

Dissertation zur Erlangung des Doktorgrades der Naturwissenschaften

vorgelegt beim Fachbereich Biochemie, Chemie und Pharmazie
der Johann Wolfgang Goethe – Universität
in Frankfurt am Main

Uncaging approach, native membrane dynamics and lipidic cubic phases in biomolecular solid-state NMR

von

Julian Martinus de Mos

aus Darmstadt

Frankfurt am Main - 2019

(D30)

vom Fachbereich Biochemie, Chemie und Pharmazie
der Johann Wolfgang Goethe - Universität
als Dissertation angenommen.

Dekan: Prof. Dr.Clemens Glaubitz
Gutachter : Prof. Dr. Clemens Glaubitz
Jun.-Prof. Dr. Nina Morgner

Datum der Disputation: 10.03.2020

Summary

It was previously shown for the *Escherichia coli* diacylglycerol kinase (DgkA) that enzyme-reactions at the membrane interface can be monitored by solid-state NMR. However, such studies can face problems due to limited accessibility of the active sites: Natural substrates for membrane enzymes, but also ligands for membrane proteins or lipid mediators, are either partitioning into the membrane and cannot be added easily, or if soluble exhibit accessibility restrictions, as they cannot freely pass through lipid bilayers. This situation complicates quantitative kinetic analysis of biochemical processes such as enzyme activity, ligand binding, but also oligomerization or folding reactions in the membrane or at its interface under MAS-NMR conditions.

To overcome these limitations the feasibility and possible advantages of the uncaging approach as a new tool for biomolecular solid-state NMR to trigger reactions by light have been explored. DgkA's enzymatic activity, exemplary of a biochemical process on the membrane interface, was thereby triggered *in situ* during MAS by light-induced release of its substrates that were rendered inactive with photolabile protecting groups. To be capable of uncaging sufficient amounts of substrate during MAS to follow the enzymatic reaction via ^{31}P real-time NMR measurements, several illumination variants including an existing illumination setup to study retinal proteins under cryogenic conditions via DNP enhanced NMR were tested. As uncaging of micromole amounts of substrates requires a higher flux compared to initiation of a photocycle in retinal proteins, a new illumination setup was built with Bruker Biospin and Leoni Fibertech. It consists of a modified MAS probe and a suitable fiber bundle, allowing to efficiently couple light from high power LEDs into a sapphire rotor containing the sample, without disturbing the magnetic field homogeneity or sample rotation. By reducing the sample volume to the illuminated area up to 60 mM ATP were released by uncaging NPE-ATP to initiate DgkA's activity in several tested membrane mimetics. These mimetics included liposomes and bicelles, which are well established in the field of biomolecular solid-state NMR as well as the optically transparent lipidic cubic phase of monoolein, widely used in membrane protein crystallography, but not yet well characterized as membrane mimetic under MAS conditions. A unique and powerful but compared to time and spatial resolution often underrepresented advantage of the uncaging approach for biophysical studies has been demonstrated by successful uncaging of a non-miscible lipid substrate to trigger DgkA's kinase reaction: Initiation

of processes that cannot easily be triggered by mixing. Examples of these are reactions involving highly hydrophobic, membrane partitioning compounds including lipid substrates, ligands or interaction partners, but also oligomerization or folding of biomacromolecules. The herein performed experiments therefore serve as a first demonstration of the uncaging-approach's feasibility and compatibility with a wide variety of membrane mimetics and give a first indication of its potential for a variety of biomolecular solid-state NMR experiments.

As high accessibility for solutes has been a second focus for the choice of membrane mimetics, DgkA's activity in the lipidic cubic phases of monoacylglycerols with its two continuous networks of water channels has been further characterized. Kinetic parameters obtained from ^{31}P real-time solid-state NMR experiments revealed that DgkA's activity is similar to activities obtained in swollen cubic phases in a bath solution with wider water channels. Diffusion of ATP in a non-swollen cubic phase was however strongly reduced compared to ATP in solution as diffusion measurements showed. Therefore, saturation of the enzyme required distinctly higher ATP concentrations. These results thereby underline the advantage of a non-invasive and label-free method like NMR to directly gain information about enzymatic reactions of immobilized enzymes in porous materials. The obtained wealth of information from ^{31}P real-time NMR experiments and biochemical assays in different membrane mimetics in presence and absence of lipid substrates and activators also provided further insight into DgkA's enzymatic activity. It confirms ATP binding and hydrolysis in the absence of a lipid substrate, in agreement with the proposed mode of substrate binding, and allowed to estimate the *in vivo* relevance of previously observed ATPase activity in liposomes.

Further exploration of the cubic phase as membrane mimetic for protein solid-state NMR revealed its high stability under MAS at elevated temperatures and capacity to reconstitute sufficient amounts of DgkA. Unlike monoolein, DgkA was cross-polarizable in a cubic phase and exhibited similar dynamics compared to DgkA reconstituted into liposomes, allowing to acquire the herein shown dipolar coupling based 2D protein spectra. As lipidic cubic phases are not containing phospholipids, monoacylglycerols could be especially useful as membrane mimetics for ^{31}P correlation spectra. Initial experiments under DNP conditions, where in liposomes line broadening causes severe overlap of phospholipid signals and unspecific cross polarization highlight this aspect.

In summary, herein reported results of the experiments performed with lipidic cubic phases demonstrate that they are robust and versatile membrane mimetics. They could be of advantage for a variety of solid-state NMR experiments where either optical transparency for efficient illumination is desired, accessibility for solutes and membrane components under MAS is required, or interference of phosphorous signals of other membrane mimetics must be avoided.

In the second chapter of this thesis ^1H solid-state NMR as a label free method to probe membrane order and dynamics directly within a cellular and disease relevant context was used to observe the effects of soluble epoxide hydrolase (sEH) encoding gene knock-outs on membrane dynamics. Knock-out of the sEH encoding gene changed the overall membrane dynamics in the physiological temperature range of native membranes derived from mouse brains, making the bulk membrane more dynamic. To confirm that these effects are related to the enzymatic activity of sEH, substrates and products of sEH were added to evaluate their effects on membrane dynamics. 19,20-dihydroxydocosapentaenoic acid (DHDP), a product of sEH, partially reversed the knock-out phenotype in a concentration dependent manner whereas the substrate 19,20-epoxydocosapentaenoic acid did not cause any effects. As both polyunsaturated fatty acids did not show differences in phase behavior in a simple phospholipid bilayer these results provide evidence that the previously observed concentration dependent DHDP induced relocation of cholesterol away from detergent resistant lipid raft fractions is associated with alteration of membrane dynamics. Therefore, also the effect of cholesterol removal via cyclodextrin on membrane dynamics was analyzed. Removal of cholesterol led to a similar temperature profile of wild-type and knock-out membranes thereby supporting the hypothesis that DHDP induced relocation of cholesterol is causing altered membrane dynamics. These alterations have been shown by the lead authors of the collaborative research project to induce relocation of various membrane proteins and are involved in the development of diabetic retinopathy. Furthermore, in this context inhibition of sEH has been shown to inhibit diabetic retinopathy and proposed as target for prevention of one of the leading causes of blindness in the developed world.

Zusammenfassung

Wie in einer vorangegangenen Arbeit am Beispiel der *Escherichia coli* Diacylglycerinkinase (DgkA) gezeigt, können enzymatisch katalysierte Reaktionen an der Grenzfläche zwischen Lösung und biologischen Membranen mittels Festkörper-Kernspinresonanzspektroskopie (NMR-Spektroskopie) verfolgt werden.

Solche Studien können jedoch aufgrund eingeschränkter Zugänglichkeit der Substrate zu den aktiven Zentren unter *In-vitro*-Bedingungen mit verschiedenen Problemen konfrontiert sein. Membranständige Substrate für Membranenzyme, aber auch Liganden für Membranproteine oder Lipidmediatoren, sind meist stark hydrophob und nicht wasserlöslich. Sie formen oftmals Aggregate in wässrigen Lösungen und können daher nicht einfach hinzugegeben werden, was die Initiation solcher Reaktionen durch einfache Hinzugabe erschwert. Lösliche Substrate wiederum sind oftmals in ihrer freien Diffusion gestört, da sie Lipiddoppelschichten nicht überwinden können und erreichen oftmals nicht alle aktiven Zentren, was ebenfalls die quantitative kinetische Analyse biochemischer Prozesse wie Enzymaktivität oder Ligandenbindung erschwert. Phasentrennung unter Bedingungen schneller Probenrotation, die für die so genannte "magic angle spinning" (MAS) NMR-Spektroskopie verwendet wird, ist ein weiterer Aspekt der die Analyse solche Prozesse in der Membran oder an ihrer Grenzfläche sowie Oligomerisierungs- oder Faltungsreaktionen erschweren kann.

Um diese Probleme zu überwinden, wurde die Machbarkeit untersucht biochemische Reaktionen *in situ* durch lichtinduzierte Abspaltung von photolabilen Schutzgruppen auszulösen. Dabei wurde der so genannte Uncaging-Ansatz als neues Werkzeug für Festkörper-NMR Versuche etabliert und mögliche Vorteile dieses Ansatzes zur Initiierung von biochemischen Prozessen aufgezeigt. Die enzymatische Aktivität von DgkA, beispielhaft für einen biochemischen Prozess an der Membrangrenzfläche, wurde dabei im Spektrometer unter MAS Bedingungen durch lichtinduzierte Freisetzung ihrer Substrate ausgelöst, die zuvor mit photolabilen Schutzgruppen inaktiviert wurden. Um ausreichende Mengen an Substrat unter MAS Bedingungen für ^{31}P -Echtzeit-NMR-Messungen zur Verfolgung der enzymatischen Reaktion freisetzen zu können, wurden mehrere Beleuchtungsvarianten getestet, einschließlich eines bereits vorhandenen Beleuchtungsaufbaus, der verwendet wurde um Retinalproteine unter kryogenen Bedingungen mittels DNP-verstärkter NMR zu untersuchen. Da das Freisetzen von Mikromol-Mengen an Substraten einen höheren

Lichtstrom erfordert als für die Induzierung eines Photozyklus in Retinalproteinen benötigt wird, konnte dieser Aufbau trotz mehrerer Tests mit zwei verschiedenen photolabilen Schutzgruppen, den Anforderungen nicht gerecht werden. Daher wurden zum einen stärkere, kollimierte und kohärente Lichtquellen, wie ein UV-Laser, der für Uncaging-Experimente in Flüssig-NMR-Studien verwendet wurde, getestet und zum anderen in Zusammenarbeit mit Bruker Biospin und Leoni Fibertech ein neuer Beleuchtungsaufbau entwickelt. Der Aufbau besteht aus einem modifizierten MAS-Probenkopf mit geweiteter Spule und einem geeigneten Faserbündel mit dem selbst schon Licht von Hochleistungs-LEDs effizient in die Probe eingekoppelt werden kann, ohne das Magnetfeld oder die Rotation des die Probe enthaltenden Saphirrotors zu stören. Durch Verringerung des Probenvolumens auf die beleuchtete Fläche wurden bis zu 60 mM ATP durch Abspaltung der photolabilen Nitrophenylethyl-Schutzgruppe (NPE-Schutzgruppe) freigesetzt um die Aktivität von DgkA in mehreren getesteten Membranmimetika zu initiieren. Zu diesen Membranmimetika gehörten die für biomolekulare Festkörper-NMR-Spektroskopie gut etablierten Liposomen und Bicellen sowie die optisch transparente lipidische kubische Phase von Monoolein, die häufig in der Membranproteinkristallographie verwendet wird, aber bisher nicht detailliert für ihre Eignung als Membranmimetikum für Festkörper-NMR Untersuchungen unter MAS charakterisiert wurde.

Das erfolgreiche Entschützen eines bei der Herstellung von Liposomen eingefügten, nicht wasserlöslichen Lipidsubstrats zur Initiierung der Kinase-Reaktion von DgkA zeigt dabei einen sehr großen, jedoch im Vergleich zur zeitlichen und räumlichen Auflösung in der Literatur oft unterrepräsentierten Vorteil des Uncaging-Ansatzes für biophysikalische Studien auf: Die Möglichkeit der Induzierung von Prozessen, die nicht einfach durch Mischen ausgelöst werden können. Beispiele hierfür sind Reaktionen, an denen stark hydrophobe, membranpartitionierende Stoffe einschließlich Lipidsubstraten, Liganden oder Lipidmediatoren beteiligt sind sowie Oligomerisierung oder Faltung von Biomakromolekülen. Die hier durchgeführten Experimente dienen daher als erste Demonstration der Durchführbarkeit des Uncaging-Ansatzes und zeigen seine Kompatibilität mit einer Vielzahl von Membranmimetika auf. Sie geben damit erste Hinweise auf das Anwendungspotenzial und Vorteile des Uncaging-Ansatzes sowie mögliche Anwendungsbereiche für lichtinduzierte Reaktionen in verschiedensten Bereichen biomolekularer Festkörper-NMR.

Da die Zugänglichkeit von löslichen Stoffen und Verhinderung von Phasentrennung unter MAS für eine quantitative Untersuchung biochemischer Reaktionen mittels Festkörper NMR verbessert werden sollte, wurde die Aktivität von DgkA in den kubischen Lipidphasen von Monoacylglyceriden, weiter charakterisiert. Diese Lipidphasen sollten sich besonders eignen, da die Lipiddoppelschicht aus Monoacylglyceriden den Raum in zwei kontinuierliche Netzwerke aus Wasserkanälen aufteilen und daher im Gegensatz zu Liposomen eine hohe Erreichbarkeit für lösliche Stoffe gegeben sein sollte. Weiterhin wurde in Experimenten zur Charakterisierung der kubischen Phase unter MAS keine erkennbare Phasentrennung beobachtet, sodass die Verteilung aller Komponenten über das Volumen der Probe auch unter MAS als gleichmäßig angenommen werden kann. Ein weiterer Vorteil der kubischen Phasen aus Monoacylglyceriden spezifisch für DgkA ist, dass Monoacylglyceride ebenfalls als Substrat für die Kinase-Reaktion dienen können und daher Lipidsubstratsättigung in kubischen Phasen angenommen werden kann, was die Reaktionsordnung verringert. Kinetische Parameter erhalten aus ^{31}P -Echtzeit-Festkörper-NMR-Experimenten zeigten, dass die Aktivität von DgkA ähnlich ist zur Aktivität, die mittels biochemischer Verfahren in geschwollenen kubischen Phasen mit breiteren Wasserkanälen in einer Badlösung gemessen wurde. Wie Diffusionsmessungen zeigten, war die Diffusion von ATP in einer nicht geschwollenen kubischen Phase jedoch im Vergleich zu ATP in Lösung stark verringert. Die Sättigung des Enzyms erforderte daher deutlich höhere ATP-Konzentrationen. Diese Ergebnisse unterstreichen den Vorteil einer nicht-invasiven und markierungsfreien Methode wie die NMR-Spektroskopie, um Informationen über enzymatische Reaktionen von immobilisierten Enzymen in porösen Materialien zu erhalten, wie sie für biotechnologische Applikationen in Frage kommen.

Die Informationsfülle aus ^{31}P -Echtzeit-NMR-Experimenten und biochemischen Analysen in verschiedenen Membranimimetika in Gegenwart und Abwesenheit von Lipidsubstraten und Aktivatoren lieferte weitere Einblicke in die enzymatische Aktivität von DgkA. Dabei wurde besonderes Augenmerk auf die zuvor mittels ^{31}P -Echtzeit-NMR beobachtete ATPase-Aktivität in Liposomen gelegt, die mit steigender Lipidsubstratkonzentration zunahm. Durchgeführte ^{31}P -Echtzeit-NMR-Experimente unter Lipidsubstratsättigungsbedingungen in Detergens und in der kubischen Phase von Monoolein zeigten, dass die Kinase-Reaktion ATP-Hydrolyse, die unter diesen Bedingungen unterhalb des Nachweisbereichs der verwendeten

Methoden war, weit übersteigt. Weiterhin zeigten durchgeführte Messungen in Liposomen und Detergens mit erhöhten Proteinkonzentrationen, dass enzymatisch katalysierte ATP-Hydrolyse in Abwesenheit eines Lipidsubstrates stattfindet. Damit wurde ebenfalls ATP-Bindung in Abwesenheit eines Lipidsubstrats nachgewiesen und die in anderen Studien vorgeschlagene zufällige Reihenfolge der Substratbindung für DgkA bestätigt. Kinetische Analyse dieser Experimente zeigten zusätzlich, dass Aktivatoren von DgkA, wie Phospholipide die ATP Konzentration der Halbsättigung, welche ein Indikator für Substrataffinität sein kann, verringern und somit notwendig sind um Sättigung der ATP Bindestellen unter *In-vivo*-Bedingungen in Abwesenheit von Lipidsubstraten zu erreichen.

Weitere Untersuchungen der kubischen Phase als Membranmimetikum für die Festkörper-NMR-Analyse von Proteinen ergaben eine hohe Stabilität unter MAS und die Fähigkeit, ausreichende Mengen an DgkA zu rekonstituieren. Im Gegensatz zu Monoolein, dass durch Diffusion entlang der stark gekrümmten Membrannormalen eine schnelle isotrope Orientierungsänderung erfährt, war DgkA in einer kubischen Phase kreuzpolarisierbar. Initiale Messungen in LCP zeigten im Vergleich zu DgkA, das in Liposomen rekonstituiert wurde, eine ähnliche Dynamik, wodurch die hier gezeigten, auf dipolaren Kopplungen basierenden, 2D-Proteinspektren erhalten werden konnten. Da kubische Lipidphasen keine Phospholipide enthalten, können Monoacylglyceride insbesondere als Membranmimetika für ^{31}P -Korrelationspektren nützlich sein. Anfängliche Experimente unter DNP-Bedingungen, bei denen die Phospholipide der Liposomen weitere Signale durch unspezifische Kreuzpolarisation verursachen, die zusätzlich durch die starke Linienverbreiterung unter kryogenen Bedingungen oftmals eine starke Überlappung mit anderen relevanten Signalen aufweisen, unterstreichen diesen Aspekt.

Zusammenfassend zeigen die hier berichteten Ergebnisse der mit kubischen Lipidphasen durchgeführten Experimente, dass es ein robustes und vielseitiges Membranmimetikum für biomolekulare Festkörper-NMR ist. Kubische Phasen könnten für eine Vielzahl von Festkörper-NMR-Experimenten von Vorteil sein, bei denen entweder optische Transparenz für eine effiziente Beleuchtung erwünscht ist, die Zugänglichkeit für gelöste Stoffe und Membrankomponenten unter MAS erforderlich ist oder störende Phosphorlipidsignale anderer Membranmimetika vermieden werden müssen.

Im zweiten Kapitel dieser Arbeit wurde ^1H -Festkörper-NMR als markierungsfreie Methode zur Untersuchung der Membranordnung und -dynamik in einem zellulären und krankheitsrelevanten Kontext verwendet, um die Auswirkungen des Knock-outs der löslichen Epoxidhydrolase (sEH) auf die Membrandynamik zu untersuchen. Knock-out des sEH kodierenden Gens in Mäusen erhöhte die allgemeine Membrandynamik im physiologischen Temperaturbereich von aus Mäusehirnen gewonnenen nativen Membranen. Um zu bestätigen, dass diese Effekte mit der enzymatischen Aktivität von sEH zusammenhängen, wurden Substrate und Produkte der sEH hinzugefügt, um ihre Auswirkungen auf die Membrandynamik zu analysieren. 19,20-Dihydroxydocosapentaensäure (DHDP), ein Produkt von sEH, kehrte den Phänotyp des Knock-outs um, während das korrespondierende Substrat 19,20-Epoxydocosapentaensäure keine Auswirkungen hatte. Da beide mehrfach ungesättigten Fettsäuren keine Unterschiede in einer Phospholipid-Modellmembran zeigten, sind diese Ergebnisse ein Hinweis, dass die zuvor beobachtete DHDP-induzierte Verdrängung des Cholesterins aus so genannten Detergens-resistenten Lipid-Raft Fraktionen mit einer Änderung der Membrandynamik zusammenhängt. Daher wurde in einem nächsten Schritt auch die Wirkung der Cholesterinentfernung über Zugabe von Cyclodextrin auf die Membrandynamik analysiert. Die Entfernung von Cholesterin führte zu einem ähnlichen Temperaturprofil von Wildtyp- und Knock-out-Membranen, was die Hypothese stützt, dass die durch DHDP induzierte Verlagerung von Cholesterin eine veränderte Membrandynamik verursacht. Eine Fülle von Ergebnissen, die von den Hauptautoren des viele weitere Forschungsdisziplinen umfassenden Projektes zusammengefasst wurden, zeigen dabei, dass DHDP induzierte Cholesterin Verlagerung die Lokalisation verschiedenster Membranproteine oder membranassoziierter Proteine verändert und damit Signalkaskaden, die Entzündungsreaktionen hervorrufen, aktiviert, die wiederum zu Schädigung der Blutgefäße in der Retina führen. Erhöhte DHDP Level sind dabei ein Risikofaktor für die Entwicklung der diabetischen Retinopathie, eine maßgeblich im Rahmen von Diabetes mellitus auftretende Schädigung der Retina, wie Mausmodelle und Untersuchungen an menschlichen Retinas belegen. Durch dieses Forschungsprojekt konnte weiterhin gezeigt werden, dass die Hemmung von sEH und damit Reduktion der DHDP Konzentration die Entwicklung der diabetischen Retinopathie hemmt und daher ein möglicher Angriffspunkt für die Prävention einer der häufigsten Erblindungsursachen in Europa und Nordamerika darstellt.

Table of Contents

| | |
|---|----|
| Summary | i |
| Zusammenfassung..... | v |
| Table of Contents | xi |
| I Uncaging approach and lipidic cubic phases to study biochemical reactions via solid-state NMR..... | 17 |
| I.1 Introduction..... | 18 |
| I.1.1 Applications for sample illumination in NMR and illumination setups developed so far | 18 |
| I.1.2 Fiber optics and radiometric units..... | 22 |
| I.1.3 Uncaging approach..... | 25 |
| I.1.4 Structures, phases and topology of amphiphilic compounds | 30 |
| I.1.4.1 Lamellar phases..... | 32 |
| I.1.4.2 Non-lamellar liquid-crystalline phases | 33 |
| I.1.4.2.1 Two-dimensional liquid-crystalline phases | 34 |
| I.1.4.2.2 Three-dimensional liquid-crystalline phases | 35 |
| I.1.4.2.3 Isotropic phases | 36 |
| I.1.4.3 Phase transitions by water content in binary lipid/water systems | 36 |
| I.1.4.4 Biomembranes | 38 |
| I.1.5 Common membrane mimetics used for membrane proteins..... | 40 |
| I.1.5.1 Liposomes | 40 |
| I.1.5.2 Bicelles..... | 41 |
| I.1.5.3 Lipidic cubic phases of monoacylglycerols | 43 |
| I.1.6 Diacylglycerol kinases | 47 |
| I.1.6.1 <i>E. coli</i> diacylglycerol kinase | 48 |
| I.1.6.2 Enzymology of DgkA | 49 |
| I.1.6.3 Stability and Folding of DgkA..... | 55 |
| I.1.6.4 Structure and mechanism of DgkA | 57 |
| I.1.7 Solid-state NMR spectroscopy..... | 61 |
| I.1.7.1 Theoretical background..... | 61 |
| I.1.7.1.1 Chemical shielding and dipolar coupling | 61 |
| I.1.7.1.2 Magic angle spinning (MAS) | 63 |
| I.1.7.1.3 Cross polarization | 64 |
| I.1.7.2 Multi-dimensional NMR experiments | 64 |
| I.1.7.3 Dipolar coupling based experiments under MAS conditions..... | 65 |
| I.1.7.3.1 Homonuclear correlation based on proton driven spin diffusion..... | 65 |

| | | |
|-------------|---|----|
| 1.1.7.3.2 | Heteronuclear correlation (HETCOR) | 66 |
| 1.1.7.3.2.1 | Double cross polarization experiments | 66 |
| 1.1.7.3.2.2 | Transferred echo double resonance experiments | 67 |
| 1.1.8 | Aim and scope | 69 |
| I.2 | Materials and Methods | 71 |
| I.2.1 | Molecular biological methods | 71 |
| I.2.1.1 | Site-directed mutagenesis | 71 |
| I.2.1.2 | Restriction-site free cloning | 71 |
| I.2.1.3 | Agarose gel electrophoresis..... | 72 |
| I.2.1.4 | Transformation | 73 |
| I.2.2 | Biochemical methods | 73 |
| I.2.2.1 | Production, purification and reconstitution of DgkA | 73 |
| I.2.2.1.1 | Production of DgkA | 73 |
| I.2.2.1.2 | Production of U ¹³ C ¹⁵ N labelled DgkA | 73 |
| I.2.2.1.3 | Purification of DgkA..... | 74 |
| I.2.2.1.4 | SDS-PAGE..... | 75 |
| I.2.2.1.5 | Western Blot | 76 |
| I.2.2.1.6 | Size exclusion chromatography | 76 |
| I.2.2.1.7 | Reconstitution into LCP for ³¹ P real-time activity measurements. | 76 |
| I.2.2.1.8 | Reconstitution into LCP for protein ssNMR measurements. | 77 |
| I.2.2.1.9 | Reconstitution into liposomes | 77 |
| I.2.2.1.10 | Reconstitution into anisotropic bicelles | 78 |
| I.2.2.2 | DgkA activity measurements | 79 |
| I.2.2.2.1 | Photometric coupled ATPase assays..... | 79 |
| I.2.2.2.1.1 | <i>in surfo</i> coupled assay | 79 |
| I.2.2.2.1.2 | <i>in meso</i> coupled assay | 80 |
| I.2.2.2.1.3 | Bicelle coupled assay | 81 |
| I.2.2.2.2 | Molybdenum blue assay..... | 81 |
| I.2.2.2.3 | ³¹ P NMR real-time activity measurements..... | 82 |
| I.2.3 | UV-Vis absorbance measurements of a lipidic cubic phase | 83 |
| I.2.4 | Solid-state NMR measurements | 84 |
| I.2.4.1 | Protein spectra of DgkA in liposomes and LCP | 84 |
| I.2.4.2 | ³¹ P real-time measurements | 84 |
| I.2.4.3 | High field MAS NMR illumination setup | 85 |
| I.2.4.4 | DNP MAS NMR illumination setup | 85 |
| I.2.5 | DNP measurements with monoolein as membrane mimetic..... | 85 |
| I.2.6 | LCP liquid-state NMR measurements..... | 86 |
| I.2.6.1 | ³¹ P DOSY on ATP in LCP and solution..... | 86 |
| I.2.7 | List of Buffers | 88 |
| I.2.8 | List of compounds | 89 |
| I.2.9 | List of equipment..... | 91 |

| | | |
|-----------|---|-----|
| I.3 | Results..... | 93 |
| I.3.1 | Purification of DgkA..... | 93 |
| I.3.2 | Characterization of LCP for MAS solid-state NMR applications | 94 |
| I.3.2.1 | Parameters of LCP studied by solid-state NMR | 94 |
| I.3.2.2 | Properties of a nucleotide in LCP | 96 |
| I.3.3 | Uncaging approach for solid-state NMR | 99 |
| I.3.3.1 | Evaluation of MAS rotors for illumination experiments | 100 |
| I.3.3.2 | Testing a DNP illumination setup for uncaging applications | 101 |
| I.3.3.3 | Development of a high field MAS NMR illumination setup..... | 106 |
| I.3.3.3.1 | Light guide variants | 107 |
| I.3.3.3.2 | Light source variants..... | 108 |
| I.3.3.3.3 | Illumination area..... | 109 |
| I.3.3.3.4 | Efficiency of <i>in situ</i> uncaging..... | 110 |
| I.3.3.3.5 | Alternative light path variants..... | 111 |
| I.3.4 | Membrane mimetics for triggering enzymatic activity by uncaging | 114 |
| I.3.4.1 | Enzymatic activity of DgkA in tested membrane mimetics..... | 115 |
| I.3.4.2 | Uncaging of a non-miscible component in a biological membrane..... | 120 |
| I.3.5 | DgkA and ATPase activity..... | 125 |
| I.3.5.1 | In environments with fast lipid substrate diffusion in excess of a lipid substrate | 125 |
| I.3.5.2 | Effect of phospholipids on ATPase activity in absence of lipid substrates | 126 |
| I.3.6 | LCP for biomolecular solid-state NMR..... | 129 |
| I.3.6.1 | Kinetic parameters of DgkA's activity in LCP | 129 |
| I.3.6.2 | Protein ssNMR of DgkA reconstituted in LCP..... | 133 |
| I.3.6.3 | Monoolein as membrane mimetic for DNP measurements | 135 |
| I.4 | Discussion..... | 139 |
| I.4.1 | Uncaging approach for solid-state NMR | 139 |
| I.4.1.1 | Illumination setup | 139 |
| I.4.1.2 | <i>In situ</i> uncaging experiments in different membrane mimetics to initiate enzymatic activity of DgkA | 141 |
| I.4.2 | ATPase activity of DgkA..... | 144 |
| I.4.3 | LCP, a novel membrane mimetic for solid-state NMR..... | 146 |
| I.5 | Conclusion and Outlook | 151 |

| | | |
|--------|---|-----|
| II | Effect of polyunsaturated fatty acid metabolites on membrane fluidity..... | 155 |
| II.1 | Introduction..... | 155 |
| II.1.1 | Lipid rafts | 155 |
| II.1.2 | DHA and lipid raft modulation | 156 |
| II.1.3 | sEH and DHA derived epoxides and diols in lipid raft modulation..... | 157 |
| II.1.4 | ¹ H MAS NMR for analysis of lipid dynamics | 158 |
| II.2 | Materials and Methods..... | 160 |
| II.2.1 | Studies on DMPC model membranes | 160 |
| II.2.2 | Studies on native membranes derived from mouse brains | 160 |
| II.2.3 | Solid-state NMR measurements..... | 161 |
| II.2.4 | List of compounds | 162 |
| II.3 | Results and Discussion..... | 163 |
| II.3.1 | Studies on DMPC model membranes | 163 |
| II.3.2 | Studies on native membranes derived from mouse brains | 165 |
| II.4 | Conclusion and Outlook..... | 169 |
| III | References..... | 171 |
| IV | Appendix..... | 199 |
| IV.1 | Plasmid and primer sequences | 199 |
| IV.2 | WB MAS NMR probe temperature calibration | 202 |
| IV.3 | Uncaging approach for solid-state NMR | 203 |
| IV.3.1 | Chemical shifts and couplings of NPE-ATP..... | 203 |
| IV.3.2 | 2D NMR spectra of NdiEt-tcAA..... | 207 |
| IV.3.3 | pH titration curve of Pi ³¹ P chemical shift | 209 |
| IV.3.4 | Verification of anisotropic bicelles | 209 |
| IV.3.5 | Enzymatic activity and ATP hydrolysis in presence of saturating amounts of monoolein..... | 210 |
| IV.3.6 | ATP hydrolysis in DgkA containing liposomes in absence of Mg ²⁺ | 210 |
| IV.3.7 | Phosphorylation of DOG in liposomes containing varying lipid ratios of DOG | 211 |
| IV.4 | NCA DgkA Trp112 peak width | 212 |
| IV.5 | Scalar couplings of lipid products in ³¹ P NMR spectra | 213 |
| IV.6 | Photometric coupled ATPase assays..... | 214 |
| IV.7 | Molybdenum blue assay..... | 215 |

| | | |
|--------|---|-----|
| IV.8 | ³¹ P real-time solid-state NMR measurements..... | 216 |
| IV.9 | Scripts for analyzing ³¹ P real-time NMR experiments | 218 |
| IV.9.1 | AU program to add up FID's of 1D experiments as sets in incremented experiment numbers | 218 |
| IV.9.2 | AU program for conversion of 1D experiments with consecutive experiment numbers into a pseudo 2D spectrum | 218 |
| IV.9.3 | AU program for conversion of pseudo 2D NMR spectra to 1D spectra in consecutive processing numbers | 218 |
| IV.9.4 | Matlab script for sequential import of 1D spectra in ASCII format to Matlab, peak fitting using peakfit.m and sorting of results..... | 219 |
| IV.10 | Effect of polyunsaturated fatty acid metabolites on membrane fluidity of DMPC model membranes..... | 220 |
| IV.11 | Published data on DgkA's enzymatic activity | 221 |
| V | List of Figures..... | 251 |
| V.1 | Figures..... | 251 |
| V.2 | Appendix Figures..... | 262 |
| VI | List of Tables | 266 |
| VI.1 | Tables | 266 |
| VI.2 | Appendix Tables | 266 |
| VII | Declarations | 268 |
| VII.1 | Declaration of contributions | 268 |
| VII.2 | Declaration of published data | 269 |
| VII.3 | Declaration of figures obtained from published work | 269 |
| VIII | List of abbreviations | 272 |
| IX | Acknowledgements | 275 |
| X | Curriculum vitae | 277 |

I Uncaging approach and lipidic cubic phases to study biochemical reactions via solid-state NMR

In the main chapter of this thesis, the feasibility and possible advantages of the uncaging approach as a tool for solid-state NMR to trigger reactions by light are evaluated. Furthermore, lipidic cubic phases as novel membrane mimetics for biomolecular NMR have been explored. Therefore, an existing DNP illumination setup was tested, advantages and disadvantages of different possible illumination and light source variants experimentally explored, and ultimately a new illumination setup for a high field MAS probe built. Successful application of the uncaging approach for solid-state NMR has been demonstrated via ^{31}P real-time NMR by releasing ATP as well as a co-reconstituted lipid substrate *in situ*, triggering enzymatic activity of the membrane enzyme diacylglycerol kinase. Experiments were performed in different membrane mimetics including liposomes, bicelles and a lipidic cubic phase, thereby highlighting the approach's general applicability for a variety of scenarios.

The optically transparent lipidic cubic phase, not containing phospholipids, has been further characterized and evaluated for biomolecular MAS NMR applications, including ^{31}P detected DNP and acquisition of 2D protein spectra. The performed enzyme kinetic studies on DgkA reconstituted in LCP highlight thereby the unique advantages of solid-state NMR to study reactions in porous materials and yield, in combination with biochemical assays, new insights into the previously observed basal ATPase activity of DgkA.

I.1 Introduction

I.1.1 Applications for sample illumination in NMR and illumination setups developed so far

The first NMR application utilizing sample illumination was a hyperpolarization method, namely chemically induced dynamic nuclear polarization (CIDNP)¹⁻³. The method relies on the generation of an unpaired electron and transfer of its polarization onto nuclei in its vicinity, often via the radical pair mechanism and not via classic DNP mechanisms⁴⁻⁶. In the case of photo-CIDNP for liquid-state NMR applications, the unpaired electron is usually generated upon blue light illumination using flavin as a photosensitizer⁷. Upon absorption of the photon, flavin can undergo intersystem crossing into a triplet state with high electron affinity. Phenols or polyaromatics like histidine, tryptophan and tyrosine then act as electron donors forming a triplet spin-correlated radical pair with flavin. This can lead to non-Boltzmann polarization of the phenol or other polyaromatic nuclei upon intersystem crossing of the radical pair into a singlet state and back transfer of the electron enhancing the NMR signal⁸, allowing it to be used as surface probe⁷.

Photo-CIDNP was later also introduced in solid-state NMR (ssNMR) to study photosynthetic reaction centers, where the reaction center is both the target of interest and photosensitizer, requiring the first illumination setups to be built for magic angle spinning (MAS) solid-state NMR probes⁹⁻¹⁰. In liquid-state NMR sample insert and eject port allowed relatively easy coupling of high-power coherent light into the sample the by using prism setups¹¹ and later on conical-shaped tapered fiber ends¹² as well as step-wise etched¹³ or abraded¹⁴ fibers for more homogeneous light distribution. Compared to liquid-state NMR illumination setups MAS however requires more complex modifications to the probe or rotor.

For the first published MAS NMR illumination setup at a Bruker system a plexiglass rod was bend to illuminate a sample from the top through a translucent rotor cap (Figure 1f)¹⁵. Shortly after, the first Chemagnetics MAS probe was modified by guiding a fiber bundle through the probe and the coil pedestal to illuminate the sample in a sapphire rotor from the side through the coil windings (Figure 1a)⁹. The robust and simple solution to induce photo-CIDNP required however modifications to the probe to allow installation of the fiber bundle and, despite usage of a stretched thin

wire coil later on (Figure 1d)¹⁶, was not the optimal solution for other types of experiments requiring homogeneous sample illumination.

Inspired by the first illumination experiments, ssNMR on photointermediates of retinal proteins soon evolved from illumination and freeze trapping outside the spectrometer to illumination inside the spectrometer. This progression however required more homogeneous sample illumination, sparking the evolution of more intricate and complex systems¹⁷⁻¹⁸. On the one hand, stators were heavily modified to insert fibers from different directions between the coil windings, with the danger to lose homogeneity of magnetic susceptibility around the coil (Figure 1b)¹⁹⁻²⁰. On the other hand, with the danger of rotor crashes, rotors were engineered to allow illumination through a fused silica window²¹, and later on a roughened fused silica cone²², in the rotor end cap via a fiber inserted from the top of the spectrometer (Figure 1c). This type of illumination was however only efficiently possible in Jeol and Varian systems, where drive for sample spinning is opposite to Bruker's approach performed at the bottom of the rotor and sample exchange is done by lowering the probe. Illumination through the cap as performed initially in a Bruker system (Figure 1f)¹⁵ also abolishes the possibility to use in place sample exchange via a transfer line to the top of the spectrometer. Thus, illumination along the long axis whilst retaining access from the top would therefore need to be performed through the bottom of the rotor. For a Bruker system equipped with a gas injection system at the top of the stator to allow continuous flow experiments, this was done by modifying the stator bottom to allow simultaneous UV/Vis measurements using a bifurcated fiber bundle (Figure 1e)²³.

In a next step to enhance signals of thermodynamic trapped intermediates, our group performed illumination experiments on retinal proteins under DNP conditions. These experiments yielded important insights into the photocycle of channelrhodopsin-2²⁴, proteorhodopsin²⁵ and krokinobacter rhodopsin 2²⁶. However, modifications of an already highly intricate cryo-DNP probe were limited in this case to not interfere with microwave coupling. Placing of a small fiber bundle was therefore only possible further away from coil and sample (Figure 32a), which required reduction of sample amounts to observe spectral changes upon illumination.

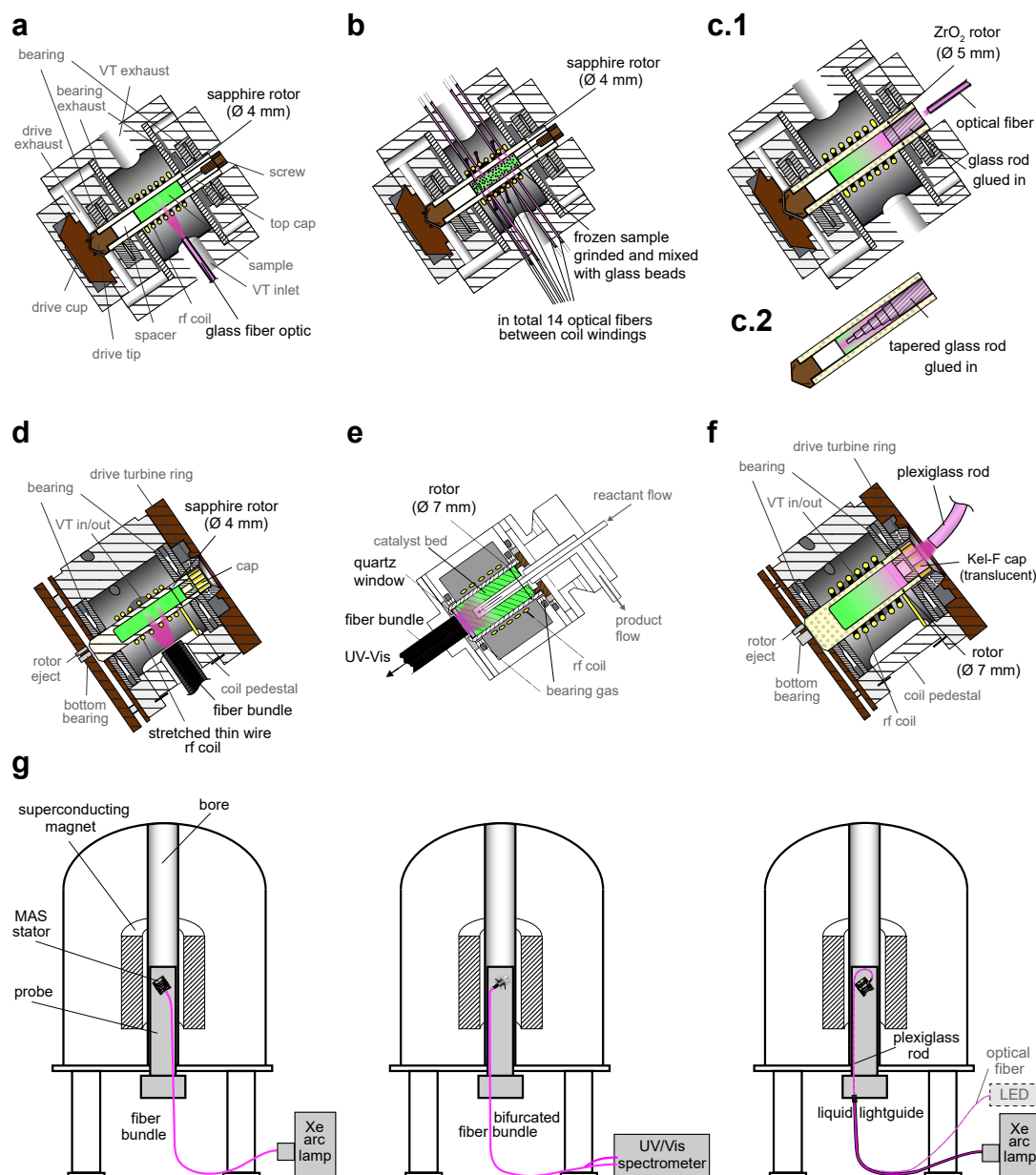


Figure 1: Schematics of MAS NMR illumination setups described in literature. **a** to **c**: Illumination setups based on Chemmagnetics and Varian type MAS NMR systems **d** to **f**: Illumination setups based on Bruker type MAS NMR systems. **a**) Potential design of the first Chemmagnetics illumination setup by Zysmilich and Mc Dermott using a glass fiber optic to illuminate a sapphire rotor from the side inducing photo-CIDNP in photosynthetic reaction centers of *Rhodobacter sphaeroides*⁹. **b**) Potential design of a modified Varian stator by Concistre and Levitt et al housing 14 optical fibers placed from various angles between coil windings to achieve homogeneous sample illumination using two 250 W quartz halogen lamps and band pass filters¹⁹⁻²⁰. For better light penetration in the studied optical dense Rhodopsin samples, frozen samples were grinded and mixed with glass beads¹⁹. **c**) Illumination via the top of zirconia rotors in a Chemmagnetics MAS system by modification of the rotor cap to allow light penetration into the sample²¹. By using a tapered glass rod (**c.2**) irradiation in optically dense samples was improved²². The setups have been used in the group of Prof. Akira Naito to study photointermediates of bacteriorhodopsin (*Halobacterium salinarum*)²¹ and sensory rhodopsin II

(*Natronomonas pharaonis*)²² using light from LED sources coupled into an optical fiber. **d)** Schematic depicting illumination from the side using a fiber bundle placed through the coil pedestal of a Bruker type MAS system equipped with a stretched thin wire coil to allow more efficient illumination to induce photo-CIDNP in photosynthetic reaction centers¹⁶. **e)** Schematic adapted from Hunger and Wang²³ depicting the modification of a continuous flow MAS system to allow simultaneous acquisition of UV/Vis spectra via a bifurcated fiber bundle through the bottom of the stator and a quartz window inside the MAS rotor. **f)** Schematics of the first described illumination setup used in the group of Prof. Hub de Groot to study photosynthetic reaction centers of *Rhodobacter sphaeroides* by illumination from the top via a plexiglass rod through a translucent Kel-F rotor cap¹⁵. **g)** Schematics of the potential light routing through the probe for the in a and c to f depicted illumination variants.

In contrast to retinal proteins, light triggered chemical reactions, another main focus of illumination experiments¹⁴, are nearly exclusively studied via liquid-state NMR as they often fall into the domain of small soluble compounds. Sample illumination is used in this application to trigger the reaction inside the spectrometer, allowing to observe and characterize intermediates and define reaction pathways that may be invisible to other spectroscopy methods.

Exhibiting a different focus than light triggered chemical reactions or retinal proteins, where the main aspect is to follow and understand native light driven processes, are tools to initiate processes with light or induce a non-equilibrium *in situ*.

From NMR perspective more desirable, because several measurements can be performed with the same sample, is reversible initiation of a non-equilibrium by light that could be achieved with photoswitches²⁷. These can switch back and forth between two states, such as two conformations²⁸ or protonation states²⁹, depending on the wavelength of the applied light. Their application however suffers from inherent difficulties to generate efficient switches that are fast and allow a high population difference or achieve conformational changes upon introduction into macromolecules, requiring further development to be an effective tool for NMR.

Irreversible initiation of biochemical processes by rendering compounds or biomacromolecules inactive with photolabile protection groups (PPG) and cleaving these off with light has been termed uncaging by Kaplan and Forbusch³⁰. This approach has been mostly developed for cell biology³¹⁻³² experiments but has seen already some applications in protein^{12, 33} and RNA³⁴⁻³⁵ liquid-state NMR folding studies. Its principles and use for NMR are elucidated further in section I.1.3 as it could be considered a helpful tool in a variety of systems. Elucidation of its applicability for solid-state NMR experiments is thereby a part of the thesis scope.

I.1.2 Fiber optics and radiometric units

Optical quantities can be either expressed in radiometric units that describe the distribution of electromagnetic radiation power in space, or in photometric units, how a standard human eye perceives light, or in photon units based on photon quantities. Whereas photometric units are restricted to visible light, radiometric and photon units can also be used to characterize radiation in the non-visible spectral range. Wavelengths (λ), the spatial period of a periodic wave and wavenumbers ($\tilde{\nu}$), the inverse of the wavelength, are related to the frequency (ν) via the speed of light in vacuum (c) by

$$\lambda = \frac{1}{\tilde{\nu}} = \frac{c}{\nu} \quad (1)$$

The energy of a photon (E_p) is related to the wavelength via the Planck constant (h) by

$$E_p = \frac{hc}{\lambda} \quad (2)$$

The radiometric unit of power, the radiant power or radiant flux (Φ_E) is radiant energy (Q_E) per time. The correlating photon unit, the number of photons (N_p) per time, the photon flux (Φ_p), for a monochromatic beam at the wavelength λ is thus connected by

$$\Phi_{p\lambda} = \frac{dN_{p\lambda}}{dt} = \frac{\Phi_E}{E_p} \quad (3)$$

Most other radiometric quantities such as emittance, the radiant flux emitted from a surface per unit area and irradiance, the radiant flux received by a surface per unit area are defined for a point, even though the unit of area suggest a large area³⁶. Directionality of the electromagnetic radiation is often included in units such as radiant intensity (I), the radiant flux emitted, reflected, transmitted or received, per unit solid angle, or radiance, the radiant flux emitted (also termed brightness), reflected, transmitted or received by a surface, per unit solid angle per unit area. However, the term light intensity is also often used to denote radiance or irradiance. Addition of the term "spectral" before radiometric quantities implies consideration of the wavelength dependence and the measurement wavelength should be stated.

For flat surfaces, radiation per unit solid angle (radiant intensity) varies with the cosine of the angle to the surface normal (θ), termed Lambert's cosine law:

$$I_\theta = I_0 \cdot \cos\theta \quad (4)$$

To describe light gathering capability of optics such as lenses the F-number ($F/\#$) and, more common in microscopy and fiber optics, the numerical aperture (NA) is used. The F-number can be approximated for small half angles of radiation (θ) by using the paraxial approximation ($\sin \theta \approx \theta$) as the ratio of the system's focal length to the clear aperture (f/D) (Figure 2).

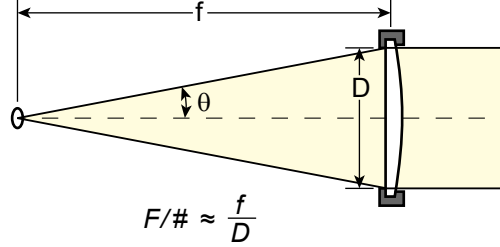


Figure 2: Lens with a clear aperture D collecting and collimating light from a source at focal length f .

The F-number taking also into account the refractive index (n) is defined as:

$$F/\# = \frac{1}{2n \sin \theta} \quad (5)$$

The F-number is connected to the numerical aperture via:

$$NA = n \sin \theta = \frac{1}{2 F/\#} \quad (6)$$

All optical fibers operate by total internal reflection. Total internal reflection occurs according to Snell's law ($\sin \theta_1 \cdot n_1 = \sin \theta_2 \cdot n_2$) if light through media with a high refractive index (n_1) strikes the interface to another medium with a lower refractive index ($n_2 < n_1$) at an angle (θ) that is greater than the critical angle (θ_c).

$$\theta_c = \sin^{-1} \frac{n_2}{n_1} \quad (7)$$

The difference of refractive indices also defines the acceptance angle (a) and if the refractive index of the environment (n_0) becomes one, also the numerical aperture of the fiber (Formula 8, Figure 3).

$$\sin a = \frac{1}{n_0} \sqrt{n_1^2 - n_2^2} \quad \text{if } n_0 = 1 \quad NA = \sin a = \sqrt{n_1^2 - n_2^2} \quad (8)$$

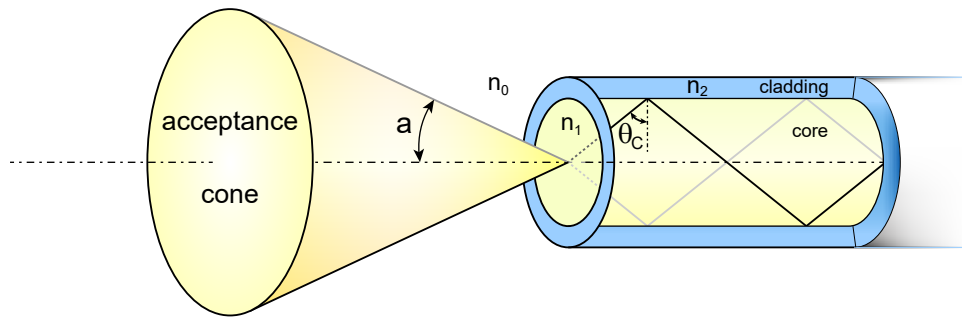


Figure 3: Coupling of light into a fiber. A fiber accepts light incident within the acceptance cone, which is determined by the differences of the refractive indices of the medium (n_0), the core (n_1) and the cladding (n_2). If light is incident at an angle greater than the acceptance angle (a), it exceeds the critical angle (θ_c) for total internal reflection.

For highly directional, collimated light sources such as lasers, to maximize the flux that is coupled into a fiber requires to focus the beam to a spot diameter equaling the active area, whilst the angle of incidence is kept below the acceptance angle (Figure 4a). The radiance of diffuse light sources that emit light into all directions, with its radiant intensity independent of direction, from an extended area however can only be projected 1:1 onto the active area of the fiber, by imaging it with a lens or via direct coupling. Due to the limited area and the fixed acceptance angle, the accepted flux (radiance \cdot area \cdot solid angle) is constant³⁷⁻³⁸. Therefore, increase of flux by increase of emitter size is not possible if the emitter area exceeds the active area of the fiber (Figure 4b). To achieve a higher flux in these cases, the radiance (brightness) of the light source would need to be increased. On the fiber side, higher transmission can be achieved by increasing the active fiber area and acceptance angle.

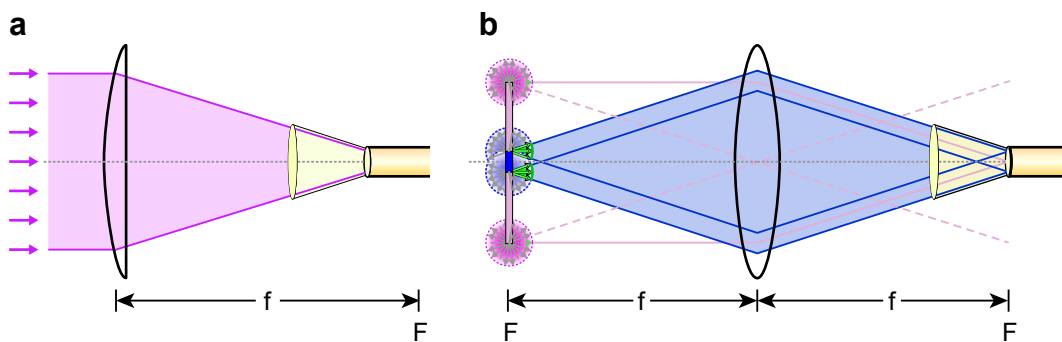


Figure 4: Coupling of highly directional, collimated light (a) and non-coherent light from diffuse light sources emitting light into all directions (b). Light from a diffuse source with an emitter area (dark blue) equating the active area of the fiber can be optimally coupled into a fiber as light paths depicted in blue from the edge of the emitter surface (circles / green arrows) onto the fiber within its acceptance cone (yellow) show. Increasing the emitter area (rose) does not increase the flux, as radiance does not add up for non-coherent light beams. F denotes focal point of the lens at focal length f .

I.1.3 Uncaging approach

Rendering a compound inactive with a photolabile protection group and triggering biochemical processes by cleaving off the so-called cage with light has enabled experiments with high spatial and temporal resolution in a variety of cell biology applications^{31-32, 39}.

The first deprotection of a biologically relevant compound with light is attributed to Barltrop and Schofield⁴⁰, who succeeded to release glycine from *N*-benzyloxycarbonyl glycine⁴¹. The early success in rendering ATP, a key molecule for energy conversion, inactive towards ATP binding proteins with a photolabile nitrophenylethyl (NPE) moiety and triggering a biochemical reaction by light led Kaplan et al to name the compound caged ATP³⁰. This name set the terminology for photolabile protecting groups in biological applications as cages, with cleavage and activation of the caged molecule termed uncaging⁴⁰. In case of NPE and other 2-nitrobenzyl derivatives release of the caged compound upon illumination proceeds via several intermediates after the primary photochemical process of intramolecular H abstraction upon a $n \rightarrow \pi^*$ transition of the nitro group (Figure 5). The mechanism has been extensively studied and undergone several revisions⁴² since the first comprehensive review⁴³. These revisions include that the cyclization is found to be irreversible and occurs from the *aci*-nitro form and not via the upon solvent mediated proton abstraction generated *aci*-nitro anion⁴⁴. Furthermore, in this study it was found that the last step in the reaction can become rate limiting at $\text{pH} < 8$ for poor leaving groups such as methanol.

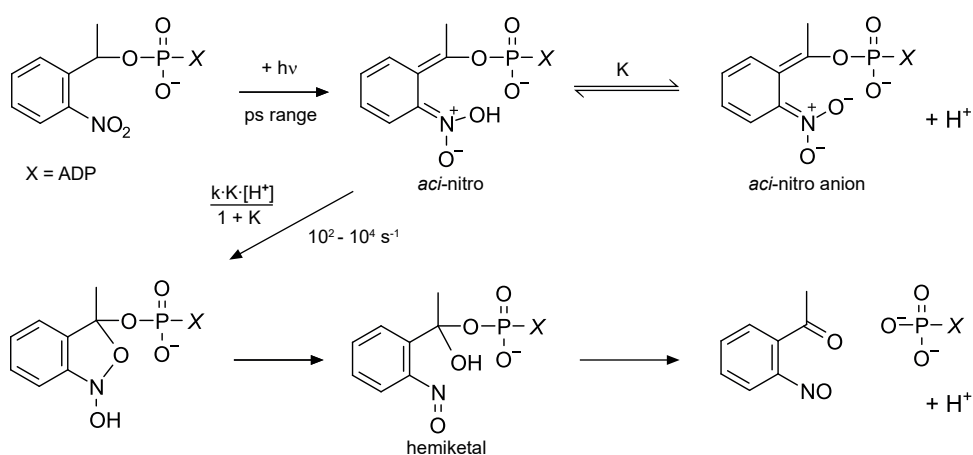


Figure 5: Revised reaction mechanism of NPE-ATP photocleavage according to the revised general mechanism for 2-nitrobenzyl derivatives by Il'ichev et al⁴⁴ summarized by Klan et al⁴².

The uncaging approach has been over time further expanded by utilization of 2-photon absorption and multi wavelength-selective uncaging to create ever more complex scenarios of light-control with new cages and caged compounds⁴². Caging of biologically relevant compounds has been achieved at a broad range spanning from protons and ions like calcium, to neurotransmitters, inositols, nucleotides, lipids, peptides up to proteins and enzymes, RNA and DNA, creating a powerful toolset to gain insight into biological questions^{31, 45-46}.

Thus temporal control, wavelength selective uncaging and high versatility of the caging approach offer a variety of possibilities for NMR and other biophysical applications to trigger biochemical reactions as well as oligomerization or folding of macromolecules *in situ*. With lipids a focus of caged compounds⁴⁵ it is surprising that the uncaging approach has so far only been used in liquid-state NMR to trigger folding reactions^{12, 34-35} even though the general possibility for uncaging with existing ssNMR illumination setups has been shown⁴⁷. Caged compounds have advantages especially for ssNMR where due to sample composition mixing compounds to initiate a reaction can be impractical. This is for example the case when compounds have to be entrapped in compartments or vesicles beforehand, are non-water soluble, highly hydrophobic membrane components like lipids or interactions leading to early association or oligomerization have to be prevented. The applicability of spatial control, a key factor for microscopy applications³¹ but also in the hope to utilize caged compounds as drugs for targeted treatment^{31, 48}, is less clear for NMR as, with exception of imaging applications, normally no direct spatial information is collected.

Comparison of photochemical properties of caged compounds that could be useful for ssNMR (Table 1) to the prototype retinal protein bacteriorhodopsin with a quantum efficiency for proton transport of 0.6-0.7⁴⁹ and an extinction coefficient of 63000 M⁻¹cm⁻¹ at 570 nm⁵⁰ reveal space for improvement. Especially a measure for the efficacy of photocleavage, the product of quantum yield and molar absorption coefficient ($\epsilon_{\text{exc}} \cdot \Phi_{\text{chem}}$), which is proportional to the amount of release at the given wavelength⁴² illustrates in one number that bacteriorhodopsin ($\epsilon_{\text{exc}} \cdot \Phi = 37800\text{-}44100 \text{ M}^{-1}\text{cm}^{-1}$) is two orders of magnitude more efficient than the first nitrobenzyl based NPE and DMNPE cages (Table 1). The uncaging efficiency is therefore also posing a challenge to illumination setups for applications requiring to uncage high concentrations like NMR^{12, 34-35}, whilst illuminating at multiple wavelengths³³.

Therefore, modification and development of novel classes of cages has been an ongoing effort to improve their properties with a variety of factors next to photochemical properties key for successful application. These additional properties include good aqueous solubility of cage and caged compound, stability in solution, a clean photochemical reaction with cleavage a primary photochemical process, creating inert photoproducts that do not absorb at the uncaging wavelength and strong absorption of the cage at wavelengths above 300 nm^{40, 42}. Due to the manifold of requirements, the currently most common cages for biomacromolecules^{42, 45} are being based on the few classes shown in Figure 6.

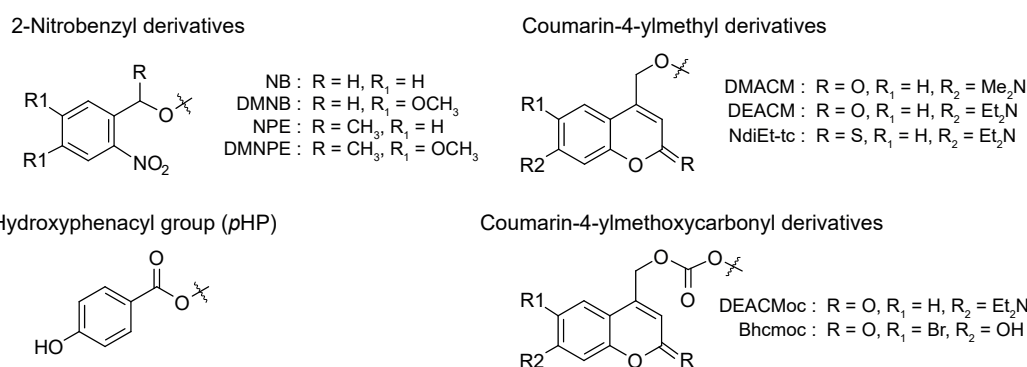


Figure 6: Chemical structures of a selection of published PPGs based on the 2-nitrobenzyl and coumarin backbone as well as the *p*-hydroxyphenacyl group.

Coumarin-4-yl derivatives have some advantages compared to nitrobenzyl derivatives and the *p*-hydroxyphenacyl group like red-shifted absorption maxima and their photoproducts are less absorbing in the uncaging wavelength. By adding electron-donating groups in the 7 position and electron-withdrawing groups in the 2- or 2- and 3 positions their absorption maxima could be red-shifted up to 472 nm⁵¹. Photocleavage of coumarin-4-yl cages proceeds via generation of an ion pair and recombination leading to heterolytic bond cleavage at rates of up to $2 \cdot 10^{10} \text{ s}^{-1}$, exceeding by far the rate for photocleavage of 2-nitrobenzyl derivatives⁵².

They are however suffering from low solubility in aqueous environments and very low quantum yields. NPE-ATP has remained the only commercially available caged ATP next to the slightly red-shifted DMNPE-ATP, a photochemically inferior derivative due to very low quantum yield and slow rate of photolysis⁵³. This is even more surprising, considering that its photoproducts are potentially highly active³⁰ and strongly absorb at the uncaging wavelength⁴². Furthermore, the initial but still widely used quantum yield for NPE-ATP (0.63 at 300-350 nm with a Xenon-arc lamp)⁵⁴ has

been highly overestimated and was later on corrected by another group⁵⁵. The initial quantum yield was determined by comparison to a known caged compound, NPE caged phosphate. The used literature quantum yield (0.58) for the release of NPE caged phosphate was however already critically discussed by the authors as quantum yields determined in the same study at the absorption maximum of the NPE group were found to be roughly half³⁰.

Compared to phosphates, carboxylates, carbonyls or diols, efficient uncaging of hydroxyl functionality, relevant sites of sugars, amino acids, lipid mediators and many other biomacromolecules, poses to be difficult due to the hydroxyl group exhibiting a higher pK_a and therefore being a poor leaving group. A common motive to enhance uncaging efficiency for caged hydroxyl groups is introduction of an oxycarbonyl linker at the cleavage site, which is readily eliminated by forming carbon dioxide in a decarboxylation reaction after initial photocleavage⁵⁶⁻⁵⁸. This method allowed more efficient photocleavage from alcohols, which is important for caged lipids and second messengers such as diacylglycerols to investigate cellular signalling^{45, 59-65}. However, quantum yields for these are still reduced compared to compounds where the same cage is directly attached to phosphates (Table 1).

Table 1: Reported photochemical properties of selected caged compounds. Maxima of single-photon absorption (λ_{\max}), molar absorption coefficients for absorption (ϵ_{exc}), quantum yield of photolysis after excitation (Φ_{chem}) and action uncaging cross section ($\epsilon_{\text{exc}} \cdot \Phi_{\text{chem}}$) at excitation wavelength (λ_{exc}).

| | λ_{\max} (nm) | λ_{exc} (nm) | ϵ_{exc} ($\text{M}^{-1} \text{cm}^{-1}$) | Φ_{chem} | $\epsilon_{\text{exc}} \cdot \Phi_{\text{chem}}$ ($\text{M}^{-1} \text{cm}^{-1}$) | |
|-------------------------------|-----------------------------------|--------------------------------|---|-------------------------------|--|---|
| NPE-ATP ³⁰ | 265 ³⁰ (for NPE-Pi) | 308 ⁵⁵ | 1720 ⁵⁵ | 0.32 ⁵⁵ | 550 | pH 7.5, 130 mM NaCl, 3 mM MgCl ₂ , 25 mM imidazole |
| | | 308 ⁵⁵ | 1670 ⁵⁵ | 0.48 ⁵⁵ | 800 | pH 6.0, 130 mM NaCl, 3 mM MgCl ₂ , 25 mM imidazole |
| | | 347 ⁶⁶ | 660 ⁶⁶ | 0.63 ^{54 a} | | pH 7.1 |
| DMNPE-ATP ⁶⁷ | 350 ⁶⁸ | 350 ⁶⁸ | 5100 ⁶⁸ | | | H ₂ O |
| | | 347 | 170 ⁶⁷ | 0.07 ⁶⁸ | 350 ⁶⁸ | H ₂ O |
| pHP-ATP ⁶⁹ | 286 ⁶⁹ | 286 ⁶⁹ | 14600 ⁶⁹ | | | CH ₃ CN/H ₂ O |
| | | 300 ⁶⁹ | | 0.3 ⁶⁹ | | pH 7.3, 50 mM Tris |
| | | 308 ⁵⁵ | 5800 ⁵⁵ | 0.21 ⁵⁵ | 1200 | pH 7.5, 130 mM NaCl, 3 mM MgCl ₂ , 25 mM imidazole |
| DMNB-DiOctaG ⁶⁰ | | 365 ⁶⁰ | 5500 ⁶⁰ | 0.09 ⁶⁰ | | pH 7.2, CH ₃ CN:H ₂ O 7:3 (v/v), 10 mM K ⁺ -MOPS |
| DMACM-ATP ⁷⁰ | 385 ⁷⁰ | 385 ⁷⁰ | 15300 ⁷⁰ | 0.086 ^{70 b} | 1300 | pH 7.2, 240 mM KCl, 20 mM HEPES |
| DEACM-ATP ⁷¹ | 392 ⁷¹ | 392 ⁷¹ | 17700 ⁷¹ | 0.076 - 0.038 ^{71 c} | 1350 | pH 7.0, H ₂ O |
| DEACMoc-Gal ⁵⁷ | 396 ⁵⁷ | 396 ⁵⁷ | 17300 ⁵⁷ | | | pH 7.2, K ⁺ -MOPS, 25% acetonitrile |
| | | 350 ⁵⁷ | 6300 ⁵⁷ | 0.0058 ^{57 d} | 37 ⁵⁷ | pH 7.2, K ⁺ -MOPS, 25% acetonitrile |
| DEACMoc-DiOctaG ⁶⁵ | 380 ⁶⁵ | 360 ⁶⁵ | | 0.011 ^{65 e} | | pH 7.4, 0.2% (v/v) Triton X-100, 20 mM HEPES |
| Bhcmoc-Gal ⁵⁷ | 374 ⁵⁷ | 374 ⁵⁷ | 15000 ⁵⁷ | | | pH 7.2, K ⁺ -MOPS, 0.1% DMSO |
| | | 350 ⁵⁷ | 11500 ⁵⁷ | 0.015 ^{57 d} | 173 ⁵⁷ | pH 7.2, K ⁺ -MOPS, 0.1% DMSO |
| Bhcmoc-DiOctaG ⁵⁷ | 343 ⁵⁷ | | 11600 ⁵⁷ | | | pH 7.2, K ⁺ -MOPS, 0.1% DMSO |
| | | 350 ⁵⁷ | | 0.014 ^{57 d} | 160 ⁵⁷ | pH 7.2, K ⁺ -MOPS, 0.1% DMSO |
| NdiEt-tcBA ⁵¹ | 472 ⁵¹ | 472 ⁵¹ | 31000 ⁵¹ | 0.18 ± 0.02 ⁵¹ | 5600 ± 600 ^{51 f} | pH 7.5, acetonitrile/H ₂ O, 20 mM Tris 1:1 (v/v) |
| | | 365 ⁵¹ | 2500 ⁵¹ | 0.12 ± 0.05 ⁵¹ | 320 ± 130 ⁵¹ | pH 7.5, acetonitrile/H ₂ O, 20 mM Tris 1:1 (v/v) |

a) at 300-350 nm with Xenon-arc lamp, determined by comparison to NPE-Pi using $\Phi_{\text{chem}} = 0.58^{30}$, see text for discussion. **b)** determined by comparison to α -DEACM-caged 8-BrcGMP⁷⁰. **c)** for 0.05 – 0.45 mM DEACM-ATP at 390 nm. **d)** with a Rayonet 350 nm lamp. **e)** at 360 nm (slit 10 nm) with 0.23 μ M DEACM-DiOctaG. **f)** 0.025 mM NdiEt-tcBA.

I.1.4 Structures, phases and topology of amphiphilic compounds

Lipids, detergents and other amphiphilic compounds exhibit immiscible hydrophilic and hydrophobic parts within the same molecule (Figure 7).

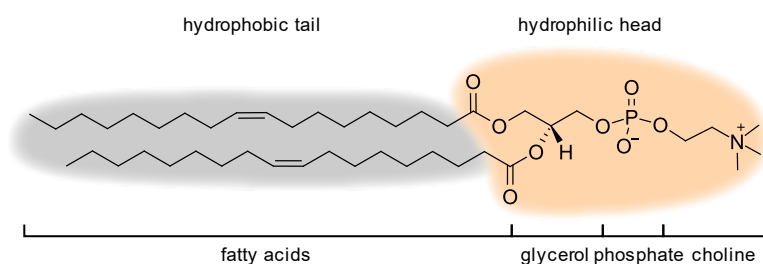


Figure 7: Structure of the glycerophospholipid dioleoylphosphatidylcholine (DOPC).

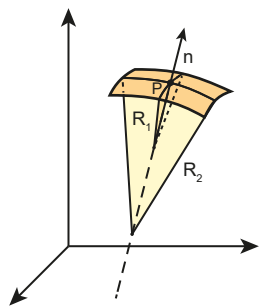
In aqueous solution, they can exhibit various phases and form a variety of supramolecular structures. The adopted phases and formed structures are a result of energy minimization as polar and apolar regions of amphiphilic compounds arrange through micro-phase segregation to reduce hydrophobic mismatch and optimize inter- as well as intramolecular interactions in a given environment. An important parameter determining the type of phase formed by an amphiphilic compound is their packing parameter⁷². It is the ratio of surfactant tail volume (v_o) to tail length (l_o) and equilibrium area per molecule at the aggregate surface (a_e).

$$\text{packing parameter} = \frac{v_o}{a_e \cdot l_o} \quad (9)$$

A value between 0 and 1 indicates curvature towards the tail, whereas a value >1 indicates curvature to the headgroup⁷³.

Formed structures of lipid-water systems can be seen as lyotropic liquid crystals, a state of matter exhibiting properties of liquids and solid crystals, as they form in a certain concentration range by more than one component and exhibit order in one or more dimensions whilst allowing motion of its components within the structure⁷⁴.

To describe and characterize lyotropic phases formed by amphiphilic molecules characterization of the interface plane between the polar and non-polar regions of the amphiphilic components yields valuable information. This plane at which the interfacial tension acts within a monolayer should be close to the neutral surface, i.e. the surface at which there is no change in area per molecule⁷⁵. It can be characterized by its mean (H) and Gaussian (K) curvature, which are related to the principal radii of curvature R_1 and R_2 as shown in Figure 8.



$$H = \left(\frac{1}{R_1} + \frac{1}{R_2} \right) / 2 \quad (10)$$

$$K = \frac{1}{R_1 \cdot R_2} \quad (11)$$

Figure 8: Definition of local curvature. Principal radii of curvature R_1 and R_2 at a point P of the interface plane, with n the surface normal vector at point P . Redrawn from Seddon⁷⁶.

By convention, positive values for principal radii describe thereby curvature towards the surfactant tail and negative radii curvature towards the water region. The Gaussian curvature determines the qualitative nature of the surface. If one of the principal curvatures is zero, Gaussian curvature is zero and the surface is parabolic or flat if both are zero, with hexagonal and lamellar phases falling in these categories. Surfaces that have positive Gaussian curvature are elliptic and form closed shells, such as micelles but also inverse micelles. If the principal curvatures are of opposite sign Gaussian curvature is negative and surfaces are hyperbolic, exhibiting saddle points. If the principal curvatures are everywhere equal in magnitude, but have an opposite sign, the mean curvature is zero. Such surfaces are termed minimal surfaces and if possible to extend periodically in space are called triply periodic minimal surfaces (TPMS) or infinite periodic minimal surfaces (IPMS), which are separating the space into two congruent volumes.

In a systematic classification of lipid phases a normal phase is defined as oil in water and exhibits positive mean curvature, thus the curvature is towards the surfactant chains, whereas an inverse phase (water in oil) exhibits curvature towards water resulting in negative mean curvature. Furthermore, phases can exhibit a bilayer or monolayer structure or continuity, thus exhibiting one continuous surface.

Classification of phases is performed mainly according to their crystallographic lattice type with structures named according to the nomenclature introduced by Luzzati⁷⁷ using L for lamellar, M for micellar, H for hexagonal and Q for cubic phases. Normal and inverse phases are in this nomenclature indicated with subscripts I and II. Subscripts c , β and α denote order of lipid chains, with c for crystalline or subgel, β for ordered or gel and α for liquid-crystalline order. Lipid phases can be classified into three major groups that will be discussed in the following sections: Lamellar phases,

micellar aggregates and non-lamellar liquid-crystalline phases exhibiting various topologies such as two or three dimensional symmetry⁷⁸.

I.1.4.1 Lamellar phases

At low temperatures or low water content most lipids arrange in a crystalline or subgel lamellar phase (L_c) that exhibits packing with long- and short-range order and hydrocarbon chains in all-*trans* conformation. Upon increase of temperature or hydration phospholipids and glycolipids undergo phase transformation into ordered or gel phases. In these phases lipids can undergo rotation around their longitudinal axis but still exhibit ordered packing. The ordered phases can be subdivided into phases with hydrocarbon chains oriented parallel to the bilayer normal (L_β), tilted hydrocarbon chains (L_β') or interdigitated chains (L_β^{int}) as well as rippled gel (P_β') phases exhibiting periodic ripples of their bilayer (Figure 9). These phases are adopted by different lipid classes under various conditions⁷⁵. Polymorphic transitions between a variety of these structures have been found such as a sub-transition from L_c to L_β' and pre-transition L_β' to P_β' in phosphatidylcholines (PC)⁷⁹. Rippled phases have been observed for a variety of biological relevant lipid classes such as phosphatidylcholines, phosphatidylethanolamines (PE), phosphatidylglycerols (PG) and phosphatidic acids (PA)⁷⁵.

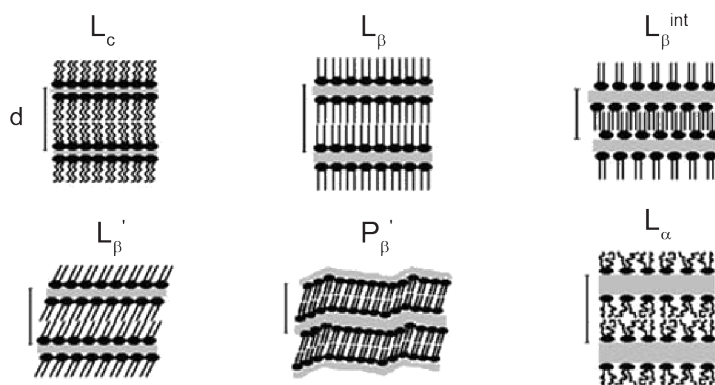


Figure 9: Structures of lamellar lipid phases: subgel or also termed crystalline phase (L_c), gel phase (L_β), gel phase with tilted hydrocarbon chains (L_β'), gel phase with interdigitated chains (L_β^{int}), rippled gel phase (P_β') and liquid-crystalline phase (L_α). Modified from Koynova and Tenchov⁷⁸.

Upon further increase of temperature, motion and occupied volume of hydrocarbon chains continually increases. At a certain temperature, the hydrocarbon chain packing melts and transition into a fluidic phase (L_α) occurs if hydration is sufficient. Most lipids containing two hydrocarbon chains melt into a fluidic or liquid-crystalline phase that exhibits not only fast axial rotation, but also fast lateral diffusion and strong

increase in bending elasticity^{78, 80}. This phase transition is the main transition in lipid bilayers with a major enthalpy change involving rotameric disordering of the hydrocarbon chains, increased headgroup hydration and increased intermolecular entropy^{78, 81}. In fully hydrated lipids this transition leads to large lipid surface area increases, a increase of specific volume against attractive van der Waals interactions and increased hydrophobic exposure at the lipid interface. These factors are thereby strongly contributing to the large transition enthalpy change of 20 to 40 kJ/mol^{78, 82}. The melting temperature is strongly dependent on the length of the hydrocarbon chains and saturation, with more saturated and longer hydrocarbon chains exhibiting higher phase transition temperatures⁸³⁻⁸⁴.

Intermediate lipid states such as the liquid-ordered (l_o) state⁸⁵ (Figure 10) between a gel (L_β) also termed solid ordered phase (s_o) and the liquid-crystalline (L_α) also termed liquid-disordered phase (l_d) have been found in complex lipid mixtures exhibiting phase separation and are thought to be of functional relevance to biological systems⁸⁶. These intermediate liquid ordered states, are thought to be required for proper function of some membrane proteins and clustering these in so called lipid-rafts, which are introduced in detail in the respective chapter of this thesis (see section II.1).

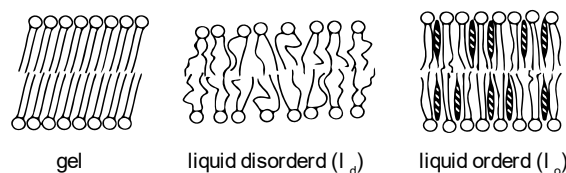


Figure 10: Structures of lamellar lipid phases. Simple phospholipid bilayers form a gel phase (L_β or also termed s_o) at low temperatures that melts to a liquid disordered phase also termed liquid-crystalline phase (l_d or also termed L_α). The presence of cholesterol or other components (hatched ovals) orders the acyl chains of the latter phase and can fluidize the former phase to an intermediate state for which the term liquid-ordered (l_o) was coined⁸⁵. Adapted from Munro⁸⁷.

I.1.4.2 Non-lamellar liquid-crystalline phases

Next to transition into lamellar liquid-crystalline phases non-lamellar phases are formed in the majority of lipids upon further increase of temperature if water content is held constant. Low hydration levels lead to tighter packing and a smaller surface area that lipid headgroups can occupy resulting in negative interfacial curvature leading to the observed tendency to form inverted micelles or inverted two or three-dimensional phases such as the inverted hexagonal (Figure 11) or cubic phases (Figure 12)^{78, 88}.

A typical phase sequence of membrane forming phospholipids and glycolipids with increasing temperature at constant water content would therefore be: $L_c \leftrightarrow L_\beta \leftrightarrow L_\alpha \leftrightarrow Q^{B_{II}} \leftrightarrow H_{II} \leftrightarrow Q^{M_{II}} \leftrightarrow M_{II}$ with $Q^{B_{II}}$ denoting a inverted bilayer cubic phase and $Q^{M_{II}}$ a inverted micellar cubic phase⁸⁹. At the same temperature, liquid phases are often existing with increasing water content in the following sequence: inverted phases (M_{II} , $Q^{M_{II}}$, H_{II} , $Q^{B_{II}}$) \leftrightarrow lamellar phase (L_α) \leftrightarrow normal phases (Q^{B_I} , H_I , Q^{M_I}) \leftrightarrow micellar solutions and finally monomers⁷⁶. The concave interface of inverted phases thereby transforms with increasing water content into a flat interface and depending on the packing parameter can then further convert into a convex interface of normal two and three-dimensional phases that eventually disintegrate into micellar aggregates and monomeric solutions below the critical micellar concentration (CMC)⁷⁸.

However, typical membrane forming double-chain lipids exhibit only inverted and L_α liquid-crystalline phases forming liposomes at high water content. They, unlike single-chain lipids, do not form normal two or three-dimensional phases or segregate into other micellar aggregates in solution and finally monomers like detergents⁷⁸.

I.1.4.2.1 Two-dimensional liquid-crystalline phases

Periodic two-dimensional liquid-crystalline phases are seen upon formation of indefinitely long, aligned rod like structures. The most typical observed two-dimensional phases are the hexagonal phases with the 2D space group $p6m$ (Figure 11).

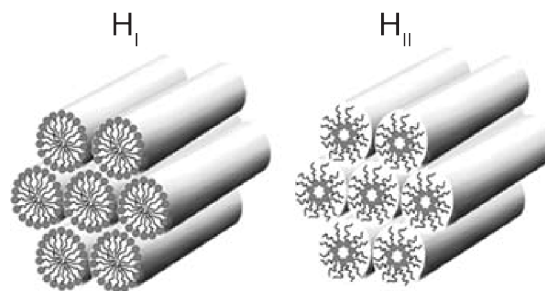


Figure 11: Normal (H_I) and inverted (H_{II}) hexagonal phase. Modified from Koynova and Tenchov⁷⁸.

In the normal hexagonal phase H_I lipids form cylindrical micelles that are packed in a hexagonal lattice with water filling the voids forming a continuous network. This phase, common in simple surfactants, is not often formed by membrane forming lipids⁷⁵. The inverse hexagonal phase however is also very common in phospholipids. Especially lipids that exhibit a small headgroup area, are weakly hydrated and exhibit intermolecular headgroup interactions, such as PE, tend to form this phase. In this

inverse phase cylinders filled with water are surrounded by the polar headgroups of the lipids and the remaining volume filled by the hydrocarbon chains⁷⁶.

However, also other hexagonal phases based on curved lipid bilayers have been reported. Furthermore, deviation of cylindrical shape can also lead to alternative packing, with two-dimensional rectangular or oblique phases observed as well⁷⁵.

I.1.4.2.2 Three-dimensional liquid-crystalline phases

Lipid water phases with a cubic symmetry account for the majority of three-dimensional liquid-crystalline phases, with tetragonal, rhombohedral and orthorhombic phases observed only in a very few cases⁷⁵. Cubic phases are in general named according to their crystallographic space group and can be separated into two classes: Micellar cubic phases, whose separated micelles exhibit cubic packing and bicontinuous cubic phases (Figure 12).

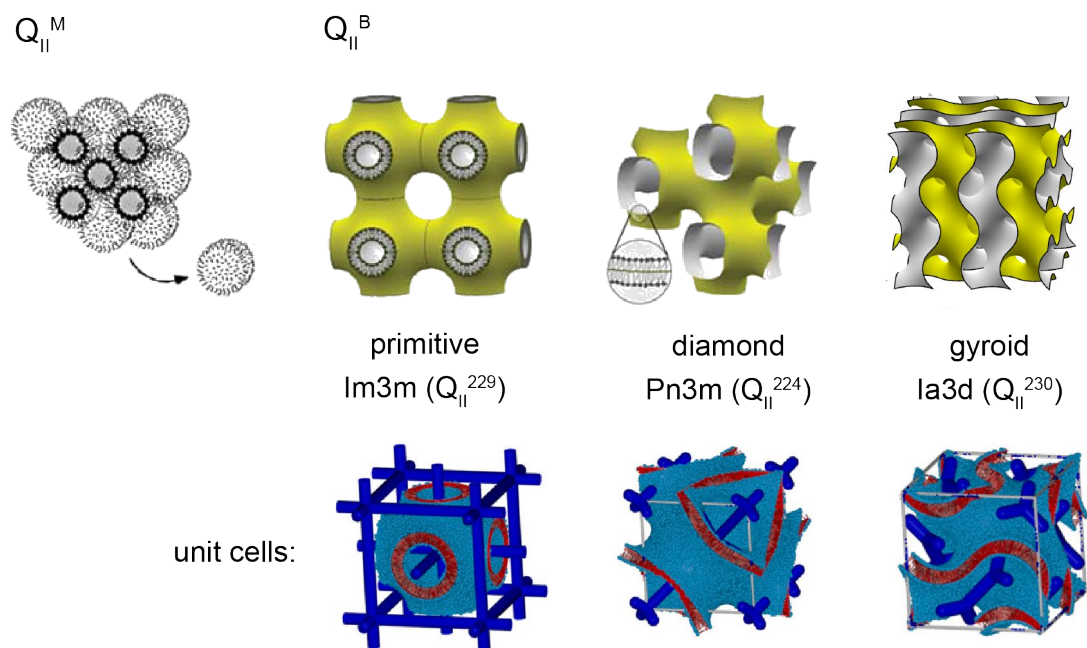


Figure 12: Inverse micellar and inverse bilayer cubic phases, with representation of their unit cells as well as symmetry axes. Combined from Koynova and Tenchov⁷⁸ and de Campo, Castle and Hyde⁹⁰.

They can exist in a normal and inverse form, with the inverse form typical for monoacylglycerol water mixtures⁹¹. Inverse bicontinuous cubic phases are formed by a continuous lipid bilayer that exhibits periodicity in all three dimensions separating the space into two non-intersecting networks of water channels⁷⁵. Their shape can be described by triply periodic minimal surfaces (TPMS) that exhibit cubic symmetry, thus surfaces that have minimal area equating to zero mean curvature and exhibit a crystallographic space group belonging to the cubic family⁷⁵. The first reported

structure of a inversed bicontinuous cubic phase formed by a lipid-water system exhibited a gyroid symmetry ($Ia3d$, Q^{230})⁹². The two other major forms of the seven bicontinuous cubic phases found in lipid-water systems exhibit primitive ($Im3m$, Q^{229}) and diamond ($Pn3m$, Q^{224}) symmetry^{78, 93} that can be described by the Schwarz' P and Schwarz' D minimal surfaces⁷⁵ (Figure 12).

I.1.4.2.3 Isotropic phases

Translationally disordered phases that exhibit isotropic behavior, comprehend various micellar aggregates, emulsions, the normal and inverted fluid isotropic phases (L_1 and L_2) as well as the so-called sponge phase (L_3), resembling thermally disordered and swollen three-dimensional liquid-crystalline phases^{75, 94-95}. As described above, mainly surfactants or mixtures of short and long chain lipids are observed to form micellar aggregates, but not membrane forming phospholipids alone. At high temperatures and low hydration however, inverse micellar phases so called fluidic inverse phases (L_2) have also been observed in membrane forming short chain or single-chain lipids⁷⁵.

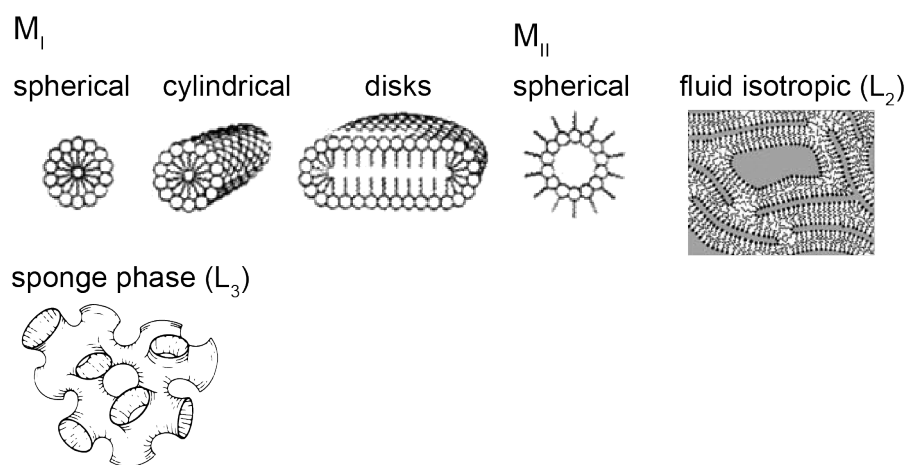


Figure 13: Graphical representation of selected disordered isotropic phases: Spherical, cylindrical (tubules) and disk-shaped micellar aggregates of the normal type M_I . Inverse spherical micelles and the fluid inverse isotropic phase (L_2) belonging to M_{II} . The sponge phase (L_3), an isotropic but disordered phase formed upon swelling of cubic phases or cooling of fluid isotropic phases⁷³. Combined and modified from Koynova and Tenchov⁷⁸, Cherezov, Clogston, Papiz and Caffrey⁹⁶ and Strey and Winkler⁹⁵.

I.1.4.3 Phase transitions by water content in binary lipid/water systems

A ‘‘ideal’’ hypothetical sequence of phase transitions of binary lipid/water systems with increasing amphiphile concentration starts above the critical micellar concentration by formation of the normal micellar phase (M_I) and proceeds via the

normal hexagonal phase (H_I) to lamellar phases (L). Upon further increase of amphiphile concentration reversed hexagonal (H_{II}) and finally reversed micellar (M_{II}) phases occur (Figure 14a). Intermediate phases are often of cubic structure and similarly occur with increasing water content in the following order: Micellar cubic phase (Q_I^M), bicontinuous cubic phase (Q_I^B), inverted bicontinuous phase (Q_{II}^B) and inverted micellar cubic phase (Q_{II}^M). However, often only a subset of these phases is formed by binary lipid/water systems as exemplified by the temperature water phase composition diagram for the glycerophospholipid DOPC (Figure 14b). Lamellar, hexagonal and phases with isotropic lipid motion such as micellar and cubic phases can be distinguished by ^{31}P NMR as they exhibit characteristic lineshapes due to differences in motional averaging of their chemical shift tensor (Figure 14c).

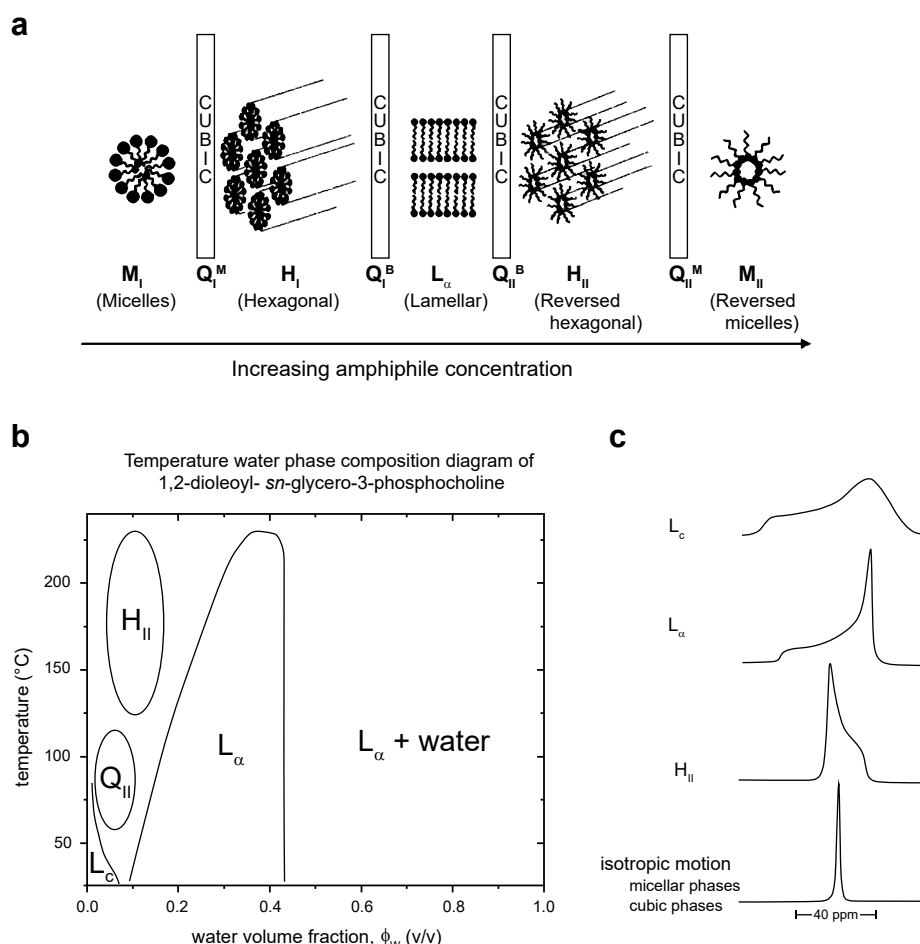


Figure 14: Binary lipid/water phase diagrams and characteristic ^{31}P NMR lineshapes. **a**) Hypothetical phase diagram, with the full sequence containing cubic intermediate phases of phase transitions by varying amphiphile concentration. Reproduced from Kaasgard and Drummond⁹⁷. **b**) Binary lipid/water phase diagram of DOPC according to Bergenstaahl and Stenius⁹⁸. Reproduced from Marsh Handbook of Lipid Bilayers⁸². **c**) Characteristic ^{31}P NMR lineshapes of phases adopted by binary glycerophospholipid/water systems. Adapted from Yao et al⁹⁹ and Cullis et al¹⁰⁰.

I.1.4.4 Biomembranes

Biological membranes are enclosing or separating compartments. In case of the cell membrane, it separates the interior of a cell from the environment and thereby defines the extent of a cell. Biological membranes are selective permeable and control movement of substances such as ions and organic molecules in and out of cells or membrane-enclosed compartments inside cells that serve special purposes such as catabolism, metabolism, energy conversion, uptake, protein production or transport and therefore exhibit altered pH or altered concentration of ions or other compounds. They are containing various proteins to mediate not only transport and selective permeability of substances, allowing to create pH, concentration and charge gradients, but also control membrane properties and composition, anchor the membrane to intracellular filaments, allow adhesion to other cells or scaffolds like the cytoskeleton, sense environmental conditions as well as signaling. The cell membrane serves furthermore as attachment for extracellular structures such as a cell wall or a polysaccharide coat (glycocalyx) that can form a capsule or slime layer for protection and is for example allowing bacteria to form biofilms or adhere to inert surfaces.

This manifold of functions require homeostasis of the membrane properties that is achieved by modulators like cholesterol and modulation of lipid composition. However, biomembranes contain also high amounts of lipids that have the ability to form non-lamellar structures⁷⁸. These lipids create membrane curvature frustration and may lead to temporary formation of non-bilayer structures thought to allow membrane fusion and fission⁷⁸. They are also supposed to support high curvature found in prolamellar bodies, cisternae, cristae, thylakoids or other formations that can even exhibit cubic phase morphology^{78, 101-102}. Lipid phase as well as membrane curvature frustration have been found to be important for modulation of membrane protein activity and alterations can influence conformational changes of membrane proteins¹⁰³⁻¹⁰⁷. Furthermore, certain proteins are localized in highly curved regions and some have been found to induce membrane curvature or cubic phase formation¹⁰⁸⁻¹¹¹.

However not only the transmembrane lipid composition of biomembranes and proteins is non-uniform, but also their lateral organization. Observation of formation of liquid-ordered microdomains in membranes, so called lipid rafts, containing high contents of cholesterol, sphingomyelin and saturated phospholipids¹¹²⁻¹¹³ thereby represent a case of lipid demixing transition⁸⁶ and liquid-liquid immiscibility¹¹⁴. Mounting evidence that this lipid lateral heterogeneity and domain formation has

functional relevance^{86, 113, 115-116} led to a growing desire to expand the fluid-mosaic model of Singer and Nicolson in which proteins freely float along the bilayer to also include lipid-rafts and cytoskeleton anchoring as membrane organizing principles¹¹⁷⁻¹²⁰. Lipid lateral heterogeneity and lipid-raft formation in a cellular context are further discussed in Section II.1.

I.1.5 Common membrane mimetics used for membrane proteins

The focus of the following section lies on widely used membrane mimetics made entirely of lipids such as liposomes, bicelles and lipidic cubic phases of monoacylglycerols (for a graphical representation see Figure 18). Other successfully applied systems are Nanodiscs, which are discoidal particles made of a lipid bilayer surrounded by a belt of membrane scaffold proteins¹²¹⁻¹²² and lipodisqs, which are formed using styrene-maleic acid copolymers instead of membrane scaffold proteins. The properties of these scaffolds allow extraction of membrane proteins from native membranes without detergents and formation of very small particles that are capable of providing a bilayer environment for embedded membrane proteins¹²³⁻¹²⁴. These aspects are especially promising for liquid-state NMR. The bilayer in lipodisqs however does not exhibit clear phase transition behavior as the majority of lipids interact with the copolymer compared to the more popular nanodisc where only a fraction of lipids is perturbed¹²⁵⁻¹²⁶. Compared to mixed detergent micelles or other membrane mimetics¹²⁷⁻¹²⁸ (for an extensive review see Catoire, Warnet and Warschawski¹²⁹) as well as liposomes, bicelles and lipidic cubic phases discussed below both systems do not provide sufficient capacity for lipid substrates or lipid diffusion, but can be a useful tool to study lipid-protein interactions^{125, 130}.

I.1.5.1 Liposomes

A typical membrane mimetic for protein solid-state NMR applications are liposomes formed by phospholipids that form lamellar phases upon hydration¹²⁸. Hydrated phospholipids form multilamellar vesicles of micrometer size that scatter light¹³¹. Methods like freeze-thawing or sonication can be applied to form unilamellar vesicles (Figure 15).

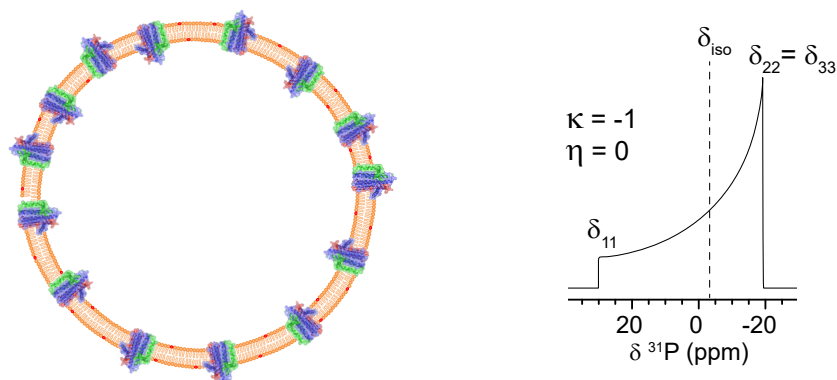


Figure 15: Artwork depicting a cross section of a unilamellar proteoliposome, with DgkA non-directional inserted. Fast axial rotation of the lipids in the fluid $L\alpha$ (l_d) phase leads to axial symmetry of the chemical shift tensor ($\delta_{22} = \delta_{33}$, in case of phospholipids) resulting in static ^{31}P spectra similar to the depicted powder spectrum. PDB: 3ZE4.

Their size can also be changed via sonication and freeze-thawing to create smaller sized liposomes or fuse liposomes depending on the conditions, ion concentrations¹³² and type of lipid¹²⁷. A defined and homogeneous liposome size¹³² can be achieved as well via extrusion. Membrane proteins purified in detergent micelles can be incorporated into liposomes via reconstitution, a process where ideally liposomes are softened with detergent allowing efficient insertion into the bilayer and subsequent removal of detergent¹³³, but also other methods have been successfully applied¹²⁷. Lipid to protein ratios can be varied to a high degree. They are typically around 5000:1 or even higher for assays and down to 50:1 for protein solid-state NMR¹³³⁻¹³⁵ allowing high capacity for lipid components or high amounts of reconstituted protein depending on the application.

I.1.5.2 Bicelles

So called anisotropic bicelles are another membrane mimetic that has been applied mainly for static solid-state NMR¹²⁸. They align with respect to an applied magnetic field and allow to gain information via angular dependent parameters like dipolar-couplings¹³⁶⁻¹³⁹. Anisotropic bicelles have also been used as alignment medium in liquid-state NMR experiments utilizing residual dipolar couplings¹³⁷ as well as polarized light spectroscopy as they exhibit less scattering compared to liposomes¹³¹. Bicelles, membrane disc-like structures, are made of long chain lipids that prefer lamellar phases and short chain lipids that would form detergent micelles, often 1,2-dimyristoyl-*sn*-glycero-3-phosphocholine (DMPC) and 1,2-dihexanoyl-*sn*-glycero-3-phosphocholine (DHPC) (Figure 16). The molar ratio between long and

short chain lipid is called q value and determines bicelle properties¹⁴⁰⁻¹⁴¹. The lower the q value the more similar bicelles become to micelles¹⁴². Isotropic tumbling disc-like bicelles used as membrane mimetic for liquid-state NMR often exhibit q values between 0.5 and 0.6¹⁴². At q values 2 or bigger anisotropic structures can form¹⁴³⁻¹⁴⁴ and align to an external magnetic field due to the dielectric tensors of long chain lipids adding up to a macroscopic magnetic susceptibility tensor that can affect the orientation^{141, 145-147}. Due to the negative sign of the DMPC anisotropy tensor they typically align with their bilayer normal perpendicular to the magnetic field, but can be "flipped" to align parallel by introducing a larger, positive magnetic susceptibility like lanthanide ions that interact with the lipids^{139, 146, 148-151} (Figure 16b).

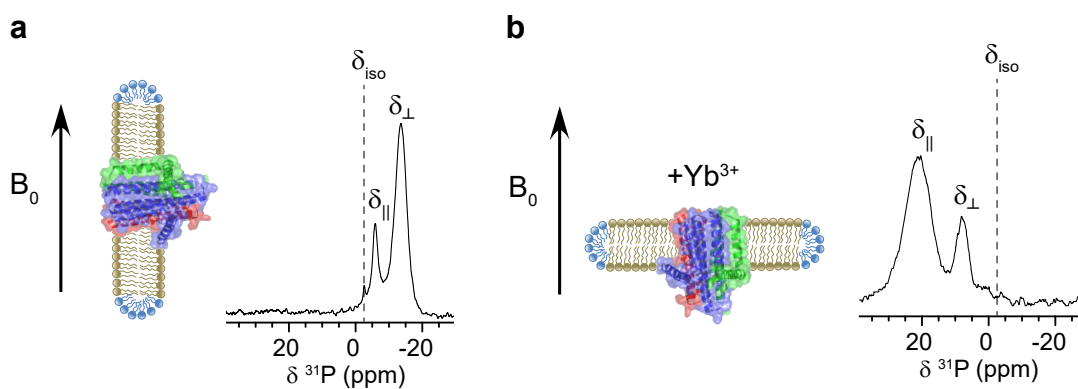


Figure 16: Artwork depicting cross sections of an anisotropic bicelle containing DgkA aligning with its bilayer normal perpendicular (a) or upon introduction of a lanthanide ion parallel (b) to an external magnetic field. Short chain lipids (blue) form a belt around a bilayer consisting of long chain lipids (olive). In case of magnetically aligning anisotropic bicelles the structure is most likely worm-like and not discoidal. The static ^{31}P spectra of these systems represents the chemical shift component of parallel and orthogonal aligned short and long-chain lipids (excerpts of Appendix Figure 10). PDB: 3ZE4.

At higher concentrations and a q value of 3.2, which is often used for static solid-state NMR^{145, 149, 152}, bicelle preparations exhibit isotropic properties at low temperatures and are clear and fluid, but become a chiral nematic resembling worm-like structures at room-temperature that is highly viscous and aligns to an external magnetic field¹⁴⁴. This transition from isotropic signals to the angular dependent signals of DMPC aligned parallel to the magnetic field and DHPC aligned perpendicular as well as its flipping is readily observed by ^{31}P or ^2H NMR^{149, 153-154}. At even higher q values above 5 the orientation of short and long chain lipid is reversed. Thus, long lamellar structures interspersed with holes formed by short chain lipids are the predominant form^{149, 152, 155}. Bicelle morphology and stability depends not only on q value but also on many

other factors such as lipid composition and concentration, temperature, pH and ionic strength^{143, 156}. Therefore, work has also been focused to increase their stability and discern transitions between different morphologies^{144, 157-159}. Membrane proteins are often reconstituted into bicelles from proteoliposomes, but can for example be also extracted from nanodiscs¹⁶⁰. After preparation of proteoliposomes short chain lipids that form detergent micelles are added at the desired molar ratio to generate bicelles via several freeze-thaw cycles¹⁶¹.

I.1.5.3 Lipidic cubic phases of monoacylglycerols

Direct mixing of the detergent solubilized membrane protein with the lipid of choice in contrast is often performed for formation and reconstitution of membrane proteins into optically transparent cubic phases of monoacylglycerols¹⁶²⁻¹⁶⁴, also termed meso phases due to their high viscosity¹⁶⁵. These lipidic cubic phases are relatively stable under different conditions¹⁶⁵⁻¹⁷⁰ as well as pressure¹⁷¹⁻¹⁷³ and were first introduced as membrane mimetics for protein crystallization by Landau and Rosenbusch¹⁷⁴. Application of LCPs for membrane protein crystallography often termed *in meso* or *in cubo* crystallization has led to an "explosive growth" of available crystal structures of membrane proteins accelerated by the first structures of G protein-coupled receptors¹⁶² and detailed characterization of their phase behaviour¹⁶⁵⁻¹⁷³.

Lipidic cubic phases form spontaneously upon hydration and mixing over a wide range of temperatures above 20 °C as detailed temperature composition phase diagrams obtained by X-ray diffraction of monoacylglycerols revealed^{165, 175-176}. A later study determining the temperature composition phase diagram by starting from a lamellar crystal phase demonstrated that the cubic phases of monoolein exhibit metastability and can be under-cooled¹⁷⁰ leading to the previously described phase diagram (Figure 17)⁹⁶.

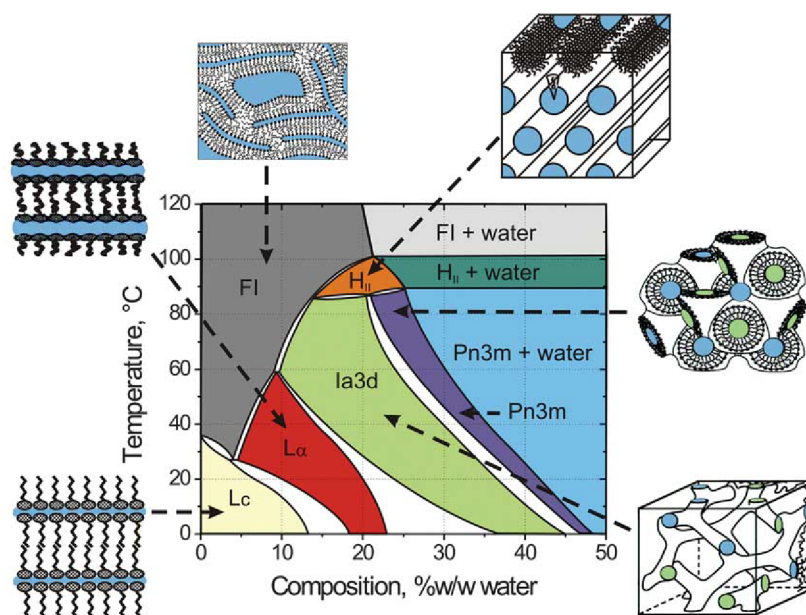


Figure 17: Temperature-composition phase diagram of the monoolein/water system determined under "conditions of use" in the heating and cooling directions starting from 20 °C. A cartoon representation of the various phase states in which colored zones represent water. FI refers to fluid isotropic (L_2), a inverse micellar phase (M_{II}) that forms at high temperatures with random isotropic ordering and fluid-like flow behavior⁷³. Figure published by Cherezov, Clogston, Papiz and Caffrey⁹⁶.

The effects of various maltosides and glucosides on phase transition with respect to detergent concentration, water content and temperature have been extensively characterized^{166, 169, 177}. Introduction of high amounts of detergent destabilizes cubic phases and shifts the equilibrium to lamellar phases, thereby limiting the amount of detergent that can be introduced^{162, 166, 178}. However, denatured membrane proteins can also be refolded into the cubic phase using acidic urea to solubilize the precipitate avoiding detergents¹⁷⁹. The lattice parameter for the Pn3m cubic phase of monoolein at a 3:2 (w/w) ratio of monoolein to water at room temperature is approximately 100 Å and contains around 500 lipid molecules¹⁸⁰ at a bilayer thickness of 34.7 Å⁹⁶. The diameter of its water channels is approximately 45 Å¹⁸¹ with water channel diameter decreasing at higher temperatures¹⁶⁵. The lattice parameters, thickness and curvature of the membrane as well as the diameter of water channels of the cubic phases depend on the lipid type and can be modified by altering lipid chain length and saturation, parameters that have been screened in protein crystallization trials¹⁶⁷. Diffusion of lipids along the highly curved surface in a cubic phase is similar compared to lipid diffusion in lamellar environments and leads to fast orientation change of the lipid molecules, averaging their chemical shift anisotropy^{80, 182}, leading to solution-state-like NMR spectra¹⁸³ (Figure 18).

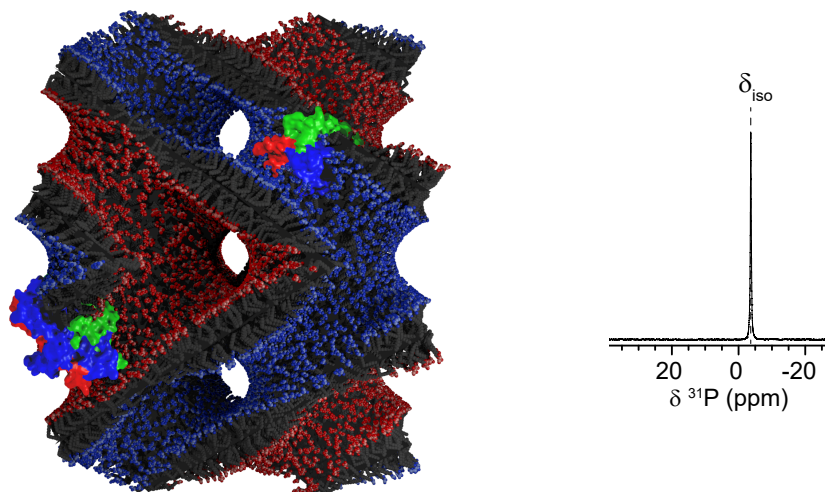


Figure 18: Graphical representation of DgkA embedded in $2 \times 2 \times 2$ unit cells of the lipidic cubic (Pn3m) mesophase at a molar monoolein to DgkA ratio used herein for 2D MAS NMR experiments (1300:1). The two leaflets of the single monoolein bilayer are colored in blue and red to highlight the two non-intersecting networks of water channels of the bicontinuous system created by the triply periodic minimal surface. Model generated from the Schwarz D surface¹⁸⁴⁻¹⁸⁶ using PyMOL¹⁸⁷ and Blender to add monoolein and DgkA. Fast, isotropic orientation change due to diffusion along the highly curved bilayer results in isotropic line shape of phospholipids embedded in a cubic phase otherwise devoid of phosphorous nuclei. PDB: 3ZE4.

However, diffusion of D_2O and sodium ions through the water channels was determined to be three orders of magnitude lower than in neat solution^{182, 188}. Nevertheless, it allows diffusion of soluble biomacromolecules that exceed the assumed size of the water channels, when in excess water, making it a potential drug delivery system¹⁸¹ in the form of dispersed cubic phase particles called cubosomes for controlled release of drugs¹⁸⁹⁻¹⁹⁰.

Excess water in combination with detergents^{166, 169} or other agents⁹⁶ leads to swelling of the cubic phase and transition into sponge phases along with loss of symmetry but not loss of isotropic behavior⁷⁵. These sponge phases exhibit wide water channels and reduced curvature⁹⁶. Additives to induce swelling include guanidinium hydrochloride and urea but also various other common agents in crystallization screens with the amount of swelling correlating to crystal formation⁹⁶. High concentrations of D_2O and glycerol, often used in DNP applications to form a glassy matrix and increase enhancement¹⁹¹, in contrast only slightly decrease lattice parameters¹⁹²⁻¹⁹³. Swelling is thought to facilitate crystallogenesis as it might promote formation of membrane protein interactions in patches of lamellar regions⁹⁶. A possible mechanism driving

clustering of membrane proteins and crystal formation *in meso* is the combination of a hydrophobic mismatch between membrane proteins and the highly curved cubic phase and a continuous bilayer allowing free diffusion of membrane proteins^{180, 194-195}. However, several crystallization conditions might also support local hexagonal H_{II} phases, where proteins can diffuse along the H_{II} phase water-filled rods to associate^{162, 196-197}. It seems likely that these are coexisting with cubic phases⁹¹ as continuity of the bilayer might be essential for crystal growth acting as infinite reservoir as well as creating pre-alignment reducing the orientation space¹⁶².

Despite its robustness, wide use in membrane protein crystallization and potential drug delivery vector as well as potential membrane mimetic for solution-state NMR¹⁸³ only a few NMR studies have been performed so far on LCPs. These have mainly focused on determining the diffusion rates of its components¹⁸² as well as phase behavior and interactions in presence of other lipids and a polypeptide¹⁹⁸⁻¹⁹⁹. A first study using saturation transfer difference spectroscopy²⁰⁰ and up to 5 kHz MAS trying to elucidate cholesterol binding to the β_2 adrenergic receptor²⁰¹ highlights the potential the cubic phase might offer for protein MAS solid-state NMR.

I.1.6 Diacylglycerol kinases

Diacylglycerol kinases (DGKs) are intracellular lipid kinases that phosphorylate diacylglycerols (DAGs) thereby forming phosphatidic acids²⁰²⁻²⁰³. DAG is a main signaling molecule and a common second messenger in eukaryotes^{64, 204-205} where it is generated by phospholipase C via hydrolysis of phosphoinositides in response to a variety of stimuli²⁰⁶. DAG activates protein kinase C^{62, 65, 207}, a family of lipid-activated protein kinases, which is a key mediator of cell proliferation and differentiation²⁰⁸. It also influences activators of proteins of the G protein families Ras and Rac that belong to the small GTPases, like Rac-GTPase activating proteins such as α - and β -chimaerins²⁰⁷, guanyl nucleotide exchange factors, such as Ras guanyl-releasing proteins²⁰⁹, Ca^{2+} and DAG-regulated guanine nucleotide exchange factor I (CalDAG-GEFI)²¹⁰ and protein kinase D²¹¹. Next to cellular signaling for proliferation and differentiation DAGs are also found to regulate localization of GPCRs⁵⁹, modulate immune function by inhibition of T-cell receptor signaling⁶³ and limit the response of macrophages and dendritic cells to intracellular pathogens²¹². Therefore, DGKs play a crucial role in regulating DAG levels and cellular signaling^{205, 212-215}. Multiple isoforms are found in eukaryotic organisms, with 10 isozymes denoted α till κ found in mammals, that can be grouped into 5 classes²¹⁶. DGKs can be targeted isoform specific to regulate activity and localization²¹⁷⁻²²⁰. Therefore DAGs and DGKs are important coordinators of spatial orientation of signaling²²¹ and could potentially act as drug targets for autoimmunity, cancer, epilepsy, cardiac hypertrophy, hypertension and type II diabetes^{202, 222-224}.

These DGKs and the DGK of gram-positive bacteria encoded by the *dgkB* gene are typically water-soluble and have at least one conserved catalytic domain exhibiting typical kinase motifs and kinase fold²²⁵⁻²²⁶.

The DGK found in gram-negative bacteria like *E. coli* is a small transmembrane enzyme encoded by the *dgkA* gene. A homolog of the gene is also found in gram-positive bacteria, which in *Bacillus subtilis* and *Streptococcus mutans* does not exhibit DGK activity and is instead encoding for a undecaprenol kinase (UDPK) that exhibits a high lipid substrate specificity^{225, 227}. Both do not share considerable homology with other known kinases and do not feature any common kinase motifs, which strongly suggests that the membrane enzymes encoded by *dgkA* are evolutionary unrelated to eukaryotic DGKs and other DGKs of gram-positive bacteria not encoded by *dgkA*^{216, 228}.

I.1.6.1 *E. coli* diacylglycerol kinase

The DGK of *E. coli* has been an object of interest since the first description of diacylglycerol kinase activity²²⁹ and isolation of the protein²³⁰ in 1965 and 1973 respectively. Terminology therefore ranges from diglyceride kinase and diacylglycerol kinase in the early studies via abbreviations like DAG kinase, DAGK and DGK to DgkA (see Appendix Table 5), its name based on the gene name according to the usual bacterial protein nomenclature, which is used hereafter for the *E. coli* variant.

DgkA is a small, 121 amino acid containing, homotrimeric membrane enzyme that catalyzes ATP-dependent phosphorylation of diacylglycerols in the cytoplasmic leaflet of the inner membrane as part of several metabolic cycles^{228, 231-232}. In *E. coli* DAGs are not known to serve as second messengers, but are generated in large quantities as byproducts during membrane-derived oligosaccharide (MDO) synthesis in the periplasm upon environmental stress such as low osmolarity²³³⁻²³⁴ by transfer of *sn*-1-glycerol-phosphate (GP) from phosphatidylglycerols (PGs) onto nascent MDOs²³⁵⁻²³⁶. The generated DAGs transverse from the periplasmic side along their concentration gradient across the membrane to the cytoplasmic leaflet, where DgkA can readily phosphorylate them avoiding potentially toxic concentrations of non-bilayer phase inducing DAGs. The generated phosphatidic acids (PAs) are a central intermediate of glycerophospholipid synthesis in bacteria^{203, 237}. Phosphorylation of DAGs by DgkA is thereby the first step for restoring the PG that is consumed during MDO synthesis, creating a phosphate shuttle over the inner membrane (Figure 19)^{228, 231-232, 236}. A second major shuttle system generating DAGs in the periplasm and relying on recycling of the used lipid is an initial step in lipopolysaccharide (LPS) synthesis, which are the main constituents of the bacterial outer membrane²³⁸. Here DAGs are generated when phosphoethanolamine (pEtN) from phosphatidylethanolamines (PE) is transferred onto glucosamines of lipid A as well as sugars of the inner LPS core, which is attached to lipid A²³⁹⁻²⁴⁴.

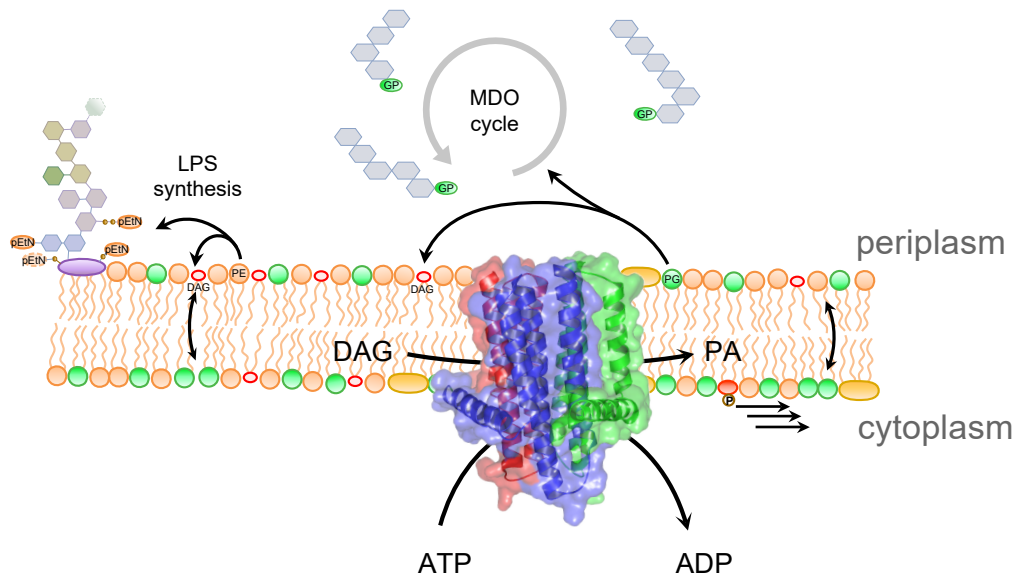


Figure 19: Physiological role of DgkA in the inner membrane. DAGs (red) are generated in the periplasmic leaflet during the MDO synthesis cycle where the *sn*-1-glycerol-phosphate (GP) from PGs (green) is transferred onto MDOs. A second source of DAGs is LPS synthesis where phosphoethanolamine (pEtN) transferases transfer pEtN from PEs (green) onto glucosamines of lipid A (purple) as well as the depicted inner LPS core²⁴¹ often using phosphate as linker (gold). Transbilayer diffusion along their concentration gradient into the cytoplasmic leaflet allows phosphorylation of DAGs via DgkA using ATP as phosphoryl donor. The generation of PA a key intermediate in lipid synthesis is thereby the first step to regenerate PG and PE. A potent activator of DgkA, cardiolipin, is depicted in yellow. Different concentrations resemble the asymmetry of the inner membrane bilayer²⁴⁵. PDB: 3ZE4

I.1.6.2 Enzymology of DgkA

The enzymatic properties of DgkA have been studied to great detail for the past 50 years and answered many questions (Appendix Table 5). The long chronicle of enzymatic studies, reflects the many challenges that have been overcome by subsequent advances of methods and facets explored, yielding to a complex picture, that also highlights the difficulties associated with determining enzymatic parameters for an interfacial membrane enzyme.

Despite initially only harsh detergents available, with assays performed in Triton X-100 mixed micelles, and purification with organic solvents, which is now known to cause protein unfolding that led to the low specific activities²⁴⁶⁻²⁴⁷, initial experiments often performed with ³²P-ATP or tritiated compounds detecting phosphorylated products yielded valuable information. Stereospecificity for *sn*-1,2-diacylglycerols²⁴⁸, broad substrate specificity towards monoolein²⁴⁹, several ceramides and alcohols^{230, 250}, absolute requirement for a divalent ion²⁵⁰, adenine nucleotide specificity²⁵⁰ as well

as first determination of altered DAG contents in *E. coli* cells upon knock-out of diacylglycerol kinase activity^{231, 251} were the main results of these experiments. performed by Pieringer and Kunnes, Chang, Schneider and Kennedy, Raetz and Newmann as well as Bohnenberger and Sandermann.

After the the *dgk* locus had been found²⁵² and sequenced²⁵³, the sequence of the under the λp_L promoter subcloned and reversed-phase purified protein was confirmed to be a diacylglycerol kinase²⁴⁷. Discovery of irreversible misfolding during purification led to the first solvent-free purification of DgkA with octyl- β -D-glucopyranosid (OG) as detergent²⁵⁴ by Loomis, Walsh and Bell. Activity assays performed using OG/phospholipid mixed micelles showed clearly increased activity, with subsequent ³²P-ATP assays performed exploring lipid substrate, lipid cofactor, divalent ion, salt, ionic strength, and pH dependence in great detail²⁵⁴⁻²⁵⁵ and summarized below.

- Lipid cofactor requirement for DgkA's activity in OG is in contrast to DgkA in Triton X-100²⁵⁰ absolute with bovine-cardiolipin the strongest activator, but also major classes of phospholipids, sulfolipids, neutral lipids and long chain diacylglycerols including non-substrates like 1,3-dioleoylglycerol cooperatively activate and stabilize DgkA in OG mixed micelles²⁵⁴⁻²⁵⁵.
- Mg²⁺ shows highest activity as divalent cation followed by Mn²⁺ but also activity with, Co²⁺, Cd²⁺, Zn²⁺, Fe²⁺ or Ni²⁺ as divalent cation was observed, with Calcium inhibitory to Mg²⁺ and Mn²⁺ activity²⁵⁴.
- Free Mg²⁺ is needed for full activity²⁵⁵.
- Activity is enhanced by removing contaminating metal ions or Ca²⁺ with EGTA²⁵⁴.
- Optimum for ionic strength and pH was found to be at 100 mM and pH 6.4, with LiCl yielding slightly higher activities than NaCl²⁵⁴.
- Activity of DgkA is dependent on the mole fraction of DAG and cardiolipin and independent of micelle number²⁵⁴
- DgkA exhibits substrate cooperativity²⁵⁵
- Diffusion of DAG between OG micelles is faster or at least as fast as enzymatic turnover²⁵⁵.
- Dioleoylglycerol and dioctanoylglycerol exhibit inhibitory effects at high concentrations, likely due to inactivation of DgkA, as enhanced inactivation is observed at higher temperatures²⁵⁴⁻²⁵⁵.

- Mg^{2+} , Mg^{2+} + AMP-PNP and lipid cofactors stabilize DgkA against dioctanoylglycerol dependent inactivation proportional to their amount of activation²⁵⁴⁻²⁵⁵.

The results of these two studies by Walsh et al laid the basis for following DgkA activity assays. Composition of assays developed later often closely resembled the found optimal conditions for high DgkA activity, which is expressed in units and mostly defined as $\mu\text{mol ATP consumed per minute per milligram DgkA}$. A subsequent study by Walsh et al focused on lipid substrate dependence of DgkA in OG²⁵⁶ and in combination with previous studies^{230, 248-250} defines our current understanding of DgkA's substrate specificity. DgkA does not exhibit strong selectivity concerning fatty acyl chains as it is also able to phosphorylate ceramides, MAGs and several alcohols, with modifications of the acyl chain and alterations of chain length down to butyl as well as modifications of the sn-2-ester of DAGs mostly altering K_M but not v_{max} . However, DgkA exhibits a strong stereoselectivity for the sn-1,2-DAG isomer and does not phosphorylate 1,3-DAGs. Modifications of the sn-1-ester, sn-3-methylene and hydroxyl moiety are strongly impairing v_{max} , without leading to pronounced changes in K_M . These results, defining DgkA's lipid substrate specificity, imply that DgkA is not selective for acyl chains, but its active site interacts directly with the glycerol backbone and ester linkages to allow correct coordination for phosphoryl transfer.

Nucleotide selectivity of DgkA compared to the broad lipid substrate selectivity is very high, with ATP most likely being its only main substrate under *in vivo* conditions^{250, 257}. With K_M most likely between 0.12-0.5 mM^{134-135, 254, 257-260}, ATP concentrations *in vivo*, which are above 3 mM²⁶¹, should saturate active sites of DgkA. In a fluorescence thin layer chromatography activity assay ADP was found to be a very weak phosphoryl donor in contrast to ATP as judged by a six orders of magnitude lower v_{max} , whilst adenosine tetraphosphate exhibited a very low affinity for DgkA²⁵⁷. The ribose and adenine moiety were found to be important for correct nucleotide coordination by DgkA as assays performed with 2'-deoxy-ATP, guanosine triphosphate (GTP) and inosine triphosphate (ITP) exhibit a strongly decreased v_{max} and triphosphate alone was not a substrate²⁵⁷.

Progress in protein production and purification led to introduction of a polyhistidine tagged construct via synthesis of the gene and cloning into the pTrcHisB vector creating pSD004²⁶²⁻²⁶³ that allowed affinity purification using detergent micelles.

During the first studies, which also showed that the polyhistidine tag was unstructured and did not alter DgkA's activity²⁶², it was discovered that this construct exhibited mutations (W117R, S118T) compared to the wild-type sequence²⁶³. Despite early discovery of the error, the sequence was only corrected several years later with introduction of the plasmid pSD005²⁶⁰. Therefore, a manifold of enzymatic and folding studies as well as cysteine-less mutants and mutational studies are based on this construct, which seems to exhibit a very similar enzymatic behavior compared to wild-type DgkA (see Appendix Table 5). The last study using this construct was published nearly a decade after correction of the construct²⁶⁴. Nevertheless, affinity purification resulted in highly increased yields²⁶³ and allowed reconstitution of DgkA into a manifold of model membrane systems such as lysophospholipid micelles²⁶⁵, amphipols²⁶⁶, bicelles²⁶⁷, liposomes^{134-135, 268}, LCPs²⁶⁹ and nanodiscs²⁷⁰. It also led to a subsequent change from harsh OG to EmpigenBB with detergent exchange during affinity purification to DM²⁶² yielding higher thermostability^{255, 260, 265} as well as enzymatic activity in presence of activators^{228, 267-268} (see Appendix Table 5) and allows long term storage at -20 °C without loss of activity^{268, 271}. In contrast to OG where no activity is observed without activators, DgkA exhibits already low activity in DM and DDM micelles with short chain DAGs^{246, 265-267, 272}. Concomitant rediscovery of a NADH coupled photometric ATPase assay that regenerates consumed ATP using pyruvate kinase and lactate dehydrogenase, which was developed by Pieringer and Kunnes²²⁹ and adapted for membrane proteins by Warren et al²⁷³, allowed to study DgkA's ATP consumption under ATP steady state conditions²⁶²⁻²⁶³. These advances allowed Badola and Sanders not only to explore the mentioned nucleotide specificity but also substrate binding and phosphoryl transfer modes of DgkA by using a bisubstrate analogue (putative: adenosine 5'-tetrphosphoryl-*O*-(*sn*-1,2-dihexanoyl)-glycerol) as competitive inhibitor²⁵⁷. Reaction rates determined in the presence and absence of this bisubstrate analogue at varying ATP and DHG concentrations could be fitted to a random equilibrium model in which nucleotide and lipid substrate binding can occur independently of each other and a bisubstrate analogue should be a strong inhibitor²⁷⁴. The observed high binding affinity of the bisubstrate analogue also indicated formation of a ternary complex and direct phosphoryl transfer as it ruled out a ping-pong mechanism, which could be expected if the reaction proceeds via formation of an enzyme-phosphate intermediate^{257, 274}.

Badola and Sanders were also raising the question of DgkA being an evolutionary optimized enzyme²⁷⁵ in terms of its activity approaching substrate diffusion rate limits and put the available wealth of data about DgkA's activity, lipid diffusion and DAG generation into a cellular context²⁵⁷. The high activity in DM micelles, reaching later up to 110 U equating to roughly 1500 lipids phosphorylated by an active site per minute at 30 °C with cardiolipin as activator and saturating concentration of DAGs^{269, 272, 276} (see Appendix Table 5), is still modest compared to the most efficient water-soluble kinases²⁷⁷⁻²⁷⁸. However, also substrate diffusion for DAGs from the periplasmic site, where they are generated, to DgkA's active site is assumed to be roughly 4 orders of magnitude slower than diffusion of solutes like ATP to the active site²⁵⁷. Trans-bilayer diffusion from the periplasmic to the cytoplasmic leaflet though still fast for spontaneous flip-flop²⁷⁹⁻²⁸⁰ had been thought to be the rate-limiting step herein before rates were available^{257, 281}. Diffusion of lipids along the bilayer in membranes is only a magnitude slower than similar sized compounds in solution²⁸², but as the bilayer reduces dimensionality²⁸³ and allows predisposition of a correct orientation²⁸⁴ rates in DAG-DgkA complex formation could be slightly higher than rates for solutes at comparable diffusion²⁵⁷. MDO synthesis upon low osmotic stress is the major source of DAGs in *E. coli*^{232, 251}. It could consume up to 10^7 PG molecules in 30 min²⁸⁵⁻²⁸⁶, far more than the estimated $4 \cdot 10^6$ PG molecules per cell²⁸⁵, which comprise 18-22 mol% of lipids in the inner membrane²⁸⁷, of the roughly $2 \cdot 10^7$ lipids a *E. coli* cell contains²⁸⁸. The DAG concentration is under normal conditions approx. 0.6 mol%²³¹, which is around the K_M obtained for longer chain DAGs reflecting DAGs found in *E. coli*^{251, 257} (see Appendix Table 5). Surprisingly, the DAG concentration only increased slightly under these stress conditions²⁸¹ despite high amounts of MDOs and DAGs created suddenly²³³⁻²³⁴. DAG concentrations upon knock-out of *dgkA* in comparison reached up to 8 mol% and impaired proliferation²³². Together with unaltered expression levels of DgkA upon low osmotic stress²⁸¹ and a constant copy number of 15-18 DgkA molecules per cell upon various influences²⁸⁹ it is clear that enzymatic activity and substrate affinity of DgkA has been evolutionary evolved to be not rate limiting the regeneration of lipids upon LPS or stress induced MDO synthesis²⁵⁷.

Activities in the same range, though always lower than the highest reported values for DM micelles, were also observed in lyso-myristoyl-phosphatidylcholine (LMPC) micelles²⁶⁵, amphipols²⁶⁶, bicelles²⁶⁷, lipidic cubic phases of monoacylglycerols

(LCP)²⁶⁹ and liposomes^{134-135, 264, 290} (see Appendix Table 5), indicating that maximal activity in this range can be assumed *in vivo*²²⁸. However direct comparison of specific activities between studies can have its caveats as a range of absorption coefficients for DgkA were used over time by different groups as well as different ATP and lipid substrate concentrations or lipid substrates, which are not always reaching saturation in the measured environments (see Appendix Table 5).

Pilot, East and Lee performed detailed studies evaluating DgkA's activity in liposomes with respect to lipid chain length and headgroup specificity¹³⁴⁻¹³⁵. They found that DgkA's activity is highest in liposomes made of phosphatidylcholines (PC)¹³⁵, which are non-native in *E. coli*. Activity at 5 mM ATP and 10 mol% dihexanoylglycerol (DHG) is also lower for liposomes made of anionic phospholipids or PC liposomes containing these, with activity lowest in liposomes only containing phosphatidic acid, a product of DgkA¹³⁵. In addition, K_M values for dihexanoylglycerol were higher for DOPC liposomes containing 20 mol% anionic phospholipids with PA the highest but also PS as well as PI increasing the K_M above 10 mol%. Variation of length and saturation of lipid acyl chains revealed that DgkA's activity is highest when both acyl chains of PC are monounsaturated with di(C18:1)-PC e.g. dioleoyl phosphatidylcholine (DOPC) supporting highest activity and lowest K_M of DgkA in a series from 14 to 24 carbon chain long symmetric monounsaturated PCs¹³⁴.

A mixture resembling closely the lipid composition of *E. coli*²⁸⁵ showed a specific activity of 26.5 U at 25 °C, roughly half the activity observed in DOPC liposomes and is attributed to the PE content in the membrane. Activity of DgkA was low in liposomes at gel phase and PE lipids inducing the hexagonal H_{II} phase, with higher temperatures favoring hexagonal phases decreasing activity and increasing K_M compared to the lamellar phase¹³⁵. Similar results in terms of decreased v_{max} were later also obtained in activity assays performed in lipidic cubic phases of monoacylglycerols, which serve a dual purpose as membrane mimetic and lipid substrate, compared to v_{max} obtained with the same monoacylglycerols in mixed detergent micelles²⁶⁹.

Solid-state NMR studies to obtain the interfacial enzyme kinetics by simultaneous and direct observation of substrates and products via time-resolved ³¹P MAS NMR yielded a similar K_M for ATP and also^{255, 257, 265} showed substrate cooperativity but revealed a strong ATPase activity relative to the very low observed kinase activity²⁹¹. ATPase activity, not described previously for DgkA, was found to be stimulated with

increasing concentrations of lipid substrate. Experiments performed with more membrane partitioning dioctanoylglycerol (DiOctaG) compared to dibutyrylglycerol (DBG) with its short acyl chain showed however an initial lack phase for formation of inorganic phosphate. ATPase and kinase activity modes and stimulation of ATPase activity in the presence of lipid substrates could be altered or uncoupled by ATP and phosphate analogues. Addition of orthovanadate, which is a structural mimic of phosphate and is known to inhibit kinases by formation of a pentavalent transition state, abolished kinase activity but still showed ATPase activity that can be stimulated by addition of DBG. ATP γ S in contrast serves as kinase substrate as seen by formation of thiophosphatidic acid (ThioPA), but also increases ATPase activity 10-fold. The increased ATPase activity is however not stimulated by addition of DBG. Determination of v_{\max} and K_M in dependence to both substrates confirmed Badola and Sanders experiments²⁵⁷, which are in agreement with DgkA following a random-equilibrium mechanism.

I.1.6.3 Stability and Folding of DgkA

DgkA is a remarkably thermostable protein and is resistant to irreversible inactivation in native membranes up to several minutes at temperatures close to 100 °C^{229, 292}. Even in DM, DDM and DDMB detergent micelles half times of inactivation at 70 °C are in the range of several hours^{265, 272}. In stronger detergents like Triton X-100 and OG stability is lower^{229, 292}, but activators, phospholipids and long chain DAGs as well as AMP-PNP increase stability towards inactivation at room temperature²⁵⁴⁻²⁵⁵ and 50 °C²⁵⁸.

Unfolding of DgkA using SDS, a harsh denaturing detergent, is reversible and allowed to assess its thermodynamic stability in micelles²⁶³ and to create mixed trimers of wild-type and mutant DgkA monomers²⁵⁹. It was found that SDS induced unfolding appears in two cooperative transitions with the second transition attributed to transmembrane segments exhibiting a remarkable stability of 16 kcal/mol²⁶³.

High thermodynamic stability is also attributed to cause DgkA's tolerance towards mutations, especially in the first transmembrane helix²⁵⁸. Misfolding of DgkA, which is produced in inclusion bodies upon overexpression²⁶⁸ or cell-free production²⁹³, can often be avoided or corrected using reconstitutive refolding²⁶⁸. In this method reversible misfolded DgkA in kinetically trapped states or non-native oligomerization states is solubilized in harsh detergent, which is removed after mixing with lipid

containing mixed micelles allowing to successfully refold a variety of misfolded single cysteine mutants²⁶⁸. Folding appears in these cases to happen in the late stages of detergent removal during vesicle formation.

Properly folded mutants were later on used to identify active site residues and map DgkA's oligomeric interface^{264, 294}. Subsequent mutational studies could show that the risk of becoming misfolded or trapped in non-native states is higher for mutants which insert slower into liposomes or fold slower^{290, 295-297}. Similarly kinetic and thermodynamic stability is correlated with folding efficiency as mutations, which destabilize DgkA, are causing reduced folding efficiency²⁹⁶⁻²⁹⁷. Aggregation prone mutants, which are not destabilized, are interestingly all found at or near the active site and are often produced at low levels²⁶⁴. However, irreversible misfolding has been shown to occur on a monomer level independent of aggregation and prior to insertion into membranes²⁹⁷.

A kinetic study on DgkA's insertion into lipid vesicles from a partially denatured state found that misfolding is faster than insertion into the membrane and the likely cause of aggregation, which reduces the amounts of inserted DgkA²⁹⁸. Rate and efficiency of folding and insertion into DOPC liposomes is also dependent on lipid composition. It is increased in presence of DOPG and decreased in lyso-PC, which is attributed to changes in membrane curvature stress and differences in lateral pressure of the headgroup regions²⁹⁹. Insertion and refolding into lipidic cubic phases of monoolein from a partially denatured state using chaotrophic compounds was highly efficient as it yielded similar activities than DgkA reconstituted into the LCP from detergent micelles. It also did not lead to misfolding as renatured DgkA exhibited the same structure¹⁷⁹.

Certain mutations, constituting roughly 10% of purified mutants, on the other hand increased thermostability²⁵⁹. Combination of mutations to enhance thermostability led to two impressively thermostable mutants, which were later on crystallized: a quadruple-mutant $\Delta 4$ -DgkA (I53C, I70L, M96L, V107D)²⁶⁰ and a septuple-mutant $\Delta 7$ -DgkA (A41C, C46A, I53V, I70L, M96L, V107D, C113A), which has wild-type like specific activity, but slightly lower thermostability than the quadruple mutant³⁰⁰. Both mutants exhibit nearly unaltered activity in DM after 10 min at 95 °C with half times in the range of hours, whereas activity is completely abolished at 95 °C for wild-type DgkA³⁰⁰.

I.1.6.4 Structure and mechanism of DgkA

DgkA, a homotrimer²⁴⁶, is with 43 kDa the smallest known kinase²²⁸ as its monomeric unit exhibits only 121 residues²⁴⁷. Its topology had been explored by protein fusion³⁰¹ and FTIR²⁶², with thiol cross-linking²⁹⁴ pointing to three transmembrane helices per monomer and a N-terminal amphipathic helix. A proposed second amphipathic helix between the first and second transmembrane helices was however not confirmed by detailed topology analysis and high-resolution structures. Mutational studies soon after first topology analysis using monomer mixing and activity assays revealed that DgkA exhibits three active sites, which are shared between subunits²⁵⁹.

Its thermostability and size also made it a model membrane protein to explore sample preparation and detergents for their feasibility to provide a good membrane mimetic for liquid-state NMR applications^{246, 302-303}. Despite the progress in backbone assignment³⁰³ and later on calculation of backbone structure based on restraints from residual dipolar coupling experiments and paramagnetic relaxation enhancement as well as contentious³⁰⁰ disulfide mapping²⁶⁴ and substrate as well as product titrations, results from liquid-state NMR unfortunately were often ambiguous. Signals arising from YodA, an impurity, were first assumed to represent a conformational specific misfolded state²⁷⁶ and also the calculated structure of the transmembrane part with a domain-swapped architecture²⁶⁴ is neither in agreement with layered packing seen in crystal structures of DgkA³⁰⁰ nor the topology determined by solid-state NMR experiments³⁰⁴⁻³⁰⁵. First MAS solid-state NMR experiments confirmed disorder of the N-terminal polyhistidine-tag used for affinity purification²⁶² and showed alterations in backbone mobility in different lipid phases using selective labelling³⁰⁶ 2D correlation spectra on microcrystals demonstrated its possibility for assignment. Solid-state NMR studies later on yielded assignment of approximately 80% of its residues and together with H/D exchange experiments allowed a detailed topology analysis of a thermostable triple mutant (I53C, I70L, V107D), which is except for the third transmembrane helix in good agreement with the crystal structure³⁰⁴. However, variances in helix and cytoplasmic loop length are also observed between crystal structures of wild-type DgkA and two thermostable mutants³⁰⁰ and hint together with high B-factors to a high plasticity in this area.

Highly diffracting crystals of DgkA and its thermostable mutants with bound MAG were initially obtained in a shorter acyl chain MAG than monoolein³⁰⁰. DgkA was still active in these conditions and is thought to resemble a native conformation. As

ATP binding according to a solid-state NMR study only leads to small chemical shift changes along the lipid binding interface³⁰⁷, crystallization and a high-resolution structure of a ternary complex of monoolein and AMP-PCP bound in one active site achieved later³⁰⁸ closely resemble the initial crystal structure. Later on in a detailed solid-state NMR analysis by our group on the global response of substrate binding using 2D and 3D MAS NMR experiments it was found that AMP-PCP can most likely occupy all three binding sites of the trimer simultaneously as no peak splitting was observed³⁰⁵. Furthermore, the obtained data suggests that DgkA adopts a symmetric conformation in the apo state as well as substrate bound states under saturating conditions. Nucleotide substrate binding not only induced extensive chemical shift perturbations in DgkA at the cytosolic part but also at large parts of the transmembrane helices. The presence of diacylglycerol on the opposite lead only to minor chemical shift perturbations compared to the apo state and none in presence of AMP-PCP. These results indicate that nucleotide binding might induce positive heteroallostery, which is supported by kinetic studies that indicate enhanced affinity for lipid substrate in presence of a nucleotide substrate²⁵⁷.

High-resolution structures also detailed the structure of the shared active site being formed by the transmembrane helices of one subunit and the amphipathic helix of an adjacent subunit (Figure 20a). The ternary complex allowed to pinpoint functionally important protein and substrate interactions on a structural basis, previously explored in great detail by mutational studies and led to the proposal of a detailed catalytic mechanism via a pentahedral transition state supported by molecular dynamics (MD) simulations³⁰⁸ (Figure 20b). The rate-limiting step of the phosphoryl transfer, as explored by density functional theory (DFT) simulations, was thereby found to be not proton abstraction from the lipid substrate but phosphate cleavage. Further insight into alternate conformations of critical glutamate (Glu) residues on a molecular level supporting molecular dynamics (MD) simulations was gained in the same study via serial femtosecond crystallography at room temperature using the Linac Coherent Light Source (LCLS) a free electron laser at the SLAC National Accelerator Laboratory. Glu69, responsible for proton abstraction as well as Glu34, which increases the pK_a of Glu69 by H-bond formation making it a stronger base, and Glu76, which partakes in the coordination of divalent ions at the active site, exhibited two alternative conformations, which can be attributed to different protonation states. It is thought that deprotonation of Glu34 upon substrate binding leads to the observed

conformational rearrangement of Glu69 extending deeper into the membrane and promotes proton abstraction of the lipid substrate hydroxyl group by Glu69. Nucleophilic attack of the alkoxide creates a pentahedral transition state²⁷⁴ with the nucleotide, which could be stabilized via H-bond interaction between protonated Glu69 and Glu34. Upon collapse of the transition state, forming ADP and phosphorylated lipid, Glu69 is deprotonated by Glu34 and Glu34 returns to resting state conformation forming a H-bond with Glu69. The phosphorylated lipid is expected to be released through the opening between the aliphatic helix and first transmembrane helix and may be facilitated by electrostatic push by Glu69 and Glu76 and pull by arginine 9 (Arg9) and lysine 12 (Lys12). ADP is opposite to ATP in MD simulations positional unstable in the active site and dissociates as well.

At last structural comparison with other kinases like protein kinase A, which exhibit a similar mechanism, revealed a very similar chemical architecture of the active site despite being evolutionary unrelated and essentially not exhibiting any structural similarities³⁰⁸.

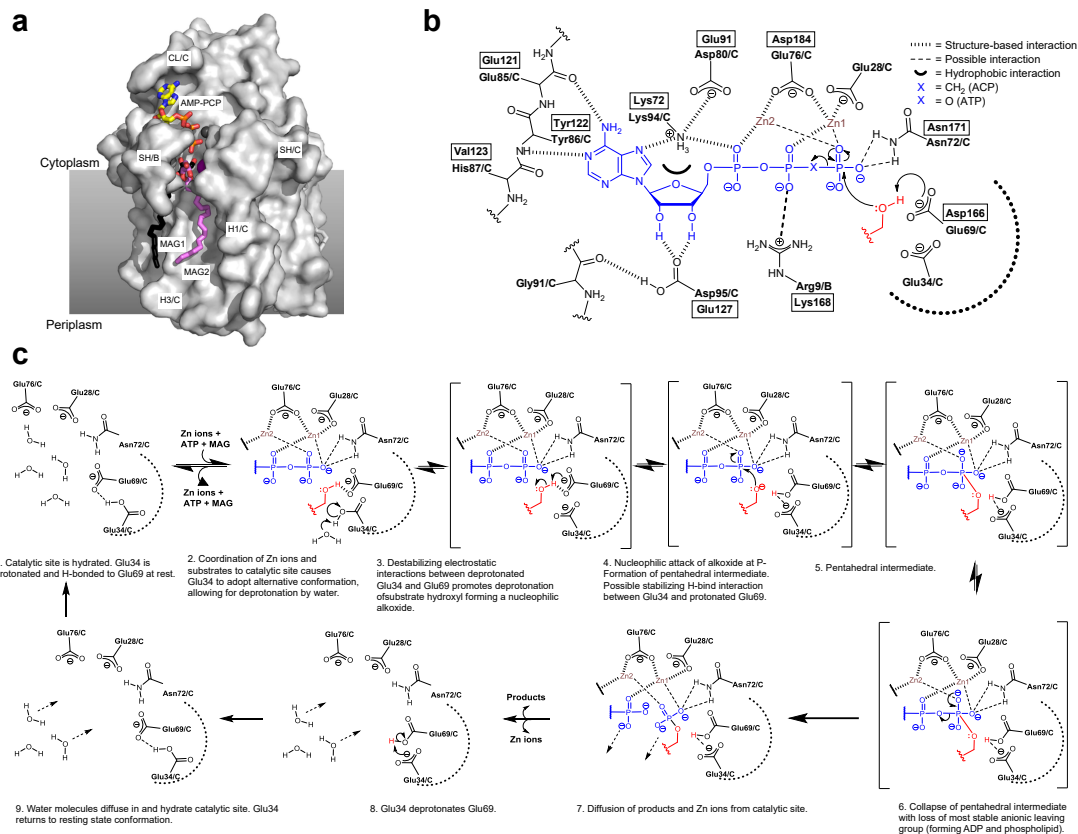


Figure 20: Structure and mechanism of DgkA according to Li et al.³⁰⁸ **a)** Structure of the $\Delta 4$ -DgkA ternary complex with AMP-PCP and monoolein bound in one active site. **b)** Two dimensional representation of the active and substrate-binding site of DgkA. Hashed bonds indicate hydrogen bond and ionic interactions with AMP-PCP and monoolein. Dashed bonds indicate interactions that are likely and possible, but that are not supported by structure data. Hydrophobic interactions are highlighted as a black semicircle. Residues with numbers in boxes indicate structurally equivalent residues in the cAMP-dependent protein kinase A according to PDB entry: 1ATP. **c)** Proposed mechanism of the phosphoryl transfer reaction. Figures modified from Li et al.³⁰⁸.

I.1.7 Solid-state NMR spectroscopy

I.1.7.1 Theoretical background

Nuclear spins are influenced by their environment. Their internal interactions can be separated into chemical shielding (chemical shift, CS), dipolar coupling (D), J -coupling or indirect nuclear spin-spin coupling (J) and quadrupolar interactions (Q). The interaction Hamiltonian of a nuclear spin is therefore defined as

$$\hat{H}_{int} = \hat{H}_{CS} + \hat{H}_D + \hat{H}_J + \hat{H}_Q \quad (12)$$

All of these interactions are tensor quantities and thus anisotropic. While J -couplings and chemical shielding are reduced in fast tumbling molecules to an isotropic scalar term, dipolar couplings and quadrupolar interactions are averaged out. Quadrupolar interactions can also only be observed in nuclei with spins greater than one-half that have non-spherical charge distribution.

I.1.7.1.1 Chemical shielding and dipolar coupling

Chemical shielding depends on the external magnetic field (B_0) applied that induces currents in electrons in the molecular orbitals in turn creating local magnetic fields. Diamagnetic and paramagnetic influences such as ring currents in aromatic residues, solvent environment and local geometry including binding partners, bond lengths and angles, affect electron distribution. As those effects lead to different local magnetic fields, nuclei exhibit different chemical shielding. The chemical shift, the resonance frequency of a nucleus relative to a standard compound in a magnetic field, therefore yields information on the local chemical environment a nucleus experiences.

The dependence of the chemical shift on the orientation is termed chemical shift anisotropy (CSA) representing a second rank tensor that can be described by the principal components δ_{xx} , δ_{yy} and δ_{zz} ³⁰⁹. If a molecule's isotropic tumbling is fast enough, the chemical shift tensor is reduced to its average value, the isotropic average (Figure 18):

$$\delta_{iso} = \frac{1}{3} (\delta_{xx} + \delta_{yy} + \delta_{zz}) \quad (13)$$

In the Haeberlen notation³¹⁰ the principal components are defined by:

$$|\delta_{zz} - \delta_{iso}| \geq |\delta_{xx} - \delta_{iso}| \geq |\delta_{yy} - \delta_{iso}| \quad (14)$$

Thus, δ_{zz} is the component farthest from and δ_{yy} closest to the isotropic value leading to two possible orders: $\delta_{zz} \geq \delta_{yy} \geq \delta_{xx}$ or $\delta_{xx} \geq \delta_{yy} \geq \delta_{zz}$ depending on the chemical system.

Another nomenclature that does not rely on knowledge of the isotropic average, allowing to accurately enumerate systems that may exhibit anisotropic motional averaging is the Mehring notation³¹¹, which uses numerical subscripts and numbers the components in order of increasing shielding:

$$\delta_{11} \leq \delta_{22} \leq \delta_{33} \quad (15)$$

Next to the isotropic average two other parameters of the chemical shift are thereby of interest³⁰⁹. Its shielding anisotropy (ζ) or ($\Delta\delta$), which are related by $\Delta\delta = 3/2 \zeta$, characterizes the width of the spectrum and its shielding asymmetry (η), which characterizes the shape or symmetry of the spectrum. They are expressed in the Haeberlen notation as follows:

$$\zeta = \delta_{ZZ} - \delta_{iso} \quad (16)$$

$$\Delta\delta = \delta_{ZZ} - \frac{1}{2}(\delta_{xx} + \delta_{yy}) \quad (17)$$

$$\eta = \frac{\delta_{YY} - \delta_{XX}}{\zeta} \quad (18)$$

Shielding anisotropy can be positive ($\delta_{zz} > \delta_{iso}$), negative ($\delta_{zz} < \delta_{iso}$) or zero. Shielding asymmetry can range from zero to one. It is zero for an axial symmetric tensor ($\delta_{xx} = \delta_{yy}$) and one in the case of $\delta_{yy} = \frac{1}{2}(\delta_{xx} + \delta_{zz}) = \delta_{iso}$. If the molecule rotates around an axis with a rate larger than ζ , the anisotropic interactions are cancelled leading to an axial symmetric tensor and the asymmetry parameter becomes zero (Figure 15).

In the Mehring notation the relationships for anisotropy and asymmetry are more difficult to express as they depend on the position of δ_{22} between δ_{11} and δ_{33} and can be replaced by span (Ω) and skew (κ)³¹²:

$$\Omega = \delta_{11} - \delta_{33} \quad (19)$$

$$\kappa = \frac{3(\delta_{22} - \delta_{iso})}{\Omega} \quad (20)$$

However, shielding anisotropy and asymmetry are recommended over span and skew by IUPAC³⁰⁹.

The Hamiltonian of the orientation-dependent chemical shift with dependence to the laboratory frame defined by B_0 can also be expressed using Euler angles by:

$$\hat{H}_{CS} = -\gamma \cdot I_z \left(\delta_{iso} + \frac{1}{2} \zeta (3 \cdot \cos^2 \beta - 1 - \eta \cdot \sin^2 \beta \cdot \cos 2\alpha) \right) \cdot B_0 \quad (21)$$

Another anisotropic interaction is the dipolar coupling. The Hamiltonians for the homo and heteronuclear dipolar coupling are:

$$\hat{H}_{IS} = -d_{IS} \cdot \frac{1}{2} (3\cos^2\beta_{IS} - 1) (3 \cdot I_Z S_Z - I \cdot S) \quad (22)$$

$$\hat{H}_{IS} = -d_{IS} \cdot \frac{1}{2} (3\cos^2\beta_{IS} - 1) \cdot 2 \cdot I_Z S_Z \quad (23)$$

The dipolar coupling constant (d_{IS}) characterizes the dipolar interaction through space between two spins (I, S) and can be defined as:

$$d_{IS}(r_{IS}) = \frac{\gamma_I \gamma_S \mu_0 \hbar}{4\pi r_{IS}^3} \quad (24)$$

Dipolar coupling is thereby dependent on the distance between the spins (r_{IS}), the angle of their internuclear vector with respect to an external magnetic field (β_{IS}) as well as the gyromagnetic ratios (γ) of the coupling spins. Angular dependence of the dipolar coupling and probability distribution of orientation lead in powders to a so called Pake doublet³¹³.

I.1.7.1.2 Magic angle spinning (MAS)

If these anisotropic contributions are not averaged out by fast isotropic motion they result in strong line broadening that leads to substantial signal overlap, leading to a loss of resolution. These interactions can be however also averaged out by fast sample spinning. If the spinning is faster than chemical shift anisotropy, an axial symmetric tensor is created along the spinning axis and the asymmetry parameter (η) becomes zero thereby reducing the chemical shift anisotropy to an axially symmetric tensor.

If the sample is spun faster than the anisotropic interactions around the so-called magic angle, the angle of the space diagonal of a cube and any of its connecting edges, approximately 54.74° with respect to the external magnetic field the angles of these interactions are projected onto this axis. If the angle of these interactions is the magic angle, the term $(3\cos^2\beta_{IS} - 1)$ becomes zero and dipolar couplings as well as the CSA are cancelled or reduced to its isotropic average.

If sample spinning is not fast enough, spinning sidebands (SSBs) appear separated by the spinning frequency from the centerband. At low spinning speeds these can be used to calculate chemical shift tensors. Especially strong proton dipolar couplings often cannot be eliminated completely by magic angle sample spinning alone and would lead to line broadening of centerband and spinning sidebands. In case of heteronuclear

detection, decoupling allows to efficiently eliminate broadening caused by dipolar couplings.

I.1.7.1.3 Cross polarization

High abundance as well as a high natural abundance and a high gyromagnetic ratio are two advantages of ^1H for NMR. However, in slowly tumbling molecules the strong dipolar network of the highly abundant ^1H spins would require fast MAS (>100 kHz) to be eliminated and therefore leads to severe line broadening at moderate MAS frequencies (10-20 kHz). Hence, more sparse and less strongly dipolar coupled heteronuclei like ^{13}C and ^{15}N are often detected. Their smaller gyromagnetic ratio however leads to lower bulk magnetization and thus weaker signal intensities.

To increase their signal intensity, magnetization can be transferred from protons or other nuclei with a higher gyromagnetic ratio via cross polarization (CP). Magnetization is thereby exchanged between two spins (I , S) by simultaneous application of two radio frequency fields, B_1 , at the respective resonance frequencies to fulfill the Hartmann-Hahn matching condition:

$$\gamma^I B_1^I = \gamma^S B_1^S \quad (25)$$

For the static and magic angle spinning case this results in:

$$\text{static: } \omega_1^I = \omega_1^S \quad (26)$$

$$\text{MAS: } \omega_1^I = \omega_1^S \pm n\omega_{rot} \quad (27)$$

Thereby allowing dipolar interaction between the two spins and polarization transfer. Cross polarization enhances the signal of the spin with lower gyromagnetic ratio (S) relative to the difference of gyromagnetic ratios:

$$\frac{S}{N} \propto \frac{\gamma_I}{\gamma_S} \quad (28)$$

As in a simple CP experiment the created net X magnetization on S originates from X magnetization via a 90° pulse on the spin with a high gyromagnetic ratio (I), the required recycle delay is dependent on T_1 of I , which in case of protons is usually shorter than for heteronuclei, allowing to also acquire more transients per time.

I.1.7.2 Multi-dimensional NMR experiments

To resolve signal overlap from spectral crowding the NMR signals can be recorded as a function of several time domains, during which magnetization can evolve. This allows to separate signals in several dimensions and gain for example information

about spin correlations. A simple 2D experiment consists of a preparation, evolution (t_1), mixing and detection period (t_2) (Figure 21). During preparation usually transverse magnetization is generated, which evolves in the time period t_1 experiencing various nuclear spin interactions. During the mixing time usually spin communication via cross relaxation, exchange or spin coupling is introduced via pulse sequences e.g. dipolar recoupling sequences under MAS. The t_1 modulated signals of the direct dimension are then detected during t_2 . Fourier transformation of the two-dimensional set of time domain information in both dimensions allows to generate a two-dimensional spectrum containing frequency information in both dimensions.

Homonuclear and heteronuclear correlation experiments allowed to gain insight into complex biomacromolecules such as peptides, proteins or nucleic acids via NMR and are now key tools used in biomolecular NMR³¹⁴⁻³¹⁶.

I.1.7.3 Dipolar coupling based experiments under MAS conditions

Dipolar coupling based experiments can be applied under MAS conditions to study molecules like membrane proteins that do not exhibit sufficient motion to cancel dipolar interactions.

I.1.7.3.1 Homonuclear correlation based on proton driven spin diffusion

One example of 2D correlation spectroscopy used herein for protein solid-state NMR is a homonuclear through space correlation experiment based on proton driven spin diffusion (PDSD)³¹⁷. Spin diffusion allows homonuclear transfer of magnetization usually between ^{13}C - or ^{15}N -nuclei through space driven by the proton spin network³¹⁸. After generation of transverse magnetization on heteronuclei, proton decoupling is applied and spins evolve under influence of their chemical environment according to the time t_1 (Figure 21). Thereafter, magnetization is flipped to the z-axis. Without proton decoupling spin diffusion of the heteronuclei by flip-flop interactions takes place. Due to line broadening from dipolar ^1H - ^{13}C and ^1H - ^1H coupling, nutation frequencies of ^{13}C spin pairs with different chemical shifts can overlap, allowing proton driven spin diffusion between the nuclei. As this correlation is proportional to the distance of two spins by r^{-6} , mixing times determine the distance of magnetization transfer. At short mixing times (10 – 20 ms), the magnetization is mostly transferred between neighboring atoms, leading to intra-residue contacts. At longer mixing times (100 ms - 3 s) magnetization can be transferred further and more distant interactions between different residues can be observed after flipping magnetization back into the

xy-plane for detection in t_2 ³¹⁹. If spin diffusion occurs, cross peaks corresponding to the chemical shifts of both nuclei can be observed in the 2D spectrum, whereas magnetization that has not been transferred is projected onto the diagonal at the respective chemical shifts.

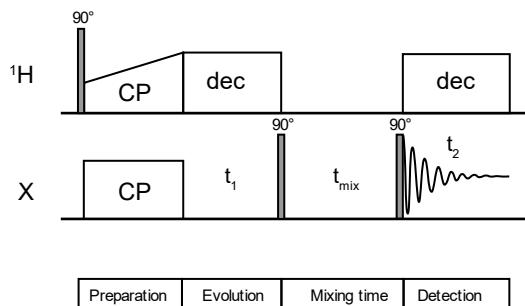


Figure 21: Pulse sequence of a 2D PDSM experiment for homonuclear correlation of heteronuclei in a densely coupled proton network via proton driven spin diffusion.

I.1.7.3.2 Heteronuclear correlation (HETCOR)

I.1.7.3.2.1 Double cross polarization experiments

To correlate for example ^{13}C and ^{15}N nuclei, magnetization is often transferred via two cross polarization steps from ^1H to ^{15}N in the preparation phase to ^{13}C after evolution of ^{15}N magnetization³²⁰. As the second CP transfer can be band-selective due to pronounced differences of chemical shifts of ^{13}C nuclei C-N correlations can be performed in peptides and proteins between the amide to the neighboring $\text{C}\alpha$ (NCA) or CO (NCO)³¹⁹. NCA experiments correlate the ^{15}N chemical shift with the ^{13}C chemical shift of $\text{C}\alpha$ of the same residue, whereas in a NCO experiment the ^{15}N chemical shift is correlated with the chemical shift of the CO group of the preceding residue. To allow matching of the Hartmann-Hahn condition and efficient cross polarization of nuclei that exhibit different chemical shifts not only the frequency of the B_1 field and contact time is optimized before but also the strength of the applied B_1 field is ramped during the cross polarization step.

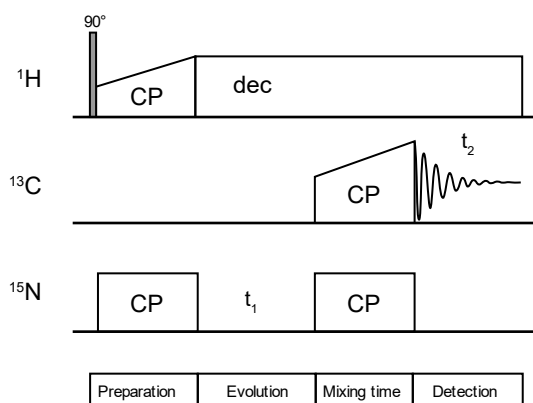


Figure 22: Pulse sequence of a 2D NCO or NCA double cross polarization experiment. Depending on the band-selective second CP magnetization is transferred between N-CO or N-C α .

I.1.7.3.2.2 Transferred echo double resonance experiments

The transferred echo double resonance (TEDOR) experiment recouples heteronuclear dipolar couplings under MAS. It evolved from the rotational echo double resonance (REDOR)³²¹ experiment that is used to obtain distances via dipolar couplings in MAS experiments.

By applying rotor period synchronized 180° pulses on a heteronucleus the heteronuclear dipolar coupling to other spins is not averaged out during MAS as flipping of the magnetization changes the sign of the Hamiltonian of the heteronuclear coupling. In addition to this 180° pulse train a 180° pulse at the center of the REDOR mixing time is applied to refocus the magnetization on the heteronucleus who had been polarized via ^1H cross polarization in the preparation phase. To determine intermolecular distances REDOR experiments are performed with increasing numbers of pulses in the 180° pulse train and compared to reference spectra (S_0) that were performed at the same mixing times but in absence of the 180° pulse train to determine the dipolar coupling³¹⁹.

TEDOR experiments are not used to obtain distances, but provide spectra of dipolar correlations that could be recoupled. To obtain a 2D correlation spectrum between two heteronuclei (X, Y), an evolution period (t_1) is introduced between two REDOR sequences (each $t_{\text{mix}}/2$) (Figure 23). After the first REDOR sequence that recoupled dipolar interactions 90° pulses on both channels are applied with a time-delay defined by the z-filter period (Δ). This results in a coherence transfer to the other heteronucleus (Y) that evolves during t_1 according to its chemical environment before a pair of 90° pulses transfers the spin coherence back onto X followed by the second TEDOR sequence, the second part of the z-filter and acquisition of the signal in t_2 .

The z-filter is applied for ^{13}C nuclei to compensate for homonuclear J -couplings, which could affect weak dipolar couplings by causing pseudo cross peaks and phase twisted signals³²². As the experiment is based on dipolar couplings, the cross peak intensity depends on the distance and degree of dipolar coupling. It also depends on the length of the used mixing time, with long mixing times leading to observation of more long-range dipolar couplings.

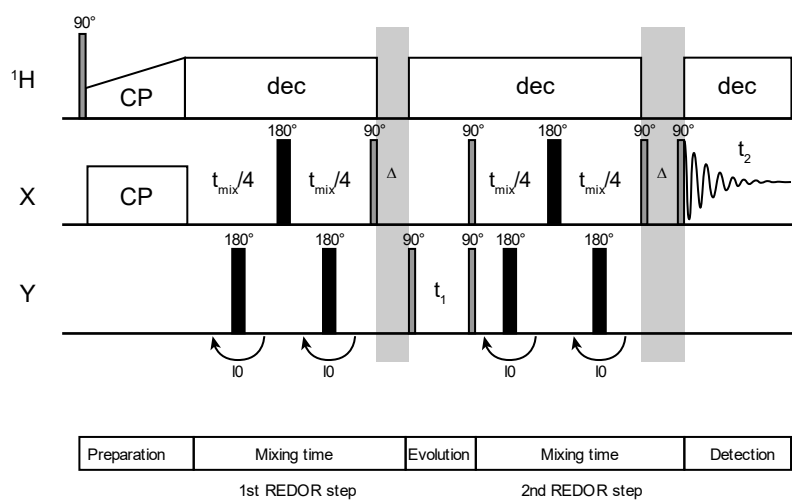


Figure 23: Pulse sequence of a z-filtered TEDOR (ZF-TEDOR) experiment³²². Δ marks the z-filter periods. l_0 is the loop number of rotor period synchronized 180° pulses applied during $t_{\text{mix}}/4$.

I.1.8 Aim and scope

In this chapter the uncaging approach's practicability for solid-state NMR will be evaluated in different membrane environments including a lipidic cubic phase to trigger biochemical reactions on the example of the interfacial membrane enzyme DgkA. Therefore, release of a caged nucleotide and a caged lipid substrate *in situ* to initiate enzymatic activity (Figure 24) is aspired.

Especially uncaging a non-miscible lipid substrate to trigger DgkA's kinase reaction will be further used to point out unique advantages the uncaging approach could offer for a variety of solid-state NMR applications. Construction, testing and comparison of a new illumination setup based on LED light sources to alternative illumination variants to achieve *in situ* uncaging is demonstrating the challenges for sample illumination under MAS NMR conditions that are overcome as well as the approach's feasibility thereby expanding the toolkit for solid-state NMR.

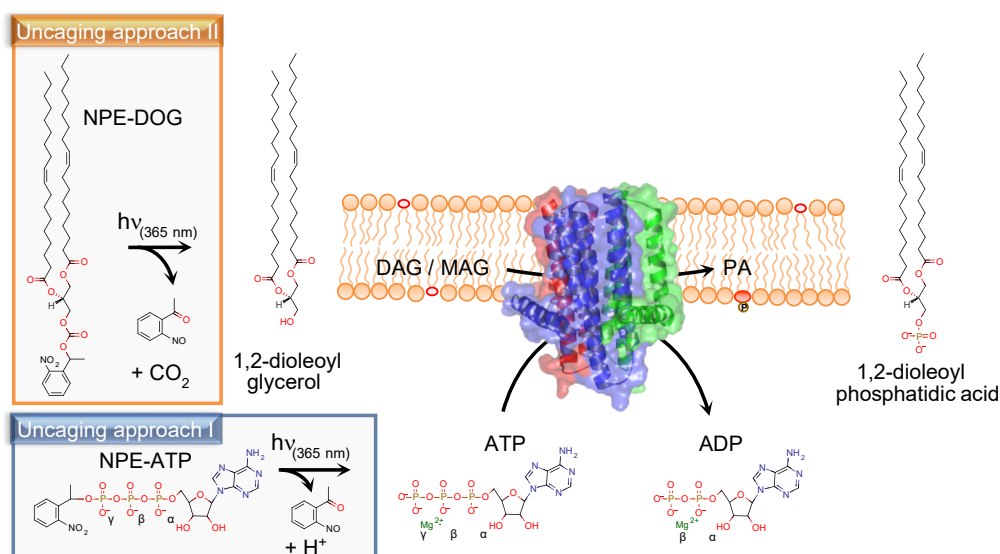


Figure 24: Caged compounds and applied uncaging approaches to trigger DgkA's enzymatic activity in various membrane mimetics.

A second focus whilst establishing the uncaging approach in solid-state NMR had been placed on utilization of optical transparent membrane mimetics to allow efficient illumination under MAS conditions. Therefore, the optically transparent LCP of monoolein is characterized with respect to its behavior and its general applicability for protein solid-state NMR. As LCPs are not commonly used in biological solid-state NMR despite their wide use in membrane protein crystallography, potential advantages of this porous bicontinuous membrane mimetic are explored. Especially its potentially high accessibility for solutes and membrane components compared to liposomes as

well as the absence of phosphorous signals where seen as advantageous. These aspects are subsequently explored after establishing LCP preparation and sample handling techniques and initial characterization under MAS conditions by performing ^{31}P real-time experiments following the enzymatic activity of DgkA and first DNP measurements utilizing the ^{31}P dimension to detect protein nucleotide contacts.

As its results would give valuable experimental information for theories on protein crystal formation in LCPs, experimental information on the behavior of membrane proteins in a LCP is highly desirable. Therefore, it was also aimed to acquire protein spectra of DgkA in the cubic phase to not only demonstrate its possibility but also gain first insights via NMR into dynamics and potential structural alterations of a multispan transmembrane protein in this high curvature membrane mimetic. These experiments should demonstrate that solid-state NMR is a useful non-invasive tool that can give highly valuable information on processes and dynamics within porous materials and may yield valuable information for enzyme immobilization and mechanisms of crystal formation. Its strength as a label-free and non-invasive method to observe dynamics in membranes and address specific details in a variety of fields in a collaborative environment is also highlighted in the second chapter of this thesis providing valuable information on the influence of alterations of lipid composition on membrane fluidity in a cellular and disease relevant context.

The wealth of information gained about DgkA's enzymatic activity from ^{31}P real-time NMR experiments performed under various conditions whilst exploring the cubic phase and uncaging approach as tools for solid-state NMR has also been aimed to contribute to a more detailed view on previously observed basal ATPase activity. Together with additional kinetic data from biochemical assays in presence and absence of lipid substrates and activators, these allow to estimate the *in vivo* relevance of observed ATP hydrolysis activity *in vitro* and give further direct evidence to DgkA's random equilibrium mode of substrate binding.

I.2 Materials and Methods

I.2.1 Molecular biological methods

I.2.1.1 Site-directed mutagenesis

Primer for site directed mutagenesis were designed manually. 18 base pairs in 3' direction upfront and ten base pairs in 5' direction of the mutagenesis site were chosen for primer construction. The primer were prolonged or shortened to start and end with a guanine or cytidine base. In addition a melting temperature of the primer between 56 °C and 64 °C was pursued. The melting temperature (T_m) was calculated by the number of guanine and cytidine bases as a 4 °C increment in T_m and a 2 °C increment for adenosine and thymidine bases. The resulting primer pair is listed in the Appendix. The thermal cycling reaction mixture was 20 μ l. The composition of the PCR mix and the used thermal cycling scheme are listed in Table 2 and Table 3. After thermal cycling the template was digested with 10 U DpnI for 2 hours at 37 °C. Followed by heat inactivation at 80 °C for 20 minutes and subsequent transformation of 5 μ l reaction mixture into competent *E. coli* cells.

Table 2: Composition of thermal cycling mix for site directed mutagenesis.

| | |
|--------------------|-----------------|
| Phusion buffer | 1x |
| dNTPs | 200 μ M |
| Hybrid Primer for | 1 μ M |
| Hybrid Primer rev | 1 μ M |
| Template | 70 ng |
| Phusion polymerase | 0.02 U/ μ l |

Table 3: Thermal cycling scheme used for site directed mutagenesis.

| Cycle | Temperature | Time |
|-------|-------------|-----------------|
| 1x | 95 °C | 60 s |
| 18x | 95 °C | 60 s |
| | 63 °C | 60 s |
| | 72 °C | 420 s (60 s/kB) |
| 1x | 72 °C | 420 s |

I.2.1.2 Restriction-site free cloning

The method was developed to insert any sequence at any desired position of a plasmid without the use of restriction enzymes. The procedure contains two polymerase chain

reaction (PCR) steps. The first PCR generates the insert, which serves as a megaprimer in the second PCR to elongate the target plasmid. The first PCR was performed in a volume of 50 μ l and the generated megaprimer were purified by gel electrophoresis. After the second PCR with 20 μ l reaction volume the template was digested with 10 U DpnI for 2 hours at 37 °C. After heat inactivation at 80 °C for 20 minutes 5 μ l of the reaction mixture were transformed into competent *E. coli* cells. The composition of the restriction free PCR mixes and the used PCR cycling scheme are listed in Table 4 and Table 5.

Table 4: Composition of PCR mix for restriction free cloning PCRs.

| Primary PCR | | Secondary PCR | |
|--------------------|-----------------|--------------------|-----------------|
| Phusion buffer | 1x | Phusion buffer | 1x |
| dNTPs | 200 μ M | dNTPs | 200 μ M |
| Hybrid Primer for | 0.5 μ M | Megaprimer | 1200 fmol |
| Hybrid Primer rev | 0.5 μ M | Template | 60 fmol |
| Template | 25 ng | Phusion polymerase | 0.02 U/ μ l |
| Phusion polymerase | 0.02 U/ μ l | | |

Table 5: PCR cycling scheme used for restriction free cloning.

| Primary PCR | | | Secondary PCR | | |
|-------------|-------------|----------------|---------------|-------------|-----------------|
| Cycle | Temperature | Time | Cycle | Temperature | Time |
| 1x | 95 °C | 60 s | 1x | 95 °C | 90 s |
| 35x | 95 °C | 15 s | 30x | 95 °C | 30 s |
| | 60 °C | 30 s | | 60 °C | 60 s |
| | 72 °C | 30 s (25 s/kB) | | 72 °C | 362 s (60 s/kB) |
| 1x | 72 °C | 420 s | 1x | 72 °C | 420 s |

Primers used for restriction free cloning were designed with at least 30 base pair overlap to the target vectors. The length of the primer pair used was also adjusted to achieve a similar melting temperature. The used primer pair is listed in Appendix IV.1.

I.2.1.3 Agarose gel electrophoresis

Agarose gel electrophoresis for the purification of DNA was performed with a 1% agarose gel in TAE buffer at 80 V for 40 min on an electrophoresis chamber built at the Max Planck Institute for Biophysics. The DNA was subsequently extracted from gel slices via the Qiagen gel extraction kit.

I.2.1.4 Transformation

Transformation of competent *E. coli* cells was performed via heat shock. 1-5 μ l ligation mix and 25 μ l of chemically competent DH5 α or C43(DE3) *E. coli* cells for protein production were heated to 42 °C for 35 s (Thermomixer compact 5350, Eppendorf or MHL 23, HLC BioTech). After the heat shock, the cells were incubated for 5 min on ice and then for 1 h in 750 μ l LB medium at 37 °C and 220 rpm (Thermomixer compact 5350, Eppendorf or MHL 23, HLC BioTech). They were subsequently plated onto ampicillin (100 μ g/ml) containing LB agar plates and incubated overnight at 37 °C for colony growth and selection.

I.2.2 Biochemical methods

I.2.2.1 Production, purification and reconstitution of DgkA

Production in LB and purification of DgkA were performed as described previously²⁶⁹ with minor changes. Production of DgkA in M9 medium for uniform ¹³C and ¹⁵N isotope labelling were performed as described by Möbius³⁰⁷ with minor changes.

I.2.2.1.1 Production of DgkA

C43(DE3) freshly transformed cells carrying the DgkA pET-19b plasmid were grown for 16 h at 27 °C and 220 rpm in 100 ml LB with 100 mg/l ampicillin. Cells were transferred 1:100 to 700 ml/2 l flask LB medium and grown at 37 °C and 220 rpm till an OD₆₀₀ of 0.6. Cells were induced with 1 mM IPTG, grown at 37 °C and 220 rpm for 3 h and harvested at 3,000 g for 15 min (Rotor: JLA-10.500; Centrifuge: Avanti J-E, Beckman).

I.2.2.1.2 Production of U¹³C¹⁵N labelled DgkA

For uniformly ¹³C¹⁵N labelled DgkA, C43(DE3) freshly transformed cells carrying the DgkA pET-19b plasmid were grown for 16 h at 27 °C and 220 rpm in 100 ml LB. Cells were transferred 1:100 to 700 ml/2 l flask M9 medium. M9 medium was prepared as follows: 6 g/l Na₂HPO₄, 3 g/l KH₂PO₄, 1 g/l NaCl and 1 g/l Ammonium-¹⁵N chloride were weighed and dissolved as 5x stock and pH adjusted to 7.0. The stock was distributed across flasks and H₂O added. Stocks of 0.1 M CaCl₂ (1000x), 1 M MgSO₄ (1000x) and 40% (w/v) (100x) D-glucose-¹³C₆ are autoclaved separately. The vitamin mix^{303, 323} stock (50x) was prepared as follows: 1.5 g of vitamin tablets (Centrum, Pfizer Consumer Healthcare) were grinded and dissolved in 20 ml sterile, deionized H₂O by vortexing for 5 min. The resulting suspension was

separated by centrifugation at 8000 g for 20 min at 4 °C. The supernatant was filter-sterilized (Rotilabo syringe filters CME sterile 0.22 µm pore size, Cat. KH54.1, Carl Roth) and stored at -20 °C. After autoclaving CaCl₂, MgSO₄, glucose, vitamin mix and ampicillin (100 mg/l) were added.

Cells in M9 medium were grown at 37 °C and 220 rpm till an OD₆₀₀ of 0.8. Then, cells were induced with 0.2 g/l IPTG, grown at 27 °C and 220 rpm for 16 h. Cells were harvested at 3,000 g for 15 min (Rotor: JLA-10.500; Centrifuge: Avanti J-E, Beckman).

I.2.2.1.3 Purification of DgkA

The cell pellet was resuspended with 5-10 ml buffer A (50 mM HEPES pH 7.5, 300 mM NaCl) per 500 ml medium and stored at -80 °C or directly used for purification. The resuspended cell pellet was diluted in 100 ml lysis buffer (50 mM HEPES pH 7.5, 300 mM NaCl, 5 mM MgCl₂, 2 pills protease inhibitor per liter cell medium, 0.2 mM TCEP, 0.2 mg/ml lysozyme, 0.05 mg/ml DNaseI) per liter cell medium and incubate with gentle stirring at room temperature for 30 min.

The suspension was cooled on ice and cells were broken using a probe sonicator for 10 min with a 0.3 s on - 0.7 s off duty cycle and a power setting of 40% (Model HD2200, Probe KE76, Bandelin). Lysate was mixed by gentle shaking every 2:30 min. The crude membrane suspension was then solubilized with 3% (w/v) octyl-β-D-glucopyranosid (OG) added as powder to the solution under slow stirring for 30 min on ice. The solubilisate was centrifuged in 50 ml centrifuge beakers (Cat. 357002 Beckman) at 10,000 rpm (10,500 g) and 4 °C for 10 min (Rotor: F0850; Centrifuge: GS-15R, Beckman) to get rid of debris.

4 ml Ni-NTA agarose (Cat. 1018240, Lot 148024809, Qiagen) per liter cell medium were measured by adding the same volume water in a 35 ml protino column (Cat. 745255.10, Lot 1009/001, Macherey-Nagel) marking the fill height and adding resin till the same fill height whilst letting the Ni-NTA buffer solution flow through. The Ni-NTA agarose was equilibrated by washing with 2 column volumes of water and then 2 column volumes buffer A. Before transferring the Ni-NTA agarose into a beaker for batch loading by stirring for 30 min on ice, 40 mM imidazole was added to the solubilisate. The loaded resin was then transferred back into the protino column and washed with 100 ml OG wash buffer (50 mM HEPES pH 7.5, 300 mM NaCl, 40 mM imidazole pH 7.5, 1.5% (w/v) OG, 0.2 mM TCEP) at 2 ml/min with a

peristaltic pump (pump: PLP 380, Cat. B00491218; pump head: PPH5062 Cat. B00491218; tubing: Tygon pipe 2.54 x 0.85 mm, Cat. BB00516098, behr Labor-Technik) by determining the flow rate with a small measuring cylinder.

Detergent was exchanged to DDM by washing with 100 ml at 2 ml/min with DDM wash buffer (50 mM HEPES pH 7.5, 30 mM NaCl, 0.1% (w/v) DDM, 0.2 mM TCEP).

Bound proteins were eluted with at least 4 times the resin volume elution buffer (50 mM HEPES pH 7.5, 30 mM NaCl, 400 mM imidazole pH 7.5, 0.1% (w/v) DDM, 1 mM TCEP) by letting the resin incubate with 2 times the resin volume of elution buffer for 30 min and subsequent 1-2 ml washing steps.

Protein concentration was determined via absorption at a Nanodrop ND-1000 (NanoDrop Technologies) using an extinction coefficient $\epsilon_{1\text{mg/ml}}$ of 2.16 ($30746 \text{ M}^{-1} \text{ cm}^{-1}$) for DgkA as used by several groups in the majority of recent publications (see also Appendix Table 5)^{179, 257, 262, 265, 269, 271, 300, 308, 324-326}.

For reconstitution into LCP and activity assays performed in detergent, imidazole was removed via PD-10 desalting columns according to the manufacturer protocol (Cat. 17-0851-01 Lot 12881046, GE Healthcare) using 10 mg/ml DgkA and PD-10 buffer (50 mM HEPES pH 7.5, 30 mM NaCl, 0.5% (w/v) DDM, 1 mM TCEP) for elution.

When higher protein concentrations were needed, DgkA was concentrated up to approximately 120 mg/ml without loss of activity using centrifugal filters with a NMWL of 50,000 (Amicon Ultra-15, Cat. UFC905024 or Amicon Ultra-4, Cat. UFC805096, Merck Millipore) at 2600 g (5000 rpm) and 4 °C. If longer storage was required DgkA in DDM was frozen with liquid nitrogen and stored at -80 °C without loss of activity upon thawing on ice²⁶⁸.

I.2.2.1.4 SDS-PAGE

Samples for SDS-PAGE were mixed with 4x Expedeon LDS sample buffer and 10 μl loaded onto 4-20% 12 well - 8x10 RunBlue™ SDS mini protein gels (Expedeon, Cat. BCG42012). For molecular weight estimation 7.5 μl of protein marker IV (10 - 150) was used. Electrophoresis was performed in a Mini-PROTEAN 3 cell electrophoresis system (Serial No. 67S/14943, Bio-Rad) with 0.2 M TRIS pH 8.9 as anode buffer and Expedeon RunBlue Rapid (Expedeon) as cathode buffer. 180 V per gel were applied for 30-35 min. Coomassie brilliant blue staining was performed overnight with a staining solution containing 5:4:1 (v/v/v) MeOH, H₂O, acetic acid (glacial) and 2.5 g/l

coomassie brilliant blue R250. Gels were destained with H₂O until the background was amendable.

I.2.2.1.5 Western Blot

Western blotting was performed with a semi dry blotting system (Trans-Blot Turbo, Bio-Rad) on a PVDF membrane (Bio-Rad). The PVDF membrane is first soaked in MeOH, followed by H₂O and finally Towbi transfer buffer (25 mM TRIS HCl pH 8.3, 192 mM glycine, 20% (v/v) MeOH). 8 filter paper, 4 placed underneath the gel and 4 placed on top are soaked in Towbi transfer buffer as well. Transfer for one mini gel is performed with a constant current of 1.3 A and a maximum of 25 V for 7 min.

For detection of His-tag the membranes were blocked with 2% BSA in TBST (50 mM TRIS HCl pH 7.4, 150 mM NaCl, 0.05% Tween 20) for 1 h, washed 3 times with TBST and then incubated for 1 h with 1:2000 Anti-His AP coupled antibody in TBST containing 0.5% BSA. After washing 3 times with TBST and 2 times with AP buffer (100 mM TRIS HCl pH 9.5, 100 mM NaCl, 5 mM MgCl₂) the membrane was stained by adding to 10 ml AP buffer 66 µl of 50 mg/ml NBT in 70% (v/v) DMF and 33 µl of 50 mg/ml BCIP in DMF. Staining was stopped by rinsing the blot with water.

I.2.2.1.6 Size exclusion chromatography

Size exclusion chromatography (SEC) was performed on a Superdex 200 Increase 10/300 GL (Cat. 28990944, GE Healthcare) with 100 µl purified DgkA at 10 mg/ml and filtered before injection with a Nanosep MF 0.2 µm filter (Cat. ODM02C35, Pall) at a flow-rate of 0.2 ml/min with a Bio-Rad NGC Quest 10 medium-pressure liquid chromatography system.

I.2.2.1.7 Reconstitution into LCP for ³¹P real-time activity measurements.

For activity measurements via ³¹P real-time MAS NMR DgkA was reconstituted in the cubic phase by mixing monoolein and protein solution inside the solid-state MAS rotor via repeated centrifugation.

Therefore, the respective amount monoolein, 30 mg for 4 mm rotors, 9 mg for 3.2 mm rotors, was added with a spatula as powder to the MAS rotor. The protein solution was added in a ratio of 7:3 (v/v) to the MAS rotor and contained 10 µM DgkA, 100 mM HEPES pH 7.5, 30 mM NaCl and 20 mM MgCl₂ with respect to the volume of liquid after the addition of nucleotide when a final monoolein to liquid ratio of 6:4 (v/v) is reached. All amounts added were verified by weighing the rotor after each step.

The samples were thoroughly mixed inside the MAS rotor by repeating short centrifugation steps³²⁷ to 16,000 g in a tabletop centrifuge and turning the MAS rotor by 180° at least 30 times followed by 30 min at 16,000 g. Formation of the transparent cubic phase during the centrifugation steps could be followed optically in sapphire rotors.

For activity measurements upon uncaging of NPE-ATP the volume of the 3.2 mm sapphire rotors was reduced to 15 µl to ensure complete sample illumination by inserting three rubber disks at the bottom and after sample mixing one rubber disk at the top.

I.2.2.1.8 Reconstitution into LCP for protein ssNMR measurements.

Uniformly ¹³C ¹⁵N labelled DgkA was concentrated to 60 mg/ml and mixed with monoolein at a 4:6 (v/v) ratio via a LCP mixing device (209525, Formulatrix) to form a LCP³²⁸ as described in detail in I.2.2.2.1.2. The sample was then transferred from the syringe into a 4 mm MAS rotor with a Gauge 22s needle, resulting in a sample containing 1 mg uniformly labelled DgkA with a protein to monoolein ratio of 1:30 (w/w) (L:P ~1200:1). The rotor was tightly packed with a rubber disk at the top to avoid gaps and prevent phase separation at 10 kHz MAS.

I.2.2.1.9 Reconstitution into liposomes

Lipids including long chain diacylglycerols were weighed, dissolved in chloroform/methanol 3:1 (v/v) and transferred into a round bottom flask (500 ml, NS 29/32). The solvent was first evaporated with a dry nitrogen stream and then *in vacuo* (40 mbar) over night at a rotary evaporator (Rotavapor R-200, Büchi). The lipids were then dissolved in a buffer containing 50 mM HEPES pH 7.5 and 30 mM NaCl at 4mg/ml for DOPC and *E. coli* polar liposomes and 50 mM HEPES pH 8, 300 mM NaCl and 1 mM EDTA at 45 mM for DMPC:DMPA liposomes using the rotary evaporator. Residual DMPC:DMPA lipids attached to the round bottom flask were dissolved by short sonification in a bath sonicator (Sonorex RK52, Bandelin). Lipids were softened by adding 3 mM DDM for DOPC and *E. coli* polar lipids or 15 mM DDM for DMPC:DMPA as powder before performing 8 freeze thaw cycles using liquid nitrogen.

Purified DgkA was added to the liposomes at the desired lipid molar ratio under slow stirring at room temperature. For *E. coli* polar lipids an average molar weight of 786 g/mol was assumed. The solution was incubated for 30 min at room temperature under

slow stirring. For detergent removal Bio-Beads SM-2 were degassed by autoclaving in H₂O and weighed by adding the slurry with a 5 ml pipette to a weighing dish and then removal of water by aspiration with a pipette from the weighing dish. 30 mg Bio-Beads per milligram of detergent in the solution were added and the solution agitated in a 50 ml tube on an orbital shaker (Roto-Shake Genie, Scientific Instruments) for 2 h at room temperature. The addition of Bio-Beads was repeated twice, with one incubation step over night at room temperature. If foam is still forming upon slight shaking, the addition of Bio-Beads was repeated. Bio-Beads were removed by filtration through gaze or 100 µm cell strainer (431752, Corning). Proteoliposomes were typically pelleted first at 72660 g (25000 rpm) 4 °C for 30 min (Rotor: 45 Ti; Optima LE-80K Ultracentrifuge, Beckman Coulter), then resuspended and transferred into 1.5 ml tubes and pelleted at 80696 g (28000 rpm) 4 °C for 30 min using custom built 1.5 ml tube inserts (Rotor: 70 Ti; Optima LE-80K Ultracentrifuge, Beckman Coulter). For protein ssNMR experiments proteoliposomes containing labelled DgkA were then washed 3 times with 20 mM HEPES pH 7.2 and 3 mM MgCl₂ using a tabletop centrifuge and pelleted at 311357 g (55000 rpm) 4 °C for 60 min (Rotor: 70 Ti; Optima LE-80K Ultracentrifuge, Beckman Coulter) before transferring into a MAS rotor.

I.2.2.1.10 Reconstitution into anisotropic bicelles

For reconstitution into anisotropic bicelles a lipid film was produced as described above. The lipids were then hydrated at 20 mg/ml in 50 mM HEPES pH 7.5 and 30 mM NaCl above phase transition temperature (>23 °C) in a water bath (Heating Bath B-490, Büchi) for 2 h with repeated vortexing and 15 min sonication in a bath sonicator (Sonorex RK52, Bandelin). The DMPC lipids were then softened by addition of 0.51% (w/v) OG and incubated for 15 min. DgkA was added above phase transition temperature to the lipids under slow stirring at a lipid to protein ratio of 130:1 (mol/mol) and incubated for 1 h under slow stirring above phase transition temperature. Detergent was removed as described above and the proteoliposomes first pelleted at 311357 g (55000 rpm) 4 °C for 60 min (Rotor: 70 Ti; Optima LE-80K Ultracentrifuge, Beckman Coulter), resuspended, transferred to 1.5 ml tubes and pelleted again with the same settings. The pellet was then resuspended at room temperature in 50 mM HEPES pH 7.5, 30 mM NaCl containing 10% (w/v) DHPC to a molar ratio of 3.2:1 (mol/mol) DMPC:DHPC assuming 90% recovery of DMPC

throughout the steps. For resuspension a 200 μl pipette tip with its tip flattened by pressing with another pipette tips pipette side onto the tip end was used as mixing spatula as well as vortexing and several cooling and warming cycles with an ice bath until the solution became clear and the pellet was dissolved completely. Empty bicelles were prepared the same way omitting addition of DgkA.

I.2.2.2 DgkA activity measurements

For activity measurements the concentration of ATP disodium salt dissolved in H_2O and titrated to pH 7.5 was determined by measuring absorbance at 260 nm ($\epsilon = 15400 \text{ M}^{-1}\text{cm}^{-1}$) in a buffer containing 50 mM HEPES pH 7.5. All activity measurements were performed at 30 °C. Activities are given in units (U), which are defined as the consumption of 1 μmol ATP per mg DgkA per minute.

I.2.2.2.1 Photometric coupled ATPase assays

The *in surfo* and *in meso* coupled ATPase assay³²⁹ without cardiolipin and monoolein as substrate was performed as described²⁶⁹ with the following details: The volume of the assay mix was held constant at 200 μl upon varying ATP concentrations by adding H_2O . Absorption at 340 nm was followed with an Infinite M200 plate reader (Tecan) with 15 s, 1 mm amplitude linear shaking before start of the measurement and 2 s shaking between timepoints and 2 x 2 reads per well. Samples containing no DgkA were measured as well to determine and subtract background rates. The formula used to calculate the enzymatic activity of DgkA in units (U) for the coupled assay is as follows:

$$U = \frac{n_{\text{ATP}} [\mu\text{mol}]}{t [\text{min}] \cdot m_{\text{DgkA}} [\text{mg}]} = \frac{\Delta\text{Abs} \cdot V [\mu\text{l}]}{t [\text{min}] \cdot \epsilon_{\text{NADH}} (340 \text{ nm}) \left[\frac{1}{\text{M} \cdot \text{cm}} \right] \cdot m_{\text{DgkA}} [\text{mg}] \cdot \text{path length} [\text{cm}]} \quad (29)$$

The molar extinction coefficient for NADH at 340 nm used was $6200 \text{ M}^{-1} \text{ cm}^{-1}$.

The path length in relation to the used volume for the 96 well plates (Nunc MicroWell 96-Well Microplates, Type F96, Cat. No. 167008, Thermo Scientific) used in the coupled photometric assay was calculated from the well dimensions in the manufacturers product specification sheet (diameter top 7 mm, diameter bottom 6.2 mm, well depth 11.4 mm) and is plotted in Appendix Figure 17. For 200 μl sample volume the fill height and thus the path length is 5.83 mm.

I.2.2.2.1.1 *in surfo* coupled assay

To prepare the assay mix, molten monoolein 0.25% (w/v) (25.5 mol%) was pipetted to the assay buffer containing 0.1 mM EGTA, 0.1 mM EDTA, 1 mM

phosphoenolpyruvate (PEP), 15 mM magnesium acetate, 50 mM LiCl, 0.3 mM NADH, 1% (w/v) decylmaltoside (DM) (75.5 mol%) and 75 mM PIPES pH 6.9. The solution with pipette tip was sonicated in a bath sonicator (Sonorex RK52, Bandelin) until monoolein dissolved. Thereafter 0.2 mM DTT and 28.9 U/ml pyruvate kinase and 28.9 U/ml lactate dehydrogenase were added. The reaction mixture, H₂O and ATP was added to the wells of a 96 well plate (Cat. 167008, Thermo Scientific).

To initiate the reaction 5 µl containing 343 ng DgkA diluted with 50 mM LiCl, 10 mM HEPES pH 7.5, 1 mM TCEP, 1% (w/v) DM were added per well to reach a final volume of 200 µl.

I.2.2.2.1.2 *in meso* coupled assay

For reconstitution, 3 volumes of monoolein were added as liquid to a 100-µl syringe (Cat. 7656-01, Hamilton) by heating all components with a heat gun and pipetting the molten lipid with a 200 µl pipette into the tip of the syringe. Therefore, the needle and ferrule were removed. Upon dispensing the monoolein, the plunger of the syringe was carefully pulled down to draw the monoolein into the syringe to minimize air bubbles. After removing residual air bubbles by repeated rapid moving of the plunger, the ferrule was inserted and a LCP syringe coupler (Cat. 209526, Formulatrix) mounted. The plunger was then carefully pushed up until all air is expelled from the barrel and the adaptor (4 µl dead volume). Two volumes of protein solution were added similarly into a second 100-µl syringe. The DgkA concentration used for reconstitution into the meso phase of monoolein was the same as for the ³¹P real-time activity measurements resulting in 57.2 ng DgkA per microliter LCP. The two syringes firmly connected with the LCP syringe coupler are now moved steadily back and forth to mix monoolein and liquid. If the mixture stays opaque and viscosity is not increasing slight heating or cooling may facilitate LCP formation as the sample becomes more viscous and birefringent upon LCP formation (Figure 62). If the LCP formed is stable over several hours, one syringe, containing the LCP, is disconnected and mounted into a 50-step repeating dispenser (Cat. PB600-1, Hamilton) and fitted with a 19.1 mm long gauge 22s flat-tipped needle.

Per well of a 96-well plate (Cat. 167008, Thermo Scientific) three 2 µl rod-shaped boluses were placed on the side of the wells. The assay mix containing 0.1 mM EGTA, 0.1 mM EDTA, 1 mM phosphoenolpyruvate (PEP), 0.2 mM DTT, 55 mM magnesium acetate, 50 mM LiCl, 0.4 mM NADH, 75 mM PIPES pH 6.9, as well as freshly added

28.9 U/ml pyruvate kinase and 28.9 U/ml lactate dehydrogenase was distributed in aliquots. H₂O and ATP were added to reach the desired ATP concentrations. To initiate the reaction the solution was then transferred to the wells containing the LCP boluses.

I.2.2.2.1.3 Bicelle coupled assay

The coupled photometric assay to determine DgkA's activity in bicelles was performed in a spectrophotometer (V-550, Jasco) with a 3x3 mm path length quartz cuvette (QS High Precision Cell, Art. 105-251-15-40, Hellma Analytics) by recording the absorption at 340 nm. Temperature was held at 30 °C with a water bath (F25 and MP, Julabo) calibrated by measuring the temperature in a filled cuvette with a thermometer. The assay mix contained 0.1 mM EGTA, 0.1 mM EDTA, 1 mM phosphoenolpyruvate (PEP), 15 mM magnesium acetate, 50 mM LiCl, 0.3 mM NADH, 75 mM PIPES pH 6.9 and 28.9 U/ml pyruvate kinase and 28.9 U/ml lactate dehydrogenase. DgkA loaded bicelles were diluted 1:1 with empty bicelles to prevent disintegration of bicelles and precipitation upon dilution with assay buffer. 20 µg of diluted DgkA was then added to the cuvette containing the assay buffer and transferred into the spectrophotometer for temperature equilibration. After 5 min 3 mM ATP was added and the solution mixed by pipetting. Thereafter 0.5 µl DBG synthesized by Dr. Andreas Jakob³³⁰ was added as oil and the solution mixed by pipetting to initiate kinase activity.

I.2.2.2.2 Molybdenum blue assay

The ATPase reaction of DgkA was measured via determination of orthophosphate built-up with the molybdenum blue assay³³¹ as published³³². The ATPase reaction mixture contained 50 µg DgkA in *E. coli* polar liposomes or DDM or 20 µg DgkA in DOPC liposomes (L:P 2000:1), 100 mM HEPES pH 7.5, 30 mM NaCl, 60 mM MgCl₂ and additionally 0.1% (w/v) DDM for DgkA in detergent. Adding ATP, reaching a total volume of 150 µl in 1.5 ml microcentrifuge tubes, and transferring the samples from ice to 30 °C after mixing by pipetting, initiated the reaction. After 20 min at 30 °C and 600 rpm in a heatblock (Thermomixer compact 5350, Eppendorf or MHL 23, HLC BioTech), the samples were transferred on ice and the reaction stopped by adding 150 µl solution A (20% (w/v) SDS) to denature the enzyme and prevent protein aggregation³³³. After vortexing the samples thoroughly 300 µl solution D is added freshly prepared using equal amounts of colorless solution B (12% (w/v) ascorbic acid, 1 M HCl) allowing to reduce molybdate at less acidic pH³³⁴ and solution C (2% (w/v)

ammonium molybdate, 1 M HCl) and samples vortexed again. After 5 min at room temperature where molybdate complexes free phosphate 450 μ l of solution E (2% (w/v) sodium citrate (tribasic dehydrate), 2% (w/v) sodium meta-arsenite, 2% (v/v) acetic acid) is added and samples vortexed to complex excess free molybdate and enhance the intensity of the formed molybdate phosphate complexes for 20 min³³⁵⁻³³⁷. To subtract unspecific orthophosphate built-up background samples were prepared as described above with the SDS solution added before addition of ATP. Absorption of the formed phosphate molybdate complexes was quantified to a phosphate standard row containing 0 – 400 μ M K_2HPO_4 (Appendix Figure 19) in ATPase buffer treated like the background samples.

I.2.2.2.3 ³¹P NMR real-time activity measurements

For ³¹P real-time activity measurements performed by adding ATP $MgCl_2$ was added to the ATP solution in twofold molar excess but at least 30 mM free Mg^{2+} or 1.5 fold molar excess for samples above 150 mM ATP and the volume adjusted for the varying ATP and $MgCl_2$ concentrations with H_2O . This approach was chosen as lower Mg^{2+} to ATP ratios lead to severe ³¹P line broadening due to exchange between $MgATP$ and free ATP. Mg^{2+} does not influence strongly the reaction rate above 50 mM according to Li et al²⁶⁹.

The ATP solution was added into the center of the pre-spun sample, weighed to avoid pipetting errors at high ATP concentrations due to increased viscosity, and immediately transferred into the spectrometer. Typically the time between adding ATP and start of the measurement was 3.5 min.

For ³¹P real-time activity measurements initiated by uncaging of NPE-ATP the nucleotide analog and a twofold molar excess of $MgCl_2$ but at least 30 mM free Mg^{2+} was added to the sample before forming the cubic phase. ATP was released by illuminating the sample for 5 min inside the spectrometer. The measurement was started immediately after illumination.

To be able to compare ATP concentrations between experiments adding ATP and uncaging NPE-ATP the concentration of NPE-ATP dissolved in 100 mM HEPES pH 7.5 was determined via NMR by comparing the ³¹P signals of NPE-ATP to the ATP signals in a mixed sample containing a defined concentration of ATP.

For ³¹P real-time activity measurements, using anisotropic bicelles dioctanoylglycerol was dissolved in chloroform to form a lipid film upon solvent removal *in vacuo*. Then,

empty bicelles were added and 8 freeze-thaw cycles with vortexing steps upon thawing were performed to dissolve dioctanoylglycerol at a maximum concentration of 15 mM. The DgkA containing bicelles were diluted with empty bicelles to reach a final amount of 2.5 μg DgkA per MAS rotor (50 μl) upon addition of dioctanoylglycerol containing bicelles and 25 μl of ATP MgCl₂, 30 mM NaCl and 100 mM HEPES pH 7.5 containing solution. To mix DgkA and dioctanoylglycerol containing bicelles 4 freeze-thaw cycles were carried out before addition of ATP.

To determine initial reaction rates progress curves were extracted from the acquired real-time spectra by integration of well separated peaks within Topspin or deconvolution in Matlab.

As deconvolution is dependent on signal to noise combining several increments, thereby however reducing time resolution, might be necessary beforehand. Therefore, an AU program was written for Topspin 2.1 that adds up FID's of 1Ds as sets in incremented expno's (Appendix IV.8.1). The 1Ds are converted back to a pseudo 2D spectrum using another custom written AU program (Appendix IV.8.2). For deconvolution, spectra were exported by writing 1D spectra of the pseudo 2D spectrum into consecutive procno's and converting these to ASCII files (Appendix IV.8.3). These spectra were then imported into Matlab and fitted in several parts with Gaussian/Lorentzian blends using a custom written script (Appendix IV.8.4) and the plugin peakfit.m³³⁸. For a graphical comparison of a spectrum detail and its deconvolution see Appendix Figure 24. The script also filters and sorts fit results of deconvoluted peaks according to their chemical shift and peak width to allow export to Origin for further analysis.

To determine initial reaction rates, progress curves for substrate and product signals were extracted from integration or deconvolution results and extrapolated with exponential functions to the start of the reaction.

I.2.3 UV-Vis absorbance measurements of a lipidic cubic phase

To perform UV-Vis absorbance measurements on a LCP without voids a special cuvette had to be built as addition of LCP into normal cuvettes by injection from a syringe or centrifugation created voids compromising the measurement. The holder consisted of two quartz windows from a broken CD cuvette (100-QS 1 mm, Hellma Analytics) planar grinded by the glass workshop of the Goethe University, a black painted aluminium mask to define the optical window, held together with a metal clip

and two spacers, to keep the two plates 9 mm apart after addition of the LCP onto one quartz window.

I.2.4 Solid-state NMR measurements

All temperatures given are referenced to KBr ^{79}Br T_1 relaxation times³³⁹ via an empirically determined formula (see Appendix IV.2 WB MAS NMR probe temperature calibration) at same spinning speed, variable temperature gas flow and frame cooling gas flow (Appendix Figure 2). ^{13}C and ^{15}N chemical shifts are referenced to DSS using a chemical shift of 179.85 ppm for the carbonyl function of microcrystalline alanine as external reference. ^{31}P spectra are referenced to 85% H_3PO_4 using a chemical shift of 58.62 ppm for triethylphosphine as external reference. All LCP samples were spun in a MAS unit a day before measurements to achieve homogeneous distribution. Pulse widths ($\pi/2$) on ^1H , ^{31}P , ^{13}C , and ^{15}N were typically 3.0, 4.0, 5.0, and 6.5 μs .

I.2.4.1 Protein spectra of DgkA in liposomes and LCP

Spectra of labelled DgkA in liposomes and LCP were acquired at 10 kHz MAS on a Bruker Avance 600 WB spectrometer operating at a ^1H frequency of 600.13 MHz equipped with a 4 mm triple resonance probe. PDSM (Figure 21) mixing time was 20 ms, 540 increments in F1, in F2 104 increments for liposomes, 144 increments for LCP. Cross polarization was performed for 1 ms with an 80-100% ramp. For NCA (Figure 22) CP times were 1 ms with an 80-100% ramp for 1st CP and 4 ms with a 90-100% ramp for 2nd CP, 60 increments in F1, 416 increments in F2. ^1H decoupling using the SPINAL-64 decoupling scheme was performed at same power level corresponding to 83 kHz for LCP and 70 kHz for liposome samples.

I.2.4.2 ^{31}P real-time measurements

For ^{31}P real-time measurements following the enzymatic activity upon addition of ATP a 4 mm double resonance probe was used on a Bruker Avance 600 WB spectrometer operating at a ^1H frequency of 600.13 MHz. To allow comparison with assay data all ^{31}P real-time activity measurements were performed at 30 °C as well. Care was taken to limit sample heating and temperature gradients. Therefore, no decoupling was used and MAS kept low. ^{31}P real-time experiments with LCP samples were performed at 3 kHz MAS. For ^{31}P real-time experiments in detergent MAS was adjusted to ~1 kHz by manually controlling bearing and drive pressures due to rotor instability at higher

MAS speeds in automatic mode. Experiments following DgkA's kinase reaction upon uncaging of NPE-DOG in DOPC liposomes were performed at 10 kHz MAS to avoid signal overlap with spinning sidebands.

I.2.4.3 High field MAS NMR illumination setup

Sample illumination during MAS was performed on a Bruker Avance III 850 WB spectrometer operating at 850.31 MHz ^1H frequency. Therefore, a 3.2 mm MAS WB double resonance probe was modified by Bruker to fit a custom build 2 mm diameter LUV 70 μm fiber bundle with macor ferrules (Leoni Fibertech) through a hole in the coil pedestal of a stretched thin wire coil. Thus, allowing to position the fiber guide close to the coil and sample. (Figure 38) For illumination at 365 nm a 22 mm clear aperture collimated UV LED with 500 mW radiant power connected to the fiber bundle via a light guide adapter in combination with a computer controlled LED driver was used (LED: LCS-0365-11-22; Light guide adapter: LCS-0365-11-22; Driver: SLC-AV02-US, Mightex Systems).

I.2.4.4 DNP MAS NMR illumination setup

A simple sample illumination setup for illumination under DNP conditions in a Bruker Avance II 400 WB spectrometer operating at a ^1H frequency of 400.20 MHz has been built by Bruker by insertion of a bifurcated fiber cable commonly used for the MAS revolution counter into an unused bore hole of the stator. For illumination at 365 nm the above mentioned UV LED in combination with the computer controlled LED driver was used (LED: LCS-0365-11-22; Driver: SLC-AV02-US, Mightex Systems). For illumination at 405 and 470 nm 22 mm clear aperture collimated high power LEDs with 2.5 and 3.3 W radiant power in combination with a high power LED driver were used (LEDs: LCS-0405-50-22 and LCS-0470-50-22; Driver: BLS-13000-1, Mightex Systems). The collimated light was focused with a light guide adapter (LCS-0365-11-22, Mightex Systems) on a liquid light guide (LLG-03-59-300-0650-2; Mightex Systems), which was coupled to the bifurcated fiber cable at the bottom of the probe with a cut pipette tip to transfer the light to the sample.

I.2.5 DNP measurements with monoolein as membrane mimetic

Samples for DNP measurements at a Bruker Avance II 400 WB spectrometer operating at a ^1H frequency of 400.20 MHz to evaluate the feasibility of monoacylglycerols as membrane mimetics for DNP were prepared as follows. For

enhancement tests purified DgkA was concentrated to 107 mg/ml after imidazole removal. DgkA was mixed at room temperature with monoolein, AMUpol, D₂O, glycerol, HEPES, MgCl₂ and NaCl in the indicated amounts (Table 10) via a LCP mixing device (209525, Formulatrix) as described in detail in I.2.2.2.1.2 to form a LCP³²⁸ for homogeneous sample distribution. The samples were then transferred from the syringe into 3.2 mm sapphire MAS rotors with a Gauge 22s needle. Samples were spun at room temperature in a MAS unit before storage to achieve homogeneous sample distribution within the rotors.

For exploration of ¹³C protein ³¹P nucleotide contacts via z-filtered transferred echo double resonance (ZF-TEDOR) experiments (Figure 23)³²² 20.5 mM AMP-PCP was added to uniformly ¹³C ¹⁵N labelled DgkA after imidazole removal, but before concentration to 59 mg/ml to avoid ligand depletion. DgkA with 20.5 mM AMP-PCP, 40 mM MgCl₂, 10 mM AMUpol, 100 mM HEPES pH 7.5, 30% (v/v) glycerol and 50% (v/v) D₂O was mixed at room temperature with monoolein via a LCP mixing device (209525, Formulatrix), transferred into a 3.2 mm sapphire MAS rotor and spun in a MAS unit as described above. All experiments were performed at 100 K and 8 kHz MAS. Pulse widths ($\pi/2$) on ¹H were typically 2.5 μ s and on ³¹P and ¹³C 5.0 μ s in ¹³C/³¹P probe mode.

I.2.6 LCP liquid-state NMR measurements

LCP samples for liquid-state NMR were prepared by mixing monoolein and liquid in a LCP mixing device at a 6:4 (w/w) ratio. The LCP samples contained with respect to the liquid fraction 15 mM ATP, 30 mM MgCl₂, 6 mM NaCl, 10 mM HEPES pH 7.5 and 10% (v/v) D₂O. The LCP was injected from a syringe (81165, Hamilton) into the bottom of a 4 mm PTFE NMR tube liner (DTL-5-4-7, Deutero) as centrifugation was unsuccessful. For comparison a solution containing the same amounts over the whole sample (6 mM ATP, 12 mM MgCl₂, 2.4 mM NaCl, 4 mM HEPES pH 7.5 and 4% (v/v) D₂O) was prepared. Experiments were performed on a Bruker Avance I 600 spectrometer operating at 600.03 MHz ¹H frequency equipped with a 5 mm HCP probe and a z-gradient coil capable of creating a maximum gradient of 55 G cm⁻¹.

I.2.6.1 ³¹P DOSY on ATP in LCP and solution

To determine diffusion rates of ATP in solution and LCP ³¹P DOSY experiments were performed. For the sample in solution a standard pulsed field gradient spin echo

(PGSE) sequence (Figure 25) with ^1H decoupling a 5 ms gradient (δ), 200 ms diffusion time (Δ) was applied and 128 transients per increment were recorded.

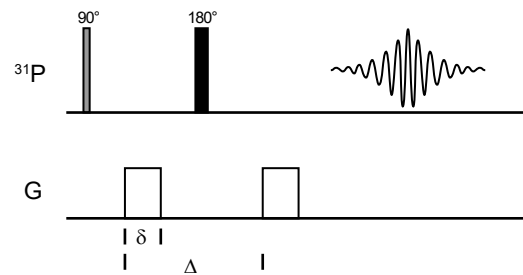


Figure 25: Pulse sequence of a pulsed field gradient spin echo (PGSE) experiment. δ denotes the gradient time and Δ the diffusion time.

For LCP the PGSE experiment and a pulsed field gradient stimulated spin echo (PFG-SSE) experiment (Figure 26) with ^1H decoupling, a 0.5 ms gradient (δ), 50 ms (Δ) diffusion time were tried with 512 transients per increment due to decay of signal.

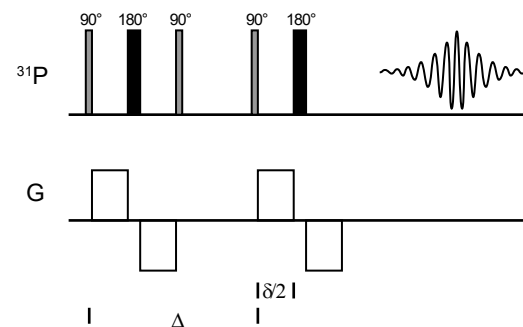


Figure 26: Pulse sequence of a pulsed field gradient stimulated spin echo (PFG-SSE) experiment. δ denotes the gradient time and Δ the diffusion time.

I.2.7 List of Buffers

AP buffer: 100 mM TRIS HCl pH 9.5, 100 mM NaCl, 5 mM MgCl₂

TAE buffer: 4.84 g/l TRIS, 1.14 ml/l glacial acetic acid, 0.37 g/l EDTA

Towbi transfer buffer: 25 mM TRIS HCl pH 8.3, 192 mM glycine, 20% (v/v) MeOH

TBST: 50 mM TRIS HCl pH 7.4, 150 mM NaCl, 0.05% Tween 20

LB agar: 25 g/l LB powder, 15 g/l agar

M9: 6 g/l Na₂HPO₄, 3 g/l KH₂PO₄, 1 g/l NaCl, 1 g/l NH₄Cl, 0.1 mM CaCl₂, 1 mM MgSO₄, 0.4 % (w/v) glucose, 0.15 g/l grinded vitamin pills (Centrum, Pfizer Consumer Healthcare), 0.1 g/l ampicillin, pH 7.0

SDS-PAGE staining solution: 5:4:1 (v/v/v) MeOH, H₂O, acetic acid (glacial) and 2.5 g/l coomassie brilliant blue R250

Buffer A: 50 mM HEPES pH 7.5, 300 mM NaCl

Lysis buffer: 50 mM HEPES pH 7.5, 300 mM NaCl, 5 mM MgCl₂, 1 pill protease inhibitor per 500 ml cell medium, 0.2 mM TCEP, 0.2 mg/ml lysozyme, 0.05 mg/ml DNaseI

OG wash buffer: 50 mM HEPES pH 7.5, 300 mM NaCl, 40 mM imidazole pH 7.5, 1.5% (w/v) OG, 0.2 mM TCEP

DDM wash buffer: 50 mM HEPES pH 7.5, 30 mM NaCl, 0.1% (w/v) DDM, 0.2 mM TCEP

Elution buffer: 50 mM HEPES pH 7.5, 30 mM NaCl, 400 mM imidazole pH 7.5, 0.1% (w/v) DDM, 1 mM TCEP

PD-10 buffer: 50 mM HEPES pH 7.5, 30 mM NaCl, 0.5% (w/v) DDM, 1 mM TCEP

DMPC:DMPA lipid buffer: 50 mM HEPES pH 8, 300 mM NaCl, 1 mM EDTA

DMPC:DMPA NMR buffer: 20 mM HEPES pH 7.2, 3 mM MgCl₂

in surfo assay buffer: 0.1 mM EGTA, 0.1 mM EDTA, 1 mM PEP, 15 mM magnesium acetate, 50 mM LiCl, 0.3 mM NADH, 1% (w/v) DM (75.5 mol%), 75 mM PIPES pH 6.9

in meso assay buffer: 0.1 mM EGTA, 0.1 mM EDTA, 1 mM PEP, 0.2 mM DTT, 55 mM magnesium acetate, 50 mM LiCl, 0.4 mM NADH, 75 mM PIPES pH 6.9

Molybdenum blue assay solution A: 20% (w/v) SDS

Molybdenum blue assay solution B: 12% (w/v) ascorbic acid, 1 M HCl

Molybdenum blue assay solution C: 2% (w/v) ammonium molybdate, 1 M HCl

Molybdenum blue assay solution D: 1:1 (v/v) assay solution B and assay solution C

Molybdenum blue assay solution E: 2% (w/v) sodium citrate (tribasic dehydrate), 2% (w/v) sodium meta-arsenite, 2% (v/v) acetic acid

1.2.8 List of compounds

1,2-Dibutyrylglycerol (DBG), 3-((1-(2-Nitrophenyl)ethoxy)carbonyl)-*sn*-1,2-dioleoylglycerol (NPE-DOG) and [7-(Diethylamino)-2-sulfanylidenechromen-4-yl] methyl acetic acid (NdiEt-tcAA) were synthesized by Dr. Andreas Jakob³³⁰.

Triethylphosphine sulfide (Cat. 30392.04, Lot D06K25) was purchased from Alfa Aesar (Haverhill MA, USA). Adenosine 5'-triphosphate disodium salt (ATP, Cat. A1348, Lot 40008777), 5-bromo-4-chloro-3'-indolylphosphate (BCIP, Cat. A1117, Lot 3P005086), DNase I (Cat. A3778, Lot 3O009479), 1,4-dithiothreitol (DTT, Cat. A1101, Lot 1M007995), ethylenediaminetetraacetic acid (EDTA, Cat. A1103, Lot 9D002526), ethylene glycol-bis(β -aminoethyl ether)-*N,N,N',N'*-tetraacetic acid (EGTA), D(+)-glucose (Cat. A1422, Lot 3L009476), glycine (Cat. A3707), 4-(2-Hydroxyethyl)piperazine-1-ethanesulfonic acid sodium salt (HEPES, Cat. A1070, Lot 1E009339), imidazole (Cat. A1073, Lot 4H015478), isopropyl β -D-1-thiogalactopyranoside (IPTG, Cat. A1008, Lot 6501055), KH_2PO_4 (Cat. A1043, Lot 6U014139), lysozyme (Cat. A3711, Lot 8N010154), $\text{MgCl}_2 \cdot 6\text{H}_2\text{O}$ (Cat. A1036, Lot 7T000254), $\text{MgSO}_4 \cdot 7\text{H}_2\text{O}$ (Cat. A1368, Lot 4E015735), NaCl (Cat. A1149, Lot 4M014937), Na_2HPO_4 (Cat. A1046, Lot 4Y009229), NaOH 4 M solution (Cat. A4239), NaOH pellets (Cat. A0991, Lot 1W008135), NH_4Cl (Cat. A0984, Lot 3V003116), β -nicotinamide adenine dinucleotide (NADH) reduced disodium salt hydrate (Cat. A1393, Lot 2B001042), nitro-blue tetrazolium (NBT, Cat. A1243, Lot 3V004156), *n*-octyl- β -D-glucopyranoside (OG, Cat. A1010, Lot 6P012262), sodium dodecyl sulfate (Cat. A7249, Lot 6I008927) were purchased from AppliChem (Darmstadt, Germany). 1,2-dihexanoyl-*sn*-glycero-3-phosphocholine (DHPC, Cat. 850305), 1,2-dioctanoyl-*sn*-glycerol (DioctaG, diC₈, Cat. 800800, Lot 80DG-108), 1,2-dioleoyl-*sn*-glycerol (DOG, Cat. 800811, Lot 800811-01-058), 1,2-dioleoyl-*sn*-glycero-3-phosphocholine (DOPC, Cat. 850375P, Lot 181PC-264), 1,2-dimyristoyl-*sn*-glycero-3-phosphocholine (DMPC, Cat. 850345, Lot 850345-02-270), 1,2-dimyristoyl-*sn*-glycero-3-phosphate sodium salt (DMPA, Cat. 830845P, Lot 140PA-54) were purchased from Avanti Polar Lipids (Alabaster AL, USA). Bio-Beads SM-2 (Cat. 152-3920, Lot 64162628) were purchased from Bio-Rad (Hercules CA, USA). D-glucose-¹³C₆ (Cat. CLM-1396-10, Lot PR-28591) was purchased from Cambridge

Isotope Laboratories (Tewksbury MA, USA). Albumin fraction V (BSA, Cat 8076.4, Lot 193198891), ampicillin sodium salt (Cat. K029.2, Lot 164213247), CHCl_3 (Cat Y015.1), LB broth (Cat. X968.4, Lot 416250436), *N,N*-dimethylformamide (DMF, Cat. T921.1), 1,4-piperazinediethanesulfonic acid (PIPES, Cat. 9156.2, Lot 14570869), Tween 20 (Cat. 9127.1, Lot 444221271) were purchased from Carl Roth (Karlsruhe, Germany). 15-({[(7-oxyl-3,11-dioxa-7-azadispiro[5.1.5.3]hexadec-15-yl)carbamoyl][2-(2,5,8,11-tetraoxatridecan-13-ylamino)}]-[3,11-dioxa-7-azadispiro[5.1.5.3]hexadec-7-yl])oxidanyl (AMUpol), Ammonium- ^{15}N chloride (99% at., Lot 15ACLG0317D289) were purchased from Cortecnet (Voisins-Le-Bretonneux, France). LDS Sample Buffer (Cat. B31010, Lot 150720003-10) was purchased from Expedeon (Cambridge, UK). Magnesium acetate tetrahydrate (Cat. 63047, Lot 422691) was purchased from Fluka (Buchs, Switzerland). Decyl β -D-maltopyranoside (DM, Cat. D9903, Lot MR1852), *n*-dodecyl β -D-maltoside (DDM, Cat. D97002-C, Lot MR2807/4) were purchased from Glycon Biochemicals (Luckenwalde, Germany). 1-Oleoyl-*rac*-glycerol (M239-J17-Z) was purchased from Nu-Chek Prep (Elysian MN, USA). Ni-NTA (Cat. 1018240, Lot 148024809) was purchased from Qiagen (Hilden, Germany). cOmplete protease inhibitor cocktail tablets (Ref 11836145001, Lot 11767900), lactate dehydrogenase (Ref 0127230001, Lot 14350325), pyruvate kinase (Ref 10128155001 Lot 10668528, 10993122) were purchased from Roche (Basel, Switzerland). Adenosine 5'-monophosphate sodium salt (Cat. A1752, Lot 105K7037) Adenosine 5'-triphosphate disodium salt (ATP, Cat. A26209, Lot MKBW6572V), adenosine 5'-[γ -thio]triphosphate tetralithium salt (ATP γ S, Cat. A1388), 2,6-di-*tert*-butyl-4-methylphenol (BHT, Cat. B1378, Lot BCBP4244V), $\text{CaCl}_2 \cdot 2\text{H}_2\text{O}$ (Cat. C3881, Lot SLBB9179V), CDCl_3 (Cat 151858, Lot MKBT0824V), ethylenediaminetetraacetic acid dipotassium salt dihydrate (EDTA, Cat. ED2P, Lot BCBH8567V), β,γ -methyleneadenosine 5'-triphosphate disodium salt (AMP-PCP, Cat. M7510, Lot SLBR7914V), phospho(enol)pyruvic acid monopotassium salt (PEP, Cat. 860077, Lot MKBD9032V), tris(2-carboxyethyl)phosphine hydrochloride (TCEP, Cat C4706, Lot 095K1188), $\text{YbCl}_3 \cdot 6\text{H}_2\text{O}$ (Cat 337927) were purchased from Sigma-Aldrich (St Louis MO, USA). Adenosine 5'-triphosphate, P^3 -(1-(2-nitrophenyl)ethyl) ester disodium salt (NPE-ATP, Cat. A1048, Lot 1644953, 1711735, 1780843, 1798352) was purchased from Thermo Fisher Scientific (Waltham MA, USA). Centrum vitamin pills (product no. 14006-01, Lot AVB024) were purchased from Pfizer Consumer Healthcare

(Berlin, Germany). LiCl (Cat. 3739, Lot 0942148) was purchased from Roth (Karlsruhe, Germany). Acetic acid glacial (Cat. 20104.298, Lot17E034008), HCl 37% (Cat. 20252.335, Lot 17L134014) were purchased from VWR (Radnor PA, USA).

I.2.9 List of equipment

| Type of equipment | Modell, Manufacturer |
|--|---|
| Agarose gel electrophoresis chamber | custom built, MPI for Biophysics |
| Centrifuge cell harvesting | Avanti J-E, Beckman |
| Centrifuge cell harvesting rotor | JLA 10.500, Beckman |
| Centrifuge 15 – 50 ml tubes | GS-15R, Beckman |
| Centrifuge 15 – 50 ml tubes rotor | F0850, Beckman |
| Centrifuge microtubes | 1-14K, Sigma |
| Centrifuge microtubes rotor | 12094, Sigma |
| Centrifuge microtubes | Hereaus Pico 17, Thermo Scientific |
| Centrifuge microtubes rotor | 75003424, Thermo Electron |
| Centrifuge microtubes | Biofuge pico, Heraeus |
| Centrifuge microtubes rotor | Sorvall 3328, Heraeus |
| Heat block shaker | Thermomixer compact 5350, Eppendorf |
| Heat block shaker | MHL 23, HLC BioTech |
| Incubator | Incucell, Medcenter Einrichtungen |
| Incubator shaker | Innova44, Brunswick Scientific |
| 355 nm laser | Paladin Advanced 355-8000, Coherent, 8 W output power |
| Laser power meter | Nova Display power meter 1Z01500, Ophir |
| Laser power meter sensor | 1Z02146, Ophir |
| LED 365 nm | LCS-0365-11-22, Mightex Systems, 0.5 W output power |
| LED 365 nm driver | SLC-AV02-US, Mightex Systems |
| LED 405 nm | LCS-0405-50-22, Mightex Systems, 2.5 W output power |
| LED 470 nm | LCS-0470-50-22, Mightex Systems, 3.3 W output power |
| LED visible light driver | BLS-13000-1, Mightex Systems |
| LED beam combiner | LCS-BC25-0380, Mightex Systems |
| LED lightguide adaptor | LCS-LGA22-0515, Mightex Systems |
| Liquid light guide | LLG-03-59-300-0650-2, Mightex Systems |
| Lyophilizer | Alpha1-2 LD 101021, Christ |
| Lyophilizer pump | J96, Sogevac |
| Medium pressure liquid chromatography system | NGC Quest 10, Bio-Rad |
| 5 mm NMR tubes | Boroeco-5-7, Deutero |
| PTFE NMR tube liner | DTL-5-4-7, Deutero |
| | |
| Orbital shaker | Roto-Shake Genie, Scientific Instruments |
| Peristaltic pump | PLP 380, Cat. B00491218, behr Labor-Technik |
| Peristaltic pump head | PPH5062 Cat. B00491218, behr Labor-Technik |
| Peristaltic pump tubing | Tygon 2.54 x 0.85 mm, Cat. BB00516098, behr Labor-Technik |
| pH meter standard buffers | FiveEasy Plus, Mettler-Toledo |
| pH electrode standard buffers | InLab Routine –L 7048503, Mettler-Toledo |
| pH meter ATP solutions | SevenCompact, Mettler-Toledo |
| pH electrode ATP solutions | InLab Micro 51343160, Mettler-Toledo |
| Platform shaker | Duomax 1030, Heidolph |
| Pipette controller | Easypet 3, Eppendorf |
| Pipette controller | Pipetboy 2, Integra |
| Power supply electrophoresis | PowerPac basic, Bio-Rad |
| Magnetic stirrer | RCT basic, IKA |

| | |
|---|--|
| Magnetic stirrer | Agitateur megnetique chauffant 10515, Fisher Bioblock Scientific |
| MAS Pneumatic Control Unit | H2620, Bruker |
| Micropipettes | Research plus and Research, Eppendorf |
| MilliQ water unit | Nanopure Diamond, Barnstead |
| Rotary evaporator | Rotavapor R-200, Büchi |
| Rotary evaporator heating bath | Heating Bath B-490, Büchi |
| Rotary evaporator vacuum control | CVC 3000, vacuubrand |
| Rotary evaporator vacuum pump | 3 EKF 63cx-4, Greiffenberger Antriebstechnik |
| Scale | Explorer E12145, OHAUS |
| Scale | PFB 2000, Kern |
| SDS-PAGE electrophoresis chamber | Mini-PROTEAN 3 cell electrophoresis system, Bio-Rad |
| SEC column | Superdex 200 Increase 10/300 GL, GE Healthcare |
| Syringe for LCP mixing | 7656-01, Hamilton |
| Syringe for LCP mixing INMR | 81165, Hamilton |
| Syringe coupler | 209526, Formulatrix |
| Syringe repeating dispenser | PB600-1, Hamilton |
| Thermo Cycler | Veriti 96-Well Thermal Cycler, Applied Biosystems |
| Tungsten lamp | KL 1500 LCD, Zeiss |
| Ultracentrifuge | Optima LE-80K Ultracentrifuge, Beckman Coulter |
| Ultracentrifuge fixed angle rotors | 45 Ti and 70 Ti, Beckman Coulter |
| Ultracentrifuge swinging bucket rotors | SW 28 and SW 50.1, Beckman Coulter |
| UV-Vis spectrophotometer | V-550, Jasco |
| UV-Vis spectrophotometer water temperature regulation | F25 and MP, Julabo |
| UV-Vis quartz cuvette 3x3 mm | QS High Precision Cell, Art. 105-251-15-40, Hellma Analytics |
| UV table | N90 MW 312 nm, Konrad Benda |
| 600 nm spectrophotometer | Ultrospec 10 Cell Density Meter, biochrom |
| Vacuum pump | MZ 2C Synchro, vacuubrand |
| Vortexer | Vortex Genie 2, Scientific Industries |
| Non UV yellow room light | UVL-520-150-101274-SCE, ASMETEC |
| Sonication bath | Sonorex RK52, Bandelin |
| Probe sonicator | D2200, Bandelin |
| Probe sonicator probe | KE76, Bandelin |

I.3 Results

I.3.1 Purification of DgkA

The expression and purification strategy led to pure and monodisperse DgkA preparations as judged by SDS-PAGE and SEC. As an additional 766 bp long sequence containing a second ribosome binding site and a IS1 transposase sequence was found between the *trc* promoter and *dgkA* by sequencing multiple pSD005 plasmid stocks, *dgkA* was cloned into a pET expression vector. Cloning *dgkA* and cell disruption via sonication increased the yields for DgkA without alteration in activity. Yields for DgkA produced in LB as well as in M9 medium were typically 50 mg per liter medium. Enzymatic activity of purified DgkA (Table 9) was comparable to previously published specific activities of a coupled assay with DM/monoolein mixed micelles at 3 mM ATP.²⁶⁹

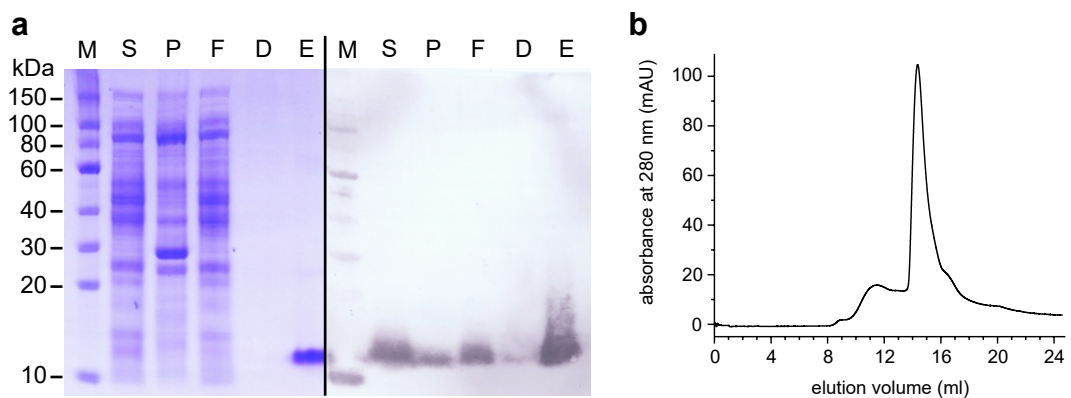


Figure 27: Purification of DgkA. **a)** SDS-PAGE and Western Blot. Lanes are: 7.5 μ l protein marker IV 10-150 (M). In 1:10 dilution (0.75 μ l), equating to 7.5 μ l cell medium: supernatant (S), pellet (P), Ni-NTA column flow-through (F). 7.5 μ l of 100 ml OG to DDM detergent exchange wash (D). Eluate containing 2 μ g DgkA (E). **b)** Size exclusion chromatogram of purified DgkA on a Superdex 200 Increase 10/300 GL.

I.3.2 Characterization of LCP for MAS solid-state NMR applications

The lipidic cubic phases of monoacylglycerols are not extensively characterized by MAS NMR. Their high viscosity (Figure 44a, Figure 28), comparable to grease, needs special handling methods. Most of these methods were developed for crystallization applications. We explored several methods to prepare solid-state NMR samples and developed procedures to allow precise control of the components and their amounts added to NMR rotors, as outlined in the materials and methods section.

We first explored the LCPs stability under varying MAS speeds and temperatures. Embedding a membrane protein at concentrations allowing the acquisition of 2D protein spectra without disintegration of the cubic phase under MAS solid-state NMR conditions was successfully tested. LCPs are thereby shown to be feasible membrane mimetics for protein solid-state NMR. Exploring its unique properties of optical transparency and accessibility of solutes for membrane proteins by studying DgkA's enzymatic activity and uncaging its nucleotide substrate in LCP broadens the scope of applications, expands the toolkit for solid-state NMR and highlights solid-state NMR for the study of biochemical reactions inside porous materials.

I.3.2.1 Parameters of LCP studied by solid-state NMR

Formation of a lipidic cubic phase can be followed by ssNMR as the high membrane curvature leads to fast angular changes caused by diffusion along the bilayer normal, resulting in liquid-state like spectra (Figure 44b, Figure 29) observable with INMR.¹⁸³ As stability of the LCP under MAS conditions was successfully tested so far only up to 5 kHz^{199,201} in 4 mm MAS rotors. Here, MAS rates up to 10 kHz, typical for protein ssNMR experiments were tested. Using fully packed rotors, sealed with rubber disks to avoid a hole forming in the center, neither a LCP nor a LCP containing 10 mol% DMPC showed pronounced changes in static ¹³C or ³¹P spectra after MAS (Figure 29a, b). Thus, even with hydrophobic mismatch no separation occurred between DMPC and monoolein. Furthermore, classical cross polarization based experiments at 10 kHz MAS with 1 mg DgkA embedded do not detect monoolein signals (Figure 63a), giving evidence that the cubic phase is maintained during MAS even with high amounts of LCP destabilizing detergent¹⁶⁶ and membrane protein. In addition, the optical transparency, high viscosity and adhesion of the LCP samples is maintained upon unpacking of MAS rotors after experiments (Figure 28).

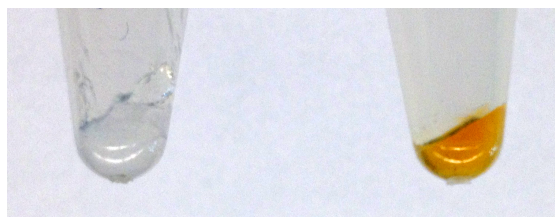


Figure 28: LCP unpacked after MAS experiments. Optical transparency and viscosity are maintained after MAS experiments. Illumination and release of NPE-ATP during MAS leads to NPE-ATP concentration dependent coloring from photoproducts (Figure 39b) but does not change optical transparency and viscosity (right).

The temperature phase diagram of monoolein water mixtures show that the cubic phase at a monoolein:liquid ratio of 6:4 (w/w) is usually stable between 20 and 80 °C and meta-stable when under-cooled.^{165, 170} MAS in this temperature range had no effect on the static ^{13}C and ^{31}P NMR spectra of a LCP containing 10 mol% DMPC (Figure 29c, d). Above 80 °C line broadening is observed in ^{13}C and ^{31}P spectra, which is non-reversible upon heating to 95 °C, most likely due to loss of water. Cooling below 20 °C is possible without alterations in the ^{31}P spectra (Figure 29d). After freezing the sample however, line broadening is observed even above 20 °C, where a cubic phase can form spontaneously, and increases with the amount of freeze-thaw cycles. The line broadening is an indication that a phase separation occurred between DMPC and monoolein or lipids and liquid, which prevents full phase transition from an Lc or $\text{L}\alpha$ phase back to a cubic phase.

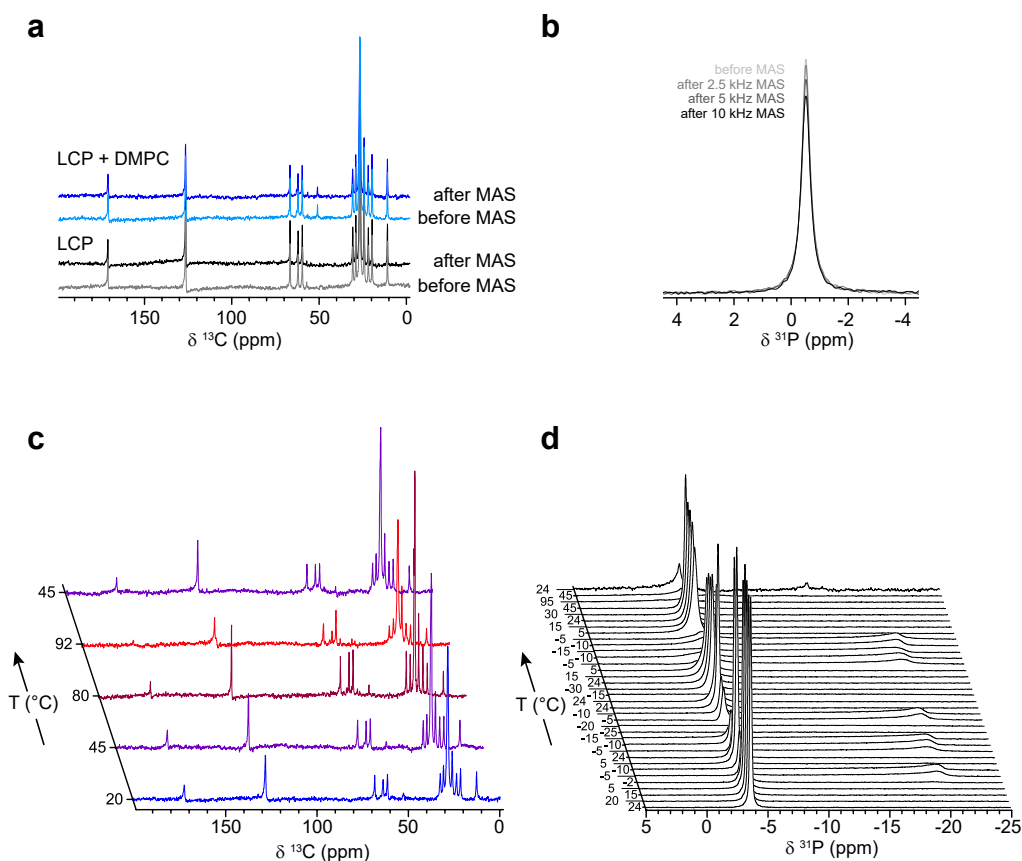


Figure 29: Stability of LCP at different MAS speeds and temperatures. **a**) Static ^{13}C spectra at 20 °C of LCP formed by centrifugation with a monoolein:liquid ratio of 6:4 (w/w) and an LCP additionally containing 10 mol% DMPC before and after 10 kHz MAS. **b**) Static ^{31}P spectra of the LCP containing 10 mol% DMPC before and after different MAS speeds. **c**) and **d**) ^{13}C and ^{31}P static temperature scan spectra of LCP samples containing 10 mol% DMPC spun at 2.5 kHz MAS between measurements. Arrow indicates order of temperature scan acquisition from bottom to top.

I.3.2.2 Properties of a nucleotide in LCP

Mg^{2+} is an essential cofactor required for DgkA's activity²⁵⁴ as seen by lack of ATPase and kinase activity in experiments omitting the divalent ion (Appendix Figure 12). Mg^{2+} is forming complexes with ATP leading to ^{31}P NMR line broadening due to intermediate exchange rates at certain molar ratios of Mg^{2+} and ATP³⁴⁰⁻³⁴¹. Therefore, ^{31}P spectra of ATP in LCP with different molar ratios of MgCl_2 were measured (Figure 30a). It was found that the βP - and γP -ATP ^{31}P signals without MgCl_2 in LCP were already severely broadened, which is in contrast to ATP in solution³⁴¹. Broadening increased and peaks shifted to a lower field upon addition of sub-stoichiometric amounts of MgCl_2 . The downfield shift is maximal at a 1 to 1 stoichiometric ratio (Figure 30c), with βP - and γP -ATP peak broadening the most severe at a MgCl_2 to ATP ratio of 1 to 2 (Figure 30d), which can be understood as

formation of a 1:1 Mg:ATP complex. The linewidths however reach their minimum only above a molar ratio of 2 and show a slight increase again at a molar ratio of 5, which is accompanied by a slight upfield shift of the peaks starting already above a molar ratio of 1. As linewidths of ATP in LCP are broad compared to liposomes or liquids where $^3J_{31P,1H}$ couplings can be observed with long acquisition times (Appendix Figure 15), a temperature scan of ATP/ADP (1:1 molar ratio) in LCP was performed (Figure 30b). Linewidths increase severely with higher temperature, but no spinning sidebands are observed even at high temperatures. Therefore, chemical exchange might be the cause of ATP and ADP linebroadening in LCP, especially as NPE-ATP signals, which do not complex with divalent ions exhibit more narrow lines in LCP than the ATP released upon uncaging (Figure 43).

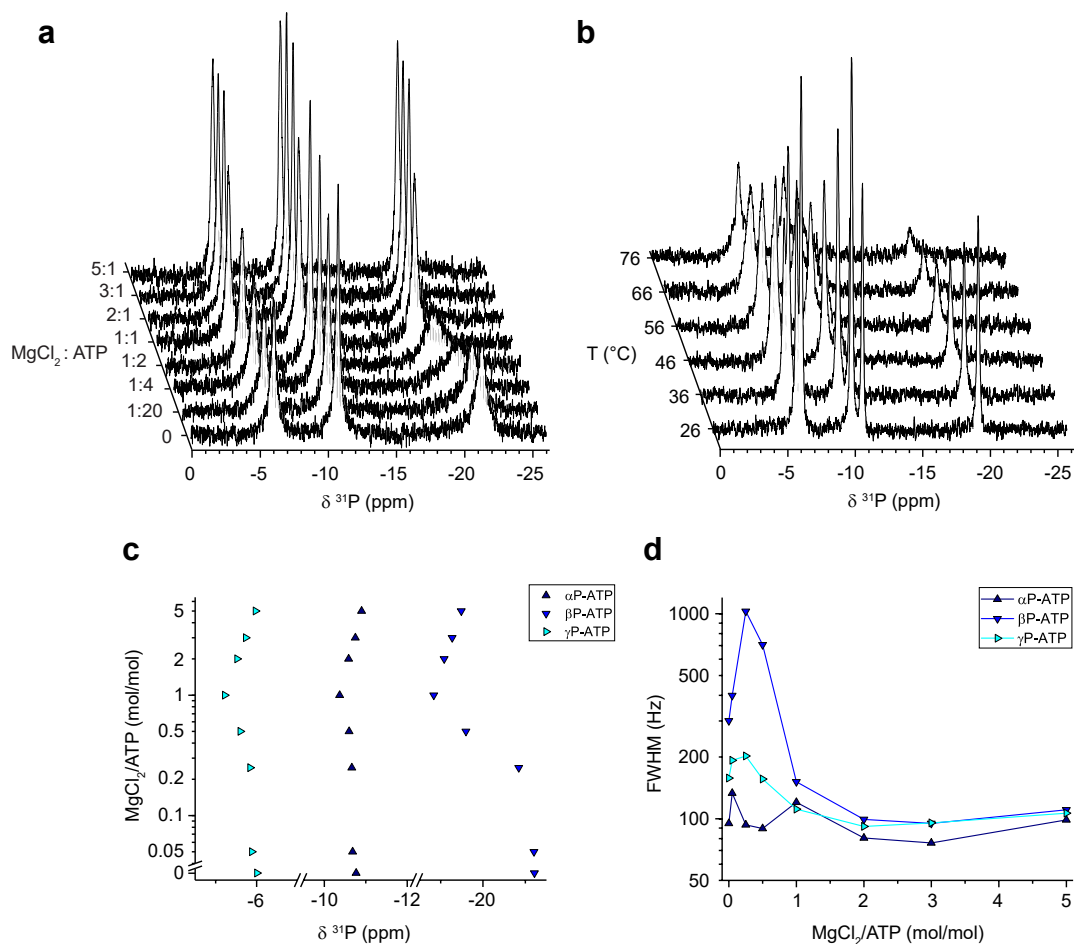


Figure 30: ³¹P MAS NMR spectra of a nucleotide in LCP upon MgCl₂ and temperature variation at 3 kHz MAS. **a)** Spectra of LCP samples containing 20 mM ATP with increasing molar ratios of MgCl₂ in 30 mM NaCl and 50 mM HEPES pH 7.5 with respect to the liquid fraction at 303 K. **b)** Temperature scan of a LCP sample containing 30 mM ATP and 30 mM ADP in 120 mM MgCl₂, 30 mM NaCl and 100 mM HEPES pH 7.5 with respect to the liquid fraction. **c)** Semi-logarithmic plot of chemical shifts of peaks from (a) with respect to the MgCl₂/ATP ratio. **d)** Semi-logarithmic plot of full widths at half maximum (FWHM) of peaks from (a) with respect to the MgCl₂/ATP ratio.

Comparison of ATP diffusion rates in solution and LCP would give useful insights into the extent of limited diffusion in cubic phases. As diffusion-ordered spectroscopy (DOSY) requires pulsed field gradients (PFG) a LCP sample for liquid-state NMR in a PTFE tube liner was prepared. The LCP formed in a LCP mixing device and injected through the bottom of the tube liner was stable as judged by viscosity, birefringence and NMR spectra of the sample (Figure 31a, b) acquired by Dr. Boris Fürtig. However, sample shimming with the PTFE tube liner was impaired, which partially contributes to the observed line broadening compared to ATP in solution. As the high content of monoolein impedes ^1H measurements of ATP, ^{31}P detected DOSY was performed (Figure 31c). The diffusion rate for ATP in solution was $2.5 \cdot 10^{-10} \text{ m}^2\text{s}^{-1}$. The diffusion rate of ATP in LCP could not be determined even by recording 512 transients per increment in a pulsed field gradient stimulated spin echo (PFG-SSE) due to fast signal decay preventing longer gradient or diffusion times. However, these experiments still yielded valuable information as the diffusion rate of ATP in LCP is below the lower limit of observable diffusion rates in the performed DOSY experiments ($1.5 \cdot 10^{-13} \text{ m}^2\text{s}^{-1}$), and therefore at least 3 orders of magnitude lower than in solution.

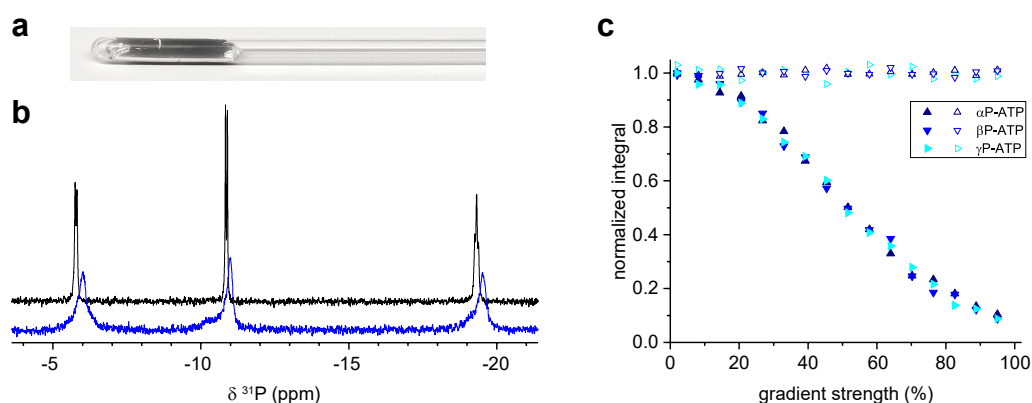


Figure 31: ^{31}P liquid-state NMR of 15 mM ATP with twofold molar excess of MgCl_2 in solution and LCP performed by Dr. Boris Fürtig. **a)** Picture of the LCP injected through the bottom into a 4 mm PTFE NMR tube liner. **b)** ^{31}P INMR spectra of ATP in solution (black, 8 transients) and in LCP (blue, 128 transients). **c)** Normalized integrals of ATP signals in solution (filled symbols) and LCP (non-filled symbols) from ^{31}P DOSY experiments in relation to applied gradient strength (at 242.89 MHz).

I.3.3 Uncaging approach for solid-state NMR

To uncage a caged compound during MAS NMR experiments inside the spectrometer two aspects had to be explored and results are described in this chapter. First, the sample needs to allow light penetration at the needed wavelength. Thus, it should not absorb or scatter too much, which judging by optical appearance might be a problem for liposomes often used in ssNMR on membrane proteins.

Second, an illumination setup capable of illuminating the whole sample at the needed wavelength with sufficient light intensity is needed. However, setups for sample illumination during MAS are not commercially available and just a few setups are known to have been built in varying complexity for different applications^{16, 19, 21-24, 342} as detailed in the introduction. The existing DNP illumination setup in our group was tested and a new high field MAS NMR illumination setup built to allow efficient uncaging *in situ* (Figure 32 and Section I.2.4).

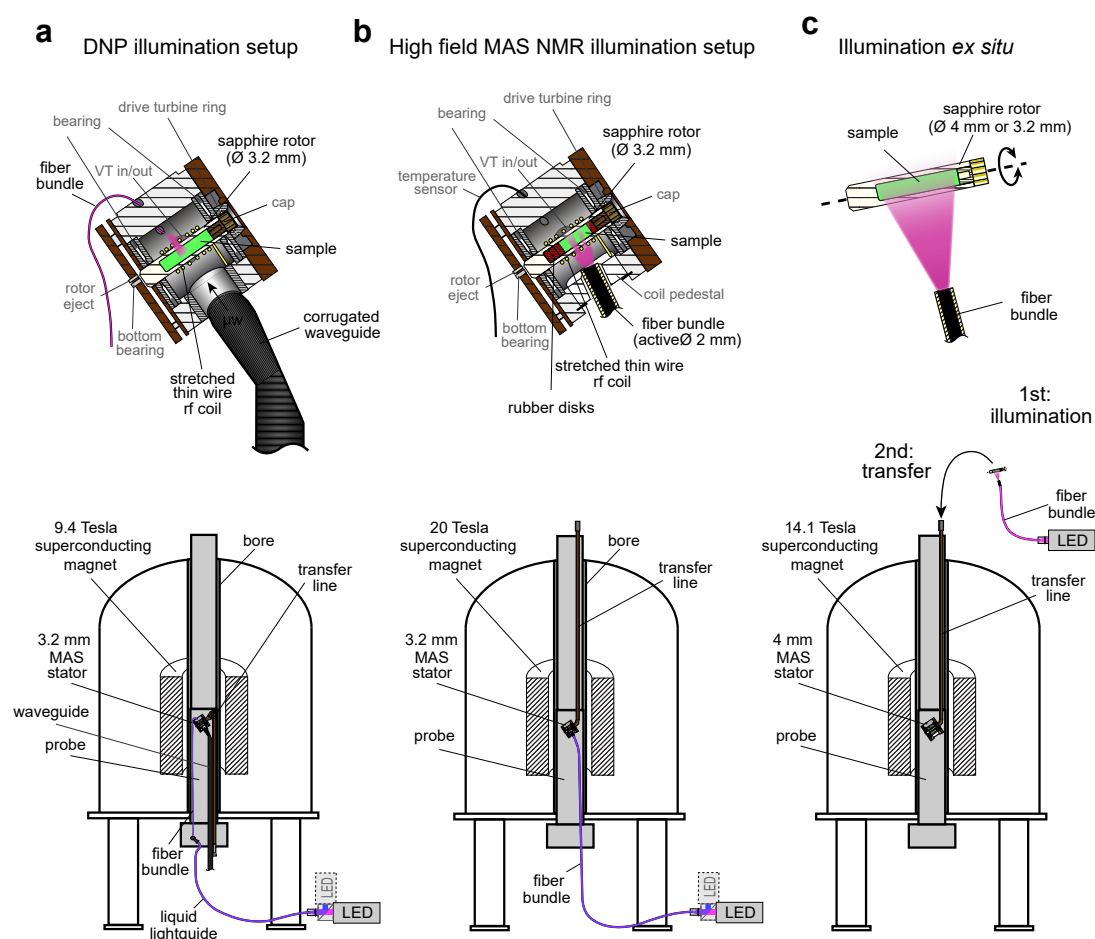


Figure 32: Illumination variants and setups used for uncaging experiments. **a)** The existing DNP illumination setup successfully used to study photointermediates of retinal proteins²⁴⁻²⁶. Schematic of the MAS stator with a narrow fiber bundle from a MAS spinning speed counter inserted through a hole in the stator otherwise used for a temperature sensor. With introduction of new lightsources as part of

the thesis, light from several LED's can be coupled into a liquid lightguide via beam combiners connected to a LED lightguide adaptor. The liquid lightguide is then coupled to the fiber bundle exiting the probe. **b)** Schematics of the new high field MAS NMR setup developed for efficient *in situ* sample illumination. A custom manufactured fiber bundle with an active diameter of 2 mm and macor ferules is inserted into the stator through a hole drilled into the coil pedestal of a custom manufactured stretched thin wire coil to allow efficient coupling of light from LEDs into the sample. The sample volume is restricted with rubber disks inside the stator to align with the illuminated area. **c)** Illumination of the sample in a MAS rotor outside the spectrometer was performed as well to test chosen light sources and lightguide variants for uncaging. After illumination, the sample was transferred into a ssNMR spectrometer for acquisition as depicted for *ex situ* uncaging experiments using a 600 MHz NMR spectrometer equipped with a 4 mm MAS probe. Illumination setups are described in detail in materials and methods (Section I.2.4).

I.3.3.1 Evaluation of MAS rotors for illumination experiments

MAS rotors for standard ssNMR experiments are typically made of zirconia (ZrO_2), a white ceramic material, which absorbs in the visible wavelength spectrum. To test if zirconia rotors can be used for UV light illumination, the absorbance of zirconia rotors was compared to optical transparent sapphire rotors used for DNP applications and illumination experiments with visible light (Figure 33) in a normal UV-Vis spectrometer (V-550, Jasco).

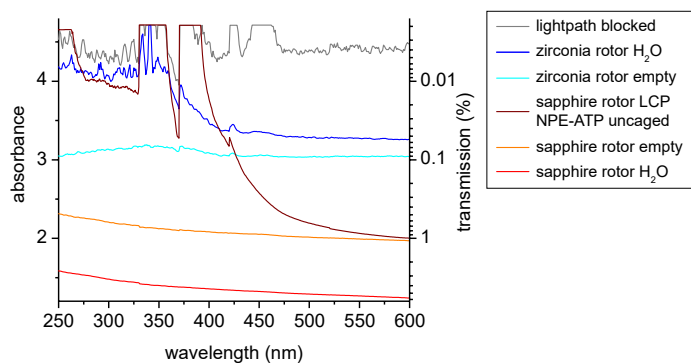


Figure 33: UV-Vis spectra of empty as well as filled 4 mm sapphire and zirconia MAS rotors. To prevent light passing around the sides of the rotors, a black painted aluminum mask was installed in the cuvette holder chamber.

This rather simple experiment shows that zirconia rotors have also higher absorbance in the UV range compared to sapphire rotors. Therefore, all ssNMR uncaging experiments were performed in sapphire rotors.

I.3.3.2 Testing a DNP illumination setup for uncaging applications

The simple DNP illumination setup used in our group for illumination of retinal proteins at low temperatures under DNP conditions²⁴⁻²⁶ was tested for possible uncaging applications at low temperatures. The illumination setup had been built by Bruker by insertion of a bifurcated fiber cable commonly used for the MAS revolution counter into an unused bore hole of the stator. As the stator material is of boron nitride, which is not absorbing visible light³⁴³, a missing alignment of the beam emitted from the fiber tip onto the sample was not considered an issue. Also due to the use of a non-coherent light source, a thin fiber and non-optimal coupling, light intensity, which reached the sample, was low, as sample amounts had to be minimized to thin films to allow excitation of retinal proteins²⁴⁻²⁵.

Uncaging of NPE-ATP upon illumination with UV light from a LED outside the spectrometer leads to an increased absorbance at 314 nm in UV-Vis spectra (Figure 34a) as the various photoproducts of the primary and secondary reactions have higher absorbance than NPE-ATP^{69, 344}. Uncaging can also be followed by ³¹P NMR observing the decrease of NPE-ATP and increase of ATP signals (Figure 34b). As caging the γ -phosphate of ATP with the NPE group introduces a chiral center in proximity to the phosphoesters and synthesis is not performed stereoselectively, the diastereomeric mixture³⁴⁵ is observable in ³¹P and ¹H NMR spectra acquired in solution (Figure 34d, Appendix Figure 4, Appendix Table 1). Diastereomers have, according to Walker et al⁵⁴, identical photolytic properties. Illumination of 15 mM NPE-ATP outside the spectrometer in a sapphire rotor through a fiber bundle showed likewise efficient and fast uncaging (Figure 34c) with a half time <10 s as followed by ³¹P signals of NPE-ATP.

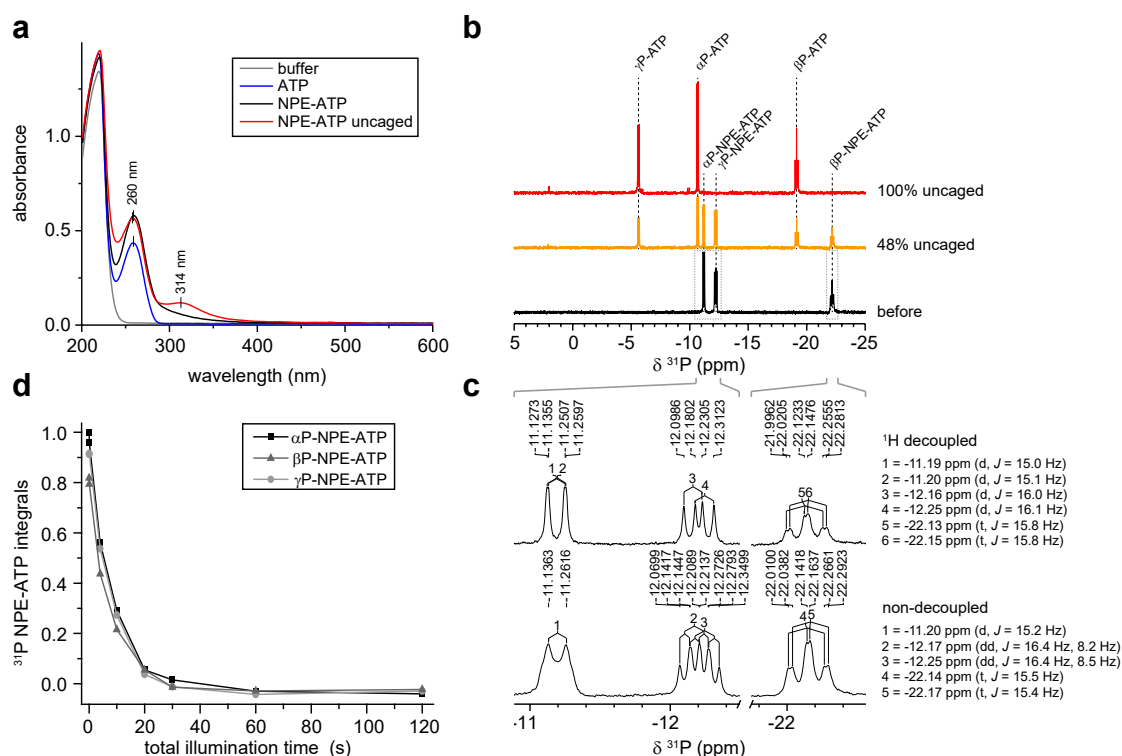


Figure 34: Uncaging of NPE-ATP outside the spectrometer by illumination with a UV LED through the custom-built fiber bundle manufactured for the high field MAS NMR illumination setup. **a**) UV-Vis absorbance spectra of 0.1 mM NPE-ATP before and after uncaging in 100 mM HEPES, 30 mM NaCl pH 7.5 as well as 0.1 mM ATP and the buffer alone in a 3 mm path length quartz cuvette. **b**) ^{31}P liquid-state NMR spectra of 7.5 mM NPE-ATP in 100 mM HEPES, 30 mM NaCl, 60 mM MgCl_2 pH 7.5 before, upon 48% uncaging and after uncaging (121.45 MHz). **c**) Detail of NPE-ATP peaks of ^{31}P liquid-state NMR spectra with and without ^1H decoupling before uncaging with J -couplings. Peak doubling is observed due to the diastereomeric mixture (121.45 MHz). **d**) Progress of uncaging 15 mM NPE-ATP in a 3.2 mm sapphire MAS rotor upon illumination with 365 nm light outside the spectrometer followed by the ^{31}P signals of NPE-ATP.

First trials to uncage 5 mM NPE-ATP inside the DNP spectrometer at room temperature with the same light source revealed that UV light intensity reaching the sample is too low for uncaging significant amounts of NPE-ATP (Figure 35).

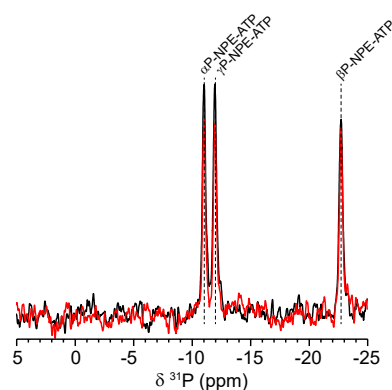


Figure 35: Uncaging of 5 mM NPE-ATP in 100 mM HEPES pH 7.5 with the illumination setup at the DNP spectrometer at room temperature and MAS in manual mode at ~ 1 kHz. In black: ^{31}P spectrum before illumination. In red: ^{31}P spectrum after 30 min illumination at 365 nm. Release of ATP from its cage could not be detected.

To avoid having to use UV light, whose non-coherent light sources are less intense, and which does not reflect but gets absorbed by boron nitride of the stator and copper of the coil, we tried a photocage, which can be uncaged in the visible wavelength range.

A red shifted coumarin photocage protecting acetic acid (NdiEt-tcAA, [7-(diethylamino)-2-sulfanylidenechromen-4-yl]methyl acetic acid) was synthesized by Dr. Andreas Jakob as described for a similar synthesis of the benzoic acid derivative⁵¹ in a project exploring red shifted photocages. Assignment for ^1H and ^{13}C resonances can be found in Table 6. As these caging groups are not water soluble⁵¹, we studied uncaging in organic solvent compositions which can form a glassy matrix upon freezing required for increased DNP enhancements, namely DMSO + 33% (v/v) H_2O (1:2 molar ratio)³⁴⁶ and tetrachloroethene (TCE)³⁴⁷. Solubility of NdiEt-tcAA in DMSO was >200 mM, in DMSO + 33% (v/v) H_2O 10 mM and in TCE 15 mM. UV-Vis spectra revealed that the absorbance maximum of NdiEt-tcAA was with 433 nm in TCE and 477 nm in DMSO + 33% (v/v) H_2O (Figure 36b) strongly solvent dependent. Uncaging outside the spectrometer resulted in altered absorbance spectra of the photoproducts compared to the caged compound and alterations in the ^1H NMR spectra, which describe the release of the caged compound, namely acetic acid (Figure 36b-d).

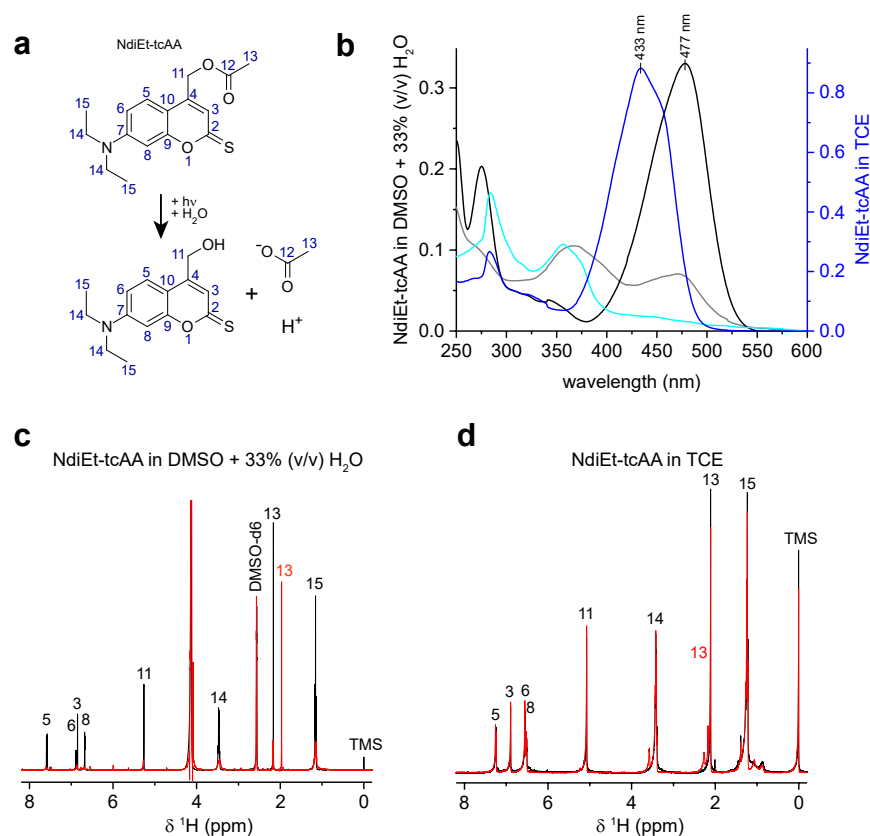


Figure 36: Uncaging of NdiEt-tcAA outside the spectrometer. **a**) Uncaging reaction scheme and structural formula of NdiEt-tcAA with atom numbering for the assignment of ¹³C and ¹H chemical shifts (Table 6). **b**) UV-Vis absorbance spectra of NdiEt-tcAA in different solvents, before (blue and black) and after (cyan and gray) illumination of the sample at 470 nm for 5 min. **c**) ¹H INMR spectra before (black) and after (red) uncaging of NdiEt-tcAA at 470 nm for 5 min in DMSO-d₆ + 33% (v/v) H₂O and TCE **d**) at 500.18 MHz with assignment of peaks according to (a).

Table 6: Assignment of NdiEt-tcAA ¹H and ¹³C chemical shifts in DMSO-d₆ and TCE obtained via HSQC and HMBC spectra referenced to TMS (Appendix Figure 7, Appendix Figure 8). Atom numbers refer to Figure 36a.

| Atom number | DMSO-d ₆ | | TCE | |
|-------------|----------------------|-----------------------|----------------------|-----------------------|
| | ¹ H (ppm) | ¹³ C (ppm) | ¹ H (ppm) | ¹³ C (ppm) |
| 2 | - | 196.17 | - | 195.27 |
| 3 | 6.858 | 119.26 | 6.892 | 121.91 |
| 4 | - | 144.56 | - | 137.98 |
| 5 | 7.586 | 126.20 | 7.242 | 108.40 |
| 6 | 6.880 | 111.54 | 6.547 | 97.17 |
| 7 | - | 151.63 | - | 149.66 |
| 8 | 6.680 | 96.28 | 6.522 | 108.34 |
| 9 | - | 159.11 | - | 158.37 |
| 10 | - | 107.70 | - | 108.10 |
| 11 | 5.267 | 61.17 | 5.070 | 60.38 |
| 12 | - | 171.19 | - | 167.90 |
| 13 | 2.166 | 20.81 | 2.108 | 19.76 |
| 14 | 3.477 | 44.65 | 3.416 | 44.26 |
| 15 | 1.163 | 12.53 | 1.228 | 12.14 |

As signals from carbons via cross polarization from attached protons would hinder NMR experiments and illumination of NdiEt-tcAA in DMSO + 33% (v/v) H₂O resulted in black precipitate, we tried to uncage 5 mM NdiEt-tcAA in TCE inside the DNP spectrometer at room temperature under MAS with a 405 nm and 470 nm light source. However, illumination for 15 min at both wavelengths did not cause a significant change in the absorbance spectra or ¹H NMR spectra recorded at the DNP spectrometer (Figure 37). The NMR spectra however are difficult to interpret as they exhibit spinning side bands at the low MAS speeds possible with solutions, most likely caused by surface adhesion at rotor walls, insufficient shimming or, less likely because not visible, aggregation of NdiEt-tcAA.

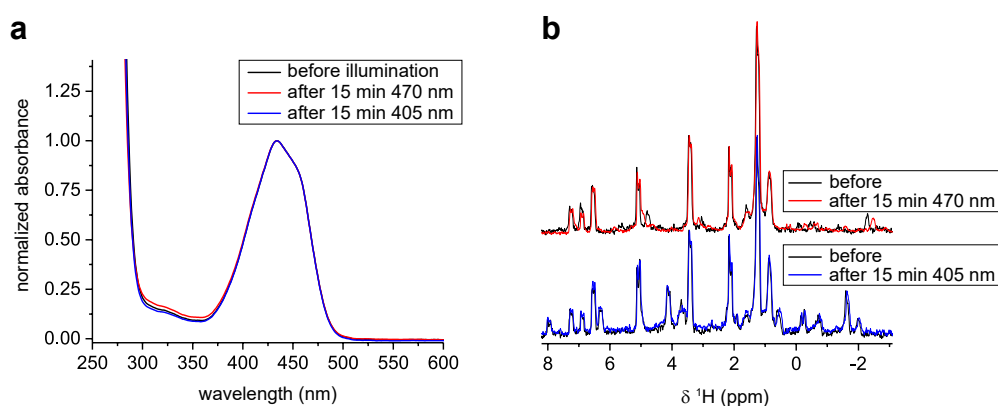


Figure 37: Uncaging of NdiEt-tcAA for illumination experiments inside the DNP spectrometer. Samples containing 5 mM NdiEt-tcAA in TCE were illuminated for 15 min at different wavelengths inside the DNP spectrometer at room temperature at ~ 1 kHz MAS in manual mode. **a)** Normalized UV-Vis absorbance spectra of samples before illumination (black) and after illumination at 470 nm (red) and 405 nm (blue). **b)** ¹H NMR spectra recorded at the DNP spectrometer (400.20 MHz) before (black) and after 15 min illumination at 470 nm (red) and 405 nm (blue) at room temperature and ~ 1 kHz MAS in manual mode.

Thus, the current light routing at the DNP spectrometer does not provide enough light intensity to the sample in the tested UV-Vis light range to uncage even low concentrations of tested caged compounds in a reasonable time (Table 7).

Table 7: Summary of success (✓) or failure (x) to uncage tested caged compounds inside the DNP spectrometer compared to uncaging outside the spectrometer with the same light sources.

| caged compound | Wavelength of used LED | uncaging <i>ex situ</i> (outside spectrometer) | uncaging <i>in situ</i> DNP setup |
|----------------|------------------------|--|-----------------------------------|
| NPE-ATP | 365 nm | ✓ | x |
| NdiEt-tcAA | 405 nm | ✓ | x |
| NdiEt-tcAA | 470 nm | ✓ | x |

I.3.3.3 Development of a high field MAS NMR illumination setup

Accessibility for illuminating a sample inside a MAS probe is limited. Therefore, all known illumination setups so far developed relied on fiber optics. Due to the construction of Bruker type MAS probes having the non-transparent cap for drive at the top, illumination onto the rotor as realized in illumination setups based on Varian or Jeol probe types¹⁷⁻¹⁸ is not possible. Because the bottom contains bearing and the eject port, illumination from the bottom²³ at 3.2 or 4 mm rotor sizes would allow only for a narrow additional bore to insert a fiber. A small diameter fiber is a drawback for the intended use of non-coherent light sources but using coherent light sources it would allow to irradiate a high active volume via total reflection along the rotor wall as shown at the end of this chapter by experiments outside the spectrometer. Thus, for modifications the focus was on illumination variants from the side, which can be intricate, placing fibers between the coil windings¹⁹, or simpler by placing a fiber bundle directed at the sample with distance to the coil¹⁶. For higher robustness and less need for modifications the latter approach was chosen and Norbert Forger from Bruker Biospin was modifying a 3.2 mm 850 MHz WB HX probe to house a light guide and manufactured a stretched thin wire coil to allow wider gaps for the light beam emitted from the light guide to reach the sample (Figure 38).

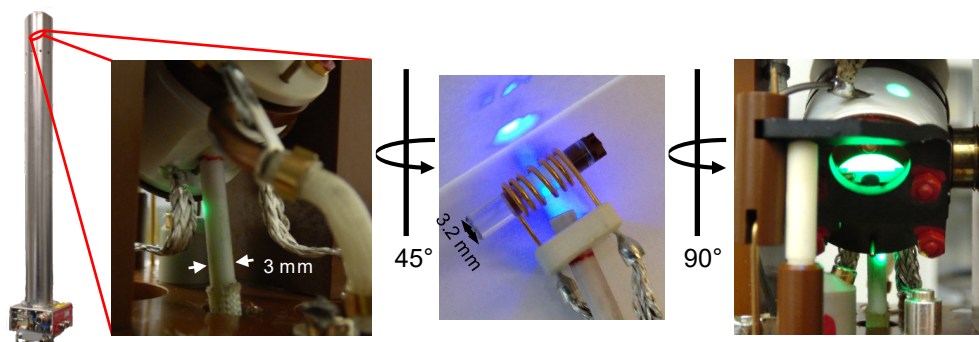


Figure 38: Modified probe for illumination under MAS conditions with inserted light guide. Pictures show the stator with the light guide inserted through a hole in the coil pedestal during illumination. The position of the light guide compared to the sample and the stretched thin wire coil is highlighted in the center picture of the disassembled coil pedestal.

I.3.3.3.1 Light guide variants

Optimal light routing with a light guide for illumination with non-coherent light sources necessitates a high acceptance angle and maximized active core area of the light guide combined with high transmittance. Therefore, liquid light guides, which have a larger acceptance angle and higher transmittance in the UV range down to 300 nm compared to fused silica fibers would be the first choice.

Liquid light guides like the tested 2 m UV-Vis type LLG-03-59-300-0650-2 (Mightex Systems) with a 5 mm ferrule housing, a 3 mm core and a numerical aperture (NA) of 0.59 are used in strong magnetic fields without complications (personal communication Bernhard Wondra, AMS Technologies). The allowed temperature range of -5 till 35 °C would limit their use for illumination experiments to ambient temperatures. Because ferrules and sheathing of available or semi-custom manufactured liquid light guides are made of stainless steel, their magnetic permeability and electric permittivity would strongly interfere with applying radio frequency (RF) pulses, detection and shimming due to the proximity to the RF coil.

Therefore, we focused on fused silica fibers as light guides. Typically, single fibers are only produced up to 1 mm core diameter, which we used for testing illumination with a 355 nm laser (Paladin Advanced 355-8000, Coherent). The high short and long-term break radius for 1 mm core fibers, typically 15 respectively 30 cm, needs careful handling and is limiting use of even wider diameters in flexible light guides.

To increase the active fiber core area and allow lower bend radii we chose to commission a 3.5 m, 2.5 mm diameter fiber bundle consisting of ~700 70 µm diameter core LUV fused silica fibers (LUV70 P05240700300200). This fiber bundle similar to one used in a publication for photo-CIDNP³⁴⁸ allows efficient transmission (>50% at 2 m fiber length) of light between 250 and 900 nm with a specified NA of 0.22 (at 587 nm).

To have less interference from differences in magnetic permeability and electric permittivity, the fiber bundle is sheathed with a fiberglass sleeve and the ferrules consist of Macor (Corning), a glass-ceramic made of fluorophlogopite in a borosilicate glass matrix³⁴⁹⁻³⁵⁰. Macor is however containing some, in our experiments not studied, NMR active nuclei, which could interfere in certain experiments due to the proximity to the RF coil. It is typically comprised of 46% SiO₂, 17% MgO, 16% Al₂O₃, 10% K₂O, 7% B₂O₃ and 4% F³⁵⁰.

I.3.3.3.2 Light source variants

Due to the high costs of high-power (>100 mW radiant power) collimated and coherent light emitting UV lasers, the light source bought for illumination under MAS conditions consists of a collimated (22 mm diameter clear aperture), 500 mW radiant power UV LED operating at a peak wavelength of 365 nm with a computer controlled LED driver (LED: LCS-0365-11-22; Driver: SLC-AV02-US, Mightex Systems). The UV LED used, had the highest radiance at the time of purchase of known commercially available non-coherent light sources for illumination at 365 nm. In combination with a light guide adapter (LCS-LGA22-0515, Mightex Systems), focusing the collimated light onto the light guide core, the radiant power at the end of the custom manufactured fused silica fiber bundle was 22 mW as determined by a laser thermal power sensor (P/N 1Z02146, Ophir) connected to a Nova Display power meter (1Z01500, Ophir). Collimated LEDs were used instead of directly coupling a LED to the fiber bundle to couple light of different wavelengths into a light guide using multi-wavelength beam combiners. These allow combining light from several LEDs for wavelength selective sequential uncaging, such as a 405 nm peak wavelength LED for release of coumarin protection groups and a 365 nm peak wavelength LED for release of NPE protection groups (LCS-BC25-0380, Mightex Systems).

In cooperation with Dr. Boris Fürtig, a 355 nm, 8 W radiant power diode pumped quasi CW (80 MHz repetition rate, > 15 ps pulse length) UV laser (Paladin Advanced 355-8000, Coherent) used for uncaging of NPE protection groups in INMR experiments was tested for sample illumination under MAS conditions. Therefore the probe and a MAS Pneumatic Control Unit (H2620, Bruker) were transferred to the laser and set up on site. The laser increased the light output at the end of a 1 mm core diameter fused silica fiber (Optran UV 1000/1100 N (high OH (700 ppm), 1000 μm core, 1100 μm cladding, NA 0.22, silicone buffer, nylon jacket), Ceram Optec) used for illumination inside the probe to 6 W radiant power compared to 22 mW obtained with the LED connected to the fiber bundle. Due to the high power in the UV range, which can cause solarization damage, but more often thermal damage to the core and cladding caused by impurities in the fiber, illumination with the fiber bundle was not tested. As the laser beam diameter is specified to be $1\text{ mm} \pm 15\%$ with a divergence smaller than 550 μrad , using the fiber bundle would most likely not increase radiant power as the active core area in the fiber bundle is decreased, due to packing factor losses.

I.3.3.3.3 Illumination area

It was tested next how much of the sample volume is illuminated under MAS conditions inside the probe using the 365 nm LED. Upon illumination of the samples NPE-ATP concentration dependent discoloration is observed (Figure 39b), most likely caused by photoproducts of the uncaging reaction. This was used to advantage by uncaging NPE-ATP in LCP, which due its high viscosity limits diffusion of the colored photoproducts, allowing to visualize the illuminated volume (Figure 39a). Discoloration in the center of a LCP sample shows that the illuminated volume is lesser than the rotors sample volume due to the fiber bundles numerical aperture limiting beam divergence and stronger light blockage from the coil at a higher angle of incidence combined with decreasing coil pitch at the sides (Figure 39d, c).

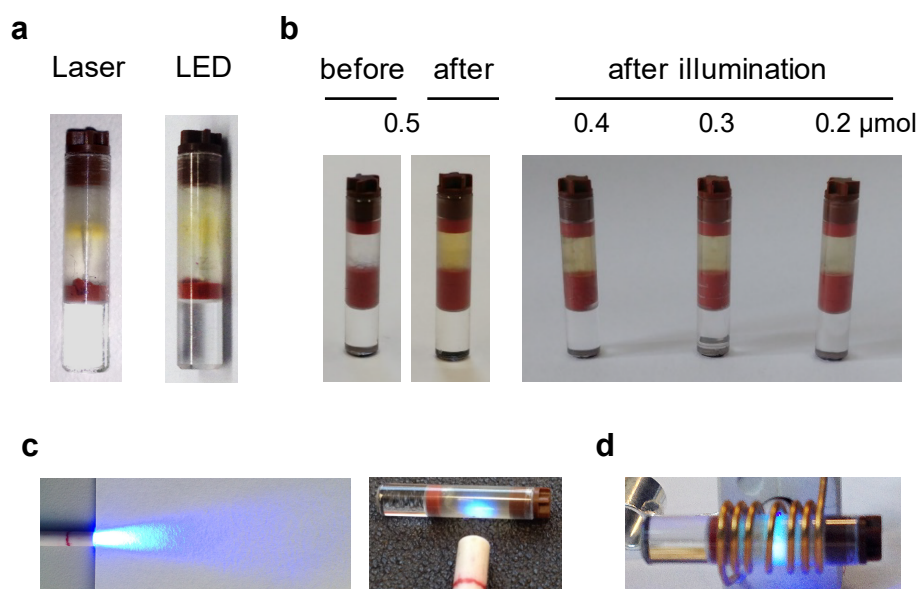


Figure 39: Illuminated area of NPE-ATP containing LCP samples. **a)** 30 μl LCP samples containing 0.45 μmol NPE-ATP illuminated inside the probe at 3 kHz MAS for 1 s with the 355 nm laser or 12 min with the 365 nm LED. **b)** Concentration dependent discoloration of samples with sample volume reduced to the active area containing 15 μl LCP upon illumination for 5 min with the 365 nm LED at 3 kHz MAS. **c)** Picture of beam divergence of the fiber bundle at 365 nm with a LED as light source **d)** Top view of the disassembled coil pedestal with an inserted sapphire MAS rotor containing LCP during illumination at 365 nm via the fiber bundle with a LED as light source.

This is further supported by ^{31}P spectra before and after uncaging showing only a 50% NPE-ATP signal reduction. Reducing the sample volume to 15 μl by placing 3 rubber disks into the bottom and 1 at the top of the rotor, leads to even discoloration and up to 95% NPE-ATP uncaging as judged by ^{31}P NMR (Figure 41). Therefore, the sample volume was reduced with this method in all further uncaging experiments even though

reduction of the sample amount also reduces the amount of signal, which is a considerable drawback as ssNMR is typically sensitivity-limited.

I.3.3.3.4 Efficiency of *in situ* uncaging

Uncaging times for 0.4 μmol NPE-ATP in LCP ($t_{1/2} = 80$ s) and 3 mg of DOPC liposomes ($t_{1/2} = 84$ s) are comparable (Figure 40), but significantly slower than illumination with the LED outside the spectrometer in solution (Figure 34). Due to the elevated risk of rotor crashes with solutions under MAS and a comparable optical transparency of cubic phases an experiment to uncage NPE-ATP in solution *in situ* was not deemed useful.

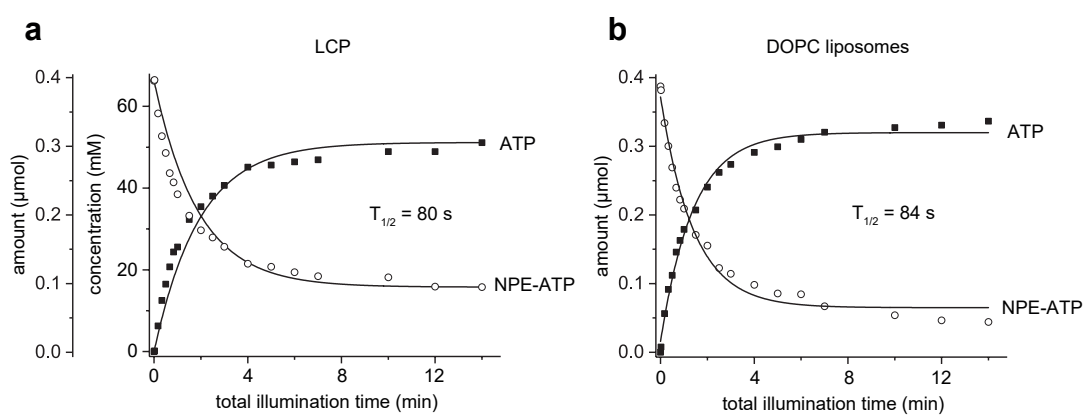


Figure 40: Stepwise uncaging of 0.4 μmol NPE-ATP at 303 K with the developed high-field MAS NMR illumination setup *in situ* at 365 nm followed by ^{31}P ATP and NPE-ATP signals in **a)** 15 μl LCP (monoolein:liquid 6:4 (w/w)) at 3 kHz MAS. Amounts as well as concentrations with respect to the liquid fraction given. **b)** 3 mg DOPC liposomes at 10 kHz MAS. Both samples were prepared with 50 mM HEPES pH 7.5 and 30 mM NaCl.

Uncaging of NPE-ATP is concentration dependent, with the uncaging efficiency decreasing from 95% at 10 mM to less than 70% at NPE-ATP concentrations above 60 mM (Figure 41) as judged by ^{31}P NPE-ATP signals before and after illumination.

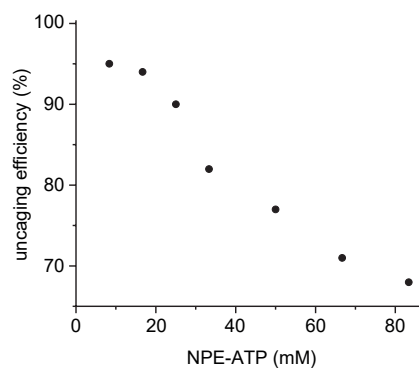


Figure 41: NPE-ATP uncaging efficiency in LCP upon illumination with the developed high-field MAS NMR illumination setup *in situ* at 365 nm for 5 min at different NPE-ATP concentrations with respect to the liquid fraction at 303 K and 3 kHz MAS followed via ^{31}P NPE-ATP signals. Samples contained 2.8 μg DgkA, 100 mM HEPES pH 7.5, 30 mM NaCl and respective MgCl_2 concentration according to Section I.2.2.2.3.

Uncaging efficiency, determined after 5 min illumination, cannot be significantly increased by increasing illumination time as shown in Figure 40. A pH shift caused by the proton released during the uncaging reaction is not considered a major factor, when using 100 mM HEPES to buffer the solution. By following the pH dependent ^{31}P chemical shift of Pi (Appendix Figure 9) a strong pH shift was not observed in the real-time experiments (Figure 47).

The primary cause for lower uncaging efficiencies at high concentrations is most likely the amount of irradiance as trials to increase the illuminated sample volume by moving the fiber bundle further away resulted in lower uncaging yields. This is further supported by fast and highly efficient uncaging in the illuminated area upon 1 s of sample illumination with the 355 nm laser setup (Figure 43). However, due to the highly focused beam from the laser, only a small part of the sample is illuminated (Figure 39). To increase the illuminated volume, modifications to the light path available for single fibers like sculpted silica fiber tips, could increase beam divergence when illuminating from the side.

I.3.3.3.5 Alternative light path variants

Illumination through the bottom of the MAS rotors, avoiding shading from the coil and insufficient beam divergence, allowing to use the complete sample volume were tested outside the probe. Compared to illumination from the side, the whole sample was illuminated as can be seen visually by light emitting from the whole sample and the cap end using the 365 nm LED (Figure 42).

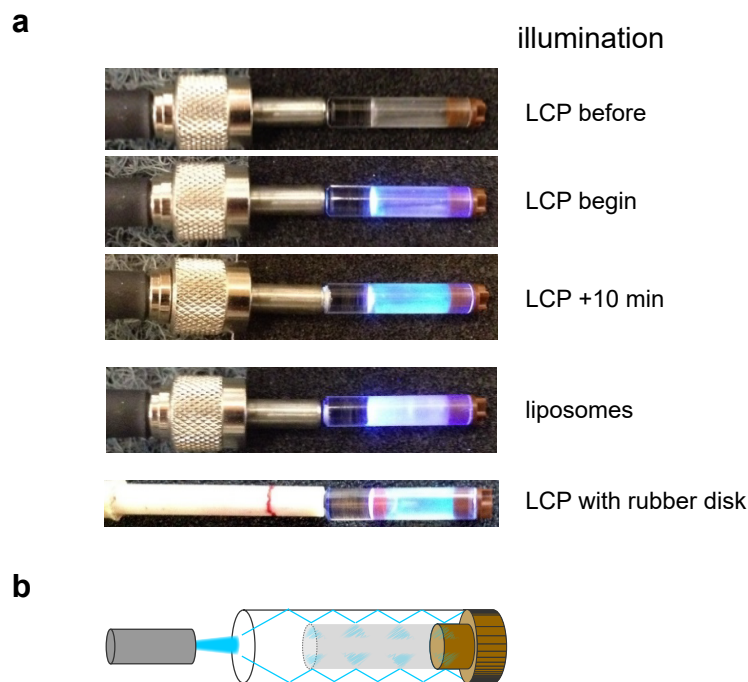


Figure 42: Illumination of sapphire MAS rotors from the bottom. **a)** Rotors contained $0.45 \mu\text{mol}$ NPE-ATP in LCP or 3 mg DOPC containing liposomes and are illuminated with the 365 nm LED. Illumination of the whole sample area persists upon insertion of a rubber disk at the bottom blocking the direct light path. **b)** Schematic of possible total reflection along the outer rotor wall and scattering at the rough inner rotor wall.

Illumination with a 1 mm diameter core fused silica fiber therefore led to high uncaging efficiencies ($>80\%$) with the 365 nm LED despite the supposedly far longer path length. To achieve high uncaging efficiencies with short laser pulses the fiber had to be aligned in a 45° angle to the sapphire rotor allowing total reflection inside the rotor as the critical angle for total internal reflection of sapphire ($n = 1.8$ at 355 nm) to air is 56.2° . 2 s of laser illumination with rotation of the rotor along its longitudinal axis between pulses resulted in equally high uncaging efficiencies as 10 min illumination with the 365 nm LED (Figure 43). To show that total reflection along the polished outside of the rotor and scattering into the sample at the rough inner surface is responsible for the high uncaging efficiencies placing a rubber disk at the bottom of the rotor did not abolish light being emitted from the whole sample upon illumination (Figure 42).

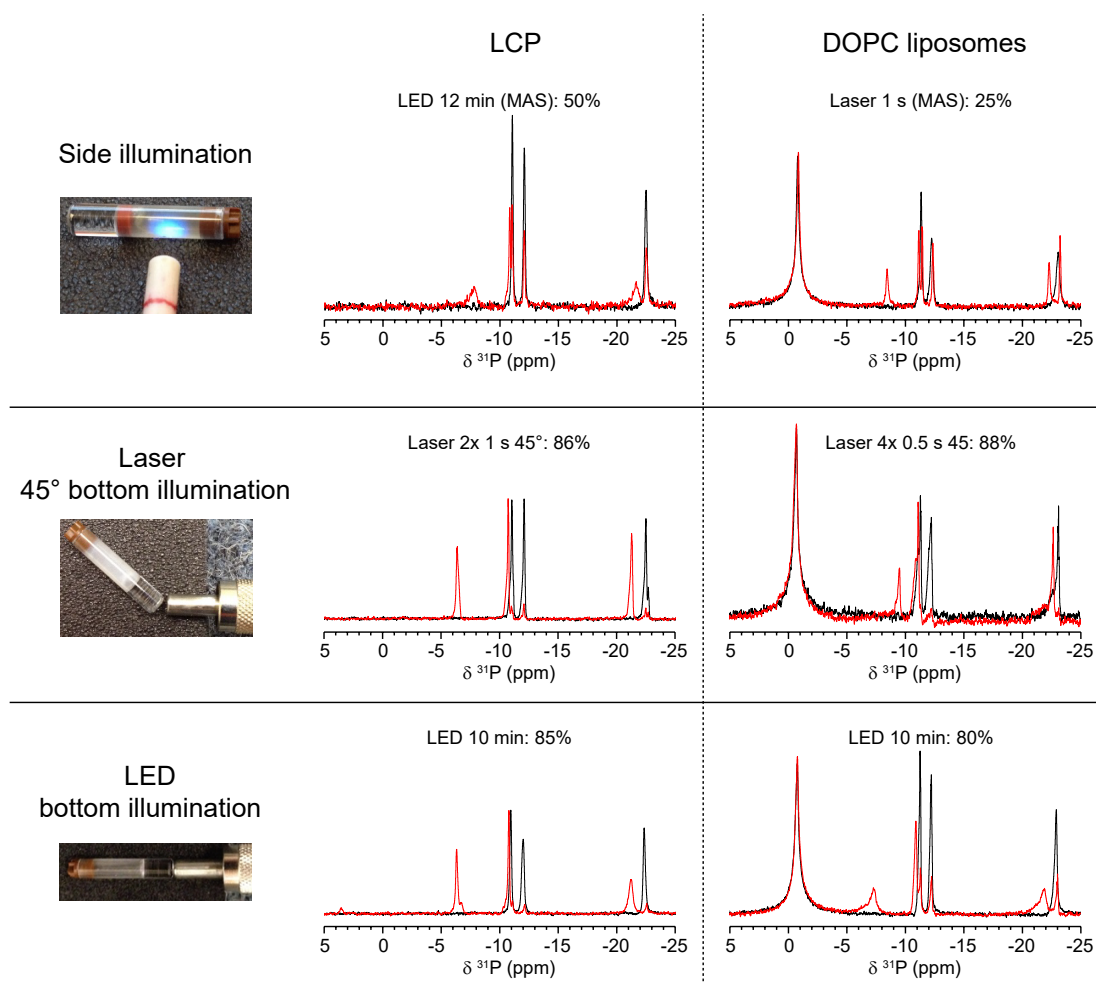


Figure 43: ^{31}P spectra and uncaging efficiencies of tested illumination configurations at full sample volume (30 μl). Comparison of illumination from the side during MAS inside the probe, illumination via short laser pulses through the bottom at a 45° angle and illumination through the bottom using the 365 nm LED. Samples contained 0.45 μmol NPE-ATP (15 mM with respect to the rotor volume) in LCP or 3 mg DOPC containing liposomes with 50 mM HEPES pH 7.5 and 30 mM NaCl.

I.3.4 Membrane mimetics for triggering enzymatic activity by uncaging

Membrane mimetics for triggering DgkA's enzymatic activity by uncaging its substrates *in situ* should maintain DgkA's enzymatic activity by allowing substrate accessibility and varying substrate concentrations, should not be highly absorbing at the uncaging wavelength and should allow to follow the enzymatic activity preferentially via ^{31}P real-time NMR. Therefore, we choose to qualitatively evaluate the lipidic cubic phase of monoolein, DOPC liposomes and anisotropic bicelles (DMPC:DHPC 3.2:1 (mol/mol)) for these parameters and their feasibility to initiate biochemical reactions by light (Figure 44). A quantitative kinetic analysis of DgkA's enzymatic activity in LCP by addition of ATP and via *in situ* uncaging of NPE-ATP is the topic of chapter I.3.6.1. Similarly, an analysis of observed ATPase activity in the tested membrane mimetics as well as DgkA's ATPase activity in absence of a lipid substrate are the topic of chapter I.3.5.

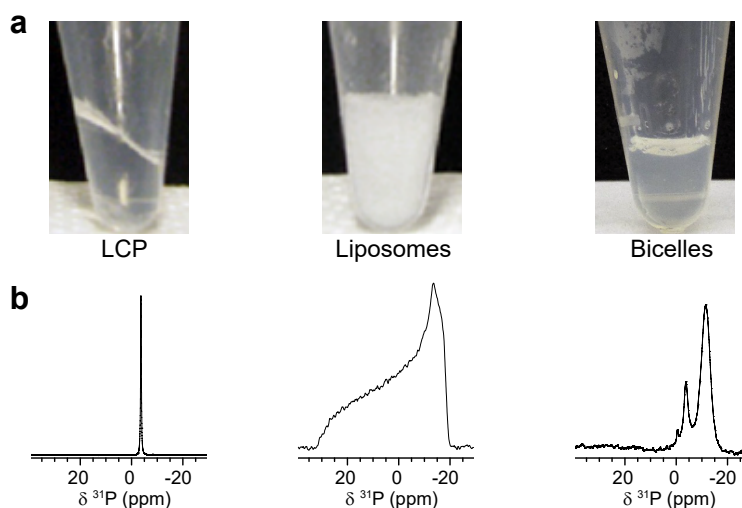


Figure 44: Comparison of LCP, DOPC liposomes and anisotropic bicelles. **a)** Optical comparison of membrane mimetics tested for uncaging experiments. **b)** Comparison of static ^{31}P spectra of LCP + 10 mol% DMPC, DOPC liposomes and magnetically aligned anisotropic bicelles (3.2:1 (mol/mol) DMPC:DHPC).

I.3.4.1 Enzymatic activity of DgkA in tested membrane mimetics

DgkA shows activity in all three tested membrane environments (Figure 45).

The lipidic cubic phase, a membrane mimetic made of MAGs, is not containing any phospholipids and is not yet commonly used in biomolecular solid-state NMR. The high membrane curvature results in isotropic linewidths of lipids diffusing along the bilayer normal (Figure 44b, Figure 29). MAGs, thus the whole membrane, are a substrate for DgkA²⁴⁹. Therefore, variation of lipid substrate concentration is not possible. By adding all components to the rotor and then forming the cubic phase, the amount of added lipids, protein and liquid volumes are precisely known compared to liposomes or bicelles. Thus, the shown addition of 2 μmol ATP (Figure 45), equates to 100 mM ATP with respect to the liquid fraction of the cubic phase. Extraction of the initial reaction rate from the progress curves for this experiment reveals an activity of 2.9 ± 0.2 U. Furthermore, ATP hydrolysis activity is not observed in LCP (Figure 45, Appendix Figure 11) as will be discussed further in chapters I.3.5.1 and I.4.2. As explored in detail in chapter I.3.2, the cubic phase is stable under MAS without phase separation being observed. Thus, in combination with the ability to precisely determine sample components and full substrate accessibility (see chapters I.3.6.1 and I.4.3) v_{max} and K_{M} values of DgkA's enzymatic activity in LCP with respect to ATP as nucleotide substrate can be determined. The results of the kinetic analysis are detailed in chapter I.3.6.1, which focusses on evaluating the influence of reduced nucleotide diffusion (Section I.3.2.2 and Figure 31) through the network of narrow water channels on enzyme kinetics in comparison to data from indirect biochemical assays performed in LCP surrounded by a bath solution.

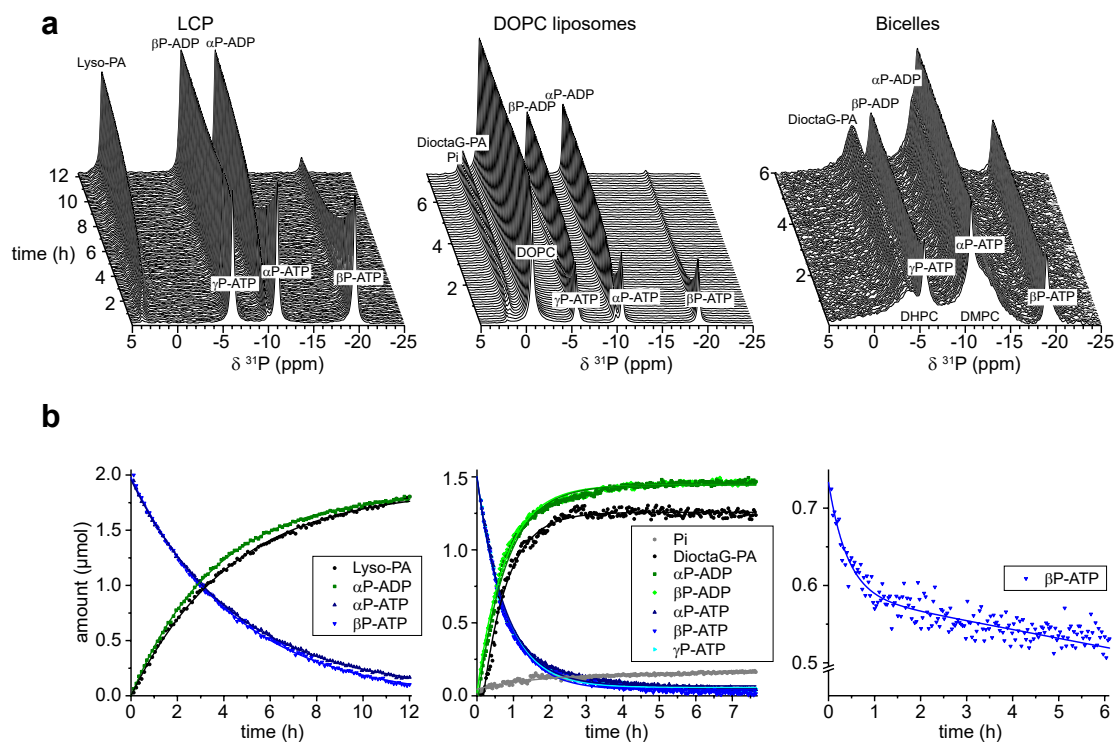


Figure 45: Enzymatic activity of DgkA in LCP, liposomes and anisotropic bicelles in the presence of lipid substrates (5 and 0.25 μmol diocetanolglycerol for liposomes and bicelles respectively). **a**) ^{31}P real-time ssNMR spectra following DgkA's enzymatic activity upon addition of 2, 1.5 and 0.75 μmol ATP for LCP, liposomes and bicelles equating to .40, 30 and 15 mM ATP with respect to the rotor volume. Sample amount of DgkA was 5 μg for LCP (L:P 240400:1), 500 μg for liposomes (L:P 120:1) and 2.5 μg for bicelles (L:P \sim 15600:1). L:P is not including diocetanolglycerol. Experiments performed at 30 $^{\circ}\text{C}$ and 3 kHz MAS for LCP, 10 kHz MAS for liposomes and without MAS for bicelles. **b**) Progress curves of integrals from well-separated peaks of (a). Monoexponential fits for LCP and biexponential fits for liposomes and bicelles of the time traces to determine initial reaction rates are shown as solid lines.

Liposomes commonly used for protein solid-state NMR applications on the other hand exhibit reaction rates under MAS NMR conditions, which are a magnitude lower²⁹¹ than published values from biochemical assays^{134-135, 271, 298}. This is also reflected in the need for higher DgkA amounts compared to bicelles and LCP to observe enzymatic activity in reasonable time with solid-state NMR (Figure 45b). An initial reaction rate of 0.04 U for DgkA in DOPC liposomes obtained from this experiment is confirming the low activity. MAS NMR, which leads to phase separation of liposomes and bulk water, most likely restricts substrate accessibility and does not alter the enzymatic activity, as published K_M values²⁹¹ are similar to assay conditions. MAS is however an unfortunate necessity, as the static lipid powder spectra would severely compromise detection of the kinase lipid product (Figure 44b).

Observation of the kinase product in static ssNMR experiments is also hindered in bicelles by the broad ^{31}P signals from the phospholipids of the magnetically aligned bicelles (Appendix Figure 10) overlapping most ATP and ADP signals (Figure 45a, Figure 47). The phospholipid signals unfortunately change their shape during the course of the experiments and therefore cannot easily be subtracted to analyze the overlapping signals (Figure 47b). The necessity for two rate constants to fit the increased activity in the beginning of the real-time measurement, transitioning into a slower nucleotide substrate consumption rate, may serve as indirect evidence that kinase activity takes place in the beginning. Upon lipid substrate consumption, ATPase activity becomes the dominating enzymatic activity (Figure 45b). Bicelles are strongly influenced by pH, lipid composition, lipid concentration, ionic strength and salt concentration^{144, 161}, as can be seen by changes in the phosphorous lipid signals during the course of the experiments, especially as DgkA's kinase activity alters lipid composition. Variation of ATP or DAG concentration, keeping the other parameters constant, was therefore limited to a small range without causing aggregation and precipitation, preventing experiments to obtain K_M and v_{\max} values for ATP or a DAG. The initial reaction rate obtained via static ^{31}P real-time NMR of 3.2 ± 0.8 U (Figure 45) with 7.5 mM dioctanoylglycerol and 15 mM ATP is in the same range to the enzymatic activity of 1.5 ± 0.2 U obtained via a coupled photometric assay with 18 mM DBG synthesized by Dr. Andreas Jakob³³⁰ and 3 mM ATP (Appendix Figure 16). Despite differences in substrate concentration and used lipid substrate, necessary due to different conditions between assay and real-time NMR experiments, these results show that substrate accessibility in bicelles is given.

Optical transparency and low absorption at the wavelength used for uncaging are important parameters for successful uncaging experiments. The lipidic cubic phase is optically transparent and absorbance does not increase significantly in the UV range until 310 nm as determined by measuring a UV-Vis spectrum of a LCP in a custom built LCP quartz holder (Figure 46) as described in section I.2.3. Attempts to transfer an LCP into a normal quartz cuvette by syringe injection or centrifugation created voids compromising the measurements thereby hindering a completely exact comparison to liposome and bicelle samples. As liposomes and bicelles have similar absorption¹³¹, scattering in liposomes comes to play a crucial role limiting absorbance measurements to very diluted solutions or thin films, making them appear optically dense compared to bicelles (Figure 44), especially in concentrations (>35 mg/ml

DOPC) used in solid-state NMR (Figure 46). By reduction of sample amounts to create thin films it is however possible to uncage a nucleotide (Figure 47) and a lipid substrate (Figure 51) in liposomes as well.

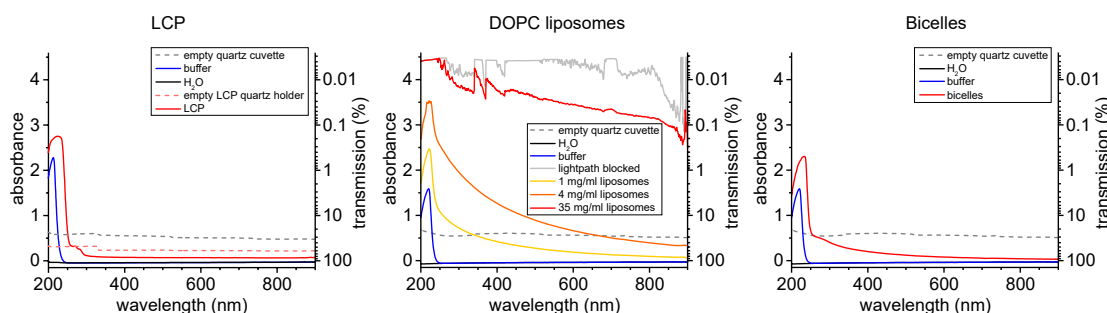


Figure 46: UV-Vis absorbance spectra of LCP (monoolein:liquid 6:4 (w/w)), DOPC liposomes (1, 4 and 35 mg/ml) and anisotropic bicelles (DMPC:DHPC 3.2:1 (mol/mol), 390 mg/ml). The absorbance spectrum of LCP was measured in a custom built quartz holder with 0.9 mm path length. Other samples and comparison to the used buffer (100 mM HEPES pH 7.5, 30 mM NaCl) and H₂O was performed in a standard 3 mm path length quartz cuvette. Dotted lines represent subtracted background spectra of the empty cuvette or holder.

It is possible to uncage NPE-ATP in all three tested membrane environments to trigger DgkA's enzymatic activity (Figure 47). LCPs allow the release of high ATP concentrations due to their optical transparency and comparably high stability. Release is limited by the light power that can be applied to the sample as with increasing NPE-ATP concentrations the uncaging efficiency drops in illumination experiments performed inside the spectrometer (Figure 41), compared to illumination with a coherent light source (Figure 43). The reduction of sample volume to 15 μ l, due to 3.2 mm rotors instead of 4 mm rotors and the illuminated area not spanning the entire rotor, reduces signal to noise and requires longer acquisition times.

Due to limited amounts of NPE-ATP, measurement time and the need to optimize bicelle and liposome sample composition for efficient uncaging as well as sample stability, the experiments shown here were simplified by omitting diacylglycerols. Nevertheless, enzymatic catalyzed ATP hydrolysis in absence of a lipid substrate was observed upon uncaging in both liposomes and bicelles. As a divalent cation, natively Mg²⁺, is a required cofactor for DgkA's enzymatic activity²⁵⁰ and Mg²⁺ does not influence hydrolysis rates in solution³⁵¹⁻³⁵², strongly reduced ATP hydrolysis in the same experiment with DOPC liposomes performed in absence of Mg²⁺ (Appendix Figure 12) confirms that the observed ATP hydrolysis in presence of Mg²⁺ is indeed enzymatically catalyzed. Whilst in liposomes scattering is the limiting factor for liposome concentration at a given light power due to increased absorbance, in bicelles

it is the stability upon release of ATP, which unlike NPE-ATP is complexing with divalent ions, and the release of a proton during the uncaging reaction. These alterations combined with bicelle destabilizing diacylglycerols severely restrict the space to vary bicelle composition, concentration of substrates, or other components.

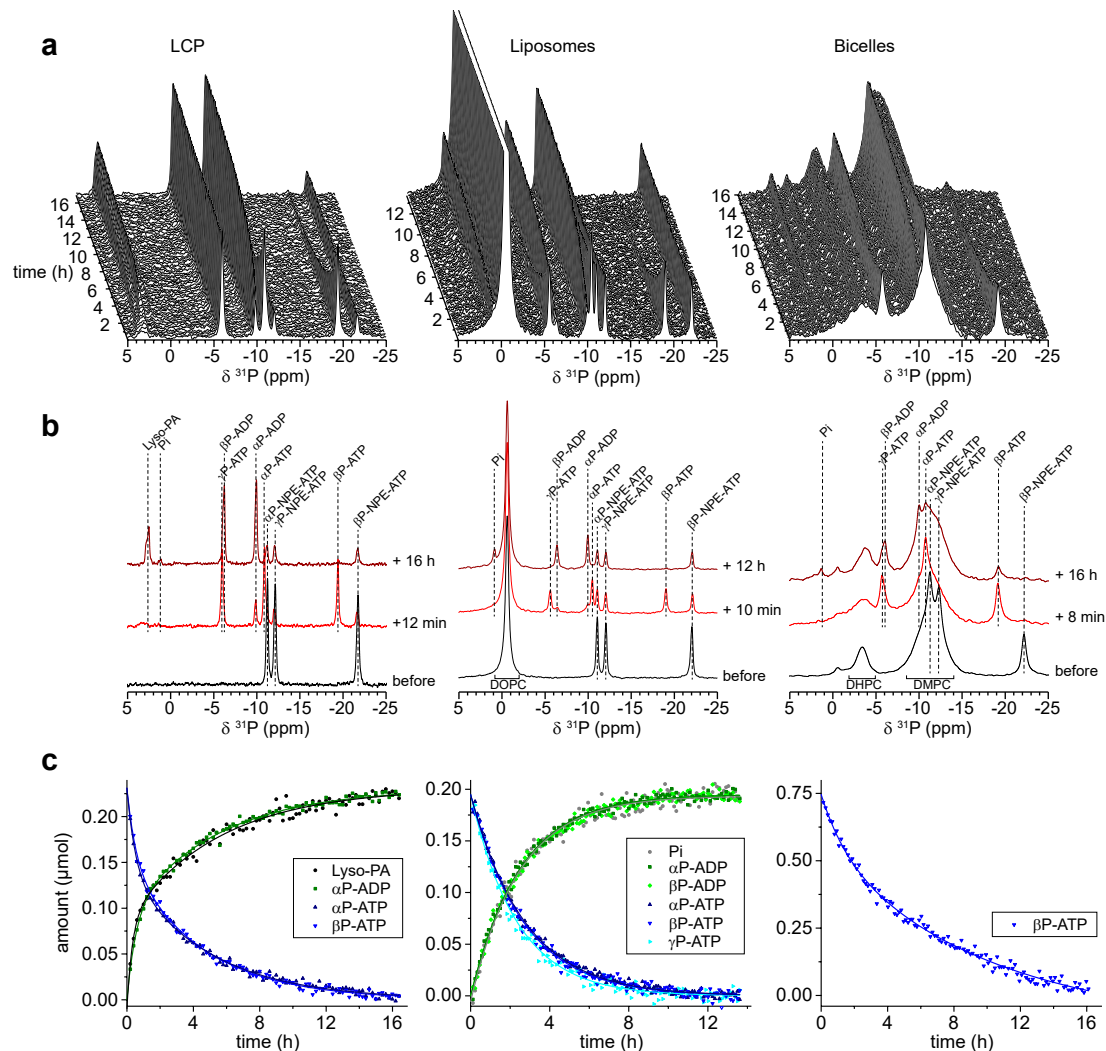


Figure 47: Uncaging of NPE-ATP to initiate DgkA's enzymatic activity in LCP, liposomes and anisotropic bicelles. **a**) ^{31}P real-time ssNMR spectra following DgkA's enzymatic activity upon 5 min illumination to initiate uncaging of 0.3 μmol NPE-ATP for LCP and DOPC liposomes and 0.75 μmol NPE-ATP for bicelles. These amounts equate to 15 mM NPE-ATP for all samples with respect to the rotor volume as illumination for bicelles was performed in a 4 mm sapphire rotor outside the spectrometer. Sample amount of DgkA was 0.97 μg for LCP (L:P 371200:1), 300 μg for liposomes (L:P 120:1) and 500 μg for bicelles (L:P 130:1). Experiments performed at 30 $^{\circ}\text{C}$ and 3 kHz MAS for LCP, 10 kHz MAS for liposomes and without MAS for bicelles. **b**) Comparison of selected ^{31}P spectra with annotations before uncaging (black), directly after uncaging (red) and at the end of the in (a) shown real-time NMR experiments (dark red). **c**) Progress curves of integrals from well-separated peaks of (a). Biexponential fit for LCP and monoexponential fits for liposomes and bicelles of the time traces are shown as solid lines. The amount of released ATP was 0.23 μmol for LCP equating to 38.5 mM with respect to the liquid fraction, 0.2 μmol for DOPC liposomes and 0.75 μmol for bicelles.

I.3.4.2 Uncaging of a non-miscible component in a biological membrane

By uncaging a native, non-water soluble lipid substrate to initiate DgkA's kinase reaction in liposomes we explore the uncaging approach as a tool to trigger biochemical reactions involving non-miscible or highly hydrophobic membrane components.

As common lipidic cubic phases used in structural biology are comprised of MAGs¹⁶², which are substrates of DgkA, release of a caged DAG was performed in DOPC liposomes. Due to their high hydrophobicity, native long chain DAGs like dioleoglycerol (DOG) have to be mixed with DOPC before liposome formation to insert into the membrane and yield a homogeneous distribution. As DAGs are non-bilayer forming lipids and are disrupting liposomes at high concentrations, screening of different DOPC:DOG ratios was performed. It was found that proteoliposome formation leading to a pellet upon centrifugation is possible without visible alterations in pellet size up to 20 mol% whilst concentrations above 25 mol% are leading to a smaller pellet and debris formation (Figure 48). In a similar range, dipalmitoylphosphatidylcholine (DPPC) bovine liver phosphocholine lipid mixtures containing more than 25 mol% DOG or DAGs derived from egg-PC extracts have been found to form non-bilayer phases³⁵³.

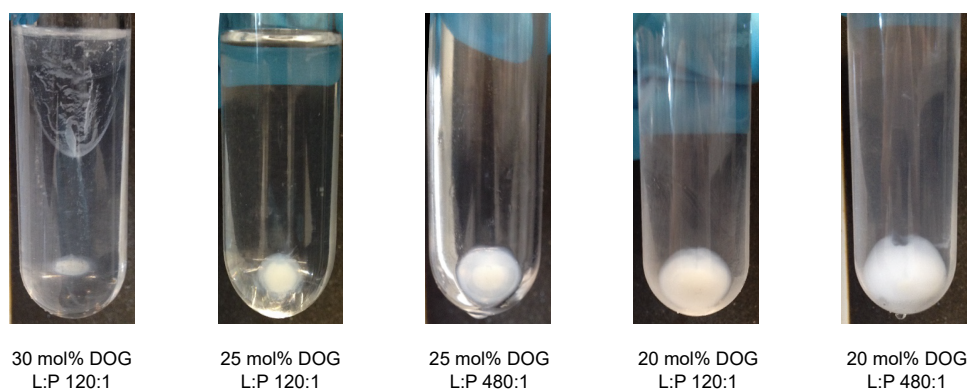


Figure 48: Pellets of DOPC proteoliposomes containing DgkA and DOG in varying ratios (18 μmol total lipid) after ultracentrifugation at 72660 g (25000 rpm) 4 $^{\circ}\text{C}$ for 30 min (Rotor: 45 Ti; Optima LE-80K Ultracentrifuge, Beckman Coulter).

DOPC liposomes containing 20 mol% DOG also exhibit a static ^{31}P powder spectrum typical for lamellar phases such as neat DOPC or DMPC:DMPA liposomes (Appendix Figure 13). DOG was retained in a quantitative manner in the liposomes during protein reconstitution as judged by DOPC and dioleoylphosphatidic acid (DOPA) ^{31}P signals upon phosphorylation of DOG by DgkA (Figure 49, Appendix Table 3).

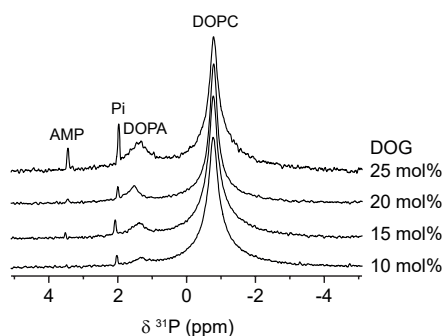


Figure 49: ^{31}P MAS NMR spectra after phosphorylation of DOG by 0.25 mg DgkA upon addition of 1 μmol ATP in DOPC liposomes containing varying lipid molar ratios of DOG (L:P 480:1) at 303 K and 10 kHz MAS. For percentage and deviation of DOPA signal to DOPC signal see Appendix Table 3.

It is therefore possible to use long-chain DAGs as lipid substrates for DgkA in liposomes. However, addition of these substrates has to occur before reconstitution as they cannot be added homogeneously in solution, with DOG not even soluble in DM micelles²⁵⁸.

To be able to first study basal ATPase activity and then initiate the kinase reaction we used the uncaging approach, rendering DAG inaccessible as substrate for DgkA until photocleavage of the protection group by illumination inside the spectrometer. Therefore, the phosphorylation site of commercially available DOG was protected with a photolabile NPE moiety with a oxycarbonyl linker (Figure 24) to enhance the uncaging efficiency by subsequent decarboxylation after initial photocleavage⁵⁸ in a 3-step synthesis by Dr. Andreas Jakob³³⁰.

After following basal ATPase activity the caged DOG was released with UV light inside the spectrometer during MAS. Built-up of phosphorylated product was in these restricted sample amounts not visible due to comparably low amounts of released DOG potentially being phosphorylated, in combination with broad linewidths, overlap with the DOPC signal and partial overlap with the Pi signal (Figure 49). However, up to 40 fold stimulation in ATP consumption can be measured by screening different lipid to protein ratios (Figure 50a-c, Appendix Table 4), which is not caused by UV light alone as illumination of a sample not containing NPE-DOG shows (Figure 50d).

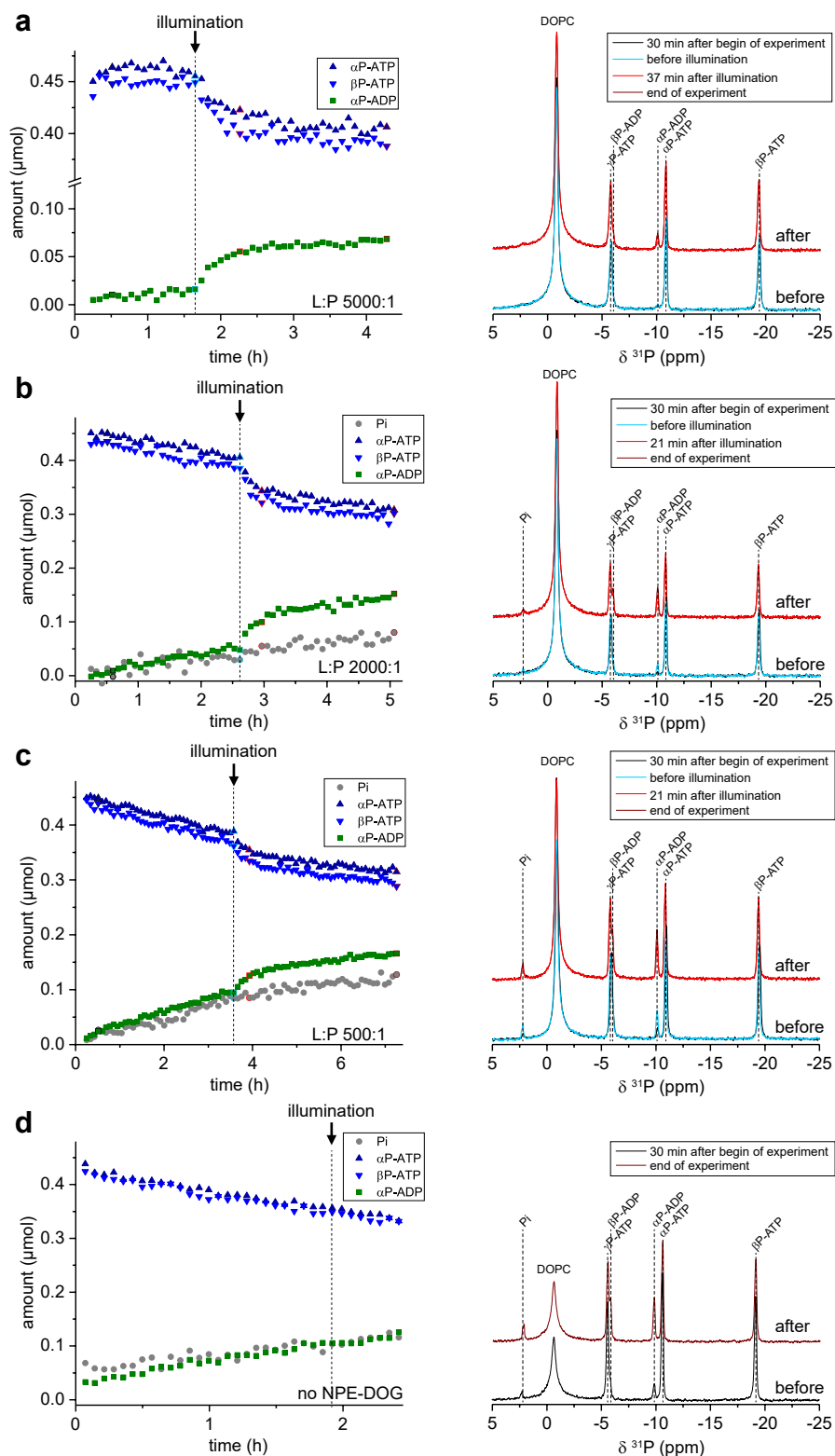


Figure 50: Time traces and selected spectra from ^{31}P real-time MAS NMR experiments following DgkA's basal ATPase activity in liposomes upon addition of $0.45\ \mu\text{mol}$ ATP followed by 5 min illumination to uncage membrane incorporated NPE-DOG triggering enhanced enzymatic activity. **a to c:** 15, 40 and 500 μg DgkA reconstituted into DOPC liposomes containing 20 mol% NPE-DOG at L:P ratios of 5000:1, 2000:1 and 500:1. Determined basal activity and stimulated activity upon illumination for these experiments are given in Appendix Table 4. **d)** Illumination does not enhance enzymatic activity of 54 μg DgkA reconstituted in DOPC liposomes (L:P 480:1) not containing a lipid substrate.

To verify that NPE-DOG was successfully uncaged and triggered DgkA's kinase reaction we used ATP γ S, a thiophosphate analog of ATP, as phosphoryl donor to resolve overlap of the phosphatidic acids ^{31}P chemical shift with the bulk lipid signal and Pi. Transfer of thiophosphate from ATP γ S by DgkA's kinase reaction leads to formation of a thiophosphatidic acid³⁵⁴, which is shifted downfield by 42 ppm compared to the corresponding phosphatidic acid. Successful application of this approach is shown in Figure 51 by built up of ThioPA after uncaging of NPE-DOG. As ATP γ S exhibits a 10 fold higher basal ATPase activity²⁹¹, the increase of ATP γ S turnover in the progress curves upon uncaging is not as pronounced (Figure 51b). Furthermore, available ATP γ S concentrations reduce the amount of liposomes that can be added in the restricted sample volumes and severely impair temporal resolution due to low signal intensity. Thus, restricting analysis of these experiments to qualitative descriptions.

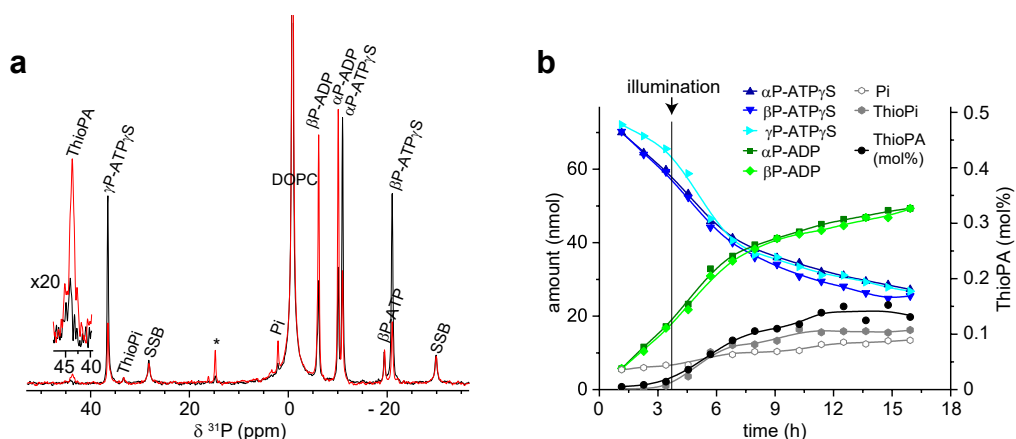


Figure 51: Formation of DgkA's kinase product thiophosphatidic acid after uncaging of NPE-DOG in presence of 75 nmol ATP γ S. **a)** Spectra of a ^{31}P real-time NMR experiment before (black) and after uncaging of NPE-DOG (red) triggering kinase activity of 13.3 μg DgkA reconstituted in DOPC liposomes (L:P 2000:1) containing 20 mol% NPE-DOG. The asterisk denotes a degradation product of the formed thiophosphate during hydrolysis of ATP γ S. **b)** Progress curves of the ^{31}P real-time NMR experiment depict basal ATPase activity before uncaging of NPE-DOG and kinase activity in conjunction with enhanced ATPase activity after uncaging as can be seen by formation of the thiophosphatidic acid product and enhanced built-up of ThioPi. Spectra consist of 6272 transients per increment.

The signal at 44 ppm assigned to ThioPA is further verified as membrane component by ^{31}P cross polarization spectra and is retained in the membrane fraction upon washing of the membrane pellet (Figure 52).

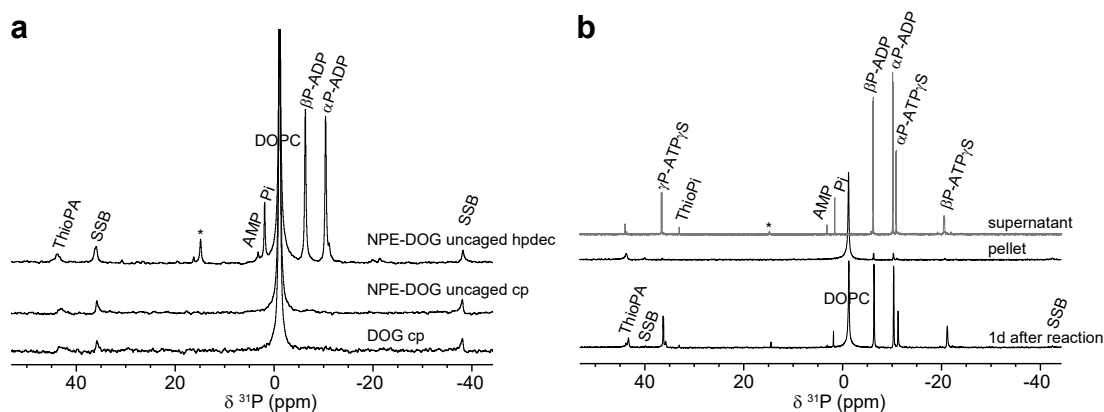


Figure 52: Formation of thiophosphatidic acid by DgkA with ATP γ S as nucleotide substrate. ^{31}P spectra confirm that the signal at 44 ppm forming after uncaging of NPE-DOG is the kinase product ThioPA as it can be cross polarized, exhibits the same chemical shift when utilizing non-caged DOG as substrate (a) and upon washing of the membrane pellet is mainly found in the pellet fraction (b). Spectra recorded at 280 K with 9 kHz MAS to avoid overlap with spinning side bands of repacked samples at 14.09 Tesla, 243 MHz ^{31}P . The spectrum of the supernatant was acquired with a liquid-state NMR spectrometer at 11.75 Tesla, 202 MHz ^{31}P .

The additional signal at 15 ppm seen in another study but not assigned³⁵⁵ or omitted by skipping the relevant spectral range in some spectra³⁵⁶ is a degradation product of ThioPi, as it also formed in a sample containing only ThioPi and MgCl₂ adjusted to pH 7.5 (Figure 53).

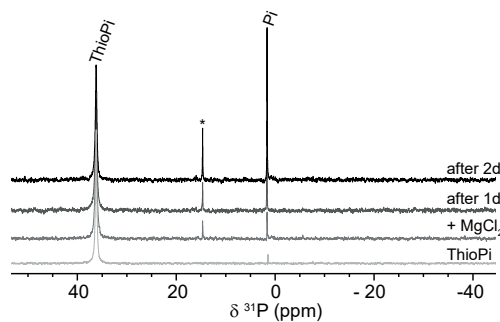


Figure 53: ^{31}P NMR spectra of thiophosphate and a 2 fold molar excess of MgCl₂ at pH 7.5 recorded at different times show built up of a signal at 15 ppm which can be attributed to a degradation product of thiophosphate. Spectra acquired with a liquid-state NMR spectrometer at 7.05 Tesla, 121 MHz ^{31}P .

I.3.5 DgkA and ATPase activity

Activity measurements in liposomes via ^{31}P real-time solid-state NMR revealed that DgkA exhibits a basal ATPase activity, which is further enhanced in presence of the short-chain diacylglycerol DBG in a concentration dependent manner²⁹¹. ATP hydrolysis activity in presence of lipid substrates is observed in the herein shown experiments with dioleoylglycerol (Figure 49, Figure 50), dioctanoylglycerol (Figure 45) in DOPC and DBG in DOPC and DMPC/DMPA liposomes (Figure 54) as well.

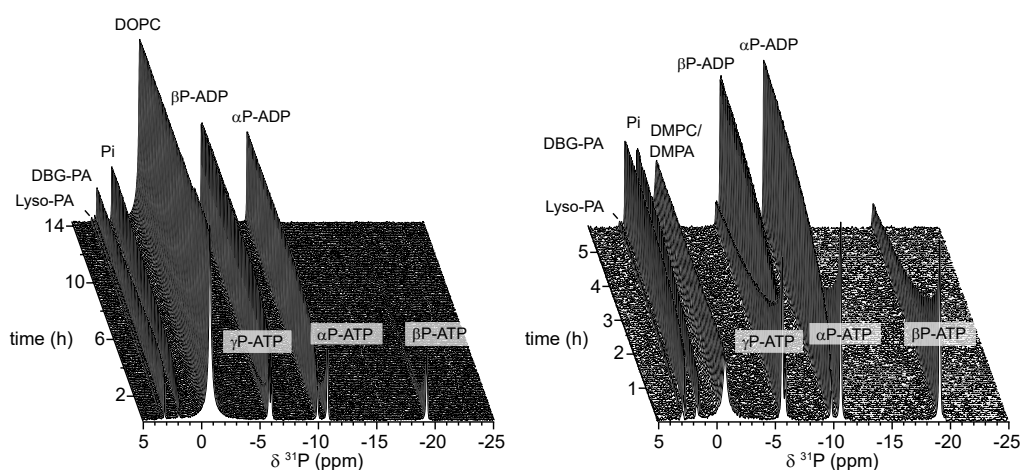


Figure 54: ^{31}P real-time NMR spectra following enzymatic activity of 0.8 mg DgkA in DOPC (L:P 120:1) and 9:1 mol/mol DMPC:DMPA (L:P 50:1) liposomes upon addition of 2.1 μmol DBG and 0.75 μmol respectively 1.5 μmol ATP. A signal at 3.7 ppm was attributed to lyso-PA based on its chemical shift and observable $^3J_{31\text{P},1\text{H}}$ coupling ($t, J = 6.5$ Hz), most likely a degradation product of DBG ($t, J = 6.0$ Hz) (Appendix Figure 15).

From the previously available data, it was unclear if ATP hydrolysis is an essential part of DgkA's activity. Coupled photometric or radiometric assays performed so far did follow either substrate phosphorylation or ATP consumption in presence of a lipid substrate but activities were not directly compared due to different assay conditions or determined in absence of lipid substrates.

I.3.5.1 In environments with fast lipid substrate diffusion in excess of a lipid substrate

^{31}P real-time NMR allows to quantitatively measure ATP hydrolysis and phosphoryl transfer in one sample. By following substrate consumption and product build-up simultaneously, it is shown that DgkA in DDM or reconstituted in an LCP of monoolein, a membrane mimetic comprised entirely of substrate, does exhibit a highly efficient phosphoryl transfer as seen by the lack of inorganic phosphorous being

created when a lipid substrate is present (Figure 45, Figure 47 and Figure 55). To confirm that the upcoming signals can be attributed to the phosphorylation products inorganic phosphorous was added to the LCP sample (Appendix Figure 11) and a DDM sample where the more water soluble DBG was used as lipid substrate for better resolution (Figure 55b). The ^{31}P chemical shift for Pi is distinct from the formed phosphatidic acids, which are by far the major product of DgkA's enzymatic activity under these conditions.

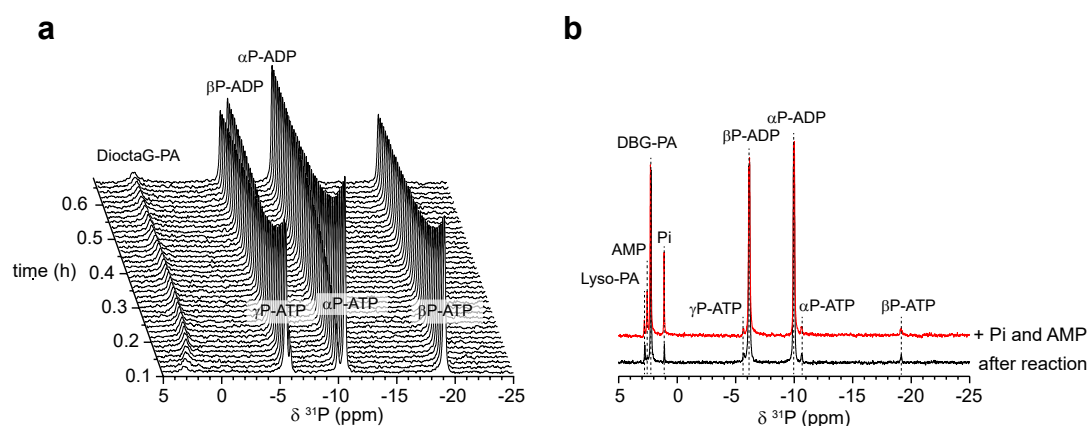


Figure 55: Enzymatic activity of DgkA in DDM in the presence of lipid substrates does not exhibit strong ATPase activity. **a)** ^{31}P real-time MAS NMR spectra following the enzymatic activity of 90 μg DgkA in 0.5% (w/v) DDM with 1.5 μmol dioctanoylglycerol added as lipid substrate at 1.35 kHz MAS. The enzymatic reaction was initiated by addition of 1.5 μmol ATP (equates to 30 mM ATP). **b)** ^{31}P MAS spectra after consumption of ATP (black) and after addition of Pi and AMP (red) with 2.1 μmol DBG as lipid substrate instead of dioctanoylglycerol. Observed Pi formation can be attributed to non-enzymatic hydrolysis of ADP as seen by built-up of an AMP signal.

In the DDM mixed micellar sample with DBG synthesized by Dr. Andreas Jakob³³⁰ as substrate a signal built-up was observed, which has a different chemical shift than added Pi or AMP. Based on its chemical shift and observable $^3J_{31\text{P},1\text{H}}$ coupling in non-decoupled ^{31}P spectra in experiments with DMPC:DMPA liposomes ($t, J = 6.5$ Hz), it can be attributed to lyso-PA formed upon phosphorylation of a monoacylglycerol, most likely a degradation product of DBG ($t, J = 6.0$ Hz) (Appendix Figure 15).

I.3.5.2 Effect of phospholipids on ATPase activity in absence of lipid substrates

To determine if the basal ATPase activity observed in liposomes and bicelles is caused or enhanced by the lipid environment we followed Pi built-up via molybdenum blue based activity assays without a lipid substrate or activator in detergent and liposomes

(Figure 56). Basal ATPase activity of DgkA in DDM micelles was observed. The protein preparation is free of phospholipids as judged by ^{31}P NMR, which is in agreement with Boland and coworkers³²⁴ who did not detect any co-purified phospholipids in a similar preparation. Thus, ATP can bind to DgkA in the absence of phospholipid activators or lipid substrates. However, the K_M was an order of magnitude higher in DDM than in DOPC or *E. coli* polar lipid extract liposomes (Table 8). The lower K_M in liposomes shows that the lipid environment increases DgkA's affinity for ATP in terms of K_M to similar values observed in presence of lipid substrates.^{134-135, 254, 257, 265-266, 271}

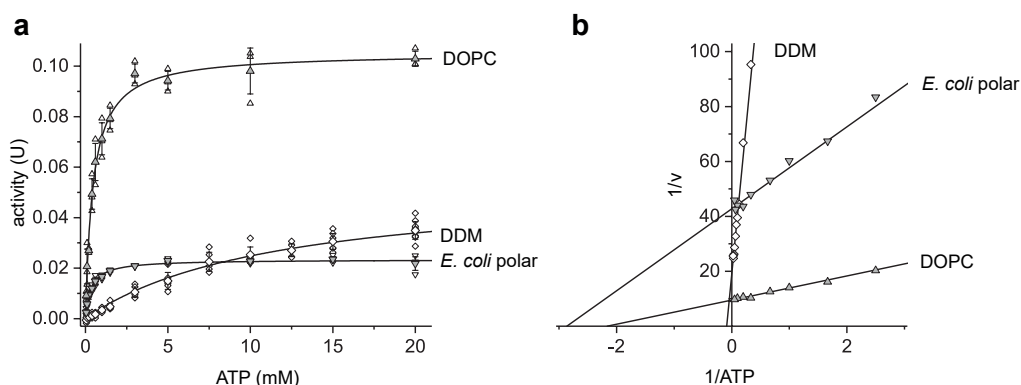


Figure 56: Basal ATPase activity of DgkA in different environments. **a)** Activity in dependence to ATP concentration without a lipid substrate was determined for DgkA in DDM and reconstituted in DOPC and *E. coli* polar lipid liposomes via molybdenum blue assay. **b)** Lineweaver-Burk representation of basal ATPase activity with fitted kinetic parameters obtained from a). Error bars represent standard deviation of four independent replications. Values of replicates are shown as small symbols.

As basal ATPase activity for DDM in terms of v_{\max} was in the same range compared to DOPC and *E. coli* polar extract liposomes only the presence of lipid substrates and not lipid activators^{135, 228, 254} alone seem to enhance DgkA's activity.

Table 8: Basal ATPase activity of DgkA in different environments. Obtained kinetic parameters in dependence to ATP concentration without a lipid substrate.

| Method | environment | v_{\max} (U) | K_M (mM) |
|-----------------------|--|-------------------|-----------------|
| ^{31}P NMR | DDM | 0.053 ± 0.002 | 7.9 ± 0.8 |
| Molybdenum blue assay | DDM | 0.054 ± 0.002 | 11.6 ± 0.9 |
| Molybdenum blue assay | DOPC liposomes | 0.105 ± 0.002 | 0.46 ± 0.03 |
| Molybdenum blue assay | <i>E. coli</i> polar extract liposomes | 0.023 ± 0.004 | 0.35 ± 0.03 |

Specific basal ATPase activity for DgkA was linear with protein concentration in DDM, DOPC and *E. coli* polar lipid liposomes (Figure 57). Raw data and background

measurements for this experiment (Appendix Figure 20) show that ATPase activity of DgkA is completely abolished by addition of SDS as the absorbance in background measurements is not significantly increasing with higher DgkA concentrations. It also highlights that there are no unspecific concentration dependent sources of Pi formation or increase in absorbance at 850 nm from a concomitant increase of DDM or DOPC and *E. coli* polar lipid liposomes.

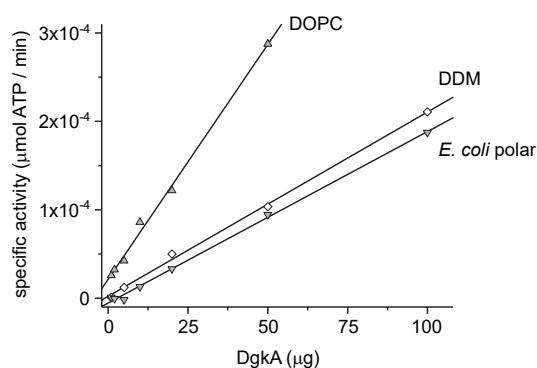


Figure 57: Specific basal ATPase activity ($\mu\text{mol ATP} / \text{min}$) of DgkA in DDM and reconstituted in DOPC and *E. coli* polar lipid liposomes at 20 mM ATP in dependence to varying DgkA amounts via molybdenum blue assay.

Very similar kinetic parameters for basal ATPase activity in DDM in comparison to the molybdenum blue assay were obtained via ^{31}P real-time MAS NMR (Figure 58, Table 8). Thus, assays and real-time MAS NMR measurements yield comparable kinetic parameters if temperatures are calibrated and homogeneous distribution as well as substrate accessibility are similar.

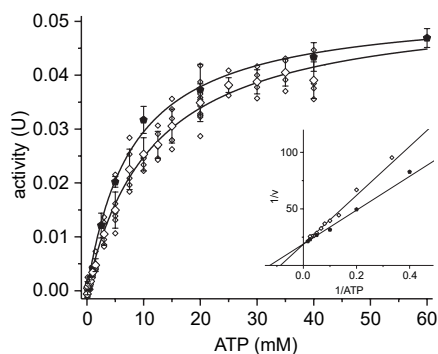


Figure 58: Comparison of DgkA's basal ATPase activity in DDM determined via initial reaction rates from ^{31}P real-time MAS NMR experiments (filled circles) and molybdenum blue assay (open diamonds) in dependence to ATP concentration. Insets show Lineweaver-Burk representations of the datasets with fitted kinetic parameters obtained from the saturation curves (Table 8). Error bars reported for ^{31}P real-time MAS NMR measurements represent standard deviation of the four analyzed signals for determination of the initial reaction rate. Error bars reported for the coupled assay represent standard deviation of four independent replications. Values of replicates are shown as small symbols.

I.3.6 LCP for biomolecular solid-state NMR

I.3.6.1 Kinetic parameters of DgkA's activity in LCP

The lipidic cubic phase of monoolein swells with higher liquid to monoolein ratios¹⁶⁹ and can change into a more unordered so-called sponge phase^{96, 162}. Kinetic parameters obtained by photometric assays therefore describe a swollen lipidic cubic phase with wider water channels and enhanced diffusion of soluble substrates as they are performed with a bath solution surrounding an LCP bolus. ³¹P real-time NMR allows to study reaction rates at defined liquid to MAG ratios without the need of a bath solution as it detects substrates and products directly, thereby emphasizing NMR as a method to study biochemical processes in porous materials.

Precisely defined liquid and lipid volumes are also important for correct determination of kinetic parameters for enzymatic activity, which is difficult to achieve with liposomes. As activity depends on substrate and product concentrations in their respective membrane or liquid volume, those cannot be expressed in amounts. This basic principle of enzyme kinetics can be seen by comparison of DgkA's enzymatic activity in LCP at different monoolein to liquid ratios in dependence to the ATP concentration with respect to the liquid fraction (Figure 59a) or as amount over the whole sample (Appendix Figure 23).

As activity of an enzyme should not be affected by limited substrate diffusion, the maximum rate should stay constant. Therefore, a similar v_{\max} for DgkA in LCP determined via ³¹P real-time NMR compared to a v_{\max} determined by reproduction of a published coupled photometric assay²⁶⁹ *in meso* confirms that the activity of DgkA in both conditions is the same (Figure 59, Table 9).

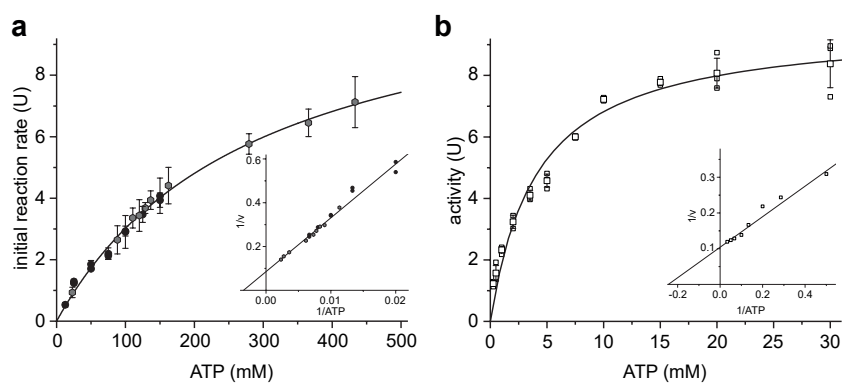


Figure 59: DgkA's enzymatic activity in LCP determined via ^{31}P real-time MAS NMR and *in meso* coupled assay. **a)** ATP saturation curve of initial reaction rates in a non-swollen LCP via ^{31}P real-time MAS NMR experiments upon addition of ATP. Depicted in black are rates from measurements with a final monoolein:liquid ratio of 6:4 (w/w) after addition of ATP. For higher ATP concentrations (in gray) the lipidic cubic phase was formed at a constant monoolein:liquid ratio of 6:4 (w/w). Addition of ATP yielded a maximum monoolein:liquid ratio of 4.4:5.6 (w/w). ATP concentrations are given with respect to the liquid fraction of the samples. **b)** ATP saturation curve of DgkA's activity in a swollen cubic phase determined via the *in meso* coupled ATPase assay.

Insets show Lineweaver-Burk representations of the datasets with fitted kinetic parameters obtained from the saturation curves (Table 9). Error bars reported for ^{31}P real-time MAS NMR measurements represent standard deviation of the four analyzed signals for determination of the initial reaction rate. Error bars reported for the coupled assay represent standard deviation of three independent replications. Values of replicates are shown as small symbols.

Table 9: Kinetic parameters of DgkA's enzymatic activity in LCP and mixed micelles with monoolein as lipid substrate.

| Method | environment | v_{\max} (U) | K_M (mM) |
|---------------------|--------------------------------|----------------|-----------------|
| ^{31}P NMR | LCP | 11.7 ± 0.5 | 288 ± 20 |
| coupled assay | <i>in meso</i> | 10.4 ± 1.2 | 5.3 ± 1.5 |
| coupled assay | <i>in surfo</i> (DM/monoolein) | 32.4 ± 1.4 | 0.35 ± 0.06 |

The determined apparent K_M however is dependent on substrate diffusion rates and differs by nearly two orders of magnitude between the real-time ssNMR measurements and the *in meso* coupled photometric assay (Table 9). Magic angle sample spinning, necessary to achieve better resolution, does not cause a reduction of the apparent K_M by itself as ^{31}P NMR MAS experiments to follow DgkA's basal ATPase activity in DDM resulted in similar kinetic parameters compared to the molybdenum blue activity assay determining phosphate build-up (Table 8). Phase separation or phase transitions of the cubic phase, which could lead to reduced substrate accessibility under MAS, were not observed either. Isotropic peaks are retained after MAS and cross polarization

of the lipids during MAS is not possible (Figure 63a). Furthermore, starting the reaction by uncaging of NPE-ATP equally distributed throughout the sample by addition upon formation of the LCP resulted in similar initial reaction rates (Figure 60), verifying high accessibility for solutes in LCP under MAS conditions in the observable concentration range. These results are thereby validating ATP addition as a feasible method to initiate DgkA's enzymatic activity. Saturation of enzymatic activity however could not be reached despite uncaging up to 0.34 μmol NPE-ATP (equating to 56.7 mM with respect to the liquid fraction). Higher ATP concentrations could not be achieved by uncaging inside the spectrometer, because uncaging efficiency at higher NPE-ATP concentrations decreases ever more (Figure 41).

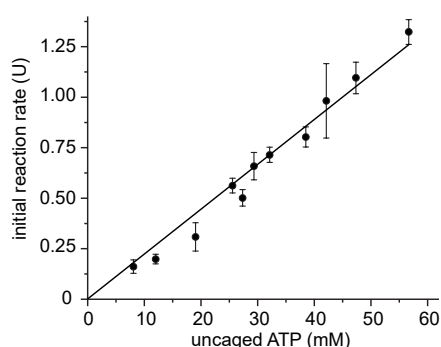


Figure 60: Initial reaction rates of DgkA's enzymatic activity in LCP initiated by uncaging NPE-ATP in dependence to released ATP concentrations obtained from progress curves of ^{31}P real-time MAS NMR experiments. ^{31}P real-time NMR spectra and progress curves for the 38.5 mM uncaged ATP datapoint are shown in Figure 47. A linear fit of the datapoints visualizes the lack of saturation at ATP concentrations achievable by uncaging inside the spectrometer.

Thus, the increased K_M obtained via MAS NMR ^{31}P real-time experiments reflects major differences in substrate diffusion between a lipidic cubic phase with a maximum liquid to monoolein ratio of 6:5 and a swollen lipidic cubic phase in a bath solution. Comparison with results from reproduction of a published assay performed *in surfo* with monoolein as substrate (Figure 61, Table 9) show that saturation with nucleotide substrate could be achieved at even lower concentrations. However, the activity of DgkA in terms of v_{max} is also higher in the used DM monoolein mixed micelles. Thus, either diffusion of lipid substrate or product is enhanced in detergent compared to LCP or the detergent environment is enhancing the activity of the enzyme itself compared to a LCP made of MAGs²⁶⁹.

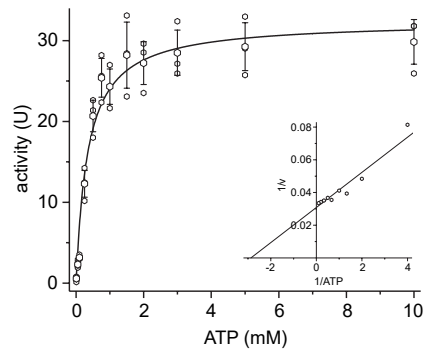


Figure 61: ATP saturation curve of DgkA's enzymatic activity in detergent micelles with monoolein as substrate determined via the *in surfo* coupled assay. Inset shows Lineweaver-Burk representation of basal ATPase activity with fitted kinetic parameters obtained from the saturation curve (Table 9). Error bars represent standard deviation of three independent replications. Values of replicates are shown as small symbols.

I.3.6.2 Protein ssNMR of DgkA reconstituted in LCP

Reconstitution of DgkA into the lipidic cubic phase in amounts sufficient for protein solid-state NMR by mixing detergent solubilized DgkA with molten monoolein in a LCP mixing device lead to a highly viscous and optically transparent sample, typical for successful LCP formation (Figure 62).

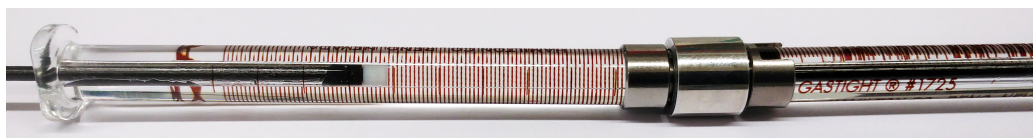


Figure 62: Reconstitution of DgkA at a concentration of 14.3 mg/ml in LCP, feasible for protein ssNMR measurements, via a LCP mixing device. Reconstitution resulted in an optical transparent and birefringent LCP as can be seen on the minor scale marks on the rear side of the Hamilton syringe.

Static measurements performed after MAS next to optical transparency and high viscosity further indicate that the protein loaded cubic phase is stable during MAS in the observed range of up to 10 kHz as isotropic lines of monoolein signals are retained (Figure 63a). Furthermore, direct evidence that the LCP is stable during MAS is provided by classical cross polarization experiments. As chemical shift anisotropy is averaged and dipolar couplings removed in a cubic phase, monoolein signals are not cross polarizable and were therefore only detected in direct polarization experiments.

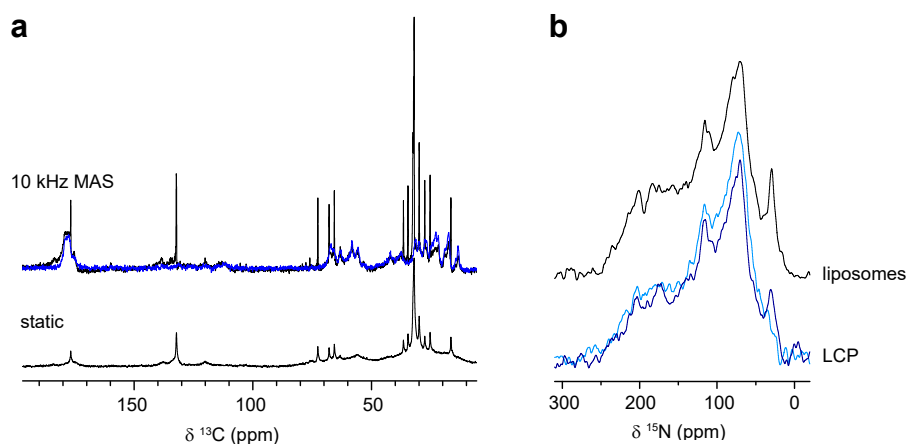


Figure 63: 1D protein solid-state NMR spectra of $U^{13}C^{15}N$ labelled DgkA in LCP and DMPC:DMPA liposomes. **a**) ^{13}C cross polarization (blue) and direct polarized 1D spectra (black) of DgkA in LCP under static and 10 kHz MAS conditions at 303 K. **b**) ^{15}N static cross polarization spectra of DgkA in liposomes with 8 ms contact time (black) and DgkA in LCP with 1 ms (light blue) and 8 ms (blue) contact time (20480 transients) at 303 K.

DgkA embedded in the cubic phase however did not exhibit isotropic linewidths indicating that the protein does not undergo the same fast diffusion driven angular changes as monoolein. It can be cross polarized and shows a typical ^{15}N static powder

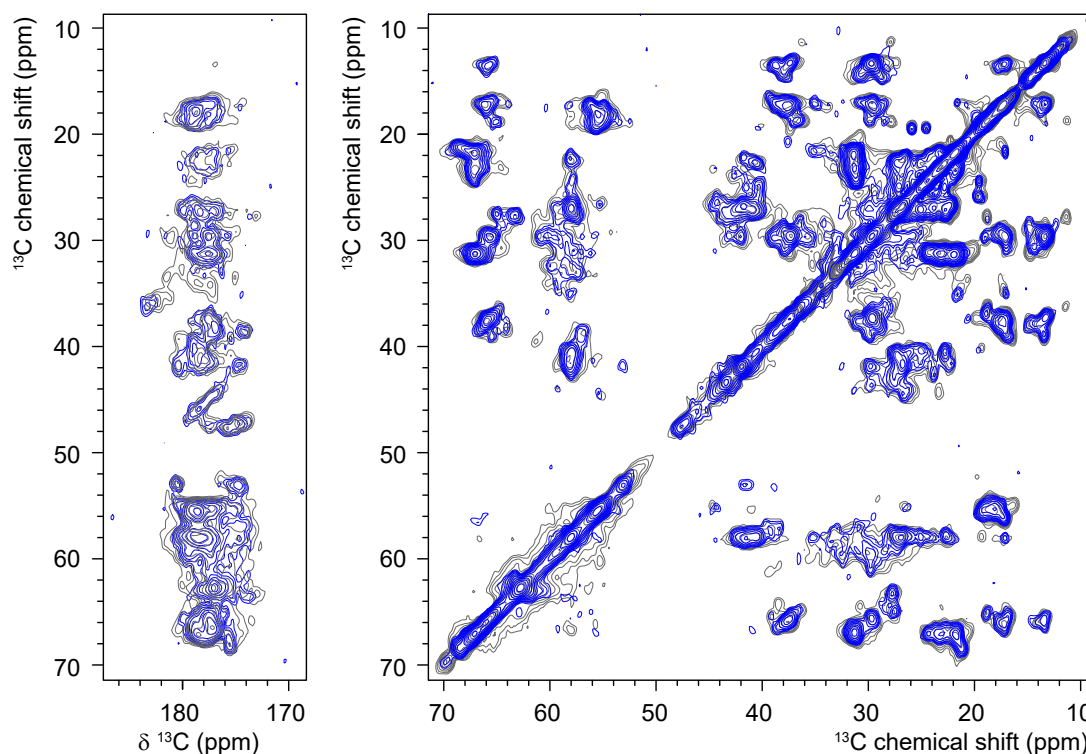


Figure 65: PDSD spectra of $U^{13}C^{15}N$ labelled DgkA in LCP (blue) and DMPC:DMPA liposomes (gray) at 10 kHz MAS, 303 K and 20 ms mixing time. 540 increments in F1, 104 transients for liposomes and 144 transients for LCP in F2.

I.3.6.3 Monoolein as membrane mimetic for DNP measurements

^{31}P correlation experiments performed with common liposomes as membrane mimetic to study for example protein nucleotide contacts suffer from signal overlap and unspecific magnetization transfers from phospholipids. Therefore, other nuclei, which require labelling such as ^{15}N or ^{13}C and are unlike phosphorous often not directly involved in enzymatic or energy transfer reactions, were used³⁵⁷⁻³⁵⁸.

Monoacylglycerols as membrane mimetics that do not contain phospholipids could offer a unique advantage over liposomes for ^{31}P experiments. Especially under DNP conditions, where cryogenic temperatures cause severe line broadening³⁵⁹⁻³⁶¹ a membrane environment without phospholipids might be necessary to resolve signal overlap. Because no reports on the use of monoacylglycerols as a membrane environment for DNP applications had been found, conditions to achieve good signal enhancements were screened. Therefore, non-labelled DgkA was reconstituted with different monoolein to lipid ratios as well as different glycerol and AMUpol concentrations by forming a cubic phase at room temperature for homogeneous sample distribution before freezing the sample for storage or upon insertion into the DNP spectrometer (Table 10). Indirect DNP ^{13}C signal enhancements in cross polarization

spectra measured on monoolein (methyl, methylene) and glycerol signals as the ratio between microwave on and off were comparable except for a sample that did not contain DgkA. Enhancements were not strongly dependent on storage temperature over the observed time range, but increased more than fourfold with glycerol content (0% - 30% with respect to the liquid fraction) from 6.7 ± 0.2 to the maximum observed ^{13}C signal enhancement of 25.8 ± 0.8 (Table 10, Figure 66a).

Table 10: Utilizing monoolein as membrane mimetic for DNP experiments. Optimization of sample compositions for increased ^{13}C signal enhancement under DNP conditions in cross polarization experiments at 100 K and 8 kHz MAS comparing peak heights of monoolein and glycerol $\text{mw}_{\text{on}} / \text{mw}_{\text{off}}$ signals.

| MO | liquid | | | | | | | | | | | $\text{mw}_{\text{on}} / \text{mw}_{\text{off}}$ | |
|-----|--------|-------------|--------------|----------------------|----------------------|------------------------|------------|-----------|-----------|----------|-----------|--|----------|
| | | AMUpol (mM) | glycerol (%) | D ₂ O (%) | H ₂ O (%) | MgCl ₂ (mM) | HEPES (mM) | NaCl (mM) | DgkA (mM) | DDM (mM) | stored at | MO | glycerol |
| 60% | 40% | 10 | 0% | 50% | 50% | 15 | 25 | 15 | 3.75 | ~150 | RT 48 h | 6.9 | 6.5 |
| 40% | 60% | 10 | 15% | 30% | 55% | 15 | 25 | 15 | 3.75 | ~150 | RT 48 h | 10.8 | 12.5 |
| 40% | 60% | 10 | 15% | 30% | 55% | 15 | 25 | 15 | 3.75 | ~150 | -80 °C | 12.3 | 13.4 |
| 40% | 60% | 10 | 30% | 20% | 50% | 0 | 25 | 15 | 3.75 | ~150 | -80 °C | 25.1 | 26.7 |
| 40% | 60% | 20 | 30% | 60% | 10% | 0 | 0 | 0 | 0 | 0 | -80 °C | 14.4 | 32.8 |

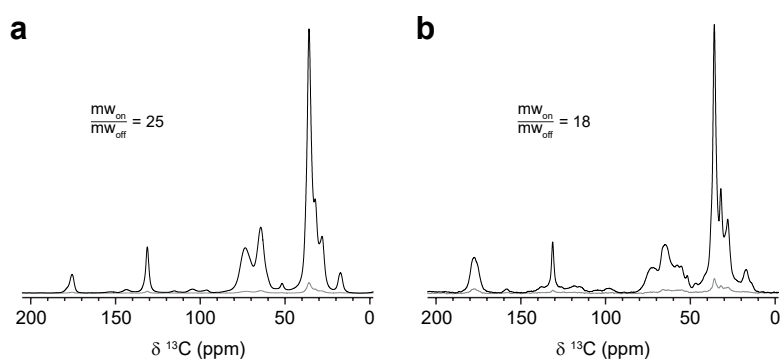


Figure 66: ^{13}C cross polarization spectra acquired under DNP conditions with mw_{on} (black) and mw_{off} (gray) of samples containing 40% (w/v) monoolein, 10 mM AMUpol, 30% (v/v) glycerol and 50% (v/v) D₂O (with respect to the liquid fraction) with **a**) 1 mg non-labelled DgkA in 25 mM HEPES pH 7.5 and 15 mM NaCl (128 transients) and **b**) 0.7 mg U $^{13}\text{C}^{15}\text{N}$ labelled DgkA with 20.5 mM AMP-PCP, 40 mM MgCl₂ and 100 mM HEPES pH 7.5 reconstituted (8 transients) at 100 K and 8 kHz MAS.

The monoolein, glycerol and D₂O content that led to the highest signal enhancement was further used for reconstitution of U $^{13}\text{C}^{15}\text{N}$ labelled DgkA with the ATP analogue AMP-PCP, which is known to bind to DgkA³⁰⁸, MgCl₂ and a higher HEPES concentration for DNP experiments to study protein nucleotide contacts utilizing the

^{31}P dimension. Acquired ^{31}P cross polarization DNP spectra reveal line broadening of the AMP-PCP peaks under DNP conditions. The line broadening leads to overlap of βP - and γP -AMP-PCP peaks (Figure 67a), which are well separated at room temperature³⁶². Comparison of a ^{31}P - ^{13}C TEDOR spectrum acquired at 8 ms mixing time with the spectrum of a liposome sample courtesy of Hundeeep Kaur highlights the severity of background from phospholipids and the advantage of a membrane mimetic not exhibiting phospholipid signals (Figure 67c).

1D ^{31}P - ^{13}C TEDOR spectra at shorter mixing times with AMP-PCP as nucleotide substrate for DgkA, revealed peaks at 177, 74 and 65 ppm (Figure 67b). The latter two are most likely intramolecular contacts to the ribose moiety (comparison ATP ^{13}C chemical shifts: Appendix Table 2). A putative protein nucleotide contact can be seen at 177 ppm in 1D ^{31}P - ^{13}C TEDOR spectra at 1, 2 and 6 ms mixing times (Figure 67b). It could correspond to γC of Asn72 (178.2 ppm apo³⁰⁷), which is with a distance of 5.5 Å to γP of AMP-PCP in close proximity according to the crystal structure of the ternary complex³⁰⁸ (PDB: 4UXX). However, this distance is already at the upper range for TEDOR and the contact could not be confirmed by subsequently acquired 2D TEDOR spectra.

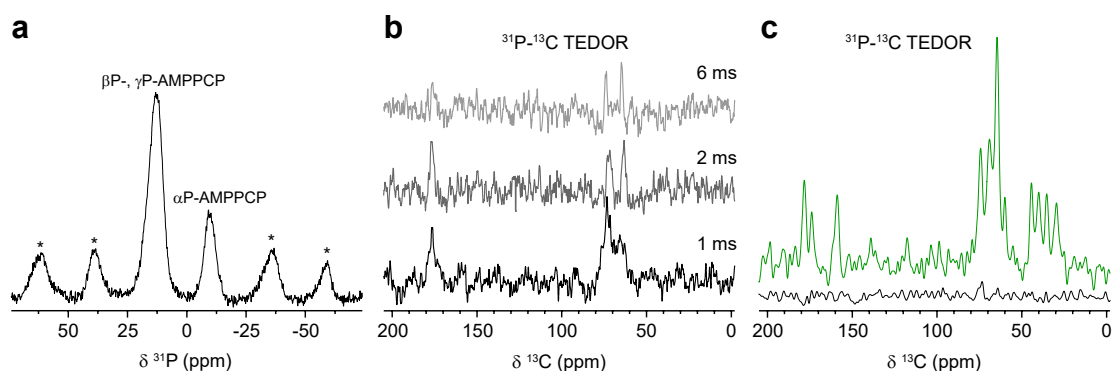


Figure 67: **a)** ^{31}P cross polarization DNP spectrum of a sample containing 0.7 mg $\text{U}^{13}\text{C}^{15}\text{N}$ labelled DgkA (51 nmol) and 20.5 mM AMP-PCP (246 nmol) reconstituted into 40% (w/v) monoolein with 40 mM MgCl_2 , 10 mM AMUpol, 100 mM HEPES pH 7.5, 30% (v/v) glycerol and 50% (v/v) D_2O (with respect to the liquid fraction) (128 transients). Asterisks denote spinning side bands. **b)** ^{31}P - ^{13}C TEDOR DNP spectra of the same sample as in (a) with 1, 2 and 6 ms mixing time (4096 transients). **c)** Comparison of the empty ^{31}P - ^{13}C TEDOR DNP spectrum at 8 ms mixing time and 24576 transients (black) with a DMPC/DMPA liposome sample containing non-labelled MsbA with 1024 transients courtesy of Hundeeep Kaur (green) at 100 K and 8 kHz MAS. The comparison is highlighting the absence of unspecific background signals in LCP samples otherwise occurring in samples containing phospholipids.

Despite variation of mixing times and high number of transients, only one peak with a maximum at 74 ppm in the ^{13}C and -9 ppm in the ^{31}P dimension was observed in 2D ^{31}P - ^{13}C TEDOR spectra (Figure 68). The peak can be attributed to an intramolecular contact between αP and natural abundance ^{13}C 2' and/or 3' nuclei of the ribose moiety (comparison ATP ^{13}C chemical shifts: Appendix Table 2) of AMP-PCP. Another possible intramolecular contact between βP or γP to the methylene group was not observed.

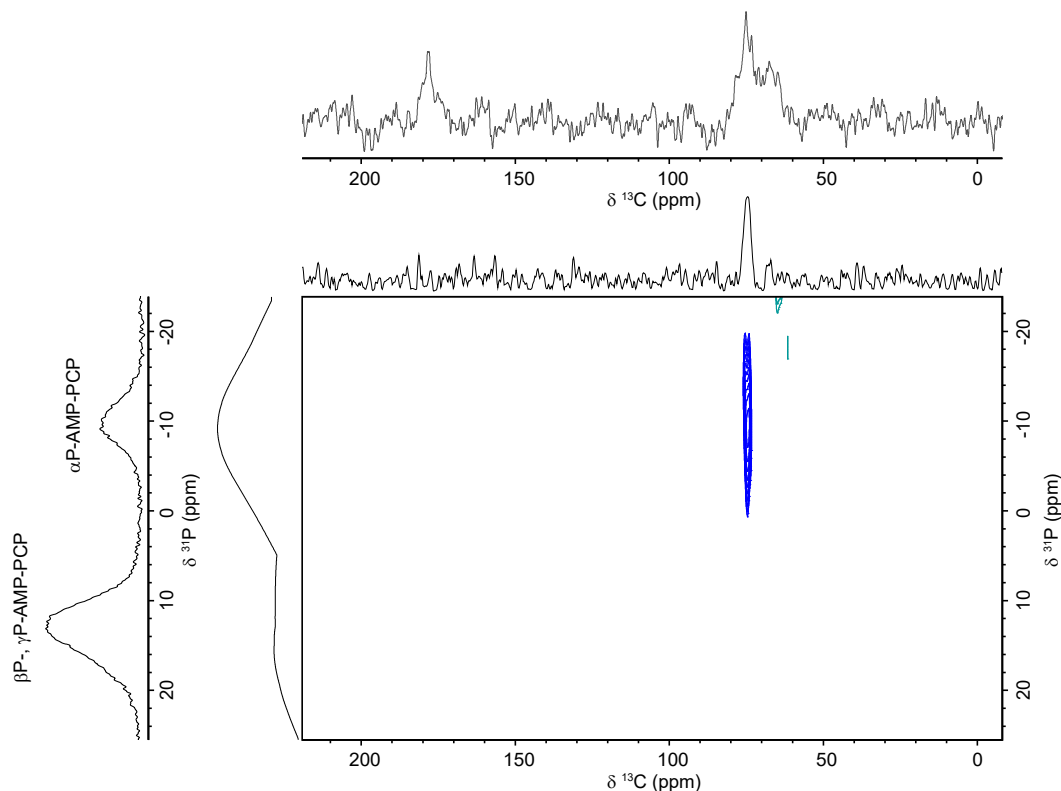


Figure 68: ^{31}P - ^{13}C 2D TEDOR DNP spectrum of a sample containing 0.7 mg $\text{U}^{13}\text{C}^{15}\text{N}$ labelled DgkA (51 nmol) and 20.5 mM AMP-PCP (246 nmol) reconstituted into 40% (w/v) monoolein with 40 mM MgCl_2 , 10 mM AMUpol, 100 mM HEPES pH 7.5, 30% (v/v) glycerol and 50% (v/v) D_2O (with respect to the liquid fraction). 1 ms mixing time, 10 increments in F1, 2048 transients in F2, 100 K, 8 kHz MAS and respective projections. The ^{31}P cross polarization spectrum with 128 transients and the ^{31}P - ^{13}C TEDOR 1D spectrum with 1 ms mixing time and 4096 transients at same conditions for the recorded spectral width are depicted along the respective axes for comparison.

I.4 Discussion

I.4.1 Uncaging approach for solid-state NMR

I.4.1.1 Illumination setup

Various tests of the existing DNP illumination setup used to excite retinal proteins²⁴⁻²⁶, showed that it is not sufficient to release observable amounts of caged compounds in neither the UV nor visible light range. In comparison to excitation of retinal proteins uncaging is more demanding as photochemical properties of caged compounds (Table 1) compared to retinal proteins like bacteriorhodopsin ($\epsilon_{\text{exc}} \cdot \Phi = 37800\text{-}44100 \text{ M}^{-1}\text{cm}^{-1}$ at 570 nm)⁴⁹⁻⁵⁰ reveal an often more than two order of magnitude lower efficiency. In light of the special sample preparations with thin films and substantially reduced amounts of isotope labelled retinal used in the published studies²⁴⁻²⁶, it is clear that the main cause is insufficient light intensity reaching the sample. As fast and efficient uncaging is seen with the same light sources and a custom manufactured fiber bundle outside the spectrometer these heavy loss of light intensity are caused by a non-optimal light path.

The efficient uncaging of reasonable concentrations of NPE-ATP with LED light sources also demonstrated that their brightness and especially luminance is enough to create a sufficient photon flux through fiber optics and present a feasible alternative to the used lasers in previous NMR studies. Even though the acceptance cone of the fibers, here 25.4° (NA 0.22), and coil windings partially blocking the emergent beam, are requiring a reduction of sample volume to the illuminated area, a fiber bundle allows illumination of a reasonable sample volume without additional optics using non-coherent and highly divergent light from LED sources. Making LEDs, when coupled to fiber bundles with a large active area, simple, reliable and cost-effective light sources for uncaging experiments at intermediate uncaging times and concentrations in the near UV to visible light range. Especially as continuous development of diode composition led to already remarkable brightness and is expected to further increase their luminance in the future³⁶³.

The tested laser's highly focused beam in contrast would require additional optics to increase divergence, like sculpted fiber tips, to illuminate a reasonable volume from the side. Its highly directional coherent beam with a small diameter and low divergence can however provide vastly more light through fused silica fibers that have limited

acceptance angles and core diameters as non-coherent LEDs that are Lambertian emitters. This was also reflected in power measures at the end of the fiber, which revealed more than a hundred-fold lesser light power was transmitted from the UV LED compared to the laser. It provided enough light to uncage within the illuminated area in seconds compared to the UV LED, whose half time was in the minute range. These uncaging experiments also revealed that LED power is not sufficient to efficiently uncage high NPE-ATP concentrations as uncaging efficiency dropped with higher NPE-ATP concentration in an illumination time independent manner. Thus, the fraction of released ATP could not be increased with longer illumination times most likely due to high absorption of photoproducts and insufficient light intensity.

Therefore, a laser would prove highly advantageous when illuminating through the bottom of the rotor with a small fiber as illumination through the bottom of the rotor with an angle allowing total reflection on the outer surface of the rotor walls and scattering into the sample at the rough inner surface has several advantages. It reduces the pathlength through the highly absorbing sample and leads to sample illumination over the whole rotor and high uncaging efficiencies even with a highly focused beam as demonstrated in tests outside the spectrometer. However, only a narrow fiber could be fitted at the bottom of the stator, as the space at the bottom is very limited due to housing of bearing and eject ports as well. To achieve efficient illumination through the narrow fiber would require however a narrow, collimated and bright beam that only a laser source can provide. Such a far more intricate to build and due to the requirement of a laser vastly more expensive setup would however be the optimal solution if even higher light intensities are required. In addition it would also not interfere with coil design and would not cause potential shimming issues, because the fiber is further away from the active area. However, the high concentrations (>10 mM) of NPE-ATP a low molecular weight compound and the in turn needed high light intensities would be barely achieved, when biomacromolecules like peptides or proteins are caged or modified with photoswitches to trigger folding, refolding, binding events, oligomerization or interactions with membrane mimetics.

Therefore, the illumination system used is a cost effective, mobile, robust and simple alternative to more complex, heavy and immobile lasers and optic tables for the shown applications. Especially as modular coupling of LEDs via beam combiner units allows to couple light of different wavelengths into the system, a necessity to toggle photoswitches between two states as well as wavelength selective uncaging.

I.4.1.2 *In situ* uncaging experiments in different membrane mimetics to initiate enzymatic activity of DgkA

The simple and robust illumination setup built for high field MAS NMR provides with matching LEDs enough light for uncaging at the near UV to visible light range. Liposomes are often used as membrane mimetic for solid-state NMR but have high absorbance due to scattering¹³¹. Results of absorption measurements performed even far below the concentrations typically used for protein solid-state NMR experiments (approximately 400-500 mg/ml) and comparison with bicelles whose lipids exhibit similar absorption¹³¹ highlight this issue. Therefore, other membrane mimetics with far lower absorption like bicelles and cubic phases are in terms of optical properties of advantage. However, with reduction of liposome concentration uncaging was possible to trigger DgkA's enzymatic reaction in all tested environments.

Despite the possibility to simply add ATP in the tested scenarios uncaging of NPE-ATP proved to be an important control for the determination of DgkAs activity in a non-swollen cubic phase. Similar reaction rates obtained by uncaging different concentrations of NPE-ATP in LCP and following the enzymatic reaction with ³¹P MAS NMR compared to initial reaction rates obtained by adding ATP verified that addition of ATP is a feasible method to initiate the enzymatic reaction in LCP. This was especially important because slow diffusion of ATP through the water channels of the LCP, which was found in ³¹P DOSY experiments to be at least three orders of magnitude slower than in solution, could have caused lower initial reaction rates when adding ATP as it would require more time to evenly distribute over the whole sample. As insufficient signal to noise limits time resolution in most MAS solid-state NMR experiments, uncaging compared to simple addition of a compound, which typically takes 3.5 min from addition of the compound to acquisition of a first free induction decay (FID), does not pose an advantage. Its true advantage for biophysical studies, including liquid-state NMR, which can make use of rapid mixing devices to reduce mixing times to less than 1 s³⁶⁴, lies in triggering reactions that cannot be initiated by simple addition or mixing. Therefore, release of a non-water soluble, highly hydrophobic compound, in our case a caged long chain DAG, was chosen to demonstrate this aspect. As MAGs are substrates of DgkA and bicelles showed to be not very stable to changes in membrane composition uncaging of NPE-DOG to trigger DgkA's kinase reaction was performed in liposomes, with the caged compound incorporated before liposome formation. Addition of ATP or ATP γ S led to observation

of basal ATPase reaction with a small amount of non-caged DOG being initially phosphorylated. Upon uncaging ATP consumption increased as kinase and basal ATPase reaction occurred. Using ATP γ S to resolve peak overlap the kinase reaction product, ThioPA, was also directly detected, demonstrating a successful first proof of concept of a reaction that cannot be started by mixing.

However, liposomes are not the ideal membrane mimetics to perform interfacial enzyme activity measurements under MAS conditions as separation of liposomes to the rotor walls and excess solution in the center occurs. A previous study from our group by Ullrich et al on DgkA's activity with liposomes under MAS reported dramatically reduced activities compared to activity assays¹³⁴⁻¹³⁵ and observed high ATPase activity²⁹¹. The v_{\max} in dependence to ATP concentration in this study and the activities obtained here under MAS conditions are in the range of basal ATPase activity determined herein by molybdenum blue assays in liposomes without lipid substrate. It can be speculated that due to phase separation accessibility of solutes is limited and therefore ATP reaches only a small fraction of active sites. An alternative interpretation that would fit the nearly unaltered K_M for ATP under MAS conditions²⁹¹ could be that accessibility for ATP is given but the added diacylglycerols are depleted fast within DgkA containing liposomes as lipid to protein ratios were markedly different between published assays (L:P 6000:1)¹³⁴⁻¹³⁵ and ssNMR experiments (L:P 120:1)²⁹¹. Therefore, kinase activity is heavily reduced as lipid substrate levels in DgkA containing liposomes are below their K_M or drop rapidly to sub K_M concentrations after a short initial phase of high kinase activity. This would also explain why ATPase activity at magnitudes similar to basal ATPase activity in absence of a lipid substrate is observed as a major coexisting mode of action next to kinase activity. The observed high initial kinase activity, without significant ATPase activity, upon use of more hydrophobic long chain DAGs that mainly partition into the membranes²⁹¹ support this interpretation as well as experiments using liposomes with higher lipid to protein ratios. Potential heterogeneity in liposome composition and limited diffusion of DAGs between liposomes could also be a factor that could lead to early depletion in some liposomes containing more DgkA and less DAG than other liposomes thereby contributing to the observed coexistence of ATPase activity and kinase activity. As ATPase activity is enhanced in the presence of DAGs²⁹¹, it however cannot be the only factor. Partial occupation of active sites by lipid substrates with nucleotides bound also at active sites lacking a lipid substrate and cooperativity

between subunits^{265, 291} is a likely mechanism that can explain the observed enhanced ATPase activity.

The used anisotropic DMPC:DHPC bicelles above their phase transition temperature are a chiral mematic consisting of long, entangled wormlike ribbons instead of disk-like bicellar structures¹⁴⁴. They align with the magnetic field and static spectra can be acquired to gain information about orientation of lipids, proteins and other components inside membranes, which is their main use in NMR^{140, 365}, as their chemical shift tensors are aligned as well. The orientation selective anisotropic chemical shifts of the magnetically aligned lipids in static ³¹P spectra are in the same region as most ATP and ADP signals but do not overlap with the β P-ATP signal. Because no phase separation occurs, activities obtained from static real-time ³¹P NMR experiments following the β P-ATP signal, despite use of a different DAG and different concentrations due to the necessities of the different methods and limited bicelle stability, are in the same range as determined by a coupled photometric ATPase assay. Thus, static NMR experiments with bicelles can yield results comparable to assays performed in bicelles. However, stability and phase behavior of bicelles is highly dependent on lipid composition, concentration¹⁴³, pH¹⁴⁵, ionic strength³⁶⁶ and other factors^{140, 156, 365} that do not allow huge variations in DAG or ATP content²⁶⁷.

Due to these limitations, it was abstained to determine further kinetic parameters from experiments performed in liposomes or bicelles. Instead, the uncaging approach's feasibility, wide applicability and potential advantages, especially for folding, oligomerization or in this case initiation of biochemical processes in membranes are demonstrated in-depth by initiation of DgkA's enzymatic activity via *in situ* uncaging in three different membrane mimetics as well as triggering its kinase activity by uncaging a non-miscible long chain DAG in liposomes.

Synthesis of the first NPE caged DAG, a caged compound with an absorption in the UV range and most likely inferior photochemical properties compared to published coumarin caged DAGs, even when considering the use of a oxycarbonyl linker⁴², was chosen to create the possibility for two wavelength selective uncaging. To demonstrate its feasibility for NMR it was thought to sequentially uncage first a red-shifted coumarin caged ATP to initiate DgkA's basal ATPase activity and subsequent uncaging of NPE-DOG to trigger the kinase reaction. However, several synthesis routes tried by Dr. Andreas Jakob failed to yield a coumarin caged ATP. As published synthesis pathways for coumarin caged nucleotides often showed very low yields or

unclear purity of the preparations, demonstration of two wavelength selective uncaging for NMR using beam combiners to couple light from different LEDs into the fiber bundle was not pursued further.

Wavelength selective uncaging could however become a very useful feature for NMR and other biophysical methods if for example sequential folding or oligomerization should be triggered. On the other hand, illumination using two different wavelengths is a necessity for studies using photoswitches to alter pH²⁹ or conformation of biomacromolecules^{28, 367} as thermal relaxation, a unwanted process, should be too slow for efficient back conversion. Especially photoswitches who can toggle between two protonation states²⁹ might be useful to create alternating proton gradients across liposomes to drive secondary active transporters or enzymes who utilize proton motive force. Undirected insertion of these proteins combined with toggling of the photoswitch would thereby allow to repeat the transport processes and measurements by repeatedly altering the direction of the proton gradient and therewith direction of transport induced by light.

I.4.2 ATPase activity of DgkA

Compared to the long history of enzymatic studies on DgkA ATPase activity had been found only recently via time-resolved ³¹P MAS NMR experiments on liposomes upon use of high amounts of DgkA due to low observed activity under these conditions²⁹¹. Initial experiments, which explored DgkA's substrate specificity, determined directly substrate phosphorylation rates via thin layer chromatography, radioactivity assays and fluorescent-labelled substrates and could not report on the rate of ATP consumption. Later on, with application of the photometric NADH coupled ATPase assay rates of ATP consumption were determined in the presence of known lipid substrates. Detection of differences between substrate phosphorylation and ATP consumption is however difficult as kinase activity is in the majority of membrane mimetics and methods several orders of magnitude higher in the presence of a lipid substrate than ATPase activity. The in this work performed ³¹P MAS NMR experiments and assays with LCP, bicelles and DDM in the presence and absence of lipid substrates also highlight this aspect. Therefore, combined with difficulties to compare results due to altered assay conditions, no noticeable discrepancies between the different assays can be observed or have been pointed out.

Measurements in the absence of lipid substrate, as performed here using the molybdenum blue assay instead of the coupled ATPase assay, were also previously performed as control to subtract unspecific ATP hydrolysis³⁰⁶. Most likely due to the used enzyme amounts in these experiments ATPase activity was small compared to DgkA concentration independent unspecific ATP hydrolysis or NADH oxidation and did not allow to detect a saturation curve, which would indicate specific enzymatic activity. In light of the comparable low ATPase activity, this is not surprising as the coupled assay with two enzymes and NADH oxidation as readout generates a strong background. In addition, the inability of performed experiments to rule-out or observe and determine specific ATPase activity in presence of saturating lipid substrate concentrations via ³¹P experiments demonstrates the challenges in dynamic range to simultaneously observe reactions with vastly different rates. Also, direct detection of inorganic phosphate using the highly sensitive molybdenum blue assay to determine DgkA's activity in presence of lipid substrate could lead to wrong conclusions if even a small fraction of generated PA's is hydrolyzed under the conditions needed to generate the color reaction.

ATPase activity in the absence of lipid substrates and even in the absence of activators such as phospholipids or cardiolipin demonstrates that ATP can bind to DgkA independently of a lipid substrate. Next to crystal structures showing MAG binding in absence of a nucleotide substrate³⁰⁰, these results complete the direct evidence for a random-equilibrium mechanism of substrate binding initially deduced from kinetic measurements^{257, 291}. Furthermore, the K_M for ATP in absence of lipid substrates in phospholipid environments is in the same range as K_M values obtained in the presence of lipid substrates and activators^{134-135, 265, 271} (see Appendix Table 5) allowing to assume only modest cooperativity for ATP binding in presence of bound lipid substrate. In absence of phospholipids or other activators the K_M for ATP is elevated indicating that activators are important for efficient ATP binding when assuming binding equilibrium is rapid compared to ATP hydrolysis. Compared to the K_M of lipid substrates, which is strongly influenced by the membrane environment such as lipid headgroup and lipid chain length or other activators nucleotide, ATP binding seems to be less influenced and only fundamentally reduced in complete absence of phospholipids or activators by comparison with available data^{134-135, 265, 271} (Appendix Table 5). ATPase activity in terms of v_{max} however is more or less independent of the studied environments, thus ATPase activity contrary to kinase activity, which might

need lipid activators for efficient lipid substrate binding¹³⁴⁻¹³⁵, is not stimulated by the surrounding lipid environment.

I.4.3 LCP, a novel membrane mimetic for solid-state NMR

The lipidic cubic phases of monoacylglycerols are a promising porous membrane mimetic for biological solid-state NMR applications. They led to a revolution in X-ray crystallography, allowed high-resolution structures of a manifold of functional membrane proteins reconstituted into the lipidic cubic phase, and has a remarkable stability in a wide range of conditions.

Its continuous and highly curved membrane allows not only solution-state like NMR spectra of membrane components, but unlike nanodiscs or liposomes where diffusion of membrane components is mainly limited to single vesicles it also allows diffusion of membrane components as well as solutes through the whole membrane mimetic. Compared to anisotropic bicelles, a membrane mimetic that would allow similar diffusion, LCPs exhibit superior stability towards alteration in membrane composition, pH and ionic strength or alterations of shape upon variation of temperature^{162, 166, 169-170, 177, 198}. However, cubic phases require elevated temperatures e.g. room temperature to form and exhibit reasonable long-term stability even though they can be undercooled¹⁷⁰. Despite cubic phase formation termed spontaneous, formation of lamellar phases at lower temperatures under MAS conditions as well as sample freezing leads to phase separation that prevents reformation of a cubic phase without additional mixing as temperature scans demonstrated.

For protein solid-state NMR applications, proteins of interest have to be reasonably temperature stable to achieve long-term stability of the formed cubic phase using elevated temperatures. They also have to withstand strong concentration at low detergent amounts to reduce destabilization of the cubic phase through detergents^{166, 169, 177}, similarly required for successful crystallization^{162, 178}. However, required concentrations may be reduced using the so-called cubicon method to concentrate the protein of interest in the cubic phase¹⁷⁸⁻¹⁷⁹. First protein spectra of DgkA, known to be sufficiently temperature stable²²⁸, demonstrated that despite formation of a cubic phase, membrane proteins can be cross-polarized and therefore seem to not partake in the same angular change inducing diffusion like membrane lipids, which are not cross-polarizable. Comparison with protein spectra acquired in liposomes at the same temperature in a liquid phase reveal also high similarity of the spectra and similar

linewidths. Signals missing in both spectra or shifted compared to the assignment of DgkA at low temperatures above freezing are mostly in the flexible loop regions due to increased mobility, which is a drawback for using LCP in cross polarization based experiments. Highly mobile residues however might be again visible at higher temperatures in J -coupling based experiments upon further increased mobility³⁶⁸.

It is likely that membrane proteins reconstituted in a cubic phase, create a lamellar domain around them, due to their architecture evolved for lamellar phases. Induction of a lamellar microenvironment is also thought to be a driving factor for protein crystal formation in the lipidic cubic phase^{162, 180, 195}. Detection of these lamellar microdomains however remains elusive and would require more specific solid-state NMR experiments. In performed cross polarization experiments exchange rates of lipids from these microdomains to the cubic phase or their small percentile compared to the cubic phase lipids could prevent efficient cross polarization and would be the reason why this population was not observed. Similarly, broad components indicating lamellar phases in static direct polarization spectra would require a reasonable population to be observable next to the protein signals.

As reported¹⁹⁸ and demonstrated in case of DMPC a phosphatidylcholine exhibiting a hydrophobic mismatch compared to monoolein, lipids can be added easily to a cubic phase without causing phase separation. Therefore, LCP might be useful to determine specific membrane components that bind to receptors, transporters, channels, enzymes or other membrane proteins and characterize their interaction. As these experiments often suffer from high background of cross-polarized molecules that are non-bound, cross polarization experiments in a cubic phase could act as a first filter reducing the signal of non-bound membrane components or lipids to the fraction exhibiting interaction with the protein of interest.

Similarly, the absence of phospholipids when using monoacylglycerols as membrane mimetics would be of advantage for phosphorous DNP measurements. Phosphoryl groups are a major form used for energy storage and transfer to drive transporters or enzymes including signaling cascades. Direct observation of this nucleus and interactions at active sites would therefore yield valuable information of energy transfer processes that can drive enzymatic reactions or conformational changes.

For membrane mimetics relying on phospholipids, conformational heterogeneity of phospholipid headgroups is observed under cryogenic conditions resulting in severe line broadening with signal overlap a major factor hindering observation of

interactions in the ^{31}P dimension³⁵⁸. The performed experiments under DNP conditions upon freezing samples prepared by forming a lipidic cubic phase for higher sample homogeneity demonstrate this advantage. However, interactions between labelled DgkA and a nucleotide analogue could not be observed yet. Despite screening of different sample compositions, low enhancements reveal a need for further optimization to be able to achieve enhancement sufficient to observe protein nucleotide contacts, which are unfortunately often at the upper distance limit for NMR, as interactions can be indirect via coordination with divalent ions. Also the freezing process itself could displace the ATP analogue from the active site in DgkA as the active site is not closed upon nucleotide binding unlike in ABC proteins where protein nucleotide ^{13}C - ^{15}N contacts were already observed³⁵⁷.

Absence of phospholipids, high stability without phase separation and porous nature allowing diffusion of membrane components as well as solutes through the whole sample are interesting parameters of LCPs for ^{31}P real-time NMR activity measurements. In case of DgkA LCPs of monoacylglycerols additionally serve a dual purpose as membrane mimetic and lipid substrate for the kinase reaction, thereby most likely saturating lipid binding sites. Lipid substrate saturation however can only be assumed, as the needed variation of MAG content without loss of cubic phase for experimental determination of a K_M is most likely not possible¹⁹⁸. However saturation is highly likely, as lipid diffusion in cubic phases is in a similar range compared to lamellar phases¹⁸² where saturation was observed¹³⁴⁻¹³⁵ even though half of the cubic phases racemic mixture of monoolein is assumed to be not a substrate for DgkA²⁵⁶.

Compared to previous ^{31}P real-time experiments in liposomes²⁹¹, which were started by addition of lipid substrate and saw saturation but also very low activities, the v_{\max} of DgkA was comparable to a published *in meso* assay²⁶⁹ indicating full accessibility for both substrates. The comparably^{134-135, 264, 267, 271} low kinase activity in liposomes reported under MAS²⁹¹ reflects most likely limitation of accessibility and homogeneous distribution of DAGs over the whole sample due to limited diffusion between liposomes and high protein to lipid ratios, that is not the case in LCPs due to its continuous nature. The high percentile of ATPase activity, whilst K_M for DBG and ATP remained unaltered compared to biochemical assays^{134-135, 264, 267, 271}, is a further hint that DAG saturation may have not been achieved for all enzymes that see sufficient amounts of nucleotide.

In contrast, an unaltered v_{\max} , but strongly increased K_M for ATP in a cubic phase with defined liquid to monoolein ratios hints to reduced diffusion of the nucleotide compared to assays performed with bath solutions. In these assays measured LCP boluses exhibit a high surface area to the surrounding bath solution and can swell due to excess liquid thereby increasing the diameter of the water channels and diffusion into and out of the bolus^{96, 169, 269}. Attempts to measure the diffusion rate of ATP via ³¹P DOSY in a LCP revealed that diffusion is reduced by at least three orders of magnitude, which is in comparison to reported strongly reduced diffusion of D₂O¹⁸² and sodium ions¹⁸⁸ in cubic phases plausible and could explain a high K_M . Activity of DgkA, which itself diffuses very slow through the LCP, would thereby very fast deplete the ATP pool in its vicinity in one of the two-non-intersecting networks of water channels depending on its insertion. ATP consumption would in turn also create a high local concentration of ADP that can bind to DgkA²⁵⁷ and might be a competitive inhibitor leading to the observed high concentrations of ATP needed to reach saturation³⁶⁹⁻³⁷¹.

The reduced activity in terms of v_{\max} of DgkA in cubic phases, irrespective of the applied method, compared to assays performed in detergent could be explained by limited diffusion of lipid substrate or reduced activity of the enzyme itself due to high curvature. It is known that gel phase as well as hexagonal phase H_{II} inducing PE lipids are creating so called bilayer frustration that leads to lower activities for DgkA¹³⁵. However, whereas increase of temperature leads also to an increased K_M for a lipid substrate in liposomes that have higher tendency to form hexagonal phases, in gel phases mainly v_{\max} is reduced. The reduced v_{\max} in gel phases was in this study attributed to potential misalignment of the substrates in the active site or high activation energy for kinetically important conformational changes¹³⁵.

As diffusion of monoolein in cubic phases should be similar to lipid diffusion in lamellar phases¹⁸², it seems very likely that high curvature inducing membrane mimetics reduce DgkA's activity compared to detergent micelles and not limited diffusion of lipid substrates or products. This is further supported by a series of enzymatic studies detailing a pronounced influence of different detergents, various lipid headgroups and bilayer thickness on the activity of DgkA in liposomes¹³⁴⁻¹³⁵ and mixed micelles^{254-255, 265, 272} where lipid substrate diffusion as underlying rate limiting factor was ruled out with extensive effort for OG mixed micelles²⁵⁴.

I.5 Conclusion and Outlook

Successful application of uncaging NPE-ATP to initiate DgkA's enzymatic activity in various membrane mimetics demonstrates the broad feasibility of the developed robust and cost-effective illumination setup to initiate biochemical reactions *in situ* during MAS and represent the first known application of the uncaging approach in solid-state NMR. Potential advantages of the uncaging approach for solid-state NMR experiments are demonstrated by uncaging a membrane-incorporated diacylglycerol to trigger DgkA's kinase reaction. Uncaging of compounds to trigger biochemical reactions inside or at the membrane interface that cannot easily be initiated as highly hydrophobic compounds are non-miscible is an often under-represented advantage of caged compounds for biophysical studies similar to initiation of interactions like oligomerization or folding as already demonstrated for liquid-state NMR³⁴⁻³⁵. These aspects will be most likely the main focus of the uncaging approach in NMR as advantages in time and spatial resolution, proclaimed hallmarks of the uncaging approach for cell biology applications, microscopy and potential photodynamic therapy³¹, are less clear. Time resolution especially in solid-state NMR is not limited by mixing times in the minutes range but mainly by the signal to noise ratio and number of transients required. Similarly, no clear advantage in time resolution exists in liquid-state NMR, where mixing devices achieve similar resolution with sub second mixing^{33, 364}. Spatial control is as well not likely to be soon of advantage in NMR as with the exception of imaging in most experiments no direct spatial information is gained. However, next to irreversible release of compounds to create a non-equilibrium photoswitches are promising tools for certain biophysical studies as they would allow to repeatedly induce a non-equilibrium²⁸. Especially in solid-state NMR, repetition of processes driven by induction of a non-equilibrium and relaxation towards equilibrium would allow to acquire sufficient signal at reasonable sample amounts. A possible example allowing to repeatedly perform experiments would thereby be creation of pH gradients²⁹ over membranes to drive enzymes or secondary active transporters that rely on proton motive force.

Thus, introduction of caged compounds and successful demonstration of their advantages for solid-state NMR expanded their scope of applications with emphasis on non-miscible membrane compounds and biomembranes. In addition, it considerably expanded the applications for solid-state NMR experiments utilizing

illumination from retinal proteins, photosystems and photo-CIDNP to triggering a wide variety of biochemical processes via light. Application of caged compounds as well as photoswitches allows thereby to trigger not only enzymatic reactions but also transport processes, macromolecular interactions, oligomerization, transitions between different states including membrane dynamics or thickness and folding.

The first direct observation of reactants of an interfacial enzymatic reaction via ^{31}P real-time MAS NMR led previously to the observation of ATPase activity in DgkA²⁹¹, which has been explored in the present work further, both in absence as well as at saturating amounts of lipid substrate. The obtained results suggest that under saturating conditions of lipid substrate, the kinase reaction is highly efficient as no ATP hydrolysis was observed in DDM mixed micelles and LCP of monoolein, the latter functioning as membrane mimetic and substrate. The previously observed low kinase activities compared to the fraction of ATPase activity in liposomes under MAS thereby indicate that accessibility issues in liposomes under MAS exist preventing to reach saturating lipid substrate concentrations using a water-soluble short chain DAG to initiate the reaction.

In absence of lipid substrate, ATPase activity could also be observed in *E. coli* polar lipid liposomes and detergent micelles, demonstrating that ATP can bind in absence of lipid substrate according to the random-equilibrium mechanism of substrate binding initially deduced from kinetic measurements^{257,291}. A elevated K_M in DDM in absence of activators like phospholipids, cardiolipin or even long chain DAGs is indicating that activators are important for efficient ATP binding and reducing the K_M for ATP to similar values obtained in the presence of saturating lipid substrate concentrations. These results additionally support the assumption that ATP binding sites are saturated in absence of a lipid substrate *in vivo*, allowing efficient phosphorylation when lipid substrates bind to DgkA^{228,257}. ATPase activity could also occur *in vivo* but is in face of the obtained results most likely very minor compared to kinase activity when MDO and LPS synthesis produce high amounts of DAGs.

Lipidic cubic phases of monoacylglycerols have led to an "explosive growth" of membrane protein structures obtained by X-ray crystallography¹⁶² but have so far been mostly evaded by protein solid-state NMR.

Despite the requirement of elevated temperatures, optically transparent LCPs exhibit comparably high stability and accessibility for solutes and membrane components during MAS as various experiments to characterize this membrane mimetic and its solute diffusion as well as ^{31}P real-time solid-state NMR following DgkA's enzymatic activity demonstrate. The high K_M for ATP obtained from ^{31}P real-time NMR experiments performed at a defined solute to lipid ratio hints to differences in solute diffusion compared to published activity assays performed in a bath solution where LCP boluses can swell and exhibit a high surface to the surrounding medium. Therefore, NMR as label-free and non-invasive method should be a favored method to directly study processes in porous materials, which yielded for example also valuable information on accumulators³⁷²⁻³⁷³ and enzyme immobilization³⁷⁴.

Reconstitution of uniformly labelled DgkA into a lipidic cubic phase allowed first acquisition of protein spectra in this membrane mimetic that does not exhibit phospholipids, making MAGs also ideal for phosphorous correlation spectra especially under DNP conditions. Surprisingly DgkA can be unlike monoolein cross-polarized and exhibits a ^{15}N powder spectrum indicating that DgkA does not undergo fast angular change due to diffusion along the highly curved bilayer like monoolein. High similarity between acquired 2D spectra further suggest that DgkA reconstituted into LCP exhibits a similar structure and dynamics compared to DgkA reconstituted in liposomes. The protein could therefore be inducing a lamellar microenvironment as it is most likely evolved for a lamellar bilayer and also exhibits lower activity in environments inducing high membrane curvature¹³⁵. It is thought as well that the high membrane curvature and resulting hydrophobic mismatch with membrane proteins evolved for lamellar phases initiates 2D crystal formation. Therefore, exploration of protein lipid interactions and formation of microdomains would not only contribute to a more general understanding of lipid curvature stress on membrane proteins or curvature inducing membrane proteins but also contribute to a better understanding of the mechanisms leading to *in meso* protein crystallization.

Lipidic cubic phases are therefore robust and versatile membrane mimetics that could be of advantage for a variety of solid-state NMR experiments including protein solid-state NMR where accessibility for solutes and membrane components under MAS is required, optical transparency for efficient illumination is needed or interference of phosphorous signals of other membrane mimetics has to be avoided.

II Effect of polyunsaturated fatty acid metabolites on membrane fluidity

It was found previously by Hu et al³⁷⁵ that a diol derivative of docosahexanoic acid (DHA) formed by the soluble epoxide hydrolase (sEH) influences cholesterol distribution between raft and non-raft fractions as well as protein location in Müller glia cells concomitantly leading to a variety of effects altering retinal angiogenesis. Continuation of this study found that elevated levels of sEH and its product 19,20-dihydrodocosapentaenoic acid (DHDP) influence diabetic retinopathy by compromising pericyte-endothelial cell interactions and inter-endothelial cell junctions by altering distribution of cell adhesion molecules between raft and non-raft fractions. Supported by a rich set of biochemical and cell biological data, evidence mounted that DHDP is exerting the observed effects by modulating membrane dynamics. To determine if altered DHDP levels have an effect on membrane dynamics, solid-state NMR experiments on model membranes and membranes derived from mouse brains were performed in collaboration with Dr. Jiong Hu and Prof. Ingrid Fleming³⁷⁶. The results of these experiments, which showed altered membrane dynamics in membranes from brains of sEH knock-out mice that can be partially reversed by addition of DHDP³⁷⁶, are presented in detail in this chapter.

II.1 Introduction

II.1.1 Lipid rafts

Shortly after the fluid mosaic model for biomembrane organization was proposed by Singer and Nicholson¹¹⁸, first observations of lateral membrane heterogeneity in biological membranes emerged as membrane fractions could be separated into detergent-soluble (DSM) and detergent-resistant membrane (DRM) fractions³⁷⁷. The lipid raft hypothesis formed proposing that specific lipids such as cholesterol, sphingolipids and saturated or glycosylated lipids form more ordered regions³⁷⁸⁻³⁸⁰, important for cellular function, by recruitment of proteins and lipids^{86, 115-116}. Despite biophysical evidence of the existence of large scale liquid ordered lateral domains in a variety of biomimetic model membranes¹¹², relevance and presence of ordered domains *in vivo* were debated due to the former¹¹³ lack of direct observation as their size is eluding most microscopy techniques³⁸¹.

A consensus definition³⁸² describes lipid rafts as transient, heterogeneous, dynamic cholesterol and sphingolipid-enriched membrane nanodomains with sizes between 10 and 200 nm, that have the potential to form microscopic domains upon clustering induced by protein–protein and protein–lipid interactions. Hydrophobic matching thereby plays a role in separating longer saturated and shorter unsaturated lipids³⁸³ as well as hydrophobicity of outward facing amino acids of membrane proteins with transmembrane domains³⁸⁴⁻³⁸⁵ into raft or non-raft domains. Lipid anchored proteins tend to follow their respective anchor such as glycosylphosphatidylinositol (GPI) or palmitoyl anchoring favoring ordered domains and anchoring to prenyl groups leading to localization in non-raft domains³⁸⁶⁻³⁸⁷. Vice versa the actin scaffold determines supramolecular membrane organization³⁸⁸ and diffusion dynamics³⁸⁹ depending on the lipid species being coupled to the filaments³⁹⁰, thereby being capable of reorganizing the plasma membrane³⁹¹.

II.1.2 DHA and lipid raft modulation

One specific lipid raft modulator, the polyunsaturated fatty acid (PUFA) DHA, is also a common dietary fatty acid component of fish oil, whose consumption is associated to have anti-inflammatory³⁹² and cardioprotective³⁹³ effects. It is directly taken up, incorporated into cellular membranes³⁹⁴⁻³⁹⁷ and accumulates mainly in the *sn*-2 position of phospholipids³⁹⁸ with preference of phosphatidylethanolamines³⁹⁹, inducing a variety of changes in lipid composition and biophysical properties. Its biophysical characterization in model membranes was mainly performed in solid-state NMR studies, which revealed that it is highly dynamic⁴⁰⁰⁻⁴⁰², behaving like a shorter oleic acid⁴⁰³, making bilayers thinner and more fluid⁴⁰³, with higher water permeability⁴⁰⁴, increasing lipid flip-flop rates⁴⁰⁵ and prefers non-lamellar phases⁴⁰⁶. Addition of DHA, itself termed to form "the ultimate non-raft membrane domain"⁴⁰⁷, stabilizes lipid rafts by increasing interdomain order disparity. This effect lead in DHA containing model membranes⁴⁰⁷⁻⁴⁰⁸ and giant plasma membrane vesicles derived from DHA supplemented cells³⁹⁹ to an increase in the temperature at which microscopic domains are observed. The magnitude of the effect is surprisingly high and comparable to major membrane perturbations induced by bile acids or liquid anesthetics⁴⁰⁹⁻⁴¹⁰. Even more, stabilization of raft phases was also observed in mice *in vivo* upon fish oil rich diets⁴¹¹⁻⁴¹² or cloning of *fat-1* encoding a n-3 fatty acid desaturase⁴¹³.

However, conflicting results have been obtained on the mode of action DHA increases fluidity of non-raft domains and thereby disparity^{399, 407-408} but also modulating cholesterol dependent protein lateral organization and signaling^{375, 414-416}. A general property of PUFA-containing phospholipids is that they are cholesterol-phobic⁴¹⁷⁻⁴¹⁹ displacing cholesterol in their respective domain⁴¹⁹. Thus, the highly dynamic PUFAs were observed to form PUFA-lipid-rich, cholesterol depleted, highly disordered domains^{407-408, 420}, but on the other hand were also observed to accumulate in ordered domains associated with lipid-rafts^{408, 411, 419, 421} reducing cholesterol content in the raft fractions^{375, 414, 419, 422}. In line with the observations that PUFAs can invade rafts they could even be incorporated into sphingolipids or esterify cholesterol^{411, 415}.

One determinant, explaining the seemingly contradictory behavior, of the observed discrepancies in partitioning was recently highlighted to be the headgroup type of lipids PUFAs are incorporated into⁴¹⁹. It was found that DHA incorporated into PEs prefers a non-raft environment^{408, 423-425} increasing cholesterol content in rafts and DHA incorporated into PCs invades raft-like domains^{411, 421} decreasing their cholesterol content.

The docosahexaenoic acyl chain content in tissues is normally below 5%³⁹⁶. However, in select tissues, such as synaptosomes⁴²⁶, sperm⁴²⁷ and the retinal rod outer segment⁴²⁸ DHA derived acyl chains are found in large amounts constituting up to 50% of all acyl chains³⁹⁴.

II.1.3 sEH and DHA derived epoxides and diols in lipid raft modulation

Tightly controlled levels of cyclooxygenase-derived prostaglandins⁴²⁹, but also lipid mediators derived from epoxygenation of PUFAs like arachidonic acid⁴³⁰⁻⁴³⁴ or DHA³⁷⁵ mainly via the cytochrome P450 (CYP) isoforms of the CYP2C family (mainly CYP2C8, CYP2C9) and CYP2J2 were found to influence angiogenesis in different tissues. Retinal angiogenesis was for example found to be dependent on the generation of a diol via the soluble epoxide hydrolase (sEH) from the epoxygenated DHA derivative 19,20-epoxydocosapentaenoic acid (EDP)³⁷⁵, with a knock-out of the sEH encoding gene *Ephx2* delaying retinal angiogenesis. Addition of this diol, 19,20-dihydroxydocosapentaenoic acid (DHDP), but not the sEH substrate EDP redistributed cholesterol from raft to non-raft fractions and suppressed Notch signaling via displacement of at least one component, presenilin 1, of the γ -secretase complex, which is localized in lipid rafts⁴³⁵⁻⁴³⁶, to non-raft fractions³⁷⁵.

Increased DHDP levels, as observed in diabetic retinopathy by overexpression of sEH, lead to pericyte loss and vascular permeability. These effects were caused by disruption of VE-cadherin and N-cadherin localization in rafts due to a loss of cholesterol mediated interaction with presenilin 1 thereby compromising pericyte-endothelial cell interactions and inter-endothelial cell junctions⁴¹⁶.

Furthermore, reduced EDP levels, due to overexpression of sEH, are also attributed to increase retinal vascular inflammation in diabetic retinopathy⁴³⁷. Addition of EDP and sEH inhibition where thereby reducing leukostasis, which can cause vaso-occlusive thrombi, also seen in stroke⁴³⁸, by reducing TNF α -induced NF κ B activity, which reduces expression of vascular cell adhesion molecule 1 (VCAM1) and intercellular adhesion molecule 1 (ICAM1)⁴³⁷.

In face of the many effects elevated or decreased DHDP levels have, with sEH inhibition as a potential drug target for prevention of diabetic retinopathy^{376, 437} and single-target multi-aspect treatment in stroke related injuries⁴³⁸⁻⁴³⁹ biophysical studies are yet at their onset. Even though such studies could lead to important insights into the modulation of cell membrane composition and dynamics, causing altered location of a manifold of proteins. The performed NMR measurements therefore demonstrate the feasibility to extract differences in membrane dynamics in a cellular and disease relevant context.

II.1.4 ¹H MAS NMR for analysis of lipid dynamics

Analysis of global lipid dynamics in complex membrane systems, such as influenza virus particles or red blood cell ghost membranes, is possible without introduction of additional compounds or isotope labelling using non-invasive and sensitive ¹H MAS NMR⁴⁴⁰. Due to fast lipid axial motions in liquid ordered and fluid states (see also section I.1.4.1) MAS can restore the proton resonances into spinning centerband and sidebands, which are inhomogeneously broadened due to weak dipole-dipole interactions⁴⁴¹. Spinning sideband intensities are therefore depending on lipid order parameters and MAS frequency⁴⁴²⁻⁴⁴⁴, with higher orders and lower MAS frequencies distributing intensity from the center- to the sidebands. In solid and liquid ordered phases axial motion is restricted to an extent that strong inter- and intramolecular dipole-dipole interactions occur^{440, 444-445}. It leads to homogeneous broadening that cannot be fully averaged out at MAS frequencies achievable with 3.2 mm or 4 mm rotors causing centerband and sideband resonance linewidths to be dependent on the

MAS frequency^{440, 444}. At the chosen spinning frequency of 10 kHz, typical linewidths of methylene resonances are 25-100 Hz for saturated lipid acyl chains in the liquid disordered (l_d) phase, 500-1000 Hz in the liquid ordered (l_o) and larger than 1.5 kHz in the solid ordered (s_o) gel phase⁴⁴⁰. As a consequence of the huge differences in linewidth between the disordered phase and ordered phases the former is the major contributor to peak height. Therefore, formation of disordered phases in complex systems can be followed directly with minimal error by measuring peak height, which is inversely related to peak width⁴⁴⁶.

Despite broad methylene linewidths in l_o and s_o phases, transitions between these phases could also be observed in model membranes via analysis of centerband to sideband ratios as *gauche-trans* isomerization and therefore order parameters are markedly different^{440, 445}. Thus, the centerband to sideband ratio reflects average order in the membrane and gives information similar to order parameters. Centerband to sideband ratios indicating s_o or l_o are however not universal, depend on sample composition and have to be determined for each lipid composition⁴⁴⁰.

^1H MAS NMR also proved successful for detection of coexistence of l_d and s_o ⁴⁴⁴ as well as l_d and l_o ⁴⁴⁵⁻⁴⁴⁶ domains in model membranes. In these cases ordered domains were large enough that lipids were mostly in slow exchange, thus residing in an ordered domain for milliseconds allowing detection of isosbetic points in temperature scan spectra, which indicate superposition of two states⁴⁴⁵. As fluid and gel phase domains exhibit different diffusion rates, determination of domain sizes of coexisting fluid and gel phase domains was possible with ^1H PFG-MAS experiments⁴⁴⁴. However measurements of domain sizes of coexisting l_d and liquid ordered phases, attributed to lipid rafts in biological membranes, are not known to have been successfully performed yet⁴⁴⁴ even though l_d and l_o should exhibit different diffusion rates⁴⁴⁷.

Standard ^1H MAS-NMR might not provide insight into domain sizes, diffusion rates or specific lipid order parameters due to limited resolution in the ^1H dimension and high complexity of biological systems. It is however, a unique, non-invasive tool to probe membrane order in a cellular context allowing a descriptive and comparative analysis of bulk membrane dynamics with reasonable sample amounts.

II.2 Materials and Methods

II.2.1 Studies on DMPC model membranes

As PUFAs like EDP and DHDP are prone to oxidation⁴⁴⁸, sample preparation was carried out under dry nitrogen atmosphere in a glove bag. Samples were handled under argon atmosphere during solvent removal at a rotary evaporator with a set-up following the Schlenk line principle as well as ultracentrifugation and lyophilization. All solvents and buffers were purged for 2 h with nitrogen gas before use to remove oxygen. To prevent oxidation BHT dissolved in MeOH was added before solvent removal in a 1:250 (mole/mole) BHT:lipid ratio⁴⁴⁹.

Due to limited amounts of PUFAs available, samples for ¹H MAS NMR temperature scans were prepared as follows: 5 mg DMPC respectively 4.7 mg for samples containing 20 mol% EDP or DHDP was dissolved in MeOH and the respective amount of PUFA in EtOH added. Solvent was removed *in vacuo* with a rotary evaporator (Rotavapor R-200, Büchi). Samples were hydrated with 1 ml D₂O and transferred into 1.5 ml tubes. Excess D₂O and lipids were separated by ultracentrifugation at 311357 g (55000 rpm) 4 °C for 1 h (Rotor: 70 Ti; Optima LE-80K Ultracentrifuge, Beckman Coulter) using custom built 1.5 ml tube inserts and D₂O removed with a syringe. Samples were lyophilized (Alpha1-2 LD 101021, Christ; pump: J96, Sogevac) over night and rehydrated with 2.5 µl D₂O (50 wt%) containing 100 mM DSS in case of the DMPC sample. For homogeneous liposome formation 8 freeze-thaw cycles and 2 times 10 s sonication in a bath sonicator (Sonorex RK52, Bandelin) were performed¹³² before the samples were spun into 3.2 mm sapphire MAS rotors and the void filled with 2 PTFE inserts (big).

II.2.2 Studies on native membranes derived from mouse brains

Mouse brains of wild-type and *Ephx2*^{-/-} knock-out mice were collected by Dr. Jiong Hu in ice-cold PBS and homogenized with a tissue homogenizer (Kinematica) at 15000 rpm for 1 min on ice. After centrifugation at 1500 g for 2 min, the pellet was resuspended by Dr. Jiong Hu in 10 ml PBS and incubated with DMSO, EDP (100 µM), DHDP (10 or 100 µM) or with 10 mg/ml methyl-β-cyclodextrin for 1 h at room temperature with gentle shaking. For EDP and DHDP delivered in EtOH, solvent was removed and PUFAs were dissolved in DMSO. Thereafter, samples were pelleted at 30000 g (average) (20300 rpm) for 30 min at 4 °C (Rotor: 70 Ti; Optima LE-80K

Ultracentrifuge, Beckman Coulter), washed with 10 ml PBS and centrifuged again (30000 g, 30 min, 4 °C) before being transferred into 4 mm zirconia MAS rotors and immediately measured.

II.2.3 Solid-state NMR measurements

Solid-state NMR measurements were performed at 10 kHz MAS on a Bruker Avance III 850 WB spectrometer operating at 850.31 MHz ^1H frequency. For studies on DMPC model membranes a 3.2 mm HCN and for studies on mouse brain membranes a 4 mm HCN probe was used. All temperatures given are referenced to KBr ^{79}Br T_1 relaxation times³³⁹ measured before each measurement time via an empirically determined formula (see Appendix IV.2 WB MAS NMR probe temperature calibration) at same spinning speed, variable temperature gas flow and frame cooling gas flow (Appendix Figure 2). Chemical shifts are referenced to DSS. For temperature and sample equilibration, acquisition was performed 10 min after the sensor reached the target temperature.

For measurements on DMPC model membranes 16 transients per temperature increment were recorded. Peak area was normalized with respect to the obtained peak area at 27 °C set to 1. The difference of normalized peak area of PUFA signals to respective DMPC signals was created by subtracting the normalized peak area of PUFA signals with the normalized peak area of the respective DMPC signals.

For measurements performed on mouse brain membranes 64 transients per temperature increment were recorded and water suppression by presaturation (approx. 0.02 Hz) was applied. The pulse width ($\pi/2$) on ^1H was 3.0 μs . Baseline correction was performed automatically by cubic spline correction, with baseline points equal for all spectra to prevent bias. Viability of automatic baseline correction was confirmed by equivalent results obtained from manually baseline corrected spectra. Peak heights were normalized to peak height at 53.4 °C, the temperature maximum reached by all temperature scans.

II.2.4 List of compounds

1,2-dimyristoyl-*sn*-glycero-3-phosphocholine (DMPC, Cat 850345, Lot 850345-02-270) was purchased from Avanti Polar Lipids (Alabaster AL, USA). (±)19,20-dihydroxy docosapentaenoic acid (DHDP, (±)19(20)-DiHDPA, Cat. 10007001, Lot 0464130-14), (±)19,20-epoxy docosapentaenoic acid (EDP, (±)19(20)-EpDPA, Cat. 10175, Lot 0437249-65, 0437249-67) were purchased from Cayman Chemical (Ann Arbor MI, USA).

II.3 Results and Discussion

First trials were performed on DMPC model membranes to observe different effects of sEH substrates and products, EDP and DHDP respectively. To gain insight if differences in the overall membrane dynamics can be observed in a cellular context, studies on native membranes derived from brains of wild-type and sEH deficient *Ephx2*^{-/-} mice were performed.

II.3.1 Studies on DMPC model membranes

As EDP and DHDP amounts are limited due to high costs, the initial studies of membrane dynamics via MAS NMR were restricted to analysis of phase transitions by ¹H NMR spectroscopy^{440, 445-446} in model membranes containing these PUFAs. Above phase transition temperature the ¹H spectra of the model membranes are well resolved at 10 kHz MAS and could be assigned according to literature for DMPC⁴⁵⁰ and DHA⁴⁰⁰, the ω-3 fatty acid precursor of EDP and DHDP (Figure 69).

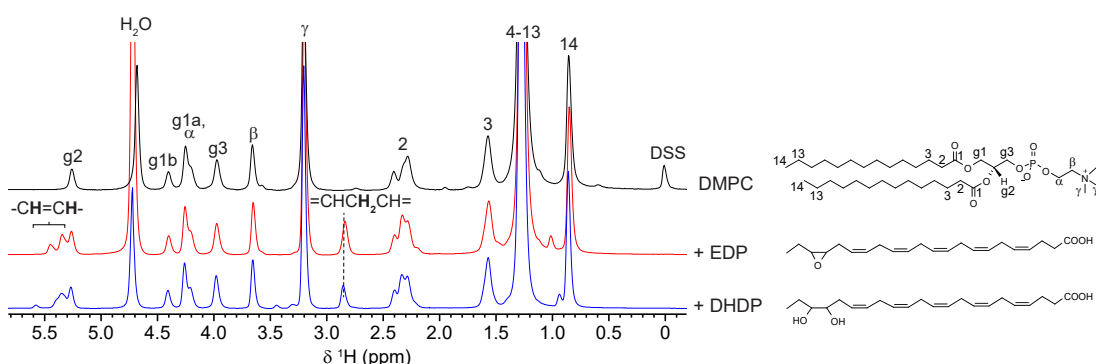


Figure 69: ¹H MAS NMR spectra of DMPC (black) and DMPC + 20 mol% EDP (red) or DHDP (blue) in D₂O (50 wt%). 16 transients at 22 °C and 10 kHz MAS, chemical structures and assignment of DMPC⁴⁵⁰ and PUFA⁴⁰⁰ signals are shown.

Introduction of the PUFAs EDP and DHDP into DMPC liposomes lowered the phase transition temperature of DMPC acyl chains from 18.2 °C to 15.3 respectively 14.8 °C (Figure 70). The phase transition in the presence of PUFAs is broadened, which in terms of slope at the phase transition temperature leads to a decrease from 0.59 °C⁻¹ to 0.16 respectively 0.15 °C⁻¹. Methylene signals from the PUFAs have a distinct chemical shift and can therefore be separately analyzed as well. Their phase transition temperature in DMPC liposomes is 15.1 °C for EDP and 16.0 °C for DHDP. Even though DHDP is causing a slightly stronger reduction of DMPC phase transition temperature as EDP, its own phase transition temperature determined by bulk

=CHCH₂CH= methylene peak area is higher compared to EDP. Phase transition of the PUFAs is significantly broader than for the respective DMPC transition, but with 0.086 °C⁻¹ and 0.081 °C⁻¹ very similar. Both aspects can be easily visualized as difference of normalized peak area between EDP or DHDP and DMPC (Figure 70c).

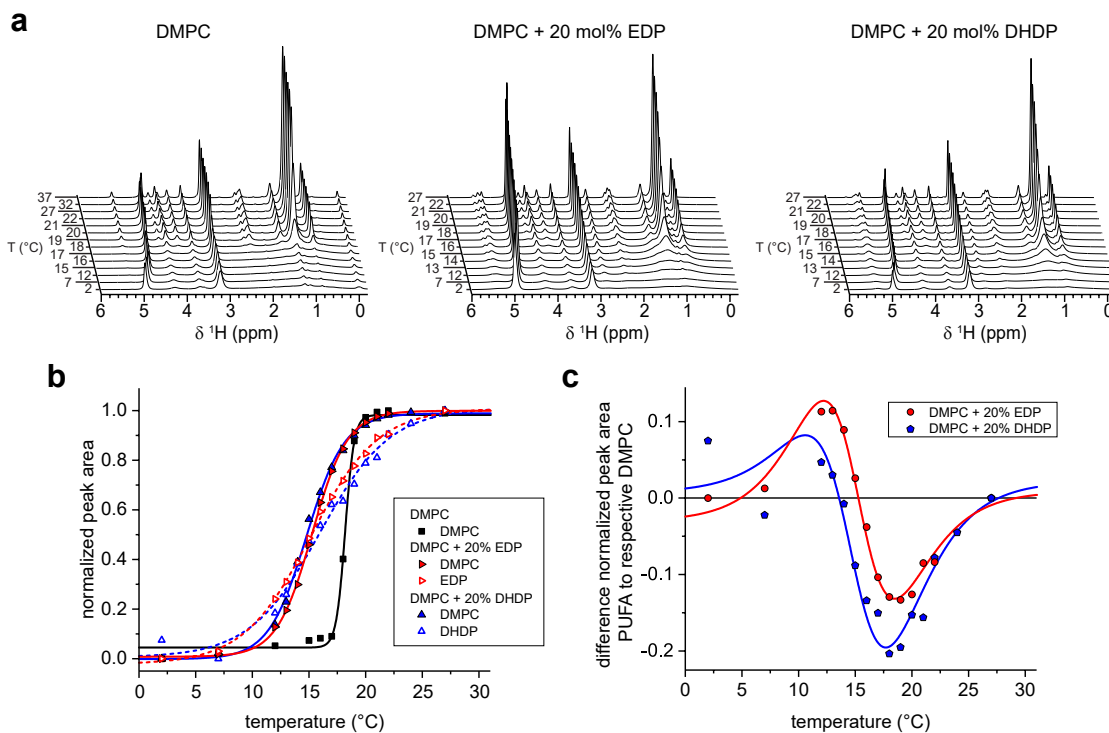


Figure 70: ¹H MAS NMR temperature scans of DMPC and DMPC + 20 mol% EDP or DHDP in D₂O (50 wt%) at 10 kHz MAS. **a**) Acquired ¹H spectra with respect to increasing temperature. 16 transients per increment. **b**) Normalized peak area and fits of analyzed acyl chain methylene DMPC (filled symbols and solid lines) and PUFA (non-filled symbols and dashed lines) peaks (see Appendix Figure 25) of DMPC (black) and DMPC + 20 mol% EDP (red) or DHDP (blue) with respect to increasing temperature using the Boltzmann sigmoid function. **c**) Difference of normalized peak area of EDP or DHDP signals to respective DMPC signals of DMPC + 20 mol% EDP (red) or DHDP (blue) as depicted in (b).

These results suggest that the PUFAs are mixing with DMPC and exhibit very similar effects in terms of altering the phase transition behavior, with the exception of a slightly higher difference in phase transition temperature between DMPC and DHDP compared to EDP. Thus, the observed effects *in vivo* are most likely not caused by general differences in phase transition induced by EDP and DHDP. Experiments in model membranes are however of limited value for providing further biophysical information as the primary mechanism *in vivo* ought to be redistribution of lipids between raft and non-raft domains, which would require very complex, raft-forming model membrane systems to reflect eukaryotic membranes.

II.3.2 Studies on native membranes derived from mouse brains

The substrates and products of sEH, EDP and DHDP, are associated to cause different partitioning of cholesterol and cholesterol binding proteins between lipid raft and non-raft fractions in eukaryotic membranes, especially in neurons and Müller cells^{375-376, 439}. Therefore, a very complex or native membrane environment is needed to emulate and observe these biologically relevant differences in biophysical properties of membranes caused by different levels of EDP and DHDP.

As sample complexity, amounts and possibilities for lipid isotope labelling are limited, it was chosen to study the overall membrane dynamics as biophysical indicator of membrane alterations with ¹H MAS NMR, a sensitive and non-invasive method⁴⁴⁰.

First trials with HEK 293 cells however were unsuccessful due to non-sufficient sample amounts and severe background from the probe in ¹H MAS NMR experiments. To contribute biophysical information to the same system studied³⁷⁶, brain membranes derived from wild-type and sEH deficient *Ephx2*^{-/-} mice were used. Experiments were carefully planned and aimed to yield a qualitative insight to reduce needed sample amounts.

¹H MAS NMR spectra of mouse brain membranes revealed three distinct peaks, which can be assigned to methyl, methylene and choline resonances, with methylene resonances also clearly observable in spinning sidebands (Figure 71). Few minor sharp peaks were observable in the spectra resulting from water-soluble components. Extremely wide bands in the spectra, underlying the more narrow methylene and choline signals of lipids, arise from proteins, DNA and RNA due to slower motions and rigidity compared to lipids⁴⁴⁰. These contributions are therefore pronounced in the sideband regions as well.

Temperature scans reveal a very broad transition from more solid-ordered or liquid-ordered states to more fluid phases as the linewidth of lipid resonances and spinning sideband intensities gradually decrease, leading to an increase in centerband peak heights, which can be determined with minimal error⁴⁴⁵. Analysis of spinning sideband intensities was strongly influenced by strong unspecific background, which could not be sufficiently compensated by manual or automatic baseline correction to yield reliable values due to low sideband intensity of lipid signals. Therefore, we abstained from interpretation of sideband to centerband ratios, which would be a more sensitive reporter of changes in *gauche-trans* conformation, and focused on the centerband peak height as the strongest spectroscopic marker for bulk membrane dynamics.

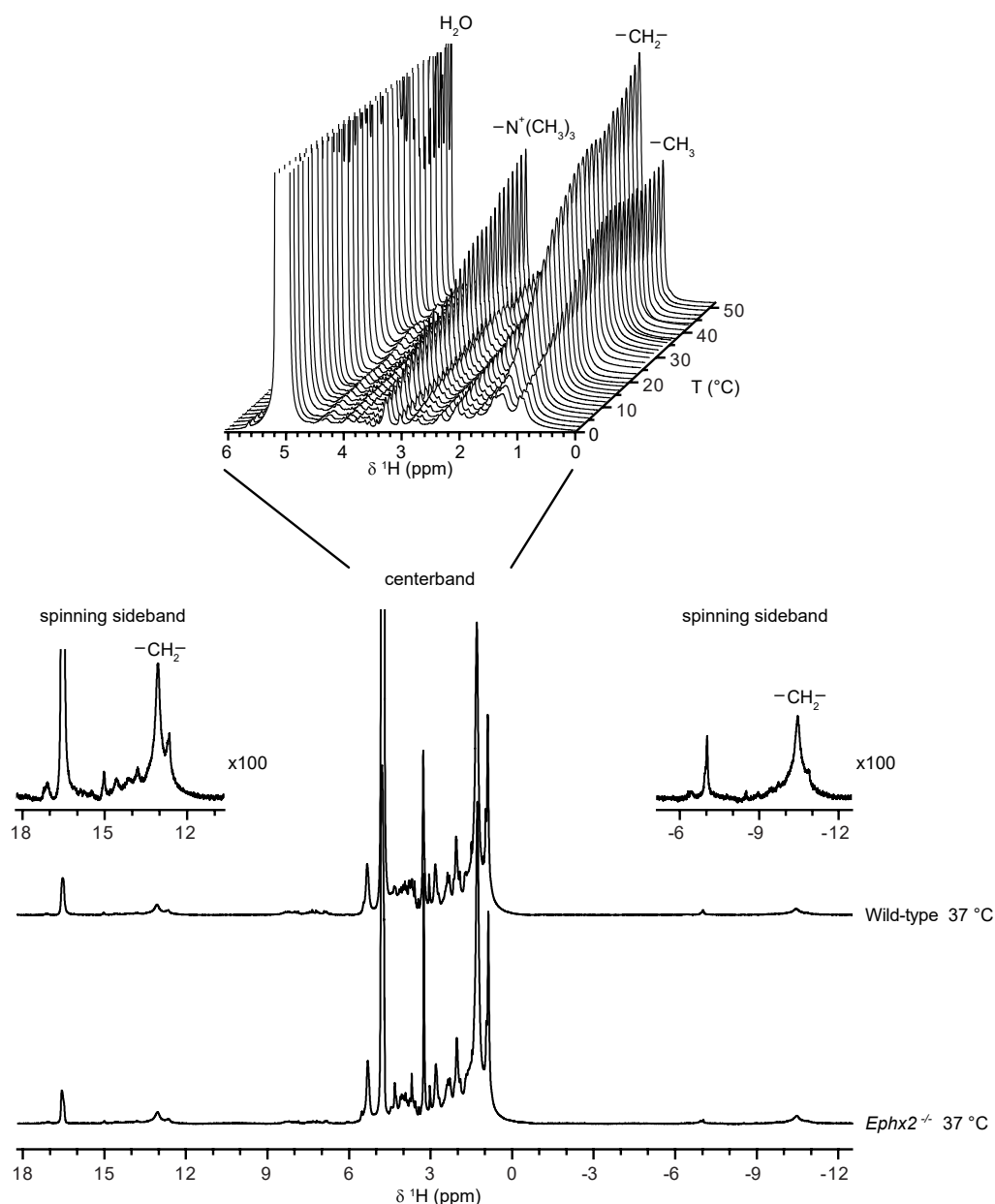


Figure 71: ^1H MAS NMR spectra of native membranes derived from wild-type and *Ephx2*^{-/-} mouse brains at 37 °C and 10 kHz MAS with first order spinning sidebands at 100 times magnification as well as centerband region of temperature scan spectra of the wild-type mouse brain membrane.

Comparison of methylene peak heights between native membranes derived from wild-type and sEH deficient *Ephx2*^{-/-} mouse brains revealed a higher bulk lipid dynamic and accordingly lower lipid order in the physiological temperature range⁴⁵¹ as judged by $13 \pm 1\%$ increase of normalized peak intensity at 37 °C (Figure 72a). Addition of the sEH product DHDP, but not its substrate EDP, to membranes derived from *Ephx2*^{-/-} mouse brains did reduce the difference to $4 \pm 1\%$ compared to the wild-type in a concentration dependent manner. Even more, these differences occurred only in the physiological temperature range, where methylene chain dynamics for

membranes derived from wild-type but also *Ephx2*^{-/-} mouse brains is not significantly altered by a temperature increase or decrease of up to 5 °C from body temperature, which is a striking reflection of homeostasis.

¹H choline signals on the opposite respond to changes in the lipid headgroup environment around phosphocholine lipids as the P⁻-N⁺-dipole realigns under the influence of the surface electrical field, indicating differences in headgroup hydration⁴⁵² and surface charge⁴⁵³. Therefore, introduction of EDP or DHDP, both having identical headgroups, into membranes derived from *Ephx2*^{-/-} mouse brains causes a similar concentration dependent change of choline peak heights from a *Ephx2*^{-/-} to a more wild-type like temperature profile (Figure 72b). Even though choline signals alter in a more complex way, as they are susceptible to variations of a manifold of different parameters⁴⁵³, the observed trend supports the hypothesis that the diol DHDP causes specific effects in the bulk dynamics of native membranes which are not related to general fatty acid or EDP content.

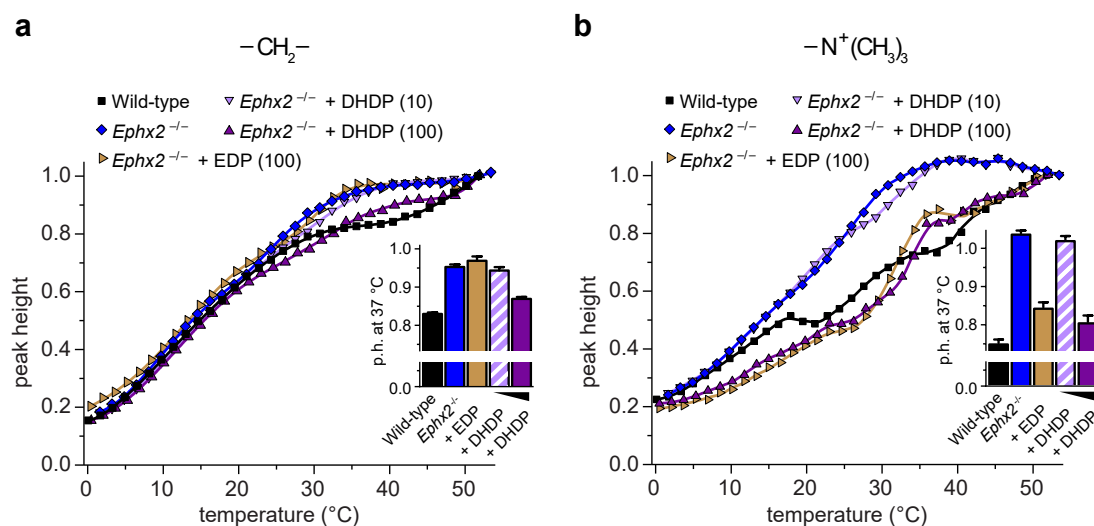


Figure 72: Normalized ethylene (a) and choline (b) peak heights obtained from ¹H MAS NMR temperature scan measurements of native membranes derived from wild-type, *Ephx2*^{-/-} and *Ephx2*^{-/-} mouse brains treated with EDP (100 μM) or DHDP (10 or 100 μM). Bar diagrams show normalized peak height at 37 °C. Error bars represent uncertainty calculated from signal to noise, baseline correction and temperature referencing.

As the sEH product DHDP is sought to redistribute cholesterol from detergent insoluble lipid raft fractions into non-raft fractions³⁷⁵, thereby leading to the observed differences in membrane dynamics, experiments to compare membrane dynamics in cholesterol-depleted membranes were performed. Native membranes derived from wild-type and *Ephx2*^{-/-} mouse brains were incubated with methyl-β-cyclodextrin to

reduce cholesterol content⁴⁵⁴. This treatment lead to slightly lower bulk membrane dynamics between 0 and 20 °C and diminution of the plateau between 32 and 42 °C as observed by methylene peak intensity of ¹H temperature scan measurements, which might be an indication for reduced cholesterol content (Figure 73). In the physiological temperature range, where differences between wild-type and *Ephx2*^{-/-} derived membranes were observed, removal of cholesterol led to convergence of differences in peak intensity from $13 \pm 1\%$ to $2 \pm 1\%$ at 37 °C between wild-type and *Ephx2*^{-/-} derived membranes (Figure 73). The high similarity of bulk membrane dynamics of membranes derived from wild-type and *Ephx2*^{-/-} mouse brains after cyclodextrin treatment suggests that the observed differences upon sEH knock-out are indeed not caused by a drastic difference in membrane composition, which is also in agreement with a lipidomics analysis on the effects of sEH knock-out in HEK 293 cells³⁷⁵. Instead, alterations in raft and non-raft fractions such as the observed DHDP induced redistribution of cholesterol from lipid raft fractions into non-raft fractions³⁷⁵ seem to be capable to cause the observed alterations in bulk membrane dynamics.

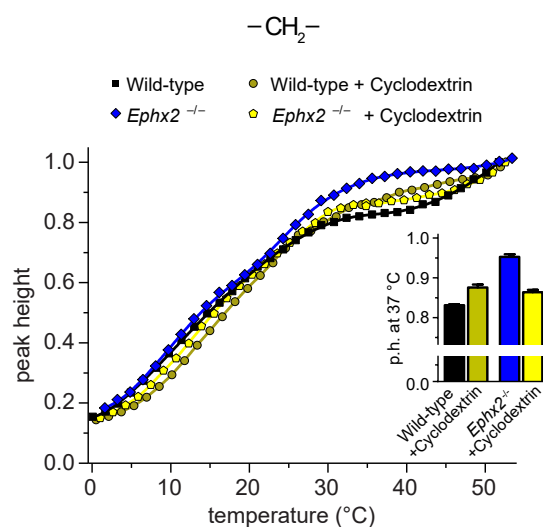


Figure 73: Normalized ethylene peak heights obtained from ¹H MAS NMR temperature scan measurements of native membranes derived from wild-type and *Ephx2*^{-/-} mouse brains and native membranes treated with 10 mg/ml methyl- β -cyclodextrin. Bar diagrams show normalized peak height at 37 °C. Error bars represent uncertainty calculated from signal to noise, baseline correction and temperature referencing.

II.4 Conclusion and Outlook

The results of ^1H MAS NMR experiments following membrane dynamics give first biophysical evidence in a cellular context to the model that DHDP, a product of sEH, causes alterations in membrane fluidity and dynamics by redistribution of lipids between raft and non-raft domains³⁷⁵⁻³⁷⁶. The corresponding sEH substrate EDP exhibits a similar phase behavior in model membranes compared to DHDP and choline headgroup temperature profile in native membranes, but unlike DHDP does not cause any alterations in bulk membrane dynamics.

This study should thereby serve as an example that non-invasive ^1H MAS NMR and ssNMR in general can be performed in a cellular context and can contribute biophysical insight into cell biological and disease relevant questions. Further biophysical questions such as structure of lipids, changes of domain sizes, dynamics and diffusion rates in different domains and the effects causing altered protein locations could be tackled by NMR^{407, 440, 449, 455-458} in a cellular context as well but would require in most cases introduction of isotope labelled compounds and higher sample amounts. Nevertheless, these examples show the possible potential of ssNMR to answer a manifold of relevant questions on a cellular level by transferring established techniques for the study of biomimetic model membranes to native eukaryotic systems or systems derived thereof, like GPMVs^{399, 459}, in an interdisciplinary effort, including MD simulation⁴⁶⁰⁻⁴⁶¹, mass spectrometry^{375, 462} and ultra-resolution microscopy^{113, 381, 463}. To provide further insight into the studied effects combination of the aforementioned methods will be crucial to determine incorporation ratios of EDP and DHDP into different lipid types, their distribution between raft and non-raft fractions and their interactions with cholesterol.

III References

1. Bargon, J.; Fischer, H., Kernresonanz-Emissionslinien während rascher Radikalreaktionen. *Z. Naturforsch. A* **1967**, *22* (10), 1556.
2. Bargon, J.; Fischer, H.; Johnsen, U., Kernresonanz-Emissionslinien während rascher Radikalreaktionen. *Z. Naturforsch. A* **1967**, *22* (10), 1551.
3. Ward, H. R.; Lawler, R. G., Nuclear magnetic resonance emission and enhanced absorption in rapid organometallic reactions. *J. Am. Chem. Soc.* **1967**, *89* (21), 5518-5519.
4. Kaptein, R., Simple Rules for Chemically Induced Dynamic Nuclear Polarization. *J. Chem. Soc., Chem. Commun.* **1971**, (14), 732-&.
5. Kaptein, R.; Oosterhoff, J. L., Chemically induced dynamic nuclear polarization II: (Relation with anomalous ESR spectra). *Chem. Phys. Lett.* **1969**, *4* (4), 195-197.
6. Closs, G. L.; Closs, L. E., Induced dynamic nuclear spin polarization in reactions of photochemically and thermally generated triplet diphenylmethylene. *J. Am. Chem. Soc.* **1969**, *91* (16), 4549-4550.
7. Kaptein, R.; Dijkstra, K.; Nicolay, K., Laser photo-CIDNP as a surface probe for proteins in solution. *Nature* **1978**, *274* (5668), 293-294.
8. Mok, K. H.; Hore, P. J., Photo-CIDNP NMR methods for studying protein folding. *Methods* **2004**, *34* (1), 75-87.
9. Zysmilich, M. G.; McDermott, A., Photochemically Induced Dynamic Nuclear Polarization in the Solid-State ¹⁵N Spectra of Reaction Centers from Photosynthetic Bacteria *Rhodospira rubra* R-26. *J. Am. Chem. Soc.* **1994**, *116* (18), 8362-8363.
10. Matysik, J.; Diller, A.; Roy, E.; Alia, A., The solid-state photo-CIDNP effect. *Photosynthesis Res.* **2009**, *102* (2-3), 427-435.
11. Kuprov, I.; Goetz, M.; Abbott, P. A.; Hore, P. J., Design and performance of a microsecond time-resolved photo-chemically induced dynamic nuclear polarization add-on for a high-field nuclear magnetic resonance spectrometer. *Rev. Sci. Instrum.* **2005**, *76* (8), 084103.
12. Kühn, T.; Schwalbe, H., Monitoring the Kinetics of Ion-Dependent Protein Folding by Time-Resolved NMR Spectroscopy at Atomic Resolution. *J. Am. Chem. Soc.* **2000**, *122* (26), 6169-6174.
13. Kuprov, I.; Hore, P. J., Uniform illumination of optically dense NMR samples. *J. Magn. Reson.* **2004**, *171* (1), 171-175.
14. Feldmeier, C.; Bartling, H.; Riedle, E.; Gschwind, R. M., LED based NMR illumination device for mechanistic studies on photochemical reactions--versatile and simple, yet surprisingly powerful. *J. Magn. Reson.* **2013**, *232*, 39-44.
15. Fischer, M. R.; De Groot, H. J. M.; Raap, J.; Winkel, C.; Hoff, A. J.; Lugtenburg, J., Carbon-13 magic angle spinning NMR study of the light-induced and temperature-dependent changes in *Rhodospira rubra* R26 reaction centers enriched in [4'-¹³C]tyrosine. *Biochemistry* **1992**, *31* (45), 11038-11049.
16. Matysik, J.; Alia, H.; Hollander, J. G.; Egorova-Zachernyuk, T.; Gast, P.; de Groot, H. J., A set-up to study photochemically induced dynamic nuclear polarization in photosynthetic reaction centres by solid-state NMR. *Indian J. Biochem. Biophys.* **2000**, *37* (6), 418-23.
17. Naito, A.; Makino, Y.; Kawamura, I., In-Situ Photo Irradiation Solid-State NMR Spectroscopy Applied to Retinal-Binding Membrane Proteins. In *Modern*

Magnetic Resonance, Webb, G. A., Ed., Springer International Publishing: Cham, 2017; pp 1-22.

18. Naito, A.; Makino, Y.; Tasei, Y.; Kawamura, I., Photoirradiation and Microwave Irradiation NMR Spectroscopy. In *Experimental Approaches of NMR Spectroscopy, Methodology and Application to Life Science and Materials Science*, 1 ed.; Naito, A., Ed., Springer Singapore: Singapore, 2018; pp 135-170.

19. Concistre, M.; Gansmuller, A.; McLean, N.; Johannessen, O. G.; Marin Montesinos, I.; Bovee-Geurts, P. H.; Brown, R. C.; DeGrip, W. J.; Levitt, M. H., Light penetration and photoisomerization in rhodopsin studied by numerical simulations and double-quantum solid-state NMR spectroscopy. *J. Am. Chem. Soc.* **2009**, *131* (17), 6133-40.

20. Concistre, M.; Gansmuller, A.; McLean, N.; Johannessen, O. G.; Marin Montesinos, I.; Bovee-Geurts, P. H.; Verdegem, P.; Lugtenburg, J.; Brown, R. C.; DeGrip, W. J.; Levitt, M. H., Double-quantum ¹³C nuclear magnetic resonance of bathorhodopsin, the first photointermediate in mammalian vision. *J. Am. Chem. Soc.* **2008**, *130* (32), 10490-1.

21. Kawamura, I.; Kihara, N.; Ohmine, M.; Nishimura, K.; Tuzi, S.; Saito, H.; Naito, A., Solid-state NMR studies of two backbone conformations at Tyr185 as a function of retinal configurations in the dark, light, and pressure adapted bacteriorhodopsins. *J. Am. Chem. Soc.* **2007**, *129* (5), 1016-7.

22. Tomonaga, Y.; Hidaka, T.; Kawamura, I.; Nishio, T.; Ohsawa, K.; Okitsu, T.; Wada, A.; Sudo, Y.; Kamo, N.; Ramamoorthy, A.; Naito, A., An active photoreceptor intermediate revealed by in situ photoirradiated solid-state NMR spectroscopy. *Biophys. J.* **2011**, *101* (10), L50-2.

23. Hunger, M.; Wang, W., Formation of cyclic compounds and carbenium ions by conversion of methanol on weakly dealuminated zeolite H-ZSM-5 investigated via a novel in situ CF MAS NMR/UV-Vis technique. *Chem. Commun.* **2004**, (5), 584-585.

24. Becker-Baldus, J.; Bamann, C.; Saxena, K.; Gustmann, H.; Brown, L. J.; Brown, R. C. D.; Reiter, C.; Bamberg, E.; Wachtveitl, J.; Schwalbe, H.; Glaubitz, C., Enlightening the photoactive site of channelrhodopsin-2 by DNP-enhanced solid-state NMR spectroscopy. *Proc. Natl. Acad. Sci. U. S. A.* **2015**, *112* (32), 9896-9901.

25. Mehler, M.; Eckert, C. E.; Leeder, A. J.; Kaur, J.; Fischer, T.; Kubatova, N.; Brown, L. J.; Brown, R. C. D.; Becker-Baldus, J.; Wachtveitl, J.; Glaubitz, C., Chromophore Distortions in Photointermediates of Proteorhodopsin Visualized by Dynamic Nuclear Polarization-Enhanced Solid-State NMR. *J. Am. Chem. Soc.* **2017**, *139* (45), 16143-16153.

26. Kaur, J.; Kriebel, C. N.; Eberhardt, P.; Jakdetchai, O.; Leeder, A. J.; Weber, I.; Brown, L. J.; Brown, R. C. D.; Becker-Baldus, J.; Bamann, C.; Wachtveitl, J.; Glaubitz, C., Solid-state NMR analysis of the sodium pump *Krokinobacter* rhodopsin 2 and its H30A mutant. *J. Struct. Biol.* **2018**.

27. Szymanski, W.; Beierle, J. M.; Kistemaker, H. A.; Velema, W. A.; Feringa, B. L., Reversible photocontrol of biological systems by the incorporation of molecular photoswitches. *Chem. Rev.* **2013**, *113* (8), 6114-78.

28. Beharry, A. A.; Woolley, G. A., Azobenzene photoswitches for biomolecules. *Chem. Soc. Rev.* **2011**, *40* (8), 4422-37.

29. Halbritter, T.; Kaiser, C.; Wachtveitl, J.; Heckel, A., Pyridine-Spiropyran Derivative as a Persistent, Reversible Photoacid in Water. *J. Org. Chem.* **2017**, *82* (15), 8040-8047.

30. Kaplan, J. H.; Forbush, B., 3rd; Hoffman, J. F., Rapid photolytic release of adenosine 5'-triphosphate from a protected analogue: utilization by the Na:K pump of human red blood cell ghosts. *Biochemistry* **1978**, *17* (10), 1929-35.
31. Ellis-Davies, G. C., Caged compounds: photorelease technology for control of cellular chemistry and physiology. *Nat. Methods* **2007**, *4* (8), 619-28.
32. Yu, H.; Li, J.; Wu, D.; Qiu, Z.; Zhang, Y., Chemistry and biological applications of photo-labile organic molecules. *Chem. Soc. Rev.* **2010**, *39* (2), 464-73.
33. Wirmer, J.; Kühn, T.; Schwalbe, H., Millisecond Time Resolved Photo-CIDNP NMR Reveals a Non-Native Folding Intermediate on the Ion-Induced Refolding Pathway of Bovine α -Lactalbumin. *Angew. Chem. Int. Ed.* **2001**, *40* (22), 4248-4251.
34. Wenter, P.; Furtig, B.; Hainard, A.; Schwalbe, H.; Pitsch, S., A caged uridine for the selective preparation of an RNA fold and determination of its refolding kinetics by real-time NMR. *ChemBioChem* **2006**, *7* (3), 417-20.
35. Fürtig, B.; Wenter, P.; Reymond, L.; Richter, C.; Pitsch, S.; Schwalbe, H., Conformational dynamics of bistable RNAs studied by time-resolved NMR spectroscopy. *J. Am. Chem. Soc.* **2007**, *129* (51), 16222-9.
36. Drozdowicz, Z.; Fernandes, N., *The Book of Photon Tools*. Oriel Instruments: Stratford.
37. Technical Note: Focusing and Collimating. <https://www.newport.com/n/focusing-and-collimating> (accessed 2018.12.06).
38. Technical Note: Fiber Optic Coupling. <https://www.newport.com/n/fiber-optic-coupling> (accessed 2018.12.06).
39. Corrie, J. E. T.; Furuta, T.; Givens, R.; Yousef, A. L.; Goeldner, M., Photoremovable Protecting Groups Used for the Caging of Biomolecules. In *Dynamic studies in biology*, Goeldner, M.; Givens, R., Eds., Wiley-VCH: Weinheim, 2005; pp 1-94.
40. Horspool, W. M.; Lenci, F., *CRC handbook of organic photochemistry and photobiology*. 2nd ed. ed.; CRC Press: Boca Raton, 2004; p 1 volume (various).
41. Barltrop, J. A.; Schofield, P., Photosensitive Protecting Groups. *Tetrahedron Lett.* **1962**, *3* (16), 697-699.
42. Klan, P.; Solomek, T.; Bochet, C. G.; Blanc, A.; Givens, R.; Rubina, M.; Popik, V.; Kostikov, A.; Wirz, J., Photoremovable protecting groups in chemistry and biology: reaction mechanisms and efficacy. *Chem. Rev.* **2013**, *113* (1), 119-91.
43. McCray, J. A.; Trentham, D. R., Properties and uses of photoreactive caged compounds. *Annu. Rev. Biophys. Biophys. Chem.* **1989**, *18*, 239-70.
44. Il'ichev, Y. V.; Schwörer, M. A.; Wirz, J., Photochemical Reaction Mechanisms of 2-Nitrobenzyl Compounds: Methyl Ethers and Caged ATP. *J. Am. Chem. Soc.* **2004**, *126* (14), 4581-4595.
45. Hoglinger, D.; Nadler, A.; Schultz, C., Caged lipids as tools for investigating cellular signaling. *Biochim. Biophys. Acta* **2014**, *1841* (8), 1085-1096.
46. Shigeri, Y.; Tatsu, Y.; Yumoto, N., Synthesis and application of caged peptides and proteins. *Pharmacol. Ther.* **2001**, *91* (2), 85-92.
47. Cherepanov, A. V.; Doroshenko, E. V.; Matysik, J.; Vries, S. d.; de Groot, H. J. M., A view on phosphate ester photochemistry by time-resolved solid state NMR. Intramolecular redox reaction of caged ATP. *Phys. Chem. Chem. Phys.* **2008**, *10* (45), 6820-6828.
48. Anstaett, P.; Pierroz, V.; Ferrari, S.; Gasser, G., Two-photon uncageable enzyme inhibitors bearing targeting vectors. *Photochem. Photobiol. Sci.* **2015**, *14* (10), 1821-1825.

49. Govindjee, R.; Balashov, S. P.; Ebrey, T. G., Quantum efficiency of the photochemical cycle of bacteriorhodopsin. *Biophys. J.* **1990**, *58* (3), 597-608.
50. Bogomolni, R. A.; Baker, R. A.; Lozier, R. H.; Stoerkenius, W., Action spectrum and quantum efficiency for proton pumping in *Halobacterium halobium*. *Biochemistry* **1980**, *19* (10), 2152-9.
51. Fournier, L.; Aujard, I.; Le Saux, T.; Maurin, S.; Beaupierre, S.; Baudin, J.-B.; Jullien, L., Coumarinylmethyl caging groups with redshifted absorption. *Chemistry – A European Journal* **2013**, *19* (51), 17494–17507.
52. Schade, B.; Hagen, V.; Schmidt, R.; Herbrich, R.; Krause, E.; Eckardt, T.; Bendig, J., Deactivation Behavior and Excited-State Properties of (Coumarin-4-yl)methyl Derivatives. 1. Photocleavage of (7-Methoxycoumarin-4-yl)methyl-Caged Acids with Fluorescence Enhancement. *J. Org. Chem.* **1999**, *64* (25), 9109-9117.
53. Goeldner, M.; Givens, R., *Dynamic studies in biology: Phototriggers, photoswitches and caged biomolecules*. Wiley-VCH: Weinheim, 2005; p xxvii, 557.
54. Walker, J. W.; Reid, G. P.; McCray, J. A.; Trentham, D. R., Photolabile 1-(2-nitrophenyl)ethyl phosphate esters of adenine nucleotide analogs. Synthesis and mechanism of photolysis. *J. Am. Chem. Soc.* **1988**, *110* (21), 7170-7177.
55. Geibel, S.; Barth, A.; Amslinger, S.; Jung, A. H.; Burzik, C.; Clarke, R. J.; Givens, R. S.; Fendler, K., P3-[2-(4-hydroxyphenyl)-2-oxo]ethyl ATP for the Rapid Activation of the Na⁺,K⁺-ATPase. *Biophys. J.* **2000**, *79* (3), 1346-1357.
56. Furuta, T.; Hirayama, Y.; Iwamura, M., Anthraquinon-2-ylmethoxycarbonyl (Aqmoc): A New Photochemically Removable Protecting Group for Alcohols. *Org. Lett.* **2001**, *3* (12), 1809-1812.
57. Suzuki, A. Z.; Watanabe, T.; Kawamoto, M.; Nishiyama, K.; Yamashita, H.; Ishii, M.; Iwamura, M.; Furuta, T., Coumarin-4-ylmethoxycarbonyls as phototriggers for alcohols and phenols. *Org. Lett.* **2003**, *5* (25), 4867-70.
58. Hasan, A.; Stengele, K.-P.; Giegrich, H.; Cornwell, P.; Isham, K. R.; Sachleben, R. A.; Pfleiderer, W.; Foote, R. S., Photolabile protecting groups for nucleosides: Synthesis and photodeprotection rates. *Tetrahedron* **1997**, *53* (12), 4247-4264.
59. Robu, V. G.; Pfeiffer, E. S.; Robia, S. L.; Balijepalli, R. C.; Pi, Y.; Kamp, T. J.; Walker, J. W., Localization of functional endothelin receptor signaling complexes in cardiac transverse tubules. *J. Biol. Chem.* **2003**, *278* (48), 48154-61.
60. Harootunian, A. T.; Kao, J. P.; Paranjape, S.; Adams, S. R.; Potter, B. V.; Tsien, R. Y., Cytosolic Ca²⁺ oscillations in REF52 fibroblasts: Ca(2+)-stimulated IP3 production or voltage-dependent Ca²⁺ channels as key positive feedback elements. *Cell Calcium* **1991**, *12* (2-3), 153-64.
61. Huang, X. P.; Sreekumar, R.; Patel, J. R.; Walker, J. W., Response of cardiac myocytes to a ramp increase of diacylglycerol generated by photolysis of a novel caged diacylglycerol. *Biophys. J.* **1996**, *70* (5), 2448-57.
62. Sreekumar, R.; Pi, Y. Q.; Huang, X. P.; Walker, J. W., Stereospecific protein kinase C activation by photolabile diglycerides. *Bioorg. Med. Chem. Lett.* **1997**, *7* (3), 341-346.
63. Quann, E. J.; Merino, E.; Furuta, T.; Huse, M., Localized diacylglycerol drives the polarization of the microtubule-organizing center in T cells. *Nat. Immunol.* **2009**, *10*, 627.
64. Nadler, A.; Reither, G.; Feng, S.; Stein, F.; Reither, S.; Müller, R.; Schultz, C., The Fatty Acid Composition of Diacylglycerols Determines Local Signaling Patterns. *Angew. Chem. Int. Ed. Engl.* **2013**, *52* (24), 6330-6334.

65. Goedhart, J.; Gadella, T. W. J., Photorelease of Diacylglycerol Increases the Amplitude and Duration of Protein Kinase C-BetaII Relocation in cyto. *bioRxiv* **2017**.
66. McCray, J. A.; Herbette, L.; Kihara, T.; Trentham, D. R., A new approach to time-resolved studies of ATP-requiring biological systems; laser flash photolysis of caged ATP. *Proc. Natl. Acad. Sci. U. S. A.* **1980**, *77* (12), 7237-41.
67. Trentham, D. R.; Corrie, J. E. T.; Reid, G. P., A new caged ATP with rapid photolysis kinetics. *Biophys. J.* **1992**, *61*, A295.
68. Wotton, J. W. T., D. R., 'CAGED' Compounds to Probe the Dynamics of Cellular Processes: Synthesis and Properties of some Novel Photosensitive P-2-Nitrobenzyl Esters of Nucleotides. In *Photochemical Probes in Biochemistry*, Nielsen, P. E., Ed., Springer Netherlands: 1989; Vol. 272, *NATO Science Series, Series C*, pp 277-296.
69. Park, C.-H.; Givens, R. S., New Photoactivated Protecting Groups. 6. p-Hydroxyphenacyl: A Phototrigger for Chemical and Biochemical Probes^{1,2}. *J. Am. Chem. Soc.* **1997**, *119* (10), 2453-2463.
70. Geissler, D.; Kresse, W.; Wiesner, B.; Bendig, J.; Kettenmann, H.; Hagen, V., DMACM-caged adenosine nucleotides: ultrafast phototriggers for ATP, ADP, and AMP activated by long-wavelength irradiation. *ChemBioChem* **2003**, *4* (2-3), 162-70.
71. Pinheiro, A. V.; Baptista, P.; Lima, J. C., Light activation of transcription: photocaging of nucleotides for control over RNA polymerization. *Nucleic Acids Res.* **2008**, *36* (14), e90.
72. Nagarajan, R., Molecular Packing Parameter and Surfactant Self-Assembly: The Neglected Role of the Surfactant Tail. *Langmuir* **2002**, *18* (1), 31-38.
73. Kulkarni, C. V.; Wachter, W.; Iglesias-Salto, G.; Engelskirchen, S.; Ahualli, S., Monoolein: a magic lipid? *Phys. Chem. Chem. Phys.* **2011**, *13* (8), 3004–3021.
74. Gruner, S. M.; Cullis, P. R.; Hope, M. J.; Tilcock, C. P., Lipid polymorphism: the molecular basis of nonbilayer phases. *Annu. Rev. Biophys. Biophys. Chem.* **1985**, *14*, 211-38.
75. Seddon, J. M.; Templer, R. H., Chapter 3 - Polymorphism of Lipid-Water Systems. In *Handbook of Biological Physics*, Lipowsky, R.; Sackmann, E., Eds., North-Holland: 1995; Vol. 1, pp 97-160.
76. Seddon, J. M., Structure of the inverted hexagonal (HII) phase, and non-lamellar phase transitions of lipids. *Biochim. Biophys. Acta* **1990**, *1031* (1), 1-69.
77. Luzzati, V., X-ray diffraction studies of lipid-water systems. In *Biol. Membr.*, Chapman, D., Ed., Academic Press: New York, 1968; Vol. 1, pp 71-123.
78. Koynova, R.; Tenchov, B., Transitions between lamellar and non-lamellar phases in membrane lipids and their physiological roles. *OA Biochemistry* **2013**, *1* (1), 1-9.
79. Koynova, R.; Caffrey, M., Phases and phase transitions of the phosphatidylcholines. *Biochim. Biophys. Acta* **1998**, *1376* (1), 91-145.
80. Lindblom, G.; Wennerström, H., Amphiphile diffusion in model membrane systems studied by pulsed NMR. *Biophys. Chem.* **1977**, *6* (2), 167-171.
81. Nagle, J. F., Theory of lipid monolayer and bilayer phase transitions: effect of headgroup interactions. *J. Membr. Biol.* **1976**, *27* (3), 233-50.
82. Marsh, D., *Handbook of Lipid Bilayers*. 2 ed.; CRC Press: Boca Raton, 2013; p 1174.
83. Seddon, J. M.; Cevc, G.; Marsh, D., Calorimetric studies of the gel-fluid (L beta-L alpha) and lamellar-inverted hexagonal (L alpha-HII) phase transitions in dialkyl- and diacylphosphatidylethanolamines. *Biochemistry* **1983**, *22* (5), 1280-9.

84. Koynova, R.; Caffrey, M., Phases and phase transitions of the hydrated phosphatidylethanolamines. *Chem. Phys. Lipids* **1994**, *69* (1), 1-34.
85. Ipsen, J. H.; Karlstrom, G.; Mouritsen, O. G.; Wennerstrom, H.; Zuckermann, M. J., Phase equilibria in the phosphatidylcholine-cholesterol system. *Biochim. Biophys. Acta* **1987**, *905* (1), 162-72.
86. Simons, K.; Ikonen, E., Functional rafts in cell membranes. *Nature* **1997**, *387* (6633), 569-72.
87. Munro, S., Lipid rafts: elusive or illusive? *Cell* **2003**, *115* (4), 377-88.
88. Tenchov, B.; Koynova, R., Cubic phases in membrane lipids. *Eur. Biophys. J.* **2012**, *41* (10), 841-50.
89. Tenchov, B., On the reversibility of the phase transitions in lipid-water systems. *Chem. Phys. Lipids* **1991**, *57* (2-3), 165-77.
90. de Campo, L.; Castle, T.; Hyde, S. T., Optimal packings of three-arm star polyphiles: from tricontinuous to quasi-uniformly striped bicontinuous forms. *Interface Focus* **2017**, *7* (4).
91. Caffrey, M., Kinetics and mechanism of transitions involving the lamellar, cubic, inverted hexagonal, and fluid isotropic phases of hydrated monoacylglycerides monitored by time-resolved X-ray diffraction. *Biochemistry* **1987**, *26* (20), 6349-63.
92. Luzzati, V.; Spegt, P. A., Polymorphism of Lipids. *Nature* **1967**, *215*, 701.
93. Longley, W.; McIntosh, T. J., A bicontinuous tetrahedral structure in a liquid-crystalline lipid. *Nature* **1983**, *303*, 612.
94. Porte, G.; Appell, J.; Bassereau, P.; Marignan, J., $L\alpha$ to $L3$: a topology driven transition in phases of infinite fluid membranes. *J. Phys. France* **1989**, *50* (11), 1335-1347.
95. Strey, R.; Winkler, J.; Magid, L., Small-angle neutron scattering from diffuse interfaces. 1. Mono- and bilayers in the water-octane-pentaoxyethylene monododecyl ether (C12Es) system. *J. Phys. Chem.* **1991**, *95* (19), 7502-7507.
96. Cherezov, V.; Clogston, J.; Papiz, M. Z.; Caffrey, M., Room to move: crystallizing membrane proteins in swollen lipidic mesophases. *J. Mol. Biol.* **2006**, *357* (5), 1605-18.
97. Kaasgaard, T.; Drummond, C. J., Ordered 2-D and 3-D nanostructured amphiphile self-assembly materials stable in excess solvent. *Phys. Chem. Chem. Phys.* **2006**, *8* (43), 4957-4975.
98. Bergenstaahl, B. A.; Stenius, P., Phase diagrams of dioleoylphosphatidylcholine with formamide, methylformamide and dimethylformamide. *J. Phys. Chem.* **1987**, *91* (23), 5944-5948.
99. Yao, H.; Lee, M. W.; Waring, A. J.; Wong, G. C. L.; Hong, M., Viral fusion protein transmembrane domain adopts β -strand structure to facilitate membrane topological changes for virus-cell fusion. *Proc. Natl. Acad. Sci. U. S. A.* **2015**, *112* (35), 10926-10931.
100. Cullis, P. R.; de Kruijff, B.; Hope, M. J.; Verkleij, A. J.; Nayar, R.; Farren, S. B.; Tilcock, C.; Madden, T. D.; Bally, M. B., Structural Properties of Lipids and Their Functional Roles in Biological Membranes. In *Concepts of Membrane Structure*, Aloia, R. C., Ed., Academic Press: 1983; *Membrane Fluidity in Biology, 1*, pp 39-81.
101. Landh, T., From entangled membranes to eclectic morphologies: cubic membranes as subcellular space organizers. *FEBS Lett.* **1995**, *369* (1), 13-7.
102. Almsherqi, Z. A.; Kohlwein, S. D.; Deng, Y., Cubic membranes: a legend beyond the Flatland* of cell membrane organization. *J. Cell Biol.* **2006**, *173* (6), 839-44.

103. Gruner, S. M., Coupling between Bilayer Curvature Elasticity and Membrane Protein Activity. In *Biomembrane Electrochemistry*, Blank, M.; Vodyanoy, I., Eds., American Chemical Society: 1994; Vol. 235, *Advances in Chemistry*, 235, pp 129-149.
104. Gruner, S. M., Intrinsic curvature hypothesis for biomembrane lipid composition: a role for nonbilayer lipids. *Proc. Natl. Acad. Sci. U. S. A.* **1985**, 82 (11), 3665-9.
105. McIntosh, T. J.; Simon, S. A., Roles of bilayer material properties in function and distribution of membrane proteins. *Annu. Rev. Biophys. Biomol. Struct.* **2006**, 35, 177-98.
106. Lee, A. G., How lipids affect the activities of integral membrane proteins. *Biochim. Biophys. Acta* **2004**, 1666 (1-2), 62–87.
107. de Kruijff, B., Biomembranes. Lipids beyond the bilayer. *Nature* **1997**, 386 (6621), 129-30.
108. Hahn, A.; Parey, K.; Bublitz, M.; Mills, D. J.; Zickermann, V.; Vonck, J.; Kuhlbrandt, W.; Meier, T., Structure of a Complete ATP Synthase Dimer Reveals the Molecular Basis of Inner Mitochondrial Membrane Morphology. *Mol. Cell* **2016**, 63 (3), 445-56.
109. Wang, T.; Hong, M., Investigation of the Curvature Induction and Membrane Localization of the Influenza Virus M2 Protein Using Static and Off-Magic-Angle Spinning Solid-State Nuclear Magnetic Resonance of Oriented Bicelles. *Biochemistry* **2015**.
110. Yang, Y.; Yao, H.; Hong, M., Distinguishing bicontinuous lipid cubic phases from isotropic membrane morphologies using (31)P solid-state NMR spectroscopy. *J. Phys. Chem. B* **2015**, 119 (15), 4993-5001.
111. McMahon, H. T.; Boucrot, E., Membrane curvature at a glance. *J. Cell Sci.* **2015**, 128 (6), 1065-70.
112. Simons, K.; Vaz, W. L., Model systems, lipid rafts, and cell membranes. *Annu. Rev. Biophys. Biomol. Struct.* **2004**, 33, 269-95.
113. Toulmay, A.; Prinz, W. A., Direct imaging reveals stable, micrometer-scale lipid domains that segregate proteins in live cells. *J. Cell Biol.* **2013**, 202 (1), 35-44.
114. McConnell, H. M.; Vrljic, M., Liquid-liquid immiscibility in membranes. *Annu. Rev. Biophys. Biomol. Struct.* **2003**, 32, 469-92.
115. Varma, R.; Mayor, S., GPI-anchored proteins are organized in submicron domains at the cell surface. *Nature* **1998**, 394 (6695), 798-801.
116. Friedrichson, T.; Kurzchalia, T. V., Microdomains of GPI-anchored proteins in living cells revealed by crosslinking. *Nature* **1998**, 394 (6695), 802-5.
117. Nicolson, G. L., The Fluid—Mosaic Model of Membrane Structure: Still relevant to understanding the structure, function and dynamics of biological membranes after more than 40years. *Biochim. Biophys. Acta* **2014**, 1838 (6), 1451 - 1466.
118. Singer, S. J.; Nicolson, G. L., The fluid mosaic model of the structure of cell membranes. *Science* **1972**, 175 (4023), 720-31.
119. Mouritsen, O. G.; Andersen, O. S., *In search of a new biomembrane model*. Munksgaard: Copenhagen, 1998.
120. Lingwood, D.; Simons, K., Lipid rafts as a membrane-organizing principle. *Science* **2010**, 327 (5961), 46-50.
121. Ritchie, T. K.; Grinkova, Y. V.; Bayburt, T. H.; Denisov, I. G.; Zolnerciks, J. K.; Atkins, W. M.; Sligar, S. G., Chapter 11 - Reconstitution of membrane proteins in phospholipid bilayer nanodiscs. *Methods Enzymol.* **2009**, 464, 211–231.

122. Inagaki, S.; Ghirlando, R.; Grisshammer, R., Biophysical characterization of membrane proteins in nanodiscs. *Methods* **2013**, *59* (3), 287–300.
123. Dorr, J. M.; Koorengevel, M. C.; Schafer, M.; Prokofyev, A. V.; Scheidelaar, S.; van der Crujisen, E. A.; Dafforn, T. R.; Baldus, M.; Killian, J. A., Detergent-free isolation, characterization, and functional reconstitution of a tetrameric K⁺ channel: the power of native nanodiscs. *Proc. Natl. Acad. Sci. U. S. A.* **2014**, *111* (52), 18607–12.
124. Orwick, M. C.; Judge, P. J.; Procek, J.; Lindholm, L.; Graziadei, A.; Engel, A.; Grobner, G.; Watts, A., Detergent-free formation and physicochemical characterization of nanosized lipid-polymer complexes: Lipodisq. *Angew. Chem. Int. Ed. Engl.* **2012**, *51* (19), 4653–7.
125. Denisov, I. G.; Sligar, S. G., Nanodiscs in Membrane Biochemistry and Biophysics. *Chem. Rev.* **2017**, *117* (6), 4669–4713.
126. Martinez, D.; Decossas, M.; Kowal, J.; Frey, L.; Stahlberg, H.; Dufourc, E. J.; Riek, R.; Habenstein, B.; Bibow, S.; Loquet, A., Lipid Internal Dynamics Probed in Nanodiscs. *ChemPhysChem* **2017**, *18* (19), 2651–2657.
127. Seddon, A. M.; Curnow, P.; Booth, P. J., Membrane proteins, lipids and detergents: not just a soap opera. *Biochim. Biophys. Acta* **2004**, *1666* (1), 105–117.
128. Warschawski, D. E.; Arnold, A. A.; Beaugrand, M.; Gravel, A.; Chartrand, É.; Marcotte, I., Choosing membrane mimetics for NMR structural studies of transmembrane proteins. *Biochim. Biophys. Acta* **2011**, *1808* (8), 1957–1974.
129. Catoire, L. J.; Warnet, X. L.; Warschawski, D. E., Micelles, Bicelles, Amphipols, Nanodiscs, Liposomes, or Intact Cells: The Hitchhiker’s Guide to the Study of Membrane Proteins by NMR. In *Membrane Proteins Production for Structural Analysis*, Mus-Veteau, I., Ed., Springer New York: New York, NY, 2014; pp 315–345.
130. Schuler, M. A.; Denisov, I. G.; Sligar, S. G., Nanodiscs as a new tool to examine lipid-protein interactions. *Methods Mol. Biol.* **2013**, *974*, 415–33.
131. Kogan, M.; Norden, B.; Beke-Somfai, T., High anisotropy of flow-aligned bicellar membrane systems. *Chem. Phys. Lipids* **2013**, *175–176*, 105–15.
132. Traikia, M.; Warschawski, D. E.; Recouvreur, M.; Cartaud, J.; Devaux, P. F., Formation of unilamellar vesicles by repetitive freeze-thaw cycles: characterization by electron microscopy and ³¹P-nuclear magnetic resonance. *Eur. Biophys. J.* **2000**, *29* (3), 184–95.
133. Rigaud, J. L.; Levy, D., Reconstitution of membrane proteins into liposomes. *Methods Enzymol.* **2003**, *372*, 65–86.
134. Pilot, J. D.; East, J. M.; Lee, A. G., Effects of bilayer thickness on the activity of diacylglycerol kinase of *Escherichia coli*. *Biochemistry* **2001**, *40* (28), 8188–8195.
135. Pilot, J. D.; East, J. M.; Lee, A. G., Effects of phospholipid headgroup and phase on the activity of diacylglycerol kinase of *Escherichia coli*. *Biochemistry* **2001**, *40* (49), 14891–14897.
136. Marassi, F. M.; Opella, S. J., Using Pisa pies to resolve ambiguities in angular constraints from PISEMA spectra of aligned proteins. *J. Biomol. NMR* **2002**, *23* (3), 239–242.
137. Bax, A.; Kontaxis, G.; Tjandra, N., Dipolar couplings in macromolecular structure determination. *Methods Enzymol.* **2001**, *339*, 127–74.
138. Warschawski, D. E.; Arnold, A. A.; Beaugrand, M.; Gravel, A.; Chartrand, E.; Marcotte, I., Choosing membrane mimetics for NMR structural studies of transmembrane proteins. *Biochim. Biophys. Acta* **2011**, *1808* (8), 1957–74.

139. Nolandt, O. V.; Walther, T. H.; Grage, S. L.; Ulrich, A. S., Magnetically oriented dodecylphosphocholine bicelles for solid-state NMR structure analysis. *Biochim. Biophys. Acta* **2012**, *1818* (5), 1142-7.
140. Durr, U. H.; Gildenberg, M.; Ramamoorthy, A., The magic of bicelles lights up membrane protein structure. *Chem. Rev.* **2012**, *112* (11), 6054-74.
141. Opella, S. J.; Marassi, F. M., Structure determination of membrane proteins by NMR spectroscopy. *Chem. Rev.* **2004**, *104* (8), 3587-606.
142. Piai, A.; Fu, Q.; Dev, J.; Chou, J. J., Optimal Bicelle Size q for Solution NMR Studies of the Protein Transmembrane Partition. *Chemistry* **2017**, *23* (6), 1361-1367.
143. Beaugrand, M.; Arnold, A. A.; Henin, J.; Warschawski, D. E.; Williamson, P. T.; Marcotte, I., Lipid concentration and molar ratio boundaries for the use of isotropic bicelles. *Langmuir* **2014**, *30* (21), 6162-70.
144. Nieh, M.-P.; Raghunathan, V. A.; Glinka, C. J.; Harroun, T. A.; Pabst, G.; Katsaras, J., Magnetically alignable phase of phospholipid "bicelle" mixtures is a chiral nematic made up of wormlike micelles. *Langmuir* **2004**, *20* (19), 7893-7897.
145. Losonczy, J. A.; Prestegard, J. H., Improved dilute bicelle solutions for high-resolution NMR of biological macromolecules. *J. Biomol. NMR* **1998**, *12* (3), 447-51.
146. Sanders, C. R.; Prosser, R. S., Bicelles: a model membrane system for all seasons? *Structure* **1998**, *6* (10), 1227-34.
147. Luckhurst, G. R.; Sluckin, T. J., *Biaxial Nematic Liquid Crystals: Theory, Simulation and Experiment*. Wiley: 2015.
148. Park, S. H.; Loudet, C.; Marassi, F. M.; Dufourc, E. J.; Opella, S. J., Solid-state NMR spectroscopy of a membrane protein in biphenyl phospholipid bicelles with the bilayer normal parallel to the magnetic field. *J. Magn. Reson.* **2008**, *193* (1), 133-8.
149. Prosser, R. S.; Hunt, S. A.; DiNatale, J. A.; Vold, R. R., Magnetically Aligned Membrane Model Systems with Positive Order Parameter: Switching the Sign of S_{zz} with Paramagnetic Ions. *J. Am. Chem. Soc.* **1996**, *118* (1), 269-270.
150. Prosser, R. S.; Bryant, H.; Bryant, R. G.; Vold, R. R., Lanthanide chelates as bilayer alignment tools in NMR studies of membrane-associated peptides. *J. Magn. Reson.* **1999**, *141* (2), 256-60.
151. Prosser, R. S.; Hwang, J. S.; Vold, R. R., Magnetically aligned phospholipid bilayers with positive ordering: a new model membrane system. *Biophys. J.* **1998**, *74* (5), 2405-18.
152. Dvinskikh, S. V.; Durr, U. H.; Yamamoto, K.; Ramamoorthy, A., High-resolution 2D NMR spectroscopy of bicelles to measure the membrane interaction of ligands. *J. Am. Chem. Soc.* **2007**, *129* (4), 794-802.
153. Arnold, A.; Labrot, T.; Oda, R.; Dufourc, E. J., Cation modulation of bicelle size and magnetic alignment as revealed by solid-state NMR and electron microscopy. *Biophys. J.* **2002**, *83* (5), 2667-80.
154. Beaugrand, M.; Arnold, A. A.; Juneau, A.; Gambaro, A. B.; Warschawski, D. E.; Williamson, P. T.; Marcotte, I., Magnetically Oriented Bicelles with Monoalkylphosphocholines: Versatile Membrane Mimetics for Nuclear Magnetic Resonance Applications. *Langmuir* **2016**, *32* (49), 13244-13251.
155. Nieh, M.-P.; Glinka, C. J.; Krueger, S.; Prosser, R. S.; Katsaras, J., SANS Study of the Structural Phases of Magnetically Alignable Lanthanide-Doped Phospholipid Mixtures. *Langmuir* **2001**, *17* (9), 2629-2638.
156. Bjorneras, J.; Nilsson, M.; Maler, L., Analysing DHPC/DMPC bicelles by diffusion NMR and multivariate decomposition. *Biochim. Biophys. Acta* **2015**, *1848* (11 Pt A), 2910-7.

157. Vácha, R.; Frenkel, D., Stability of Bicelles: A Simulation Study. *Langmuir* **2014**, *30* (15), 4229-4235.
158. Wu, H.; Su, K.; Guan, X.; Sublette, M. E.; Stark, R. E., Assessing the size, stability, and utility of isotropically tumbling bicelle systems for structural biology. *Biochim. Biophys. Acta* **2010**, *1798* (3), 482-8.
159. Morrison, E. A.; Henzler-Wildman, K. A., Reconstitution of integral membrane proteins into isotropic bicelles with improved sample stability and expanded lipid composition profile. *Biochim. Biophys. Acta* **2012**, *1818* (3), 814–820.
160. Laguerre, A.; Lohr, F.; Henrich, E.; Hoffmann, B.; Abdul-Manan, N.; Connolly, P. J.; Perozo, E.; Moore, J. M.; Bernhard, F.; Dotsch, V., From Nanodiscs to Isotropic Bicelles: A Procedure for Solution Nuclear Magnetic Resonance Studies of Detergent-Sensitive Integral Membrane Proteins. *Structure* **2016**, *24* (10), 1830-1841.
161. De Angelis, A. A.; Opella, S. J., Bicelle samples for solid-state NMR of membrane proteins. *Nat. Protoc.* **2007**, *2* (10), 2332–2338.
162. Caffrey, M., A comprehensive review of the lipid cubic phase or in meso method for crystallizing membrane and soluble proteins and complexes. *Acta Crystallogr. Sect. D. Biol. Crystallogr.* **2015**, *71* (Pt 1), 3-18.
163. Caffrey, M.; Cherezov, V., Crystallizing membrane proteins using lipidic mesophases. *Nat. Protoc.* **2009**, *4* (5), 706-31.
164. Iwata, S., *Methods and results in crystallization of membrane proteins*. International University Line: La Jolla, Calif., 2003; p XVIII, 355.
165. Briggs, J.; Chung, H.; Caffrey, M., The Temperature-Composition Phase Diagram and Mesophase Structure Characterization of the Monoolein/Water System. *J. Phys. II* **1996**, *6* (5), 723–751.
166. Misquitta, Y.; Caffrey, M., Detergents destabilize the cubic phase of monoolein: implications for membrane protein crystallization. *Biophys. J.* **2003**, *85* (5), 3084-96.
167. Cherezov, V.; Clogston, J.; Misquitta, Y.; Abdel-Gawad, W.; Caffrey, M., Membrane protein crystallization in meso: lipid type-tailoring of the cubic phase. *Biophys. J.* **2002**, *83* (6), 3393-407.
168. Cherezov, V.; Fersi, H.; Caffrey, M., Crystallization screens: Compatibility with the lipidic cubic phase for in meso crystallization of membrane proteins. *Biophys. J.* **2001**, *81* (1), 225–242.
169. Ai, X.; Caffrey, M., Membrane protein crystallization in lipidic mesophases: detergent effects. *Biophys. J.* **2000**, *79* (1), 394-405.
170. Qiu, H.; Caffrey, M., The phase diagram of the monoolein/water system: metastability and equilibrium aspects. *Biomaterials* **2000**, *21* (3), 223-34.
171. Conn, C. E.; Ces, O.; Squires, A. M.; Mulet, X.; Winter, R.; Finet, S. M.; Templer, R. H.; Seddon, J. M., A pressure-jump time-resolved X-ray diffraction study of cubic-cubic transition kinetics in monoolein. *Langmuir* **2008**, *24* (6), 2331–2340.
172. Kraineva, J.; Nicolini, C.; Thiyagarajan, P.; Kondrashkina, E.; Winter, R., Incorporation of alpha-chymotrypsin into the 3D channels of bicontinuous cubic lipid mesophases. *Biochim. Biophys. Acta* **2006**, *1764* (3), 424–433.
173. Winter, R., Synchrotron X-ray and neutron small-angle scattering of lyotropic lipid mesophases, model biomembranes and proteins in solution at high pressure. *Biochim. Biophys. Acta* **2002**, *1595* (1-2), 160–184.
174. Landau, E. M.; Rosenbusch, J. P., Lipidic cubic phases: a novel concept for the crystallization of membrane proteins. *Proc. Natl. Acad. Sci. U. S. A.* **1996**, *93* (25), 14532–14535.

175. Aomori, H.; Ishiguro, T.; Kuwata, K.; Kaneko, T.; Ogino, K., Study on Thermal and Structural Behavior of Monoacylglycerol-Water Systems. II The Phase Behavior of Monooleoylglycerol-Water Systems. *Journal of Japan Oil Chemists' Society* **1995**, *44* (11), 1004-1011.
176. Lutton, E. S., Phase behavior of aqueous systems of monoglycerides. *J. Am. Oil Chem. Soc.* **1965**, *42* (12), 1068-1070.
177. Khvostichenko, D. S.; Ng, J. J.; Perry, S. L.; Menon, M.; Kenis, P. J., Effects of detergent beta-octylglucoside and phosphate salt solutions on phase behavior of monoolein mesophases. *Biophys. J.* **2013**, *105* (8), 1848-59.
178. Ma, P.; Weichert, D.; Aleksandrov, L. A.; Jensen, T. J.; Riordan, J. R.; Liu, X.; Kobilka, B. K.; Caffrey, M., The cubicon method for concentrating membrane proteins in the cubic mesophase. *Nat. Protoc.* **2017**, *12* (9), 1745–1762.
179. Li, D.; Caffrey, M., Renaturing membrane proteins in the lipid cubic phase, a nanoporous membrane mimetic. *Sci. Rep.* **2014**, *4*, 5806.
180. Khelashvili, G.; Albornoz, P. B.; Johner, N.; Mondal, S.; Caffrey, M.; Weinstein, H., Why GPCRs behave differently in cubic and lamellar lipidic mesophases. *J. Am. Chem. Soc.* **2012**, *134* (38), 15858-68.
181. Clogston, J.; Caffrey, M., Controlling release from the lipidic cubic phase. Amino acids, peptides, proteins and nucleic acids. *J. Controlled Release* **2005**, *107* (1), 97-111.
182. Eriksson, P. O.; Lindblom, G., Lipid and water diffusion in bicontinuous cubic phases measured by NMR. *Biophys. J.* **1993**, *64* (1), 129-36.
183. Boyle-Roden, E.; Hofer, N.; Dey, K. K.; Grandinetti, P. J.; Caffrey, M., High resolution ¹H NMR of a lipid cubic phase using a solution NMR probe. *J. Magn. Reson.* **2007**, *189* (1), 13–19.
184. Anderson, S.; Jacob, M.; Lidin, S.; Larsson, K., Structure of the cubosome – a closed lipid bilayer aggregate. *zkri* **1995**, *210* (5), 315.
185. Angelova, A.; Angelov, B.; Papahadjopoulos-Sternberg, B.; Bourgaux, C.; Couvreur, P., Protein driven patterning of self-assembled cubosomic nanostructures: long oriented nanoridges. *J. Phys. Chem. B* **2005**, *109* (8), 3089-93.
186. Angelov, B. Schwarz' D Minimal Surface and the {6, 4} tiling. <http://library.wolfram.com/infocenter/MathSource/6868/> (accessed 2018.11.27).
187. Schrodinger, LLC, The PyMOL Molecular Graphics System, Version 1.7. 2015.
188. Momot, K. I.; Kuchel, P. W.; Whittaker, D., Enhancement of Na⁺ diffusion in a bicontinuous cubic phase by the ionophore monensin. *Langmuir* **2004**, *20* (7), 2660-6.
189. Spicer, P. T., Cubosomes: Bicontinuous Liquid Crystalline Nanoparticles. In *Dekker Encyclopedia of Nanoscience and Nanotechnology*, 1 ed.; Schwarz, J. A.; Lyshevski, S. E.; Putyera, K.; Contescu, C. I., Eds., CRC Press: Boca Raton, 2004; p 4200.
190. Angelov, B.; Angelova, A.; Mutafchieva, R.; Lesieur, S.; Vainio, U.; Garamus, V. M.; Jensen, G. V.; Pedersen, J. S., SAXS investigation of a cubic to a sponge (L3) phase transition in self-assembled lipid nanocarriers. *Phys. Chem. Chem. Phys.* **2011**, *13* (8), 3073-81.
191. Japan, T. N. M. R. S. o., *Experimental Approaches of NMR Spectroscopy, Methodology and Application to Life Science and Materials Science*. 1 ed.; Springer Singapore: Singapore, 2018; p XII, 636.

192. Takahashi, H.; Jojiki, K., Water isotope effect on the lipidic cubic phase: Heavy water-Induced interfacial area reduction of monoolein-Water system. *Chem. Phys. Lipids* **2017**, *208*, 52–57.
193. Richardson, S. J.; Staniec, P. A.; Newby, G. E.; Rawle, J. L.; Slaughter, A. R.; Terrill, N. J.; Elliott, J. M.; Squires, A. M., Glycerol prevents dehydration in lipid cubic phases. *Chem. Commun.* **2015**, *51* (57), 11386–11389.
194. Caffrey, M., On the Mechanism of Membrane Protein Crystallization in Lipidic Mesophases. *Cryst. Growth Des.* **2008**, *8* (12), 4244–4254.
195. Johner, N.; Mondal, S.; Morra, G.; Caffrey, M.; Weinstein, H.; Khelashvili, G., Protein and lipid interactions driving molecular mechanisms of in meso crystallization. *J. Am. Chem. Soc.* **2014**, *136* (8), 3271–84.
196. Caffrey, M. In *Crystallizing Membrane Proteins for Structure-Function Studies Using Lipidic Mesophases*, Advancing Methods for Biomolecular Crystallography, Dordrecht, 2013//; Read, R.; Urzhumtsev, A. G.; Lunin, V. Y., Eds. Springer Netherlands: Dordrecht, 2013; pp 33–46.
197. Caffrey, M., Crystallizing membrane proteins for structure-function studies using lipidic mesophases. *Biochem. Soc. Trans.* **2011**, *39* (3), 725–32.
198. Chupin, V.; Killian, J. A.; Kruijff, B. d., Effect of phospholipids and a transmembrane peptide on the stability of the cubic phase of monoolein: implication for protein crystallization from a cubic phase. *Biophys. J.* **2003**, *84* (4), 2373–2381.
199. Gater, D. L.; Reat, V.; Czaplicki, G.; Saurel, O.; Milon, A.; Jolibois, F.; Cherezov, V., Hydrogen bonding of cholesterol in the lipidic cubic phase. *Langmuir* **2013**, *29* (25), 8031–8.
200. Nagaraja, C. S., Heteronuclear saturation transfer difference (HSTD) experiment for detection of ligand binding to proteins. *Chem. Phys. Lett.* **2006**, *420* (4), 340–346.
201. Gater, D. L.; Saurel, O.; Iordanov, I.; Liu, W.; Cherezov, V.; Milon, A., Two classes of cholesterol binding sites for the β 2AR revealed by thermostability and NMR. *Biophys. J.* **2014**, *107* (10), 2305–2312.
202. Merida, I.; Avila-Flores, A.; Merino, E., Diacylglycerol kinases: at the hub of cell signalling. *Biochem. J.* **2008**, *409* (1), 1–18.
203. Berg, J. M.; Stryer, L.; Tymoczko, J. L.; Gatto jr, G. J., *Stryer Biochemie*. 8 ed.; Springer Berlin Heidelberg: Berlin, Heidelberg, 2018.
204. Brose, N.; Betz, A.; Wegmeyer, H., Divergent and convergent signaling by the diacylglycerol second messenger pathway in mammals. *Curr. Opin. Neurobiol.* **2004**, *14* (3), 328–40.
205. Kanoh, H.; Yamada, K.; Sakane, F., Diacylglycerol kinases: emerging downstream regulators in cell signaling systems. *J. Biochem.* **2002**, *131* (5), 629–33.
206. Kadamur, G.; Ross, E. M., Mammalian phospholipase C. *Annu. Rev. Physiol.* **2013**, *75*, 127–54.
207. Ron, D.; Kazanietz, M. G., New insights into the regulation of protein kinase C and novel phorbol ester receptors. *FASEB J.* **1999**, *13* (13), 1658–76.
208. Rosse, C.; Linch, M.; Kermorgant, S.; Cameron, A. J.; Boeckeler, K.; Parker, P. J., PKC and the control of localized signal dynamics. *Nat. Rev. Mol. Cell Biol.* **2010**, *11* (2), 103–12.
209. Stone, J. C., Regulation and Function of the RasGRP Family of Ras Activators in Blood Cells. *Genes Cancer* **2011**, *2* (3), 320–34.
210. Kawasaki, H.; Springett, G. M.; Toki, S.; Canales, J. J.; Harlan, P.; Blumenstiel, J. P.; Chen, E. J.; Bany, I. A.; Mochizuki, N.; Ashbacher, A.; Matsuda, M.; Housman, D. E.; Graybiel, A. M., A Rap guanine nucleotide exchange factor

- enriched highly in the basal ganglia. *Proc. Natl. Acad. Sci. U. S. A.* **1998**, *95* (22), 13278-83.
211. Brose, N.; Rosenmund, C., Move over protein kinase C, you've got company: alternative cellular effectors of diacylglycerol and phorbol esters. *J. Cell Sci.* **2002**, *115* (Pt 23), 4399-411.
212. Wattenberg, B. W.; Raben, D. M., Diacylglycerol kinases put the brakes on immune function. *Sci. STKE* **2007**, *2007* (398), pe43.
213. Topham, M. K.; Prescott, S. M., Diacylglycerol kinases: regulation and signaling roles. *Thromb. Haemost.* **2002**, *88* (6), 912-8.
214. Topham, M. K., Signaling roles of diacylglycerol kinases. *J. Cell. Biochem.* **2006**, *97* (3), 474-84.
215. Sakane, F.; Kanoh, H., Molecules in focus: diacylglycerol kinase. *Int. J. Biochem. Cell Biol.* **1997**, *29* (10), 1139-43.
216. Gupta, R. S.; Epand, R. M., Phylogenetic analysis of the diacylglycerol kinase family of proteins and identification of multiple highly-specific conserved inserts and deletions within the catalytic domain that are distinctive characteristics of different classes of DGK homologs. *PLoS ONE* **2017**, *12* (8), e0182758.
217. Sanjuan, M. A.; Pradet-Balade, B.; Jones, D. R.; Martinez, A. C.; Stone, J. C.; Garcia-Sanz, J. A.; Merida, I., T cell activation in vivo targets diacylglycerol kinase alpha to the membrane: a novel mechanism for Ras attenuation. *J. Immunol.* **2003**, *170* (6), 2877-83.
218. Topham, M. K.; Bunting, M.; Zimmerman, G. A.; McIntyre, T. M.; Blackshear, P. J.; Prescott, S. M., Protein kinase C regulates the nuclear localization of diacylglycerol kinase-zeta. *Nature* **1998**, *394* (6694), 697-700.
219. van Baal, J.; de Widt, J.; Divecha, N.; van Blitterswijk, W. J., Translocation of diacylglycerol kinase theta from cytosol to plasma membrane in response to activation of G protein-coupled receptors and protein kinase C. *J. Biol. Chem.* **2005**, *280* (11), 9870-8.
220. Shulga, Y. V.; Topham, M. K.; Epand, R. M., Regulation and functions of diacylglycerol kinases. *Chem. Rev.* **2011**, *111* (10), 6186-208.
221. Almena, M.; Merida, I., Shaping up the membrane: diacylglycerol coordinates spatial orientation of signaling. *Trends Biochem. Sci.* **2011**, *36* (11), 593-603.
222. Goto, K.; Hozumi, Y.; Nakano, T.; Saino-Saito, S.; Martelli, A. M., Lipid messenger, diacylglycerol, and its regulator, diacylglycerol kinase, in cells, organs, and animals: history and perspective. *Tohoku J. Exp. Med.* **2008**, *214* (3), 199-212.
223. Sakane, F.; Imai, S.; Kai, M.; Yasuda, S.; Kanoh, H., Diacylglycerol kinases as emerging potential drug targets for a variety of diseases. *Curr. Drug Targets* **2008**, *9* (8), 626-40.
224. Sakane, F.; Mizuno, S.; Komenoi, S., Diacylglycerol Kinases as Emerging Potential Drug Targets for a Variety of Diseases: An Update. *Front. Cell Dev. Biol.* **2016**, *4*, 82.
225. Jerga, A.; Lu, Y. J.; Schujman, G. E.; de Mendoza, D.; Rock, C. O., Identification of a soluble diacylglycerol kinase required for lipoteichoic acid production in *Bacillus subtilis*. *J. Biol. Chem.* **2007**, *282* (30), 21738-45.
226. Miller, D. J.; Jerga, A.; Rock, C. O.; White, S. W., Analysis of the *Staphylococcus aureus* DgkB structure reveals a common catalytic mechanism for the soluble diacylglycerol kinases. *Structure* **2008**, *16* (7), 1036-46.
227. Lis, M.; Kuramitsu, H. K., The Stress-Responsive dgk Gene from *Streptococcus mutans* Encodes a Putative Undecaprenol Kinase Activity. *Infect. Immun.* **2003**, *71* (4), 1938-1943.

228. Van Horn, W. D.; Sanders, C. R., Prokaryotic diacylglycerol kinase and undecaprenol kinase. *Annu. Rev. Biophys.* **2012**, *41*, 81-101.
229. Pieringer, R. A.; Kunnes, R. S., The Biosynthesis of Phosphatidic Acid and Lysophosphatidic Acid by Glyceride Phosphokinase Pathways in Escherichia Coli. *J. Biol. Chem.* **1965**, *240*, 2833-8.
230. Schneider, E. G.; Kennedy, E. P., Phosphorylation of ceramide by diglyceride kinase preparations from Escherichia coli. *The Journal of biological chemistry* **1973**, *248* (10), 3739-41.
231. Raetz, C. R.; Newman, K. F., Neutral lipid accumulation in the membranes of Escherichia coli mutants lacking diglyceride kinase. *J. Biol. Chem.* **1978**, *253* (11), 3882-3887.
232. Raetz, C. R. H.; Newman, K. F., Diglyceride Kinase Mutants of Escherichia coli: Inner Membrane Association of 1,2-Diglyceride and Its Relation to Synthesis of Membrane-Derived Oligosaccharides. *J. Bacteriol.* **1979**, *137* (2), 860-868.
233. Yamashita, Y.; Takehara, T.; Kuramitsu, H., Molecular characterization of a Streptococcus mutans mutant altered in environmental stress responses. *J. Bacteriol.* **1993**, *175* (19), 6220-6228.
234. Chen, P.; Novak, J.; Kirk, M.; Barnes, S.; Qi, F.; Caufield, P. W., Structure-activity study of the lantibiotic mutacin II from Streptococcus mutans T8 by a gene replacement strategy. *Appl. Environ. Microbiol.* **1998**, *64* (7), 2335-2340.
235. Yao, J.; Rock, C. O., Phosphatidic acid synthesis in bacteria. *Biochim. Biophys. Acta* **2013**, *1831* (3), 495-502.
236. Vance, D. E.; Vance, J. E., *Biochemistry of Lipids, Lipoproteins and Membranes*. Elsevier Science: 2002.
237. Sohlenkamp, C.; Geiger, O., Bacterial membrane lipids: Diversity in structures and pathways. *FEMS Microbiol. Rev.* **2016**, *40* (1), 133-159.
238. Zhang, Y.-M.; Rock, C. O., Membrane lipid homeostasis in bacteria. *Nature Reviews Microbiology* **2008**, *6* (3), 222.
239. Raetz, C. R.; Guan, Z.; Ingram, B. O.; Six, D. A.; Song, F.; Wang, X.; Zhao, J., Discovery of new biosynthetic pathways: the lipid A story. *J. Lipid Res.* **2009**, *50* Suppl, S103-8.
240. Whitfield, C.; Trent, M. S., Biosynthesis and export of bacterial lipopolysaccharides. *Annu. Rev. Biochem.* **2014**, *83*, 99-128.
241. Salazar, J.; Alarcon, M.; Huerta, J.; Navarro, B.; Aguayo, D., Phosphoethanolamine addition to the Heptose I of the Lipopolysaccharide modifies the inner core structure and has an impact on the binding of Polymyxin B to the Escherichia coli outer membrane. *Arch. Biochem. Biophys.* **2017**, *620*, 28-34.
242. Herrera, C. M.; Hankins, J. V.; Trent, M. S., Activation of PmrA inhibits LpxT-dependent phosphorylation of lipid A promoting resistance to antimicrobial peptides. *Mol. Microbiol.* **2010**, *76* (6), 1444-60.
243. Cullen, T. W.; Trent, M. S.; Raetz, C. R. H., A link between the assembly of flagella and lipooligosaccharide of the Gram-negative bacterium Campylobacter jejuni. *Proc. Natl. Acad. Sci. U. S. A.* **2010**, *107* (11), 5160-5165.
244. Cullen, T. W.; Madsen, J. A.; Ivanov, P. L.; Brodbelt, J. S.; Trent, M. S., Characterization of unique modification of flagellar rod protein FlgG by Campylobacter jejuni lipid A phosphoethanolamine transferase, linking bacterial locomotion and antimicrobial peptide resistance. *J. Biol. Chem.* **2012**, *287* (5), 3326-36.
245. Goldfine, H., Bacterial membranes and lipid packing theory. *J. Lipid Res.* **1984**, *25* (13), 1501-1507.

246. Vinogradova, O.; Badola, P.; Czerski, L.; Sonnichsen, F. D.; Sanders, C. R., 2nd, Escherichia coli diacylglycerol kinase: a case study in the application of solution NMR methods to an integral membrane protein. *Biophys. J.* **1997**, *72* (6), 2688-701.
247. Loomis, C. R.; Walsh, J. P.; Bell, R. M., sn-1,2-Diacylglycerol kinase of Escherichia coli. Purification, reconstitution, and partial amino- and carboxyl-terminal analysis. *J. Biol. Chem.* **1985**, *260* (7), 4091-7.
248. Chang, Y. Y.; Kennedy, E. P., Pathways for the synthesis of glycerophosphatides in Escherichia coli. *J. Biol. Chem.* **1967**, *242* (3), 516-9.
249. Bohnenberger, E.; Sandermann, H., Lipid dependence of diacylglycerol kinase from Escherichia coli. *Eur. J. Biochem.* **1983**, *132* (3), 645-650.
250. Schneider, E. G.; Kennedy, E. P., Partial purification and properties of diglyceride kinase from Escherichia coli. *Biochim. Biophys. Acta* **1976**, *441* (2), 201-212.
251. Roterling, H.; Raetz, C. R., Appearance of monoglyceride and triglyceride in the cell envelope of Escherichia coli mutants defective in diglyceride kinase. *J. Biol. Chem.* **1983**, *258* (13), 8068-8073.
252. Lightner, V. A.; Larson, T. J.; Tailleur, P.; Kantor, G. D.; Raetz, C. R.; Bell, R. M.; Modrich, P., Membrane phospholipid synthesis in Escherichia coli. Cloning of a structural gene (plsB) of the sn-glycerol-3-phosphate acyltransferase. *J. Biol. Chem.* **1980**, *255* (19), 9413-20.
253. Lightner, V. A.; Bell, R. M.; Modrich, P., The DNA sequences encoding plsB and dgk loci of Escherichia coli. *J. Biol. Chem.* **1983**, *258* (18), 10856-10861.
254. Walsh, J. P.; Bell, R. M., sn-1,2-Diacylglycerol kinase of Escherichia coli.: Mixed micellar analysis of the phospholipid cofactor requirement and divalent cation dependence. *J. Biol. Chem.* **1986**, *261* (14), 6239-6247.
255. Walsh, J. P.; Bell, R. M., sn-1,2-Diacylglycerol kinase of Escherichia coli.: Structural and kinetic analysis of the lipid cofactor dependence. *J. Biol. Chem.* **1986**, *261* (32), 15062-15069.
256. Walsh, J. P.; Fahrner, L.; Bell, R. M., sn-1,2-diacylglycerol kinase of Escherichia coli. Diacylglycerol analogues define specificity and mechanism. *J. Biol. Chem.* **1990**, *265* (8), 4374-4381.
257. Badola, P.; Sanders, C. R., Escherichia coli diacylglycerol kinase is an evolutionarily optimized membrane enzyme and catalyzes direct phosphoryl transfer. *J. Biol. Chem.* **1997**, *272* (39), 24176-24182.
258. Zhou, Y.; Wen, J.; Bowie, J. U., A passive transmembrane helix. *Nat. Struct. Biol.* **1997**, *4* (12), 986-990.
259. Lau, F. W.; Chen, X.; Bowie, J. U., Active sites of diacylglycerol kinase from Escherichia coli are shared between subunits. *Biochemistry* **1999**, *38* (17), 5521-5527.
260. Zhou, Y.; Bowie, J. U., Building a thermostable membrane protein. *J. Biol. Chem.* **2000**, *275* (10), 6975-9.
261. Buckstein, M. H.; He, J.; Rubin, H., Characterization of nucleotide pools as a function of physiological state in Escherichia coli. *J. Bacteriol.* **2008**, *190* (2), 718-726.
262. Sanders, C. R., 2nd; Czerski, L.; Vinogradova, O.; Badola, P.; Song, D.; Smith, S. O., Escherichia coli diacylglycerol kinase is an alpha-helical polytopic membrane protein and can spontaneously insert into preformed lipid vesicles. *Biochemistry* **1996**, *35* (26), 8610-8.
263. Lau, F. W.; Bowie, J. U., A method for assessing the stability of a membrane protein. *Biochemistry* **1997**, *36* (19), 5884-92.

264. Van Horn, W. D.; Kim, H. J.; Ellis, C. D.; Hadziselimovic, A.; Sulistijo, E. S.; Karra, M. D.; Tian, C.; Sonnichsen, F. D.; Sanders, C. R., Solution nuclear magnetic resonance structure of membrane-integral diacylglycerol kinase. *Science* **2009**, *324* (5935), 1726-9.
265. Koehler, J.; Sulistijo, E. S.; Sakakura, M.; Kim, H. J.; Ellis, C. D.; Sanders, C. R., Lysophospholipid micelles sustain the stability and catalytic activity of diacylglycerol kinase in the absence of lipids. *Biochemistry* **2010**, *49* (33), 7089–7099.
266. Gorzelle, B. M.; Hoffman, A. K.; Keyes, M. H.; Gray, D. N.; Ray, D. G.; Sanders, C. R., Amphipols can support the activity of a membrane enzyme. *J. Am. Chem. Soc.* **2002**, *124* (39), 11594–11595.
267. Czerski, L.; Sanders, C. R., Functionality of a membrane protein in bicelles. *Anal. Biochem.* **2000**, *284* (2), 327–333.
268. Gorzelle, B. M.; Nagy, J. K.; Oxenoid, K.; Lonzer, W. L.; Cafiso, D. S.; Sanders, C. R., Reconstitutive Refolding of Diacylglycerol Kinase, an Integral Membrane Protein†. *Biochemistry* **1999**, *38* (49), 16373-16382.
269. Li, D.; Caffrey, M., Lipid cubic phase as a membrane mimetic for integral membrane protein enzymes. *PNAS* **2011**, *108* (21), 8639-44.
270. Hopper, J. T.; Yu, Y. T.; Li, D.; Raymond, A.; Bostock, M.; Liko, I.; Mikhailov, V.; Laganowsky, A.; Benesch, J. L.; Caffrey, M.; Nietlispach, D.; Robinson, C. V., Detergent-free mass spectrometry of membrane protein complexes. *Nat. Methods* **2013**, *10* (12), 1206-8.
271. Jittikoon, J.; East, J. M.; Lee, A. G., A fluorescence method to define transmembrane alpha-helices in membrane proteins: Studies with bacterial diacylglycerol kinase. *Biochemistry* **2007**, *46* (38), 10950–10959.
272. Hutchison, J. M.; Lu, Z.; Li, G. C.; Travis, B.; Mittal, R.; Deatherage, C. L.; Sanders, C. R., Dodecyl-β-melibioside Detergent Micelles as a Medium for Membrane Proteins. *Biochemistry* **2017**, *56* (41), 5481–5484.
273. Warren, G. B.; Toon, P. A.; Birdsall, N. J.; Lee, A. G.; Metcalfe, J. C., Reconstitution of a Calcium-Pump Using Defined Membrane Components. *Proc. Natl. Acad. Sci. U. S. A.* **1974**, *71* (3), 622-626.
274. Lassila, J. K.; Zalatan, J. G.; Herschlag, D., Biological phosphoryl-transfer reactions: understanding mechanism and catalysis. *Annu. Rev. Biochem.* **2011**, *80*, 669–702.
275. Albery, W. J.; Knowles, J. R., Efficiency and evolution of enzyme catalysis. *Angew. Chem. Int. Ed. Engl.* **1977**, *16* (5), 285-93.
276. Oxenoid, K.; Sonnichsen, F. D.; Sanders, C. R., Conformationally specific misfolding of an integral membrane protein. *Biochemistry* **2001**, *40* (17), 5111–5118.
277. Tsai, M. D.; Yan, H. G., Mechanism of adenylate kinase: site-directed mutagenesis versus X-ray and NMR. *Biochemistry* **1991**, *30* (28), 6806-18.
278. Fersht, A., *Enzyme Structure and Mechanism*. 2 ed.; W.H. Freeman & Co.: New York, 1985.
279. Allan, D.; Thomas, P.; Michell, R. H., Rapid transbilayer diffusion of 1,2-diacylglycerol and its relevance to control of membrane curvature. *Nature* **1978**, *276* (5685), 289-90.
280. Hamilton, J. A.; Bhamidipati, S. P.; Kodali, D. R.; Small, D. M., The interfacial conformation and transbilayer movement of diacylglycerols in phospholipid bilayers. *J. Biol. Chem.* **1991**, *266* (2), 1177-86.
281. Walsh, J. P.; Loomis, C. R.; Bell, R. M., Regulation of diacylglycerol kinase biosynthesis in *Escherichia coli*: A trans-acting *dgkR* mutation increases transcription of the structural gene. *J. Biol. Chem.* **1986**, *261* (24), 11021–11027.

282. Gennis, R. B., *Biomembranes: Molecular Structure and Function*. Springer-Verlag: New York, 1989; p XVII, 533.
283. McCloskey, M. A.; Poo, M. M., Rates of membrane-associated reactions: reduction of dimensionality revisited. *J. Cell Biol.* **1986**, *102* (1), 88-96.
284. Berg, O. G.; von Hippel, P. H., Diffusion-controlled macromolecular interactions. *Annu. Rev. Biophys. Biophys. Chem.* **1985**, *14*, 131-60.
285. Shibuya, I., Metabolic regulations and biological functions of phospholipids in *Escherichia coli*. *Prog. Lipid Res.* **1992**, *31* (3), 245-299.
286. Larson, T. J.; Dowhan, W., Ribosomal-associated phosphatidylserine synthetase from *Escherichia coli*: purification by substrate-specific elution from phosphocellulose using cytidine 5'-diphospho-1,2-diacyl-sn-glycerol. *Biochemistry* **1976**, *15* (24), 5212-8.
287. Morein, S.; Andersson, A.; Rilfors, L.; Lindblom, G., Wild-type *Escherichia coli* cells regulate the membrane lipid composition in a "window" between gel and non-lamellar structures. *J. Biol. Chem.* **1996**, *271* (12), 6801-9.
288. Milo, R.; Phillips, R., *Cell biology by the numbers*. Garland Science, Taylor & Francis Group: New York, 2015; p 400.
289. Schmidt, A.; Kochanowski, K.; Vedelaar, S.; Ahrne, E.; Volkmer, B.; Callipo, L.; Knoops, K.; Bauer, M.; Aebersold, R.; Heinemann, M., The quantitative and condition-dependent *Escherichia coli* proteome. *Nat. Biotechnol.* **2016**, *34* (1), 104-110.
290. Nagy, J. K.; Lonzer, W. L.; Sanders, C. R., Kinetic study of folding and misfolding of diacylglycerol kinase in model membranes. *Biochemistry* **2001**, *40* (30), 8971-80.
291. Ullrich, S. J.; Hellmich, U. A.; Ullrich, S.; Glaubitz, C., Interfacial enzyme kinetics of a membrane bound kinase analyzed by real-time MAS-NMR. *Nat. Chem. Biol.* **2011**, *7* (5), 263-70.
292. Russ, E.; Kaiser, U.; Sandermann, H., Lipid-dependent membrane enzymes. Purification to homogeneity and further characterization of diacylglycerol kinase from *Escherichia coli*. *Eur. J. Biochem.* **1988**, *171* (1-2), 335-342.
293. Boland, C.; Li, D.; Shah, S. T.; Haberstock, S.; Dotsch, V.; Bernhard, F.; Caffrey, M., Cell-free expression and in meso crystallisation of an integral membrane kinase for structure determination. *Cell. Mol. Life Sci.* **2014**.
294. Nagy, J. K.; Lau, F. W.; Bowie, J. U.; Sanders, C. R., Mapping the oligomeric interface of diacylglycerol kinase by engineered thiol cross-linking: homologous sites in the transmembrane domain. *Biochemistry* **2000**, *39* (14), 4154-64.
295. Nagy, J. K.; Sanders, C. R., A critical residue in the folding pathway of an integral membrane protein. *Biochemistry* **2002**, *41* (29), 9021-5.
296. Nagy, J. K.; Sanders, C. R., Destabilizing mutations promote membrane protein misfolding. *Biochemistry* **2004**, *43* (1), 19-25.
297. Mi, D. H.; Kim, H. J.; Hadziselimovic, A.; Sanders, C. R., Irreversible misfolding of diacylglycerol kinase is independent of aggregation and occurs prior to trimerization and membrane association. *Biochemistry* **2006**, *45* (33), 10072-10084.
298. Lorch, M.; Booth, P. J., Insertion kinetics of a denatured alpha helical membrane protein into phospholipid bilayer vesicles. *J. Mol. Biol.* **2004**, *344* (4), 1109-21.
299. Seddon, A. M.; Lorch, M.; Ces, O.; Templer, R. H.; Macrae, F.; Booth, P. J., Phosphatidylglycerol lipids enhance folding of an alpha helical membrane protein. *J. Mol. Biol.* **2008**, *380* (3), 548-56.

300. Li, D.; Lyons, J. A.; Pye, V. E.; Vogeley, L.; Aragao, D.; Kenyon, C. P.; Shah, S. T.; Doherty, C.; Aherne, M.; Caffrey, M., Crystal structure of the integral membrane diacylglycerol kinase. *Nature* **2013**, *497* (7450), 521-4.
301. Smith, R. L.; O'Toole, J. F.; Maguire, M. E.; Sanders, C. R., Membrane topology of Escherichia coli diacylglycerol kinase. *J. Bacteriol.* **1994**, *176* (17), 5459–5465.
302. Vinogradova, O.; Sönnichsen, F.; Sanders, C. R., On choosing a detergent for solution NMR studies of membrane proteins. *J. Biomol. NMR* **1998**, *11* (4), 381–386.
303. Oxenoid, K.; Kim, H. J.; Jacob, J.; Sönnichsen, F. D.; Sanders, C. R., NMR assignments for a helical 40 kDa membrane protein. *J. Am. Chem. Soc.* **2004**, *126* (16), 5048–5049.
304. Chen, Y.; Zhang, Z.; Tang, X.; Li, J.; Glaubitz, C.; Yang, J., Conformation and topology of diacylglycerol kinase in E.coli membranes revealed by solid-state NMR spectroscopy. *Angew. Chem. Int. Ed. Engl.* **2014**, *53* (22), 5624-8.
305. Möbius, K.; Kazemi, S.; Güntert, P.; Jakob, A.; Heckel, A.; Becker-Baldus, J.; Glaubitz, C., Global response of diacylglycerol kinase towards substrate binding observed by 2D and 3D MAS NMR. *Sci. Rep.* **2019**, *9* (1).
306. Yamaguchi, S.; Tuzi, S.; Bowie, J. U.; Saitô, H., Secondary structure and backbone dynamics of Escherichia coli diacylglycerol kinase, as revealed by site-directed solid-state ¹³C NMR. *Biochim. Biophys. Acta* **2004**, *1698* (1), 97–105.
307. Möbius, K., Structural and Functional Studies on E.coli Diacylglycerol Kinase by MAS NMR Spectroscopy. Goethe-Universität Frankfurt: Frankfurt, 2018.
308. Li, D.; Stansfeld, P. J.; Sansom, M. S. P.; Keogh, A.; Vogeley, L.; Howe, N.; Lyons, J. A.; Aragao, D.; Fromme, P.; Fromme, R.; Basu, S.; Grotjohann, I.; Kupitz, C.; Rendek, K.; Weierstall, U.; Zatsepin, N. A.; Cherezov, V.; Liu, W.; Bandaru, S.; English, N. J.; Gati, C.; Barty, A.; Yefanov, O.; Chapman, H. N.; Diederichs, K.; Messerschmidt, M.; Boutet, S.; Williams, G. J.; Marvin Seibert, M.; Caffrey, M., Ternary structure reveals mechanism of a membrane diacylglycerol kinase. *Nat. Commun.* **2015**, *6*, 10140.
309. Harris, R. K.; Becker, E. D.; Cabral de Menezes, S. M.; Granger, P.; Hoffman, R. E.; Zilm, K. W., Further conventions for NMR shielding and chemical shifts (IUPAC Recommendations 2008). *Pure Appl. Chem.* **2008**, *80* (1), 59–84.
310. Haeberlen, U., *High Resolution NMR in Solids Selective Averaging: Supplement 1 Advances in Magnetic Resonance*. Academic Press: New York, 1976.
311. Mehring, M., *High Resolution NMR Spectroscopy in Solids*. Springer-Verlag: Berlin Heidelberg New York, 1976.
312. Saito, H.; Ando, I.; Ramamoorthy, A., Chemical shift tensor - the heart of NMR: Insights into biological aspects of proteins. *Prog. Nucl. Magn. Reson. Spectrosc.* **2010**, *57* (2), 181-228.
313. Pake, G. E., Nuclear Resonance Absorption in Hydrated Crystals: Fine Structure of the Proton Line. *J. Chem. Phys.* **1948**, *16* (4), 327-336.
314. Dingley, A. J.; Pascal, S. M., *Biomolecular NMR Spectroscopy*. IOS Press: Amsterdam, Washington, 2011.
315. James, T. L., *Nuclear Magnetic Resonance of Biological Macromolecules*. Academic Press: 2005; Vol. C.
316. James, T. L.; Dötsch, V.; Schmitz, U., *Nuclear Magnetic Resonance of Biological Macromolecules*. Academic Press: 2005; Vol. A, B.
317. Szeverenyi, N. M.; Sullivan, M. J.; Maciel, G. E., Observation of spin exchange by two-dimensional fourier transform ¹³C cross polarization-magic-angle spinning. *J. Magn. Reson.* **1982**, *47* (3), 462 - 475.

318. Takegoshi, K.; Nakamura, S.; Terao, T., ^{13}C - ^1H dipolar-assisted rotational resonance in magic-angle spinning NMR. *Chem. Phys. Lett.* **2001**, *344* (5), 631 - 637.
319. Apperley, D. C.; Harris, R. K.; Hodgkinson, P., *Solid-State NMR: Basic Principles and Practice*. Momentum Press: New York, 2012.
320. Baldus, M.; Petkova, A. T.; Herzfeld, J.; Griffin, R. G., Cross polarization in the tilted frame: assignment and spectral simplification in heteronuclear spin systems. *Mol. Phys.* **1998**, *95* (6), 1197-1207.
321. Gullion, T.; Schaefer, J., Rotational-echo double-resonance NMR. *J. Magn. Reson.* **1989**, *81* (1), 196 - 200.
322. Jaroniec, C. P.; Filip, C.; Griffin, R. G., 3D TEDOR NMR experiments for the simultaneous measurement of multiple carbon-nitrogen distances in uniformly $(^{13}\text{C},^{15}\text{N})$ -labeled solids. *J. Am. Chem. Soc.* **2002**, *124* (36), 10728-42.
323. Roberts, G. C. K., *NMR of macromolecules : a practical approach*. IRL Press at Oxford University Press: Oxford; New York, 1993; p 399.
324. Boland, C.; Li, D.; Shah, S. T.; Haberstock, S.; Dötsch, V.; Bernhard, F.; Caffrey, M., Cell-free expression and in meso crystallisation of an integral membrane kinase for structure determination. *Cell. Mol. Life Sci.* **2014**.
325. Li, D.; Shah, S. T.; Caffrey, M., Host Lipid and Temperature as Important Screening Variables for Crystallizing Integral Membrane Proteins in Lipidic Mesophases. Trials with Diacylglycerol Kinase. *Cryst. Growth Des.* **2013**, *13* (7), 2846-2857.
326. Li, D.; Pye, V. E.; Caffrey, M., Experimental phasing for structure determination using membrane-protein crystals grown by the lipid cubic phase method. *Acta Crystallogr. D Biol. Crystallogr.* **2015**, *71* (Pt 1), 104–122.
327. Nollert, P., Practical Aspects of Membrane Protein Crystallization in Lipidic Cubic Phases. In *Methods and results in crystallization of membrane proteins*, 1 ed.; Iwata, S., Ed., International University Line: La Jolla, Calif., 2003; *IUL biotechnology series*, *4*, pp 57-72.
328. Caffrey, M.; Porter, C., Crystallizing membrane proteins for structure determination using lipidic mesophases. *J. Vis. Exp.* **2010**, (45).
329. Tanzer, M. L.; Gilvarg, C., Creatine and creatine kinase measurement. *J. Biol. Chem.* **1959**, *234*, 3201-4.
330. Jakob, A. Synthese von Zwei-Photonen-Schutzgruppen für Oligonukleotide und Peptide. Dissertation, Goethe-Universität Frankfurt, Fachbereich 14 Biochemie, Chemie und Pharmazie, Frankfurt am Main, 2018.
331. Fiske, C. H.; Subbarow, Y., The colorimetric determination of phosphorus. *J. Biol. Chem.* **1925**, *66* (2), 375-400.
332. González-Romo, P.; Sánchez-Nieto, S.; Gavilanes-Ruíz, M., A modified colorimetric method for the determination of orthophosphate in the presence of high ATP concentrations. *Anal. Biochem.* **1992**, *200* (2), 235–238.
333. Chifflet, S.; Torriglia, A.; Chiesa, R.; Tolosa, S., A method for the determination of inorganic phosphate in the presence of labile organic phosphate and high concentrations of protein: Application to lens ATPases. *Anal. Biochem.* **1988**, *168* (1), 1–4.
334. Saheki, S.; Takeda, A.; Shimazu, T., Assay of inorganic phosphate in the mild pH range, suitable for measurement of glycogen phosphorylase activity. *Anal. Biochem.* **1985**, *148* (2), 277-81.
335. Baginski, E. S.; Epstein, E.; Zak, B., Review of phosphate methodologies. *Ann. Clin. Lab. Sci.* **1975**, *5* (5), 399–416.

336. Nagul, E. A.; McKelvie, I. D.; Worsfold, P.; Kolev, S. D., The molybdenum blue reaction for the determination of orthophosphate revisited: Opening the black box. *Anal. Chim. Acta* **2015**, *890*, 60–82.
337. Baginski, E.; Zak, B., Micro-determination of serum phosphate and phospholipids. *Clin. Chim. Acta* **1960**, *5*, 834-8.
338. O'Haver, T. C. 7.45; Department of Chemistry and Biochemistry, University of Maryland at College Park.
339. Thurber, K. R.; Tycko, R., Measurement of sample temperatures under magic-angle spinning from the chemical shift and spin-lattice relaxation rate of ^{79}Br in KBr powder. *Journal of magnetic resonance* **2009**, *196* (1), 84-7.
340. Cohn, M.; Hughes, T. R., Jr., Nuclear magnetic resonance spectra of adenosine di- and triphosphate. II. Effect of complexing with divalent metal ions. *J. Biol. Chem.* **1962**, *237*, 176-81.
341. Vasavada, K. V.; Ray, B. D.; Nageswara Rao, B. D., ^{31}P NMR lineshapes of beta-P (ATP) in the presence of Mg^{2+} and Ca^{2+} : estimate of exchange rates. *J. Inorg. Biochem.* **1984**, *21* (4), 323–335.
342. Mak-Jurkauskas, M. L.; Bajaj, V. S.; Hornstein, M. K.; Belenky, M.; Griffin, R. G.; Herzfeld, J., Energy transformations early in the bacteriorhodopsin photocycle revealed by DNP-enhanced solid-state NMR. *Proc. Natl. Acad. Sci. U. S. A.* **2008**, *105* (3), 883–888.
343. Singh, B.; Kaur, G.; Singh, P.; Singh, K.; Kumar, B.; Vij, A.; Kumar, M.; Bala, R.; Meena, R.; Singh, A.; Thakur, A.; Kumar, A., Nanostructured Boron Nitride With High Water Dispersibility For Boron Neutron Capture Therapy. *Sci. Rep.* **2016**, *6*, 35535.
344. Barth, A.; Corrie, J. E. T.; Gradwell, M. J.; Maeda, Y.; Mäntele, W.; Meier, T.; Trentham, D. R., Time-Resolved Infrared Spectroscopy of Intermediates and Products from Photolysis of 1-(2-Nitrophenyl)ethyl Phosphates: Reaction of the 2-Nitrosoacetophenone Byproduct with Thiols. *J. Am. Chem. Soc.* **1997**, *119* (18), 4149-4159.
345. Corrie, J. E. T.; Reid, G. P.; Trentham, D. R.; Hursthouse, M. B.; Mazid, M. A., Synthesis and absolute stereochemistry of the two diastereoisomers of P3-1-(2-nitrophenyl)ethyl adenosine triphosphate ('caged' ATP). *J. Chem. Soc., Perkin Trans. I* **1992**, (8), 1015-1019.
346. Catalan, J.; Diaz, C.; Garcia-Blanco, F., Characterization of binary solvent mixtures of DMSO with water and other cosolvents. *J. Org. Chem.* **2001**, *66* (17), 5846–5852.
347. Yarava, J. R.; Chaudhari, S. R.; Rossini, A. J.; Lesage, A.; Emsley, L., Solvent suppression in DNP enhanced solid state NMR. *J. Magn. Reson.* **2017**, *277*, 149–153.
348. Daviso, E.; Diller, A.; Alia, A.; Matysik, J.; Jeschke, G., Photo-CIDNP MAS NMR beyond the T1 limit by fast cycles of polarization extinction and polarization generation. *J. Magn. Reson.* **2008**, *190* (1), 43–51.
349. Beall, G. H. High strength machinable glass-ceramics. US8298970B2, 2011.
350. Macor Machinable Glass Ceramic. <https://precision-ceramics.com/materials/macor-machinable-glass-ceramic/> (accessed 06.12.018).
351. Williams, N. H., Magnesium Ion Catalyzed ATP Hydrolysis. *J. Am. Chem. Soc.* **2000**, *122* (48), 12023-12024.
352. Herschlag, D.; Jencks, W. P., The effect of divalent metal ions on the rate and transition-state structure of phosphoryl-transfer reactions. *J. Am. Chem. Soc.* **1987**, *109* (15), 4665-4674.

353. De Boeck, H.; Zidovetzki, R., Effects of diacylglycerols on the structure of phosphatidylcholine bilayers: a deuterium and phosphorus-31 NMR study. *Biochemistry* **1989**, *28* (18), 7439-7446.
354. Bonnel, S. I.; Lin, Y. P.; Kelley, M. J.; Carman, G. M.; Eichberg, J., Interactions of thiophosphatidic acid with enzymes which metabolize phosphatidic acid. Inhibition of phosphatidic acid phosphatase and utilization by CDP-diacylglycerol synthase. *Biochim. Biophys. Acta* **1989**, *1005* (3), 289–295.
355. Jaffe, E. K.; Cohn, M., ³¹P nuclear magnetic resonance spectra of the thiophosphate analogues of adenine nucleotides; effects of pH and Mg²⁺ binding. *Biochemistry* **1978**, *17* (4), 652-7.
356. Spoerner, M.; Nuehs, A.; Herrmann, C.; Steiner, G.; Kalbitzer, H. R., Slow conformational dynamics of the guanine nucleotide-binding protein Ras complexed with the GTP analogue GTPgammaS. *FEBS J.* **2007**, *274* (6), 1419-33.
357. Kaur, H.; Abreu, B.; Akhmetzyanov, D.; Lakatos-Karoly, A.; Soares, C. M.; Prisner, T.; Glaubitz, C., Unexplored Nucleotide Binding Modes for the ABC Exporter MsbA. *J. Am. Chem. Soc.* **2018**, *140* (43), 14112-14125.
358. Kaur, H. Probing the enzymatic and structural mechanism of the catalytic cycle of the E. coli exporter MsbA, using MAS-NMR spectroscopy. Dissertation, Goethe-Universität Frankfurt, Fachbereich 14 Chemie, Biochemie und Pharmazie, Frankfurt am Main, 2017.
359. Siemer, A. B.; McDermott, A. E., Solid-state NMR on a type III antifreeze protein in the presence of ice. *J. Am. Chem. Soc.* **2008**, *130* (51), 17394-9.
360. Bauer, T.; Dotta, C.; Balacescu, L.; Gath, J.; Hunkeler, A.; Bockmann, A.; Meier, B. H., Line-Broadening in Low-Temperature Solid-State NMR Spectra of Fibrils. *J. Biomol. NMR* **2017**, *67* (1), 51-61.
361. Wiegand, T.; Liao, W.-C.; Ong, T. C.; Däpp, A.; Cadalbert, R.; Copéret, C.; Böckmann, A.; Meier, B. H., Protein-nucleotide contacts in motor proteins detected by DNP-enhanced solid-state NMR. *J. Biomol. NMR* **2017**.
362. Vogel, H. J.; Bridger, W. A., Phosphorus-31 nuclear magnetic resonance studies of the methylene and fluoro analogues of adenine nucleotides. Effects of pH and magnesium ion binding. *Biochemistry* **1982**, *21* (2), 394–401.
363. Hoelen, C.; Antonis, P.; Boer, D. d.; Koole, R.; Kadijk, S.; Li, Y.; Vanbroekhoven, V.; Voorde, P. V. D. In *Progress in extremely high brightness LED-based light sources*, SPIE Optical Engineering + Applications, SPIE: 2017; p 19.
364. Zeeb, M.; Balbach, J., Protein folding studied by real-time NMR spectroscopy. *Methods* **2004**, *34* (1), 65–74.
365. Durr, U. H.; Soong, R.; Ramamoorthy, A., When detergent meets bilayer: birth and coming of age of lipid bicelles. *Prog. Nucl. Magn. Reson. Spectrosc.* **2013**, *69*, 1-22.
366. Struppe, J.; Whiles, J. A.; Vold, R. R., Acidic phospholipid bicelles: a versatile model membrane system. *Biophys. J.* **2000**, *78* (1), 281-9.
367. Beharry, A. A.; Sadowski, O.; Woolley, G. A., Photo-control of peptide conformation on a timescale of seconds with a conformationally constrained, blue-absorbing, photo-switchable linker. *Org. Biomol. Chem.* **2008**, *6* (23), 4323–4332.
368. Zhong, L.; Bamm, V. V.; Ahmed, M. A.; Harauz, G.; Ladizhansky, V., Solid-state NMR spectroscopy of 18.5 kDa myelin basic protein reconstituted with lipid vesicles: spectroscopic characterisation and spectral assignments of solvent-exposed protein fragments. *Biochim. Biophys. Acta* **2007**, *1768* (12), 3193-205.
369. Rees, D. C., A general solution for the steady-state kinetics of immobilized enzyme systems. *Bull. Math. Biol.* **1984**, *46* (2), 229-34.

370. Cooney, M. J., Kinetic Measurements for Enzyme Immobilization. In *Enzyme Stabilization and Immobilization: Methods and Protocols*, Minter, S. D., Ed., Humana Press: Totowa, NJ, 2011; pp 207-225.
371. Laidler, K. J.; Bunting, P. S., The kinetics of immobilized enzyme systems. *Methods Enzymol.* **1980**, *64*, 227-48.
372. Key, B.; Bhattacharyya, R.; Morcrette, M.; Seznec, V.; Tarascon, J. M.; Grey, C. P., Real-time NMR investigations of structural changes in silicon electrodes for lithium-ion batteries. *J. Am. Chem. Soc.* **2009**, *131* (26), 9239-49.
373. Tang, M.; Sarou-Kanian, V.; Melin, P.; Leriche, J. B.; Menetrier, M.; Tarascon, J. M.; Deschamps, M.; Salager, E., Following lithiation fronts in paramagnetic electrodes with in situ magnetic resonance spectroscopic imaging. *Nat. Commun.* **2016**, *7*, 13284.
374. Kuchler, A.; Yoshimoto, M.; Luginbuhl, S.; Mavelli, F.; Walde, P., Enzymatic reactions in confined environments. *Nat. Nanotechnol.* **2016**, *11* (5), 409-20.
375. Hu, J.; Popp, R.; Frömel, T.; Ehling, M.; Awwad, K.; Adams, R. H.; Hammes, H.-P.; Fleming, I., Müller glia cells regulate Notch signaling and retinal angiogenesis via the generation of 19,20-dihydroxydocosapentaenoic acid. *J. Exp. Med.* **2014**, *211* (2), 281-295.
376. Hu, J.; Dziumbila, S.; Lin, J.; Bibli, S. I.; Zukunft, S.; de Mos, J.; Awwad, K.; Fromel, T.; Jungmann, A.; Devraj, K.; Cheng, Z.; Wang, L.; Fauser, S.; Eberhart, C. G.; Sodhi, A.; Hammock, B. D.; Liebner, S.; Muller, O. J.; Glaubitz, C.; Hammes, H. P.; Popp, R.; Fleming, I., Inhibition of soluble epoxide hydrolase prevents diabetic retinopathy. *Nature* **2017**, *552* (7684), 248-252.
377. Yu, J.; Fischman, D. A.; Steck, T. L., Selective solubilization of proteins and phospholipids from red blood cell membranes by nonionic detergents. *J. Supramol. Struct.* **1973**, *1* (3), 233-48.
378. Ahmed, S. N.; Brown, D. A.; London, E., On the origin of sphingolipid/cholesterol-rich detergent-insoluble cell membranes: physiological concentrations of cholesterol and sphingolipid induce formation of a detergent-insoluble, liquid-ordered lipid phase in model membranes. *Biochemistry* **1997**, *36* (36), 10944-53.
379. van Meer, G.; Stelzer, E. H.; Wijnaendts-van-Resandt, R. W.; Simons, K., Sorting of sphingolipids in epithelial (Madin-Darby canine kidney) cells. *J. Cell Biol.* **1987**, *105* (4), 1623-35.
380. Pralle, A.; Keller, P.; Florin, E. L.; Simons, K.; Horber, J. K., Sphingolipid-cholesterol rafts diffuse as small entities in the plasma membrane of mammalian cells. *J. Cell Biol.* **2000**, *148* (5), 997-1008.
381. Sezgin, E.; Levental, I.; Mayor, S.; Eggeling, C., The mystery of membrane organization: composition, regulation and roles of lipid rafts. *Nat. Rev. Mol. Cell Biol.* **2017**, *18*, 361.
382. Pike, L. J., Rafts defined: a report on the Keystone Symposium on Lipid Rafts and Cell Function. *J. Lipid Res.* **2006**, *47* (7), 1597-8.
383. Heberle, F. A.; Petruziolo, R. S.; Pan, J.; Drazba, P.; Kucerka, N.; Standaert, R. F.; Feigenson, G. W.; Katsaras, J., Bilayer thickness mismatch controls domain size in model membranes. *J. Am. Chem. Soc.* **2013**, *135* (18), 6853-9.
384. Jensen, M. O.; Mouritsen, O. G., Lipids do influence protein function-the hydrophobic matching hypothesis revisited. *Biochim. Biophys. Acta* **2004**, *1666* (1-2), 205-26.
385. Kaiser, H. J.; Orłowski, A.; Rog, T.; Nyholm, T. K.; Chai, W.; Feizi, T.; Lingwood, D.; Vattulainen, I.; Simons, K., Lateral sorting in model membranes by

- cholesterol-mediated hydrophobic matching. *Proc. Natl. Acad. Sci. U. S. A.* **2011**, *108* (40), 16628-33.
386. Levental, I.; Lingwood, D.; Grzybek, M.; Coskun, U.; Simons, K., Palmitoylation regulates raft affinity for the majority of integral raft proteins. *Proc. Natl. Acad. Sci. U. S. A.* **2010**, *107* (51), 22050-4.
387. Levental, I.; Grzybek, M.; Simons, K., Greasing their way: lipid modifications determine protein association with membrane rafts. *Biochemistry* **2010**, *49* (30), 6305-16.
388. Koster, D. V.; Mayor, S., Cortical actin and the plasma membrane: inextricably intertwined. *Curr. Opin. Cell Biol.* **2016**, *38*, 81-9.
389. Fritzsche, M.; Erlenkamper, C.; Moeendarbary, E.; Charras, G.; Kruse, K., Actin kinetics shapes cortical network structure and mechanics. *Sci. Adv.* **2016**, *2* (4), e1501337.
390. Honigsmann, A.; Sadeghi, S.; Keller, J.; Hell, S. W.; Eggeling, C.; Vink, R., A lipid bound actin meshwork organizes liquid phase separation in model membranes. *eLife* **2014**, *3*, e01671.
391. Gowrishankar, K.; Ghosh, S.; Saha, S.; C, R.; Mayor, S.; Rao, M., Active remodeling of cortical actin regulates spatiotemporal organization of cell surface molecules. *Cell* **2012**, *149* (6), 1353-67.
392. Calder, P. C., n-3 polyunsaturated fatty acids, inflammation, and inflammatory diseases. *Am. J. Clin. Nutr.* **2006**, *83* (6 Suppl), 1505S-1519S.
393. Wang, C.; Harris, W. S.; Chung, M.; Lichtenstein, A. H.; Balk, E. M.; Kupelnick, B.; Jordan, H. S.; Lau, J., n-3 Fatty acids from fish or fish-oil supplements, but not alpha-linolenic acid, benefit cardiovascular disease outcomes in primary- and secondary-prevention studies: a systematic review. *Am. J. Clin. Nutr.* **2006**, *84* (1), 5-17.
394. Salem, N.; Kim, H.-Y.; Yergey, J. A., Docosahexaenoic acid: membrane function and metabolism. In *Health Effects of Polyunsaturated Fatty Acids in Seafoods*, Simopoulos, A. P.; Kifer, R. R.; Martin, R. E., Eds., Academic Press: New York, 1986; pp 263-317.
395. Stillwell, W., The role of polyunsaturated lipids in membrane raft function. *Scand. J. Food Nutr.* **2006**, *50* (sup2), 107-113.
396. Stillwell, W.; Wassall, S. R., Docosahexaenoic acid: membrane properties of a unique fatty acid. *Chem. Phys. Lipids* **2003**, *126* (1), 1-27.
397. Stillwell, W.; Shaikh, S. R.; Zerouga, M.; Siddiqui, R.; Wassall, S. R., Docosahexaenoic acid affects cell signaling by altering lipid rafts. *Reprod. Nutr. Dev.* **2005**, *45* (5), 559-79.
398. Anderson, R. E.; Sperling, L., Lipids of ocular tissues. VII. Positional distribution of the fatty acids in the phospholipids of bovine retina rod outer segments. *Arch. Biochem. Biophys.* **1971**, *144* (2), 673-7.
399. Levental, K. R.; Lorent, J. H.; Lin, X.; Skinkle, A. D.; Surma, M. A.; Stockenbojer, E. A.; Gorfe, A. A.; Levental, I., Polyunsaturated Lipids Regulate Membrane Domain Stability by Tuning Membrane Order. *Biophys. J.* **2016**, *110* (8), 1800-1810.
400. Eldho, N. V.; Feller, S. E.; Tristram-Nagle, S.; Polozov, I. V.; Gawrisch, K., Polyunsaturated docosahexaenoic vs docosapentaenoic acid-differences in lipid matrix properties from the loss of one double bond. *J. Am. Chem. Soc.* **2003**, *125* (21), 6409-6421.

401. Feller, S. E.; Gawrisch, K.; MacKerell, A. D., Polyunsaturated fatty acids in lipid bilayers: intrinsic and environmental contributions to their unique physical properties. *J. Am. Chem. Soc.* **2002**, *124* (2), 318–326.
402. Huber, T.; Rajamoorthi, K.; Kurze, V. F.; Beyer, K.; Brown, M. F., Structure of docosahexaenoic acid-containing phospholipid bilayers as studied by (2)H NMR and molecular dynamics simulations. *J. Am. Chem. Soc.* **2002**, *124* (2), 298–309.
403. Holte, L. L.; Peter, S. A.; Sinnwell, T. M.; Gawrisch, K., 2H nuclear magnetic resonance order parameter profiles suggest a change of molecular shape for phosphatidylcholines containing a polyunsaturated acyl chain. *Biophys. J.* **1995**, *68* (6), 2396–403.
404. Huster, D.; Jin, A. J.; Arnold, K.; Gawrisch, K., Water permeability of polyunsaturated lipid membranes measured by 17O NMR. *Biophys. J.* **1997**, *73* (2), 855–864.
405. Armstrong, V. T.; Brzustowicz, M. R.; Wassall, S. R.; Jenki, L. J.; Stillwell, W., Rapid flip-flop in polyunsaturated (docosahexaenoate) phospholipid membranes. *Arch. Biochem. Biophys.* **2003**, *414* (1), 74–82.
406. Gawrisch, K.; Holte, L. L., NMR investigations of non-lamellar phase promoters in the lamellar phase state. *Chem. Phys. Lipids* **1996**, *81* (2), 105–116.
407. Wassall, S. R.; Stillwell, W., Docosahexaenoic acid domains: the ultimate non-raft membrane domain. *Chem. Phys. Lipids* **2008**, *153* (1), 57–63.
408. Soni, S. P.; LoCascio, D. S.; Liu, Y.; Williams, J. A.; Bittman, R.; Stillwell, W.; Wassall, S. R., Docosahexaenoic acid enhances segregation of lipids between : 2H-NMR study. *Biophys. J.* **2008**, *95* (1), 203–14.
409. Zhou, Y.; Maxwell, K. N.; Sezgin, E.; Lu, M.; Liang, H.; Hancock, J. F.; Dial, E. J.; Lichtenberger, L. M.; Levental, I., Bile acids modulate signaling by functional perturbation of plasma membrane domains. *J. Biol. Chem.* **2013**, *288* (50), 35660–70.
410. Gray, E.; Karslake, J.; Machta, B. B.; Veatch, S. L., Liquid general anesthetics lower critical temperatures in plasma membrane vesicles. *Biophys. J.* **2013**, *105* (12), 2751–9.
411. Rockett, B. D.; Teague, H.; Harris, M.; Melton, M.; Williams, J.; Wassall, S. R.; Shaikh, S. R., Fish oil increases raft size and membrane order of B cells accompanied by differential effects on function. *J. Lipid Res.* **2012**, *53* (4), 674–85.
412. Teague, H.; Harris, M.; Fenton, J.; Lallemand, P.; Shewchuk, B. M.; Shaikh, S. R., Eicosapentaenoic and docosahexaenoic acid ethyl esters differentially enhance B-cell activity in murine obesity. *J. Lipid Res.* **2014**, *55* (7), 1420–33.
413. Kim, W.; Fan, Y. Y.; Barhoumi, R.; Smith, R.; McMurray, D. N.; Chapkin, R. S., n-3 polyunsaturated fatty acids suppress the localization and activation of signaling proteins at the immunological synapse in murine CD4+ T cells by affecting lipid raft formation. *J. Immunol.* **2008**, *181* (9), 6236–43.
414. Grimm, M. O.; Kuchenbecker, J.; Grosgen, S.; Burg, V. K.; Hundsdorfer, B.; Rothhaar, T. L.; Friess, P.; de Wilde, M. C.; Broersen, L. M.; Penke, B.; Peter, M.; Vigh, L.; Grimm, H. S.; Hartmann, T., Docosahexaenoic acid reduces amyloid beta production via multiple pleiotropic mechanisms. *J. Biol. Chem.* **2011**, *286* (16), 14028–39.
415. Teague, H.; Fhaner, C. J.; Harris, M.; Duriancik, D. M.; Reid, G. E.; Shaikh, S. R., n-3 PUFAs enhance the frequency of murine B-cell subsets and restore the impairment of antibody production to a T-independent antigen in obesity. *J. Lipid Res.* **2013**, *54* (11), 3130–8.
416. Hu, J.; Dziuombla, S.; Lin, J.; Bibli, S.-I.; Zukunft, S.; Mos, J. d.; Awwad, K.; Frömel, T.; Jungmann, A.; Devraj, K.; Cheng, Z.; Wang, L.; Fauser, S.; Eberhart, C.

- G.; Sodhi, A.; Hammock, B. D.; Liebner, S.; Müller, O. J.; Glaubitz, C.; Hammes, H.-P.; Popp, R.; Fleming, I., Inhibition of soluble epoxide hydrolase prevents diabetic retinopathy. *Nature* **2017**, *552* (7684), 248–252.
417. Brzustowicz, M. R.; Cherezov, V.; Caffrey, M.; Stillwell, W.; Wassall, S. R., Molecular organization of cholesterol in polyunsaturated membranes: microdomain formation. *Biophys. J.* **2002**, *82* (1 Pt 1), 285-98.
418. Shaikh, S. R.; Cherezov, V.; Caffrey, M.; Soni, S. P.; LoCascio, D.; Stillwell, W.; Wassall, S. R., Molecular organization of cholesterol in unsaturated phosphatidylethanolamines: X-ray diffraction and solid state ²H NMR reveal differences with phosphatidylcholines. *J. Am. Chem. Soc.* **2006**, *128* (16), 5375-83.
419. Shaikh, S. R.; Kinnun, J. J.; Leng, X.; Williams, J. A.; Wassall, S. R., How polyunsaturated fatty acids modify molecular organization in membranes: Insight from NMR studies of model systems. *Biochim. Biophys. Acta* **2015**, *1848* (1, Part B), 211-219.
420. Georgieva, R.; Chachaty, C.; Hazarosova, R.; Tessier, C.; Nuss, P.; Momchilova, A.; Staneva, G., Docosahexaenoic acid promotes micron scale liquid-ordered domains. A comparison study of docosahexaenoic versus oleic acid containing phosphatidylcholine in raft-like mixtures. *Biochim. Biophys. Acta* **2015**, *1848* (6), 1424-35.
421. Williams, J. A.; Batten, S. E.; Harris, M.; Rockett, B. D.; Shaikh, S. R.; Stillwell, W.; Wassall, S. R., Docosahexaenoic and eicosapentaenoic acids segregate differently between raft and nonraft domains. *Biophys. J.* **2012**, *103* (2), 228–237.
422. Schley, P. D.; Brindley, D. N.; Field, C. J., (n-3) PUFA alter raft lipid composition and decrease epidermal growth factor receptor levels in lipid rafts of human breast cancer cells. *J. Nutr.* **2007**, *137* (3), 548-53.
423. Shaikh, S. R.; Cherezov, V.; Caffrey, M.; Stillwell, W.; Wassall, S. R., Interaction of cholesterol with a docosahexaenoic acid-containing phosphatidylethanolamine: trigger for microdomain/raft formation? *Biochemistry* **2003**, *42* (41), 12028-37.
424. Shaikh, S. R.; Dumauval, A. C.; Castillo, A.; LoCascio, D.; Siddiqui, R. A.; Stillwell, W.; Wassall, S. R., Oleic and docosahexaenoic acid differentially phase separate from lipid raft molecules: a comparative NMR, DSC, AFM, and detergent extraction study. *Biophys. J.* **2004**, *87* (3), 1752-66.
425. Shaikh, S. R.; Locascio, D. S.; Soni, S. P.; Wassall, S. R.; Stillwell, W., Oleic- and docosahexaenoic acid-containing phosphatidylethanolamines differentially phase separate from sphingomyelin. *Biochim. Biophys. Acta* **2009**, *1788* (11), 2421-6.
426. Breckenridge, W. C.; Gombos, G.; Morgan, I. G., The lipid composition of adult rat brain synaptosomal plasma membranes. *Biochim. Biophys. Acta* **1972**, *266* (3), 695-707.
427. Neill, A. R.; Masters, C. J., Metabolism of fatty acids by bovine spermatozoa. *Biochem. J.* **1972**, *127* (2), 375-85.
428. Wiegand, R. D.; Anderson, R. E., Phospholipid molecular species of frog rod outer segment membranes. *Exp. Eye Res.* **1983**, *37* (2), 159-73.
429. Salvado, M. D.; Alfranca, A.; Haeggstrom, J. Z.; Redondo, J. M., Prostanoids in tumor angiogenesis: therapeutic intervention beyond COX-2. *Trends Mol. Med.* **2012**, *18* (4), 233-43.
430. Munzenmaier, D. H.; Harder, D. R., Cerebral microvascular endothelial cell tube formation: role of astrocytic epoxyeicosatrienoic acid release. *Am. J. Physiol. Heart Circ. Physiol.* **2000**, *278* (4), H1163-7.

431. Zhang, C.; Harder, D. R., Cerebral capillary endothelial cell mitogenesis and morphogenesis induced by astrocytic epoxyeicosatrienoic Acid. *Stroke* **2002**, *33* (12), 2957-64.
432. Medhora, M.; Daniels, J.; Munday, K.; Fisslthaler, B.; Busse, R.; Jacobs, E. R.; Harder, D. R., Epoxygenase-driven angiogenesis in human lung microvascular endothelial cells. *Am. J. Physiol. Heart Circ. Physiol.* **2003**, *284* (1), H215-24.
433. Michaelis, U. R.; Fisslthaler, B.; Medhora, M.; Harder, D.; Fleming, I.; Busse, R., Cytochrome P450 2C9-derived epoxyeicosatrienoic acids induce angiogenesis via cross-talk with the epidermal growth factor receptor (EGFR). *FASEB J.* **2003**, *17* (6), 770-2.
434. Wang, Y.; Wei, X.; Xiao, X.; Hui, R.; Card, J. W.; Carey, M. A.; Wang, D. W.; Zeldin, D. C., Arachidonic acid epoxygenase metabolites stimulate endothelial cell growth and angiogenesis via mitogen-activated protein kinase and phosphatidylinositol 3-kinase/Akt signaling pathways. *J. Pharmacol. Exp. Ther.* **2005**, *314* (2), 522-32.
435. Vetrivel, K. S.; Cheng, H.; Lin, W.; Sakurai, T.; Li, T.; Nukina, N.; Wong, P. C.; Xu, H.; Thinakaran, G., Association of gamma-secretase with lipid rafts in post-Golgi and endosome membranes. *J. Biol. Chem.* **2004**, *279* (43), 44945-54.
436. Hur, J. Y.; Welander, H.; Behbahani, H.; Aoki, M.; Franberg, J.; Winblad, B.; Frykman, S.; Tjernberg, L. O., Active gamma-secretase is localized to detergent-resistant membranes in human brain. *FEBS J.* **2008**, *275* (6), 1174-87.
437. Capozzi, M. E.; Hammer, S. S.; McCollum, G. W.; Penn, J. S., Epoxygenated Fatty Acids Inhibit Retinal Vascular Inflammation. *Sci. Rep.* **2016**, *6*, 39211.
438. Yilmaz, G.; Granger, D. N., Cell adhesion molecules and ischemic stroke. *Neurol. Res.* **2008**, *30* (8), 783-93.
439. Chen, Y.; Tian, H.; Yao, E.; Tian, Y.; Zhang, H.; Xu, L.; Yu, Z.; Fang, Y.; Wang, W.; Du, P.; Xie, M., Soluble epoxide hydrolase inhibition Promotes White Matter Integrity and Long-Term Functional Recovery after chronic hypoperfusion in mice. *Sci. Rep.* **2017**, *7* (1), 7758.
440. Polozov, I. V.; Bezrukov, L.; Gawrisch, K.; Zimmerberg, J., Progressive ordering with decreasing temperature of the phospholipids of influenza virus. *Nat. Chem. Biol.* **2008**, *4* (4), 248-255.
441. Oldfield, E.; Bowers, J. L.; Forbes, J., High-resolution proton and carbon-13 NMR of membranes: why sonicate? *Biochemistry* **1987**, *26* (22), 6919-23.
442. Herzfeld, J.; Berger, A. E., Sideband intensities in NMR spectra of samples spinning at the magic angle. *J. Chem. Phys.* **1980**, *73* (12), 6021-6030.
443. Munowitz, M. G.; Griffin, R. G., Two-dimensional nuclear magnetic resonance in rotating solids: An analysis of line shapes in chemical shift-dipolar spectra. *J. Chem. Phys.* **1982**, *76* (6), 2848-2858.
444. Polozov, I. V.; Gawrisch, K., Domains in binary SOPC/POPE lipid mixtures studied by pulsed field gradient 1H MAS NMR. *Biophys. J.* **2004**, *87* (3), 1741-1751.
445. Polozov, I. V.; Gawrisch, K., Characterization of the liquid-ordered state by proton MAS NMR. *Biophys. J.* **2006**, *90* (6), 2051-2061.
446. Veatch, S. L.; Polozov, I. V.; Gawrisch, K.; Keller, S. L., Liquid domains in vesicles investigated by NMR and fluorescence microscopy. *Biophys. J.* **2004**, *86* (5), 2910-2922.
447. Filippov, A.; Oradd, G.; Lindblom, G., The effect of cholesterol on the lateral diffusion of phospholipids in oriented bilayers. *Biophys. J.* **2003**, *84* (5), 3079-86.
448. Lyberg, A.-M.; Fasoli, E.; Adlercreutz, P., Monitoring the oxidation of docosahexaenoic acid in lipids. *Lipids* **2005**, *40* (9), 969-979.

449. Huster, D.; Arnold, K.; Gawrisch, K., Influence of docosaehaenoic acid and cholesterol on lateral lipid organization in phospholipid mixtures. *Biochemistry* **1998**, *37* (49), 17299–17308.
450. Nomura, K.; Lintuluoto, M.; Morigaki, K., Hydration and temperature dependence of ¹³C and ¹H NMR spectra of the DMPC phospholipid membrane and complete resonance assignment of its crystalline state. *The journal of physical chemistry. B* **2011**, *115* (50), 14991–15001.
451. Hart, J. S., Average body temperature in mice. *Science* **1951**, *113* (2934), 325–6.
452. Ulrich, A. S.; Watts, A., Molecular response of the lipid headgroup to bilayer hydration monitored by 2H-NMR. *Biophys. J.* **1994**, *66* (5), 1441–9.
453. Doux, J. P.; Hall, B. A.; Killian, J. A., How lipid headgroups sense the membrane environment: an application of (1)(4)N NMR. *Biophys. J.* **2012**, *103* (6), 1245–53.
454. Klein, U.; Gimpl, G.; Fahrenholz, F., Alteration of the myometrial plasma membrane cholesterol content with beta-cyclodextrin modulates the binding affinity of the oxytocin receptor. *Biochemistry* **1995**, *34* (42), 13784–93.
455. Gawrisch, K.; Soubias, O.; Mihailescu, M., Insights from biophysical studies on the role of polyunsaturated fatty acids for function of G-protein coupled membrane receptors. *Prostaglandins Leukot. Essent. Fatty Acids* **2008**, *79* (3–5), 131–134.
456. Polozova, A.; Litman, B. J., Cholesterol dependent recruitment of di22:6-PC by a G protein-coupled receptor into lateral domains. *Biophys. J.* **2000**, *79* (5), 2632–2643.
457. Gawrisch, K.; Eldho, N. V.; Holte, L. L., The structure of DHA in phospholipid membranes. *Lipids* **2003**, *38* (4), 445–452.
458. Aussenac, F.; Tavares, M.; Dufourc, E. J., Cholesterol dynamics in membranes of raft composition: a molecular point of view from 2H and 31P solid-state NMR. *Biochemistry* **2003**, *42* (6), 1383–1390.
459. Sezgin, E.; Kaiser, H. J.; Baumgart, T.; Schwille, P.; Simons, K.; Levental, I., Elucidating membrane structure and protein behavior using giant plasma membrane vesicles. *Nat. Protoc.* **2012**, *7* (6), 1042–51.
460. Eggeling, C.; Honigsmann, A., Closing the gap: The approach of optical and computational microscopy to uncover biomembrane organization. *Biochim. Biophys. Acta* **2016**, *1858* (10), 2558–2568.
461. Sodt, A. J.; Sandar, M. L.; Gawrisch, K.; Pastor, R. W.; Lyman, E., The molecular structure of the liquid-ordered phase of lipid bilayers. *J. Am. Chem. Soc.* **2014**, *136* (2), 725–732.
462. Derogis, P. B. M. C.; Freitas, F. P.; Marques, A. S. F.; Cunha, D.; Appolinário, P. P.; Paula, F. d.; Lourenço, T. C.; Murgu, M.; Di Mascio, P.; Medeiros, M. H. G.; Miyamoto, S., The development of a specific and sensitive LC-MS-based method for the detection and quantification of hydroperoxy- and hydroxydocosaehaenoic acids as a tool for lipidomic analysis. *PLoS ONE* **2013**, *8* (10), e77561.
463. Eggeling, C.; Ringemann, C.; Medda, R.; Schwarzmann, G.; Sandhoff, K.; Polyakova, S.; Belov, V. N.; Hein, B.; von Middendorff, C.; Schonle, A.; Hell, S. W., Direct observation of the nanoscale dynamics of membrane lipids in a living cell. *Nature* **2009**, *457* (7233), 1159–62.
464. Shi, P.; Li, D.; Chen, H.; Xiong, Y.; Wang, Y.; Tian, C., In situ ¹⁹F NMR studies of an E. coli membrane protein. *Protein Sci.* **2012**, *21* (4), 596–600.

465. Lahiri, S.; Brehms, M.; Olschewski, D.; Becker, C. F. W., Total chemical synthesis of an integral membrane enzyme: Diacylglycerol kinase from *Escherichia coli*. *Angew. Chem. Int. Ed. Engl.* **2011**, *50* (17), 3988–3992.
466. Shi, P.; Wang, H.; Xi, Z.; Shi, C.; Xiong, Y.; Tian, C., Site-specific ¹⁹F NMR chemical shift and side chain relaxation analysis of a membrane protein labeled with an unnatural amino acid. *Protein Sci.* **2011**, *20* (1), 224–228.
467. Lorch, M.; Faham, S.; Kaiser, C.; Weber, I.; Mason, A. J.; Bowie, J. U.; Glaubit, C., How to prepare membrane proteins for solid-state NMR: A case study on the alpha-helical integral membrane protein diacylglycerol kinase from *E. coli*. *ChemBioChem* **2005**, *6* (9), 1693-700.
468. Partridge, A. W.; Melnyk, R. A.; Yang, D.; Bowie, J. U.; Deber, C. M., A transmembrane segment mimic derived from *Escherichia coli* diacylglycerol kinase inhibits protein activity. *J. Biol. Chem.* **2003**, *278* (24), 22056–22060.
469. Lau, F. W.; Nauli, S.; Zhou, Y.; Bowie, J. U., Changing single side-chains can greatly enhance the resistance of a membrane protein to irreversible inactivation. *J. Mol. Biol.* **1999**, *290* (2), 559–564.
470. Wen, J.; Chen, X.; Bowie, J. U., Exploring the allowed sequence space of a membrane protein. *Nat. Struct. Biol.* **1996**, *3* (2), 141–148.
471. Ramer, J. K.; Bell, R. M., Expression of the phospholipid-dependent *Escherichia coli* sn-1,2-diacylglycerol kinase in COS cells perturbs cellular lipid composition. *J. Biol. Chem.* **1990**, *265* (27), 16478–16483.
472. Bohnenberger, E.; Sandermann, H., Jr., Diglyceride kinase from *Escherichia coli*. Modulation of enzyme activity by glycosphingolipids. *Biochim. Biophys. Acta* **1982**, *685* (1), 44-50.
473. Bohnenberger, E.; Sandermann, H., Jr., Diglyceride kinase from *Escherichia coli*. Purification in organic solvent and some properties of the enzyme. *Eur. J. Biochem.* **1979**, *94* (2), 401-7.


```
TCGTGCGCTCTCCTGTTCCGACCCCTGCCGCTTACCGGATACCTGTCCGCTTTCTCCCTTCGGGAAGCGTGGCGCTTTCATAGCTCAGCTGTAGGTATCTCAGTTCGGTGT
AGGTCGTTGCTCCAAGCTGGGCTGTGTGCACGAACCCCGCTTCAGCCCGACCGCTGCGCCTTATCCGGTAACATCGTCTTGAGTCCAACCCGGTAAGACACGACTTATCGC
CACTGGCAGCAGCCACTGGTAACAGGATTAGCAGAGCGAGGTATGTAGGCGGTGTACAGAGTCTTGAAGTGGTGGCCTAACTACGGCTACACTAGAAGGACAGTATTTGGTA
TCTGCGCTCTGCTGAAGCCAGTTACCTTCGGAAAAAGAGTTGGTAGCTCTTGATCCGGCAACAAACCACCGCTGGTAGCGGTGGTTTTTTGTTTGAAGCAGCAGATTACGC
GCAGAAAAAGGATCTCAAGAAAGATCCTTGTATCTTTCTACGGGCTGTGACGCTCAGTGAACGAAAACTCAGCTTAAGGATTTTGGTCATGAGATTATCAAAAAGGATCT
TCACCTAGATCCTTTAAATTAATAATGAAGTTTAAATCAATCTAAAGTATATATGAGTAAACCTGGTCTGACAGTTACCAATGCTTAATCAGTGAGCCACCTATCTCAGCGA
TCTGTCTATTTGCTCATCCATAGTTGCTGACTCCCGCTCGTGTAGATAACTACGATACGGGAGGGCTTACCATCTGGCCCCAGTGTGCAATGATACCGCGAGACCCACGCT
CACCGCTCCAGATTTATCAGCAATAAACACGACGCGGAGGGCCGAGCGCAGAAAGTGGTCTTCAACTTTATCCGCTCCATCCAGTCTATTAATTGTTGCCGGGAAGCTA
GAGTAAGTAGTTCCGCAAGTTAATAGTTTCCGCAACGTTGTTGCCATTGCTGCAGGCATCGTGGTGTCAAGCTCGTCTGTTGGTATGGCTTCACTCAGCTCCGCTCCCAACGAT
CAAGCGGAGTTACATGATCCCCATGTTGTGCAAAAAAGCGGTAGCTCCTCCGTCCTCCGATCGTGTGCAAGTAAGTTGGCCGAGTGTATCACTCATGGTTATGGCAG
CACTGCATAATTTCTTACTGTATGCCATCCGTAAGATGCTTTTCTGTGACTGGTGTGACTCAACCAAGTCATTCTGAGAATAGTGTATGCCGGCAGCGAGTTGCTCTTCC
CGGCGTCAACACGGGATAATACCGCCACATAGCAGACTTAAAGTGTCTATCATTGGAACGTTCTCGGGGCGAAACTCTCAAGGATCTTACCGCTGTGAGATCCA
GTTTCATGTAACCCACTCCTGCAACCACTGATCTTCAGCATCTTTTACTTTTCAACCGCTTTCTGGGTGAGCAAAAAACAGGAAGGCAAAATCCCGCAAAAAAGGAAATAGGG
CGACACGGAATGTTGAATACTACTACTCTCTCTTTTCAATATTTAAGCATTATCAGGGTTATTGTCTCATGAGCGGATACATATTTGAATGATTTAGAAAAATAAAC
AAATAGGGGTTCCGCGCACATTTCCCGAAAAAGTGCCACCTGACGTCTAAGAAACCATTTATCATGACATTAACCTATAAAAAATAGGGGTATCAGGAGCCCTTTCGTCTTC
AAGAA
```

Sequences of primers used:

pTrcHis for: AATCTGTGTGGGCACTCG

pTrcHis rev: CTTCTGCGTTCTGATTTAATCTG

HindIIIINdeI for: CTTTCGGTTAAGCTTGGCTGTTTTGGCGGATGAGAG

HindIIIINdeI rev: CTCATCCGCCAAAAACAGCCAAGCTTAACCGAAGTGGGACCAC

RF for: GAAATAATTTTGTGTTAACTTTAAGAAGGAGATATACCATGGGGCATCATCATCATC

RF rev: GCAGCCGGATCCTCGAGCATATGTTAACCGAAGTGGGACCAC

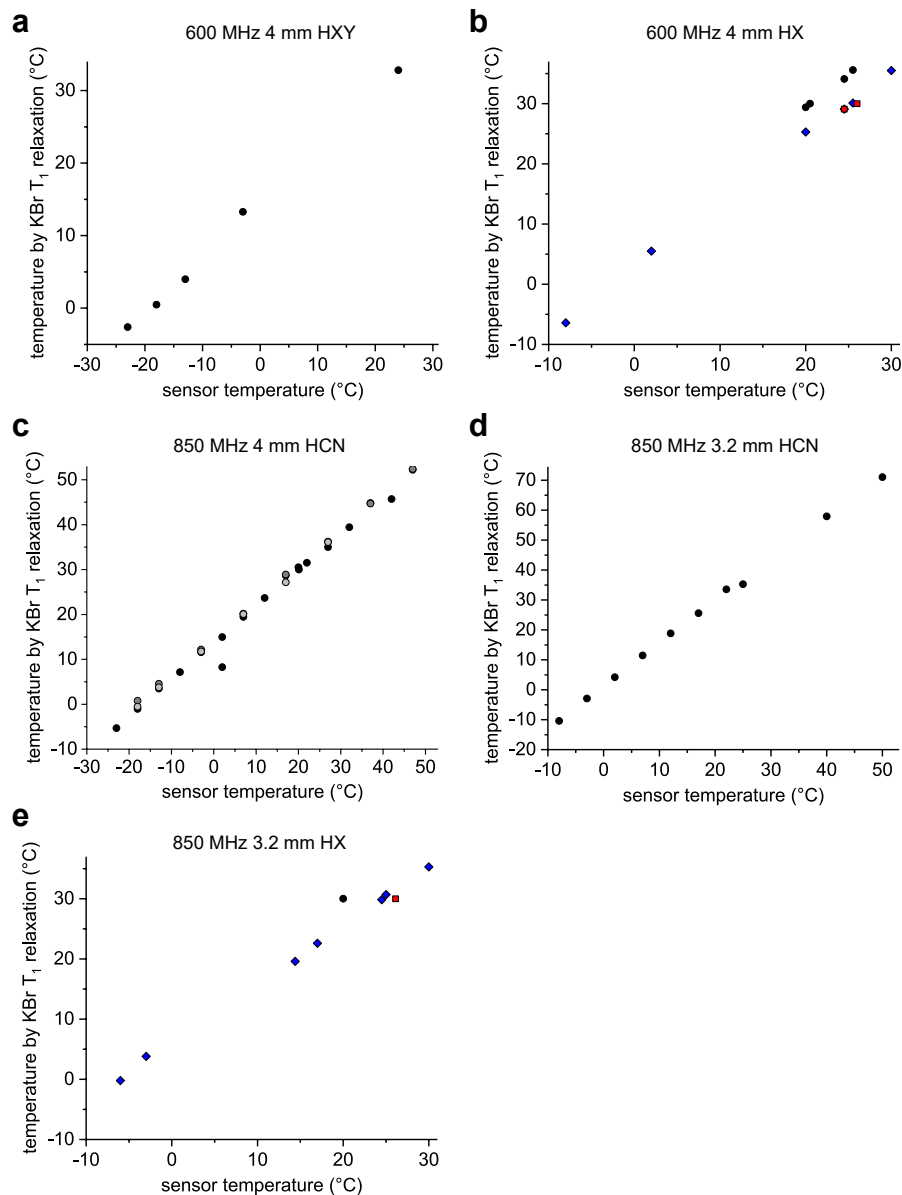
Amino acid sequence of the inserted IS1 transposase in pSD005, according to sequencing results:

```
MPGNSPHYGRWPQHDFTSLLKLRPQSVTSRIQPGSDVIVCAEMDEQWGYVGAKSQRWLFYAYDSLRLK
TVVAHVFGERTMATLGRMLSLSPFDVVIWMTDGWPLYESRLKGLHVISKRYTQRIERHNLNLRQHL
ARLGRKSLSFSKSVELHDKVIGHYLNKHYQ
```


IV.2 WB MAS NMR probe temperature calibration

The empirical formula to determine sample temperature from KBr T_1 relaxation measurements with T in K and T_1 in ms used in the Bruker AUprogram calcTfromT1 is as follows:

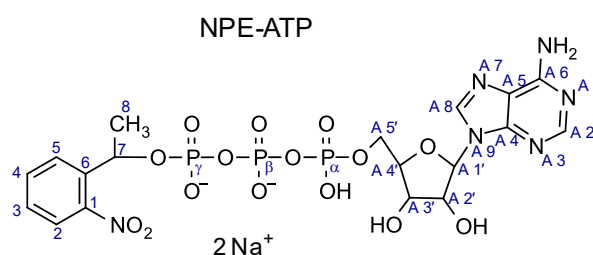
$$T = 638.28077105 - 8.42140328 T_1 + 0.06551726 T_1^2 - 0.00019694 T_1^3 \quad (30)$$



Appendix Figure 2: Temperature calibration of 600 MHz 4 mm HXY **(a)**, 4 mm HX **(b)** as well as 850 MHz 4 mm HCN **(c)**, 3.2 mm HCN **(d)**, 3.2 mm HX **(e)** WB MAS probes at 10 kHz (black to gray), 5 kHz (blue) and 3 kHz (red) MAS via ^{79}Br T_1 relaxation measurements using microcrystalline KBr. The different grayscales in (c) depict calibration before each measurement time for mouse brain membrane temperature scans.

IV.3 Uncaging approach for solid-state NMR

IV.3.1 Chemical shifts and couplings of NPE-ATP



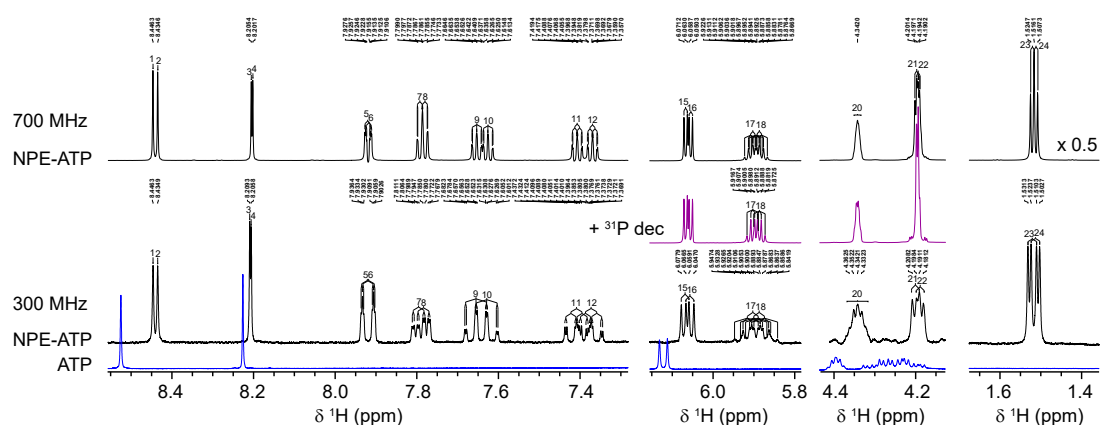
Appendix Figure 3: Structural formula and atom numbering of NPE-ATP

Appendix Table 1: ^1H and ^{13}C NMR chemical shift assignment of NPE-ATP in 100 mM HEPES, 30 mM NaCl at pH 7.5 with ^1H chemical shifts and J -couplings of the diastereomer mixture as well as the respective ^{13}C chemical shifts obtained from ^1H , ^{13}C , ^1H - ^{13}C HSQC and ^1H - ^{31}P HMBC spectra according to the atom numbering of Appendix Figure 3. Multiplets are numbered according to Appendix Figure 4, with assignment of absolute stereochemistry according to Corrie et al³⁴⁵ in brackets.

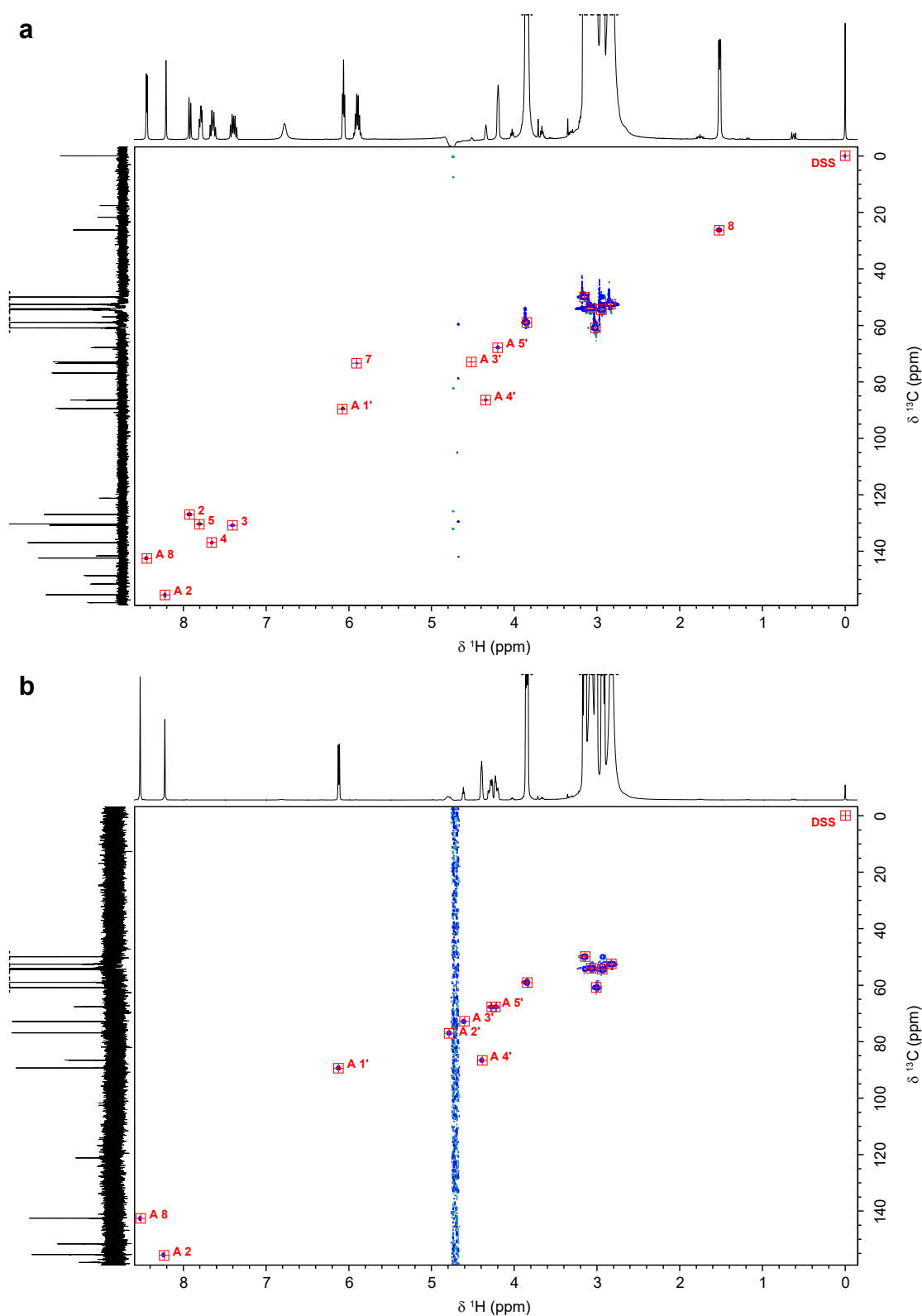
| atom number | ^1H | | | | ^{13}C | | | | |
|-----------------|--------------|----------------|------------------------------------|------------------------------------|-----------------|----------------|------------------------------------|------------------------------------|----------------|
| | # | δ (ppm) | J -couplings (at 300 MHz) | J -couplings (at 700 MHz) | # | δ (ppm) | J -couplings (at 300 MHz) | J -couplings (at 700 MHz) | δ (ppm) |
| A 2 | 3 | 8.207 | s | s | 4 | 8.204 | s | s | 155.4 |
| A 8 | 2 (S) | 8.435 | s | s | 1 (R) | 8.446 | s | s | 142.5 |
| A 1' | 16 (S) | 6.056 | d, $J = 5.82$ Hz | d, $J = 5.88$ Hz | 15 (R) | 6.068 | d, $J = 5.64$ Hz | d, $J = 5.74$ Hz | 89.6 |
| A 2' | - | - | - | - | - | - | - | - | 76.9 |
| A 3' | 19 | 4.511 | - | t, $J = 4.24$ Hz | - | - | - | - | 72.8 |
| A 4' | 20 (S) | 4.347 | t, $J = 3.12$ Hz | m | 21 (S) | 4.341 | t, $J = 2.99$ Hz | m | 86.5 |
| A 5' | 22 (S) | 4.201 | d, $J = 2.94$ Hz | d, $J = 3.01$ Hz | 23 (R) | 4.189 | d, $J = 2.97$ Hz | d, $J = 2.80$ Hz | 67.9 |
| NH ₂ | 13 | 6.790 | s | s | 14 | 6.779 | s | s | - |
| 2 | 5 | 7.921 | dd, $J = 8.22$, 0.93 Hz | dd, $J = 8.51$, 1.37 Hz | 6 | 7.918 | dd, $J = 8.27$, 0.98 Hz | dd, $J = 8.51$, 1.30 Hz | 126.9 |
| 3 | 11 | 7.408 | ddd, $J = 8.21$, 7.36, 1.39 Hz | ddd, $J = 8.37$, 7.49, 1.40 Hz | 12 | 7.371 | ddd, $J = 8.25$, 7.34, 1.44 Hz | ddd, $J = 8.45$, 7.54, 1.38 Hz | 130.8 |
| 4 | 9 | 7.645 | dt, $J = 7.65$, 1.18 Hz | dt, $J = 7.88$, 0.84 Hz | 10 | 7.624 | dt, $J = 7.66$, 1.20 Hz | dt, $J = 7.83$, 0.98 Hz | 136.9 |
| 5 | 7 | 7.794 | dd, $J = 7.88$, 1.46 Hz | dd, $J = 8.19$, 0.84 Hz | 8 | 7.782 | dd, $J = 8.03$, 1.28 Hz | dd, $J = 8.51$, 0.88 Hz | 130.4 |
| 7 | 18 (S) | 5.887 | qd, $J = 8.09$, 6.40 Hz | qd, $J = 7.77$, 6.58 Hz | 17 (R) | 5.903 | qd, $J = 7.97$, 6.23 Hz | qd, $J = 7.84$, 6.60 Hz | 73.4 |
| 8 | 24 (S) | 1.521 | d, $J = 6.30$ Hz | d, $J = 6.02$ Hz | 25 (R) | 1.512 | d, $J = 6.30$ Hz | d, $J = 6.16$ Hz | 26.3 |

Appendix Table 2: ^1H and ^{13}C NMR chemical shift assignment of ATP in 100 mM HEPES, 30 mM NaCl at pH 7.5 with ^1H chemical shifts and J -couplings as well as the respective ^{13}C chemical shifts obtained from ^1H , ^{13}C and ^1H - ^{13}C HSQC spectra according to the atom numbering of Appendix Figure 3.

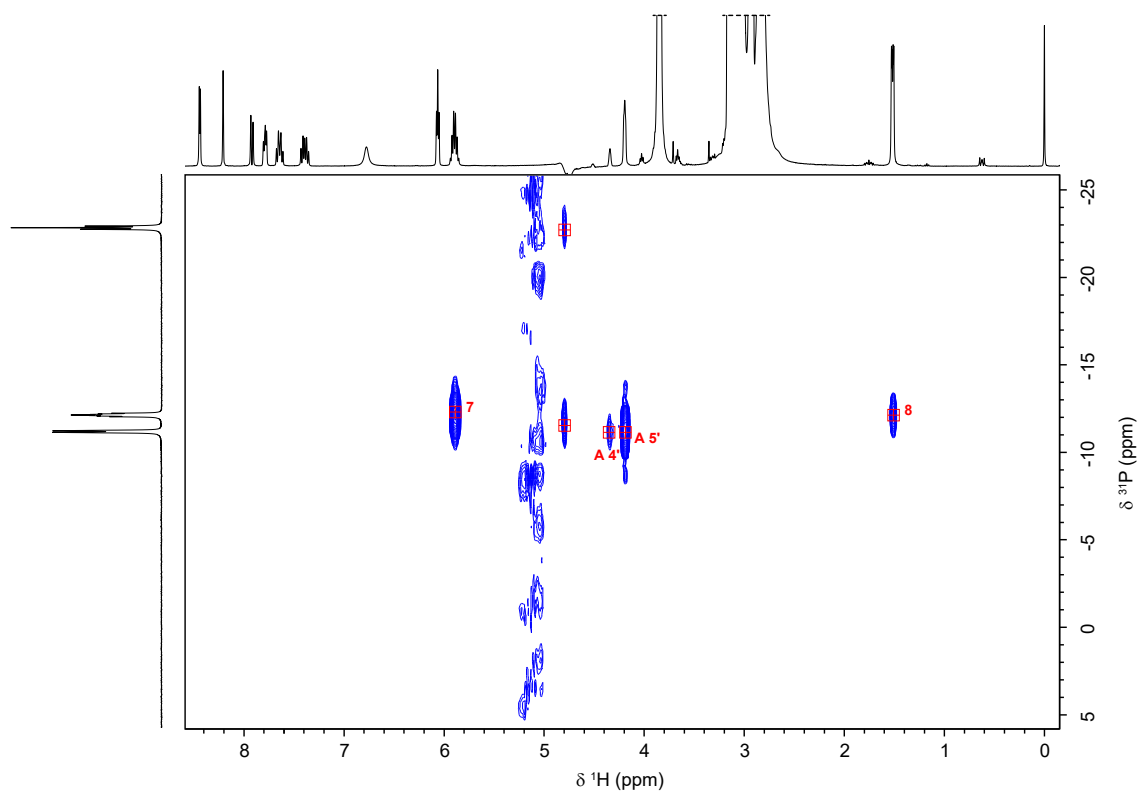
| atom number | ^1H | | ^{13}C |
|---------------|----------------|-------------------------|-----------------|
| | δ (ppm) | J -couplings | δ (ppm) |
| A 2 | 8.225 | s | 155.6 |
| A 8 | 8.524 | s | 142.6 |
| A 1' | 6.121 | d, $J = 5.79$ Hz | 89.4 |
| A 2' | 4.788 | - | 77.1 |
| A 3' | 4.615 | t, $J = 4.08$ Hz | 72.8 |
| A 4' | 4.396 | td, $J = 2.78, 6.09$ Hz | 86.7 |
| A 5' | 4.253 | m | 67.7 |
| NH_2 | 6.812 | s | - |



Appendix Figure 4: Details of ^1H NMR spectra of 12 mM NPE-ATP with (purple) and without (black) ^{31}P decoupling and 30 mM ATP (blue) in 100 mM HEPES, 30 mM NaCl pH 7.5 at 700.17 and 300.03 MHz with multiplet assignments.

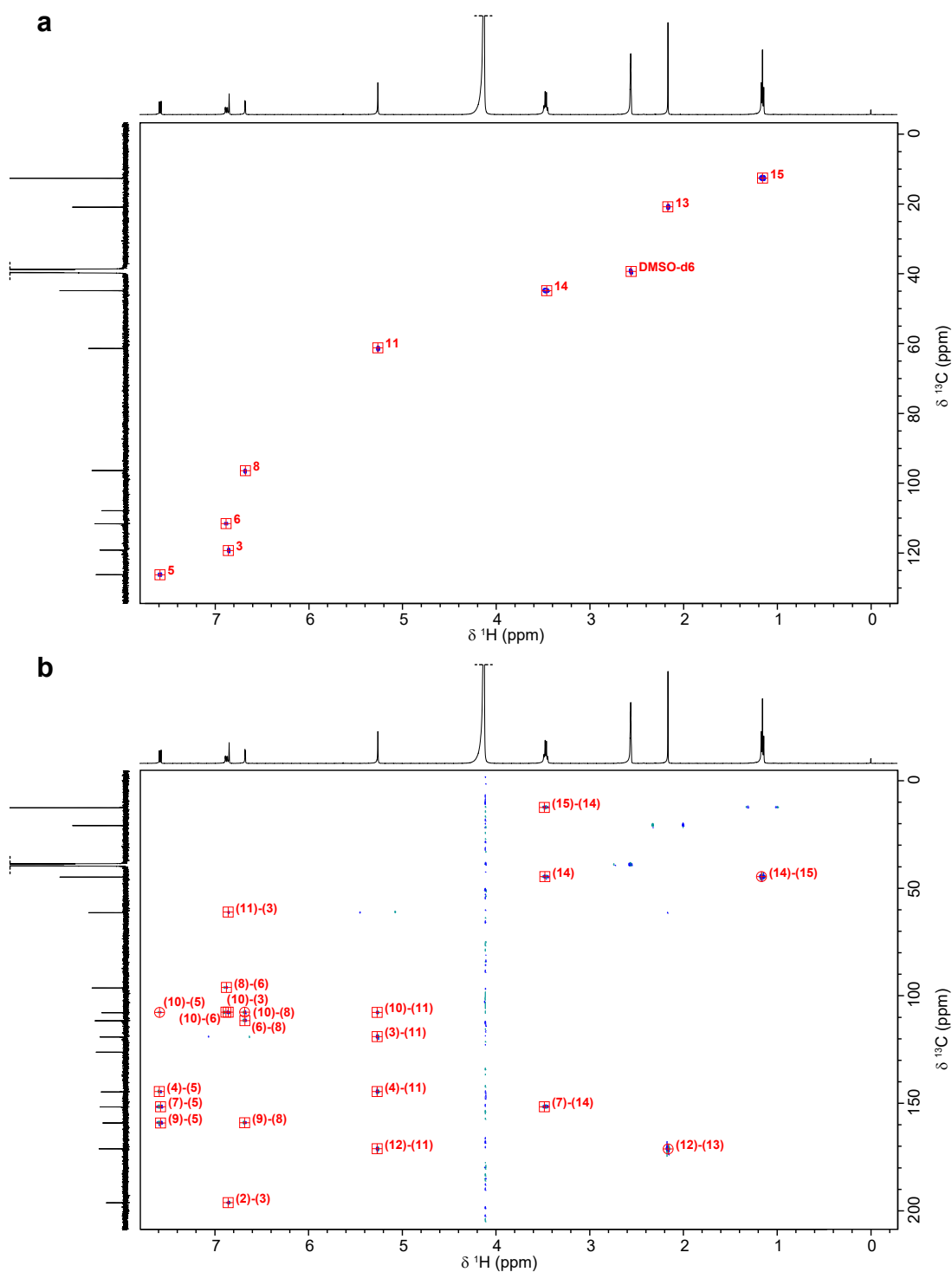


Appendix Figure 5: ^1H - ^{13}C HSQC spectra of 12 mM NPE-ATP (a) and 30 mM ATP (b) in 100 mM HEPES, 30 mM NaCl pH 7.5 with assignment according to Appendix Figure 3 (400.13 MHz) and respective ^1H and ^{13}C 1D spectra at same field except the ^{13}C spectrum of NPE-ATP (125.78 MHz).

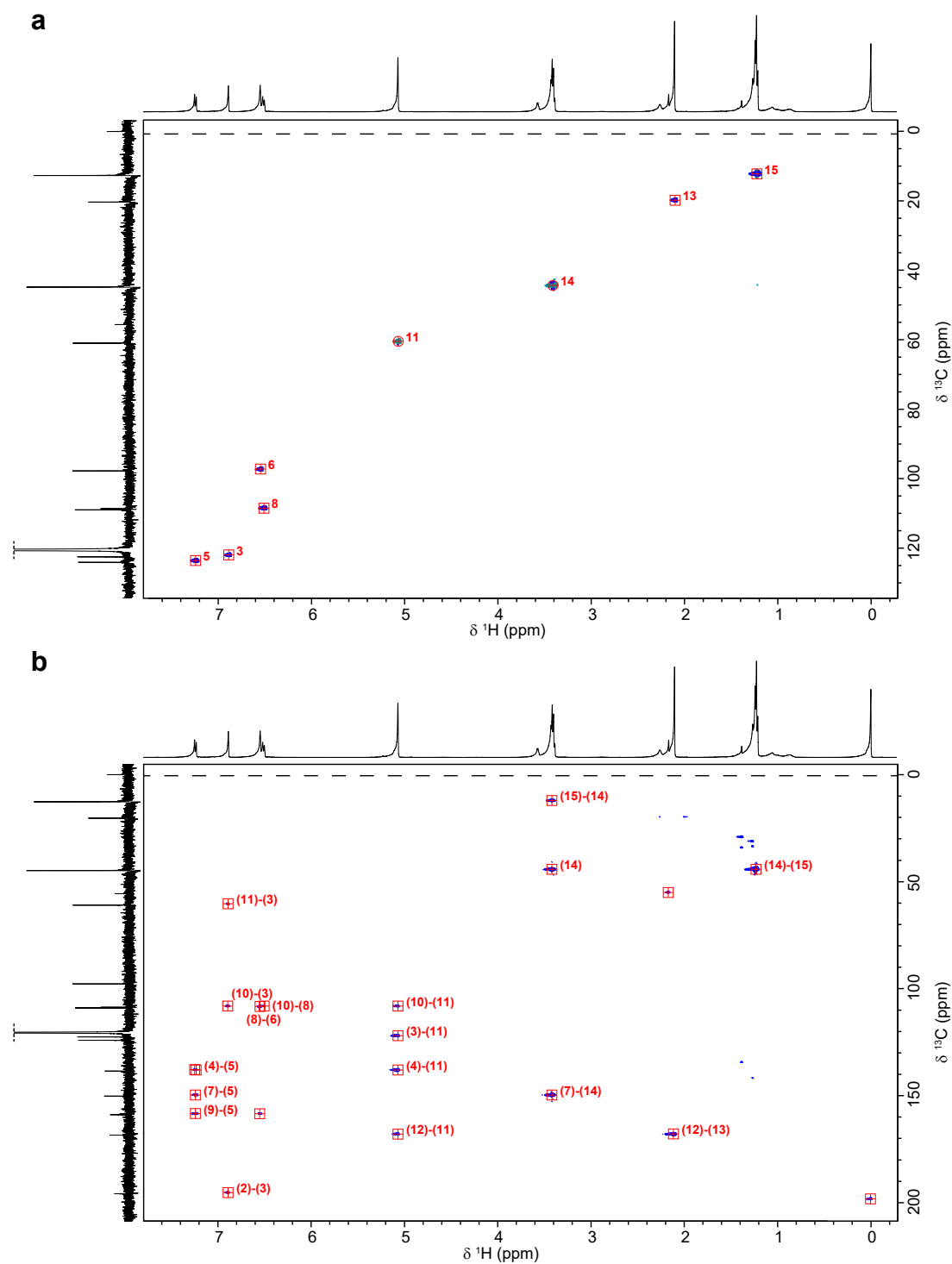


Appendix Figure 6: ^1H - ^{31}P HMBC of 12 mM NPE-ATP in 100 mM HEPES, 30 mM NaCl pH 7.5 with assignment according to Appendix Figure 3 (500.18 MHz) and respective ^1H (400.13 MHz) and ^{31}P (202.48 MHz) 1D spectra.

IV.3.2 2D NMR spectra of NdiEt-tcAA

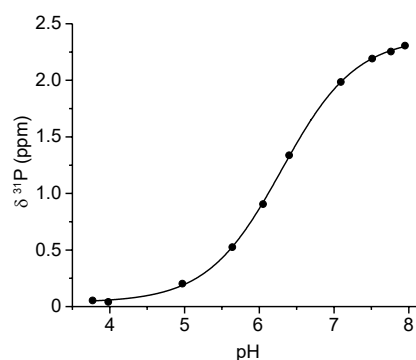


Appendix Figure 7: ^1H - ^{13}C HSQC (a) and HMBC (b) spectra of NdiEt-tcAA (400.13 MHz, DMSO- d_6) with assignment and respective ^1H and ^{13}C 1D spectra (500.18 MHz, DMSO- d_6). Atom numbers refer to Figure 36a. Dotted lines mark cut offs.



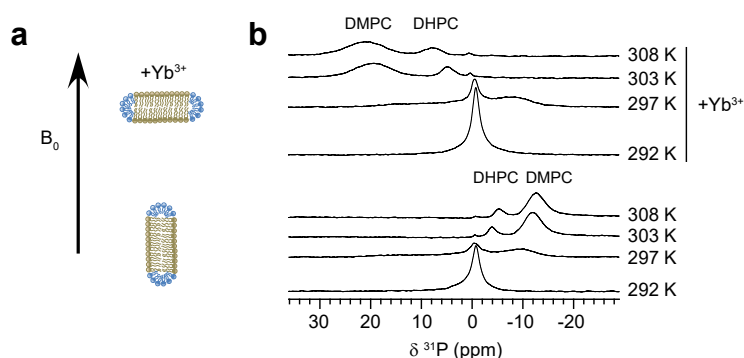
Appendix Figure 8: ^1H - ^{13}C HSQC (a) and HMBC (b) spectra of NdiEt-tcAA (500.18 MHz, TCE) with assignment and respective ^1H and ^{13}C 1D spectra. Atom numbers refer to Figure 36a. Dotted lines mark cut offs. Spectra were recorded without lock and shimming was performed on an external sample.

IV.3.3 pH titration curve of Pi ^{31}P chemical shift



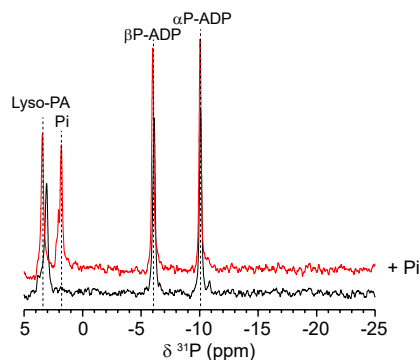
Appendix Figure 9: pH titration curve of Pi ^{31}P chemical shift. 5 mM sodium phosphate in 30 mM NaCl, 50 mM HEPES pH 7.9 at 303 K by addition of NaOH.

IV.3.4 Verification of anisotropic bicelles



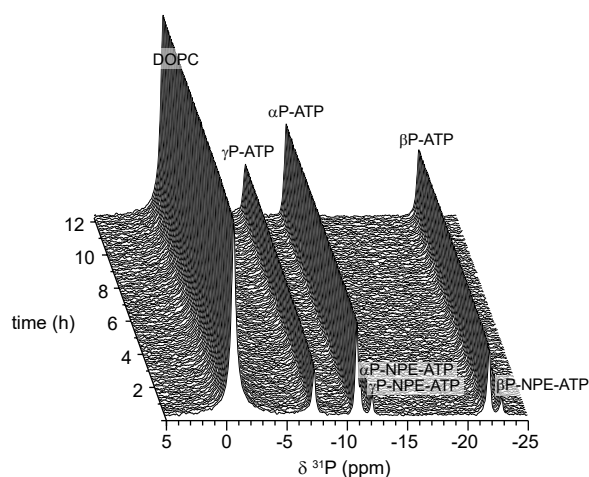
Appendix Figure 10: Verification of magnetic alignment and flipping of bicelles prepared for measuring DgkA's enzymatic activity in real-time NMR experiments and a coupled ATPase assay upon addition of ATP or uncaging of NPE-ATP. **a**) Schematic of anisotropic bicelles aligning perpendicular with their bilayer normal to a magnetic field, upon addition of a cation (Yb^{3+}) bicelles flip to align parallel to a magnetic field. Bicelle flipping is causing a change of the observed chemical shift in static ^{31}P ssNMR spectra.^{139, 146} **b**) Static ^{31}P temperature scan spectra of prepared bicelles made of 3.2:1 (mol/mol) DMPC:DHPC (bottom) and upon after addition of 1:100 (mol/mol) YbCl_3 to DMPC showing successful flipping of the anisotropic bicelles upon formation at elevated temperature.

IV.3.5 Enzymatic activity and ATP hydrolysis in presence of saturating amounts of monoolein



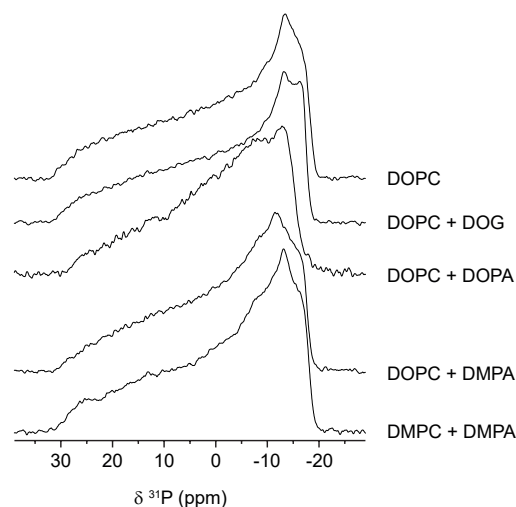
Appendix Figure 11: ^{31}P spectra after consumption of 2 μmol ATP (equates to 100 mM ATP with respect to the liquid fraction) by 5 μg DgkA in 30 mg LCP (black) and after addition of Pi (red) at 3 kHz MAS. For the real-time MAS NMR spectra of the enzymatic reaction see Figure 45.

IV.3.6 ATP hydrolysis in DgkA containing liposomes in absence of Mg^{2+}



Appendix Figure 12: ^{31}P real-time MAS NMR spectra after uncaging of 0.3 μmol NPE-ATP in DOPC liposomes containing 300 μg DgkA (L:P 120:1) 30 mM NaCl, 100 mM HEPES pH 7.5 but without MgCl_2 at 10 kHz MAS. Under these conditions in absence of Mg^{2+} ATP hydrolysis is not detected, as a divalent cation is a required cofactor for DgkA's enzymatic activity²⁵⁰.

IV.3.7 Phosphorylation of DOG in liposomes containing varying lipid ratios of DOG



Appendix Figure 13: Static ^{31}P spectra of DOPC liposomes containing 20 mol% DOG, DOPA, DMPA and DMPC liposomes containing 10 mol% DMPA at 303 K.

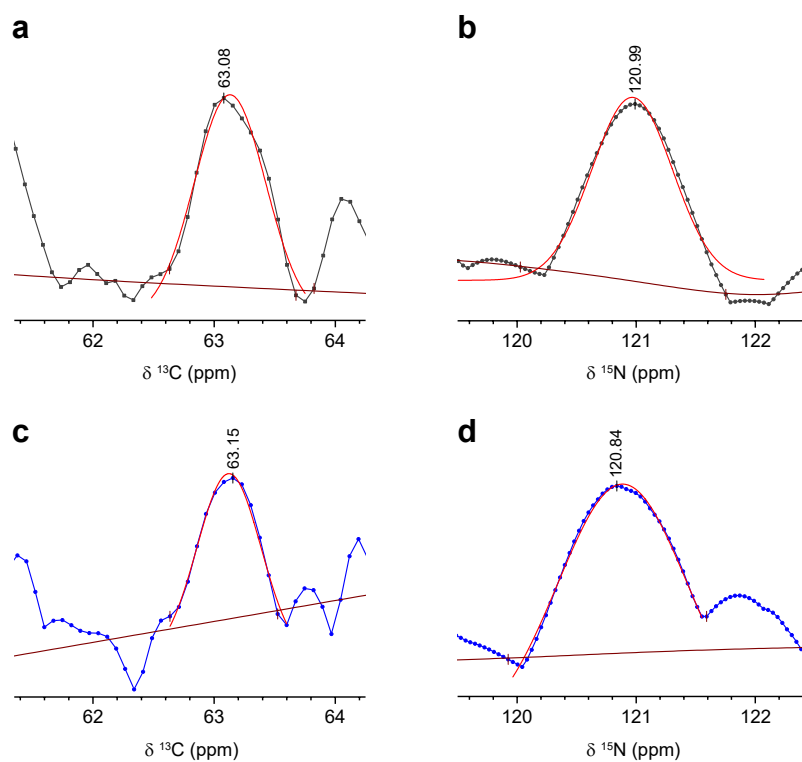
Appendix Table 3: Percentage and deviation of DOPA signal to lipid signals upon phosphorylation by DgkA of DOPC liposomes prepared with different lipid ratios of DOG from ^{31}P MAS NMR spectra (Figure 49).

| DOG:lipid molar percentage | DOPA:lipid ^{31}P signal percentage | absolute deviation | relative deviation |
|----------------------------|--|--------------------|--------------------|
| 10 mol% | 6% | 4% | 36% |
| 15 mol% | 10% | 5% | 35% |
| 20 mol% | 14% | 6% | 30% |
| 25 mol% | 21% | 4% | 17% |

Appendix Table 4: Initial rates from ^{31}P real-time MAS NMR experiments determining basal ATPase and stimulated activity in μU as well as factor of stimulation over basal ATPase activity of DgkA reconstituted at different L:P ratios in DOPC liposomes containing 20 mol% NPE-DOG upon addition of 0.45 μmol ATP. Stimulated activity is measured after 5 min illumination to uncage membrane incorporated NPE-DOG.

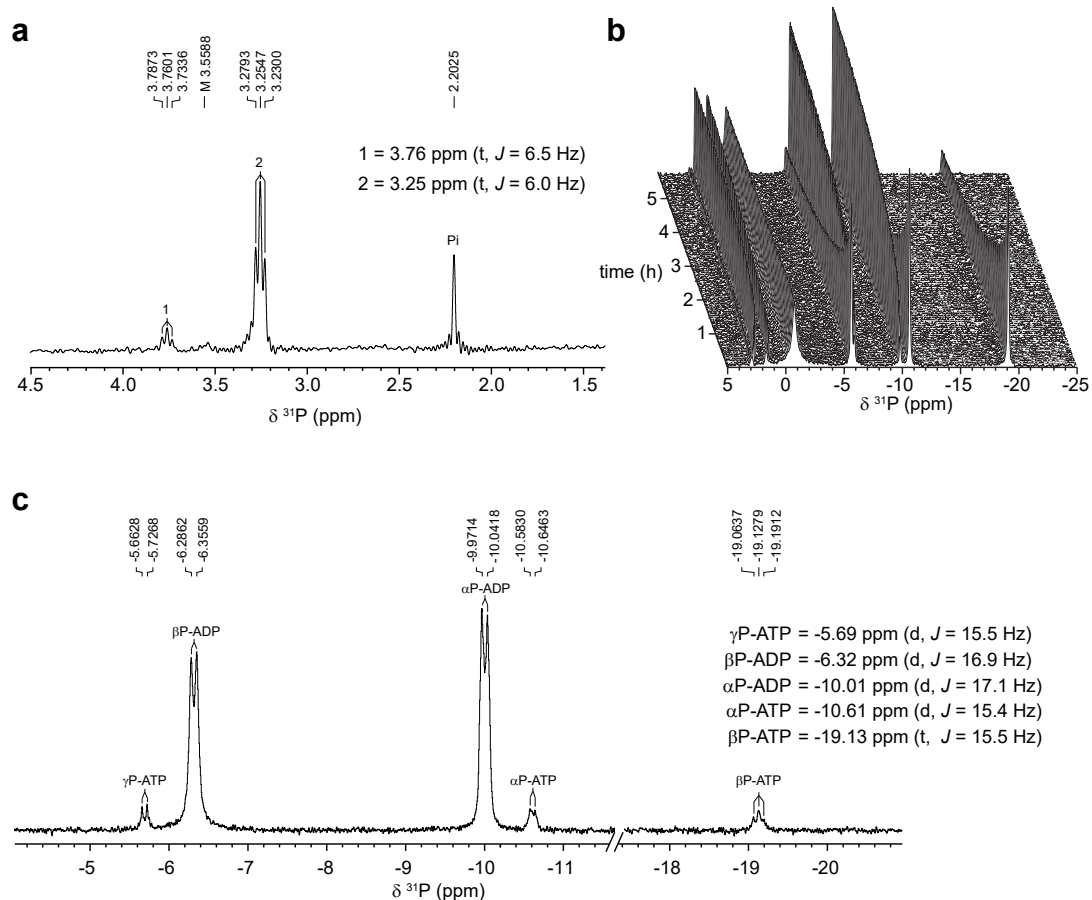
| L:P | DgkA (μg) | basal (μU) | stimulated (μU) | factor |
|--------|------------------------|-------------------------|------------------------------|--------|
| 500:1 | 500 μg | 0.8 | 4.2 | 5 |
| 2000:1 | 40 μg | 10 | 120 | 10 |
| 5000:1 | 15 μg | 4 | 160 | 40 |

IV.4 NCA DgkA Trp112 peak width



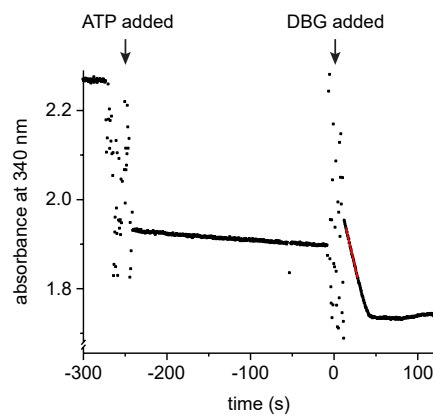
Appendix Figure 14: Projections of the acquired NCA spectra for the Trp112 peak with peak maxima (black), projected baseline and base markers (dark red) and Gaussian fits (red). **a)** F2 and **b)** F1 dimension projection of Trp112 peak of the DMPC:DMPA liposome sample. **c)** F2 and **d)** F1 dimension projection of Trp112 peak of the LCP sample.

IV.5 Scalar couplings of lipid products in ^{31}P NMR spectra

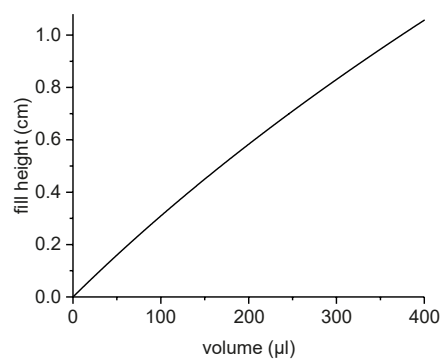


Appendix Figure 15: Formed lipid products of DgkA's enzymatic reaction in liposomes with DBG as lipid substrate. ^{31}P spectra with scalar couplings of lipid product signals (**a**) and nucleotide signals (**c**) after enzymatic activity of 0.84 mg DgkA in DMPC:DMPA liposomes (L:P 50:1) upon addition of 0.8 μl (3.45 μmol) DBG and 1.5 μmol ATP at 10 kHz MAS followed by ^{31}P real-time MAS NMR (**b**). Triplet 1 can be attributed to monobutyrylphosphatidic acid as it exhibits a typical chemical shift for lysophosphatidic acids (for comparison see Figure 45 and Figure 47) and exhibits similar J -coupling values compared to dibutyrylphosphatidic acid (Triplet 2).

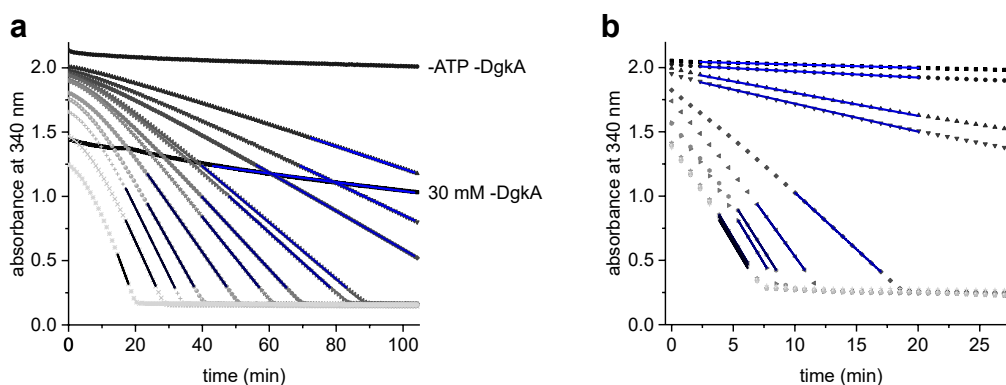
IV.6 Photometric coupled ATPase assays



Appendix Figure 16: Time trace of a coupled photometric assay performed in a cuvette following enzymatic activity of 20 μg DgkA in bicelles. Addition of 3 mM ATP and 18 mM DBG to start the kinase reaction is visible by disturbance of the absorbance recording. The linear fitted section of the time trace for rate determination after addition of DBG is depicted in red and yielded a activity of 1.5 ± 0.2 U.

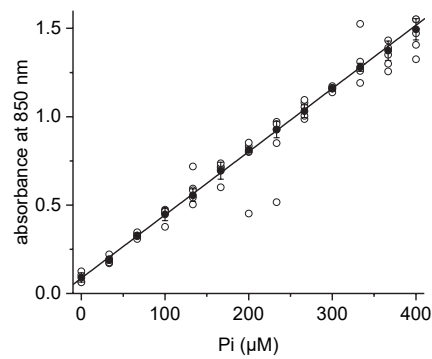


Appendix Figure 17: Fill height in relation to volume of 96 well plate wells used for the coupled photometric assays.

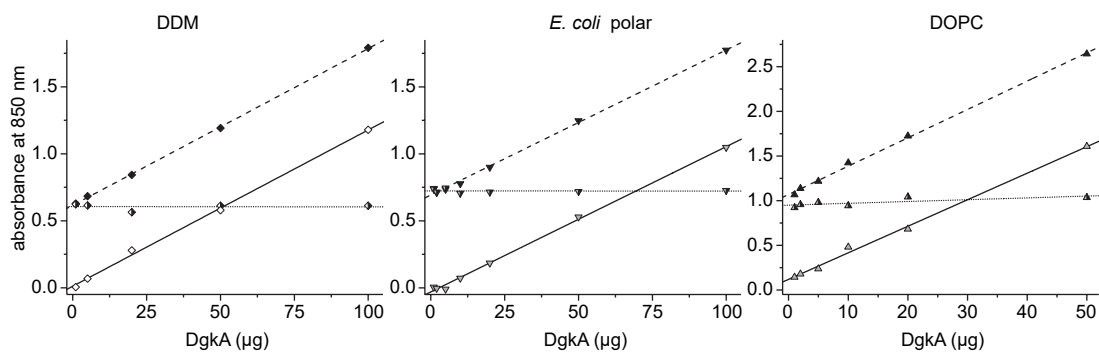


Appendix Figure 18: Representative set of time traces of *in meso* and *in surfo* coupled photometric assays performed with varying ATP concentrations. **a)** *in meso* coupled assay performed with 0.25, 0.5, 1, 1.5, 2, 3.5, 5, 7.5, 10, 15, 20, 30 mM ATP (from dark to light gray) as well as without DgkA with and without 30 mM ATP. **b)** *in surfo* coupled assay performed with 0, 0.01, 0.05, 0.1, 0.25, 0.5, 0.75, 1, 3.5, 5, 10 mM ATP (from dark to light gray). Linear fitted sections of the time traces for rate determination are depicted from blue to black with increasing ATP concentrations.

IV.7 Molybdenum blue assay

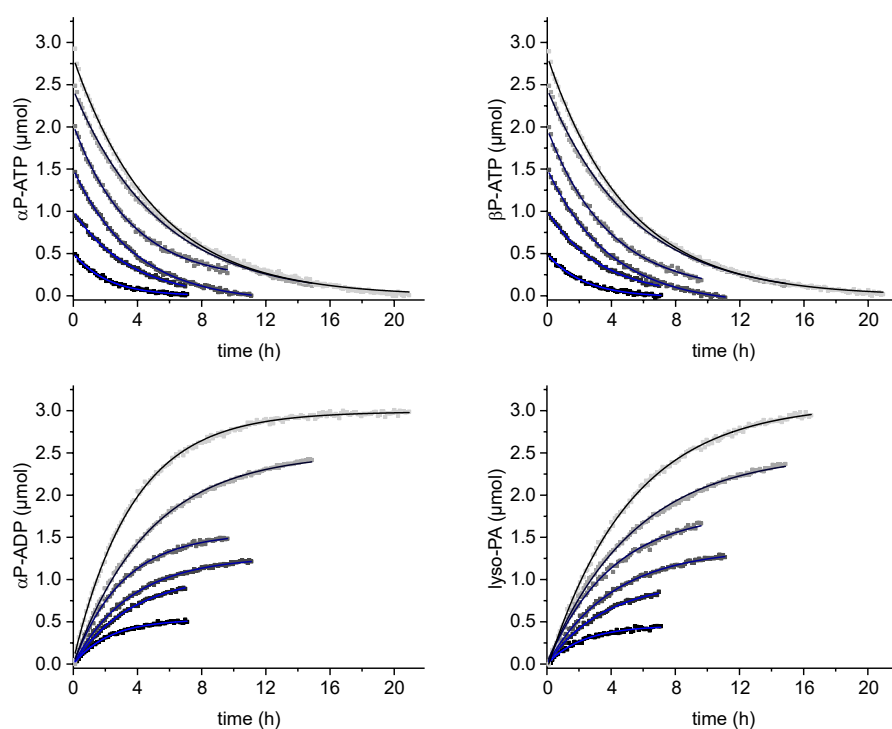


Appendix Figure 19: Molybdenum blue assay standard curve for determination of inorganic phosphorus. $n = 5$

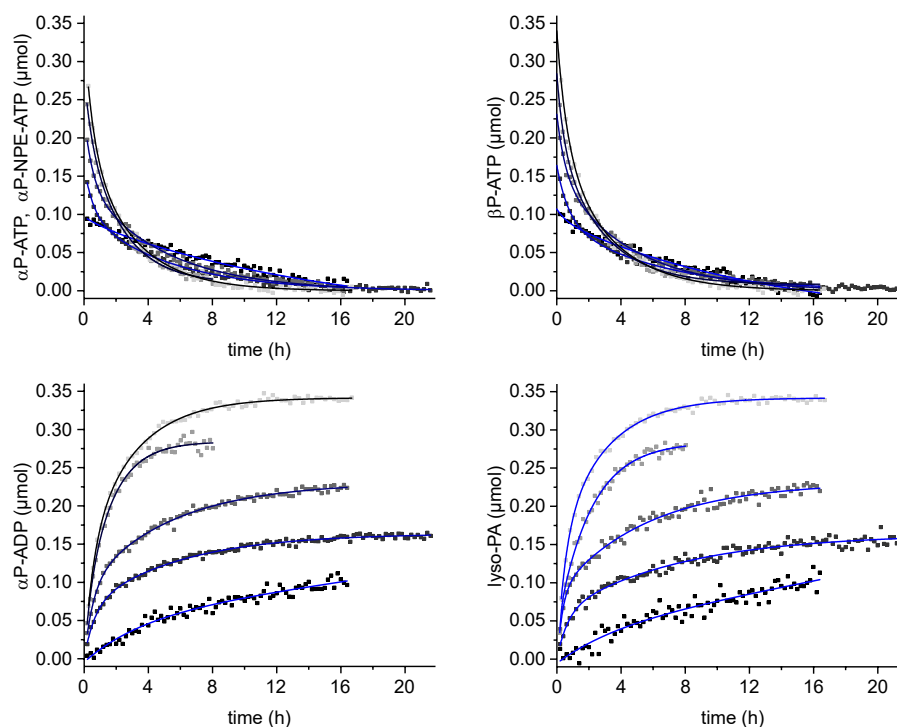


Appendix Figure 20: Absorbance measurements for the determination of specific basal ATPase activity of DgkA in DDM and reconstituted in DOPC and *E. coli* polar lipid liposomes at 20 mM ATP in dependence to varying DgkA amounts via molybdenum blue assay. Raw data: filled symbols and linear fit thereof as dashed line. Background: half filled symbols and linear fit thereof as dotted line. Background subtracted data: non-filled symbols and linear fit thereof as solid line.

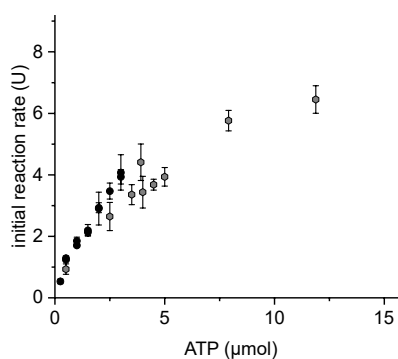
IV.8 ^{31}P real-time solid-state NMR measurements



Appendix Figure 21: Progress curves of ^{31}P real-time MAS NMR experiments following the activity of 2.8 μg DgkA in 50 mg LCP (2:3 (w/w) liquid : monoolein) upon addition of 0.5, 1, 1.5, 2, 2.5, 3 μmol ATP equating to 25, 50, 75, 100, 125, 150 mM ATP (from black to gray) with respect to the liquid fraction of the LCP. Monoexponential fits of the time traces to determine initial reaction rates are shown in blue till black from low to high ATP concentrations.



Appendix Figure 22: Progress curves of ^{31}P real-time MAS NMR experiments following the activity of $3.8\ \mu\text{g}$ DgkA in $15\ \text{mg}$ LCP (2:3 (w/w) liquid : monoolein) prepared with $0.1, 0.2, 0.3, 0.4, 0.5\ \mu\text{mol}$ NPE-ATP upon release of $0.09, 0.16, 0.23, 0.28, 0.34\ \mu\text{mol}$ ATP via uncaging equating to $15.7, 27.3, 38.5, 47.3, 56.7\ \text{mM}$ ATP with respect to the liquid fraction of the LCP. Biexponential fits of the time traces to determine initial reaction rates are shown in blue till black from low to high ATP concentrations.



Appendix Figure 23: Initial reaction rates of DgkA's enzymatic activity in LCP determined via ^{31}P real-time MAS NMR as shown in Figure 59a in dependence to ATP amounts added. Depicted in black are rates from measurements with a final monoolein:liquid ratio of 6:4 (w/w) after addition of ATP. For higher ATP concentrations (in gray) the lipidic cubic phase was formed at a constant monoolein:liquid ratio of 6:4 (w/w). Addition of ATP yielded a maximum monoolein:liquid ratio of 4.4:5.6 (w/w).

IV.9 Scripts for analyzing ³¹P real-time NMR experiments

IV.9.1 AU program to add up FID's of 1D experiments as sets in incremented experiment numbers

```

Proc_err(DEF_ERR_OPT, "In the following fields select the starting expno of consecutive expno's where multi_fidadd
should work on and continue.");
#include <inc/getdataset>
int orig, newexpno=1000+expno, stepexpno=expno, incexpno, scans, totscans;
/*char newname[0];
strcpy(newname,name);*/
GETINT("How many incremented expno's?",i1)
GETINT("How many expno's do you want to merge to one?",i2)
/* i1=4; /*i1 = number of expnos;*/
/* i2=2; /*i2 = number of expnos to be combined each;*/

if(i1 % i2 != 0)
{
Proc_err(DEF_ERR_OPT, "The experiments can not be combined! \n The modulo of the number of selected expno's divided
by how many should be merged each is not zero. \n Set a different number of expno's or how many should be merged
each. \n AU Program aborted. No files created.");
ABORT
}
GETINT("From which expno onwards should the newly merged fid's be saved?",newexpno)
/*GETSTRING("What should be the new project name",newname)*/
TIMES(i1/i2)
/*create new dataset*/
DATASET(name, stepexpno, procno, disk, user)
WRA(newexpno)
/*counting the number of scans for the expnos to be combined*/
totscans=0;
TIMES2(i2)
SETCURDATA
FETCHPARS("NS",&scans)
totscans += scans;
IEXPNO
END
/*changing the number of scans in the new dataset*/
DATASET(name, newexpno, procno, disk, user)
STOREPAR("DC",1.0)
STOREPARS("NS",totscans)
STOREPAR("TI","result of multi_fidadd")
STOREPARS("TI","result of multi_fidadd")
/*adding the FIDs of two datasets*/
incexpno = stepexpno;
TIMES2(i2-1)
DATASET2(name, newexpno, procno, disk, user)
DATASET3(name, ++incexpno, procno, disk, user)
ADDFID
END

newexpno += 1;
stepexpno += i2;
END
QUIT

```

IV.9.2 AU program for conversion of 1D experiments with consecutive experiment numbers into a pseudo 2D spectrum

```

/*This AU program has to be executed from a empty pseudo 2D expno with consecutive 1D expno's following "times",
"name", "dir" and "user" have to be filled in*/
i1="times";
i2=0;
TIMES(i1)
i2=i2+1;
WSER(i2,"name",expno,procno,"dir","user");
IEXPNO
END
END

```

IV.9.3 AU program for conversion of pseudo 2D NMR spectra to 1D spectra in consecutive processing numbers

```

/*This AU program has to be executed from a pseudo 2D procno*/
FETCHPARS("TD", &i1)
i2 = 1;
TIMES(i1)
i3=i2+100;
RSR(i2,i3)
i2=i2+1;
END
QUIT

```

IV.9.4 Matlab script for sequential import of 1D spectra in ASCII format to Matlab, peak fitting using peakfit.m and sorting of results

```

% defining import range of procnos
startprocno = 101;
endprocno = 220;
numprocnos = endprocno-startprocno+1;
delimiterIn = ',';

% create the cell array mydata where input and output is stored
mydata = cell(8, (endprocno-startprocno+1));
% loop for importing the 1D ASCII files
for procno = startprocno:endprocno
    myfilename = sprintf('X:\\%\"filepath\"\\data\\\"user\"\\nmr\\\"name\"\\\"expno\"\\pdata\\%d\\ascii-spec.txt', procno);
    mydata{1, (procno-startprocno+1)}z = importdata(myfilename,delimiterIn);
end
peak_start_values =[0.9 -0.6 -5.6 -6.3 -10 -10.5 -11.1 -12.0 -19]
peak_number_fit = [1 1 1 4 1]
window= [0.5 2 1 1 3.5 1.5]
peak_start_width=[0.05 0.5 0.2 0.2 0.2 0.2 0.2 0.2 0.2]
peakshape=1
extra=0
NumTrials=20

##### Fitting the spectra in several parts #####
for j = 1:length(peak_number_fit)
    peak_numbers=sum(peak_number_fit(1:(j)))

    peak_start_shifts=    peak_start_values((sum(peak_number_fit(1:j)) -    peak_number_fit(j)
+1):sum(peak_number_fit(1:(j))))
    peak_start_widths=    peak_start_width((sum(peak_number_fit(1:j)) -    peak_number_fit(j)
+1):sum(peak_number_fit(1:(j))))
    temp = [peak_start_shifts; peak_start_widths];
    start_values= temp(:)';
    %defining center of fitted area
    center=mean(peak_start_shifts)

    for k = 1:numprocnos

        % [FitResults,GOF,baseline,coeff,residual,xi,yi,BootResults]=peakfit(signal,center>window,NumPeaks,peaks
hape,extra,NumTrials,start,autozero,fixedparameters,plots,bipolar,minwidth,DELTA,clipheight)

        [FitResults,GOF,baseline,coeff,residual,xi,yi]=peakfit([mydata{1, k}(:,4) mydata{1, k}(:,2)],
center, window(j), peak_number_fit(j), peakshape, extra, NumTrials, start_values, 0, 0, 1);
mydata{(j*10)+2, k} = FitResults;
mydata{(j*10)+3, k} = GOF;
mydata{(j*10)+4, k} = baseline;
mydata{(j*10)+5, k} = coeff;
mydata{(j*10)+6, k} = residual;
mydata{(j*10)+7, k} = xi;
mydata{(j*10)+8, k} = yi;

    end
end

##### Transpose from the cell array into matrices

%Peak position
for l= 1:length(peak_number_fit)
    for m=1:peak_number_fit(l)
        peak_number = sum(peak_number_fit(1:l))-peak_number_fit(l)+m;
        peakposition(:,peak_number) = transpose(cellfun (@(x) x(m,2),mydata{(l*10)+2,1:numprocnos}));
        peakheight(:,peak_number) = transpose(cellfun (@(x) x(m,3),mydata{(l*10)+2,1:numprocnos}));
        peakwidth(:,peak_number) = transpose(cellfun (@(x) x(m,4),mydata{(l*10)+2,1:numprocnos}));
        peakarea(:,peak_number) = transpose(cellfun (@(x) x(m,5),mydata{(l*10)+2,1:numprocnos}));
    end
end

##### Create a 3 dimensional array to be able to filter and sort the values.
resultarray = cat(3, peakposition, peakheight, peakwidth, peakarea);

##### Apply conditions to filter out wrong fits

%Delete wrong fits based on peakposition and/or other things
spectralwidth=[-25, 5];
max_peakwidth= 0.5;
%conditions
cond1 = resultarray(:, :,1) < spectralwidth(1) | resultarray(:, :,1) > spectralwidth(2);
cond2 = resultarray(:, :,3) > max_peakwidth;

cond_all =cond1&cond2;

%create logical matrix with same dimensions as results
cond_logical = repmat (cond_all,[1,1,4]);

%apply the logical matrix and set these values to zero
resultarray(cond_logical) = 0;

##### Sort the peaks according to their shifts, leaving zeroes at their place
sortedresultarray=zeros(size(resultarray));
for row = 1:size(resultarray, 1)

```

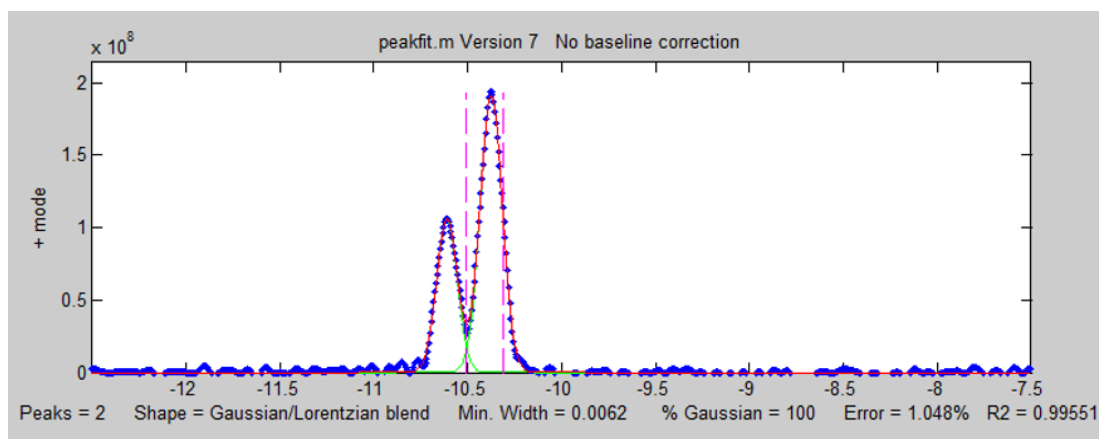
```

        [sortedresultarray(row, (resultarray(row, :1)~=0), 1), ind]=sort(resultarray(row, (resultarray(row, :1)~=0),
1), 'descend');
        resultrow=(resultarray(row, (resultarray(row, :1)~=0), 2));
        sortedresultarray(row, (resultarray(row, :1)~=0), 2)=resultrow(ind);
        resultrow=(resultarray(row, (resultarray(row, :1)~=0), 3));
        sortedresultarray(row, (resultarray(row, :1)~=0), 3)=resultrow(ind);
        resultrow=(resultarray(row, (resultarray(row, :1)~=0), 4));
        sortedresultarray(row, (resultarray(row, :1)~=0), 4)=resultrow(ind);
    end

%creates a array d with same size as array c
%goes through the arrays row by row. for each row it:
%sorts the non zero values of array c
%copies the sorted non zero values of array c into the position of array d where the non zero values in array c where
%creates an index vector how the results where sorted
%applies index vector onto third dimension of array (2,3,4, height, width, area)

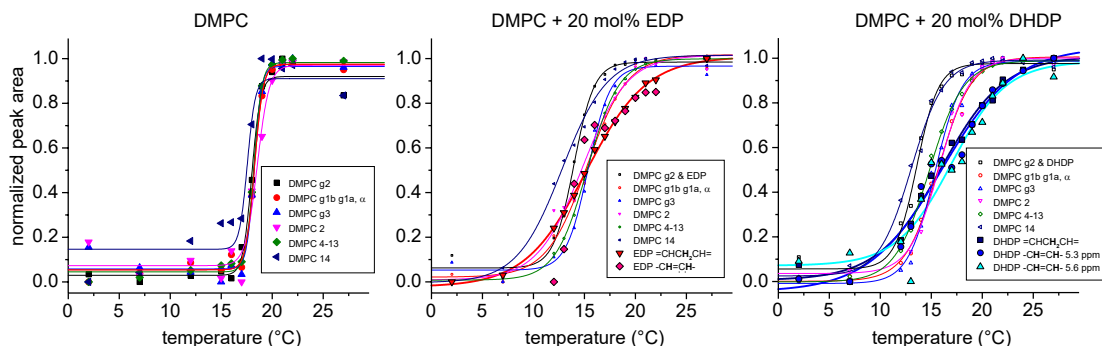
%GOF
for n = 1:length(peak_number_fit)
    GOF(:,n) = transpose(cellfun (@(x) x(1,2),mydata((n*10)+3,1:numprocnos)))
end

```



Appendix Figure 24: Deconvolution (red, green) using the Matlab plugin peakfit.m of α P-ATP and α P-ADP peaks of a 1D spectrum (blue) from a pseudo 2D ^{31}P real-time NMR spectrum with starting peak positions marked as pink dashed lines and fitting parameters given.

IV.10 Effect of polyunsaturated fatty acid metabolites on membrane fluidity of DMPC model membranes



Appendix Figure 25: Normalized peak area of analyzed DMPC (filled) and PUFA (non-filled) peaks (Figure 69, Figure 70a) of DMPC and DMPC + 20 mol% EDP or DHDP with respect to increasing temperature.

IV.11 Published data on DgkA's enzymatic activity

Appendix Table 5: Published data on DgkA's enzymatic activity. Kinetic parameters, assay conditions, type of assay, sample preparation, type of sample.

| # | Ref | Title | Authors | Published | Mutants | General comments | Protein name | Extinction coefficient as in | Assay conditions as in | Purification | DgkA stock | Assay environment | Activator | Lipid substrate | Type of assay | Km nucleotide | Km lipid substrate | vmax (DAG varied, ATP fixed) | Specific activity | ATP concentration | Mg concentration | Half-life nucleotide | Notes and special parameters | Assay temp | pH | Salt | Assay buffer composition | Protein purification |
|----|-----|--|---|-----------|---|--|--------------|------------------------------|------------------------|--------------|------------|--|---------------------|-----------------------------|--|---------------|--------------------|------------------------------|-------------------|-------------------|------------------|---|------------------------------|------------|-----------|---|---|--|
| 57 | 272 | Dodecyl-β-D-melibioside Detergent Micelles Medium for Membrane Proteins | Hutchison, J. M.; Lu, Z.; G. S.; G. S.; B.; Mihal; Deatherage S. L.; G. S.; C. R. | 2017, Oct | | | DAGK | 1.8 mg/ml/cm | 31 mg/ml/cm | 37 and 43 | DM | 0.4 μg DgkA in 1% (w/v) DM | 3 mg/ml cardiolipin | 4.5 mg/ml dihexano/glycerol | coupled assay, quartz cuvette | | | | -66 | 3 mM | 15 mM Mg acetate | 3.3 ± 1.3 h at 70 °C | | 30 °C | 6.9 | 50 mM LCI | 1 mM PEP, 0.25 mM NADH, 20 U/ml PK and DM, DDM, 1 mM MNG, PIPES, 0.1 mM EGTA, 0.1 mM EDTA, 0.2 mM DTT | Emphen BB, Ni-NiTA, To DM, DDM, MNG or |
| 58 | 338 | Ternary structure phasing for mechanism of membrane protein crystals grown by the lipid | Li, D.; Conway, M.; et al | 2015, Dec | V17 and I101 point mutations | Substrates of Δ4 (CLLD) DgkA with SeMet in DM, yield of 5 mg/l (LD) (CAVLLDA) in 7.5 MAG and FEL | DgkA | ε 1 mg/ml = 2.1 | 48 | 50 | DM | 5 μl LCP (60:40 monoolein:liquid DgkA) (total 132 μg DgkA) | 3 mg/ml cardiolipin | 4.5 mg/ml monoolein | coupled assay, microtiter plate, in meso | | | | 21 | 30 mM | 55 mM Mg acetate | 8.5 ± 0.5 h incubation at 70 °C in DDM, assay in DM; 9.9 ± 1.7 h incubation at 70 °C in DDM, assay in DM; 5.6 ± 1.3 h incubation at 70 °C in MNG, assay in DM, half life of the population sensitive to thermal inactivation (~40% of the population) | 30 °C | 6.9 | 50 mM LCI | 0.1 mM EDTA, 0.1 mM EGTA, 1 mM PEP, 0.2 mM DTT, 0.4 mM NADH, 20 U/ml PK and DM, 75 mM PIPES | Emphen BB, Ni-NiTA, DDM, SEC from HEPES pH 7.5 to TRIS pH 7.5 (100 mM and 7.5) | |
| 59 | 326 | Experimental identification of membrane protein crystals grown by the lipid phase method | Li, Dianfan; Pye, J.; G. S.; E.; G. S.; Martin | 2015, Jan | Δ4 (CLLD) | DgkA produced in MB with SeMet in DM, yield of 5 mg/l (LD) (CAVLLDA) (CLLD) | DgkA | ε 1 mg/ml = 2.1 | 48 | 50 | DM | 5 μl LCP (60:40 monoolein:liquid DgkA) (total 132 μg DgkA) | 3 mg/ml cardiolipin | 4.5 mg/ml monoolein | coupled assay, microtiter plate, in meso | | | | 17 | 20 mM | 55 mM Mg acetate | same as for normal Δ4 (CLLD) DgkA | 30 °C | 6.9 | 50 mM LCI | 0.1 mM EDTA, 0.1 mM EGTA, 1 mM PEP, 0.2 mM DTT, 0.4 mM NADH, 20 U/ml PK and DM, 75 mM PIPES | Emphen BB, Ni-NiTA, DDM, SEC from HEPES pH 7.5 to TRIS pH 7.5 (100 mM and 7.5) | |
| 60 | 326 | Experimental identification of membrane protein crystals grown by the lipid phase method | Li, Dianfan; Pye, J.; G. S.; E.; G. S.; Martin | 2015, Jan | Cye-less Δ4 (CLLD) (CAVLLDA), V107D and C113A | DgkA produced in MB with SeMet in DM, yield of 5 mg/l (LD) (CAVLLDA) (CLLD) | DgkA | ε 1 mg/ml = 2.1 | 48 | 50 | DM | 5 μl LCP (60:40 monoolein:liquid DgkA) (total 132 μg DgkA) | 3 mg/ml cardiolipin | 4.5 mg/ml monoolein | coupled assay, microtiter plate, in meso | | | | 16.5 | 20 mM | 55 mM Mg acetate | same as for normal Δ4 (CLLD) DgkA, same yield and trimer | 30 °C | 6.9 | 50 mM LCI | 0.1 mM EDTA, 0.1 mM EGTA, 1 mM PEP, 0.2 mM DTT, 0.4 mM NADH, 20 U/ml PK and DM, 75 mM PIPES | Emphen BB, Ni-NiTA, DDM, SEC from HEPES pH 7.5 to TRIS pH 7.5 (100 mM and 7.5) | |

| # | Ref Title | Authors | Pub-lished | Mutants | General comments | Protein name | Extinction coefficient as in | Assay as in | Purification | DgkA stock | Assay environment | Activator | Lipid substrate | Type of assay | Km nucleotide | Km lipid substrate | vmax (DAG varied, ATP fixed) | Specific activity | ATP concentration | Mg concentration | Half-life incubation | Notes and special parameters | Assay temp | pH | Salt | Assay buffer composition | Protein purification protocol |
|----|---|--|-------------|--------------|---|--------------|------------------------------|-------------|-----------------------------|--|---|---------------------------------|--------------------------------------|---|-----------------------------|---------------------------|------------------------------|-------------------|-------------------|------------------|---|------------------------------|------------|-----------|--|--------------------------|-------------------------------|
| 47 | Use of Lipid and Temperature as Important Screening Criteria for Crystallization of Integral Membrane Proteins in Lipidic Mesophases. Diacylglycerol Kinase | Li, D., Shah, S., T. Caffrey, M. | 2011, April | A7 (CAVLLDA) | activity under crystallization conditions | DgkA | 1 mg/ml = 2.1 | 48 | with modification as in 48. | LCP (10 µl, 12 mg/ml DgkA, 10 mg 7.8 MAG) in 1 ml solution (4.5% (v/v) 2-methyl-2,4-hexanediol (MPD), 0.1 M sodium chloride, 60 mM potassium acetate, 50 mM sodium citrate, pH 6.0) with 10 mM ATP. At 4 °C for 0, 0.5, 1, 2, 3, 5 and 10 h. | - | - | - | coupled assay, 384 microtiter plate, in surto | - | - | - | 0.05 | 15 mM MgCl2 | - | activity under crystallization conditions. 0.05 U for A7 (CAVLLDA) under these conditions for 0.5 h. For WT under these conditions (as stated in Supplementary Figure 14) | 30 °C | 6.9 | - | 1 mM PEP, 0.2 mM DTT, 0.2 mM NaOH, 20 U/ml Phosphatidylcholine, 75 mM PIPES | - | |
| 48 | in situ 19F NMR studies of an E. coli membrane protein | Shi, Pan; Li, Dong; Wang, Xiang; Xiong, Yng; Wang, Teon; Chennan | 2012, Feb | WT and CLLD | Crystallization (with Mg monolein, magnesium is an important factor (With and no effect on crystal morphology or mosaic, however, it proved to be essential for crystal growth in 7.8 MAG). Yield: 16 mg/l (LB) | DgkA | 1 mg/ml = 2.1 | - | 48. | DM | 1% w/v (21 mM) (62.9 mg/ml) DM | 0.66 mM (2.9 mg/ml) cardiolipin | 0.95 mM (4.2 mol%) dihexano/glycerol | coupled assay, microtiter plate, in surto | - | - | - | 108 ± 1.6 | 3 mM ATP | 15 mM Mg acetate | - | 30 °C | 6.9 | 50 mM LCI | 0.1 mM EDTA, 0.1 mM EGTA, 0.2 mM DTT, 0.3 mM NaOH, 20 U/ml PK and LDH, 75 mM PIPES | 8% Empigen-N30, 0.5% DM | |
| 48 | Lipid cubic phase as a membrane protein | Li, D., Caffrey, M. | 2011, May | WT | Yield: 23 mg/l (LB) synthesized by E. coli strain EcO1 same as pSD005 | DgkA | 1 mg/ml = 2.1 | - | 18. | DM | 1% w/v (21 mM) (62.9 mg/ml) DM | 0.66 mM (2.9 mg/ml) cardiolipin | 0.95 mM (4.2 mol%) dihexano/glycerol | coupled assay, microtiter plate, in surto | - | - | - | 127.6 ± 2.4 | 3 mM ATP | 15 mM Mg acetate | - | 30 °C | 6.9 | 50 mM LCI | 0.1 mM EDTA, 0.1 mM EGTA, 0.2 mM DTT, 0.3 mM NaOH, 20 U/ml PK and LDH, 75 mM PIPES | - | |
| | | | | WT | CLLD (also synthesized) | | | | | DM | 1% w/v (21 mM) (62.9 mg/ml) DM | 2.9 mol% cardiolipin | 25.2 mol% monolein | coupled assay, microtiter plate, in surto | - | - | - | 37.4 ± 0.3 | 3 mM ATP | 15 mM Mg acetate | - | 30 °C | 6.9 | 50 mM LCI | - | - | |
| | | | | WT | | | | | | DM | 1% w/v (21 mM) (62.9 mg/ml) DM | 2.9 mol% cardiolipin | 25.2 mol% monolein | coupled assay, microtiter plate, in surto | - | - | - | 26.9 ± 0.3 | 3 mM ATP | 15 mM Mg acetate | - | 30 °C | 6.9 | 50 mM LCI | - | - | |
| | | | | WT | | | | | | LCP | 5x 1µl LCP (60:40 monolein:lipid) bolus (total 132 ng DgkA) | - | monolein | coupled assay, microtiter plate, in meso | 3.5 ± 0.3 mM (with Mg xATP) | 14.4 ± 0.4 (with Mg xATP) | 16.5 ± 1.2 | 30 mM ATP | 55 mM Mg acetate | - | kinase assay, coupled assay, ATP for kinetics and not 55 mM Mg Acetate as for specific activity) | 30 °C | 6.9 | 50 mM LCI | 0.1 mM EDTA, 0.1 mM EGTA, 0.2 mM DTT, 0.3 mM NaOH, 20 U/ml PK and LDH, 75 mM PIPES | - | |
| | | | | WT | | | | | | LCP | 5x 1µl LCP (60:40:20) bolus (total 132 ng DgkA) | - | 7.11 MAG | coupled assay, microtiter plate, in meso | - | - | 16.1 | 20 mM ATP | 55 mM Mg acetate | - | 30 °C | 6.9 | 50 mM LCI | - | - | | |
| | | | | WT | | | | | | LCP | 5x 1µl LCP (60:40:20) bolus (total 132 ng DgkA) | - | 9.7 MAG | coupled assay, microtiter plate, in meso | - | - | 14.2 | 20 mM ATP | 55 mM Mg acetate | - | 30 °C | 6.9 | 50 mM LCI | - | - | | |
| | | | | WT | | | | | | LCP | MAG:liquid bolus (total 132 ng DgkA) | - | 7.7 MAG | coupled assay, microtiter plate, in meso | - | - | 9.8 | 30 mM ATP | 55 mM Mg acetate | - | 30 °C | 6.9 | 50 mM LCI | - | - | | |

| # | Ref Title | Authors | Pub-lished | Mutants | General comments | Protein name | Extinction coefficient as in | Purifi-cation | DgkA stock | Assay environment | Activator | Lipid substrate | Type of assay | Km nucleotide | Km lipid substrate | vmax (DAG varied, ATP varied) | Specific activity | ATP concen-tration | Mg concen-tration | Half-life nucleo-tidation | Notes and special parameters | Assay temp | pH | Salt | Assay buffer composition | Protein purification |
|----|-----------|---|------------------|--|--|--------------|------------------------------|---------------|------------------------------|---|-----------|--|--|---------------|--------------------|-------------------------------|-------------------|----------------------|-------------------|--|------------------------------|------------|------------|--|---|----------------------|
| | | | | WT | | | | | LCP | 5x 1µl LCP (60:40 MAC liquid) bolus (total 132 ng DgkA) | - | Branche-MAG | coupled assay, microtiter plate, in meso | | | 4.4 | 20 mM ATP | 55 mM Mg acetate | | | 30 °C | 6.9 | 50 mM LiCl | | | |
| | | | | WT | | | | | LCP | 5x 1µl LCP (60:40 MAC liquid) bolus (total 132 ng DgkA) | - | PAL | coupled assay, microtiter plate, in meso | | | 8.6 | 20 mM ATP | 55 mM Mg acetate | | | 30 °C | 6.9 | 50 mM LiCl | | | |
| | | | | WT | | | | | LCP | 5x 1µl LCP (28:72 MAC liquid) bolus (total 132 ng DgkA) | - | Phytantriol | coupled assay, microtiter plate, in meso | | | 0.7 | 20 mM ATP | 55 mM Mg acetate | | | 30 °C | 6.9 | 50 mM LiCl | | | |
| | | | | WT | | | | | LCP | 5x 1µl LCP (60:40 MAC liquid) bolus (total 132 ng DgkA) | - | Mycosol (Mycosol is a food-grade lipids containing mono-, di-, and tri-acylglycerols and free fatty acids. Predominant component is monocolin) | coupled assay, microtiter plate, in meso | | | 17.6 ± 1.2 | 20 mM ATP | 55 mM Mg acetate | | | 30 °C | 6.9 | 50 mM LiCl | | | |
| | | | | GLD | | | | | LCP | 5x 1µl LCP (60:40 monocolin:liquid) bolus (total 132 ng DgkA) | - | monocolin | coupled assay, microtiter plate, in meso | | | 16.8 ± 1.3 | 20 mM ATP | 55 mM Mg acetate | | | 30 °C | 6.9 | 50 mM LiCl | | | |
| | | | | WT | | | | | LCP | 5x 1µl LCP (60:40 monocolin:liquid) bolus (total 132 ng DgkA) | - | monocolin | coupled assay, microtiter plate, in meso | | | | Na ATP 30 mM | 0, 120 mM Mg acetate | | Magnesium Optimization: maximum activity at 55 mM Mg acetate | 30 °C | 6.9 | 50 mM LiCl | | | |
| | | | | WT | | | | | LCP | 5x 1µl LCP (60:40 monocolin:liquid) bolus >0 mg/ml -16 mg/ml | - | monocolin | coupled assay, microtiter plate, in meso | | | | Na ATP 20 mM | 55 mM Mg acetate | | Enzyme Loading Effects: The result indicates loading initially as expected, therefore that DgkA behaved catalytically. At higher concentrations, the rate dropped but became linear with loading again in the range of 0-16 mg protein/mL. | 30 °C | 6.9 | 50 mM LiCl | | | |
| | | | | WT | monocolin gets phosphorylated by DgkA | | | | LCP | 5x 1µl LCP (60:40 monocolin:liquid) bolus (total 132 ng DgkA) | - | monocolin | TLC | | | | Na ATP 20 mM | 55 mM Mg acetate | | | 30 °C | 6.9 | 50 mM LiCl | 0.1 mM EDTA, 0.1 mM EGTA, 0.2 mM DTT, 0.4 mM NADH, 20 U/mL PK and 10 U/mL PIPES, all in assay mix 2 as stated) | | |
| 47 | 485 | Lahiri, S.; Bha, M.; D. Chakraborty; D. Becker; C. F. W. Escherichia coli | 2011, March 23th | WT SR4C (for ligation purpose) | yield: 20 mg for each of the 4 segments, after ligation 4 mg | DAGK | 20 | | final step: loading into DDM | 0.5% DM | | dioleoylglycerol | | | | | | | | keat (s-1) 8 ± 2 | | | | | total chemical synthesis of 3 segments (Branche-MAG, PAL and Phytantriol) and native ligation in 8 M Urea and 20 mM LiCl in assay mix 2 in DgkA | |
| | | | | SR4C and IV25 to propionic acid with NBD fluorescent protein and N-termin bionin | NBD labelling | | | | final step: loading into DDM | 0.5% DM | | dioleoylglycerol | | | | | | | | keat (s-1) 7 ± 2 | | | | | | |

| # | Ref Title | Authors | Pub-lished | Mutants | General comments | Protein name | Extinction coefficient as in | Purifi-cation | DgGA stock | Assay environment | Activator | Lipid substrate | Type of assay | Km nucleotide | Km lipid substrate | vmax (DAG varied, ATP fixed) | Specific activity | ATP concen-tration | Mg concen-tration | Half-life | Notes and special parameters | Assay temp | pH | Salt | Assay buffer composition | Protein purification protocol |
|----|-----------|--|------------------|--|---|--------------|---------------------------------|---------------|------------|---|---------------------|-------------------------------------|---------------|---------------|-------------------------------|---|--|------------------------------|-------------------|---|---|------------|-----|------------|---|--|
| 46 | 291 | Ullrich, S.; Helmich, Ullrich, S.; Glauholz, C. | 2011, March 20th | A4 (GLLD) | 31P MAS NMR ATPγS, DAG ATP ortho vanadate | DGK | - | - | DM | 18 μmol DOPC (1:120 PL) 2.1 mg (0.15 μmol) DgGA | - | 0.175 μmol DBG (2.5 mM or 1.0 mol%) | 1P MAS NMR | 1.9 ± 1.3 mM | 3.7 ± 1.3 mM (1.4 ± 0.5 mol%) | 0.0085 min ⁻¹ (ATPase), 0.026 min ⁻¹ (ATPase), 0.0175 min ⁻¹ (ATPase), 0.3 mM (1.1 ± 0.1 mol%) | 1.45 × 10 ⁻³ min ⁻¹ (ATPase), 7.0(2) × 10 ⁻³ min ⁻¹ (ATPase) | 2 μmol (30 mM) ATP | - | - | HL: 1.4 ± 0.4 (DBG), 3.2 ± 0.4 (ATP) | - | - | - | - | - |
| 47 | 166 | Shi, P.; Wang, H.; Xu, Z.; Shi, Y.; Tian, C. | 2010, Nov | Fluo3-1/mim-DAGK | DPC micelles | DAGK | - | - | DM | 18 μmol DOPC (1:120 PL) 2.1 mg (0.15 μmol) DgGA | - | - | coupled assay | - | - | - | - | 3 mM ATP | 20 mM Mg acetate | - | before and after MAS NMR | 30 °C | 6.8 | 50 mM LiCl | 60 mM PIPES, 0.1 mM EDTA, 1 mM MgCl ₂ , 1 mM NMDH, 20 U LDH and PK | - |
| 44 | 265 | Koester, J.; Sulejro, E.; Saekura, H.; Hoshino, J.; Ehr, C.; Stenders, C. R. | 2010, July | finally real WT μSD005 also in Sanders group | - | DAGK | 2.18 (mg/mL) 1 cm ⁻¹ | 37 and 43 | DM | 21 mM DM (18 mM micellar) | 0.66 mM cardiolipin | 7.8 mM DBG | coupled assay | - | - | - | 16 | 3 mM MgATP +12 mM Mg acetate | 50 mM LiCl | - | - | 30 °C | 6.9 | 50 mM LiCl | 0.1 mM EGTA, 0.1 mM EDTA, 75 mM NTA, 1 mM PIPES, 1 mM HEP, 0.25 mM NaCl | Emgen BB NTA, detergent to exchange of cholest |
| | | | | | - | DAGK | 2.18 (mg/mL) 1 cm ⁻¹ | 37 and 43 | DM | 0.5% w/v DM | - | 7.8 mM DBG | coupled assay | - | - | 0.3 | 3 mM MgATP +12 mM Mg acetate | 50 mM LiCl | - | 7.7 ± 0.4 d (pH 7.8), 12.6 ± 0.7 d (pH 6.5), 1.7 ± 0.7 h (pH 7.8), 5.1 ± 0.3 h (pH 6.5) | half life at 45 °C, 70 °C | 30 °C | 6.9 | 50 mM LiCl | - | - |
| | | | | | - | DAGK | 2.18 (mg/mL) 1 cm ⁻¹ | 37 and 43 | LLPC | 0.5% w/v LLPC | - | 7.8 mM DBG | coupled assay | - | - | 18 ± 6 | 3 mM MgATP +12 mM Mg acetate | 50 mM LiCl | - | - | - | 30 °C | 6.9 | 50 mM LiCl | - | - |
| | | | | | - | DAGK | 2.18 (mg/mL) 1 cm ⁻¹ | 37 and 43 | DM | 0.2% w/v LMPC | - | 7.8 mM DBG | coupled assay | - | - | 66 | 3 mM MgATP +12 mM Mg acetate | 50 mM LiCl | - | - | - | 30 °C | 6.9 | 50 mM LiCl | - | - |
| | | | | | - | DAGK | 2.18 (mg/mL) 1 cm ⁻¹ | 37 and 43 | LMPC | 0.2% w/v LMPC | - | 7.8 mM DBG | coupled assay | 0.5 ± 0.02 mM | 4.7 ± 0.2 mM | 119 ± 6, 91 ± 5 (20 mM DBG, 3 mM ATP) | 3 mM MgATP +12 mM Mg acetate | 50 mM LiCl | - | 1.9 ± 0.1 d (pH 7.8), 8.0 ± 0.4 d (pH 6.5), 0.7 ± 0.2 h (pH 7.8), 4.6 ± 0.3 h (pH 6.5) | HL: 1.4 (DBG), 1.8 (ATP); half life at 45 °C, 70 °C | 30 °C | 6.9 | 50 mM LiCl | - | - |
| | | | | | - | DAGK | 2.18 (mg/mL) 1 cm ⁻¹ | 37 and 43 | LPFC | 0.2% w/v LPFC | - | 7.8 mM DBG | coupled assay | - | - | 44 ± 2 | 3 mM MgATP +12 mM Mg acetate | 50 mM LiCl | - | - | - | 30 °C | 6.9 | 50 mM LiCl | - | - |
| | | | | | - | DAGK | 2.18 (mg/mL) 1 cm ⁻¹ | 37 and 43 | DM | 0.2% w/v LMFG | - | 7.8 mM DBG | coupled assay | - | - | 22 | 3 mM MgATP +12 mM Mg acetate | 50 mM LiCl | - | - | - | 30 °C | 6.9 | 50 mM LiCl | - | - |
| | | | | | - | DAGK | 2.18 (mg/mL) 1 cm ⁻¹ | 37 and 43 | LMFG | 0.2% w/v LMFG | - | 7.8 mM DBG | coupled assay | 0.5 ± 0.02 mM | 7.9 ± 0.4 mM | 50 ± 3, 46 ± 3 (20 mM DBG, 3 mM ATP) | 3 mM MgATP +12 mM Mg acetate | 50 mM LiCl | - | 0.1 ± 0.01 d (pH 7.8), 8.8 ± 0.5 d (pH 6.5), 0.7 ± 0.1 h (pH 7.8), 3.5 ± 0.2 h (pH 6.5) | HL: 1.6 (DBG), 1.5 (ATP); half life at 45 °C, 70 °C | 30 °C | 6.9 | 50 mM LiCl | - | - |
| | | | | | - | DAGK | 2.18 (mg/mL) 1 cm ⁻¹ | 37 and 43 | LPFG | 0.2% w/v LPFG | - | 7.8 mM DBG | coupled assay | - | - | 16.6 ± 5 | 3 mM MgATP +12 mM Mg acetate | 50 mM LiCl | - | - | - | 30 °C | 6.9 | 50 mM LiCl | - | - |

| # | Ref Title | Authors | Pub-lished | Mutants | General comments | Protein name | Extinction coefficient | Assay as in | Purifi-cation | DgKA stock | Assay environment | Activator | Lipid substrate | Type of assay | Km nucleotide | Km lipid substrate | vmax (DAG varied; ATP varied) | Specific activity | ATP concen-tration | Mg concen-tration | Half-life nucle-otidation | Notes and special parameters | Assay temp | pH | Salt | Assay buffer composition | Protein purification sheet | |
|----|-----------|--|--|---|---|--------------|--|------------------------|---------------|--|--|---------------------------------|---|---------------|----------------|--------------------|---|-------------------|-------------------------------|-------------------------------|---|---|--------------------------------------|-----------|-----------|--------------------------|----------------------------|--|
| 43 | 2864 | Solution nuclear magnetic resonance studies of the structure of the C48A, C113A, and C113A/C48A double mutant of the yeast diacylglycerol kinase | Van Horn, W. D.; Kim, H. J.; Ellis, D.; Havelin, H.; Suijlo, E.; S. ; Kara, D. ; T. Ishi, C. ; Somnathsen, F. D. ; G. R. | WT (W117RS118 T) or Cytless (W117RS118T C48A, C113A or W117RS118T C48A, C113A, C113A) which one of each measurement | Catalytic activities of single-cysteine mutant forms of DAGK (Cytless) and double-cysteine mutant forms of DAGK (Cytless C48A, C113A or W117RS118T C48A, C113A, C113A) after purification and refolding into vesicles | DAGK | - | DPC | DPC | DM | 0.2% w/w TDFC | not stated | 7.8 mM DBG | coupled assay | 1.4 ± 0.07 mM | 8.9 ± 0.4 mM | 17 ± 1, 23 ± 2 (20 mM DBG, 3 mM ATP) | 10 ± 1 | 3 mM Mg/ATP +12 mM Mg acetate | 3 mM Mg/ATP +12 mM Mg acetate | 0.7 ± 0.1 d (pH 7.8), 10.1 ± 0.5 d (pH 6.5), 0.7 ± 0.1 d (pH 7.8), 5.0 ± 0.3 h (pH 6.5) | + DTI to prevent disulfide bond formations (no conc stated) | 30 °C | 6.9 | 50 mM LCI | | | |
| | | | | | | | 31 | | | DM | 0.5% w/w DPC | | 7.8 mM DBG | coupled assay | | | | 0.1 | 3 mM Mg/ATP +12 mM Mg acetate | | | 30 °C | 6.9 | 50 mM LCI | | | | |
| | | | | | | | | DPC | DPC | DM | 0.5% w/w DPC | | 7.8 mM DBG | coupled assay | | | | 0.3 | 3 mM Mg/ATP +12 mM Mg acetate | | | 30 °C | 6.9 | 50 mM LCI | | | | |
| | | | | | | | | DM | DM | DM | 0.2% w/w TDFC | | 7.8 mM DBG | coupled assay | | | | 28 | 3 mM Mg/ATP +12 mM Mg acetate | | | 30 °C | 6.9 | 50 mM LCI | | | | |
| | | | | | | | | TDFC | | DM | 0.2% w/w TDFC | | 7.8 mM DBG | coupled assay | | | | 10 ± 1 | 3 mM Mg/ATP +12 mM Mg acetate | | | 30 °C | 6.9 | 50 mM LCI | | | | |
| | | | | | | | | DM | | DM | 0.2% w/w ASB-14 | | 7.8 mM DBG | coupled assay | | | | 0.6 | 3 mM Mg/ATP +12 mM Mg acetate | | | 30 °C | 6.9 | 50 mM LCI | | | | |
| | | | | | | | | DM | | DM | the following: 0.5% CyF-7, 0.2% z3-14, 2.0% LS, 0.5% DTAB, 0.5% DMSO, 0.5% did not show activity | | 7.8 mM DBG | coupled assay | | | | -0 | 3 mM Mg/ATP +12 mM Mg acetate | | | | 30 °C | 6.9 | 50 mM LCI | | | |
| | | | | | | | | DPC | | DPC | POPC | not stated | 2.5 mM DBG | coupled assay | | | | 60 ± 10 | 10 mM ATP | 20 mM Mg acetate | | + DTI to prevent disulfide bond formations (no conc stated) | not stated. Cited paper variety of T | 6.9 | | | | |
| | | | | | | | | DPC | | DPC | DM redissolved POPC liposomes | maybe 0.66 mM (3m%) cardiolipin | dihexanoylglycerol | coupled assay | | | | 100 ± 8 | 10 mM ATP | 20 mM Mg acetate | | + DTI to prevent disulfide bond formations (no conc stated) | not stated. Cited paper variety of T | 6.9 | | | | |
| | | | | | | | | | | | E. coli native membranes | not stated | DBG | coupled assay | | | | | | | | | | | | | | |
| 42 | 271 | A fluorescence resonance energy transfer study of the interaction of the alpha-helices in membrane proteins: studies of diacylglycerol kinase | Jitticon, L. ; Lee, J. ; M. ; Lee, A. ; G. | WT (pSD004) or Cytless (pSD005) (depending when they get it) (see (32) and (34)) | NBD labelling several Cytless mutants, NBD labelling | DGK | 30800 M ⁻¹ cm ⁻¹ | 32: some modifications | 32 | DM + cholate, reconstitution of DgkA by dilution below CMC | 8 μmol DOPC (16000 P/L) | not stated | 20 mM dihexanoylglycerol co-reconstituted | coupled assay | 0.34 ± 0.03 mM | 9.2 ± 1.8 mM | 95.3 ± 8.7, 100 ± 1.5, 100 ± 1.5, 100 ± 1.5 mM ATP) | -65 | 5 mM ATP | 20 mM Mg ²⁺ | | | 25 °C | 6.9 | | | | |
| | | | | | | | | | | DM + cholate, reconstitution of DgkA by dilution below CMC | 8 μmol DOPC (16000 P/L) | | 20 mM dihexanoylglycerol co-reconstituted | coupled assay | | | | -63 | 5 mM ATP | 20 mM Mg ²⁺ | | | 25 °C | 6.9 | | | | |
| | | | | | | | | | | DM + cholate, reconstitution of DgkA by dilution below CMC | 8 μmol DOPC (16000 P/L) | | 20 mM dihexanoylglycerol co-reconstituted | coupled assay | 0.13 ± 0.01 mM | 4.9 ± 1.7 mM | 114.0 ± 12.9, 117.4 ± 1.5, 117.4 ± 1.5, 117.4 ± 1.5 mM ATP) | -63 | 5 mM ATP | 20 mM Mg ²⁺ | | | 25 °C | 6.9 | | | | |

| # | Ref Title | Authors | Published | Mutants | General comments | Protein name | Extinction coefficient | Assay as in | Purification | DgkA stock | Assay environment | Activator | Lipid substrate | Type of assay | Km nucleotide | Km lipid substrate | vmax (DAG varied; ATP varied) | Specific activity | ATP concentration | Mg concentration | Half-life nucleation | Notes and special parameters | Assay temp | pH | Salt | Assay buffer composition | Protein purification |
|----|--|---|-------------|---|------------------|--------------|--|-------------------|--------------|---|-------------------|----------------------|---------------------------|---|------------------------------|--------------------------------|---|--|------------------------|------------------------|---------------------------------------|--|-----------------|-----|------|---|----------------------|
| 36 | 4481 A transmembrane Segment Mimic Derived from Escherichia coli DgkA Lipid Kinase Inhibits Protein Activity | Partridge, A. W., Meryk, R., Escherichia coli DgkA Lipid Kinase Inhibits Protein Activity | 2003, March | WT (and Oye-C8A-C113A? also referred to as SDD004), Flg1 Sequence of TM3 is of real WT | | DGK | 25 | DM | 20 | DM | 1.5% OG | 3.5 mol% cardiolipin | 7.0 mol% dioleoylglycerol | coupled assay microtiter plate | | | 23 | | | 12.5 mM MgCl2 | | using saturating substrate concentrations (whatever these are) | not stated, RT? | 6.9 | | | |
| 35 | 266 Amphipols can support the activity of a membrane enzyme | Gozzelle, B., Hofman, A. K., Gouy, M., D. N.; Ray, D. G.; Sanders, G. R. | 2002, July | sSD004 = W117R, S118T | | DGK | 22 | DM | 20 | DM | 0.5% DM | 3 mol% cardiolipin | DGK | coupled assay | 0.8 ± 0.1 mM | | 61.4 ± 8 (10 mM varied) DBG, ATP | 51 | 3 mM ATP | | | | 30 °C | 6.9 | | | |
| | | | | | | | | | | | | | | coupled assay | | | 1.5 no Michaelis-Menten kinetics observed | 1 | 3 mM ATP | | no Michaelis-Menten kinetics observed | 30 °C | 6.9 | | | | |
| | | | | | | | | | | | | | | coupled assay | 1.0 ± 0.3 mM | 70 ± 11 (10 mM varied) | 53 | 3 mM ATP | | | | 30 °C | 6.9 | | | | |
| | | | | | | | | | | | | | | coupled assay | 1.3 ± 0.2 mM | 40 ± 5 (10 mM varied) DBG, ATP | 36 | 3 mM ATP | | | | 30 °C | 6.9 | | | | |
| | | | | | | | | | | | | | | coupled assay | | | 27 | 3 mM ATP | | | | 30 °C | 6.9 | | | | |
| | | | | | | | | | | | | | | coupled assay | | | 27 | 3 mM ATP | | | | 30 °C | 6.9 | | | | |
| | | | | | | | | | | | | | | coupled assay | | | 1 | 3 mM ATP | | | | 30 °C | 6.9 | | | | |
| | | | | | | | | | | | | | | coupled assay | | | 1 | 3 mM ATP | | | | 30 °C | 6.9 | | | | |
| | | | | | | | | | | | | | | coupled assay | | | <1 | 3 mM ATP | | | | 30 °C | 6.9 | | | | |
| 34 | 135 Effects of phospholipid headgroup and phase on the activity of diacylglycerol kinase of Escherichia coli | Eng, J. D., Erki, J. M., Lee, A. G. | 2001, Nov | WT could be sSD004/W117R, S118T or could also be sSD004 (apparently a mutant of sSD004) when they got it from Bowie (lab) | | DGK | 26200 M ⁻¹ cm ⁻¹ | DOPC (1:6000 P:L) | 32 | DM + choline reconstitution of DgkA by dilution below CMC | DOPC (1:6000 P:L) | | | 20 mol% dihexanoylglycerol co-reconstituted | coupled assay quartz cuvette | 0.31 ± 0.01 mM | 4.9 ± 0.2 mol% | 74.5 ± 1.2, 64.8 ± 0.8/20 mol% DHG, 5 mm ATP | 60.5 | 20 mM Mg ²⁺ | | | 25 °C | 6.9 | | 50 mM PIPES, 3 mM PEP, 0.2 mM NADH, 18 U PK, 22 U LDH | |
| | | | | | | | | | | | | | | coupled assay quartz cuvette | | 4.5 ± 0.2 mol% | 108.8 ± 1.7 (20 mol% DHG) | 60.5 | 20 mM Mg ²⁺ | | | 30 °C | 6.9 | | | | |
| | | | | | | | | | | | | | | coupled assay quartz cuvette | | | 0.2 | 20 mM ATP | | | | 25 °C | 6.9 | | | | |
| | | | | | | | | | | | | | | coupled assay quartz cuvette | | | 4.2 | 20 mM ATP | | | | 25 °C | 6.9 | | | | |

| # | Ref Title | Authors | Published | Mutants | General comments | Protein name | Extinction coefficient | Assay as in | Purification | DgKA stock | Assay environment | Activator | Lipid substrate | Type of assay | Km nucleotide | Km lipid substrate | vmax (DAG varied, ATP fixed) | Specific activity | ATP concentration | Mg concentration | Half-life nucleation | Notes and special parameters | Assay temp | pH | Salt | Assay buffer composition | Protein purification protocol |
|----|---|--|--|---|------------------|--------------|------------------------|---------------------------|---|--|--|-----------|--|--------------------------------|----------------|---|---|-------------------|------------------------|------------------------|----------------------|------------------------------|------------|-------------------------------------|--|--|-------------------------------|
| | | | | | | | | | | DM + cholate, reconstitution of DgKA by dilution below CMC | DOPG (1:6000 P:L) | - | 20 mol% dihexano/glycerol co-reconstituted | coupled assay quartz cuvette | | | 27.9 ± 3.7 mol% 16.7 ± 0.4 (20 mol% DHS, 5 mol% ATP) | 25 | 5 mM ATP | 20 mM Mg ²⁺ | | | 25 °C | 6.9 | - | | |
| | | | | | | | | | | DM + cholate, reconstitution of DgKA by dilution below CMC | cardiolipin (1:6000 P:L) | - | 20 mol% dihexano/glycerol co-reconstituted | coupled assay quartz cuvette | | | 4.3 | 5 mM ATP | 20 mM Mg ²⁺ | | | 25 °C | 6.9 | - | | | |
| | | | | | | | | | | DM + cholate, reconstitution of DgKA by dilution below CMC | 80% DOPC and 20% DOPG (1:6000 P:L) | - | 20 mol% dihexano/glycerol co-reconstituted | coupled assay quartz cuvette | | | 26.5 | 5 mM ATP | 20 mM Mg ²⁺ | | | 25 °C | 6.9 | - | | | |
| | | | | | | | | | | DM + cholate, reconstitution of DgKA by dilution below CMC | 75% DOPC, 20% DOPG, and 5% cardiolipin (1:6000 P:L) | - | 20 mol% dihexano/glycerol co-reconstituted | coupled assay quartz cuvette | | | 26.5 | 5 mM ATP | 20 mM Mg ²⁺ | | | 25 °C | 6.9 | - | | | |
| | | | | | | | | | | DM + cholate, reconstitution of DgKA by dilution below CMC | 75% DOPC, 15% DOPG, and 10% cardiolipin (1:6000 P:L) | - | 20 mol% dihexano/glycerol co-reconstituted | coupled assay quartz cuvette | | | 26.5 | 5 mM ATP | 20 mM Mg ²⁺ | | | 25 °C | 6.9 | - | | resembles E.coli lipid composition | |
| | | | | | | | | | | DM + cholate, reconstitution of DgKA by dilution below CMC | DMPG (1:6000 P:L) | - | 20 mol% dihexano/glycerol co-reconstituted | coupled assay quartz cuvette | 0.24 ± 0.02 mM | 27.9 ± 3.7 mol% 16.7 ± 0.4 (20 mol% DHS, 5 mol% ATP) | 47.9 ± 4.2 | 5 mM ATP | 20 mM Mg ²⁺ | | | 16 °C | 6.9 | - | | | |
| | | | | | | | | | | DM + cholate, reconstitution of DgKA by dilution below CMC | - | - | 20 mol% dihexano/glycerol co-reconstituted | coupled assay quartz cuvette | 0.38 ± 0.03 mM | 8.1 ± 0.2 mol% | 14.9 ± 0.3 | 5 mM ATP | 20 mM Mg ²⁺ | | | 20 °C (DHS) (ATP) | 6.9 | - | | | |
| | | | | | | | | | | DM + cholate, reconstitution of DgKA by dilution below CMC | 80% DOPC and 20% DOPA (1:6000 P:L) | - | 20 mol% dihexano/glycerol co-reconstituted | coupled assay quartz cuvette | 0.18 ± 0.02 mM | 19.1 ± 1.2 mol% | 25.3 ± 0.9 | 5 mM ATP | 20 mM Mg ²⁺ | | | 25 °C | 6.9 | - | | | |
| | | | | | | | | | | DM + cholate, reconstitution of DgKA by dilution below CMC | 80% DOPC and 20% DOPS (1:6000 P:L) | - | 20 mol% dihexano/glycerol co-reconstituted | coupled assay quartz cuvette | 0.25 ± 0.03 mM | 20.9 ± 2.3 mol% | 74.4 ± 4.9 | 5 mM ATP | 20 mM Mg ²⁺ | | | 25 °C | 6.9 | - | | | |
| | | | | | | | | | | DM + cholate, reconstitution of DgKA by dilution below CMC | 80% DOPC and 20% cardiolipin (1:6000 P:L) | - | 20 mol% dihexano/glycerol co-reconstituted | coupled assay quartz cuvette | 0.11 ± 0.01 mM | 3.8 ± 0.3 mol% | 42.1 ± 1.0 | 5 mM ATP | 20 mM Mg ²⁺ | | | 25 °C | 6.9 | - | | | |
| | | | | | | | | | | DM + cholate, reconstitution of DgKA by dilution below CMC | 80% DOPC and 20% DOPH (1:6000 P:L) | - | 20 mol% dihexano/glycerol co-reconstituted | coupled assay quartz cuvette | | 11.9 ± 0.7 mol% | 61.2 ± 1.7 (20 mol% DHS) | 5 mM ATP | 20 mM Mg ²⁺ | | | 25 °C | 6.9 | - | | | |
| | | | | | | | | | | DM + cholate, reconstitution of DgKA by dilution below CMC | 80% DOPC and 20% DOPG (1:6000 P:L) | - | 20 mol% dihexano/glycerol co-reconstituted | coupled assay quartz cuvette | | 5.4 ± 0.1 mol% | 86.6 ± 0.5 (20 mol% DHS) | 5 mM ATP | 20 mM Mg ²⁺ | | | 25 °C | 6.9 | - | | | |
| | | | | | | | | | | DM + cholate, reconstitution of DgKA by dilution below CMC | 50% DOPC and 50% DOPG (1:6000 P:L) | - | 40 mol% dihexano/glycerol co-reconstituted | coupled assay quartz cuvette | | 2.4 ± 0.2 mol% | 25.5 ± 0.6 (20 mol% DHS) | 5 mM ATP | 20 mM Mg ²⁺ | | | 25 °C | 6.9 | - | | | |
| | | | | | | | | | | DM + cholate, reconstitution of DgKA by dilution below CMC | 50% DOPC and 50% DOPG (1:6000 P:L) | - | 20 mol% dihexano/glycerol co-reconstituted | coupled assay quartz cuvette | | 19.2 ± 0.5 mol% | 56.8 ± 0.9 (20 mol% DHS) | 5 mM ATP | 20 mM Mg ²⁺ | | | 30 °C | 6.9 | - | | | |
| 33 | 280 Kinetic study of the effect of cardiolipin on the activity of diacylglycerol kinase in model membranes. | Nagy, J. K.; Mizer, W.; Sanders, C. R. | 2001, J. Biol. Chem. 276(11):11703-11708 | Cys-less Y11703-118 Y11703-118 C48A C113A | | DAGK | 2800.01 ± 1.3 | 22, but does not use DAG. | POPC (1:120 P:L) (reconstitutive refolding procedure as in (27)) | | | | 3 mM DAG | coupled assay microtiter plate | | | 32 | 5 mM ATP | 15 mM Mg(l) | | | 30 °C | 6.8 | 50 mM ClO ₄ ⁻ | Empan N-alkylmaleimide 1 mM EGTA, 1 mM DTT, 1 mM PEP, 0.5 mM NADH, | Empan N-alkylmaleimide 1 mM EGTA, 1 mM DTT, 1 mM PEP, 0.5 mM NADH, (1:120 P:L) | |

| # | Ref Title | Authors | Pub-lished | Mitigants | General comments | Protein name | Extinction coefficient | Assay as in | Purifi-cation | DgMA stock | Assay environment | Activator | Lipid substrate | Type of assay | Km nucleotide | Km lipid substrate | vmax (DAG varied, ATP varied) | Specific activity | ATP concen-tration | Mg concen-tration | Half-life nucle-ination | Notes and special parameters | Assay temp | pH | Salt | Assay buffer composition | Protein purification sheet |
|----|---|--------------------------|--------------------------------------|---|--|--------------|--|-------------|-------------------|--|---|------------------|-------------------------|--------------------------------|---------------|--------------------|-------------------------------|-------------------|--------------------|-------------------|-------------------------|------------------------------|------------|-----|-----------|--|----------------------------|
| | | | | | | | | | | POPC liposomes (1:120 P:L) vesicle assay with 1% DM (DMP-OPC 40:1) | 200 fold diluted into 1% fomic acid mix resulting in 2 mM vesicles and 40 nM POPC (80 nM) | - | 3 mM DBG | coupled assay microtiter plate | | | | | 3 mM ATP | 15 mM Mg(II) | | | 30 °C | 6.8 | 50 mM LCI | | |
| | | | | | | | | | | NHNTA eluted 6.5 M Urea 1% fomic acid | 200 fold diluted into 1% fomic acid mix resulting in 2 mM vesicles and 40 nM POPC (80 nM) | - | 3 mM DBG | coupled assay microtiter plate | | | | | 3 mM ATP | 15 mM Mg(II) | | | 30 °C | 6.8 | 50 mM LCI | | |
| | | | | | | | | | | NHNTA eluted 8 M GdnHCl | 200 fold diluted into 1% fomic acid mix resulting in 2 mM vesicles and 40 nM POPC (80 nM) | - | 3 mM DBG | coupled assay microtiter plate | | | | | 3 mM ATP | 15 mM Mg(II) | | | 30 °C | 6.8 | 50 mM LCI | | |
| | | | | | | | | | | NHNTA eluted 8 M GdnHCl | 200 fold diluted into 1% (21 mM) DM cardiolipin DHG mixed vesicles and 40 nM POPC (80 nM) | 3 mM cardiolipin | 5 mM dhexanoylglycerol | coupled assay microtiter plate | | | | | 3 mM ATP | 15 mM Mg(II) | | | 30 °C | 6.8 | 50 mM LCI | | |
| | | | | | | | | | | DM (POPC liposomes (1:120 P:L) vesicle assay redissolved with 1% DM (DMP-OPC 40:1)) | 200 fold diluted into 1% fomic acid mix resulting in 2 mM vesicles and 40 nM POPC (80 nM) | - | 3 mM DBG | coupled assay microtiter plate | | | | | 3 mM ATP | 15 mM Mg(II) | | | 30 °C | 6.8 | 50 mM LCI | | |
| | | | | | | | | | | BOG (POPC liposomes (1:120 P:L) vesicle assay redissolved with 1% DM (DMP-OPC 40:1)) | 200 fold diluted into 1% fomic acid mix resulting in 2 mM vesicles and 40 nM POPC (80 nM) | - | 3 mM DBG | coupled assay microtiter plate | | | | | 3 mM ATP | 15 mM Mg(II) | | | 30 °C | 6.8 | 50 mM LCI | | |
| | | | | | | | | | | SDS (POPC liposomes (1:120 P:L) vesicle assay redissolved with 1% SDS) | 200 fold diluted into 1% fomic acid mix resulting in 2 mM vesicles and 40 nM POPC (80 nM) | - | 3 mM DBG | coupled assay microtiter plate | | | | | 3 mM ATP | 15 mM Mg(II) | | | 30 °C | 6.8 | 50 mM LCI | | |
| 32 | 134 Effects of bilayer composition on the activity of diacylglycerol kinase of Escherichia coli | Pick, J. D.; Lane, A. G. | 2001, J. Biol. Chem. 276:11811-11817 | WT could be replaced by R.S1181T or pSD005 could also be replaced by pSD005 when they got it from Bowie (lab) | assay from Bowie lab pSD005 (depending when they got it) | DGK | 25200 M ⁻¹ cm ⁻¹ | as in | some modification | DM | 1.5% w/v OG | - | 5.1 mM dihexoylglycerol | coupled assay quartz cuvette | | | | 65.3 | 5 mM ATP | 20 mM Mg(II) | | | 25 °C | 6.9 | none | 2 mM MES, 0.5 mM NaOH, 18 U PKC, 22 U LDH, 80 mM Pipes | |
| | | | | | | | | | | DM | 1.5% w/v OG | - | 5.1 mM dihexoylglycerol | coupled assay quartz cuvette | | | | 1 | 5 mM ATP | 20 mM Mg(II) | | | 25 °C | 6.9 | none | | |
| | | | | | | | | | | DM | 1.5% w/v OG | cardiolipin | 5.1 mM dihexoylglycerol | coupled assay quartz cuvette | | | | 72.6 | 5 mM ATP | 20 mM Mg(II) | | | 25 °C | 6.9 | none | | |
| | | | | | | | | | | DM | 1.5% w/v OG | cardiolipin | 5.1 mM dihexoylglycerol | coupled assay quartz cuvette | | | | 24.2 | 5 mM ATP | 20 mM Mg(II) | | | 25 °C | 6.9 | none | | |
| | | | | | | | | | | DM | 1.5% w/v OG | DOPC | 5.1 mM dihexoylglycerol | coupled assay quartz cuvette | | | | 65.3 | 5 mM ATP | 20 mM Mg(II) | | | 25 °C | 6.9 | none | | |
| | | | | | | | | | | DM | 1.5% w/v OG | DOPC | 5.1 mM dihexoylglycerol | coupled assay quartz cuvette | | | | 1.5 | 5 mM ATP | 20 mM Mg(II) | | | 25 °C | 6.9 | none | | |
| | | | | | | | | | | DM | 1.5% w/v OG | DOPC | 5.1 mM dihexoylglycerol | coupled assay quartz cuvette | | | | 58.3 | 5 mM ATP | 20 mM Mg(II) | | | 25 °C | 6.9 | none | | |
| | | | | | | | | | | DM | 1.5% w/v OG | DMPG | 5.1 mM dihexoylglycerol | coupled assay quartz cuvette | | | | | 5 mM ATP | 20 mM Mg(II) | | | 25 °C | 6.9 | none | | |
| | | | | | | | | | | DM | 1.5% w/v OG | di(C22:1)PC | 5.1 mM dihexoylglycerol | coupled assay quartz cuvette | | | | | 5 mM ATP | 20 mM Mg(II) | | | 25 °C | 6.9 | none | | |
| | | | | | | | | | | DM | 1.5% w/v OG | DOPE | 5.1 mM dihexoylglycerol | coupled assay quartz cuvette | | | | | 5 mM ATP | 20 mM Mg(II) | | | 25 °C | 6.9 | none | | |
| | | | | | | | | | | DM | 1.5% w/v OG | DOPE | 5.1 mM dihexoylglycerol | coupled assay quartz cuvette | | | | | 5 mM ATP | 20 mM Mg(II) | | | 25 °C | 6.9 | none | | |
| | | | | | | | | | | DM | 1.5% w/v OG | GOPS | 5.1 mM dihexoylglycerol | coupled assay quartz cuvette | | | | | 5 mM ATP | 20 mM Mg(II) | | | 25 °C | 6.9 | none | | |
| | | | | | | | | | | DM | 1.5% w/v OG | DOPS | 5.1 mM dihexoylglycerol | coupled assay quartz cuvette | | | | | 5 mM ATP | 20 mM Mg(II) | | | 25 °C | 6.9 | none | | |
| | | | | | | | | | | DM | 1.5% w/v OG | DOPS | 5.1 mM dihexoylglycerol | coupled assay quartz cuvette | | | | | 5 mM ATP | 20 mM Mg(II) | | | 25 °C | 6.9 | none | | |

| # | Ref Title | Authors | Pub-lished | Mutants | General comments | Protein name | Extinction coefficient as in | Purification | DgkA stock | Assay environment | Activator | Lipid substrate | Type of assay | Km nucleotide | Km lipid substrate | vmax (DAG varied, ATP fixed) | Specific activity | ATP concentration | Mg concentration | Half-life nucleation | Notes and special parameters | Assay temp | pH | Salt | Assay buffer composition | Protein purification protocol |
|----|-----------|--|------------|---|---|--------------|------------------------------|--------------|---|-------------------------------------|-------------------------------------|--|------------------------------|----------------------|--------------------|--|-------------------|-------------------|------------------|---|---|------------|------------|---|--------------------------|-------------------------------|
| | | | | | | | | | DM | 1.5% w/v OG | 2.4 mol% DOPA | 5.1 mol% dioleoylglycerol | coupled assay quartz cuvette | | | | 70.3 | 5 mM | 20 mM Mg(l) | | | 25 °C | 6.9 | none | | |
| | | | | | | | | | DM | 1.5% w/v OG | 2.4 mol% DOPA | 5.1 mol% dihexanoylglycerol | coupled assay quartz cuvette | | | | 6.8 | 5 mM | 20 mM Mg(l) | | | 25 °C | 6.9 | none | | |
| | | | | | | | | | DM + cholate reconstitution of DgkA by dilution below CMC | d(C16:1)PC (1:6000 P:L) | - | 6.5 ± 6.7 mol% dihexanoylglycerol | coupled assay quartz cuvette | 1.83 ± 0.06 mM | | | -16 | 5 mM | 20 mM Mg(l) | | Specificity: Phospholipid concentration of (8 mol) and the required diacylglycerol (usually 2 μmol of DAG) were dried onto the walls of a thin glass vial. Buffer [400 μL, 60 mM Pipes (pH 6.9)] containing 0.1 mM EDTA was added, and the sample was sonicated to clarify in a bath sonicator (Ultrawave). DgkA (2 μg) was added and the reaction left at room temperature for 15 min. | 25 °C | 6.9 | none | | |
| | | | | | | | | | DM + cholate reconstitution of DgkA by dilution below CMC | d(C16:1)PC (1:6000 P:L) | - | 20 mol% dihexanoylglycerol | coupled assay quartz cuvette | -0.49 mM | -8.5 mol% | -76, -66 (20 mol% DAG, 5 mol% ATP) | -46 | 5 mM | 20 mM Mg(l) | | as above | 25 °C | 6.9 | none | | |
| | | | | | | | | | DM + cholate reconstitution of DgkA by dilution below CMC | DOPC (1:6000 P:L) | - | 20 mol% dihexanoylglycerol | coupled assay quartz cuvette | 0.21 ± 0.01 mM | 4.9 ± 0.7 mol% | -74.8 ± 1.2, -86 (20 mol% DAG, 5 mol% ATP) | -57 | 5 mM | 20 mM Mg(l) | | as above | 25 °C | 6.9 | none | | |
| | | | | | | | | | DM + cholate reconstitution of DgkA by dilution below CMC | d(C20:1)PC (1:6000 P:L) | - | 20 mol% dihexanoylglycerol | coupled assay quartz cuvette | -0.3 mM | -4 mol% | -83, -46 (20 mol% DAG, 5 mol% ATP) | -47 | 5 mM | 20 mM Mg(l) | | as above | 25 °C | 6.9 | none | | |
| | | | | | | | | | DM + cholate reconstitution of DgkA by dilution below CMC | d(C22:1)PC (1:6000 P:L) | - | 20 mol% dihexanoylglycerol | coupled assay quartz cuvette | -0.21 mM | -3 mol% | -43, -36 (20 mol% DAG, 5 mol% ATP) | -37 | 5 mM | 20 mM Mg(l) | | as above | 25 °C | 6.9 | none | | |
| | | | | | | | | | DM + cholate reconstitution of DgkA by dilution below CMC | d(C24:1)PC (1:6000 P:L) | - | 20 mol% dihexanoylglycerol | coupled assay quartz cuvette | -0.19 mM | -1.5 mol% | -26, -21 (20 mol% DAG, 5 mol% ATP) | -19 | 5 mM | 20 mM Mg(l) | | as above | 25 °C | 6.9 | none | | |
| | | | | | | | | | DM + cholate reconstitution of DgkA by dilution below CMC | d(C14:1)PC:cholesterol (1:6000 P:L) | - | 20 mol% dihexanoylglycerol | coupled assay quartz cuvette | | 31.9 ± 3.8 mol% | 87.8 ± 6.7 | | 5 mM | 20 mM Mg(l) | | as above | 25 °C | 6.9 | none | | |
| | | | | | | | | | DM + cholate reconstitution of DgkA by dilution below CMC | DOPC (1:6000 P:L) | - | 20 mol% dihexanoylglycerol in empty DOPC liposomes → 14.3 mol% DAG | coupled assay quartz cuvette | | | | 28 | 5 mM | 20 mM Mg(l) | | | 25 °C | 6.9 | none | | |
| | | | | | | | | | DM + cholate reconstitution of DgkA by dilution below CMC | DOPC (1:6000 P:L) | - | 20 mol% dihexanoylglycerol in empty DOPC liposomes → 14.3 mol% DAG | coupled assay quartz cuvette | | | | 57 | 5 mM | 20 mM Mg(l) | | | 25 °C | 6.9 | none | | |
| 31 | 267 | Charakl, L., 2000; Charakl, L., Sept C. R. | | DgkA Oye-less (W117R,S118) (T-C46A,C113) (A17,ISSC,T02) | Coupled assay with liposomes would orient in NMR, above Laipha transition | DAGK | - | 21 and 27 | DM | 21 mM DM | 0.66 mM (3 heavy bovine cardiolipin | 2.5 mM DAG | coupled assay | 1.2 ± 0.5 mM (50 °C) | | -40, -30, -20 (20 mol% DAG, 40, 45 °C) | 10 mM ATP | 20 mM acetate | | (vmax similar to specific activity, but DAG was never detected) | 20, 40, 60 °C | 6.9 | 50 mM LiCl | 5 mM PEP, 2.5 mM DTT, 10 mM PK, 34 U/ml LDH, 75 mM Pipes, 0.1 mM EDTA, 0.1 mM | | |
| | | | | | | | | | DM | 10% weight/volume DHP:DMPC 12.7 | - | 2.5 mM DAG | coupled assay | 1.2 ± 0.5 mM (40 °C) | | -18 | 10 mM ATP | 20 mM acetate | | (vmax similar to specific activity, but DAG was never detected) | 40 °C | 6.9 | 50 mM LiCl | | | |
| | | | | | | | | | DM | 10% weight/volume GHP-SO:DLPC 13.5 | - | 2.5 mM DAG | coupled assay | | | -12 | 10 mM ATP | 20 mM acetate | | | 20 °C | 6.9 | 50 mM LiCl | | | |
| | | | | | | | | | DM | 10% weight/volume DHP:DLPC 13 | - | 2.5 mM DAG | coupled assay | 1.8 ± 0.5 mM (25 °C) | | -6.7 | 10 mM ATP | 20 mM acetate | | (vmax similar to specific activity, but DAG was never detected) | 20 °C | 6.9 | 50 mM LiCl | | | |

| Ref | Title | Authors | Published | Mutants | General comments | Protein name | Extinction coefficient | Assay as in | Purification | DgMA stock | Assay environment | Activator | Lipid substrate | Type of assay | Km nucleotide | Km lipid substrate | vmax (DAG varied, ATP fixed) | Specific activity between 15°C and 55°C (15 min) and unheated | ATP concentration | Mg concentration | Half-life inactivation | Notes and special parameters | Assay temp | pH | Salt | Assay buffer composition | Protein purification protocol |
|-----|---|---|-------------|--|--|----------------------|------------------------|-------------|--|---------------------------|--------------------------------|--------------------------------|------------------|------------------|---|--------------------------------|--|---|--|--|------------------------|------------------------------|---|---|--|--------------------------|-------------------------------|
| 28 | 2860 Building a thermostable membrane protein | Zhou, Y.; Bowers, J. U. | 2000, March | Correction of plasmid sequence to read for expression in yeast (pSD009) and introduction of mutation in CLLD (D5K) | Introduction of real WT (pSD005) and CLLD Δ4 (pSD009) which has reduced activity in different detergents. Experiments found the thermostable mutations by screening Cytases (26) IS3C, I70C, I70L, I70M, I70N, I70P, I70Q, I70R, I70S, I70T, I70V, I70W, I70X, I70Y, I70Z, I70AA, I70AB, I70AC, I70AD, I70AE, I70AF, I70AG, I70AH, I70AI, I70AJ, I70AK, I70AL, I70AM, I70AN, I70AO, I70AP, I70AQ, I70AR, I70AS, I70AT, I70AU, I70AV, I70AW, I70AX, I70AY, I70AZ, I70BA, I70BB, I70BC, I70BD, I70BE, I70BF, I70BG, I70BH, I70BI, I70BJ, I70BK, I70BL, I70BM, I70BN, I70BO, I70BP, I70BQ, I70BR, I70BS, I70BT, I70BU, I70BV, I70BW, I70BX, I70BY, I70BZ, I70CA, I70CB, I70CC, I70CD, I70CE, I70CF, I70CG, I70CH, I70CI, I70CJ, I70CK, I70CL, I70CM, I70CN, I70CO, I70CP, I70CQ, I70CR, I70CS, I70CT, I70CU, I70CV, I70CW, I70CX, I70CY, I70CZ, I70DA, I70DB, I70DC, I70DD, I70DE, I70DF, I70DG, I70DH, I70DI, I70DJ, I70DK, I70DL, I70DM, I70DN, I70DO, I70DP, I70DQ, I70DR, I70DS, I70DT, I70DU, I70DV, I70DW, I70DX, I70DY, I70DZ, I70EA, I70EB, I70EC, I70ED, I70EE, I70EF, I70EG, I70EH, I70EI, I70EJ, I70EK, I70EL, I70EM, I70EN, I70EO, I70EP, I70EQ, I70ER, I70ES, I70ET, I70EU, I70EV, I70EW, I70EX, I70EY, I70EZ, I70FA, I70FB, I70FC, I70FD, I70FE, I70FF, I70FG, I70FH, I70FI, I70FJ, I70FK, I70FL, I70FM, I70FN, I70FO, I70FP, I70FQ, I70FR, I70FS, I70FT, I70FU, I70FV, I70FW, I70FX, I70FY, I70FZ, I70GA, I70GB, I70GC, I70GD, I70GE, I70GF, I70GG, I70GH, I70GI, I70GJ, I70GK, I70GL, I70GM, I70GN, I70GO, I70GP, I70GQ, I70GR, I70GS, I70GT, I70GU, I70GV, I70GW, I70GX, I70GY, I70GZ, I70HA, I70HB, I70HC, I70HD, I70HE, I70HF, I70HG, I70HH, I70HI, I70HJ, I70HK, I70HL, I70HM, I70HN, I70HO, I70HP, I70HQ, I70HR, I70HS, I70HT, I70HU, I70HV, I70HW, I70HX, I70HY, I70HZ, I70IA, I70IB, I70IC, I70ID, I70IE, I70IF, I70IG, I70IH, I70II, I70IJ, I70IK, I70IL, I70IM, I70IN, I70IO, I70IP, I70IQ, I70IR, I70IS, I70IT, I70IU, I70IV, I70IW, I70IX, I70IY, I70IZ, I70JA, I70JB, I70JC, I70JD, I70JE, I70JF, I70JG, I70JH, I70JI, I70JJ, I70JK, I70JL, I70JM, I70JN, I70JO, I70JP, I70JQ, I70JR, I70JS, I70JT, I70JU, I70JV, I70JW, I70JX, I70JY, I70JZ, I70KA, I70KB, I70KC, I70KD, I70KE, I70KF, I70KG, I70KH, I70KI, I70KJ, I70KL, I70KM, I70KN, I70KO, I70KP, I70KQ, I70KR, I70KS, I70KT, I70KU, I70KV, I70KW, I70KX, I70KY, I70KZ, I70LA, I70LB, I70LC, I70LD, I70LE, I70LF, I70LG, I70LH, I70LI, I70LJ, I70LK, I70LL, I70LM, I70LN, I70LO, I70LP, I70LQ, I70LR, I70LS, I70LT, I70LU, I70LV, I70LW, I70LX, I70LY, I70LZ, I70MA, I70MB, I70MC, I70MD, I70ME, I70MF, I70MG, I70MH, I70MI, I70MJ, I70MK, I70ML, I70MN, I70MO, I70MP, I70MQ, I70MR, I70MS, I70MT, I70MU, I70MV, I70MW, I70MX, I70MY, I70MZ, I70NA, I70NB, I70NC, I70ND, I70NE, I70NF, I70NG, I70NH, I70NI, I70NJ, I70NK, I70NL, I70NM, I70NO, I70NP, I70NQ, I70NR, I70NS, I70NT, I70NU, I70NV, I70NW, I70NX, I70NY, I70NZ, I70OA, I70OB, I70OC, I70OD, I70OE, I70OF, I70OG, I70OH, I70OI, I70OJ, I70OK, I70OL, I70OM, I70ON, I70OO, I70OP, I70OQ, I70OR, I70OS, I70OT, I70OU, I70OV, I70OW, I70OX, I70OY, I70OZ, I70PA, I70PB, I70PC, I70PD, I70PE, I70PF, I70PG, I70PH, I70PI, I70PJ, I70PK, I70PL, I70PM, I70PN, I70PO, I70PP, I70PQ, I70PR, I70PS, I70PT, I70PU, I70PV, I70PW, I70PX, I70PY, I70PZ, I70QA, I70QB, I70QC, I70QD, I70QE, I70QF, I70QG, I70QH, I70QI, I70QJ, I70QK, I70QL, I70QM, I70QN, I70QO, I70QP, I70QQ, I70QR, I70QS, I70QT, I70QU, I70QV, I70QW, I70QX, I70QY, I70QZ, I70RA, I70RB, I70RC, I70RD, I70RE, I70RF, I70RG, I70RH, I70RI, I70RJ, I70RK, I70RL, I70RM, I70RN, I70RO, I70RP, I70RQ, I70RR, I70RS, I70RT, I70RU, I70RV, I70RW, I70RX, I70RY, I70RZ, I70SA, I70SB, I70SC, I70SD, I70SE, I70SF, I70SG, I70SH, I70SI, I70SJ, I70SK, I70SL, I70SM, I70SN, I70SO, I70SP, I70SQ, I70SR, I70SS, I70ST, I70SU, I70SV, I70SW, I70SX, I70SY, I70SZ, I70TA, I70TB, I70TC, I70TD, I70TE, I70TF, I70TG, I70TH, I70TI, I70TJ, I70TK, I70TL, I70TM, I70TN, I70TO, I70TP, I70TQ, I70TR, I70TS, I70TT, I70TU, I70TV, I70TW, I70TX, I70TY, I70TZ, I70UA, I70UB, I70UC, I70UD, I70UE, I70UF, I70UG, I70UH, I70UI, I70UJ, I70UK, I70UL, I70UM, I70UN, I70UO, I70UP, I70UQ, I70UR, I70US, I70UT, I70UU, I70UV, I70UW, I70UX, I70UY, I70UZ, I70VA, I70VB, I70VC, I70VD, I70VE, I70VF, I70VG, I70VH, I70VI, I70VJ, I70VK, I70VL, I70VM, I70VN, I70VO, I70VP, I70VQ, I70VR, I70VS, I70VT, I70VU, I70VV, I70VW, I70VX, I70VY, I70VZ, I70WA, I70WB, I70WC, I70WD, I70WE, I70WF, I70WG, I70WH, I70WI, I70WJ, I70WK, I70WL, I70WM, I70WN, I70WO, I70WP, I70WQ, I70WR, I70WS, I70WT, I70WU, I70WV, I70WW, I70WX, I70WY, I70WZ, I70XA, I70XB, I70XC, I70XD, I70XE, I70XF, I70XG, I70XH, I70XI, I70XJ, I70XK, I70XL, I70XM, I70XN, I70XO, I70XP, I70XQ, I70XR, I70XS, I70XT, I70XU, I70XV, I70XW, I70XX, I70XY, I70XZ, I70YA, I70YB, I70YC, I70YD, I70YE, I70YF, I70YG, I70YH, I70YI, I70YJ, I70YK, I70YL, I70YM, I70YN, I70YO, I70YP, I70YQ, I70YR, I70YS, I70YT, I70YU, I70YV, I70YW, I70YX, I70YY, I70YZ, I70ZA, I70ZB, I70ZC, I70ZD, I70ZE, I70ZF, I70ZG, I70ZH, I70ZI, I70ZJ, I70ZK, I70ZL, I70ZM, I70ZN, I70ZO, I70ZP, I70ZQ, I70ZR, I70ZS, I70ZT, I70ZU, I70ZV, I70ZW, I70ZX, I70ZY, I70ZZ | See general comments | DM | 1.5% OG | 3.5 mol% cardiolipin | 7.0 mol% dioleoylglycerol | coupled assay microtiter plate | 0.24 ± 0.01 mM | 1.37 ± 0.02 mol% | 87.4 ± 8.8 | fractional activity between 15°C and 55°C (15 min) and unheated | 10 mM Mg ATP | 10 mM Mg ATP + 15 mM MgCl ₂ | 5.7 ± 0.2 min | Figure 3 (temperature dependent) after 10 min: OG detergents after 10 min: OG -45 °C, LDAO -45 °C, Empigen 5545 -45 °C, Cymal-5 -45 °C, half life at 55 °C, 80 °C, 1.5% OG pH 7.5 50 mM Na ₃ PO ₄ 0.3 M NaCl | RT7 | 6.9 | none? | 1 mM PEP, 2.5 mM NADH, 14 U PK, 22 U LDH, 80 mM PIPES | NINJA, OG purification in 25 | | | |
| 27 | 2868 Recombinative refolding of kinase, an integral membrane protein | Goedels, B.; M. Nagy, J. K.; Owend, W.; Loner, W.; Loner, C. R. | 1999, Nov | 63 single mutants purified and assayed for activity (basis is O ₂ less mutant), (pSD004 + C48A, C113A) | WT DNA base is likely all literature from 1997 (for historical reasons). DgMA overproduction in inclusion bodies (less mutant), (pSD004 + C48A, C113A) | DAGK | 280,011 ± 1.8 | DM and DMS | DM and FORC (1:20) PLU and after liposome back to detergent (also refer to later published, which could refer to 31) | 3.5 mol% cardiolipin | 7.0 mol% dioleoylglycerol | coupled assay microtiter plate | 0.18 ± 0.02 mM | 0.85 ± 0.03 mol% | 56.9 ± 4.6 | coupled assay microtiter plate | 10 mM Mg ATP | 10 mM Mg ATP + 15 mM MgCl ₂ | 28.7 ± 1.6 min | Figure 3 (temperature dependent) after 10 min: OG -45-75 °C, LDAO -75 °C, Empigen -85 °C, Cymal-5 -85 °C, half life at 100 °C, 1.5% OG pH 7.5 50 mM Na ₃ PO ₄ 0.3 M NaCl | RT7 | 6.9 | none? | 60 mM PIPES, 0.1 mM EDTA, 1 mM PEP, 0.25 mM NADH, 14 U LDH and PK | NINJA, OG or Empigen higher yield than other detergents (for activity data!) then DM | | |
| 26 | 489 Changing single side-chains can greatly enhance a membrane protein to irreversible inactivation | Lau, F.-W.; Nauli, S.; Zhou, Y.; Bowers, J. U. | 1999, July | Cysteine less mutants (pSD004, I70L, C48A, C113A) | Assay as in 25 which refer to specific activity to 20, when say communications (Assay used but not explained in 18. Most likely later kinetic parameters 25 refers to 23 (Triton X-100). Cysteine mutant, I53C I70C (no disulfide bridge forming) | DgK | 280,011 ± 1.8 | DM | 0.7% Triton X-100 | 3.5 mol% cardiolipin | 7.0 mol% dioleoylglycerol | coupled assay microtiter plate | 0.17 ± 0.02 mM | 1.0 ± 0.25 mol% | 56 ± 4 | coupled assay microtiter plate | 10 mM Mg ATP | 10 mM Mg ATP + 15 mM MgCl ₂ | 7 min, <1 min | half life at 50 °C, 70 °C, 1.5% OG pH 7.5 50 mM Na ₃ PO ₄ 0.3 M NaCl | not stated | 6.9 | none? | 1 mM PEP, 2.5 mM NADH, 14 U LDH, 80 mM PIPES | NINJA, OG or Empigen higher yield than other detergents (for activity data!) then DM | | |

| # | Ref Title | Authors | Published | Mutants | General comments | Protein name | Extinction coefficient | Assay as in | Purification | DgkA stock | Assay environment | Activator | Lipid substrate | Type of assay | Km nucleotide | Km lipid substrate | vmax (DAG varied; ATP constant) | Specific activity | ATP concentration | Mg concentration | Half-life nucleation | Notes and special parameters | Assay temp | pH | Salt | Assay buffer composition | Protein purification protocol |
|----|--|---|-------------|-------------------------------------|--|--------------|------------------------|----------------------|---|------------|------------------------------|-----------------------------------|--------------------------------------|--|----------------|--------------------|---------------------------------|--|-------------------|------------------|----------------------|--|----------------------|------------|---|---|-------------------------------|
| 25 | Active sites of diacylglycerol kinase from <i>Escherichia coli</i> . Enzymes are shared between subunits | Lau, F. W.; Chen, X.; Bowie, J. U. | 1989, April | psiSD004 = W117R,S118T; C115A; I35C | monomer mixing and wt W117R,S118T mutants and vmax given for A14Q, E68C, N72S, E76L, K94V, D95N, for activity. Specific activity performed as in 20, where personal assay was used but not explained in 18. Most likely later published in 22). Kinetic parameters (Triton X-100). Mutant enzyme activities were measured using a coupled assay (19, which is performed as 5). | Dgk | - | See general comments | whole <i>E. coli</i> colony expressing DgkA on DgkA purified | DM | 0.7% Triton X-100 | 3.5 mol% cardiolipin | 7.0 mol% dioleoylglycerol | coupled assay microtiter plate | 0.07 ± 0.01 mM | 0.76 ± 0.06 mol% | 48 ± 1 | given for a lot of mutants. 32P ATP colony assay and coupled assay | 10 mM Mg ATP | 15 mM MgCl2 | 23 min < 1 min | half life at 50 °C, 70 °C, 1.5% OG pH 7.5 50 mM Na3PO4, 0.3 M NaCl | not stated in detail | 6.9 | none? | none? | |
| 25 | Active sites of diacylglycerol kinase from <i>Escherichia coli</i> . Enzymes are shared between subunits | Lau, F. W.; Chen, X.; Bowie, J. U. | 1989, April | psiSD004 = W117R,S118T; C115A; I35C | monomer mixing and wt W117R,S118T mutants and vmax given for A14Q, E68C, N72S, E76L, K94V, D95N, for activity. Specific activity performed as in 20, where personal assay was used but not explained in 18. Most likely later published in 22). Kinetic parameters (Triton X-100). Mutant enzyme activities were measured using a coupled assay (19, which is performed as 5). | Dgk | - | See general comments | whole <i>E. coli</i> colony expressing DgkA on DgkA purified | DM | 0.7% Triton X-100 | 3.5 mol% cardiolipin | 7.0 mol% dioleoylglycerol | coupled assay microtiter plate | 0.07 ± 0.01 mM | 0.76 ± 0.06 mol% | 48 ± 1 | given for a lot of mutants. 32P ATP colony assay and coupled assay | 10 mM Mg ATP | 15 mM MgCl2 | 23 min < 1 min | half life at 50 °C, 70 °C, 1.5% OG pH 7.5 50 mM Na3PO4, 0.3 M NaCl | not stated in detail | 6.9 | none? | none? | |
| 24 | On choosing a detergent for purification of membrane proteins | Vinogradov, S. O.; Galeson, J. F.; Sanders, C. R. | 1998, May | psiSD004 = W117R,S118T | coupled assay microtiter plate application | DAGK | - | modified from 20 | DM | DM | 0.7% Triton X-100 1.5% OG | 3.5 mol% cardiolipin | 9 mol% dioleoylglycerol | 32P ATP coupled assay microtiter plate | 0.12 ± 0.01 mM | 1.2 ± 0.2 mol% | 48 ± 8 | high (50-100%) detergent activity in to CG + DMPC assays specific activity of detergent (except SDS) | 12.5 mM Mg ATP | 15 mM MgCl2 | not stated | RT | 6.8 | 50 mM LiCl | 50 mM imidazole, 1 mM EGTA, 1 mM MgCl2, 1 mM NaOH, 14 U PK, 22 U LDH, 60 mM PIPES | | |
| 24 | On choosing a detergent for purification of membrane proteins | Vinogradov, S. O.; Galeson, J. F.; Sanders, C. R. | 1998, May | psiSD004 = W117R,S118T | comparison of DgkA activity from different detergents. DMPC OG assay mix with and without DMPC, results written in Low (<5%) activity compared to 22 U in 1.5 % OG with DMPC (with activity except SDS) | DAGK | - | 22 | different detergents: DMPC, DHPC, LMP, Triton X-100, SDS, Triton X-100, CYMAL-4, Fos-Choline-6; | DM | 60 mM OG (38 mM micellar) | 7 mM equals 20 mol% (micellar OG) | 2.6 mM equals 7.5 mol% (micellar OG) | coupled assay quartz cuvette | 0.12 ± 0.01 mM | 1.2 ± 0.2 mol% | 48 ± 8 | All detergents compared with DMPC always "high" (50-100%) detergent activity (in comparison to CG + DMPC assays specific activity of detergent (except SDS)) | 3 mM ATP | 20 mM Mg acetate | 30 min | high DAG Km difficult to saturate and therefore difficult to calculate Km for in to CG + DMPC assays specific activity of detergent (except SDS) | 30 °C | 6.8 | 50 mM LiCl | 60 mM PIPES, 0.1 mM EDTA, 1 mM EGTA, 1 mM MgCl2, 1 mM NaOH, 14 U LDH and PK | |
| | | | | | | | | | | | 60 mM OG (38 mM micellar) | - | 2.6 mM equals 7.5 mol% (micellar OG) | coupled assay quartz cuvette | | | | | | | | 30 °C | 6.8 | 50 mM LiCl | | | |

| # | Ref | Title | Authors | Published | Mutants | General comments | Protein name | Extinction coefficient as in | Purification as in | DgKA stock | Assay environment | Activator | Lipid substrate | Type of assay | Km nucleotide | Km lipid substrate | vmax (DAG varied, ATP fixed) | Specific activity | ATP concentration | Mg concentration | Half-life nucleation | Notes and special parameters | Assay temp | pH | Salt | Assay buffer composition | Protein purification protocol |
|----|-----|---|----------------------------------|------------|---|---|--------------|------------------------------|--------------------|---------------------------|-----------------------------------|---|------------------------------|------------------------------|---|--|------------------------------|-------------------|---|--|----------------------|--|---------------------------------------|-----------|---|--|---|
| 23 | 236 | A. assava transmembrane helix | Zhou, Y.; Wen, J.; Bowles, J. U. | 1997; Dec | ΔSD004 = W17R,S118T | Thermal inactivation rates w/ ΔSD004 and +/- cardiolipin and ATP stabilize DgKA | DgK | - | - | 0.7% Triton X-100 | 3.5 mol% cardiolipin | 9 mol% dioleoylglycerol | 32P ATP | coupled assay | 0.15 ± 0.006 mM | 1.3 ± 0.25 mol% | 79 ± 9 | 72 ± 4 | 5 mM ATP | 12.5 mM MgCl2 | - | - | RT | 6.6 | 50 mM LCI | 50 mM imidazole, 1 mM EGTA | - |
| 22 | 227 | Escherichia coli diacylglycerol kinase is an integral membrane protein that optimizes membrane enzyme and phospholipid transfer | Badda, P.; Sanders, C. R. | 1997; Sept | Most likely is ΔSD004 = W17R,S118T (18) | NAOH 6110 (cmM kinetic studies) | DGK | ε 1 mg/ml = 2.1 | 18 | - | 60 mM OG (38 mM micellar) | 8 mol% Cardiolipin beef heart (micellar OG) | dihexanoylglycerol | coupled assay quartz cuvette | 1.2 ± 0.5 mM, 0.58 ± 0.25 mM (αna ⁻¹) | 5.0 ± 2.2 mol%, 2.4 mol% (dipalmitoyl) | 50 ± 7 | - | 20 mM Mg acetate | 20 mM Mg acetate | - | keat (s-1), 12, keatKm (mol-ls-1), 1000, Alpha, 0.48 ± 0.17, concentration of OG is ~22 mM, the micellar OG concentration therefore is 38 mM | 30 °C | 6.8 | 50 mM LCI | 75 mM PIPES, 0.1 mM EDTA, 1 mM EGTA, 1 mM PEP, 0.25 mM NADH, 20 U LDH and PK | Ni-NTA, Emgen and then DM elution, Lyophilisation |
| | | | | | | standard activity assays | | | | 60 mM OG (38 mM micellar) | 7 mM equals 20 mol% (micellar OG) | 2.6 mM equals 7.5 dihexanoylglycerol | coupled assay quartz cuvette | 2.6 ± 1.2 mM | - | 25 ± 5 | 22 | 3 mM ATP | 20 mM Mg acetate | - | - | 30 °C | 6.8 | 50 mM LCI | 60 mM PIPES, 0.1 mM EDTA, 1 mM PEP, 0.25 mM NADH, 20 U LDH and PK | - | |
| | | | | | | different substrate | | 18 | | 21 mM DM (19 mM micellar) | 5 mM DMPC | 1.25 mM pyrene-pyrenebutyryl-2-butyryl-sn-glycerol (PBBC) | Fluorescent/TLC-based Assay | Fluorescent/TLC-based Assay | 2.6 ± 1.2 mM | - | >0.05 | <0.0001 | more than 5 mM ATP Mg was set to [ATP]+20 mM Mg | 20 mM Mg acetate, if more than 5 mM ATP Mg was set to [ATP]+20 mM Mg | - | ATP (s-1), 6.24, keatKm (mol-ls-1), 2400 | 22 °C, 22 min incubation, 24 s ± 5 °C | 6.8 | 50 mM LCI | 60 mM PIPES, 0.2 mM EGTA, 1 mM PEP, 0.25 mM NADH, 20 U LDH and PK | - |
| | | | | | | | | | | 21 mM DM (19 mM micellar) | 5 mM DMPC | 1.25 mM pyrene-tagged DAG (1-pyrenebutyryl-2-butyryl-sn-glycerol, PBBC) | Fluorescent/TLC-based Assay | Fluorescent/TLC-based Assay | >10 mM | - | - | <0.0001 | more than 5 mM ATP Mg was set to [ATP]+20 mM Mg | 20 mM Mg acetate, if more than 5 mM ATP Mg was set to [ATP]+20 mM Mg | - | Adenosine tetraphosphate; keat (s-1), 0.012, keatKm (mol-ls-1), 0.6 | 30 °C | 6.8 | 50 mM LCI | 60 mM PIPES, 0.2 mM EDTA, 1 mM NADH, 20 U LDH and PK | - |
| | | | | | | | | | | 21 mM DM (19 mM micellar) | 5 mM DMPC | 1.25 mM pyrene-tagged DAG (1-pyrenebutyryl-2-butyryl-sn-glycerol, PBBC) | Fluorescent/TLC-based Assay | Fluorescent/TLC-based Assay | ~1 | - | - | <0.0001 | more than 5 mM ATP Mg was set to [ATP]+20 mM Mg | 20 mM Mg acetate, if more than 5 mM ATP Mg was set to [ATP]+20 mM Mg | - | ADP (s-1), <0.00025, keatKm (mol-ls-1), <0.025 | 30 °C | 6.8 | 50 mM LCI | 60 mM PIPES, 0.2 mM EDTA, 1 mM NADH, 20 U LDH and PK | - |
| | | | | | | | | | | 21 mM DM (19 mM micellar) | 5 mM DMPC | 1.25 mM pyrene-tagged DAG (1-pyrenebutyryl-2-butyryl-sn-glycerol, PBBC) | Fluorescent/TLC-based Assay | Fluorescent/TLC-based Assay | no activity observed | - | - | - | more than 5 mM ATP Mg was set to [ATP]+20 mM Mg | 20 mM Mg acetate, if more than 5 mM ATP Mg was set to [ATP]+20 mM Mg | - | Triphosphate | 30 °C | 6.8 | 50 mM LCI | 60 mM PIPES, 0.2 mM EDTA, 1 mM NADH, 20 U LDH and PK | - |
| | | | | | | | | | | 21 mM DM (19 mM micellar) | 5 mM DMPC | 1.25 mM pyrene-tagged DAG (1-pyrenebutyryl-2-butyryl-sn-glycerol, PBBC) | Fluorescent/TLC-based Assay | Fluorescent/TLC-based Assay | 4.2 ± 1.5 mM | - | 1.9 ± 0.5 | - | more than 5 mM ATP Mg was set to [ATP]+20 mM Mg | 20 mM Mg acetate, if more than 5 mM ATP Mg was set to [ATP]+20 mM Mg | - | 2 Deoxy ATP, Z, keat (s-1), 0.48, keatKm (mol-ls-1), 110 | 30 °C | 6.8 | 50 mM LCI | 60 mM PIPES, 0.2 mM EDTA, 1 mM NADH, 20 U LDH and PK | - |
| | | | | | | | | | | 21 mM DM (19 mM micellar) | 5 mM DMPC | 1.25 mM pyrene-tagged DAG (1-pyrenebutyryl-2-butyryl-sn-glycerol, PBBC) | Fluorescent/TLC-based Assay | Fluorescent/TLC-based Assay | 8.7 ± 3 mM | - | 0.0032 ± 0.001 | - | more than 5 mM ATP Mg was set to [ATP]+20 mM Mg | 20 mM Mg acetate, if more than 5 mM ATP Mg was set to [ATP]+20 mM Mg | - | GTP, keat (s-1), 0.00079, keatKm (mol-ls-1), 0.091 | 30 °C | 6.8 | 50 mM LCI | 60 mM PIPES, 0.2 mM EDTA, 1 mM NADH, 20 U LDH and PK | - |
| | | | | | | | | | | 21 mM DM (19 mM micellar) | 5 mM DMPC | 1.25 mM pyrene-tagged DAG (1-pyrenebutyryl-2-butyryl-sn-glycerol, PBBC) | Fluorescent/TLC-based Assay | Fluorescent/TLC-based Assay | 5.9 ± 4 mM | - | 0.0066 ± 0.0004 | - | more than 5 mM ATP Mg was set to [ATP]+20 mM Mg | 20 mM Mg acetate, if more than 5 mM ATP Mg was set to [ATP]+20 mM Mg | - | ATP (s-1), 0.00015, keatKm (mol-ls-1), 0.025 | 30 °C | 6.8 | 50 mM LCI | 60 mM PIPES, 0.2 mM EDTA, 1 mM NADH, 20 U LDH and PK | - |

| # | Ref | Title | Authors | Published | Mutants | General comments | Protein name | Extinction coefficient | Assay as in | Purification | Detergent stock | Assay environment | Activator | Lipid substrate | Type of assay | Km nucleotide | Km lipid substrate | vmax (DAG varied, ATP varied) | Specific activity | ATP concentration | Mg concentration | Half-life nucleation | Notes and special parameters | Assay temp | pH | Salt | Assay buffer composition | Protein purification |
|----|-----|---|---|------------|-----------------------|---|--------------|------------------------|---|--------------|-----------------|-------------------|--------------------------------|---|------------------------------|---------------|--------------------|-------------------------------|-------------------|-------------------|------------------|----------------------|------------------------------|------------|------------|--|--|----------------------|
| 21 | 248 | <i>Escherichia coli</i> diacylglycerol kinase: a case study in the accuracy of the solution NMR methods to an integral membrane protein | Vingradov, A. C.; Badda, P.; Wang, L.; Sengupta, I. F. D.; Sanders, C. R. | 1997, June | ΔSD004 = WT17R, S118T | WT ΔDFA here is ΔSD004 WT17R, S118T, yield 10-30 mg/l | DAGK | - | will be present with several modifications most likely (22) | 18 | 1% DM | 9% OG | 2 or 5 mM DMPC ? | 2.6 mM equals 7.5 meq% dihexanoylglycerol ? | coupled assay quartz cuvette | | | 15 | 3 mM ATP | 20 mM Mg acetate | | | 25 °C | 7 | 50 mM LiCl | 50 mM PIPES, 0.1 mM EDTA, 1 mM MEGTA, 1 mM NADH, 20 U LDH and PK | EMSA, NATA then DM Purification Lyophilisation | |
| | | | | | | | | | | | 1% DM | 9% OG | - | 2.6 mM equals 7.5 meq% dihexanoylglycerol ? | coupled assay quartz cuvette | | | none | 3 mM ATP | 20 mM Mg acetate | | | 25 °C | 7 | 50 mM LiCl | 50 mM PIPES, 0.1 mM EDTA, 1 mM MEGTA, 1 mM NADH, 20 U LDH and PK | | |
| | | | | | | | | | | | 1% DM | 4-14% DM | 2 or 5 mM DMPC or cardiolipin? | 2.6 mM equals 7.5 meq% dihexanoylglycerol ? | coupled assay quartz cuvette | | | 20 | 3 mM ATP | 20 mM Mg acetate | | | 25-50 °C | 6-8 | 50 mM LiCl | 50 mM PIPES, 0.1 mM EDTA, 1 mM MEGTA, 1 mM NADH, 20 U LDH and PK | | |
| | | | | | | | | | | | 1% DM | 4-14% DM | - | 2.6 mM equals 7.5 meq% dihexanoylglycerol ? | coupled assay quartz cuvette | | | 0.4 | 3 mM ATP | 20 mM Mg acetate | | | 25-50 °C | 6-8 | 50 mM LiCl | 50 mM PIPES, 0.1 mM EDTA, 1 mM MEGTA, 1 mM NADH, 20 U LDH and PK | | |
| | | | | | | | | | | | 1% DM | 10% DDM | - | 2.6 mM equals 7.5 meq% dihexanoylglycerol ? | coupled assay quartz cuvette | | | >1 | 3 mM ATP | 20 mM Mg acetate | | | 25 °C | 6-8 | 50 mM LiCl | 50 mM PIPES, 0.1 mM EDTA, 1 mM MEGTA, 1 mM NADH, 20 U LDH and PK | | |
| | | | | | | | | | | | 1% DM | 10% DHPG | 2 or 5 mM DMPC or cardiolipin? | 2.6 mM equals 7.5 meq% dihexanoylglycerol ? | coupled assay quartz cuvette | | | 15 | 3 mM ATP | 20 mM Mg acetate | | | 25 °C | 6-8 | 50 mM LiCl | 50 mM PIPES, 0.1 mM EDTA, 1 mM MEGTA, 1 mM NADH, 20 U LDH and PK | | |
| | | | | | | | | | | | 1% DM | 8% CHAPSO | 2 or 5 mM DMPC? | 2.6 mM equals 7.5 meq% dihexanoylglycerol ? | coupled assay quartz cuvette | | | >1 | 3 mM ATP | 20 mM Mg acetate | | | 25-40 °C | 7.9 | 50 mM LiCl | 50 mM PIPES, 0.1 mM EDTA, 1 mM MEGTA, 1 mM NADH, 20 U LDH and PK | | |
| | | | | | | | | | | | 1% DM | 8% CHAPSO | - | 2.6 mM equals 7.5 meq% dihexanoylglycerol ? | coupled assay quartz cuvette | | | none | 3 mM ATP | 20 mM Mg acetate | | | 25-40 °C | 7.9 | 50 mM LiCl | 50 mM PIPES, 0.1 mM EDTA, 1 mM MEGTA, 1 mM NADH, 20 U LDH and PK | | |
| | | | | | | | | | | | 1% DM | 5% Triton X-100 | 2 or 5 mM DMPC | 2.6 mM equals 7.5 meq% dihexanoylglycerol ? | coupled assay quartz cuvette | | | >5 | 3 mM ATP | 20 mM Mg acetate | | | 30-50 °C | 7.8 | 50 mM LiCl | 50 mM PIPES, 0.1 mM EDTA, 1 mM NADH, 20 U LDH and PK | | |
| | | | | | | | | | | | 1% DM | 9% DPC | not stated | 2.6 mM equals 7.5 meq% dihexanoylglycerol ? | coupled assay quartz cuvette | | | 0.7 | 3 mM ATP | 20 mM Mg acetate | | | 20-50 °C | 4.5 | 50 mM LiCl | 50 mM PIPES, 0.1 mM EDTA, 1 mM NADH, 20 U LDH and PK | | |

| # | Ref Title | Authors | Pub-lished | Mitants | General comments | Protein name | Extinction coefficient as in | Purifi-cation | DgPA stock | Assay environment | Activator | Lipid substrate | Type of assay | Km nucleotide | Km lipid substrate | vmax (DAG varied, ATP varied) | Specific activity | ATP concen-tration | Mg concen-tration | Half-life nucle-ination | Notes and special parameters | Assay temp | pH | Salt | Assay buffer composition | Protein purification | |
|----|-----------|--------------------------|------------|---------|---|----------------------|------------------------------|---------------|--|--------------------|---|----------------------------|-------------------------------------|---------------|--------------------|-------------------------------|-------------------|------------------------------|-------------------|-------------------------|------------------------------|--|-------|------------|--|--|--|
| 13 | 2255 | Wash, J., P. Bell, R. M. | 1986, Nov | WT | Tifton X-100 is not a substrate. The activities with polyoxyethylene. Tifton X-100 were entirely dependent on dioleoylglycerol, implying that the function of activator was not occurring. Relationship of lipid to the stimulation of enzyme activity (6.9 mol% dioleoylglycerol) is dependent on the apparent apparent K _a for Mg, cardiolipin, PS, PC) Fig 1 A and B 1,3. Dioleoylglycerol activates Dicylglycerol is substrate and activator in OG | dicylglycerol kinase | 12 | | membranes of DgPA overexpressin (M830/pJW10) | 11 mM Tifton X-100 | | | 0.1 mM dipalmitoylglycerol | 32P ATP | | | | 0.4 mmol | 5 mM Na ATP | 12.5 mM MgCl2 | | Self-activation of dioleoylglycerol kinase appropriate start of reaction leading to ATP at different concentrations. Phosphatidic acid as a substrate at different DDM concentrations! | 25 °C | 6.6 | 50 mM NaCl | 60mM imidazole, 1 mM EGTA, 0.03 mM DTPA, 2 mM DTT. | |
| | | | | | | | | | | 51 mM OG | | 3.7 mol% dioleoylglycerol | 32P ATP detecting phosphatidic acid | | | 1% compared to cardiolipin | 5 mM Na ATP | 12.5 mM MgCl2 | | | | 25 °C | 6.6 | 50 mM NaCl | 60mM imidazole, 1 mM EGTA, 0.03 mM DTPA, 2 mM DTT. | | |
| | | | | | | | | | | 51 mM OG | mitochondrial cardiolipin | 3.7 mol% dioleoylglycerol | 32P ATP detecting phosphatidic acid | | | -5 | 5 mM Na ATP | 12.5 mM MgCl2 | | | | 25 °C | 6.6 | 50 mM NaCl | 60mM imidazole, 1 mM EGTA, 0.03 mM DTPA, 2 mM DTT. | | |
| | | | | | | | | | | 51 mM OG | sulfidic acid | 3.7 mol% dioleoylglycerol | 32P ATP detecting phosphatidic acid | | | -5 | 5 mM Na ATP | 12.5 mM MgCl2 | | | | 25 °C | 6.6 | 50 mM NaCl | 60mM imidazole, 1 mM EGTA, 0.03 mM DTPA, 2 mM DTT. | | |
| | | | | | | | | | | 51 mM OG | Bis-phosphatidic acid | 3.7 mol% dioleoylglycerol | 32P ATP detecting phosphatidic acid | | | -5 | 5 mM Na ATP | 12.5 mM MgCl2 | | | | 25 °C | 6.6 | 50 mM NaCl | 60mM imidazole, 1 mM EGTA, 0.03 mM DTPA, 2 mM DTT. | | |
| | | | | | | | | | | 51 mM OG | DOPG | 3.7 mol% dioleoylglycerol | 32P ATP detecting phosphatidic acid | | | -5 | 5 mM Na ATP | 12.5 mM MgCl2 | | | | 25 °C | 6.6 | 50 mM NaCl | 60mM imidazole, 1 mM EGTA, 0.03 mM DTPA, 2 mM DTT. | | |
| | | | | | | | | | | 51 mM OG | 0, 1.8, 3.7, 6.9, 10 mol% DOPG | 3.7 mol% dioleoylglycerol | 32P ATP detecting phosphatidic acid | | | | 1.10 mM Na ATP | 7.5 mM free Mg ²⁺ | | | | 25 °C | 6.6 | 50 mM NaCl | 60mM imidazole, 1 mM EGTA, 0.03 mM DTPA, 2 mM DTT. | | |
| | | | | | | | | | | 51 mM OG | 2.8, 3.7, 5.1, 7.1, 8.1, 12.5 mol% DOPG | 12.5 mol% dioleoylglycerol | 32P ATP detecting phosphatidic acid | | | | 5 mM Na ATP | 12.5 mM MgCl2 | | | | 25 °C | 6.6 | 50 mM NaCl | 60mM imidazole, 1 mM EGTA, 0.03 mM DTPA, 2 mM DTT. | | |
| | | | | | | | | | | 51 mM OG | PC | 3.7 mol% dioleoylglycerol | 32P ATP detecting phosphatidic acid | | | -5 | 5 mM Na ATP | 12.5 mM MgCl2 | | | | 25 °C | 6.6 | 50 mM NaCl | 60mM imidazole, 1 mM EGTA, 0.03 mM DTPA, 2 mM DTT. | | |
| | | | | | | | | | | 51 mM OG | DOPC | 3.7 mol% dioleoylglycerol | 32P ATP detecting phosphatidic acid | | | -5 | 5 mM Na ATP | 12.5 mM MgCl2 | | | | 25 °C | 6.6 | 50 mM NaCl | 60mM imidazole, 1 mM EGTA, 0.03 mM DTPA, 2 mM DTT. | | |
| | | | | | | | | | | 51 mM OG | D-C-hexadecyl-phosphatidyl- | 3.7 mol% dioleoylglycerol | 32P ATP detecting phosphatidic acid | | | -5 | 5 mM Na ATP | 12.5 mM MgCl2 | | | | 25 °C | 6.6 | 50 mM NaCl | 60mM imidazole, 1 mM EGTA, 0.03 mM DTPA, 2 mM DTT. | | |
| | | | | | | | | | | 51 mM OG | Sarcosyl-lysophosphatidyl-choleine | 3.7 mol% dioleoylglycerol | 32P ATP detecting phosphatidic acid | | | -5 | 5 mM Na ATP | 12.5 mM MgCl2 | | | | 25 °C | 6.6 | 50 mM NaCl | 60mM imidazole, 1 mM EGTA, 0.03 mM DTPA, 2 mM DTT. | | |

| # | Ref Title | Authors | Pub-lished | Mitants | General comments | Protein name | Extinction coefficient as in | Purifi-cation | DgPA stock | Assay environment | Activator | Lipid substrate | Type of assay | Km nucleotide | Km lipid substrate | vmax (DAG varied, ATP fixed) | Specific activity | ATP concen-tration | Mg concen-tration | Half-life | Notes and special parameters | Assay temp | pH | Salt | Assay buffer composition | Protein purification |
|---|-----------|---------|------------|---------|------------------|--------------|------------------------------|---------------|------------|-------------------|------------------------------------|-----------------------------------|-------------------------------------|---------------|--------------------|------------------------------|-------------------|--------------------|-------------------|---|------------------------------|------------|-----|------------|--|----------------------|
| | | | | | | | | | | 51 mM OG | Hexadecyl phosphorylcholine | 3.7 mol% didecanoylethyl glycerol | 32P ATP detecting phosphatidic acid | | | -5 | | 5 mM Na ATP | 12.5 mM MgCl2 | protection from inactivation | Ka: 17.3 mol%, Hill: 3.8 | 25 °C | 6.6 | 50 mM NaCl | 60 mM imidazole, 1 mM EGTA, 0.03 mM DTPA, 2 mM DTT | |
| | | | | | | | | | | 51 mM OG | 1-O-alkyl-phosphatidylcholine | 3.7 mol% didecanoylethyl glycerol | 32P ATP detecting phosphatidic acid | | | -5 | | 5 mM Na ATP | 12.5 mM MgCl2 | protection from inactivation | Ka: 21.9 mol%, Hill: 3.5 | 25 °C | 6.6 | 50 mM NaCl | 60 mM imidazole, 1 mM EGTA, 0.03 mM DTPA, 2 mM DTT | |
| | | | | | | | | | | 51 mM OG | Snakehead activating factor | 3.7 mol% didecanoylethyl glycerol | 32P ATP detecting phosphatidic acid | | | -5 | | 5 mM Na ATP | 12.5 mM MgCl2 | | Ka: 22.4 mol%, Hill: 3.4 | 25 °C | 6.6 | 50 mM NaCl | 60 mM imidazole, 1 mM EGTA, 0.03 mM DTPA, 2 mM DTT | |
| | | | | | | | | | | 51 mM OG | Sodium dodecyl sulfate | 3.7 mol% didecanoylethyl glycerol | 32P ATP detecting phosphatidic acid | | 3.2 | | | 5 mM Na ATP | 12.5 mM MgCl2 | protection from inactivation | Ka: 9.8 mol%, Hill: 3.4 | 25 °C | 6.6 | 50 mM NaCl | 60 mM imidazole, 1 mM EGTA, 0.03 mM DTPA, 2 mM DTT | |
| | | | | | | | | | | 51 mM OG | D LPC | 3.7 mol% didecanoylethyl glycerol | 32P ATP detecting phosphatidic acid | | 1 | | | 5 mM Na ATP | 12.5 mM MgCl2 | | Ka: 11.9 mol%, Hill: 2.9 | 25 °C | 6.6 | 50 mM NaCl | 60 mM imidazole, 1 mM EGTA, 0.03 mM DTPA, 2 mM DTT | |
| | | | | | | | | | | 51 mM OG | 93 mol% didecanoylethyl glycerol | 7.4 mol% didecanoylethyl glycerol | 32P ATP detecting phosphatidic acid | | | | 0.08 | 5 mM Na ATP | 12.5 mM MgCl2 | no protection from inactivation | did not activate | 25 °C | 6.6 | 50 mM NaCl | 60 mM imidazole, 1 mM EGTA, 0.03 mM DTPA, 2 mM DTT | |
| | | | | | | | | | | 51 mM OG | 93 mol% didecanoylethyl glycerol | 5.7 mol% dioleylethyl glycerol | 32P ATP detecting phosphatidic acid | | | | 3.1 | 5 mM Na ATP | 12.5 mM MgCl2 | dioleylethyl glycerol is in contrast to dioleylethyl glycerol a activator of DgPA | | 25 °C | 6.6 | 50 mM NaCl | 60 mM imidazole, 1 mM EGTA, 0.03 mM DTPA, 2 mM DTT | |
| | | | | | | | | | | 51 mM OG | 16.3 mol% phosphatidylcholine | 3.7 mol% didecanoylethyl glycerol | 32P ATP detecting phosphatidic acid | | | | | 5 mM Na ATP | 12.5 mM MgCl2 | did not activate | | 25 °C | 6.6 | 50 mM NaCl | 60 mM imidazole, 1 mM EGTA, 0.03 mM DTPA, 2 mM DTT | |
| | | | | | | | | | | 51 mM OG | - | 3.7 mol% didecanoylethyl glycerol | 32P ATP detecting phosphatidic acid | | | | 0.04 | 5 mM Na ATP | 4 mM MgCl2 | | | 25 °C | 6.6 | 50 mM NaCl | 60 mM imidazole, 1 mM EGTA, 0.03 mM DTPA, 2 mM DTT | |
| | | | | | | | | | | 51 mM OG | 16.3 mol% Dimethyl-myristamide | 3.7 mol% didecanoylethyl glycerol | 32P ATP detecting phosphatidic acid | | | | 0.17 | 5 mM Na ATP | 4 mM MgCl2 | | | 25 °C | 6.6 | 50 mM NaCl | 60 mM imidazole, 1 mM EGTA, 0.03 mM DTPA, 2 mM DTT | |
| | | | | | | | | | | 51 mM OG | Dioleylethylene glycol | 1.5 mol% didecanoylethyl glycerol | 32P ATP detecting phosphatidic acid | | | | 0.34 | 5 mM Na ATP | 4 mM MgCl2 | | | 25 °C | 6.6 | 50 mM NaCl | 60 mM imidazole, 1 mM EGTA, 0.03 mM DTPA, 2 mM DTT | |
| | | | | | | | | | | 51 mM OG | 3.7 mol% 1,3-dioleylethyl glycerol | 3.7 mol% didecanoylethyl glycerol | 32P ATP detecting phosphatidic acid | | | | 1.31 | 5 mM Na ATP | 4 mM MgCl2 | | | 25 °C | 6.6 | 50 mM NaCl | 60 mM imidazole, 1 mM EGTA, 0.03 mM DTPA, 2 mM DTT | |
| | | | | | | | | | | 51 mM OG | Hexadecyl alcohol | 3.7 mol% didecanoylethyl glycerol | 32P ATP detecting phosphatidic acid | | | | 0.15 | 5 mM Na ATP | 4 mM MgCl2 | | tested to be not a substrate | 25 °C | 6.6 | 50 mM NaCl | 60 mM imidazole, 1 mM EGTA, 0.03 mM DTPA, 2 mM DTT | |
| | | | | | | | | | | 51 mM OG | 16.3 mol% Methyl-myristate | 3.7 mol% didecanoylethyl glycerol | 32P ATP detecting phosphatidic acid | | | | 0.64 | 5 mM Na ATP | 4 mM MgCl2 | | | 25 °C | 6.6 | 50 mM NaCl | 60 mM imidazole, 1 mM EGTA, 0.03 mM DTPA, 2 mM DTT | |
| | | | | | | | | | | 51 mM OG | 16.3 mol% Hexadecyl-chloride | 3.7 mol% didecanoylethyl glycerol | 32P ATP detecting phosphatidic acid | | | | 0.09 | 5 mM Na ATP | 4 mM MgCl2 | | | 25 °C | 6.6 | 50 mM NaCl | 60 mM imidazole, 1 mM EGTA, 0.03 mM DTPA, 2 mM DTT | |
| | | | | | | | | | | 51 mM OG | Myristyl acetate | 3.7 mol% didecanoylethyl glycerol | 32P ATP detecting phosphatidic acid | | | | 1.1 | 5 mM Na ATP | 4 mM MgCl2 | | | 25 °C | 6.6 | 50 mM NaCl | 60 mM imidazole, 1 mM EGTA, 0.03 mM DTPA, 2 mM DTT | |
| | | | | | | | | | | 51 mM OG | 16.3 mol% Nitro-dodecane | 3.7 mol% didecanoylethyl glycerol | 32P ATP detecting phosphatidic acid | | | | 0.5 | 5 mM Na ATP | 4 mM MgCl2 | | | 25 °C | 6.6 | 50 mM NaCl | 60 mM imidazole, 1 mM EGTA, 0.03 mM DTPA, 2 mM DTT | |
| | | | | | | | | | | 51 mM OG | Octyl acetate | 3.7 mol% didecanoylethyl glycerol | 32P ATP detecting phosphatidic acid | | | | 0.15 | 5 mM Na ATP | 4 mM MgCl2 | | | 25 °C | 6.6 | 50 mM NaCl | 60 mM imidazole, 1 mM EGTA, 0.03 mM DTPA, 2 mM DTT | |
| | | | | | | | | | | 51 mM OG | 16.3 mol% Oleoyl-chloride | 3.7 mol% didecanoylethyl glycerol | 32P ATP detecting phosphatidic acid | | | | 0.27 | 5 mM Na ATP | 4 mM MgCl2 | | | 25 °C | 6.6 | 50 mM NaCl | 60 mM imidazole, 1 mM EGTA, 0.03 mM DTPA, 2 mM DTT | |

| # | Ref Title | Authors | Pub-lished | Mitlans | General comments | Protein name | Extinction coefficient as in | Purifi-cation | DgPA stock | Assay environment | Activator | Lipid substrate | Type of assay | Km nucleotide | Km lipid substrate | vmax (DAG varied; ATP varied) | Specific activity | ATP concen-tration | Mg concen-tration | Half-life nucle-ation | Notes and special parameters | Assay temp | pH | Salt | Assay buffer composition | Protein purification |
|---|-----------|---------|------------|---------|------------------|--------------|------------------------------|---------------|------------|--------------------|--|---|-------------------------------------|---------------|--------------------|-------------------------------|-------------------|--------------------|-------------------|-----------------------|--|------------|-----|--|--------------------------|----------------------|
| | | | | | | | | | | 51 mM OG | metM octanoate, dideoxy-ribosephatidyl-diboyl-chole, 1,3-bisnaphthyl-ammonium chloride, 12 CHAPS or dicosyl sodium sulfate | 3.7 mol% dideoxy-ribosephatidyl-diboyl-chole, 1,3-bisnaphthyl-ammonium chloride, 12 CHAPS or dicosyl sodium sulfate | 32P ATP detecting phosphatidic acid | | | | | 5 mM Na ATP | 4 mM MgCl2 | 25 min | did not activate | 25 °C | 6.6 | 50 mM imidazole, 1 mM EGTA, 2 mM DTT, NaCl | | |
| | | | | | | | | | | 51 mM OG | 10 mol% DOPG | 7.4 mol% dideoxy-ribosephatidyl-diboyl-chole, 1,3-bisnaphthyl-ammonium chloride, 12 CHAPS or dicosyl sodium sulfate | 32P ATP detecting phosphatidic acid | | | | | 5 mM Na ATP | 7.5 mM MgCl2 | 25 min | Effect of adenylylimidodiphosphate on dideoxy-ribosephatidyl-diboyl-chole kinase: half life at 25 °C | 25 °C | 6.6 | 50 mM imidazole, 1 mM EGTA, 2 mM DTT, NaCl | | |
| | | | | | | | | | | 51 mM OG-10mol% PG | 10 mol% DOPG | 7.4 mol% dideoxy-ribosephatidyl-diboyl-chole, 1,3-bisnaphthyl-ammonium chloride, 12 CHAPS or dicosyl sodium sulfate | 32P ATP detecting phosphatidic acid | | | | | 5 mM Na ATP | 7.5 mM MgCl2 | 38 min | half life at 25 °C | 25 °C | 6.6 | 50 mM imidazole, 1 mM EGTA, 2 mM DTT, NaCl | | |
| | | | | | | | | | | 51 mM OG | 10 mol% DOPG | 7.4 mol% dideoxy-ribosephatidyl-diboyl-chole, 1,3-bisnaphthyl-ammonium chloride, 12 CHAPS or dicosyl sodium sulfate | 32P ATP detecting phosphatidic acid | | | | | 5 mM Na ATP | - | 25 min | 5 mM AMP-PNP: half life at 25 °C | 25 °C | 6.6 | 50 mM imidazole, 1 mM EGTA, 2 mM DTT, NaCl | | |
| | | | | | | | | | | 51 mM OG-10mol% PG | 10 mol% DOPG | 7.4 mol% dideoxy-ribosephatidyl-diboyl-chole, 1,3-bisnaphthyl-ammonium chloride, 12 CHAPS or dicosyl sodium sulfate | 32P ATP detecting phosphatidic acid | | | | | 5 mM Na ATP | - | 36 min | 5 mM AMP-PNP: half life at 25 °C | 25 °C | 6.6 | 50 mM imidazole, 1 mM EGTA, 2 mM DTT, NaCl | | |
| | | | | | | | | | | 51 mM OG | 10 mol% DOPG | 7.4 mol% dideoxy-ribosephatidyl-diboyl-chole, 1,3-bisnaphthyl-ammonium chloride, 12 CHAPS or dicosyl sodium sulfate | 32P ATP detecting phosphatidic acid | | | | | 5 mM Na ATP | - | 27 min | 1 mM AMP-PNP: half life at 25 °C | 25 °C | 6.6 | 50 mM imidazole, 1 mM EGTA, 2 mM DTT, NaCl | | |
| | | | | | | | | | | 51 mM OG-10mol% PG | 10 mol% DOPG | 7.4 mol% dideoxy-ribosephatidyl-diboyl-chole, 1,3-bisnaphthyl-ammonium chloride, 12 CHAPS or dicosyl sodium sulfate | 32P ATP detecting phosphatidic acid | | | | | 5 mM Na ATP | 12.5 mM MgCl2 | 82 min | 1 mM AMP-PNP: half life at 25 °C | 25 °C | 6.6 | 50 mM imidazole, 1 mM EGTA, 2 mM DTT, NaCl | | |
| | | | | | | | | | | 51 mM OG | 10 mol% DOPG | 7.4 mol% dideoxy-ribosephatidyl-diboyl-chole, 1,3-bisnaphthyl-ammonium chloride, 12 CHAPS or dicosyl sodium sulfate | 32P ATP detecting phosphatidic acid | | | | | 5 mM Na ATP | 1 mM MgCl2 | 25 min | 5 mM AMP-PNP: half life at 25 °C | 25 °C | 6.6 | 50 mM imidazole, 1 mM EGTA, 2 mM DTT, NaCl | | |
| | | | | | | | | | | 51 mM OG-10mol% PG | 10 mol% DOPG | 7.4 mol% dideoxy-ribosephatidyl-diboyl-chole, 1,3-bisnaphthyl-ammonium chloride, 12 CHAPS or dicosyl sodium sulfate | 32P ATP detecting phosphatidic acid | | | | | 5 mM Na ATP | 12.5 mM MgCl2 | 81 min | 5 mM AMP-PNP: half life at 25 °C | 25 °C | 6.6 | 50 mM imidazole, 1 mM EGTA, 2 mM DTT, NaCl | | |
| | | | | | | | | | | 51 mM OG | 10 mol% DOPG | 7.4 mol% dideoxy-ribosephatidyl-diboyl-chole, 1,3-bisnaphthyl-ammonium chloride, 12 CHAPS or dicosyl sodium sulfate | 32P ATP detecting phosphatidic acid | | | | | 5 mM Na ATP | 12.5 mM MgCl2 | 27 min | 5 mM AMP-PNP: half life at 25 °C | 25 °C | 6.6 | 50 mM imidazole, 1 mM EGTA, 2 mM DTT, NaCl | | |
| | | | | | | | | | | 51 mM OG-10mol% PG | 10 mol% DOPG | 7.4 mol% dideoxy-ribosephatidyl-diboyl-chole, 1,3-bisnaphthyl-ammonium chloride, 12 CHAPS or dicosyl sodium sulfate | 32P ATP detecting phosphatidic acid | | | | | 5 mM Na ATP | 17.5 mM MgCl2 | 220 min | 10 mM AMP-PNP: half life at 25 °C | 25 °C | 6.6 | 50 mM imidazole, 1 mM EGTA, 2 mM DTT, NaCl | | |
| | | | | | | | | | | 51 mM OG | 0.7, 1.8, 3.4, 6.7 mol% cardiolin | 6.9 mol% dideoxy-ribosephatidyl-diboyl-chole, 1,3-bisnaphthyl-ammonium chloride, 12 CHAPS or dicosyl sodium sulfate | 32P ATP detecting phosphatidic acid | | | | | 5 mM Na ATP | 12.5 mM MgCl2 | 120 min | relationship of lipid cofactor stabilization to the stimulation of enzyme activity | 25 °C | 6.6 | 50 mM imidazole, 1 mM EGTA, 0.03 mM DTPA, 2 mM DTT, NaCl | | |
| | | | | | | | | | | 51 mM OG | 1.8, 3.4, 6.7, 15.2 mol% PG | 6.9 mol% dideoxy-ribosephatidyl-diboyl-chole, 1,3-bisnaphthyl-ammonium chloride, 12 CHAPS or dicosyl sodium sulfate | 32P ATP detecting phosphatidic acid | | | | | 5 mM Na ATP | 12.5 mM MgCl2 | 49 min | relationship of lipid cofactor stabilization to the stimulation of enzyme activity | 25 °C | 6.6 | 50 mM imidazole, 1 mM EGTA, 0.03 mM DTPA, 2 mM DTT, NaCl | | |
| | | | | | | | | | | 51 mM OG | 10 mol% DOPG | 3.7 mol% dideoxy-ribosephatidyl-diboyl-chole, 1,3-bisnaphthyl-ammonium chloride, 12 CHAPS or dicosyl sodium sulfate | 32P ATP detecting phosphatidic acid | | | | | 5 mM Na ATP | - | 131 min | relationship of lipid cofactor stabilization to the stimulation of enzyme activity | 25 °C | 6.6 | 50 mM imidazole, 1 mM EGTA, 0.03 mM DTPA, 2 mM DTT, NaCl | | |

| # | Ref Title | Authors | Published | Mutants | General comments | Protein name | Extinction coefficient as in | Assay as in | Purification | DgMA stock | Assay environment | Activator | Lipid substrate | Type of assay | Km nucleotide | Km lipid substrate | vmax (DAG varied, ATP varied) | Specific activity | ATP concentration | Mg concentration | Half-life nucleotide | Notes and special parameters | Assay temp | pH | Salt | Assay buffer composition | Protein purification protocol |
|---|-----------|---------|-----------|---------|------------------|--------------|------------------------------|---------------------|--------------|------------|--------------------------------|--|-------------------------------------|---------------|---------------|--------------------|-------------------------------|-------------------|-------------------|------------------|----------------------|---|------------|-----|------------|--|-------------------------------|
| | | | | | | | | 51 mM OG | | | 10 mol% DOPG | 3.7 mol% dactanoyl/glycerol phosphatidic acid | 32P ATP detecting phosphatidic acid | | | | | | 5 mM Na ATP | 12.5 mM MgCl2 | 53 min | half life at 25 °C | 25 °C | 6.6 | 50 mM NaCl | 60 mM imidazole, 2 mM DTT | |
| | | | | | | | | 51 mM OG 10 mol% PG | | | 10 mol% DOPG | 3.7 mol% dactanoyl/glycerol phosphatidic acid | 32P ATP detecting phosphatidic acid | | | | | | 5 mM Na ATP | 12.5 mM MgCl2 | 150 min | half life at 25 °C | 25 °C | 6.6 | 50 mM NaCl | 60 mM imidazole, 2 mM DTT | |
| | | | | | | | | 51 mM OG | | | 10 mol% DOPG | 3.7 mol% dactanoyl/glycerol phosphatidic acid | 32P ATP detecting phosphatidic acid | | | | | | 5 mM Na ATP | 5 mM MgCl2 | 71 min | half life at 25 °C | 25 °C | 6.6 | 50 mM NaCl | 1 mM EGTA, 60 mM imidazole, 2 mM DTT | |
| | | | | | | | | 51 mM OG 10 mol% PG | | | 10 mol% DOPG | 3.7 mol% dactanoyl/glycerol phosphatidic acid | 32P ATP detecting phosphatidic acid | | | | | | 5 mM Na ATP | 5 mM MgCl2 | 157 min | half life at 25 °C | 25 °C | 6.6 | 50 mM NaCl | 1 mM EGTA, 60 mM imidazole, 2 mM DTT | |
| | | | | | | | | 51 mM OG | | | 10 mol% DOPG | 3.7 mol% dactanoyl/glycerol phosphatidic acid | 32P ATP detecting phosphatidic acid | | | | | | 5 mM Na ATP | 4 mM MgCl2 | 85 min | half life at 25 °C | 25 °C | 6.6 | 50 mM NaCl | 1 mM NTFA, 60 mM imidazole, 2 mM DTT | |
| | | | | | | | | 51 mM OG 10 mol% PG | | | 10 mol% DOPG | 3.7 mol% dactanoyl/glycerol phosphatidic acid | 32P ATP detecting phosphatidic acid | | | | | | 5 mM Na ATP | 4 mM MgCl2 | 143 min | half life at 25 °C | 25 °C | 6.6 | 50 mM NaCl | 1 mM NTFA, 60 mM imidazole, 2 mM DTT | |
| | | | | | | | | 51 mM OG | | | - | 0.04-10 mol% dioleoyl/glycerol phosphatidic acid | 32P ATP detecting phosphatidic acid | | | | | | 5 mM Na ATP | 12.5 mM MgCl2 | | Cooperativity of the dioleoyl/glycerol dependence of diacylglycerol kinase in the absence of an added lipid substrate. (Figure 2) | 25 °C | 6.6 | 50 mM NaCl | 60 mM imidazole, 1 mM EGTA, 0.03 mM DTPA, 2 mM DTT | |
| | | | | | | | | 51 mM OG | | | - | 0.04-10 mol% dioleoyl/glycerol phosphatidic acid | 32P ATP detecting phosphatidic acid | | | | | | 5 mM Na ATP | 25 mM MgCl2 | | | 25 °C | 6.6 | 50 mM NaCl | 60 mM imidazole, 1 mM EGTA, 0.03 mM DTPA, 2 mM DTT | |
| | | | | | | | | 51 mM OG | | | 5.7 mol% 1,3-Dioleoyl/glycerol | 0.04-10 mol% dioleoyl/glycerol phosphatidic acid | 32P ATP detecting phosphatidic acid | | | | | | 5 mM Na ATP | 12.5 mM MgCl2 | | | 25 °C | 6.6 | 50 mM NaCl | 60 mM imidazole, 1 mM EGTA, 0.03 mM DTPA, 2 mM DTT | |
| | | | | | | | | 51 mM OG | | | 3.7 mol% 1,3-Dioleoyl/glycerol | 0.04-10 mol% dioleoyl/glycerol phosphatidic acid | 32P ATP detecting phosphatidic acid | | | | | | 5 mM Na ATP | 25 mM MgCl2 | | | 25 °C | 6.6 | 50 mM NaCl | 60 mM imidazole, 1 mM DTPA, 2 mM DTT | |
| | | | | | | | | 51 mM OG | | | 3.7 mol% 1,3-Dioleoyl/glycerol | 0.04-10 mol% dioleoyl/glycerol phosphatidic acid | 32P ATP detecting phosphatidic acid | | | | | | 5 mM Na ATP | 4 mM MgCl2 | | | 25 °C | 6.6 | 50 mM NaCl | 60 mM imidazole, 1 mM EGTA, 0.03 mM DTPA, 2 mM DTT | |

| # | Ref Title | Authors | Pub-lished | Milants | General comments | Protein name | Extinction coefficient as in | Purifi-cation | DgPA stock | Assay environment | Activator | Lipid substrate | Type of assay | Km nucleotide | Km lipid substrate | vmax (DAG varied; ATP (text) 10.4 (table) | Specific activity | ATP concen-tration | Mg concen-tration | Half-life | Notes and special parameters | Assay temp | pH | Salt | Assay buffer composition | Protein purification |
|----|-----------|----------------------------|------------|---------|--|-----------------------|------------------------------|---|------------|-----------------------------|--------------------------------|-------------------------------------|---------------|---------------|----------------------|---|-------------------|--------------------|--|---|---|------------|------|--|--|----------------------|
| 12 | 254 | Wash, J., P., Bell, R., M. | 1986; May | WT | long chain DAGs act as substrate and activator; half-max activation at 1 μM; cardiolipin activity (pH 7.4) slightly higher than NaCl; max activity at 100 mM ionic strength; detergent removes contaminating metal ions, which reduce activity; cardiolipin activity is independent on the mode fraction of DAG and cardiolipin in the assay mix but independent of micelle DAG concentrations above 3.7 mol% inhibitory caused by cardiolipin; Activity was observed with Mn ²⁺ , Fe ²⁺ and Ni ²⁺ ; Zn ²⁺ , Cu ²⁺ and Cd ²⁺ were inactive; Synergistic activation of diacylglycerol kinase was observed with Mg ²⁺ ; Mn ²⁺ , Co ²⁺ , Zn ²⁺ , or Cd ²⁺ ; Calcium was inhibitory to the Mg ²⁺ and Mn ²⁺ activities at all concentrations tested. | diacylglycerol kinase | - | membranes of DgPA overexpressin (pGEX3/GM10), solubilised with OG | 51 mM OG | 3.5 mol% (1 mM) cardiolipin | 6.9 mol% (2 mM) diacylglycerol | 32P ATP detecting phosphatidic acid | 0.3 mM | 0.95 mol% | 10.5 or 10.4 (table) | 8.8 | 5 mM Na ATP | 12.5 mM MgCl2 | 84 min (30 min) in assay; ATP; (diacylglycerol or acetoxy) or cardiolipin; 2,3-dioleoylglycerol same as substrate (rate) | incubation at 25 °C minus MgCl2; half life at 25 °C | 25 °C | 6.6 | NaCl | 60 mM mmdazole, 1 mM EGTA, 0.3 mM DTPA, 2 mM DTT | | |
| | | | | | | | | | 51 mM OG | 3.5 mol% (1 mM) cardiolipin | 6.9 mol% (2 mM) diacylglycerol | 32P ATP detecting phosphatidic acid | | | | | | 5 mM Na ATP | 12.5 mM MgCl2 | 86 min | incubation at 25 °C minus MgCl2; half life at 25 °C | 25 °C | 6.6 | NaCl | 60 mM mmdazole, 1 mM EGTA, 0.3 mM DTPA, 2 mM DTT | |
| | | | | | | | | | 51 mM OG | 3.5 mol% (1 mM) cardiolipin | 6.9 mol% (2 mM) diacylglycerol | 32P ATP detecting phosphatidic acid | | | | | | 5 mM Na ATP | 12.5 mM MgCl2 | 84 min | incubation at 25 °C minus EGTA, DTPA; half life at 25 °C | 25 °C | 6.6 | NaCl | 60 mM mmdazole, 1 mM EGTA, 0.3 mM DTPA, 2 mM DTT | |
| | | | | | | | | | 51 mM OG | 3.5 mol% (1 mM) cardiolipin | 6.9 mol% (2 mM) diacylglycerol | 32P ATP detecting phosphatidic acid | | | | | | 5 mM Na ATP | 12.5 mM MgCl2 | 20 min | incubation at 25 °C minus cardiolipin; half life at 25 °C | 25 °C | 6.6 | NaCl | 60 mM mmdazole, 1 mM EGTA, 0.3 mM DTPA, 2 mM DTT | |
| | | | | | | | | | 51 mM OG | 3.5 mol% (1 mM) cardiolipin | 6.9 mol% (2 mM) diacylglycerol | 32P ATP detecting phosphatidic acid | | | | | | 5 mM Na ATP | 12.5 mM MgCl2 | 31 min | incubation at 25 °C minus MgCl2, cardiolipin; half life at 25 °C | 25 °C | 6.6 | NaCl | 60 mM mmdazole, 1 mM EGTA, 0.3 mM DTPA, 2 mM DTT | |
| | | | | | | | | | 51 mM OG | 3.5 mol% (1 mM) cardiolipin | 6.9 mol% (2 mM) diacylglycerol | 32P ATP detecting phosphatidic acid | | | | | | 5 mM Na ATP | 12.5 mM MgCl2 | 23 min | incubation at 25 °C minus EGTA, DTPA; cardiolipin; half life at 25 °C | 25 °C | 6.6 | NaCl | 60 mM mmdazole, 1 mM EGTA, 0.3 mM DTPA, 2 mM DTT | |
| | | | | | | | | | 51 mM OG | 3.5 mol% (1 mM) cardiolipin | 6.9 mol% (2 mM) diacylglycerol | 32P ATP detecting phosphatidic acid | | | | | | 5 mM Na ATP | 12.5 mM MgCl2 | 500 min | incubation at 25 °C minus DAG; half life at 25 °C | 25 °C | 6.6 | NaCl | 60 mM mmdazole, 1 mM EGTA, 0.3 mM DTPA, 2 mM DTT | |
| | | | | | | | | | 51 mM OG | 3.5 mol% (1 mM) cardiolipin | 6.9 mol% (2 mM) diacylglycerol | 32P ATP detecting phosphatidic acid | | | | | | 5 mM Na ATP | 12.5 mM MgCl2 | 205 min | incubation at 25 °C minus cardiolipin, DAG; half life at 25 °C | 25 °C | 6.6 | NaCl | 60 mM mmdazole, 1 mM EGTA, 0.3 mM DTPA, 2 mM DTT | |
| | | | | | | | | | 51 mM OG | 3.5 mol% (1 mM) cardiolipin | 6.9 mol% (2 mM) diacylglycerol | 32P ATP detecting phosphatidic acid | | | | | | 5 mM Na ATP | 12.5 mM MgCl2 | 230 min | incubation at 25 °C minus MgCl2, cardiolipin, and DAG; half life at 25 °C | 25 °C | 6.6 | NaCl | 60 mM mmdazole, 1 mM EGTA, 0.3 mM DTPA, 2 mM DTT | |
| | | | | | | | | | 51 mM OG | 3.5 mol% (1 mM) cardiolipin | 6.9 mol% (2 mM) diacylglycerol | 32P ATP detecting phosphatidic acid | | | | | | 5 mM Na ATP | 12.5 mM MgCl2 | | 13 diacylglycerol is activator but not a substrate; half life at 25 °C | 25 °C | 6.6 | NaCl | 60 mM mmdazole, 1 mM EGTA, 0.3 mM DTPA, 2 mM DTT | |
| | | | | | | | | | 51 mM OG | 3.5 mol% (1 mM) cardiolipin | 6.9 mol% (2 mM) diacylglycerol | 32P ATP detecting phosphatidic acid | | | | | | 5 mM Na ATP | 12.5 mM MgCl2 | | no significant activity | 25 °C | 6.6 | NaCl | 60 mM mmdazole, 1 mM EGTA, 0.3 mM DTPA, 2 mM DTT | |
| | | | | | | | | | 51 mM OG | 3.5 mol% (1 mM) cardiolipin | 6.9 mol% (2 mM) diacylglycerol | 32P ATP detecting phosphatidic acid | | | | | | 5 mM Na ATP | 12.5 mM MgCl2 | | 0.06 | 25 °C | 6.6 | NaCl | 60 mM mmdazole, 1 mM EGTA, 0.3 mM DTPA, 2 mM DTT | |

| # | Ref Title | Authors | Pub-lished | Mitants | General comments | Protein name | Extinction coefficient as in | Assay as in | Purifi-cation | DgKA stock | Assay environment | Activator | Lipid substrate | Type of assay | Km nucleotide | Km lipid substrate | vmax (DAG varied, ATP varied) | Specific activity compared at 3.5 mol%, sn-1,2-dioleoyl-glycerol | ATP concentration | Mg concentration | Half-life nucleation | Notes and special parameters | Assay temp | pH | Salt | Assay buffer composition | Protein purification protocol |
|---|-----------|---------|------------|---------|------------------|--------------|------------------------------|--------------------------------------|---------------|------------|--------------------------------------|---|--|-------------------------------------|---------------|--------------------|-------------------------------|--|-------------------|---|----------------------|---|------------|------------|--|--|-------------------------------|
| | | | | | | | | 51 mM OG | | | 51 mM OG | 3.5 mol% (1 mM) cardiolipin | 3.5 mol% sn-1,2-dioleoyl-glycerol 3.5 mol% sn-2,3-dioleoyl-glycerol | 32P ATP detecting phosphatidic acid | | | | 7% inhibition compared at 3.5 mol%, sn-1,2-dioleoyl-glycerol | 5 mM Na ATP | 12.5 mM MgCl2 | | 25 °C | 6.6 | 50 mM NaCl | 60 mM midazole, 1 mM EGTA, 0.3 mM DTPA, 2 mM DTT | | |
| | | | | | | | | 51 mM OG | | | 51 mM OG | 3.5 mol% (1 mM) cardiolipin | 6.9 mol% (2 mM) dioleoyl-glycerol | 32P ATP detecting phosphatidic acid | | | | | 5 mM Na ATP | 12.5 mM MgCl2 | | Ki Ca: 30 µM | 25 °C | 6.6 | 50 mM NaCl | 60 mM midazole, 1 mM EGTA, 0.3 mM DTPA, 2 mM DTT | |
| | | | | | | | | 51 mM OG | | | 51 mM OG | 3.5 mol% (1 mM) cardiolipin | 6.9 mol% (2 mM) dioleoyl-glycerol | 32P ATP detecting phosphatidic acid | | | | | 5 mM Na ATP | 12.5 mM MgCl2 | | Ki Mg: 3.4 mM, EGTA and EDTA needed to remove Calcium from assay (comes from membranes), 1.5 µM free MgCl2 and 1.5 µM free DTPA | 25 °C | 6.6 | 50 mM NaCl | 60 mM midazole, 1 mM EGTA, 0.3 mM DTPA, 2 mM DTT | |
| | | | | | | | | 51 mM OG | | | 51 mM OG | 3.5 mol% (1 mM) cardiolipin | 6.9 mol% (2 mM) dioleoyl-glycerol | 32P ATP detecting phosphatidic acid | | | | | 5 mM Na ATP | 12.5 mM MgCl2 | | Ki cardiolipin: 1 mg% | 25 °C | 6.6 | 50 mM NaCl | 60 mM midazole, 1 mM EGTA, 0.3 mM DTPA, 2 mM DTT | |
| | | | | | | | | 51 mM OG + 10% (v/v) DMSO | | | 51 mM OG + 10% (v/v) DMSO | 3.5 mol% (1 mM) cardiolipin | 6.9 mol% (2 mM) dioleoyl-glycerol | 32P ATP detecting phosphatidic acid | 0.35 mol% | | | | 5 mM Na ATP | 12.5 mM MgCl2 | | | 25 °C | 6.6 | 50 mM NaCl | 60 mM midazole, 1 mM EGTA, 0.3 mM DTPA, 2 mM DTT | |
| | | | | | | | | 51 mM OG + 10% (v/v) 1,4-dioxane | | | 51 mM OG + 10% (v/v) 1,4-dioxane | 3.5 mol% (1 mM) cardiolipin | 6.9 mol% (2 mM) dioleoyl-glycerol | 32P ATP detecting phosphatidic acid | 0.55 mol% | | | | 5 mM Na ATP | 12.5 mM MgCl2 | | | 25 °C | 6.6 | 50 mM NaCl | 60 mM midazole, 1 mM EGTA, 0.3 mM DTPA, 2 mM DTT | |
| | | | | | | | | 51 mM OG + 10% (v/v) Tetramethylurea | | | 51 mM OG + 10% (v/v) Tetramethylurea | 3.5 mol% (1 mM) cardiolipin | 6.9 mol% (2 mM) dioleoyl-glycerol | 32P ATP detecting phosphatidic acid | 0.35 mol% | | | | 5 mM Na ATP | 12.5 mM MgCl2 | | | 25 °C | 6.6 | 50 mM NaCl | 60 mM midazole, 1 mM EGTA, 0.3 mM DTPA, 2 mM DTT | |
| | | | | | | | | 51 mM OG | | | 51 mM OG | 3.5 mol% (1 mM) cardiolipin | 6.9 mol% (2 mM) dioleoyl-glycerol | 32P ATP detecting phosphatidic acid | 3.2 mol% | | 10.5 (leaf) 10 (table) | | 5 mM Na ATP | 12.5 mM MgCl2 | | | 25 °C | 6.6 | 50 mM NaCl | 60 mM midazole, 1 mM EGTA, 0.3 mM DTPA, 2 mM DTT | |
| | | | | | | | | 51 mM OG + 10% (v/v) DMSO | | | 51 mM OG + 10% (v/v) DMSO | 3.5 mol% (1 mM) cardiolipin | 6.9 mol% (2 mM) dioleoyl-glycerol | 32P ATP detecting phosphatidic acid | 0.84 mol% | | | | 5 mM Na ATP | 12.5 mM MgCl2 | | | 25 °C | 6.6 | 50 mM NaCl | 60 mM midazole, 1 mM EGTA, 0.3 mM DTPA, 2 mM DTT | |
| | | | | | | | | 51 mM OG + 10% (v/v) 1,4-dioxane | | | 51 mM OG + 10% (v/v) 1,4-dioxane | 3.5 mol% (1 mM) cardiolipin | 6.9 mol% (2 mM) dioleoyl-glycerol | 32P ATP detecting phosphatidic acid | 1.9 mol% | | | | 5 mM Na ATP | 12.5 mM MgCl2 | | | 25 °C | 6.6 | 50 mM NaCl | 60 mM midazole, 1 mM EGTA, 0.3 mM DTPA, 2 mM DTT | |
| | | | | | | | | 51 mM OG + 10% (v/v) Tetramethylurea | | | 51 mM OG + 10% (v/v) Tetramethylurea | 3.5 mol% (1 mM) cardiolipin | 6.9 mol% (2 mM) dioleoyl-glycerol | 32P ATP detecting phosphatidic acid | 0.92 mol% | | | | 5 mM Na ATP | 12.5 mM MgCl2 | | | 25 °C | 6.6 | 50 mM NaCl | 60 mM midazole, 1 mM EGTA, 0.3 mM DTPA, 2 mM DTT | |
| | | | | | | | | 51 mM OG | | | 51 mM OG | 3.5 mol% (1 mM) cardiolipin | 6.9 mol% (2 mM) dioleoyl-glycerol | 32P ATP detecting phosphatidic acid | | | | -3.5 | 5 mM Na ATP | 5 µM free MgCl2 (max higher Km activity, no lower the activity) | | 25 °C | 6.6 | 50 mM NaCl | 60 mM midazole, 1 mM EGTA, 0.3 mM DTPA, 2 mM DTT | | |
| | | | | | | | | 51 mM OG | | | 51 mM OG | 3.5 mol% (1 mM) cardiolipin | 6.9 mol% (2 mM) dioleoyl-glycerol | 32P ATP detecting phosphatidic acid | | | | | 2 mM Mn ATP | 5 µM free MgCl2 | | | 25 °C | 6.6 | 50 mM NaCl | 60 mM midazole, 1 mM EGTA, 0.3 mM DTPA, 2 mM DTT | |
| | | | | | | | | 51 mM OG | | | 51 mM OG | > 4 mol% cardiolipin (full stimulation) | 6.9 mol% (2 mM) dioleoyl-glycerol | 32P ATP detecting phosphatidic acid | | | | -8 | 5 mM Na ATP | 12.5 mM MgCl2 | | | 25 °C | 6.6 | 50 mM NaCl | 60 mM midazole, 1 mM EGTA, 0.3 mM DTPA, 2 mM DTT | |
| | | | | | | | | 51 mM OG | | | 51 mM OG | > 8 mol% Myristic acid (full stimulation) | 6.9 mol% (2 mM) dioleoyl-glycerol | 32P ATP detecting phosphatidic acid | | | | -4 | 5 mM Na ATP | 12.5 mM MgCl2 | | | 25 °C | 6.6 | 50 mM NaCl | 60 mM midazole, 1 mM EGTA, 0.3 mM DTPA, 2 mM DTT | |
| | | | | | | | | 51 mM OG | | | 51 mM OG | 5 mol% DOPA (full stimulation) | 6.9 mol% (2 mM) dioleoyl-glycerol | 32P ATP detecting phosphatidic acid | | | | -4 | 5 mM Na ATP | 12.5 mM MgCl2 | | | 25 °C | 6.6 | 50 mM NaCl | 60 mM midazole, 1 mM EGTA, 0.3 mM DTPA, 2 mM DTT | |
| | | | | | | | | 51 mM OG | | | 51 mM OG | 6 mol% DOPS (full stimulation) | 6.9 mol% (2 mM) dioleoyl-glycerol | 32P ATP detecting phosphatidic acid | | | | -8 | 5 mM Na ATP | 12.5 mM MgCl2 | | | 25 °C | 6.6 | 50 mM NaCl | 60 mM midazole, 1 mM EGTA, 0.3 mM DTPA, 2 mM DTT | |
| | | | | | | | | 51 mM OG | | | 51 mM OG | 10 mol% DOPS (full stimulation, no measured, no saturation) | 6.9 mol% (2 mM) dioleoyl-glycerol | 32P ATP detecting phosphatidic acid | | | | -7.8 | 5 mM Na ATP | 12.5 mM MgCl2 | | | 25 °C | 6.6 | 50 mM NaCl | 60 mM midazole, 1 mM EGTA, 0.3 mM DTPA, 2 mM DTT | |

| # | Ref Title | Authors | Pub-lished | Mitants | General comments | Protein name | Extinction coefficient as in | Purifi-cation | DgKA stock | Assay environment | Activator | Lipid substrate | Type of assay | Km nucleotide | Km lipid substrate | vmax (DAG varied; ATP varied) | Specific activity | ATP concen-tration | Mg concen-tration | Half-life nucleo-tidation | Notes and special parameters | Assay temp | pH | Salt | Assay buffer composition | Protein purification | |
|---|-----------|---------|------------|---------|------------------|--------------|------------------------------|---------------|------------|-------------------|---|----------------------------------|-------------------------------------|---------------|--------------------|-------------------------------|--------------------------------|--------------------|-------------------|---------------------------|--|------------|-------|-------------|--|--|--|
| | | | | | | | | | | 51 mM OG | 1.6 mol% (2 mM) DOPG(highest measured, no saturation) | 6.9 mol% (2 mM) dioleoyl/glycard | 32P ATP detecting phosphatidic acid | | | | -8 | 5 mM Na ATP | 12.5 mM MgCl2 | | | 25 °C | 6.6 | 50 mM NaCl | 60 mM midazole, 1 mM EGTA, 0.3 mM DTPA, 2 mM DTT | | |
| | | | | | | | | | | 51 mM OG | 3.5 mol% (1 mM) cardiolipin | 6.9 mol% (2 mM) dioleoyl/glycard | 32P ATP detecting phosphatidic acid | | | | | 5 mM Na ATP | 0.50 mM MgCl2 | | Effect of few Mg ²⁺ on dioleoyl/glycard kinase activity (Figure 6) | 25 °C | 6.6 | 50 mM NaCl | 60 mM midazole, 1 mM EGTA, 0.3 mM DTPA, 2 mM DTT | | |
| | | | | | | | | | | 51 mM OG | 3.5 mol% (1 mM) cardiolipin | 0.04-10 mol% dioleoyl/glycard | 32P ATP detecting phosphatidic acid | | | | | 5 mM Na ATP | 12.5 mM MgCl2 | | Dioleoyl/glycard kinase function of dioleoyl/glycard concentration (Figure 10) | 25 °C | 6.6 | 50 mM NaCl | 60 mM midazole, 1 mM EGTA, 0.3 mM DTPA, 2 mM DTT | | |
| | | | | | | | | | | 51 mM OG | 3.5 mol% (1 mM) cardiolipin | 0.04-15 mol% dioleoyl/glycard | 32P ATP detecting phosphatidic acid | | | | | 5 mM Na ATP | 12.5 mM MgCl2 | | | 25 °C | 6.6 | 50 mM NaCl | 60 mM midazole, 1 mM EGTA, 0.3 mM DTPA, 2 mM DTT | | |
| | | | | | | | | | | 42-102 mM OG | 0.37 mol% cardiolipin | 3.7 mol% dioleoyl/glycard | 32P ATP detecting phosphatidic acid | | | | max activity | 5 mM Na ATP | 12.5 mM MgCl2 | | Effect of mixed micelle concentration on activity of DgKA (Figure 11) | 25 °C | 6.6 | 50 mM NaCl | 60 mM midazole, 1 mM EGTA, 0.3 mM DTPA, 2 mM DTT | | |
| | | | | | | | | | | 42-102 mM OG | 0.37 mol% cardiolipin | 1.0 mM dioleoyl/glycard | 32P ATP detecting phosphatidic acid | | | | higher OS decrease | 5 mM Na ATP | 12.5 mM MgCl2 | | | | 25 °C | 6.6 | 50 mM NaCl | 60 mM midazole, 1 mM EGTA, 0.3 mM DTPA, 2 mM DTT | |
| | | | | | | | | | | 42-102 mM OG | 0.1 mM cardiolipin | 3.7 mol% dioleoyl/glycard | 32P ATP detecting phosphatidic acid | | | | higher OS decrease | 5 mM Na ATP | 12.5 mM MgCl2 | | | 25 °C | 6.6 | 50 mM NaCl | 60 mM midazole, 1 mM EGTA, 0.3 mM DTPA, 2 mM DTT | | |
| | | | | | | | | | | 42-102 mM OG | 0.1 mM cardiolipin | 1.0 mM dioleoyl/glycard | 32P ATP detecting phosphatidic acid | | | | higher OS decrease (strongest) | 5 mM Na ATP | 12.5 mM MgCl2 | | | 25 °C | 6.6 | 50 mM NaCl | 60 mM midazole, 1 mM EGTA, 0.3 mM DTPA, 2 mM DTT | | |
| | | | | | | | | | | 51 mM OG | 3.5 mol% (1 mM) cardiolipin | 6.9 mol% (2 mM) dioleoyl/glycard | 32P ATP detecting phosphatidic acid | | | | highest activity at pH 6.4 | 5 mM Na ATP | 12.5 mM MgCl2 | | pH dependence on DgKA activity (Supplementary Figure 2) | 25 °C | 5.9 | 50 mM NaCl | 60 mM midazole, 1 mM EGTA, 0.3 mM DTPA, 2 mM DTT | | |
| | | | | | | | | | | 51 mM OG | 3.5 mol% (1 mM) cardiolipin | 6.9 mol% (2 mM) dioleoyl/glycard | 32P ATP detecting phosphatidic acid | | | | -4.7 | 5 mM Na ATP | 12.5 mM MgCl2 | | Effect of Chelators on DgKA activity (No chelator) | 25 °C | 6.6 | 50 mM NaCl | 60 mM midazole, 1 mM EGTA, 0.3 mM DTPA, 2 mM DTT | | |
| | | | | | | | | | | 51 mM OG | 3.5 mol% (1 mM) cardiolipin | 6.9 mol% (2 mM) dioleoyl/glycard | 32P ATP detecting phosphatidic acid | | | | -8.6 | 5 mM Na ATP | 12.5 mM MgCl2 | | EGTA | 25 °C | 6.6 | 50 mM NaCl | 60 mM midazole, 1 mM EGTA, 2 mM DTT | | |
| | | | | | | | | | | 51 mM OG | 3.5 mol% (1 mM) cardiolipin | 6.9 mol% (2 mM) dioleoyl/glycard | 32P ATP detecting phosphatidic acid | | | | -8.4 | 5 mM Na ATP | 12.5 mM MgCl2 | | EDTA | 25 °C | 6.6 | 50 mM NaCl | 60 mM midazole, 1 mM EGTA, 2 mM DTT | | |
| | | | | | | | | | | 51 mM OG | 3.5 mol% (1 mM) cardiolipin | 6.9 mol% (2 mM) dioleoyl/glycard | 32P ATP detecting phosphatidic acid | | | | -6.7 | 5 mM Na ATP | 12.5 mM MgCl2 | | DTPA | 25 °C | 6.6 | 50 mM NaCl | 60 mM midazole, 0.3 mM DTPA, 2 mM DTT | | |
| | | | | | | | | | | 51 mM OG | 3.5 mol% (1 mM) cardiolipin | 6.9 mol% (2 mM) dioleoyl/glycard | 32P ATP detecting phosphatidic acid | | | | -5.3 | 5 mM Na ATP | 12.5 mM MgCl2 | | NFA | 25 °C | 6.6 | 50 mM NaCl | 60 mM midazole, 1 mM EGTA, 2 mM DTT | | |
| | | | | | | | | | | 51 mM OG | 3.5 mol% (1 mM) cardiolipin | 6.9 mol% (2 mM) dioleoyl/glycard | 32P ATP detecting phosphatidic acid | | | | -5.2 | 5 mM Na ATP | 12.5 mM MgCl2 | | o-Phenanthroline | 25 °C | 6.6 | 50 mM NaCl | 60 mM midazole, 1 mM EGTA, 2 mM DTT | | |
| | | | | | | | | | | 51 mM OG | 3.5 mol% (1 mM) cardiolipin | 6.9 mol% (2 mM) dioleoyl/glycard | 32P ATP detecting phosphatidic acid | | | | -5.3 | 5 mM Na ATP | 12.5 mM MgCl2 | | Deferoxamine | 25 °C | 6.6 | 50 mM NaCl | 60 mM midazole, 1 mM EGTA, 2 mM DTT | | |
| | | | | | | | | | | 51 mM OG | 3.5 mol% (1 mM) cardiolipin | 6.9 mol% (2 mM) dioleoyl/glycard | 32P ATP detecting phosphatidic acid | | | | max activity (1.5) at 50 mM | 5 mM Na ATP | 12.5 mM MgCl2 | | Effect of some strength on DgKA activity (Supplementary Figure 3) | 25 °C | 6.6 | 250 mM NaCl | 60 mM midazole, 1 mM EGTA, 0.3 mM DTPA, 2 mM DTT | | |
| | | | | | | | | | | 51 mM OG | 3.5 mol% (1 mM) cardiolipin | 6.9 mol% (2 mM) dioleoyl/glycard | 32P ATP detecting phosphatidic acid | | | | activity decrease (10 U/ml) | 5 mM Na ATP | 12.5 mM MgCl2 | | Effect of some strength on DgKA activity (Figure 3) (LCI and RCI identical) | 25 °C | 6.6 | 250 mM NaCl | 60 mM midazole, 1 mM EGTA, 0.3 mM DTPA, 2 mM DTT | | |

| # | Ref Title | Authors | Pub-lished | Mutants | General comments | Protein name | Extinction coefficient as in | Purifi-cation | DgPA stock | Assay environment | Activator | Lipid substrate | Type of assay | Km nucleotide | Km lipid substrate | vmax (DAG varied; ATP varied) | Specific activity | ATP concen-tration | Mg concen-tration | Half-life inacti-vation | Notes and special parameters | Assay temp | pH | Salt | Assay buffer composition | Protein purification protocol |
|---|-----------|--|--|-------------|------------------|---|------------------------------|---|---|---------------------------|---------------------------------|-----------------------------------|-------------------------------------|---------------|--------------------|-------------------------------|-------------------|--------------------|-------------------|-------------------------|------------------------------|------------|-------------|--|--------------------------|-------------------------------|
| 8 | 472 | Diglyceride kinase from <i>Escherichia coli</i> . Modulation of enzyme activity by phospholipase | Bomber g, E.; Sanderman, H. | 1982, Feb | | | 6 | purified with butan-1-ol in Triton X-100 | 0.66% (w/v) Triton X-100 | 0.66% (w/v) Triton X-100 | cardiolipin (0.3 mM) | 0.1 mM sn-1,2-dipalmitoylglycerol | 32P-ATP detecting phosphatidic acid | | | | | | | all in % | | | | | | |
| 7 | 252 | Membrane localization and synthesis in <i>Escherichia coli</i> . Cloning of a complementary gene for sn-1,2-dipalmitoyl-3-phosphate phosphotransferase | Lightner, V. T.; Larson, D.; Tallier, J.; Kinton, P.; Kmetz, D.; Ruetz, C. R.; Bell, M.; Modrich, P. | 1980 | | socialization of DgPA locus | | | | | | | | | | | | | | | | | | | | |
| 6 | 473 | Diglyceride kinase from <i>Escherichia coli</i> . Purification in organic solvent and some properties of the enzyme | Bomber g, E.; Sanderman, H. | 1976, March | | first purification of DgPA, isoelectric point pH 4.0 | | purified with butan-1-ol in Triton X-100 | 0.7% (w/v) Triton X-100, 0.4 mM DLPE | 0.4 mM bovine cardiolipin | 2 mM sn-1,2-dipalmitoylglycerol | 0.082 mM | 32P-ATP | 1.4 mM | 0.082 mM | | 2.2 | 5 mM ATP | 10 mM MgCl2 | | | | 100 mM NaCl | 50 mM Tris-phosphate, 1 mM mercaptoethanol | | |
| 5 | 231 | Neutral lipid accumulation in the membranes of mutants lacking diglyceride kinase | Raez, C.; Newman, K. F. | 1978 | | | | membrane prepared with purified with butan-1-ol in Triton X-100 | 0.7% (w/v) Triton X-100, 0.4 mM DLPE | 0.4 mM bovine cardiolipin | 2 mM sn-1,2-dipalmitoylglycerol | 0.25 mM | 32P-ATP | | | 0.0015 | 5 mM ATP | 10 mM MgCl2 | | | | | | | | |
| 4 | 230 | Partial purification and properties of diglyceride kinase from <i>Escherichia coli</i> | Schneider, E. G.; Kennedy, E. P. | 1976 | | partial activity in Triton X-100 seen (without lipid activator) | | | | | | | | | | | | | | | | | | | | |
| 3 | 230 | Phosphorylation of ceramide by diglyceride kinase from <i>Escherichia coli</i> | Schneider, E. G.; Kennedy, E. P. | 1973, May | | | | | | | | | | | | | | | | | | | | | | |
| 2 | 248 | Pathways for the synthesis of glycerophosphatidylserine in <i>Escherichia coli</i> | Chang, Y.; Kennedy, E. P. | 1987, Feb | | | | | | | | | | | | | | | | | | | | | | |
| 1 | 229 | The Biosynthesis of Phosphatidic Acid and Lysophosphatidic Acid by <i>Escherichia coli</i> . Phospholipase Pathways in <i>Escherichia coli</i> | Bomberg, R. A.; Kimes, R.; Kimes, S. | 1985, July | | low activity, lipid phosphorylation of diacylglycerol consuming ATP and need for Mg ²⁺ | diglyceride kinase activity | | membrane dissolved in diisobutylphosphate (partially) | | | 0.6% beta-dipalmitoylglycerol | 32P-ATP | | | | | | | | | | | | | |

| # | Ref Title | Authors | Pub- lished | Mutants | General comments | Protein name | Extinction coefficient | Assay as in | Purifi- cation | DgPA stock | Assay environment | Activator | Lipid substrate | Type of assay | Km nucleotide | Km lipid substrate | vmax (DAG varied, ATP fixed) | Specific activity | ATP concen- tration | Mg concen- tration | Half-life inacti- vation | Notes and special parameters | Assay temp | pH | Salt | Assay buffer composition | Protein purification protocol |
|-------|--|---|----------------|---------|--|-----------------|---------------------------|----------------|-------------------|------------|-------------------|-----------|-----------------|---------------|------------------|-----------------------|------------------------------------|----------------------|---------------------------|-----------------------|--------------------------------|---------------------------------|---------------|----|------|-----------------------------|-------------------------------------|
| S2273 | Reconstitution of a calcium pump using defined membrane components | Warren, G. B.; Toon, P. A.; Fagan, N. J.; Lee, A. G.; Metcalfe, J. C. | 1974, March | | First use of PK and LDH coupled ATPase assay for determination of membrane protein activity (Mg ²⁺ , Ca ²⁺ ATPase) | | | | | | | | | | | | | | | | | | | | | | |
| S1329 | Creatine and creatine kinase measurement | Tanzer, M. J.; Grainger, C. | 1959, Dec | | Invention of PK and coupled ATPase assay | | | | | | | | | | | | | | | | | | | | | | |

V List of Figures

V.1 Figures

Figure 1: Schematics of MAS NMR illumination setups described in literature. a to c: Illumination setups based on Chemagnetics and Varian type MAS NMR systems d to f: Illumination setups based on Bruker type MAS NMR systems. **a)** Potential design of the first Chemagnetics illumination setup by Zysmilich and Mc Dermott using a glass fiber optic to illuminate a sapphire rotor from the side inducing photo-CIDNP in photosynthetic reaction centers of *Rhodobacter sphaeroides*^[9]. **b)** Potential design of a modified Varian stator by Concistre and Levitt et al housing 14 optical fibers placed from various angles between coil windings to achieve homogeneous sample illumination using two 250 W quartz halogen lamps and band pass filters^[19-20]. For better light penetration in the studied optical dense Rhodopsin samples, frozen samples were grinded and mixed with glass beads^[19]. **c)** Illumination via the top of zirconia rotors in a Chemagnetics MAS system by modification of the rotor cap to allow light penetration into the sample^[21]. By using a tapered glass rod (**c.2**) irradiation in optically dense samples was improved^[22]. The setups have been used in the group of Prof. Akira Naito to study photointermediates of bacteriorhodopsin (*Halobacterium salinarum*)^[21] and sensory rhodopsin II (*Natronomonas pharaonis*)^[22] using light from LED sources coupled into an optical fiber. **d)** Schematic depicting illumination from the side using a fiber bundle placed through the coil pedestal of a Bruker type MAS system equipped with a stretched thin wire coil to allow more efficient illumination to induce photo-CIDNP in photosynthetic reaction centers^[16]. **e)** Schematic adapted from Hunger and Wang^[23] depicting the modification of a continuous flow MAS system to allow simultaneous acquisition of UV/Vis spectra via a bifurcated fiber bundle through the bottom of the stator and a quartz window inside the MAS rotor. **f)** Schematics of the first described illumination setup used in the group of Prof. Hub de Groot to study photosynthetic reaction centers of *Rhodobacter sphaeroides* by illumination from the top via a plexiglass rod through a translucent Kel-F rotor cap^[15]. **g)** Schematics of the potential light routing through the probe for the in a and c to f depicted illumination variants.

Figure 2: Lens with a clear aperture D collecting and collimating light from a source at focal length f .

Figure 3: Coupling of light into a fiber. A fiber accepts light incident within the acceptance cone, which is determined by the differences of the refractive indices of the medium (n_0), the core (n_1) and the cladding (n_2). If light is incident at an angle greater than the acceptance angle (α), it exceeds the critical angle (θ_c) for total internal reflection.

Figure 4: Coupling of highly directional, collimated light (**a**) and non-coherent light from diffuse light sources emitting light into all directions (**b**). Light from a diffuse source with an emitter area (dark blue) equating the active area of the fiber can be

optimally coupled into a fiber as light paths depicted in blue from the edge of the emitter surface (circles / green arrows) onto the fiber within its acceptance cone (yellow) show. Increasing the emitter area (rose) does not increase the flux, as radiance does not add up for non-coherent light beams. F denotes focal point of the lens at focal length f .

Figure 5: Revised reaction mechanism of NPE-ATP photocleavage according to the revised general mechanism for 2-nitrobenzyl derivatives by Il'ichev et al^[44] summarized by Klan et al^[42].

Figure 6: Chemical structures of a selection of published PPGs based on the 2-nitrobenzyl and coumarin backbone as well as the *p*-hydroxyphenacyl group.

Figure 7: Structure of the glycerophospholipid dioleoylphosphatidylcholine (DOPC).

Figure 8: Definition of local curvature. Principal radii of curvature R_1 and R_2 at a point P of the interface plane, with n the surface normal vector at point P . Redrawn from Seddon^[76].

Figure 9: Structures of lamellar lipid phases: subgel or also termed crystalline phase (L_c), gel phase (L_β), gel phase with tilted hydrocarbon chains (L_β'), gel phase with interdigitated chains (L_β^{int}), rippled gel phase (P_β') and liquid-crystalline phase (L_α). Modified from Koynova and Tenchov^[78].

Figure 10: Structures of lamellar lipid phases. Simple phospholipid bilayers form a gel phase (L_β or also termed s_o) at low temperatures that melts to a liquid disordered phase also termed liquid-crystalline phase (l_d or also termed L_α). The presence of cholesterol or other components (hatched ovals) orders the acyl chains of the latter phase and can fluidize the former phase to an intermediate state for which the term liquid-ordered (l_o) was coined^[85]. Adapted from Munro^[87].

Figure 11: Normal (H_I) and inverted (H_{II}) hexagonal phase. Modified from Koynova and Tenchov^[78].

Figure 12: Inverse micellar and inverse bilayer cubic phases, with representation of their unit cells as well as symmetry axes. Combined from Koynova and Tenchov^[78] and de Campo, Castle and Hyde^[90].

Figure 13: Graphical representation of selected disordered isotropic phases: Spherical, cylindrical (tubules) and disk-shaped micellar aggregates of the normal type M_I . Inverse spherical micelles and the fluid inverse isotropic phase (L_2) belonging to M_{II} . The sponge phase (L_3), an isotropic but disordered phase formed upon swelling of cubic phases or cooling of fluid isotropic phases^[73]. Combined and modified from Koynova and Tenchov^[78], Cherezov, Clogston, Papiz and Caffrey^[96] and Strey and Winkler^[95].

Figure 14: Binary lipid/water phase diagrams and characteristic ^{31}P NMR lineshapes. **a)** Hypothetical phase diagram, with the full sequence containing cubic intermediate phases of phase transitions by varying amphiphile concentration. Reproduced from Kaasgard and Drummond^[97]. **b)** Binary lipid/water phase diagram of DOPC according

to Bergenstaahl and Stenius^[98]. Reproduced from Marsh Handbook of Lipid Bilayers^[82]. **c)** Characteristic ³¹P NMR lineshapes of phases adopted by binary glycerophospholipid/water systems. Adapted from Yao et al^[99] and Cullis et al^[100].

Figure 15: Artwork depicting a cross section of a unilamellar proteoliposome, with DgkA non-directional inserted. Fast axial rotation of the lipids in the fluid L_α (l_d) phase leads to axial symmetry of the chemical shift tensor ($\delta_{22} = \delta_{33}$, in case of phospholipids) resulting in static ³¹P spectra similar to the depicted powder spectrum. PDB: 3ZE4.

Figure 16: Artwork depicting cross sections of a anisotropic bicelle containing DgkA aligning with its bilayer normal perpendicular (**a**) or upon introduction of a lanthanide ion parallel (**b**) to an external magnetic field. Short chain lipids (blue) form a belt around a bilayer consisting of long chain lipids (olive). In case of magnetically aligning anisotropic bicelles the structure is most likely worm-like and not discoidal. The static ³¹P spectra of these systems represents the chemical shift component of parallel and orthogonal aligned short and long-chain lipids (excerpts of Appendix Figure 10). PDB: 3ZE4.

Figure 17: Temperature-composition phase diagram of the monoolein/water system determined under "conditions of use" in the heating and cooling directions starting from 20 °C. A cartoon representation of the various phase states in which colored zones represent water. FI refers to fluid isotropic (L₂), a inverse micellar phase (M_{II}) that forms at high temperatures with random isotropic ordering and fluid-like flow behavior^[73]. Figure published by Cherezov, Clogston, Papiz and Caffrey^[96].

Figure 18: Graphical representation of DgkA embedded in 2x2x2 unit cells of the lipid cubic (Pn3m) mesophase at a molar monoolein to DgkA ratio used herein for 2D MAS NMR experiments (1300:1). The two leaflets of the single monoolein bilayer are colored in blue and red to highlight the two non-intersecting networks of water channels of the bicontinuous system created by the triply periodic minimal surface. Model generated from the Schwarz D surface^[184-186] using PyMOL^[187] and Blender to add monoolein and DgkA. Fast, isotropic orientation change due to diffusion along the highly curved bilayer results in isotropic line shape of phospholipids embedded in a cubic phase otherwise devoid of phosphorous nuclei. PDB: 3ZE4.

Figure 19: Physiological role of DgkA in the inner membrane. DAGs (red) are generated in the periplasmic leaflet during the MDO synthesis cycle where the sn-1-glycerol-phosphate (GP) from PGs (green) is transferred onto MDOs. A second source of DAGs is LPS synthesis where phosphoethanolamine (pEtN) transferases transfer pEtN from PEs (green) onto glucosamines of lipid A (purple) as well as the depicted inner LPS core^[241] often using phosphate as linker (gold). Transbilayer diffusion along their concentration gradient into the cytoplasmic leaflet allows phosphorylation of DAGs via DgkA using ATP as phosphoryl donor. The generation of PA a key intermediate in lipid synthesis is thereby the first step to regenerate PG and PE. A potent activator of DgkA, cardiolipin, is depicted in yellow. Different concentrations resemble the asymmetry of the inner membrane bilayer^[245]. PDB: 3ZE4

Figure 20: Structure and mechanism of DgkA according to Li et al.^[308] **a)** Structure of the $\Delta 4$ -DgkA ternary complex with AMP-PCP and monoolein bound in one active site. **b)** Two dimensional representation of the active and substrate-binding site of DgkA. Hashed bonds indicate hydrogen bond and ionic interactions with AMP-PCP and monoolein. Dashed bonds indicate interactions that are likely and possible, but that are not supported by structure data. Hydrophobic interactions are highlighted as a black semicircle. Residues with numbers in boxes indicate structurally equivalent residues in the cAMP-dependent protein kinase A according to PDB entry: 1ATP. **c)** Proposed mechanism of the phosphoryl transfer reaction. Figures modified from Li et al.^[308].

Figure 21: Pulse sequence of a 2D PDSO experiment for homonuclear correlation of heteronuclei in a densely coupled proton network via proton driven spin diffusion.

Figure 22: Pulse sequence of a 2D NCO or NCA double cross polarization experiment. Depending on the band-selective second CP magnetization is transferred between N-CO or N-C α .

Figure 23: Pulse sequence of a z-filtered TEDOR (ZF-TEDOR) experiment^[322]. Δ marks the z-filter periods. 10 is the loop number of rotor period synchronized 180° pulses applied during $t_{\text{mix}}/4$.

Figure 24: Caged compounds and applied uncaging approaches to trigger DgkA's enzymatic activity in various membrane mimetics.

Figure 25: Pulse sequence of a pulsed field gradient spin echo (PGSE) experiment. δ denotes the gradient time and Δ the diffusion time.

Figure 26: Pulse sequence of a pulsed field gradient stimulated spin echo (PFG-SSE) experiment. δ denotes the gradient time and Δ the diffusion time.

Figure 27: Purification of DgkA. **a)** SDS-PAGE and Western Blot. Lanes are: 7.5 μl protein marker IV 10-150 (M). In 1:10 dilution (0.75 μl), equating to 7.5 μl cell medium: supernatant (S), pellet (P), Ni-NTA column flow-through (F). 7.5 μl of 100 ml OG to DDM detergent exchange wash (D). Eluate containing 2 μg DgkA (E). **b)** Size exclusion chromatogram of purified DgkA on a Superdex 200 Increase 10/300 GL.

Figure 28: LCP unpacked after MAS experiments. Optical transparency and viscosity are maintained after MAS experiments. Illumination and release of NPE-ATP during MAS leads to NPE-ATP concentration dependent coloring from photoproducts (Figure 39b) but does not change optical transparency and viscosity (right).

Figure 29: Stability of LCP at different MAS speeds and temperatures. **a)** Static ^{13}C spectra at 20 °C of LCP formed by centrifugation with a monoolein:liquid ratio of 6:4 (w/w) and an LCP additionally containing 10 mol% DMPC before and after 10 kHz MAS. **b)** Static ^{31}P spectra of the LCP containing 10 mol% DMPC before and after different MAS speeds. **c)** and **d)** ^{13}C and ^{31}P static temperature scan spectra of LCP samples containing 10 mol% DMPC spun at 2.5 kHz MAS between

measurements. Arrow indicates order of temperature scan acquisition from bottom to top.

Figure 30: ^{31}P MAS NMR spectra of a nucleotide in LCP upon MgCl_2 and temperature variation at 3 kHz MAS. **a)** Spectra of LCP samples containing 20 mM ATP with increasing molar ratios of MgCl_2 in 30 mM NaCl and 50 mM HEPES pH 7.5 with respect to the liquid fraction at 303 K. **b)** Temperature scan of a LCP sample containing 30 mM ATP and 30 mM ADP in 120 mM MgCl_2 , 30 mM NaCl and 100 mM HEPES pH 7.5 with respect to the liquid fraction. **c)** Semi-logarithmic plot of chemical shifts of peaks from (a) with respect to the MgCl_2/ATP ratio. **d)** Semi-logarithmic plot of full widths at half maximum (FWHM) of peaks from (a) with respect to the MgCl_2/ATP ratio.

Figure 31: ^{31}P liquid-state NMR of 15 mM ATP with twofold molar excess of MgCl_2 in solution and LCP performed by Dr. Boris Fürtig. **a)** Picture of the LCP injected through the bottom into a 4 mm PTFE NMR tube liner. **b)** ^{31}P INMR spectra of ATP in solution (black, 8 transients) and in LCP (blue, 128 transients). **c)** Normalized integrals of ATP signals in solution (filled symbols) and LCP (non-filled symbols) from ^{31}P DOSY experiments in relation to applied gradient strength (at 242.89 MHz).

Figure 32: Illumination variants and setups used for uncaging experiments. **a)** The existing DNP illumination setup successfully used to study photointermediates of retinal proteins^[24-26]. Schematic of the MAS stator with a narrow fiber bundle from a MAS spinning speed counter inserted through a hole in the stator otherwise used for a temperature sensor. With introduction of new light sources as part of the thesis, light from several LED's can be coupled into a liquid lightguide via beam combiners connected to a LED lightguide adaptor. The liquid lightguide is then coupled to the fiber bundle exiting the probe. **b)** Schematics of the new high field MAS NMR setup developed for efficient *in situ* sample illumination. A custom manufactured fiber bundle with an active diameter of 2 mm and macor ferules is inserted into the stator through a hole drilled into the coil pedestal of a custom manufactured stretched thin wire coil to allow efficient coupling of light from LEDs into the sample. The sample volume is restricted with rubber disks inside the stator to align with the illuminated area. **c)** Illumination of the sample in a MAS rotor outside the spectrometer was performed as well to test chosen light sources and lightguide variants for uncaging. After illumination, the sample was transferred into a ssNMR spectrometer for acquisition as depicted for *ex situ* uncaging experiments using a 600 MHz NMR spectrometer equipped with a 4 mm MAS probe. Illumination setups are described in detail in materials and methods (Section I.2.4).

Figure 33: UV-Vis spectra of empty as well as filled 4 mm sapphire and zirconia MAS rotors. To prevent light passing around the sides of the rotors, a black painted aluminum mask was installed in the cuvette holder chamber.

Figure 34: Uncaging of NPE-ATP outside the spectrometer by illumination with a UV LED through the custom-built fiber bundle manufactured for the high field MAS NMR illumination setup. **a)** UV-Vis absorbance spectra of 0.1 mM NPE-ATP before and

after uncaging in 100 mM HEPES, 30 mM NaCl pH 7.5 as well as 0.1 mM ATP and the buffer alone in a 3 mm path length quartz cuvette. **b)** ^{31}P liquid-state NMR spectra of 7.5 mM NPE-ATP in 100 mM HEPES, 30 mM NaCl, 60 mM MgCl_2 pH 7.5 before, upon 48% uncaging and after uncaging (121.45 MHz). **c)** Detail of NPE-ATP peaks of ^{31}P liquid-state NMR spectra with and without ^1H decoupling before uncaging with J -couplings. Peak doubling is observed due to the diastereomeric mixture (121.45 MHz). **d)** Progress of uncaging 15 mM NPE-ATP in a 3.2 mm sapphire MAS rotor upon illumination with 365 nm light outside the spectrometer followed by the ^{31}P signals of NPE-ATP.

Figure 35: Uncaging of 5 mM NPE-ATP in 100 mM HEPES pH 7.5 with the illumination setup at the DNP spectrometer at room temperature and MAS in manual mode at ~ 1 kHz. In black: ^{31}P spectrum before illumination. In red: ^{31}P spectrum after 30 min illumination at 365 nm. Release of ATP from its cage could not be detected.

Figure 36: Uncaging of NdiEt-tcAA outside the spectrometer. **a)** Uncaging reaction scheme and structural formula of NdiEt-tcAA with atom numbering for the assignment of ^{13}C and ^1H chemical shifts (Table 6). **b)** UV-Vis absorbance spectra of NdiEt-tcAA in different solvents, before (blue and black) and after (cyan and gray) illumination of the sample at 470 nm for 5 min. **c)** ^1H INMR spectra before (black) and after (red) uncaging of NdiEt-tcAA at 470 nm for 5 min in $\text{DMSO-d}_6 + 33\%$ (v/v) H_2O and TCE **(d)** at 500.18 MHz with assignment of peaks according to (a).

Figure 37: Uncaging of NdiEt-tcAA for illumination experiments inside the DNP spectrometer. Samples containing 5 mM NdiEt-tcAA in TCE were illuminated for 15 min at different wavelengths inside the DNP spectrometer at room temperature at ~ 1 kHz MAS in manual mode. **a)** Normalized UV-Vis absorbance spectra of samples before illumination (black) and after illumination at 470 nm (red) and 405 nm (blue). **b)** ^1H NMR spectra recorded at the DNP spectrometer (400.20 MHz) before (black) and after 15 min illumination at 470 nm (red) and 405 nm (blue) at room temperature and ~ 1 kHz MAS in manual mode.

Figure 38: Modified probe for illumination under MAS conditions with inserted light guide. Pictures show the stator with the light guide inserted through a hole in the coil pedestal during illumination. The position of the light guide compared to the sample and the stretched thin wire coil is highlighted in the center picture of the disassembled coil pedestal.

Figure 39: Illuminated area of NPE-ATP containing LCP samples. **a)** 30 μl LCP samples containing 0.45 μmol NPE-ATP illuminated inside the probe at 3 kHz MAS for 1 s with the 355 nm laser or 12 min with the 365 nm LED. **b)** Concentration dependent discoloration of samples with sample volume reduced to the active area containing 15 μl LCP upon illumination for 5 min with the 365 nm LED at 3 kHz MAS. **c)** Picture of beam divergence of the fiber bundle at 365 nm with a LED as light source **d)** Top view of the disassembled coil pedestal with an inserted sapphire MAS rotor containing LCP during illumination at 365 nm via the fiber bundle with a LED as light source.

Figure 40: Stepwise uncaging of 0.4 μmol NPE-ATP at 303 K with the developed high-field MAS NMR illumination setup *in situ* at 365 nm followed by ^{31}P ATP and NPE-ATP signals in **a)** 15 μl LCP (monoolein:liquid 6:4 (w/w)) at 3 kHz MAS. Amounts as well as concentrations with respect to the liquid fraction given. **b)** 3 mg DOPC liposomes at 10 kHz MAS. Both samples were prepared with 50 mM HEPES pH 7.5 and 30 mM NaCl.

Figure 41: NPE-ATP uncaging efficiency in LCP upon illumination with the developed high-field MAS NMR illumination setup *in situ* at 365 nm for 5 min at different NPE-ATP concentrations with respect to the liquid fraction at 303 K and 3 kHz MAS followed via ^{31}P NPE-ATP signals. Samples contained 2.8 μg DgkA, 100 mM HEPES pH 7.5, 30 mM NaCl and respective MgCl_2 concentration according to Section I.2.2.2.3.

Figure 42: Illumination of sapphire MAS rotors from the bottom. **a)** Rotors contained 0.45 μmol NPE-ATP in LCP or 3 mg DOPC containing liposomes and are illuminated with the 365 nm LED. Illumination of the whole sample area persists upon insertion of a rubber disk at the bottom blocking the direct light path. **b)** Schematic of possible total reflection along the outer rotor wall and scattering at the rough inner rotor wall.

Figure 43: ^{31}P spectra and uncaging efficiencies of tested illumination configurations at full sample volume (30 μl). Comparison of illumination from the side during MAS inside the probe, illumination via short laser pulses through the bottom at a 45° angle and illumination through the bottom using the 365 nm LED. Samples contained 0.45 μmol NPE-ATP (15 mM with respect to the rotor volume) in LCP or 3 mg DOPC containing liposomes with 50 mM HEPES pH 7.5 and 30 mM NaCl.

Figure 44: Comparison of LCP, DOPC liposomes and anisotropic bicelles. **a)** Optical comparison of membrane mimetics tested for uncaging experiments. **b)** Comparison of static ^{31}P spectra of LCP + 10 mol% DMPC, DOPC liposomes and magnetically aligned anisotropic bicelles (3.2:1 (mol/mol) DMPC:DHPC).

Figure 45: Enzymatic activity of DgkA in LCP, liposomes and anisotropic bicelles in the presence of lipid substrates (5 and 0.25 μmol dioctanoylglycerol for liposomes and bicelles respectively). **a)** ^{31}P real-time ssNMR spectra following DgkA's enzymatic activity upon addition of 2, 1.5 and 0.75 μmol ATP for LCP, liposomes and bicelles equating to .40, 30 and 15 mM ATP with respect to the rotor volume. Sample amount of DgkA was 5 μg for LCP (L:P 240400:1), 500 μg for liposomes (L:P 120:1) and 2.5 μg for bicelles (L:P ~15600:1). L:P is not including dioctanoylglycerol. Experiments performed at 30 $^\circ\text{C}$ and 3 kHz MAS for LCP, 10 kHz MAS for liposomes and without MAS for bicelles. **b)** Progress curves of integrals from well-separated peaks of (a). Monoexponential fits for LCP and biexponential fits for liposomes and bicelles of the time traces to determine initial reaction rates are shown as solid lines.

Figure 46: UV-Vis absorbance spectra of LCP (monoolein:liquid 6:4 (w/w)), DOPC liposomes (1, 4 and 35 mg/ml) and anisotropic bicelles (DMPC:DHPC 3.2:1 (mol/mol), 390 mg/ml).

The absorbance spectrum of LCP was measured in a custom built quartz holder with 0.9 mm path length. Other samples and comparison to the used buffer (100 mM HEPES pH 7.5, 30 mM NaCl) and H₂O was performed in a standard 3 mm path length quartz cuvette. Dotted lines represent subtracted background spectra of the empty cuvette or holder.

Figure 47: Uncaging of NPE-ATP to initiate DgkA's enzymatic activity in LCP, liposomes and anisotropic bicelles. **a)** ³¹P real-time ssNMR spectra following DgkA's enzymatic activity upon 5 min illumination to initiate uncaging of 0.3 μmol NPE-ATP for LCP and DOPC liposomes and 0.75 μmol NPE-ATP for bicelles. These amounts equate to 15 mM NPE-ATP for all samples with respect to the rotor volume as illumination for bicelles was performed in a 4 mm sapphire rotor outside the spectrometer. Sample amount of DgkA was 0.97 μg for LCP (L:P 371200:1), 300 μg for liposomes (L:P 120:1) and 500 μg for bicelles (L:P 130:1). Experiments performed at 30 °C and 3 kHz MAS for LCP, 10 kHz MAS for liposomes and without MAS for bicelles. **b)** Comparison of selected ³¹P spectra with annotations before uncaging (black), directly after uncaging (red) and at the end of the in (a) shown real-time NMR experiments (dark red). **c)** Progress curves of integrals from well-separated peaks of (a). Biexponential fit for LCP and monoexponential fits for liposomes and bicelles of the time traces are shown as solid lines. The amount of released ATP was 0.23 μmol for LCP equating to 38.5 mM with respect to the liquid fraction, 0.2 μmol for DOPC liposomes and 0.75 μmol for bicelles.

Figure 48: Pellets of DOPC proteoliposomes containing DgkA and DOG in varying ratios (18 μmol total lipid) after ultracentrifugation at 72660 g (25000 rpm) 4 °C for 30 min (Rotor: 45 Ti; Optima LE-80K Ultracentrifuge, Beckman Coulter).

Figure 49: ³¹P MAS NMR spectra after phosphorylation of DOG by 0.25 mg DgkA upon addition of 1 μmol ATP in DOPC liposomes containing varying lipid molar ratios of DOG (L:P 480:1) at 303 K and 10 kHz MAS. For percentage and deviation of DOPA signal to DOPC signal see Appendix Table 3.

Figure 50: Time traces and selected spectra from ³¹P real-time MAS NMR experiments following DgkA's basal ATPase activity in liposomes upon addition of 0.45 μmol ATP followed by 5 min illumination to uncage membrane incorporated NPE-DOG triggering enhanced enzymatic activity. **a to c):** 15, 40 and 500 μg DgkA reconstituted into DOPC liposomes containing 20 mol% NPE-DOG at L:P ratios of 5000:1, 2000:1 and 500:1. Determined basal activity and stimulated activity upon illumination for these experiments are given in Appendix Table 4. **d)** Illumination does not enhance enzymatic activity of 54 μg DgkA reconstituted in DOPC liposomes (L:P 480:1) not containing a lipid substrate.

Figure 51: Formation of DgkA's kinase product thiophosphatidic acid after uncaging of NPE-DOG in presence of .75 nmol ATP_γS. **a)** Spectra of a ³¹P real-time NMR experiment before (black) and after uncaging of NPE-DOG (red) triggering kinase activity of 13.3 μg DgkA reconstituted in DOPC liposomes (L:P 2000:1) containing

20 mol% NPE-DOG. The asterisk denotes a degradation product of the formed thiophosphate during hydrolysis of ATP γ S. **b)** Progress curves of the ^{31}P real-time NMR experiment depict basal ATPase activity before uncaging of NPE-DOG and kinase activity in conjunction with enhanced ATPase activity after uncaging as can be seen by formation of the thiophosphatidic acid product and enhanced built-up of ThioPi. Spectra consist of 6272 transients per increment.

Figure 52: Formation of thiophosphatidic acid by DgkA with ATP γ S as nucleotide substrate. ^{31}P spectra confirm that the signal at 44 ppm forming after uncaging of NPE-DOG is the kinase product ThioPA as it can be cross polarized, exhibits the same chemical shift when utilizing non-caged DOG as substrate (**a**) and upon washing of the membrane pellet is mainly found in the pellet fraction (**b**). Spectra recorded at 280 K with 9 kHz MAS to avoid overlap with spinning side bands of repacked samples at 14.09 Tesla, 243 MHz ^{31}P . The spectrum of the supernatant was acquired with a liquid-state NMR spectrometer at 11.75 Tesla, 202 MHz ^{31}P .

Figure 53: ^{31}P NMR spectra of thiophosphate and a 2 fold molar excess of MgCl_2 at pH 7.5 recorded at different times show built up of a signal at 15 ppm which can be attributed to a degradation product of thiophosphate. Spectra acquired with a liquid-state NMR spectrometer at 7.05 Tesla, 121 MHz ^{31}P .

Figure 54: ^{31}P real-time NMR spectra following enzymatic activity of 0.8 mg DgkA in DOPC (L:P 120:1) and 9:1 mol/mol DMPC:DMPA (L:P 50:1) liposomes upon addition of 2.1 μmol DBG and 0.75 μmol respectively 1.5 μmol ATP. A signal at 3.7 ppm was attributed to lyso-PA based on its chemical shift and observable $^3J_{^{31}\text{P},^1\text{H}}$ coupling (t , $J = 6.5$ Hz), most likely a degradation product of DBG (t , $J = 6.0$ Hz) (Appendix Figure 15).

Figure 55: Enzymatic activity of DgkA in DDM in the presence of lipid substrates does not exhibit strong ATPase activity. **a)** ^{31}P real-time MAS NMR spectra following the enzymatic activity of 90 μg DgkA in 0.5% (w/v) DDM with 1.5 μmol dioctanoylglycerol added as lipid substrate at 1.35 kHz MAS. The enzymatic reaction was initiated by addition of 1.5 μmol ATP (equates to 30 mM ATP). **b)** ^{31}P MAS spectra after consumption of ATP (black) and after addition of Pi and AMP (red) with 2.1 μmol DBG as lipid substrate instead of dioctanoylglycerol. Observed Pi formation can be attributed to non-enzymatic hydrolysis of ADP as seen by built-up of an AMP signal.

Figure 56: Basal ATPase activity of DgkA in different environments. **a)** Activity in dependence to ATP concentration without a lipid substrate was determined for DgkA in DDM and reconstituted in DOPC and *E. coli* polar lipid liposomes via molybdenum blue assay. **b)** Lineweaver-Burk representation of basal ATPase activity with fitted kinetic parameters obtained from a). Error bars represent standard deviation of four independent replications. Values of replicates are shown as small symbols.

Figure 57: Specific basal ATPase activity ($\mu\text{mol ATP} / \text{min}$) of DgkA in DDM and reconstituted in DOPC and *E. coli* polar lipid liposomes at 20 mM ATP in dependence to varying DgkA amounts via molybdenum blue assay.

Figure 58: Comparison of DgkA's basal ATPase activity in DDM determined via initial reaction rates from ^{31}P real-time MAS NMR experiments (filled circles) and molybdenum blue assay (open diamonds) in dependence to ATP concentration. Insets show Lineweaver-Burk representations of the datasets with fitted kinetic parameters obtained from the saturation curves (Table 8). Error bars reported for ^{31}P real-time MAS NMR measurements represent standard deviation of the four analyzed signals for determination of the initial reaction rate. Error bars reported for the coupled assay represent standard deviation of four independent replications. Values of replicates are shown as small symbols.

Figure 59: DgkA's enzymatic activity in LCP determined via ^{31}P real-time MAS NMR and *in meso* coupled assay. **a)** ATP saturation curve of initial reaction rates in a non-swollen LCP via ^{31}P real-time MAS NMR experiments upon addition of ATP. Depicted in black are rates from measurements with a final monoolein:liquid ratio of 6:4 (w/w) after addition of ATP. For higher ATP concentrations (in gray) the lipidic cubic phase was formed at a constant monoolein:liquid ratio of 6:4 (w/w). Addition of ATP yielded a maximum monoolein:liquid ratio of 4.4:5.6 (w/w). ATP concentrations are given with respect to the liquid fraction of the samples. **b)** ATP saturation curve of DgkA's activity in a swollen cubic phase determined via the *in meso* coupled ATPase assay.

Figure 60: Initial reaction rates of DgkA's enzymatic activity in LCP initiated by uncaging NPE-ATP in dependence to released ATP concentrations obtained from progress curves of ^{31}P real-time MAS NMR experiments. ^{31}P real-time NMR spectra and progress curves for the 38.5 mM uncaged ATP datapoint are shown in Figure 47. A linear fit of the datapoints visualizes the lack of saturation at ATP concentrations achievable by uncaging inside the spectrometer.

Figure 61: ATP saturation curve of DgkA's enzymatic activity in detergent micelles with monoolein as substrate determined via the *in surfo* coupled assay. Inset shows Lineweaver-Burk representation of basal ATPase activity with fitted kinetic parameters obtained from the saturation curve (Table 9). Error bars represent standard deviation of three independent replications. Values of replicates are shown as small symbols.

Figure 62: Reconstitution of DgkA at a concentration of 14.3 mg/ml in LCP, feasible for protein ssNMR measurements, via a LCP mixing device. Reconstitution resulted in an optical transparent and birefringent LCP as can be seen on the minor scale marks on the rear side of the Hamilton syringe.

Figure 63: 1D protein solid-state NMR spectra of $\text{U}^{13}\text{C}^{15}\text{N}$ labelled DgkA in LCP and DMPC:DMPA liposomes. **a)** ^{13}C cross polarization (blue) and direct polarized 1D spectra (black) of DgkA in LCP under static and 10 kHz MAS conditions at 303 K. **b)** ^{15}N static cross polarization spectra of DgkA in liposomes with 8 ms contact time (black) and DgkA in LCP with 1 ms (light blue) and 8 ms (blue) contact time (20480 transients) at 303 K.

Figure 64: NCA spectra of $\text{U}^{13}\text{C}^{15}\text{N}$ labelled DgkA in LCP (blue) and

DMPC:DMPA liposomes (gray) at 10 kHz MAS and 303 K. 60 increments in F1, 416 transients in F2. For comparison, the assignment of DgkA in DMPC:DMPA liposomes at 273 K by Kristin Möbius[307] is overlaid.

Figure 65: PDSM spectra of $U^{13}C^{15}N$ labelled DgkA in LCP (blue) and DMPC:DMPA liposomes (gray) at 10 kHz MAS, 303 K and 20 ms mixing time. 540 increments in F1, 104 transients for liposomes and 144 transients for LCP in F2.

Figure 66: ^{13}C cross polarization spectra acquired under DNP conditions with mw_{on} (black) and mw_{off} (gray) of samples containing 40% (w/v) monoolein, 10 mM AMUpol, 30% (v/v) glycerol and 50% (v/v) D_2O (with respect to the liquid fraction) with **a**) 1 mg non-labelled DgkA in 25 mM HEPES pH 7.5 and 15 mM NaCl (128 transients) and **b**) 0.7 mg $U^{13}C^{15}N$ labelled DgkA with 20.5 mM AMP-PCP, 40 mM $MgCl_2$ and 100 mM HEPES pH 7.5 reconstituted (8 transients) at 100 K and 8 kHz MAS.

Figure 67: **a**) ^{31}P cross polarization DNP spectrum of a sample containing 0.7 mg $U^{13}C^{15}N$ labelled DgkA (51 nmol) and 20.5 mM AMP-PCP (246 nmol) reconstituted into 40% (w/v) monoolein with 40 mM $MgCl_2$, 10 mM AMUpol, 100 mM HEPES pH 7.5, 30% (v/v) glycerol and 50% (v/v) D_2O (with respect to the liquid fraction) (128 transients). Asterisks denote spinning side bands. **b**) ^{31}P - ^{13}C TEDOR DNP spectra of the same sample as in (a) with 1, 2 and 6 ms mixing time (4096 transients). **c**) Comparison of the empty ^{31}P - ^{13}C TEDOR DNP spectrum at 8 ms mixing time and 24576 transients (black) with a DMPC/DMPA liposome sample containing non-labelled MsbA with 1024 transients courtesy of Hundeeep Kaur (green) at 100 K and 8 kHz MAS. The comparison is highlighting the absence of unspecific background signals in LCP samples otherwise occurring in samples containing phospholipids.

Figure 68: ^{31}P - ^{13}C 2D TEDOR DNP spectrum of a sample containing 0.7 mg $U^{13}C^{15}N$ labelled DgkA (51 nmol) and 20.5 mM AMP-PCP (246 nmol) reconstituted into 40% (w/v) monoolein with 40 mM $MgCl_2$, 10 mM AMUpol, 100 mM HEPES pH 7.5, 30% (v/v) glycerol and 50% (v/v) D_2O (with respect to the liquid fraction). 1 ms mixing time, 10 increments in F1, 2048 transients in F2, 100 K, 8 kHz MAS and respective projections as well as ^{31}P and ^{31}P - ^{13}C TEDOR 1D spectra.

Figure 69: 1H MAS NMR spectra of DMPC (black) and DMPC + 20 mol% EDP (red) or DHDP (blue) in D_2O (50 wt%). 16 transients at 22 °C and 10 kHz MAS, chemical structures and assignment of DMPC^[450] and PUFA^[400] signals are shown.

Figure 70: 1H MAS NMR temperature scans of DMPC and DMPC + 20 mol% EDP or DHDP in D_2O (50 wt%) at 10 kHz MAS. **a**) Acquired 1H spectra with respect to increasing temperature. 16 transients per increment. **b**) Normalized peak area and fits of analyzed acyl chain methylene DMPC (filled symbols and solid lines) and PUFA (non-filled symbols and dashed lines) peaks (see Appendix Figure 25) of DMPC (black) and DMPC + 20 mol% EDP (red) or DHDP (blue) with respect to increasing temperature using the Boltzmann sigmoid function. **c**) Difference of normalized peak area of EDP or DHDP signals to respective DMPC signals of DMPC + 20 mol% EDP (red) or DHDP (blue) as depicted in (b).

Figure 71: ^1H MAS NMR spectra of native membranes derived from wild-type and *Ephx2*^{-/-} mouse brains at 37 °C and 10 kHz MAS with first order spinning sidebands at 100 times magnification as well as centerband region of temperature scan spectra of the wild-type mouse brain membrane.

Figure 72: Normalized ethylene **(a)** and choline **(b)** peak heights obtained from ^1H MAS NMR temperature scan measurements of native membranes derived from wild-type, *Ephx2*^{-/-} and *Ephx2*^{-/-} mouse brains treated with EDP (100 μM) or DHDP (10 or 100 μM). Bar diagrams show normalized peak height at 37 °C. Error bars represent uncertainty calculated from signal to noise, baseline correction and temperature referencing.

Figure 73: Normalized ethylene peak heights obtained from ^1H MAS NMR temperature scan measurements of native membranes derived from wild-type and *Ephx2*^{-/-} mouse brains and native membranes treated with 10 mg/ml methyl- β -cyclodextrin. Bar diagrams show normalized peak height at 37 °C. Error bars represent uncertainty calculated from signal to noise, baseline correction and temperature referencing.

V.2 Appendix Figures

Appendix Figure 1: Partial, annotated sequence of pSD005 according to sequencing results, highlighting insertion of a IS1 transposase sequence. Sequencing and PCR primers used are highlighted in yellow.

Appendix Figure 2: Temperature calibration of 600 MHz 4 mm HXY **(a)**, 4 mm HX **(b)** as well as 850 MHz 4 mm HCN **(c)**, 3.2 mm HCN **(d)**, 3.2 mm HX **(e)** WB MAS probes at 10 kHz (black to gray), 5 kHz (blue) and 3 kHz (red) MAS via ^{79}Br T₁ relaxation measurements using microcrystalline KBr. The different grayscale in **(c)** depict calibration before each measurement time for mouse brain membrane temperature scans.

Appendix Figure 3: Structural formula and atom numbering of NPE-ATP

Appendix Figure 4: Details of ^1H NMR spectra of 12 mM NPE-ATP with (purple) and without (black) ^{31}P decoupling and 30 mM ATP (blue) in 100 mM HEPES, 30 mM NaCl pH 7.5 at 700.17 and 300.03 MHz with multiplet assignments.

Appendix Figure 5: ^1H - ^{13}C HSQC spectra of 12 mM NPE-ATP **(a)** and 30 mM ATP **(b)** in 100 mM HEPES, 30 mM NaCl pH 7.5 with assignment according to Appendix Figure 3 (400.13 MHz) and respective ^1H and ^{13}C 1D spectra at same field except the ^{13}C spectrum of NPE-ATP (125.78 MHz).

Appendix Figure 6: ^1H - ^{31}P HMBC of 12 mM NPE-ATP in 100 mM HEPES, 30 mM NaCl pH 7.5 with assignment according to Appendix Figure 3 (500.18 MHz) and respective ^1H (400.13 MHz) and ^{31}P (202.48 MHz) 1D spectra.

Appendix Figure 7: ^1H - ^{13}C HSQC **(a)** and HMBC **(b)** spectra of NdiEt-tcAA (400.13 MHz, DMSO-d₆) with assignment and respective ^1H and ^{13}C 1D spectra

(500.18 MHz, DMSO-d₆). Atom numbers refer to Figure 36a. Dotted lines mark cut offs.

Appendix Figure 8: ¹H-¹³C HSQC (**a**) and HMBC (**b**) spectra of NdiEt-tcAA (500.18 MHz, TCE) with assignment and respective ¹H and ¹³C 1D spectra. Atom numbers refer to Figure 36a. Dotted lines mark cut offs. Spectra were recorded without lock and shimming was performed on an external sample.

Appendix Figure 9: pH titration curve of Pi ³¹P chemical shift. 5 mM sodium phosphate in 30 mM NaCl, 50 mM HEPES pH 7.9 at 303 K by addition of NaOH.

Appendix Figure 10: Verification of magnetic alignment and flipping of bicelles prepared for measuring DgkA's enzymatic activity in real-time NMR experiments and a coupled ATPase assay upon addition of ATP or uncaging of NPE-ATP. **a**) Schematic of anisotropic bicelles aligning perpendicular with their bilayer normal to a magnetic field, upon addition of a cation (Yb³⁺) bicelles flip to align parallel to a magnetic field. Bicelle flipping is causing a change of the observed chemical shift in static ³¹P ssNMR spectra.^[139, 146] **b**) Static ³¹P temperature scan spectra of prepared bicelles made of 3.2:1 (mol/mol) DMPC:DHPC (bottom) and upon after addition of 1:100 (mol/mol) YbCl₃ to DMPC showing successful flipping of the anisotropic bicelles upon formation at elevated temperature.

Appendix Figure 11: ³¹P spectra after consumption of 2 μmol ATP (equates to 100 mM ATP with respect to the liquid fraction) by 5 μg DgkA in 30 mg LCP (black) and after addition of Pi (red) at 3 kHz MAS. For the real-time MAS NMR spectra of the enzymatic reaction see Figure 45.

Appendix Figure 12: ³¹P real-time MAS NMR spectra upon uncaging of 0.3 μmol NPE-ATP in DOPC liposomes containing 300 μg DgkA (L:P 120:1) 30 mM NaCl, 100 mM HEPES pH 7.5 but without MgCl₂ at 10 kHz MAS. Under these conditions in absence of Mg²⁺ ATP hydrolysis is not detected, as a divalent cation is a required cofactor for DgkA's enzymatic activity^[250].

Appendix Figure 13: Static ³¹P spectra of DOPC liposomes containing 20 mol% DOG, DOPA, DMPA and DMPC liposomes containing 10 mol% DMPA at 303 K.

Appendix Figure 14: Projections of the acquired NCA spectra for the Trp112 peak with peak maxima (black), projected baseline and base markers (dark red) and Gaussian fits (red). **a**) F2 and **b**) F1 dimension projection of Trp112 peak of the DMPC:DMPA liposome sample. **c**) F2 and **d**) F1 dimension projection of Trp112 peak of the LCP sample.

Appendix Figure 15: Formed lipid products of DgkA's enzymatic reaction in liposomes with DBG as lipid substrate. ³¹P spectra with scalar couplings of lipid product (**a**) and nucleotide signals (**c**) after enzymatic activity of 0.84 mg DgkA in DMPC:DMPA liposomes (L:P 50:1) upon addition of 0.8 μl (3.45 μmol) DBG and 1.5 μmol ATP at 10 kHz MAS followed by ³¹P real-time MAS NMR (**b**).

Appendix Figure 16: Time trace of a coupled photometric assay performed in a cuvette following enzymatic activity of 20 μg DgkA in bicelles. Addition of 3 mM ATP and 18 mM DBG to start the kinase reaction is visible by disturbance of the absorbance recording. The linear fitted section of the time trace for rate determination after addition of DBG is depicted in red and yielded a activity of 1.5 ± 0.2 U.

Appendix Figure 17: Fill height in relation to volume of 96 well plate wells used for the coupled photometric assays.

Appendix Figure 18: Representative set of time traces of *in meso* and *in surfo* coupled photometric assays performed with varying ATP concentrations. **a)** *in meso* coupled assay performed with 0.25, 0.5, 1, 1.5, 2, 3.5, 5, 7.5, 10, 15, 20, 30 mM ATP (from dark to light gray) as well as without DgkA with and without 30 mM ATP. **b)** *in surfo* coupled assay performed with 0, 0.01, 0.05, 0.1, 0.25, 0.5, 0.75, 1, 3.5, 5, 10 mM ATP (from dark to light gray). Linear fitted sections of the time traces for rate determination are depicted from blue to black with increasing ATP concentrations.

Appendix Figure 19: Molybdenum blue assay standard curve for determination of inorganic phosphorus. $n = 5$

Appendix Figure 20: Absorbance measurements for the determination of specific basal ATPase activity of DgkA in DDM and reconstituted in DOPC and *E. coli* polar lipid liposomes at 20 mM ATP in dependence to varying DgkA amounts via molybdenum blue assay. Raw data: filled symbols and linear fit thereof as dashed line. Background: half filled symbols and linear fit thereof as dotted line. Background subtracted data: non-filled symbols and linear fit thereof as solid line.

Appendix Figure 21: Progress curves of ^{31}P real-time MAS NMR experiments following the activity of 2.8 μg DgkA in 50 mg LCP (2:3 (w/w) liquid : monoolein) upon addition of 0.5, 1, 1.5, 2, 2.5, 3 μmol ATP equating to 25, 50, 75, 100, 125, 150 mM ATP (from black to gray) with respect to the liquid fraction of the LCP. Monoexponential fits of the time traces to determine initial reaction rates are shown in blue till black from low to high ATP concentrations.

Appendix Figure 22: Progress curves of ^{31}P real-time MAS NMR experiments following the activity of 3.8 μg DgkA in 15 mg LCP (2:3 (w/w) liquid : monoolein) prepared with 0.1, 0.2, 0.3, 0.4, 0.5 μmol NPE-ATP upon release of 0.09, 0.16, 0.23, 0.28, 0.34 μmol ATP via uncaging equating to 15.7, 27.3, 38.5, 47.3, 56.7 mM ATP with respect to the liquid fraction of the LCP. Biexponential fits of the time traces to determine initial reaction rates are shown in blue till black from low to high ATP concentrations.

Appendix Figure 23: Initial reaction rates of DgkA's enzymatic activity in LCP determined via ^{31}P real-time MAS NMR as shown in Figure 59a in dependence to ATP amounts added. Depicted in black are rates from measurements with a final monoolein:liquid ratio of 6:4 (w/w) after addition of ATP. For higher ATP concentrations (in gray) the lipidic cubic phase was formed at a constant

monoolein:liquid ratio of 6:4 (w/w). Addition of ATP yielded a maximum monoolein:liquid ratio of 4.4:5.6 (w/w).

Appendix Figure 24: Deconvolution (red, green) using the Matlab plugin peakfit.m of α P-ATP and α P-ADP peaks of a 1D spectrum (blue) from a pseudo 2D ^{31}P real-time NMR spectrum with starting peak positions marked as pink dashed lines and fitting parameters given.

Appendix Figure 25: Normalized peak area of analyzed DMPC (filled) and PUFA (non-filled) peaks (Figure 69, Figure 70a) of DMPC and DMPC + 20 mol% EDP or DHDP with respect to increasing temperature.

VI List of Tables

VI.1 Tables

Table 1: Reported photochemical properties of selected caged compounds. Maxima of single-photon absorption (λ_{\max}), molar absorption coefficients for absorption (ϵ_{exc}), quantum yield of photolysis after excitation (Φ_{chem}) and action uncaging cross section ($\epsilon_{\text{exc}} \cdot \Phi_{\text{chem}}$) at excitation wavelength (λ_{exc}).

Table 2: Composition of thermal cycling mix for site directed mutagenesis.

Table 3: Thermal cycling scheme used for site directed mutagenesis.

Table 4: Composition of PCR mix for restriction free cloning PCRs.

Table 5: PCR cycling scheme used for restriction free cloning.

Table 6: Assignment of NdiEt-tcAA ^1H and ^{13}C chemical shifts in DMSO- d_6 and TCE obtained via HSQC and HMBC spectra referenced to TMS (Appendix Figure 7, Appendix Figure 8). Atom numbers refer to Figure 36a.

Table 7: Summary of success (\checkmark) or failure (\times) to uncage tested caged compounds inside the DNP spectrometer compared to uncaging outside the spectrometer with the same lightsources.

Table 8: Basal ATPase activity of DgkA in different environments. Obtained kinetic parameters in dependence to ATP concentration without a lipid substrate.

Table 9: Kinetic parameters of DgkA's enzymatic activity in LCP and mixed micelles with monoolein as lipid substrate.

Table 10: Utilizing monoolein as membrane mimetic for DNP experiments. Optimization of sample compositions for increased ^{13}C signal enhancement under DNP conditions in cross polarization experiments at 100 K and 8 kHz MAS comparing peak heights of monoolein and glycerol $m_{\text{w on}} / m_{\text{w off}}$ signals.

VI.2 Appendix Tables

Appendix Table 1: ^1H and ^{13}C NMR chemical shift assignment of NPE-ATP in 100 mM HEPES, 30 mM NaCl at pH 7.5 with ^1H chemical shifts and J -couplings of the diastereomer mixture as well as the respective ^{13}C chemical shifts obtained from ^1H , ^{13}C , ^1H - ^{13}C HSQC and ^1H - ^{31}P HMBC spectra according to the atom numbering of Appendix Figure 3. Multiplets are numbered according to Appendix Figure 4, with assignment of absolute stereochemistry according to Corrie et al^[345] in brackets.

Appendix Table 2: ^1H and ^{13}C NMR chemical shift assignment of ATP in 100 mM HEPES, 30 mM NaCl at pH 7.5 with ^1H chemical shifts and J -couplings as well as the respective ^{13}C chemical shifts obtained from ^1H , ^{13}C and ^1H - ^{13}C HSQC spectra according to the atom numbering of Appendix Figure 3.

Appendix Table 3: Percentage and deviation of DOPA signal to lipid signals upon phosphorylation by DgkA of DOPC liposomes prepared with different lipid ratios of DOG from ^{31}P MAS NMR spectra (Figure 49).

Appendix Table 4: Initial rates from ^{31}P real-time MAS NMR experiments determining basal ATPase and stimulated activity in μU as well as factor of stimulation over basal ATPase activity of DgkA reconstituted at different L:P ratios in DOPC liposomes containing 20 mol% NPE-DOG upon addition of 0.45 μmol ATP. Stimulated activity is measured after 5 min illumination to uncage membrane incorporated NPE-DOG.

Appendix Table 5: Published data on DgkA's enzymatic activity. Kinetic parameters, assay conditions, type of assay, sample preparation, type of sample.

VII Declarations

VII.1 Declaration of contributions

Except where stated otherwise by reference or acknowledgment, the work presented was generated by myself under the supervision of my advisors during my doctoral studies. All contributions from colleagues are explicitly referenced in the thesis. The material listed below was obtained in the context of collaborative research:

Section I.3.3.2, Figure 36, Figure 37, Table 6, Appendix Figure 7 and Appendix Figure 8: Dr. Andreas Jakob, Institute for Organic Chemistry and Chemical Biology, provided the used red-shifted coumarin photocage NdiEt-tcAA. I designed, executed and analyzed experiments.

Section I.3.3.3.2, Section I.3.3.3.5 and Figure 43: Dr. Boris Fürtig, Institute for Organic Chemistry and Chemical Biology, Centre for Biomolecular Magnetic Resonance, provided access and training to the used UV laser and thermal power meter. I designed, executed and analyzed experiments.

Section I.3.3.3, Figure 54, Appendix Figure 18 Section I.3.5.1, Figure 55 and Appendix Figure 16: Dr. Andreas Jakob, Institute for Organic Chemistry and Chemical Biology, developed a synthesis route and synthesized the used water-soluble short chain DAG DBG as substrate in the performed experiments. I designed, executed and analyzed shown experiments.

Section I.3.4.2, Figure 50, Figure 51 and Figure 52: Dr. Andreas Jakob, Institute for Organic Chemistry and Chemical Biology, developed a synthesis route and synthesized the used caged DAG NPE-DOG as substrate in the performed illumination experiments. I designed, executed and analyzed experiments.

Section I.3.2.2 and Figure 31: Dr. Boris Fürtig, Institute for Organic Chemistry and Chemical Biology, Centre for Biomolecular Magnetic Resonance, performed ^{31}P DOSY NMR experiments. I prepared the samples and analyzed experiments.

Section I.3.6.3, Figure 66, Figure 67, Figure 68 and Table 10: Sample preparation and optimization as well as DNP measurements were performed in context of an internship by the master student Christian Bonifer. Dr. Johanna Becker-Baldus, Institute for Biophysical Chemistry, Centre for Biomolecular Magnetic Resonance, designed, planned and supervised the DNP measurements and analysis. I designed, planned and supervised sample preparation and optimization and performed the analysis shown in this thesis.

Section I.3.6.3, Figure 67: ^{31}P - ^{13}C TEDOR DNP spectrum of a DMPC/DMPA liposome sample containing non-labelled MsbA courtesy of Hundeeep Kaur, Institute for Biophysical Chemistry, Centre for Biomolecular Magnetic Resonance.

Section II.3.2, Figure 71, Figure 72 and Figure 73: Design of the study and preparation of native membranes from mouse brains was performed by Dr. Jiong Hu, Institute for Vascular Signalling, Centre for Molecular Medicine. I prepared samples for studies on DMPC model membranes, performed NMR measurements and data analysis.

VII.2 Declaration of published data

The following parts of the thesis have been previously published:

Figure 71 and Figure 72a have been published in: Hu, J.; Dziumbala, S.; Lin, J.; Bibli, S. I.; Zukunft, S.; de Mos, J.; Awwad, K.; Fromel, T.; Jungmann, A.; Devraj, K.; Cheng, Z.; Wang, L.; Fauser, S.; Eberhart, C. G.; Sodhi, A.; Hammock, B. D.; Liebner, S.; Muller, O. J.; Glaubitz, C.; Hammes, H. P.; Popp, R.; Fleming, I., Inhibition of soluble epoxide hydrolase prevents diabetic retinopathy. *Nature* **2017**, 552 (7684), 248-252

VII.3 Declaration of figures obtained from published work

The following figures in the introductory part of this thesis have been obtained, are redrawn, adapted or modified from published work in accordance with copyright permissions or granted licenses by the respective copyright holders (licensors):

Figure 1e: Adapted from Figure 1 in Hunger, M.; Wang, W., Formation of cyclic compounds and carbenium ions by conversion of methanol on weakly dealuminated zeolite H-ZSM-5 investigated via a novel in situ CF MAS NMR/UV-Vis technique. *Chem. Commun.* **2004**, (5), 584–585 (Permission granted: Royal Society of Chemistry, Licence number: 4546971473534).

Figure 8: Redrawn from Figure 20 in Seddon, J. M., Structure of the inverted hexagonal (H_{II}) phase, and non-lamellar phase transitions of lipids. *Biochim. Biophys. Acta* **1990**, 1031 (1), 1-69 (Permission granted: Elsevier, Licence number: 4483061019782).

Figure 9 and Figure 11: Adapted from Figure 1 in Koynova, R.; Tenchov, B., Transitions between lamellar and non-lamellar phases in membrane lipids and their physiological roles. *OA Biochemistry* **2013** 1(1), 1-9 in accordance of the copyright of the published version under a Creative Commons Attribution License (CC BY)

Figure 10: Adapted from Figure 1 in Munro, S., Lipid rafts: elusive or illusive? *Cell* **2003**, *115* (4), 377-88 (Permission granted: Elsevier, Licence number: 4481261446551).

Figure 12: Adapted from Figure 1 in Koynova, R.; Tenchov, B., Transitions between lamellar and non-lamellar phases in membrane lipids and their physiological roles. *OA Biochemistry* **2013** *1*(1), 1-9 in accordance of the copyright of the published version under a [Creative Commons Attribution License \(CC BY\)](#) and Figure 2 in de Campo, L.; Castle, T.; Hyde, S. T., Optimal packings of three-arm star polyphiles: from tricontinuous to quasi-uniformly striped bicontinuous forms. *Interface Focus* **2017**, *7* (4) (Permission granted: Royal Society, Licence number: 4485330296384).

Figure 13: Combined from Figure 1 in Koynova, R.; Tenchov, B., Transitions between lamellar and non-lamellar phases in membrane lipids and their physiological roles. *OA Biochemistry* **2013** *1*(1), 1-9 in accordance of the copyright of the published version under a [Creative Commons Attribution License \(CC BY\)](#), Figure 1 in Cherezov, V.; Clogston, J.; Papiz, M. Z.; Caffrey, M., Room to move: crystallizing membrane proteins in swollen lipidic mesophases. *J. Mol. Biol.* **2006**, *357* (5), 1605-18 (Permission granted: Elsevier, Licence number: 4477060646142) and Figure 1 in Strey, R.; Winkler, J.; Magid, L., Small-angle neutron scattering from diffuse interfaces. 1. Mono- and bilayers in the water-octane-pentaoxyethylene monododecyl ether (C12Es) system. *J. Phys. Chem.* **1991**, *95* (19), 7502-7507 (Adapted with permission. Copyright 2018 American Chemical Society).

Figure 14: Adapted from Figure 1 in Kaasgaard, T.; Drummond, C. J., Ordered 2-D and 3-D nanostructured amphiphile self-assembly materials stable in excess solvent. *Phys Chem. Chem. Phys.* **2006**, *8* (43), 4957-4975 (Permission granted: Royal Society of Chemistry, Licence number: 4534230161647), Section II.6.1.1 Figure: 1,2-dioleoyl-sn-glycero-3-phosphocholine 1,2-(18:1c Δ^9)₂PtdCho in Marsh, D., *Handbook of Lipid Bilayers*. 2 ed.; CRC Press: Boca Raton, 2013; p 1174 (Permission granted: Taylor & Francis, Licence number: 4534240269772), Cullis, P. R.; de Kruijff, B.; Hope, M. J.; Verkleij, A. J.; Nayar, R.; Farren, S. B.; Tilcock, C.; Madden, T. D.; Bally, M. B., Structural Properties of Lipids and Their Functional Roles in Biological Membranes. In *Concepts of Membrane Structure*, Aloia, R. C., Ed. Academic Press: 1983; pp 39-81. (Permission granted: Elsevier Science & Technology Books, Licence number: 4534250113128) and Figure S7 of the Supporting Information in Yao, H.; Lee, M. W.; Waring, A. J.; Wong, G. C. L.; Hong, M., Viral fusion protein

transmembrane domain adopts β -strand structure to facilitate membrane topological changes for virus–cell fusion. *Proc. Natl. Acad. Sci. USA* **2015**, *112* (35), 10926-10931 in accordance of the copyright of the published version.

Figure 20: Modified from Figure 2, Figure 5f and Supplementary Figure 6 in Li, D.; Stansfeld, P. J.; Sansom, M. S. P.; Keogh, A.; Vogeley, L.; Howe, N.; Lyons, J. A.; Aragao, D.; Fromme, P.; Fromme, R.; Basu, S.; Grotjohann, I.; Kupitz, C.; Rendek, K.; Weierstall, U.; Zatsepin, N. A.; Cherezov, V.; Liu, W.; Bandaru, S.; English, N. J.; Gati, C.; Barty, A.; Yefanov, O.; Chapman, H. N.; Diederichs, K.; Messerschmidt, M.; Boutet, S.; Williams, G. J.; Marvin Seibert, M.; Caffrey, M., Ternary structure reveals mechanism of a membrane diacylglycerol kinase. *Nat. Commun.* **2015**, *6*, 10140. in accordance of the copyright of the published version under a [Creative Commons Attribution 4.0 International license](https://creativecommons.org/licenses/by/4.0/)

Figure 17: Adapted from Figure 1 Cherezov, V.; Clogston, J.; Papiz, M. Z.; Caffrey, M., Room to move: crystallizing membrane proteins in swollen lipidic mesophases. *J. Mol. Biol.* **2006**, *357* (5), 1605-18 (Permission granted: Elsevier, Licence number: 4477060646142), which had been adapted and modified from Figure 7 in Qiu, H.; Caffrey, M., The phase diagram of the monoolein/water system: metastability and equilibrium aspects. *Biomaterials* **2000**, *21* (3), 223-34 (Permission granted: Elsevier, Licence number: 4477070759887), which in turn had been modified from Figure 1 in Briggs, J.; Chung, H.; Caffrey, M., The Temperature-Composition Phase Diagram and Mesophase Structure Characterization of the Monoolein/Water System. *J. Phys. II* **1996**, *6* (5), 723–751 (Permission granted: EDP Sciences).

VIII List of abbreviations

| Abbreviation | Name |
|-----------------|--|
| AA | Acetic acid |
| aa | Amino acids |
| ABC | ATP-binding cassette |
| ADP | Adenosine diphosphate |
| AMP | Adenosine monophosphate |
| AMP-PCP | β,γ -Methyleneadenosine 5'-triphosphate |
| AMP-PNP | β,γ -Imidoadenosine 5'-triphosphate |
| AP | Alkaline phosphatase |
| Arg | Arginine |
| Asn | Asparagine |
| ATP | Adenosine triphosphate |
| ATPyS | Adenosine 5'-[γ -thio]triphosphate |
| AMUpol | 15-[[[(7-oxyl-3,11-dioxo-7-azadispiro[5.1.5.3]hexadec-15-yl)carbamoyl][2-(2,5,8,11-tetraoxatridecan-13-ylamino))-[3,11-dioxo-7-azadispiro[5.1.5.3]hexadec-7-yl]]oxidanyl |
| BA | Benzoic acid |
| BCIP | 5-Bromo-4-chloro-3'-indolyphosphate |
| Bhcmoc | 6-Bromo-7-hydroxycoumarin-4-ylmethoxycarbonyl |
| Bhcmoc-DioctaG | 3-(6-Bromo-7-hydroxycoumarin-4-ylmethoxycarbonyl)-1,2-dioctanoylglycerol |
| Bhcmoc-Gal | 1,2,3,4-Di-O-isopropylidene-D-galactopyranosyl 6-bromo-7-hydroxycoumarin-4-ylmethoxycarbonate |
| BHT | 2,6-Di- <i>tert</i> -butyl-4-methylphenol |
| bp | Base pair |
| BSA | Bovine serum albumin |
| cAMP | Cyclic adenosine monophosphate |
| CIDNP | Chemically induced dynamic nuclear polarization |
| CMC | Critical micellar concentration |
| CP | Cross polarization |
| CPMG | Carr-Purcell-Meiboom-Gill |
| CSA | Chemical shift anisotropy |
| CYP | Cytochrome P450 |
| DAG | Diacylglycerol |
| DBG | 1,2-Dibutylglycerol |
| DBG-PA | 1,2-Dibutylglycero-3-phosphate |
| DEACM | P^3 -[7-(dimethylamino)coumarin-4-yl]methyl |
| DEACM-ATP | P^3 -[7-(dimethylamino)coumarin-4-yl]methyl adenosine 5'-triphosphate |
| DEACMoc | P^3 -[7-(dimethylamino)coumarin-4-yl] methoxycarbonyl |
| DEACMoc-DioctaG | 3-[7-(dimethylamino)coumarin-4-ylmethoxycarbonyl]-1,2-dioctanoyl glycerol |
| DEACMoc-Gal | 1,2,3,4-Di-O-isopropylidene-D-galactopyranosyl 7-diethylaminocoumarin-4-ylmethoxycarbonate |
| DFT | Density functional theory |
| DGK | Diacylglycerol kinase |
| DgkA | <i>E. coli</i> diacylglycerol kinase |
| <i>dgkA</i> | Gene encoding DgkA |
| DDM | <i>n</i> -Dodecyl β -D-maltoside |
| DHA | Docosahexaenoic acid |
| DHDP | (\pm)19,20-Dihydroxydocosapentaenoic acid |
| DHPC | 1,2-Dihexanoyl- <i>sn</i> -glycero-3-phosphocholine |
| DioctaG | 1,2-Dioctanoyl- <i>sn</i> -glycerol |
| DioctaG-PA | 1,2-Dioctanoyl- <i>sn</i> -glycero-3-phosphate |
| DM | Decyl β -D-maltopyranoside |
| DMACM | P^3 -[7-(Dimethylamino)coumarin-4-yl]methyl |
| DMACM-ATP | P^3 -[7-(Dimethylamino)coumarin-4-yl]methyl adenosine 5'-triphosphate |
| DMF | Dimethylformamide |

| | |
|-----------------|--|
| DMNB | P^3 -(4,5-dimethoxy-2-nitrobenzyl) |
| DMNB-DiOctaG | 3-(4,5-dimethoxy-2-nitrobenzyl)- <i>sn</i> -1,2-dioctanoylglycerol |
| DMNPE | P^3 -[1-(4,5-dimethoxy-2-nitrophenyl)ethyl] |
| DMNPE-ATP | Adenosine 5'-triphosphate, P^3 -[1-(4,5-dimethoxy-2-nitrophenyl)ethyl] ester |
| DMPA | 1,2-Dimyristoyl- <i>sn</i> -glycero-3-phosphate |
| DMPC | 1,2-Dimyristoyl- <i>sn</i> -glycero-3-phosphocholine |
| DMSO | Dimethyl sulfoxide |
| DNP | Dynamic nuclear polarization |
| DOG | 1,2-Dioleoyl- <i>sn</i> -glycerol |
| DOPA | 1,2-Dioleoyl- <i>sn</i> -glycero-3-phosphate |
| DOPC | 1,2-Dioleoyl- <i>sn</i> -glycero-3-phosphocholine |
| DOSY | Diffusion-ordered spectroscopy |
| DRM | Detergent-resistant membrane |
| DSM | Detergent-soluble membrane |
| DSS | 4,4-Dimethyl-4-silapentane-1-sulfonic acid |
| DTT | 1,4-Dithiothreitol |
| EDP | (\pm)19,20-Epoxydocosapentaenoic acid |
| EDTA | Ethylenediaminetetraacetic acid |
| EGTA | Ethylene glycol-bis(β -aminoethyl ether)- N,N,N',N' -tetraacetic acid |
| EmpigenBB | N,N -Dimethyl- N -dodecylglycine betaine |
| <i>Ephx2</i> | Mouse gene encoding soluble epoxide hydrolase (sEH) |
| EtOH | Ethanol |
| FID | Free induction decay |
| FWHM | Full width at half maximum |
| Gal | 1,2,3,4-Di- O -isopropylidene-D-galactopyranose |
| Glu | Glutamate |
| GPI | Glycosylphosphatidylinositol |
| GPMV | Giant plasma membrane vesicle |
| HEPES | 4-(2-Hydroxyethyl)-1-piperazineethanesulfonic acid |
| <i>in meso</i> | Protein of interest reconstituted in a lipidic cubic mesophase |
| <i>in situ</i> | In position; on site |
| <i>in surfo</i> | Protein of interest dispersed in a surfactant solution |
| IPMS | Infinite periodic minimal surface (also TPMS) |
| kB | Kilo base pair |
| K_M | Michaelis constant |
| Kel-F | Polychlorotrifluoroethylene |
| LB | Lysogeny broth |
| LCP | Lipidic cubic phase |
| l_d | Liquid disordered |
| LDH | L-Lactate dehydrogenase |
| INMR | Liquid-state NMR |
| l_o | Liquid ordered |
| Lys | Lysine |
| LPS | Lipopolysaccharide |
| MAG | Monoacylglycerol |
| MAS | Magic-angle-spinning |
| MD | Molecular dynamics |
| MDO | Membrane-derived oligosaccharide |
| MeOH | Methanol |
| MO | Monoolein |
| MOPS | 3-(N -morpholino)propanesulfonic acid |
| mw | Microwave |
| NA | Numerical aperture |
| NADH | Nicotinamide adenine dinucleotide (reduced) |
| NB | P^3 -(2-nitrobenzyl) |
| NBT | Nitro-blue tetrazolium |
| NdiEt-tc | [7-(diethylamino)-2-sulfanylidenechromen-4-yl]methyl |

| | |
|-----------------|--|
| NdiEt-tcAA | [7-(diethylamino)-2-sulfanylidenechromen-4-yl]methyl acetic acid |
| NdiEt-tcBA | [7-(diethylamino)-2-sulfanylidenechromen-4-yl]methyl benzoic acid |
| NMWL | Nominal molecular weight limit |
| NPE | P^3 -(1-(2-nitrophenyl)ethyl) |
| NPE-ATP | Adenosine 5'-triphosphate, P^3 -(1-(2-nitrophenyl)ethyl) ester |
| NPE-DOG | 3-((1-(2-Nitrophenyl)ethoxy)carbonyl)- <i>sn</i> -1,2-dioleoylglycerol |
| OG | Octyl β -D-glucopyranoside |
| PA | Phosphatidic acid |
| PC | Phosphatidylcholine |
| PCR | Polymerase chain reaction |
| PDB | Protein data base |
| PE | Phosphatidylethanolamine |
| PEP | Phosphoenolpyruvate |
| PFG | Pulsed field gradient |
| PFG-SSE | Pulsed field gradient stimulated spin echo |
| PG | Phosphatidylglycerol |
| PGSE | Pulsed field gradient spin echo |
| <i>p</i> HP | <i>p</i> -Hydroxyphenacyl |
| <i>p</i> HP-ATP | 4-Hydroxyphenacyl adenosine 5'-triphosphate |
| Pi | Inorganic phosphate |
| PIPES | 1,4-Piperazinediethanesulfonic acid |
| PK | Pyruvate kinase |
| PTFE | Polytetrafluoroethylene |
| PUFA | Polyunsaturated fatty acid |
| PVDF | Polyvinylidene fluoride |
| RF | Radio frequency |
| RT | Room temperature |
| SDS-PAGE | Sodium dodecyl sulfate polyacrylamide gel electrophoresis |
| SEC | Size exclusion chromatography |
| sEH | Soluble epoxide hydrolase |
| s_o | Solid ordered |
| SSB | Spinning side band |
| ssNMR | Solid-state NMR |
| TBST | Tris-buffered saline with Tween20 |
| TCE | Tetrachloroethene |
| TCEP | Tris(2-carboxyethyl)phosphine |
| TEDOR | Transferred echo double resonance |
| TPMS | Triply periodic minimal surface |
| TRIS | Tris(hydroxymethyl)aminomethane |
| Triton X-100 | <i>t</i> -Octylphenoxypolyethoxyethanol |
| Tween 20 | Polysorbate 20, Polyoxyethylene (20) sorbitan monolaurate |
| U | Unit |
| UDPK | Undecaprenol kinase |
| UV | Ultraviolet |
| WB | Wide bore (refers to a NMR magnet with a bore diameter of 89 mm) |

IX Acknowledgements

I am utmost grateful to all people who supported me during the ups and downs of my my PhD and learned to cope as well.

First, I would like to thank my PhD advisor Prof. Dr. Clemens Glaubitz for the opportunity to work at these projects and giving me the freedom to carry out my research in these fields.

Further, I also want to express my gratitude to my mentoring committee members Jun.-Prof. Dr. Nina Morgner and Dr. Boris Fürtig for their insightful comments, discussions and encouragement in my research. I am especially grateful to Dr. Boris Fürtig for performing liquid-state NMR measurements and his help to use the UV-laser and power meters.

I feel beholden to the current and previous lab members for fruitful discussions as well as light hearted talk and support over the past years. I want to express my gratitude to Dr. Johanna Becker-Baldus for discussion about decisive aspects of the projects, introducing me to Topspin and solid-state NMR as well as NMR maintenance and coordination with Bruker. Manfred Strupf for his dedication in electrical as well as precision mechanic engineering, always giving helpful technical advice, sharing a nearly unlimited stock of tools and materials, but also to repair nearly everything and especially to build the temperature control unit for the FT-IR instrument. Ingrid Weber and Ramona Vogel, for all the organization and maintenance of the wet lab as well as ordering and repairs. Simone Kobylka for her immaculate administrative work. Maria Ferreira Dos Santos for her fearless and relentless contribution to a clean lab and a different, exhilarating perspective towards work.

I would especially like to thank Dr. Hundeeep Kaur, for all the fun discussions we had. Jakob Maciejko for being my silent office neighbor deep into the evenings, knowing a simple solution to many problems. Kristin Möbius for fruitful discussions, help and expertise, whilst sharing the same niche of DgkA related projects. Dr. Jiafei Mao, for creative ideas broadening my scope as well as enjoyable evening discussions about science, its circumstances and the people doing science. Dr. Jagdeep Kaur for being the most kind and supportive person, helping in the wet lab and taking care of machines. Dr. Andrea Lakatos for scrutinizing initial aspects and arguments of the proposed projects and general guidance in the first years. Dr. Roberta Spadaccini for her calm, continuous support and open ear, listening whenever needed. Tobias

Herrmann for his knowledge in Blender and together with Christian Hofmann, David Heidenreich, Dr. Michaela Mehler, Clara Nassrin Kriebel, Julian Reitz, Orawan Jakdetchai, Christian Bonifer, Phoebe Ye and Mahmoud Doroudgar for a good lab atmosphere and many scientific and non-scientific discussions.

I especially want to thank Prof. Dr. Ingrid Fleming and Dr. Jiong Hu for their determination to approach us and explore membrane biophysics on a cellular level in this successful and intriguing inter-disciplinary collaboration.

I also want to thank Dr. Andreas Jakob and Prof. Dr. Alexander Heckel for their collaboration within my graduate program and synthesizing non-commercially available substrates and caged compounds used in the study.

I am very grateful to Dr. Christian Richter as well as Gabriele Sentis for their help with liquid-state measurements in the service and manually measuring them if needed.

I also want to thank my not yet named friends and scientific discussion partners in non-scientific environments, especially Bianca Eisel, Sebastian Renelt, Dr. Sarah-Marie Renelt, Christine Molenda, Dr. Fabian Elgner, Maria Grötzinger, Jakob Gebel, Sascha Marquardt, Selena Đorđević, Dr. Matiss Reinfelds, Julia Brandstetter, Falco Peter, Jessica Huber, Philipp Graab, Christian Osterburg, Linda Schulte and of course György Pintér and László Rácz, for all their support!

Last but not least I want to thank my parents that you have supported me all the way. Thank you.

X Curriculum vitae

Family Name: de Mos
First Names: Julian Martinus
Date of Birth: October 09, 1988
Place of Birth: Darmstadt
Nationality: German



Education

PhD, Biophysical Chemistry **September 2014 – April 2019**

Goethe University Frankfurt, Frankfurt am Main

Supervisor: Prof. Dr. Clemens Glaubitz, Institute for Biophysical Chemistry

Diploma studies in Biochemistry **October 2008 – December 2013**

Diploma in Biochemistry, December 03, 2013 (grade: 1.3)

Goethe University Frankfurt, Frankfurt am Main

Thesis title: Charakterisierung der Proteinstabilität des Endothelin B Rezeptors und seiner Varianten. (Max Planck Society eDoc ID: 674783; in english)

Supervisor – Prof. Dr. Hartmut Michel, Department of Molecular Membrane Biology, Max Planck Institute of Biophysics

Pre-degree in Biochemistry, October 07, 2010 (grade: 1.0)

General University Maturity **June 04, 2008**

Certificate of general university maturity with honours from the German Mathematical Society, Immanuel-Kant-Schule, Rüsselsheim

Publications

Hu, J.; Dziumbala, S.; Lin, J.; Bibli, S. I.; Zukunft, S.; de Mos, J.; Awwad, K.; Fromel, T.; Jungmann, A.; Devraj, K.; Cheng, Z.; Wang, L.; Fauser, S.; Eberhart, C. G.; Sodhi, A.; Hammock, B. D.; Liebner, S.; Muller, O. J.; Glaubitz, C.; Hammes, H. P.; Popp, R.; Fleming, I., Inhibition of soluble epoxide hydrolase prevents diabetic retinopathy. *Nature* **2017**, *552* (7684), 248-252.

Manuscripts in preparation

de Mos, J.; Jakob, A.; Becker-Baldus, J.; Heckel, A.; Glaubitz, C., Initiation of a biochemical reaction by light under magic angle spinning conditions: Uncaging approach for solid-state NMR. (in preparation)

de Mos, J.; Glaubitz, C., Lipidic cubic phase of monoolein for biomolecular solid-state NMR applications: MAS-NMR detection of membrane bound enzyme reactions in lipidic cubic phases. (in preparation)

Conference Contributions

- Poster presentation - CRC 807 International Symposium New Horizons in Membrane Transport and Communication: *Detecting Biochemical Reactions Catalyzed by Integral Membrane Proteins within the Membrane by Time-Resolved MAS-NMR*. Frankfurt, Germany, 04. - 06.10.2017.
- Poster presentation - 39th FGMR Annual Discussion Meeting - Joint Conference of the French and German Magnetic Resonance Societies: *Light Induced Uncaging as a Tool to Study the Enzyme Kinetics of a Membrane Bound Kinase via Real-Time MAS-NMR*. Bayreuth, Germany, 25. - 28.09.2017.
- Poster presentation - Design and Light Control - Joint Conference of CEF and CLiC: *Light Induced Uncaging as a Tool to Study the Enzyme Kinetics of a Membrane Bound Kinase via Real-Time MAS-NMR*, Niedernberg, Germany, 30.08. – 01.09.2017.
- Poster presentation - 9th BMRZ Symposium Magnetic Resonance on Biomolecular Complexes: *Light Induced Uncaging as a Tool to Study the Enzyme Kinetics of a Membrane Bound Kinase via Real-Time MAS-NMR*. Bad Homburg, Germany, 26.06.2017.
- Poster presentation - 27th International Conference on Magnetic Resonance in Biological Systems (ICMRBS): *Light Induced Uncaging as a Tool to Study the Enzyme Kinetics of a Membrane Bound Kinase via Real-Time MAS-NMR*. Kyoto, Japan, 21. - 26.08.2016.
- Talk – Institutskolloquium Institute of Physical and Theoretical Chemistry Goethe University Frankfurt: *Solid-state NMR combined with light: Methods, Applications and Development*. Hirschegg, Austria, 21. - 25.03.2016.

Teaching Experience

- Supervision of a master internship, Goethe University Frankfurt (2018).
- Teaching Assistant: Practical course Biophysical Chemistry I for biochemistry students, Institute for Biophysical Chemistry, Goethe University Frankfurt (2014 - 2018).
- Tutor: Tutorium Biophysical Chemistry I for biochemistry students, Institute for Biophysical Chemistry, Goethe University Frankfurt (2011).

Previous practical work experience

- 2014 3 months, research assistant at the group of Prof. Dr. Clemens Glaubitz
Institute for Biophysical Chemistry, Goethe University Frankfurt
Overhauser DNP-NMR at high fields at ambient temperature.
- 2013 10 months, diploma thesis at the group of Prof. Dr. Hartmut Michel
Max Planck Institute of Biophysics, Frankfurt
Thermostability of the endothelin B receptor and fusion constructs.
- 2012 3-month internship at the group of Prof. Anthony Watts
Department of Biochemistry, University of Oxford
Non-uniform sampling in solid-state NMR.
- 2012 2-month internship at the group of Dr. Grez,
Georg-Speyer-Haus, Frankfurt
*Evaluation of myeloid specific promoters for gene therapy of X-CGD with
alpharetroviral vectors.*
- 2011 2-month internship at the group of Dr. Löbner
Federal institute for vaccines and sera, Paul-Ehrlich-Institute, Langen
Generation of a novel model antigen for S. typhimurium challenge tests.
- 2011 6-week internship at the group of Prof. Dr. Steinhilber
Institute of Pharmaceutical Chemistry, Goethe-University, Frankfurt
*Sirtuine as molecular targets for resveratrol in the therapy of non-alcohol
induced fatty liver diseases (NAFLD) – in vitro analysis on a cell system.*

Qualifications

- GxP-Training, erfolgreiche Teilnahme, Pharmaakademie (24. – 28.09.2018)
- Weiterbildungskurs GMP Basiswissen, Provadis Novia (29. – 30.01.2018)
- Weiterbildungskurs Gentechnikrecht - Sachkundenachweis für Projektleiter
gem. § 15 und 17 GenTSV, DECHEMA (07. – 08.11.2016)
- Eingeschränkte Sachkunde gem. § 5 Abs. 1 Nr. 7 der Chemikalien-Verbots-
Verordnung, Goethe-Universität (09.01.2014)

Otherwise applicable skills (1 day courses)

Literature search, Literature management, Adobe Photoshop, Adobe Illustrator, Excel and Origin, Good Scientific Practice, Self- and Project-management, Project presentations, Scientific writing part I, Scientific writing part II, Scientific writing part III, Presentation skills.